Genesis and alteration of the Kalahari and Postmasburg manganese deposits, Griqualand West, South Africa

by

Jens Gutzmer

THESIS

presented in fullfillment of the requirements for the degree of

PHILOSOPHIAE DOCTOR

in

Geology

UNIVERSITY OF JOHANNESBURG

in the

FACULTY OF SCIENCE

of the

RAND AFRIKAANS UNIVERSITY
JOHANNESBURG

Promoter
Prof. N. J. Beukes

May 1996

Minerals are the basic stuff of the Earth, and their study will always remain at the core of the Earth Sciences.

The message is simple: If you can't recognize minerals, you won't find mines!

Frank C. Hawthorne
Canadian Mineralogist (1993), Vol. 31, pp. 253-296

UNIVERSITY OF JOHANNESBURG

Table of Contents

Acknowledgements ..... **i**
Uittreksel ..... **iii**
Abstract ..... **vii**
Kurzfassung ..... **xi**

Chapter 1: Introduction

General 1
Previous Work 4
Postmasburg manganese field 4
Kalahari manganese field 6
Objective and outline of this thesis 9
Geological Setting 12
General 12
Geological Setting of the Kalahari manganese field 18
Geological Setting of the Postmasburg manganese field 20
References 26

Chapter 2: Metasomatic and supergene alteration of Early Proterozoic sedimentary manganese ore at Mamatwan Mine, Kalahari manganese field, South Africa.

Abstract 33
Introduction 33
Geological Setting 35
Analytical Techniques 38
Lateral macroscopic zonation in ore composition 39
Alteration along faults 39
Alteration along joints and veins 43
Lateral mineralogical variation 44
Alteration along faults 44
Alteration along veins and joints 47

UNIVERSITY JOHANNESBURG

Petrographic zonation and paragenetic relationships 49
Alteration along faults 49
Alteration around veins and joints 54
Mineral chemistry 54
Geochemistry 58
Stable isotope geochemistry 64
Discussion 67
Conclusions 72
Acknowledgements 72
References 73

Chapter 3: Minerogenesis of the Kalahari manganese field, South Africa

Abstract 75
Introduction 76
Previous mineralogical work 78
Geological setting 79
Paragenesis of the chemosedimentary braunite-lutite mineral association 84
Late diagenetic/ lower greenschist facies metamorphic mineral association 84
The Wessels event of hydrothermal alteration 86
Sugilite calc-silicate association 89
Hausmannite-rich association (Wessels-type ore) 91
Vein and vug-hosted association 96
The Mamatwan event of hydrothermal alteration 98
The Smartt event of hydrothermal alteration 102
Supergene weathering along the Kalahari unconformity 104
Discussion 105
Conclusions 107
Acknowledgements 108
References 108
Appendix 1: Minerals of the Kalahari manganese field 112

Chapter 4: Effects of mass transfer, compaction and secondary porosity on hydrothermal upgrading of Paleoproterozoic sedimentary manganese ore in the Kalahari manganese field, South Africa

Abstract 117
Introduction 117
Geology 120
Sampling and analytical methods 126
Quantitative mineralogical composition and density of manganese ores 127
Geochemistry 134
Estimating compaction amd secondary porosity 135
Mass balance calculations 140
Method 140
Ferruginous style of alteration 142
Siliceous style of alteration 143
Conclusions 144
Acknowledgements 146
References 147

UNIVERSITY OF JOHANNESBURG

Chapter 5: Tropical terrestrial weathering and vegetation in the Paleoproterozoic: Evidence from a pisolithic paleolaterite from South Africa

Abstract 149
Introduction 149
Description of the paleolaterite profile 151
Conclusions 155
References 157

Chapter 6: Petrography and geochemistry of the karst-hosted manganese deposits in the Postmasburg manganese field, Northern Cape Province, South Africa

Abstract 159
Introduction 160
Analytical techniques 162
Regional geological setting 165

Detailed geological setting 168
Eastern Belt 168
Western Belt 170
Mineralogy and petrography 177
Siliceous manganese ores 177
Fine crystalline bedded ferruginous manganese ores 181
Coarse crystalline ferruginous manganese ores 184
Supergene ores 185
Shales 186
Conglomerates 186
Geochemistry 187
Siliceous ores and Wolhaarkop breccia of the Eastern Belt 187
Ferruginous ores of the Western Belt 188
Supergene ores 191
Dolomite of the Reivilo Formation and wad 192
Geochemical associations 195
Depositional environment and evolution of the manganese ore deposits 195
Wolhaarkop breccia and siliceous manganese ore 195
Ferruginous manganese ore 198
Metamorphism 203
Conclusions 205
Acknowledgements 205
References 206

Chapter 7: Mineralogy and mineral chemistry of the manganese ores of the Postmasburg manganese field, Northern Cape Province, South Africa

Abstract 209
Introduction 209
Analytical techniques 213
Geological setting 214
Petrography of siliceous ores of the Eastern Belt 222
Petrography of ferruginous ores of the Western Belt 224
Petrography of supergene ores 226
Mineral chemistry 226
Braunite 226
Bixbyite 231
Hausmannite 234

UNIVERSITY OF JOHANNESBURG

Manganomelane group of minerals and pyrolusite 236
Gamagarite, apatite and barite 238
Diaspore and silicate minerals 240
Discussion 241
The braunite group 241
Other minerals 244
Metamorphism 245
Supergene alteration 247
Conclusions 247
Acknowledgements 248
References 248

Chapter 8: Conclusions

Genesis and alteration of manganese ores in the Kalahari manganese field 253
Genesis and alteration of manganese ores of the Postmasburg manganese field . 258
Two manganese fields - one story ? 261
Suggestions for future work 263
References 264

UNIVERSITY OF JOHANNESBURG

Appendix I: Analytical techniques

I.1 Sample preparation A1
I.2 Analytical Chemistry A1
I.2.1 X-ray fluorescence spectrometry A2
I.2.2 Inductively coupled - atomic emission spectrometry (ICP-AES) ... A4
I.2.3 Atomic absorption spectrometry (AAS) A8
I.2.4 Inductively coupled plasma - mass spectrometry (ICP-MS) A8
I.2.5 Titrimetric $Fe_{(total)}$ determination A10
I.2.6 CO_2 (total) determination by coulometric titration A10
I.2.7 H_2O^- determination by drying A11
I.2.8 Loss on ignition determination (L.O.I.) A12
I.2.9 Electron microprobe analysis (EMPA) A13
I.3 Stable ($\delta^{13}C$, $\delta^{18}O$, $\delta^{34}S$) and radiogenic ($^{87}Sr/^{86}Sr$) isotope analysis A16
I.4 Density measurement A16
I.5 X-ray powder diffraction analysis (XRD) A19

I.6 Petrography and ore petrography A20
I.7 Fluid inclusion studies A21
I.8 References A22

Appendix II: Sample Descriptions

General A25
II.1 Samples from the Postmasburg manganese field A26
II.2 Samples from the Kalahari manganese field A38

Appendix III: Whole rock geochemical data

General A41
III.1 Major and trace element geochemistry of manganese ores A42
III.2 Geochemistry of host-rocks of Mn-ores A62
III.3 Trace element and REE geochemistry of Mn-ores, KMF (ICP-MS) A64

UNIVERSITY OF JOHANNESBURG

Appendix IV: Phase chemistry

General A69
IV.1 Lower oxides of manganese A70
IV.2 Higher oxides of manganese A75
IV.3 Silicates A76
IV.4 Carbonates A81
IV.5 Hydroxides, sulphates, phosphates, and vanadates A83
IV.6 Minerals associated with bostonite dykes, KMF A85
IV.7.1 Igneous phases A85
IV.7.2 Alteration phases A86

Appendix V: Stable isotope data

Stable isotope data A89

Appendix VI: Fluid inclusion data

Fluid inclusion data A97

Appendix VII: Fault-controlled metasomatic alteration of Early Proterozoic sedimentary manganese ores in the Kalahari manganese field, South Africa.

Abstract A113
Introduction A114
Regional geology A115
Distribution of major ore types and zones of ferruginization A118
Sampling A122
Mineralogical variations A125
Petrographical variations A127
Western side of Traverse S A127
Eastern side of Traverse S A131
Traverse 28S-E A132
Traverse 43S-E A133
Mineral chemistry A135
Whole rock geochemistry A141
Discussion A143
Mineral paragenetic model A143
Conceptual hydrothermal model A146
Conclusions A150
Acknowledgements A151
References A151

UNIVERSITY OF JOHANNESBURG

Appendix VIII: Fault controlled hydrothermal alteration of Paleoproterozoic manganese ore in Wessels mine, Kalahari manganese field.

Abstract A153
Introduction A154
Regional geological setting A156
Detailed geological setting A159
Definition of ore types and lateral zonation along sections A164

Lateral mineralogical variations A167
Lateral petrographic zonation and paragenetic relationships A169
Chemical composition of selected minerals A175
Whole rock geochemistry A179
Integrated model of lateral zonation in ores A182
Conceptual genetic model A185
Conclusions A189
Acknowledgements A190
References A191

Appendix IX: Magnetic hausmannite from hydrothermally altered manganese ore in the Palaeoproterozoic Kalahari manganese deposit, Transvaal Supergroup, South Africa.

Abstract A193
Introduction A193
Geological setting A195
Petrography and sample preparation A196
Mineral chemistry A200
Crystallography A201
Magnetic mineralogy A203
Discussion A204
Conclusions A209
Acknowledgements A209
References A210

UNIVERSITY OF JOHANNESBURG

Acknowledgements

There are many people and organizations to acknowledge for contributing in different ways and means to this thesis.

I am especially indebted to my supervisor Prof. N.J. Beukes, not only for his continuous interest in this project and his great support throughout, but also for supplying me with the chance of coming to South Africa and conducting research at the Rand Afrikaans University under most favourable conditions.

I am also grateful to my parents and my brothers, without whom my stay in South Africa would not be possible. Many thanks also to my girlfriend Quirina for her unfailing support and scientific expertise.

My sincerest thanks to Dr. L. von Bezing (Kimberley) for his great interest in the minerals of the manganese deposits of then Northern Cape, and his thorough, scientific approach while collecting them. I profited many times from his expertise and his willingness to share it with me.

The geological staff of SAMANCOR (Hotazel), ASSMANG (Black Rock and Beeshoek), and RTZ (Posmasburg) provided me with the possibility to take samples at various occasions from drill core as well as from their mines. Special thanks to the following persons:

Don McIyver and Pamela Naidoo from Wessels Mine for their tremendous support and interest during my stay at Hotazel, but also N. Bleeker (Mamatwan Mine, Hotazel), R. Arnold (Hotazel), and A. Pretorius (Black Rock/ Nchwaning II) for their kind help while sampling.

W. Grobbelaar (Beeshoek) for several idea-generating discussions about the manganese deposits of the Northern Cape during my stay in Beeshoek.

The exploration staff of RTZ (then Postmasburg) for showing me around on Aucampsrust, but also for their hospitality during my stay in Postmasburg in June, 1993.

Numerous persons and institutions helped generously by providing facilities and funds for chemical analyses and isotope analyses. I wish to express my sincerest appreciation to the following persons and institutions:

MINTEK supplied considerable support to this project. I want to thank particulary Arno

Kleyenstüber (Mineralogy and Process Chemistry Division) for many friendly and constructive discussions and his support throughout the project. Thanks also to Dr. J.P.R. De Villiers, head of the Mineralogy and Process Chemistry Division, and C. Pohland-Watson, head of the Analytical Chemistry Division, for their willingness to support this project.

The staff at the Institut für Mineralogie und mineralische Rohstoffe (TU Clausthal), for allowing me to use their excellent equipment for chemical analyses free of charge. My sincerest thanks to the Abteilung Salzlagerstätten und Untergrunddeponien, especially Prof.em. A.G. Herrmann, M. Siemann, K. Herrmann (XRF), Dr. B.Knipping and Dr. A. Stascheit (ICP). Prof. B. Lehmann, A.Kausche and Dr. E. Gierth (all Abteilung für Lagerstättenforschung), Prof. G. Müller, Dr. K. Strauß, Dr. A.K. Schuster and Dr. B. Prause are acknowledged for their kindness and hospitality during my two stays in Clausthal.

V. Ritz and the staff at the Studiengesellschaft für Eisnerzaufbereitung (Othfresen) for showing me how to analyse iron and manganese ores.

Prof. Hsueh-Wen Yeh at the Academia Sinica, Taipeh, for his introduction into the secrets of stable isotope geochemistry. Dr. H. Strauß at the Ruhruniversität Bochum and S. Talma at the CSIR (Pretoria) for numerous isotope analyses.

Herman van Niekerk for translating the abstract to this thesis into Afrikaans and Andreas Pack (Bonn), Vernie Naidoo (RAU) and Wilna for sharing their knowledge on black and white photography with me.

Calvin and Hobbes for giving some deep insights into the realities of life (and how to avoid them).

I want to express my sincerest appreciation to the staff of the Department of Geology, RAU, for their invaluable help. Hennie Jonker, who made the impossible possible; Dr. B. Cairncross for his interest in mineralogy and his neverending supply with interesting samples; Dr. J.M. Huizenga, for seeding a fancy for fluid inclusions (and for working on Sundays); and M. Baloyi, H. Leteani, and D. Selepe for suffering during the preparation of my samples.

Last but by no means least I want to thank Dr. Stephanie Cronje, Herman Van Niekerk, Solly Theron, Abhen Pather, Meiring Burger, Katherine Thompson and Tzoo Mokgatlha for easing the (at times) hard life of a student by sharing it with me.

UNIVERSITY OF JOHANNESBURG

UITTREKSEL

Die ekonomies belangrike sedimentêre mangaanafsettings van die Paleoproterosoïese Kalahari en Postmasburg mangaanvelde is geografies baie naby aan mekaar geleë in die Griekeland Wesgebied van die Noordelike Kaapprovinsie, Suid-Afrika. Die proefskrif beskryf aspekte van mineralogie, petrografie en geochemie van die mangaanerts met die doel om genetiese modelle vir die onstaan en alterasie van die twee mangaanvelde daar te stel.

Die Kalahari mangaanveld, sowat 60km noord-wes van Kuruman geleë, is die grootste bekende binnelandse mangaanafsetting ter wêreld. Die mangaanerts kom tussengelaag voor met ysterformasies van die Hotazel Formasie van die Voëlwater Subgroep van die Laat Argeïese-Paleoproterosoïse Transvaal Supergroep. Die sedimentere gesteentes van die Voëlwater Subgroep is bewaar in vyf erosierelikte, waarvan die Kalahari mangaanafsettings by verre die grootste is. Dit is ook die enigste wat van ekonomiese belang is. Twee tipes erts word gemyn, laegraadse sedimentêre Mamatwan-tipe erts en hoëgraadse Wessels-tipe erts. Mamatwan-tipe erts word verteenwoordig deur mikrokristallyne gelamineerde brauniet-lutiet opgebou uit kutnahoriet, Mn-kalsiet, brauniet en hematiet wat verander is deur die voorkoms van laat diagenetiese of metamorfe hausmanniet, partridgeïet, manganiet en kalsiet. Mamatwan-tipe erts bevat tot 38 massa % Mn en verteenwoordig ongeveer 97% van die ertsreserwes in die Kalahari mangaanafsetting.

Hidrotermaal-veranderde hoëgraadse Wessels-tipe erts met 'n gemiddelde mangaaninhoud van tussen 42 en 48 massa % Mn , verteenwoordig ongeveer 3% van die ertsreserwes. Dit kom slegs voor in die noordwestelike gedeelte van die hoof Kalahari afsetting en as klein afsettings by Hotazel en Langdon in assosiasie met 'n stelsel van noord-suid strekkende normale verskuiwings. Daar word vermoed dat die Wessels-hidrotermale gebeurtenis verband hou met die Kibaran orogenese wat ongeveer 1.1 Ga gelede plaasgevind het. Verskuiwingsones is veryster en langs die verskuiwings is sedimentêre Mamatwan-tipe erts hidrotermaal opgradeer na Wessels-tipe erts. Metasomatiese sonering is ontwikkel as spesifieke mineraalassosiasies langs die verskuiwings. Gebiede van onveranderde Mamatwan-tipe erts is bewaar in die kerne van die verskuiwingsblokke. Wessels-tipe erts bestaan hoofsaaklik uit hausmanniet, bixbyiet, brauniet II en manganiet en ondergeskikte minerale soos klinochloor en andradiet. Die mineraalversameling wat tydens die Wessels hidrotermale proses gevorm het, is besonder divers. Meer as 100 minerale is geïdentifiseer waaronder agt nuwe minerale en 'n ongewone ferrimagnetiese ysterryke variëteit van hausmanniet tel.

UNIVERSITY OF JOHANNESBURG

Massabalans berekeninge wys dat die opgradering van die Wessels-tipe mangaanerts die resultaat is van die uitloging van CaO, MgO, CO_2 en SiO_2 vanaf 'n laegraadse Mamatwan-tipe voorganger. Die metasomatiese proses het 'n verhoging in sekondêre porositeit, kompaktering van die ertsliggaam tot twee derdes van die oorspronklike dikte, en gevolglik residuële verryking van mangaan in die erts veroorsaak.

Drie jonger alterasie gebeurtenisse is aanwesig in die Kalahari mangaanafsetting. Hulle is egter van weinig ekonomiese belang. Wandgesteente alterasie geassosieer met die Mamatwan alterasie gebeurtenis word gekenmerk deur reduksieloging van Fe en Mn rondom sintektoniese are en nate met piriet-chalkopiriet-karbonaat mineralisasie. Die alterasie word verklaar deur infiltrasie van epitermale oplossings wat ingevoer is langs die are of nate. Die alterasie gebeurtenis is voorlopig in die voor-Karoo tot na-Kibaran tydperk geplaas. Die Smartt alterasie gebeurtenis is geassosieer met verskuiwings en geassosieerde breksies. Dit word gekenmerk deur die vervanging van brauniet en karbonaat van Mamatwan-tipe erts deur todorokiet en mangaanomelaan. Dit is 'n proses wat redelike opgradering in kwaliteit van die mangaanerts veroorsaak by die Mamatwan-myn. Dit is ook verantwoordelik vir die vorming van todorokiet by die Smartt-myn. Die Smartt alterasie gebeurtenis het na die Mamatwan alterasie gebeurtenis plaasgevind en is tentitatief gekorreleer met pre-Kalahari grondwatersirkulasie. Supergene alterasie van die erts het plaasgevind tydens en na afsetting van die Kalaharisedimente. Die supergene alterasie word gekenmerk deur die voorkoms van kriptomalaan en pirolusiet langs die subdagsoom van die Hotazel Formasie onder die Senosoïese Kalahari Formasie.

Die Postmasburg mangaanveld is sowat 120km suid van die Kalahari mangaanveld op die Maremane koepel geleë. Twee boogvormige gordels van afsettings strek vanaf Postmasburg in die suide tot by Sishen in die noorde. Twee hooftipes erts is aanwesig. Ysterryke tipe erts bestaan hoofsaaklik uit brauniet, partridgeïet en bixbyiet en kom voor in die middelste deel van die Gamagararand of Westelike gordel. Die silikaryke tipe erts bestaan uit brauniet, kwarts en klein hoeveelhede partridgeïet en kom voor in klein afsettings lang die Klipfonteinheuwels of Oostelike gordel en die noordelike en suidelike dele van die Gamagararand.

Geologiese en geochemiese getuienis dui aan dat die mangaanerts afkomstig is van ouer mangaanaarde afsettings wat in karstdepressies, tydens die laat Paleoproterosoïkum op die Maremanekoepel versamel het, en daarna gemetamorfiseer is. Afsetting van die mangaanaarde het

blykbaar plaasgevind onder landelike toestande in 'n lateritiese omgewing. Die dolomiete van die Campbellrand Groep van die Transvaal Supergroep vorm die gasheer en die bron vir die mangaanafsettings. Kontrasterende geologiese omgewings word voorgestel vir die ontstaan van die silikaryke en die ysterryke tipes erts. Eersgenoemde het ontstaan in assosiasie met chertoplossingsbreksies in oergrotsisteme wat onder 'n dak van Kurumanysterformasies ontwikkel het. Daarteenoor het die ysterryke tipe erts versamel as 'n gemengde mangaanaarde-kleiryke sediment in oppervlakkige sinkholtes op 'n oer karstoppervlak. Die ysterryke tipe ertsliggame word konkordant oorlê deur die Doornfontein hematietrolsteen konglomeraat of alluminiumryke skalies wat behoort tot die Gamagara Formasie van die laat Paleoprotesoïse Olifantshoek Groep. Goedbewaarde laterietiese karst paleogrondprofiele, in die basale deel van die Gamagara Formasie, dui op die landelike oorsprong van die afsettings. Na afsetting is die mangaanerts van die Postmasburg mangaanveld geaffekteer deur diagenese en laer groenskisfasies metamorfose. Metamorfose veroorsaak herkristalisasie tot brauniet in die silikaryke erts van die Oostelike gordel. In die westelike gordel lei metamorfose tot die ontstaan van masiewe of mosaïek-tekstuur brauniet en idioblastiese partridgeïet. Sekondêre karstifikasie en supergene verwering is getuienis vir onlangse hernude atmosferiese blootstelling van die mangaanerts en hulle gasheer gesteentes. In hierdie resente supergene omgewing is die metamorfe mineraalversameling vervang deur romanechiet en lithiophoriet.

Vergelykings tussen die Kalahari en Postmasburg mangaanvelde dui daarop dat die mangaan onder totaal verskillende toestande gevorm het. Ooreenkomste is die gevolg van regionale geologiese gebeurtenisse wat die gebied beïnvloed het nadat die afsetting van die erts plaasgevind het. Ooreenkomste sluit in laer groenskis fasies metamorfose, 'n gebeurtenis wat verband hou met stootverskuiwings en korsverdikking gedurende die Kheis orogenese, en sin- tot na-Kalahari supergene alterasie. 'n Moontlike korrelasie tussen hidrotermale gebeurtenisse in die Kalahari en Postmasburg mangaanvelde bly onseker weens 'n tekort aan kwantitatiewe radiometriese ouderdomsbepalings op mineraalversamelings van die verskillende gebeurtenisse.

UNIVERSITY OF JOHANNESBURG

ABSTRACT

The economically important sedimentary manganese deposits of the Paleoproterozoic Kalahari and Postmasburg manganese fields, are situated in close geographic vicinity to each other in the Griqualand West region of the Northern Cape Province, South Africa. This thesis describes aspects of mineralogy, petrography and geochemistry of the manganese ores with the purpose to establish genetic models for genesis and alteration of manganese ores of both manganese fields.

The Kalahari manganese field, situated some 60 km northwest of Kuruman, is the largest known land-based manganese deposit. Manganese ores occur interbedded with iron-formations of the Hotazel Formation of the Vöelwater Subgroup of the Late Archean-Paleoproterozoic Transvaal Supergroup. The sediments of the Vöelwater Subgroup are preserved in five erosional relics, of which the Kalahari manganese deposit is by far the largest and the only one of economic importance. Two types of ore are mined, low-grade sedimentary Mamatwan-type ore and high-grade Wessels-type ore. Mamatwan-type ore is represented by microcrystalline laminated braunite-lutite composed of kutnahorite, Mn-calcite, braunite and hematite, modified by the occurrence of late diagenetic or metamorphic hausmannite, partridgeite, manganite and calcite. Mamatwan-type ore contains up to 38 mass % Mn and constitutes about 97 % of the ore reserves in the Kalahari manganese deposit.

High-grade Wessels-type ore, with a manganese content of between 42 to 48 mass % Mn (on average), constitutes about 3 % of the ore reserves. It occurs only in the northwestern part of the main Kalahari deposit, and in small deposits at Hotazel and Langdon, in association with a system of north-south striking normal faults. The Wessels alteration event is thought to be related to the Kibaran orogenetic event (about 1.1 Ga). Fault zones are ferruginized and alongside faults sedimentary Mamatwan-type ore has been hydrothermally upgraded to Wessels-type ore. Metasomatic fronts are defined by changing mineral associations. These associations clearly illustrate that decreasing degrees of alteration relate to increasing distance from the fluid feeders. Areas of unaltered Mamatwan-type ore are preserved in the core of fault blocks. Wessels-type ore consists mostly of hausmannite, bixbyite, braunite II and manganite and subordinate gangue minerals such as clinochlore and andradite but the mineral assemblage associated with the Wessels alteration event is unusually diverse. More than 100 minerals have been identified, amongst them 8 new mineral species and an unusual, ferrimagnetic, Fe-rich variety of hausmannite.

Mass balance calculations illustrate that the upgrading of the Wessels-type manganese ore is a consequence of leaching of CaO, MgO, CO_2, and SiO_2 from a low-grade Mamatwan-type precursor.

UNIVERSITY OF JOHANNESBURG

This metasomatic process results in increasing secondary porosities, compaction of the orebody to two thirds of its original thickness and consequently residual enrichment of manganese in the ores.

Three younger alteration events are observed in the Kalahari manganese deposit. These are only of minor economic importance. Wallrock alteration associated with the Mamatwan alteration event is characterized by reductive leaching of Fe and Mn around syntectonic veins and joints with pyrite-chalcopyrite-carbonate mineralization. The alteration is explained by infiltration of epithermal solutions that were introduced along veins or joints. The timing of the alteration event has tentatively been placed into the Pre-Karoo era. The Smartt alteration event is associated with intensive fault-hosted brecciation and replacement of braunite and carbonates of the Mamatwan-type ore by todorokite and manganomelane, a process that causes considerable upgrading of the manganese ore next to a fault breccia at Mamatwan mine, and the formation of stratiform cross-fibre todorokite veins at Smartt mine. The Smartt alteration event postdates the Mamatwan alteration event and has tentatively been correlated with Pre-Kalahari groundwater circulation. Supergene alteration of the ores took place in Kalahari and Post-Kalahari times. It is characterized by the occurrence of cryptomelane, pyrolusite and other typically supergene manganese oxides along the suboutcrop of the Hotazel Formation beneath the Cenozoic Kalahari Formation.

UNIVERSITY OF JOHANNESBURG

The Postmasburg manganese field is situated about 120 km to the south of the Kalahari manganese field on the Maremane dome. Two arcuate belts of deposits extend from Postmasburg in the south to Sishen in the north. Two major ore types are present. The ferruginous type of ore is composed mainly of braunite, partridgeite and bixbyite and occurs along the centre of the Gamagara Ridge, or Western belt. The siliceous type of ore consists of braunite, quartz and minor partridgeite and occurs in small deposits along the Klipfontein Hills (or Eastern belt) and the northern and southern extremities of the Gamagara Ridge.

Geological and geochemical evidence suggest that the manganese ores represent weakly metamorphosed wad deposits that accumulated in karst depressions during a period of lateritic weathering and karstification in a supergene, terrestrial environment during the Late Paleoproterozoic. The dolomites of the Campbellrand Group of the Transvaal Supergroup are host and source for the wad accumulations. Contrasting geological settings are suggested for the accumulation of the siliceous and the ferruginous types of ore respectively. The former originated as small pods and lenses of wad in chert breccia that accumulated in a karst cave system capped by

the hematitized Manganore iron-formation of the Transvaal Supergroup. The cave system finally collapsed and the hematitized iron-formation slumped into the sinkhole structures.

The ferruginous type of ore accumulated as mixed wad-clay sediment trapped in surficial sinkhole depressions in the paleokarst surface. The orebodies are conformably overlain by the Doornfontein hematite pebble conglomerate or aluminous shales belonging to the Gamagara Formation of the Late Paleoproterozoic Olifantshoek Group. Well preserved karst laterite paleosol profiles, described from the basal section of the Gamagara Formation, provide a strong argument for the terrestrial, supergene origin of the manganese ores. The manganese ores in the Postmasburg manganese field were affected by diagenesis and lower greenschist facies metamorphism. Metamorphism resulted in recrystallization to braunite in the siliceous ores of the Eastern belt, and to massive or mosaic textured braunite and idioblastic partridgeite in the ferruginous environment of the Western belt. Secondary karstification and supergene weathering are evidence for renewed subaerial exposure of the manganese ore and their host rocks. The metamorphic mineral assemblage is replaced by abundant romanechite, lithiophorite and other supergene manganese oxides.

Comparison between the Kalahari- and the Postmasburg manganese field shows that sedimentary manganese accumulation took place in entirely different depositional environments and owing to different mechanisms. Their close geographic relationship appears to be coincidental. Apparent similarities arise as a consequence of regional geological events that postdate the deposition of the manganese ores. These similarities include the lower greenschist facies metamorphic overprint, an event tentatively related to thrusting and crustal thickening during the Kheis orogenetic event, and syn- to Post-Kalahari supergene alteration. The correlation of structurally controlled hydrothermal alteration events in the Kalahari manganese field and the Postmasburg manganese field remains difficult due to the absence of the necessary geochronological constraints.

UNIVERSITY OF JOHANNESBURG

KURZFASSUNG

Die bergwirtschaftlich wichtigen frühproterozoischen, sedimentären Manganlagerstätten des Kalahari Manganerzfeldes und des Postmasburg Manganerzfeldes finden sich eng benachbart in der Griqualand West Region der nördlichen Kapprovinz Südafrikas. Die folgende Dissertation widmet sich der Mineralogie, Petrographie und Geochemie der Manganerze. Ziel der Arbeit ist die Entwicklung von Modellen für die Genese und Alteration der Lagerstätten beider Manganerzfelder.

Das Kalahari Manganerzfeld befindet sich 60 km nordwestlich von Kuruman und ist mit 13.5 Milliarden Tonnen bekannter Erzreserven (> 20 % Mn) die weltweit größte bekannte Manganerzlagerstätte. Drei flözartige Manganerzkörper sind eingeschaltet in die gebänderte Eisenformation der frühproterozoischen Hotazel Formation (2.2-2.3 Ga) der Vöelwater Gruppe der Transvaal Hauptgruppe. Von den fünf Erosionsrelikten der Vöelwater Gruppe ist das Kalahari Feld das bei weitem größte und bergwirtschaftlich einzig wichtige. Abgebaut werden carbonatreiche Mamatwan-Typ Erze (ca. 97 % der Reserven bei durchschnittlich 38 % Mn) und oxidische Wessels-Typ Reicherze (3 % der Reserven bei > 42 % Mn). Die Erze des Mamatwan-Typs sind feinkristalline, sedimentär feingeschichtete Braunit-Lutite, die sich aus Kutnahorit, Mn-Calcit, Braunit und Hämatit zusammensetzen. Lokal werden diese Mineralien von spätdiagentisch oder metamorph gebildetem Hausmannit, Partridgeit, Manganit und Calcit verdrängt.

Reicherze des Wessels-Typs sind dagegen im allgemeinen grobkristallin, massig, carbonatarm und ausgezeichnet durch ihre ungewöhnlich variable Mineralparagenese, die durch Hausmannit, Bixbyit, Braunit II, Manganit, sowie den Gangarten Clinochlor und Andradit angeführt wird. Mehr als 100 Mineralien wurden bisher identifiziert, darunter acht neue Mineralien und eine Fe-reiche, ferrimagnetische Varietät von Hausmannit. Die Reicherze finden sich ausschließlich im bruchtektonisch gestörten nordwestlichen Teil des Kalahari Feldes und in kleineren Vorkommen bei Hotazel und Langdon. Systematische Veränderungen der mineralogischen und chemischen Zusammensetzung der Wessels-Typ Erze sind Beleg für die hydrothermal-metasomatische Alteration von Mamatwan-Typ Erzen zu Wessels-Typ Erzen. Der Alterationsprozeß wurde gesteuert durch die Infiltration von hydrothermalen Lösungen entlang von Nord-Süd streichenden Störungszonen während der proterozoischen Kibaran Orogenese (1.1 Ga).

Mit Hilfe von Massenbilanzrechnungen kann nachgewiesen werden, daß die Reicherze als Produkt der residuellen Anreicherung von Mangan aus Mamatwan-Typ Erzen entstanden. Im Zuge dieses

UNIVERSITY JOHANNESBURG

Prozesses wurden Ca, Mg, CO_2 und SiO_2 gelaugt und der Erzkörper um ca. ein Drittel seiner ursprünglichen Mächtigkeit kompaktiert.

Der Wessels Alteration folgen drei weitere Alterationsprozesse, die allerdings nur bedingt von wirtschaftlicher Bedeutung sind. Syntektonische Pyrit-Chalkopyrit-Carbonat Gänge und reduktive epithermale Laugung von Mangan und Eisen aus dem die Gänge umgebenden Manganerz kennzeichnen den Mamatwan Alterationsprozeß. Dieser Alterationsprozeß hat vermutlich ein spätproterozoisches oder frühpaleozoisches Alter. Hydrothermale Breccierung und oxidierende Nebengesteinsalteration charakterisieren den Smartt Alterationsprozeß, dem ein spätmesozoisches Alter zugeordnet wird. Die Verdrängung von Braunit und Mn-Carbonaten durch Todorokit und Manganomelan während des Smartt Alterationsprozesses deutet auf die Infiltration sauerstoffreicher, niedrigthermaler Lösungen hin. Rezente supergene Alteration der Manganerze zu Pyrolusit und Cryptomelan folgt dem Ausbiß der Hotazel Formation.

Das Postmasburg Manganerzfeld findet sich südlich des Kalahari Manganerzfeldes auf der epirogenetischen Maremane Aufwölbung. Die Manganlagerstätten definieren zwei bogenförmige Gürtel, die sich von Postmasburg im Süden bis nach Sishen im Norden hinziehen. Geologie, Petrographie und Geochemie der Manganerze belegen ihre Herkunft als schwach metamorph überprägte Karstmanganerze. Residueller Wad bildete sich als Produkt der Verkarstung Fe-Mn reicher Dolomite der Campbell Gruppe der Transvaal Hauptgruppe vor der Ablagerung der frühproterozoischen Sedimente der Gamagara Formation der Olifantshoek Gruppe (2.0-2.2 Ga).

Fe-reiche und SiO_2-reiche Manganerze werden unterschieden. Erze des Fe-reichen Typs, die aus Braunit, Partridgeit, Bixbyit, Diaspor, Ephesit und Amesit bestehen, finden sich nur im Zentralteil des westlichen Lagerstättengürtels entlang des Gamagara Höhenzuges. SiO_2-reiche Erze dagegen bestehen aus Braunit, Quarz und wenig Partridgeit und finden sich in kleinen taschen- oder linsenförmigen Erzkörpern in der Wolhaarkop Chert Breccie im östlichen Lagerstättengürtel, der sich aus einer Kette von Inselbergen (Klipfontein Hills) aufbaut, und entlang der nördlichen und südlichen Ausläufer des Gamagara Höhenzugs. Den beiden Erztypen können unterschiedliche Bildungsmilieus zugeordnet werden. Die Wolhaarkop Chert Breccie und assoziierte SiO_2-reiche Manganerze akkumulierten als Karsthöhlensedimente. Eine scheinbare Inversion der Stratigraphie resultierte aus dem Kollaps des durch die hämatitisierte Manganore Eisenformation gebildeten

Daches der Karsthöhlen. Geologisch ältere Eisenerze überlagern so die jüngeren manganreichen Sedimente.

Die Fe-reichen Manganerze repräsentieren variable Mischsedimente aus lateritischen Tonen und Wad, die in offenen Karstdolinen zusammengeschwemmt wurden. Die Fe-reichen Manganerze werden konkordant überlagert von fluvialen Hämatitkonglomeraten und lateritischen Schiefern und Tonsteinen der Gamagara Formation. Paleosolprofile finden sich im basalen Teil der Gamagara Formation und sind ein weiterer Beleg für die terrestrisch-supergene Genese der Manganerze des Postmasburg Manganerzfeldes.

Diagenese und Metamorphose der unteren Grünschieferfazies (300-375 °C, 3-4 kbar) überprägten die Manganerze des Postmasburg Manganerzfeldes. Braunit, Partridgeit, Bixbyit, Diaspor, Ephesit und Amesit sind Produkte der diagenetischen und metamorphen Rekristallisation. Die metamorphe Mineralassoziation ist ausgezeichnet durch das Auftreten ungewöhnlicher Braunit-Varietäten, wie z.B. Braunit II, Si-armem Braunit und Ti-reichem Braunit.

Sekundäre Verkarstung und Verwitterungsprozesse führten zu einer erneuten Alteration der Erze. Die metamorphe Mineralparagenese wird verdrängt durch Romanechit, Lithiophorit und andere typisch supergene Manganoxide.

Der Vergleich zwischen den Lagerstätten des Kalahari Manganerzfeldes und des Postmasburg Manganerzfeldes belegt sehr deutlich, daß ihre enge geographische Vergesellschaftung rein zufällig ist. Die Lagerstätten beider Felder sind zwar von frühproterozoisch sedimentärem Ursprung, ihre Bildung beruht jedoch auf komplett unterschiedlichen lagerstättenbildenden Prozessen. Offensichtliche mineralogische Ähnlichkeiten zwischen den Erzen bildeten sich als Folge epigenetischer regionalgeologischer Prozesse, wie der Grünschiefer-faziellen Regionalmetamorphose und subrezenter Verwitterungsprozesse, heraus.

UNIVERSITY OF JOHANNESBURG

Chapter One

Introduction

General

Griqualand West (Fig. 1.1A) covers a large, sparsely populated area in the Northern Cape Province of South Africa between the small town of Prieska in the South and the border to Botswana in the North. The area is located between about 22° 30' E, 30°00' S and 25° 00'E, 27° 10' S (Fig. 1.1A). The climate is continental semiarid, with an average rainfall of 300 - 350 mm per year, mainly taking place in the summer months. The vegetation is characterized by a loose cover of small shrubs, acacia trees and grass suited as pasture for cattle, sheep or goat farming. The mean elevation in this area is between 1100 m to 1400 m; the morphology is dominated by gently sloping plains interrupted by generally N-S striking ranges of hills, such as the Asbestos Hills, the Klipfontein Hills and the Gamagara Ridge. Outcrop conditions in the hills are very good but on the plains poor because of cover by calcrete and/ or Kalahari sand.

UNIVERSITY
JOHANNESBURG

The area hosts two economically important districts of manganese deposits, the giant Kalahari manganese field (Fig. 1.1B) and the large Postmasburg manganese field (Fig. 1.1C). In addition small manganese deposits are present in the Rooinekke area to the South of Postmasburg (Fig. 1.1A). Manganese ore in Griqualand West was discovered by Cpt. L.T. Shone in 1922 close to the town of Postmasburg (Fig. 1.1C), i.e. the so-called Postmasburg manganese field (De Villiers, 1960). His discovery caused an exploration and mining boom in the Postmasburg area, resulting in the delineation of two distinct belts of manganese deposits stretching from Postmasburg in the south to Sishen in the north (Fig. 1.1C). Mining of ferruginous manganese ore along the so-called Western Belt, confined to the central part of the Gamagara Ridge (Fig. 1.1C), constituted the most important source for manganese in South Africa from 1922 to 1954. The small, siliceous manganese orebodies of the Eastern Belt or Klipfontein Hills were, in comparison, of minor importance and mined only on a small scale.

Open pit and underground mining in the Kalahari manganese field commenced in 1940 at Black Rock, a small but conspicuous hillock composed of iron-formation and interbedded manganese ore. This hillock, situated about 90 km to the northwest of Kuruman, was already marked in 1908 on a small scale map by Dr. A.W. Rogers (Boardman, 1941). It is owing to L.G. Boardman that

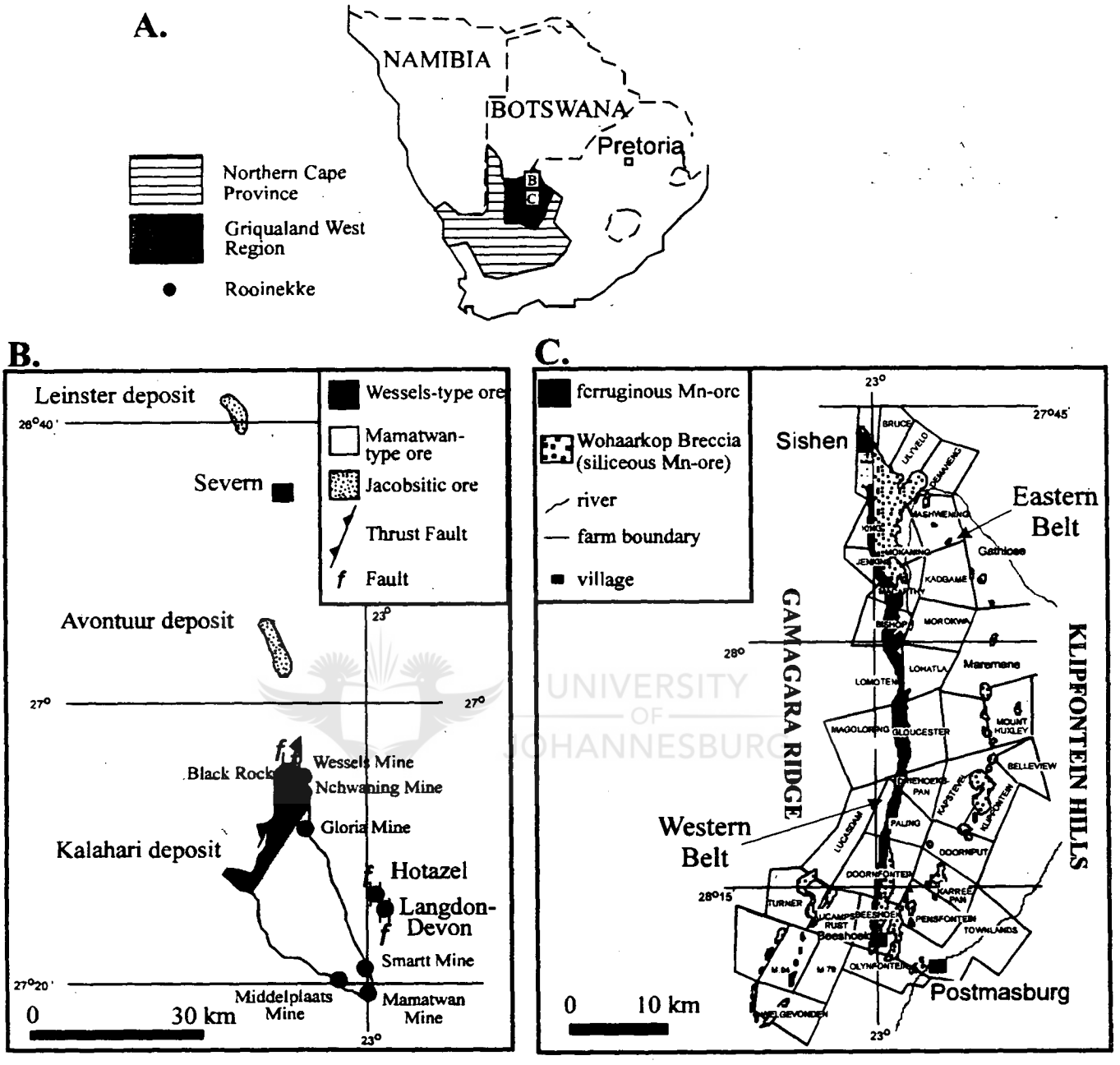

Fig. 1.1 (A) Location of the Griqualand West region and the study areas in the Northern Cape Province of South Africa; (B) Locality map of the Kalahari manganese field showing the location of the five erosionally preserved deposits, and the distribution of thrusting, major normal faulting, ore-types and location of mines; (C) Regional map of the Postmasburg manganese field showing the location of ferruginous manganese ore along the Western Belt and the occurrence of Wolhaarkop Breccia (and associated manganese ore) along the Eastern Belt, the Gamagara Ridge and in the Aucampsrust area.

the true extent of the Kalahari manganese deposits and its outliers at Hotazel and Langdon were discovered under a thick cover of Kalahari sands. Mining of concealed ores began in small open pit operations at Smartt and Devon in 1954.

The amount and quality of ores supplied by the neighbouring Kalahari manganese field forced the closure of the last of once numerous manganese mines in the Postmasburg manganese field in 1989. Factors that disadvantage the Postmasburg deposits are the irregular size and shape of individual orebodies that impose severe restrictions to the application of modern bulk mining techniques, the lack of remaining ore reserves (15 Mt of ferruginous ores, estimated by Taljaardt, 1982), and the unfavourable composition of the ores.

In the meantime mining in the Kalahari manganese field flourished and today it is one of the biggest producers of manganese ore in the world. The Kalahari manganese field, as it is known today, consists of a group of five erosional relics of the Paleoproterozoic Hotazel manganese- and iron-formation (Fig. 1.1B). Of the five relics the 35 km x 15 km measuring Kalahari manganese deposit is by far the largest and the only one of economic importance. The Hotazel and Langdon-Devon deposits are structural relics preserved in N-S striking graben structures to the east of the Kalahari deposit. These two small high-grade deposits have virtually been mined out. The Leinster and Avontuur deposits further to the North have proved to contain only subeconomic jacobsite-rich ore.

UNIVERSITY OF JOHANNESBURG

The Kalahari manganese field is, with 13500 Mt of estimated ore reserves (manganese ore at >20 wt % Mn), regarded the largest known manganese deposit on land (Taljaardt, 1982; Laznicka, 1992). The active open pits (Mamatwan, Langdon) and underground mines (Gloria, Wessels, Nchwaning) continue to be important suppliers of manganese ore to the South African and the world market. These mines are operated by three South African companies, ASSMANG (Associated Manganese Mines of South Africa Ltd.), SAMANCOR (South African Manganese Mining Corporation), and National Manganese Ltd.

The manganese deposits of the Postmasburg and Kalahari manganese fields have been subject of numerous geological and mineralogical studies (see section **1.2**). Their close geographic association led several authors to speculate about possible genetic links between the two manganese fields (Boardman, 1964; De Villiers, 1983, 1992) (see section **1.4**). The following study was conducted to compare the manganese deposits of the Postmasburg manganese field with those from the Kalahari manganese field with the aim to identify and characterize similarities and differences between the two. To accomplish this it was decided to carry out systematic studies of the mineralogy, petrography and geochemistry of the manganese ores.

Previous work

Postmasburg manganese field

The geology and mineralogy of the manganese ore deposits of Griqualand West have been studied by numerous investigators, and the origin of the deposits has been subject of many controversial discussions. Stow (1874) and Rogers (1905, 1906, 1907) pioneered the regional geology and stratigraphic subdivision, and it was Rogers (1905, 1906) who stressed the importance of regional thrusting in the area and its influence on stratigraphy. Hall (1926) contributed the first geological description of the manganese ores at Postmasburg, soon followed by Kaiser (1927). Based on the result of his regional study, Hall (1926) suggested that the manganese oxides precipitated from meteoric ground water solutions and replaced sedimentary clays.

Nel (1929) was the first to subdivide the ores of the Postmasburg manganese field into two distinct types, a ferruginous type occurring along the Gamagara Ridge or Western Belt (Fig. 1.1C), and a siliceous type, hosted in chert breccia along the Klipfontein Hills or Eastern Belt (Fig. 1.1C). He recognized the intimate association of the manganese ores with the underlying Campbellrand dolomite. Du Toit (1933) stressed the close association of the manganese ores with overlying hematitic iron ores. Truter et al. (1938) and Visser (1944) made considerable contributions to the understanding of the regional geology around the manganese deposits. It was Visser (1944) who was the first to map the thrust tectonics in detail. Beukes (1978) established that the distribution and nature of the manganese ore are controlled by the composition and type of the underlying Campbellrand dolomite. Ferruginous ores are only found in karst sinkholes in the Reivilo Formation. Siliceous ores, however, occur in close association with chert breccia overlying dolomite beds rich in diagenetic chert concretions, such as the Klipfontein Hills and Klippan Formations.

Nel (1929), Du Toit (1933), Truter et al. (1938), Boardman (1964), Borchert (1970), Söhnge (1977) and Beukes (1978) envisaged dissolution of Mn- and Fe-bearing Campbellrand dolomite by meteoric solutions as the source for Fe and Mn accumulations in the Postmasburg manganese field. Du Toit (1933) Boardman (1940, 1961, 1964), De Villiers (1944), De Villiers (1956) and De Villiers (1960) stressed the importance of fluid flow focused by thrust planes for the origin of the manganese ore. Concentrations of B, Li, Na, Cl and F in the manganese ores and the presence of typically hydrothermal textures led De Villiers (1944, 1983) to the conclusion that fluids that were responsible for the formation of the manganese ores were of magmatic origin,

an idea that found no further support by other authors. All these authors agree with Hall (1926) on a metasomatic ore forming process, i.e. that manganese oxides replace aluminous shales to form the ferruginous manganese ores of the Western Belt and chert fragments to form the siliceous ores of the Eastern Belt.

Different timings were suggested for the mineralizing event, ranging from Post-Olifantshoek (Nel, 1929; Du Toit, 1933; Truter et al. 1938) to Post-Karoo (Truter et al., 1938). Stowe (1986) and Beukes and Smit (1987) recently confirmed the presence and importance of low angle thrusts to the West of the Gamagara Ridge (Fig. 1.1C) without speculating on a possible influence of the thrusting event on the origin or alteration of the manganese ores.

Based on thorough ore petrographic studies, Schneiderhöhn (1931) and Plehwe-Leisen (1985) suggest the synsedimentary accumulation of the manganese ores prior to deposition of the overlying strata, followed by a regional metamorphic overprint. This synsedimentary model was also supported by Kaiser (1931), Richter (1933), Kupferburger et al. (1956), Button (1976), Grobbelaar and Beukes (1986), and Leisen (1987).

A number of publications were devoted to the interesting mineralogy of the manganese deposits. Investigations by De Villiers (1943a, 1943b, 1944, 1945a, 1945b) resulted in the descriptions of two new mineral species, the Ba-(Mn,Fe)-vanadate gamagarite (1943b) and partridgeite (α-Mn_2O_3) (1943a)[a]. Nel (1929) and Chudoba (1929) identified and described Mn-diaspore. Ephesite, erroneously described by Chudoba (1929) as manganophyll, was correctly identified by Coles-Phillips (1931). Nel (1930) described the rare silicate zunyite from aluminous shales immediately overlying the manganese ores. Gruner (1943) was the first to discover the Li-Al manganese oxyhydroxide lithiophorite at Postmasburg. A unique find of unusually coarse crystalline lithiophorite from Glosam mine was described by De Villiers (1945b), who later (1992) also identified braunite II in the ferruginous ores of the Western Belt[b].

---

[a] Partridgeite is not recognized as a mineral species by the IMA (International Mineralogical Association).
[b] Braunite II is up to today only known from two localities, the Kalahari manganese field (type locality) and the Postmasburg manganese field.

Kalahari manganese field

Boardman (1941) was the first to describe the occurrence of manganese ore at the Black Rock outcrop and concluded that the manganese ores formed by metasomatic replacement of iron-formation of the Upper Griquatown stage (now Koegas Subgroup). Based on a greater wealth of information from drilling and mining operations, Kupferburger et al. (1956) recognized the sedimentary nature of 'manganiferous limestone' beds interbedded with iron-formation in the Kalahari manganese field and suggested that 'prolonged supergene weathering' resulted in upgrading of this manganiferous limestone to manganese ore at Black Rock, Smartt and Devon. Frankel (1958) came to a similar conclusion when studying the petrography, chemistry and mineralogy of some samples of enriched ore from the Smartt mine. Detailed accounts of the geology of the Black Rock outcrop and general surveys of the geology and extent of the Kalahari manganese deposit and its outliers at Hotazel and Langdon-Annex were published by De Villiers (1960) and Boardman (1964). The most recent review of the geology of the structurally complex northwestern part of the Kalahari manganese deposit around the Black Rock outcrop was provided by Grobbelaar et al. (1995). It was De Villiers (1970) who performed a first regional geological and mineralogical study covering the Kalahari manganese deposit and the two graben structures to the east. He inferred a chemosedimentary origin of the carbonate-rich manganese ore and considered localized thermal metamorphism (at Hotazel and Black Rock) and supergene alteration as important factors for the enrichment of some of the ores. A microbially mediated volcano-sedimentary origin of low-grade ores followed by structurally controlled alteration caused by circulating meteoric water were important genetic processes envisaged by Söhnge (1977). De Villiers (1983, 1986, 1992) suggested a metasomatic model for the origin of the manganese ores and inferred a close genetic relationship between the ores of the Postmasburg and Kalahari manganese fields.

The review by Button (1976) was the first publication in which the correct stratigraphic position of the interbedded succession of manganese and iron formations in the Vöelwater Subgroup of the Postmasburg Group was acknowledged. Beukes et al. (1982) recognized the presence of three volcano-sedimentary cycles in the manganese-bearing succession. A detailed overview of the regional stratigraphy and the geological setting of the manganese ores was then prepared by Beukes (1983). He stressed that manganese ores occur in the Hotazel Formation of the Vöelwater Subgroup and constitute the centre of three chemosedimentary cycles composed of jaspilitic iron-formation, hematite-lutite and braunite-lutite and established a tentative model for its deposition. In his tentative genetic model transgressive-regressive cycles account for slight changes of the

Eh-pH conditions in the depositional environment resulting in the observed separation of Fe-SiO_2 from Mn-CO_3^{2-} precipitates. He also suggested deposition of the Hotazel Formation in a back arc environment rather than in a mid ocean ridge-type setting, with iron and manganese possibly introduced by a distant volcanic source. In this model iron-rich sediments precipitate more proximal and manganese-rich sediments more distal relative to the volcanic source. Very recently, Cornell and Schütte (1995) challenged this model and proposed a volcano-sedimentary origin of the Kalahari manganese deposit in a proximal mid ocean ridge-type environment, very similar to modern marine hydrothermal manganese deposits.

Several studies concentrated on the geological setting of specific mines, and the description of mineralogy, petrography and composition of the ore exploited. Nel (1984) conducted a detailed mineralogical and geochemical study of the manganese ore at Mamatwan mine, subdividing the orebody into 11 lithologically distinct subzones. Nel et al. (1986) published a comprehensive description of the Mamatwan mine. The papers by Jennings (1986) and Grobbelaar (1985) provide short descriptions of geology and mining operations at Middelplaats mine and Nchwaning mine.

UNIVERSITY OF JOHANNESBURG

The identification of 'ferrian braunite' and andradite in ores from Black Rock were the results of the first mineralogical study of manganese ores in the Kalahari manganese field (De Villiers, 1945). Later De Villiers (1970) conducted the first regional mineralogical study. Following this approach Kleyenstüber (1984, 1985) focused on the mineralogy of the Vöelwater Subgroup in general and the sediments of the Hotazel Formation in particular. His work was based on samples from 21 drill cores, 14 from the Kalahari deposit and 5 from the Leinster and 2 from the Avontuur deposit [c]. He was able to identify a number of previously unnoted minerals and subdivided the ores into 3 distinct types: Low-grade metamorphic Mamatwan-type ore, high-grade Wessels-type ore and the uneconomic jakobsitic-type. Kleyenstüber (1985) stressed that high-grade Wessels-type ore formed through a process of hydrothermal upgrading from low-grade Mamatwan-type ores, a process apparently restricted to the structurally disturbed northwestern part of the Kalahari deposit. He envisaged a close genetic relationship between the processes of hydrothermal upgrading and structural deformation (normal faulting and thrusting).

---

[c] *These two deposits are small erosional relics of the Hotazel Formation towards the north of the main Kalahari deposit (Fig. 1.1B).*
[d] *Attached as APPENDIX 7 in this thesis.*
[e] *Attached as APPENDIX 8 in this thesis.*

Based on petrographic and compositional characteristics, the Wessels-type of ore was further subdivided by some authors into Wessels-type s.s., Hotazel Supergrade-type and Black Rock-type (Kleyenstüber, 1993).

Thermodynamic calculations by Miyano and Beukes (1987, 1988) were dedicated to the delineation of physicochemical conditions of this alteration process upgrading Mamatwan-type ore to Wessels-type ore. Their results indicate that alteration took place at 0.5-1.5 kbar and 300-400 °C, low fO_2 and very low fCO_2. Dixon (1985, 1989) came to similar, qualitative conclusions (max. 450 °C, low fCO_2) based on his study of the peculiar sugilite-bearing calc-silicate assemblage associated with Wessels-type ore. Recent studies by Gutzmer (1993), Burger (1994), Gutzmer and Beukes (1995)[d] and Beukes et al. (1995)[e] established a comprehensive model for the hydrothermal alteration process. According to this model hydrothermal fluids were introduced into the manganese ore body along major N-S and minor W-E striking fault zones. Pervasive alteration led to complete removal of CO_2 and considerable leaching of SiO_2 from the sedimentary precursor. The alteration process resulted in a characteristic zonation of various ore-types and grades next to faults that acted as feeder structures for hydrothermal fluids.

Other geological events that affected the mineralogy of the manganese ores received little or no attention. Boardman (1964), De Villiers (1970) and De Villiers (1983) noted effects of contact metamorphism around bostonite dykes. De Villiers (1970), Kleyenstüber (1984, 1985, 1993) and Nel et al. (1986) briefly described the effects of supergene alteration on ore mineralogy and composition. Kleyenstüber (1993) summarized the knowledge of the mineralogical and geochemical effects of weathering related to different erosional unconformities that cut the manganese ore beds of the Hotazel Formation.

A vast number of publications deal with specific mineralogical aspects of the manganese ores of the Kalahari manganese field. The properties of 'ferrian braunite' of De Villiers (1945) were investigated (and the phase renamed to 'braunite II') by De Villiers and Herbstein (1967). Its crystal structure was solved by De Villiers (1980). Kleyenstüber (1985) identified an even more silica-deficient member of the braunite group, which he tentatively called braunite (new). The occurrence of neltnerite, the Ca-rich analogue of braunite, was recently recorded by Burger (1994). Dixon (1985, 1989) described the complex and variable association of sugilite in dense calc-silicate bodies from Wessels mine. Up to now the occurrence of more than 130 minerals was recorded in association with the manganese ore. The Kalahari manganese deposit is the type locality for eight of these minerals: sturmanite (Peacor et al., 1983), orlymanite (Peacor et al. 1990), vonbezingite (Dai and Harlow, 1992), poldervaartite (Dai et al., 1993), hennomartinite

(Armbruster et al., 1993), kornite (Armbruster et al., 1993), effenbergerite (Giester and Rieck, 1994) and nchwaningite (Nyfeler et al., 1995).

Objective and outline of this thesis

Previous authors such as Boardman (1941, 1964) and De Villiers (1983, 1986, 1992) tried to recognize features common to the Kalahari and the Postmasburg manganese fields and suggested a unique event of manganese mineralization. The close geographic association of two large deposits of manganese ore such as the Kalahari and Postmasburg manganese fields is in fact striking and calls for geological or genetic relationships.

The available literature on the Kalahari and Postmasburg manganese fields covers a wide range of geological, sedimentological, and mineralogical aspects, but there appears to be a distinct lack of information concerning the petrography, mineral paragenesis and geochemistry of the manganese ores. The objective of this study is to close some of these gaps with the aim to construct feasible models for the origin of the manganese deposits of the Kalahari and Postmasburg manganese fields and to identify possible geological events that influenced the mineralogy or geochemistry of the manganese ores in both areas.

The six chapters that form the core of this thesis (Chapters 2 to 7) were written in the form of publications. This has the disadvantage that some information in the introductory part of each chapter is redundant to the reader that studies this thesis as a whole. However, it has the great advantage that every chapter represents in itself a conclusive unit. Each chapter has its own thrust and can be read and understood separately. This may also be a great relief to the reader who wants to test the self consistency of the presented data and interpretations. Chapter 8 represents not only a comprehensive summary of the results of the seven previous chapters and an outline of some major remaining problems, but it is the attempt to draw a comparative picture for the evolution of the manganese ores and to illuminate similarities and differences between the Kalahari and Postmasburg manganese fields.

Three of the six core chapters are devoted to petrography, mineralogy, mineral chemistry and mineral paragenesis of ores in the Kalahari manganese deposit. Chapter 2 describes previously unnoted alteration events that affected the manganese ore locally and postdate the main alteration event that resulted in the formation of Wessels-type ores. Chapter 3 is an attempt to construct a consistent paragenetic sequence for the numerous mineral phases associated with the manganese

ore. In chapter 4 mass balance calculations are applied to quantify mass transfer and compaction during alteration of Mamatwan-type ore to Wessels-type ore.

Chapter 5 to 7 are devoted to the manganese deposits of the Postmasburg manganese field. In the first of these three chapters (Chapter 5) the find of very well preserved Paleoproterozoic paleo-laterite profiles is reported that overlie the manganese orebodies of the Western Belt. This discovery has important implications not only for the genesis of the manganese ore but provides also new evidence or the presence of organic matter on the continents during the Paleoproterozoic. Petrography and geochemistry of different types of manganese ore of the Postmasburg manganese field are described in Chapter 6. The chemistry of the different ore and gangue minerals present in the manganese ores of the Postmasburg deposits is discussed in Chapter 7.

Nine appendices follow the text of the thesis. Appendix 1 contains detailed descriptions of the analytical techniques used. Appendix 2 provides sample descriptions, appendix 3 whole rock geochemical data, appendix 4 phase chemistry data, appendix 5 carbonate stable isotope data and $^{87}Sr/^{86}Sr$ data on barite and celestite, and appendix 6 fluid inclusion data, compiled during the course of this study. Not all of these data have been fully evaluated in this thesis, but they may represent valuable information for the interested reader.

UNIVERSITY OF JOHANNESBURG

Three further papers that have already been published in scientific journals are added in the back of this thesis as appendices 7 to 9. It was decided to include these papers because they contain information that complements what is provided in the main part of the thesis. Appendices 7 and 8 describe major features of fault-controlled hydrothermal alteration of Mamatwan-type ore to Wessels-type ore at Nchwaning and Wessels mine respectively. These publications summarize the findings of Gutzmer (1993) and Burger (1994). Appendix 9 is a detailed study of the occurrence and the properties of magnetic hausmannite. This Fe-rich variety of hausmannite occurs in abundance in the hydrothermally altered Wessels-type ores.

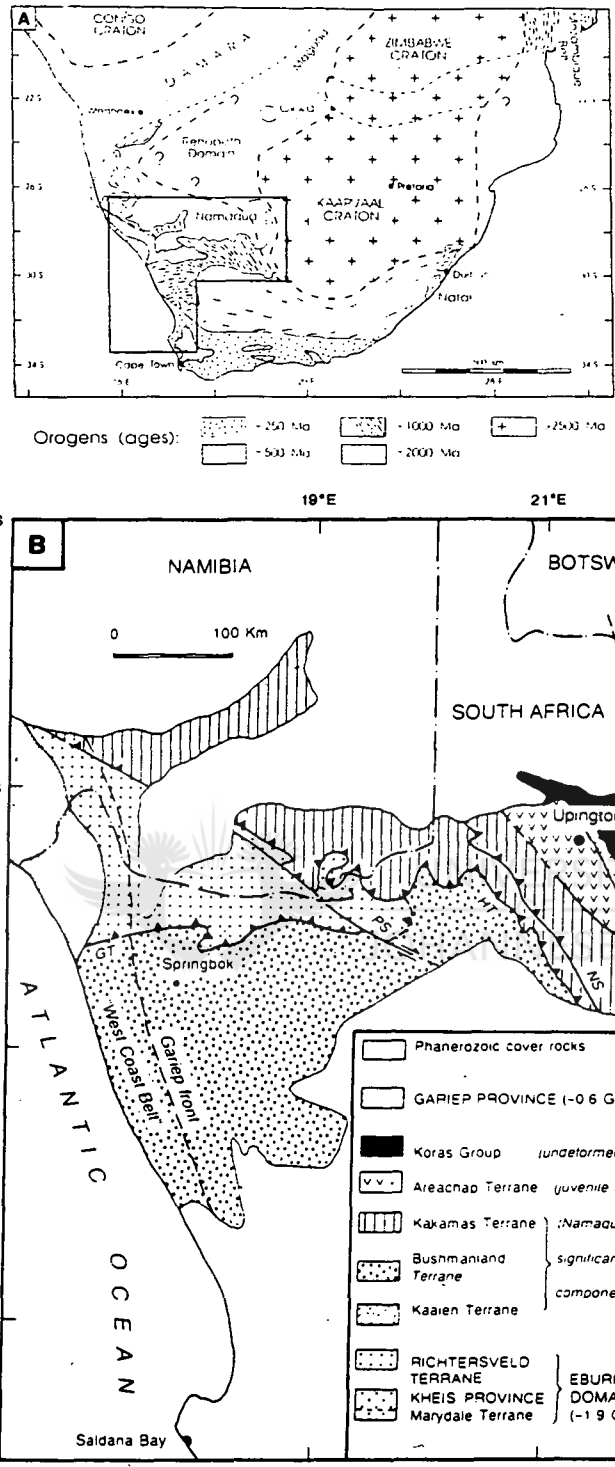

Fig. 1.2 (A) Location and regional tectonic setting of the 1.1 Ga Kibaran orogenetic belt (Namaqua-Natal Province) in Southern Africa and its relationship to pre-existing Eburnian and Archean Crustal Blocks (after Thomas et al., 1994b); (B) Tectonic subdivision of the region west of the study area. Indicated are the locations of the Kalahari manganese field (KMF) and the Postmasburg manganese field (PMF) close to the eastern border of the Kheis Province (modified after Thomas et al., 1994a) (GT - Groothoek thrust; HT - Hartebeest River thrust; PS - Pofadder shear; NS - Neusspruit shear; BoS - Boven Rugseer shear; BS - Brakbos shear; DL - Doringberg lineament).

Geological setting

General

The study area is located on the western margin of the Kaapvaal Craton (Fig. 1.2). Outcrop of weakly deformed and metamorphosed supracrustal cover rocks of the Kaapvaal Craton are cut off to the west of the study area by the Kheis thrust front (Figs. 1.2, 1.3) (Thomas et al., 1994a, 1994b). Metamorphosed and strongly deformed rocks of the Kheis province occur to the west of the Kheis front, a succession which has been correlated with the rocks of the Late Paleoproterozoic Olifantshoek Group (SACS, 1980). The deformational and metamorphic history of the Kheis Province is extremely complex and has as yet not been fully understood (Thomas et al., 1994b).

It appears, however, that the Late Proterozoic rocks of the Olifantshoek Group were deformed and thrust onto the western margin of the Kaapvaal Craton during the 1.8-1.9 Ga Kheis orogeny (Beukes and Smit, 1987). The Kheis Province is also the easternmost tectonic block of the 400 km wide N-S striking Namaqualand Metamorphic Province extending from southern Namibia into Namaqualand (Fig. 1.2). The rocks of the Namaqualand Metamorphic Province acquired a pervasive structural fabric during the 1.1 Ga Kibaran tectono-magmatic event. Older geological structures, such as the Kheis thrust front, were reactivated during this event of intense metamorphism and extensive magmatism and crustal thickening took place as response to collision of the western edge of the Kaapvaal Craton with the Bushmanland Craton. The collison of the two continental masses is characterized by northeast directed thrusting during the early collision phase, followed by pervasive northwest-southeast striking shearing due to continued convergence and crustal thickening (Stowe, 1986; Thomas et al., 1994b).

The oldest outcropping rocks in the study area are tholeeitic basalts of the Late Archean Ventersdorp Supergroup (2.9-2.7 Ga) (Fig. 1.4) that are exposed south of Koegas and Douglas (Fig. 1.3). The Ventersdorp Supergroup is conformably overlain by a thick sequence of sediments and volcanics of the 2.7 - 2.2 Ga old Transvaal Supergroup (Barton et al., 1994; Trendall, 1990). The Transvaal Supergroup in Griqualand West (former Griqualand West Sequence) consists (Fig. 1.4) of a chemical sedimentary unit, the Ghaap Group, which is unconformably overlain by the mixed volcanic-chemical sedimentary Postmasburg Group (Beukes, 1978, 1983, 1986). The Ghaap Group is subdivided into the basal Smitsdrift Group, composed of interbedded

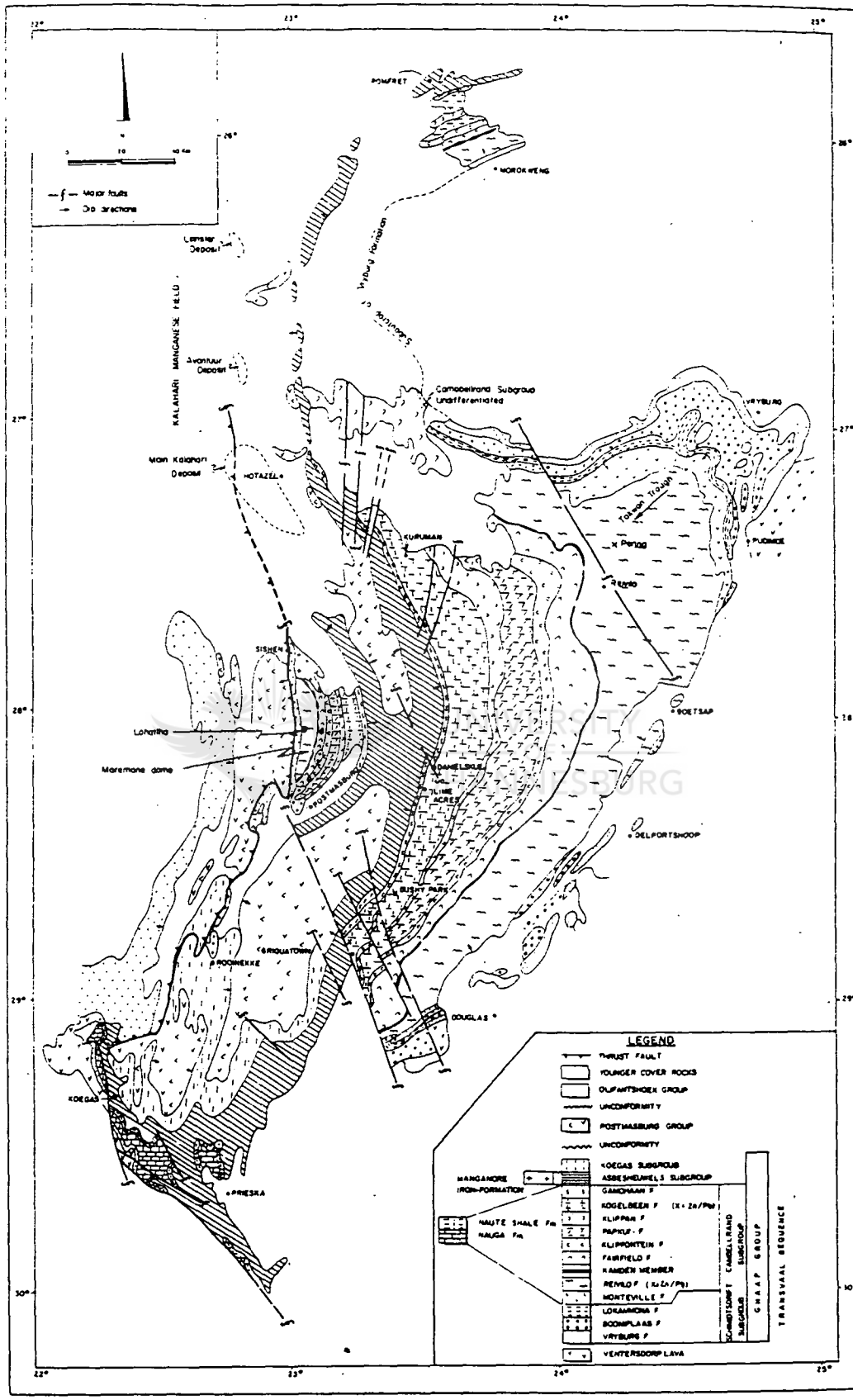

Fig. 1.3 Geological map of Griqualand West showing the distribution of major stratigraphic units and ore deposits (after Beukes, 1983).

siliciclastics and carbonate rocks, limestones and dolomites of the Campbellrand Subgroup[f], the Asbesheuwels Subgroup (iron-formation), and the Koegas Subgroup (interbedded siliciclastics and iron-formation) (Beukes, 1986). The Makganyene diamictite forms the basal unit of the Postmasburg Group, followed by a thick succession of andesitic flood basalts of the Ongeluk Formation[g], conformably overlain by the Hotazel iron- and manganese-formation and the Moodraai Formation. Beukes (1983) suggested that the deposition of the Transvaal Supergroup in Griqualand West took place on a shallow marine platform on the western edge of the Kaapvaal Craton.

The Transvaal Supergroup is overlain with an erosional unconformity by a sequence of clastic sediments (red beds, quartzite) and minor volcanics of the 2.2-1.9 Ga old, Late Palaeoproterozoic Olifantshoek Group (Fig. 1.4). The Olifantshoek Group can be subdivided into the basal Mapedi/ Gamagara Formation, composed of a basal hematite pebble conglomerate followed by red- and cream-coloured illitic shales with thin interbeds of fine-grained quartzites, overlain by quartzites of the Lucknow Formation and the mixed volcanogenic-sedimentary Hartley Formation[h] (SACS, 1980).The top of the Olifantshoek Group is formed by coarse quartzites and conglomerates of the Volop Group (Jansen, 1983).

On the Maremane dome (Fig. 1.3), between Sishen and Postmasburg, a succession of hematitized Manganore iron formation, an altered lateral equivalent of the iron-formations of the Asbesheuwels Subgroup, hematite-pebble conglomerate and black, red and white coloured aluminous shales rest unconformably on carbonates of the Campbellrand Subgroup. The highly variable terrigenous succession of hematite pebble conglomerates and aluminous shales is traditionally called Gamagara Formation and is in the areas to the north and south of the Maremane Dome (Dimoten Syncline to the northeast, Ongeluk-Witwater Syncline to the southeast) (Fig. 1.3) represented by a thin bed of hematite pebble conglomerate at the base of the Mapedi/ Gamagara shales.

Ongeluk lava and parts of the Makganyene diamictite have been thrusted from the west over the Mapedi/ Gamagara Formation along the low angle Blackridge thrust fault located west of the Gamagara Ridge (Beukes and Smit, 1987). Thrusting took place during the 1.8-1.9 Ga Kheis

(f) Barton et al. (1994) reported a single zircon U-Pb age of 2552±11 Ma for the Nauga Formation of the Campbellrand Subgroup. Sumner and Bowring (1995, reference in Sumner, 1995) established a single zircon U-Pb age of 2521±3 Ma for a tuff bed interbedded with the Gamoohan Fomration of the Campbellrand Subgroup.

(g) Cornell et al. (reference in Cornell and Schütte, 1995) report and extrusion age of 2223±13 Ma for the Ongeluk lava, in close agreement with and age of 2239±90 Ma by Armstrong (1987).

(h) Different ages for the extrusion of the Hartley lava are 2026±180 Ma (Rb-Sr isochron) and 1830±400 Ma (Pb-Pb) (Armstrong, 1987) and 1930±4 Ma (single zircon U-Pb) (Cornell et al., reference in Cornell and Schütte, 1995).

(Beukes and Smit, 1987) and/ or the 1.1 Ga Namaqua-Natal (Kibaran) orogenetic events(Thomas et al., 1994a and b). The thrust fault can be traced further to the south into the vicinity of Rooinekke (Fig. 1.3) where even the upper part of the Campbellrand Subgroup and the Asbesheuwels iron-formation have been thrust over the Mapedi/ Gamagara formation of the Olifantshoek Group (Van Wyk, 1980). Duplication of strata to the west of Black Rock in the Kalahari manganese field has also been attributed to displacement along the Blackridge thrust fault (Beukes, 1986).

The Late Carboniferous and Early Permian Dwyka glaciation of the Karoo Supergroup carved deep N-S striking valleys into the Proterozoic basement which are now filled by thick beds of diamictite. Clays, marls, windblown sands and their calcretized equivalents of the Late Mesozoic to Cenozoic Kalahari Formation cover and conceal the older rocks in the north of the study area (Fig. 1.3).

Intrusive rocks are scarce in the study area. Intrusion of a number of syenitic and gabbroic dykes into the rocks of the Transvaal Supergroup apparently predates the deposition of the Olifantshoek Group (Beukes and Gutzmer, 1995). Such dykes are present in the northwestern part of the Kalahari manganese field and in the Sishen-Postmasburg area (De Villiers, 1960). Dolerite dykes occur scattered within the study area, they are apparently of Karoo age and have a noritic, gabbroic or gabbrodioritic composition (Nel, 1929; Truter et al., 1938). Kimberlite pipes and dykes in the area (for example at Kuruman, Postmasburg, and Finsch) are of Proterozoic to Mesozoic age.

UNIVERSITY JOHANNESBURG

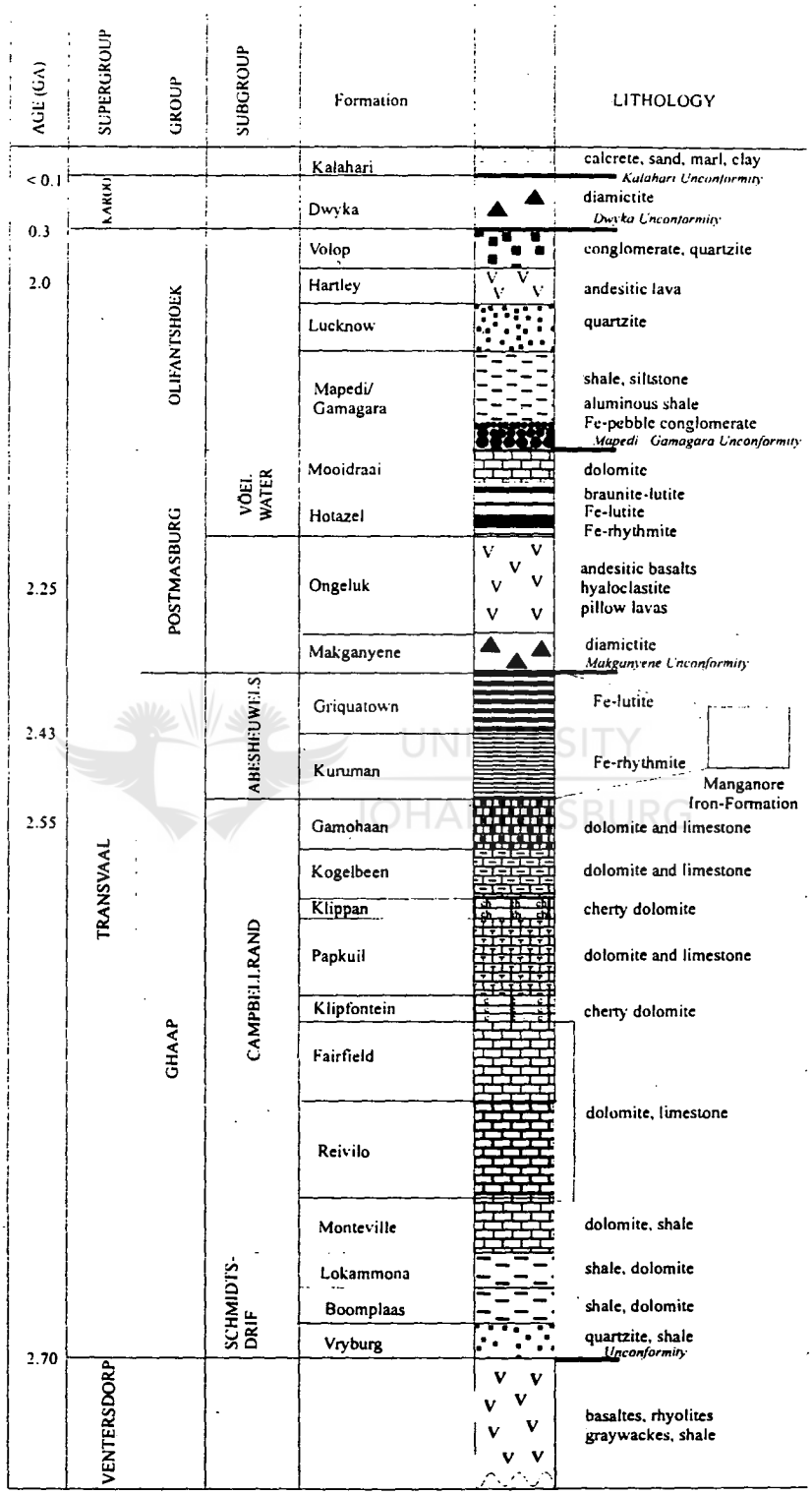

Fig. 1.4 The lithostratigraphy of the study area in Griqualand West.

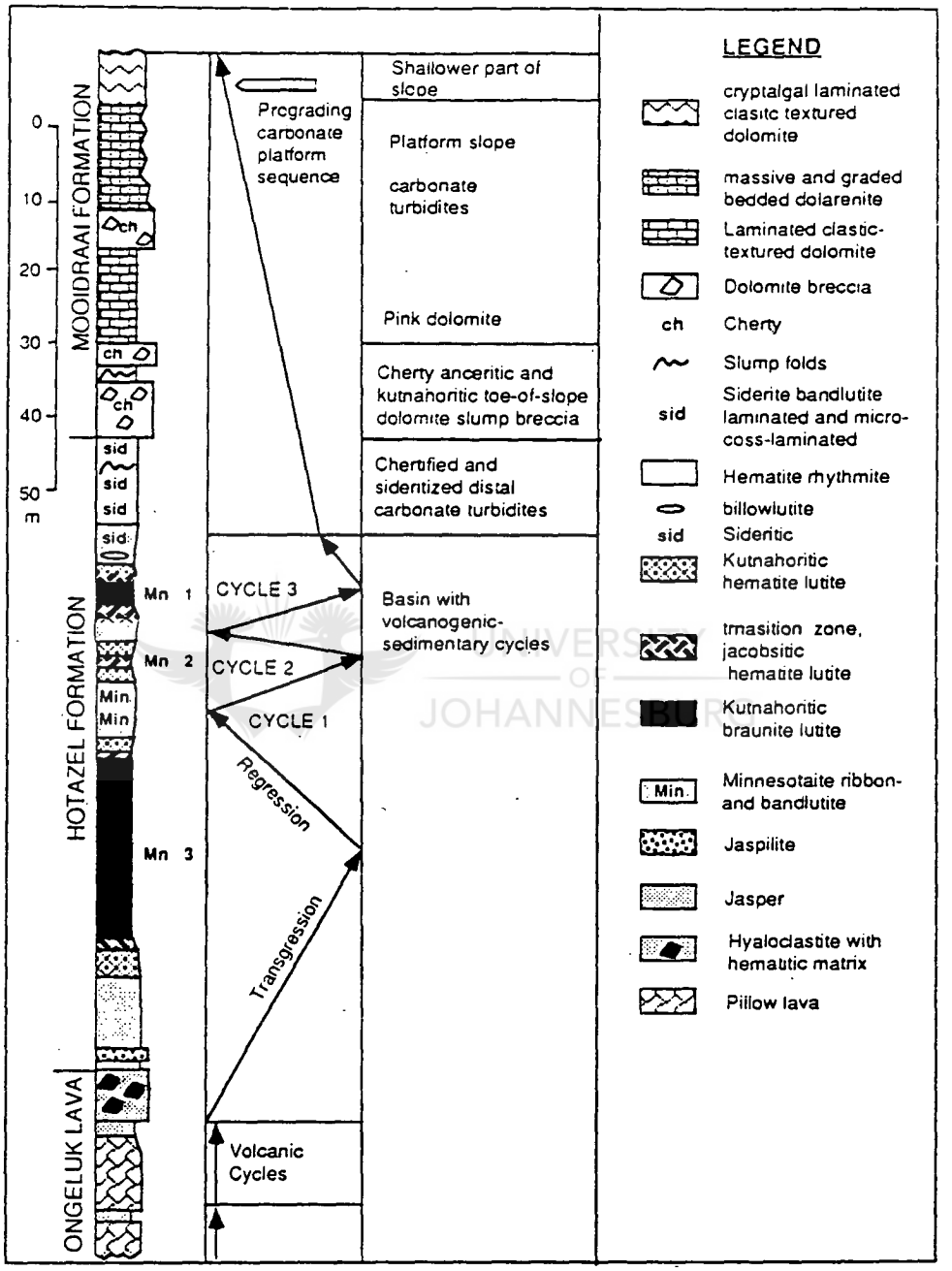

Fig. 1.5 Type profile of the Hotazel and Mooidraai Formations showing the stratigraphic setting of the three manganese ore units interbedded with iron-formation. Note the cyclical repetition of lithofacies in the Hotazel Formation and the jaspilites interbedded with hyaloclastite and pillow lava of the Ongeluk Formation (modified after Nel et al., 1986).

Geological setting of the Kalahari manganese field

The manganese deposits of the Kalahari manganese field represent structurally preserved erosional relics of the manganese-bearing Hotazel Formation below younger cover of late Palaeoproterozoic Olifantshoek red beds, late Carboniferous-early Permian Dwyka diamictite of the Karoo Supergroup and Cenozoic Kalahari beds (Fig. 1.5). Virtually all the deposits are covered by these younger sequences and natural outcrop is restricted to Black Rock, a small hill in the northwestern part of the main Kalahari deposit (Boardman, 1941).

The manganese-bearing Hotazel Formation is conformably underlain by pillow lava, hyaloclastite and jaspilite of the Ongeluk Formation and grades upwards into dolomite of the Mooidraai Formation (Fig. 1.5). Three manganese beds are present in the Hotazel Formation, each forming the centre of three symmetrical iron-formation → hematite lutite → braunite lutite sedimentary cycles (Fig. 1.5) (Beukes, 1983). Virtually all manganese ore reserves and production come from the lower manganese bed which reaches a maximum known thickness of about 45 m at Mamatwan Mine and ranges between 4 - 8 m in the Wessels and Nchwaning mining areas (Fig. 1.1C). The upper manganese bed has been mined locally where it reaches a thickness of up to 4 m. The central manganese bed is of no economic significance, being only locally developed and on average less than 1 m thick (De Villiers, 1970).

UNIVERSITY OF JOHANNESBURG

The age of the Hotazel Formation is restricted to about 2.2-2.1 Ga by radiometric dates reported for the underlying Ongeluk lava (Armstrong, 1987; Cornell et al., 1995 - reference in: Cornell and Schütte, 1995) and the Hartley lavas of the overlying Olifantshoek Group (Armstrong, 1987; Cornell, - reference in: Schütte, 1992). In the Kalahari deposit strata dip gently to the west at about 8°. However, near the western margin of the deposit, Ongeluk lava and Hotazel Formation have been duplicated by thrusting from the west (Fig. 1.6) (Boardman, 1941; Beukes and Smit, 1987; Grobbelaar et al., 1995). The sequence has also been affected by a series of north-trending normal faults. These faults post-date deposition of the overlying late Palaeoproterozoic Olifantshoek red beds but pre-date the thrust event (Fig. 1.6). Thrusting is related to the Kheiss orogeny (Stowe, 1986; Beukes and Smit, 1987). The effects of minor NNW-SSE and NNE-SSW orientated jointing and faulting is recognizable in all the mines in the Kalahari deposit. Intrusion of NNE-SSW and E-W striking 'bostonite' dykes in northern part of the Kalahari manganese field apparently predates the period of erosion prior to deposition of the Olifantshoek sediments.

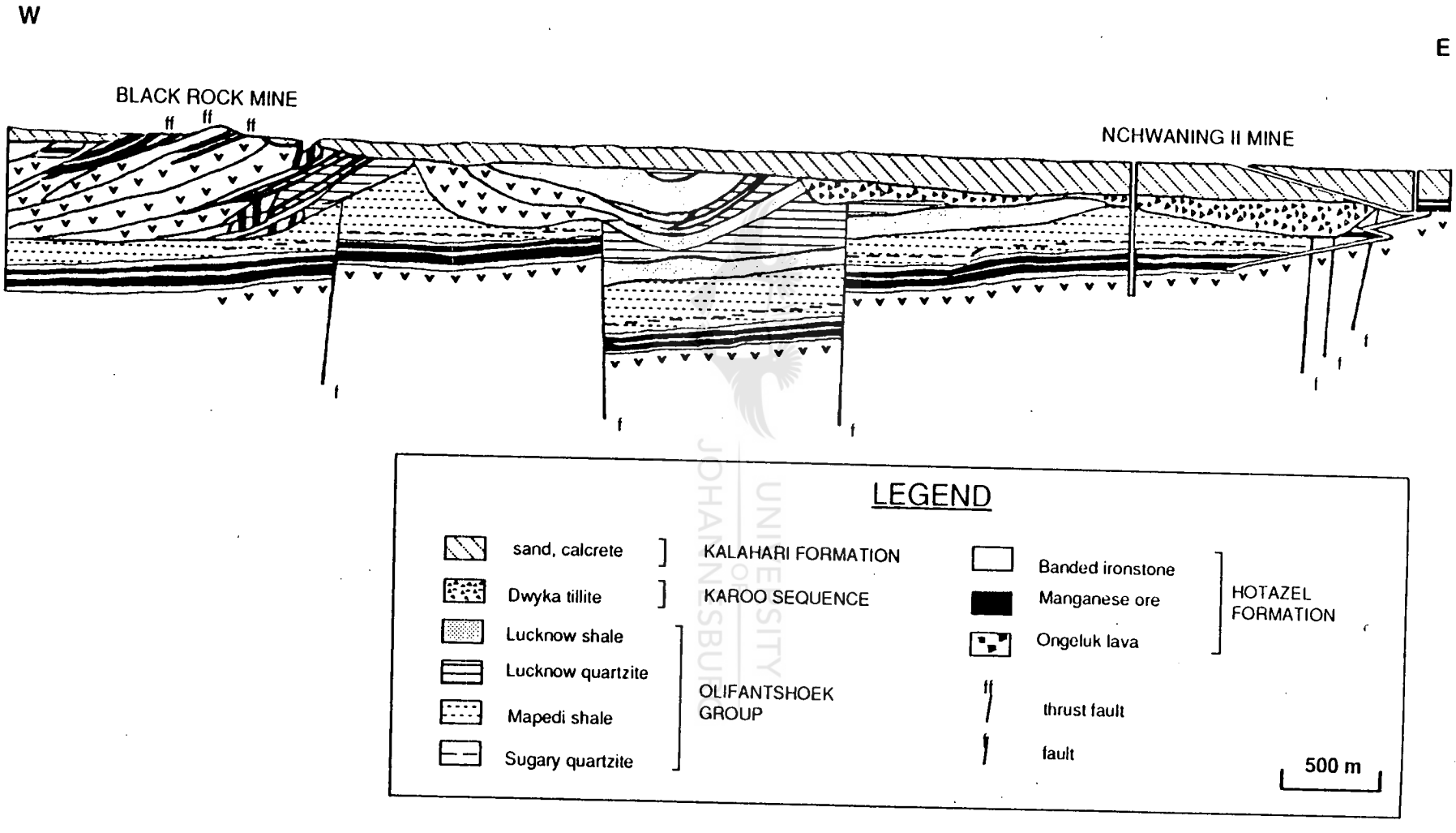

Fig. 1.6 Cross section through Black Rock and Nchwaning mines in the northwestern part of the Kalahari manganese field illustrating the displacement of the Proterozoic succession by normal faults and low-angle thrusting from the west (Blackridge thrust).

Two main ore types are present, namely low-grade primary sedimentary Mamatwan-type ore, with Mn contents of 20-38 mass %, and secondary high-grade Wessels-type ore containing 45-60 mass % Mn (Kleyenstüber, 1984). High-grade Wessels-type ore represents a hydrothermal alteration product of low-grade sedimentary Mamatwan-type ore (Kleyenstüber, 1984). Its occurrence is restricted to the faulted northwestern part of the deposit and it constitutes only about three percent of the known reserves (Taljaardt, 1982). Part of this high-grade reserve is not minable because of the presence of ferruginized zones around fault zones. The high-grade Wessels-type ore is composed predominantly of hausmannite, braunite II, bixbyite, and braunite. Many different gangue minerals occur, such as andradite, clinochlore, barite and sparitic calcite.

The Mamatwan-type ore is a finely laminated, microcrystalline braunite-lutite composed of Mn-bearing carbonates such as kutnahorite and Mn-calcite, braunite and hematite. Characteristic is the occurrence of abundant mm-sized carbonate ovoids and short, stratiform carbonate laminae that enhance the bedded appearance of the ore. Hausmannite and partridgeite, associated with Mn-poor calcite, are slightly more coarse crystalline and formed as metamorphic oxidation products of kutnahorite or Mn-calcite (Kleyenstüber, 1984, Nel et al., 1986). Kleyenstüber (1984) suggested that the Mamatwan-type ore has been subjected only to lower greenschist facies metamorphism.

UNIVERSITY OF JOHANNESBURG

Geological setting of the Postmasburg manganese field

The manganese and iron ore deposits of the Postmasburg manganese field are situated on the Maremane dome between Postmasburg in the south and Sishen in the north (Fig. 1.1B). The Maremane dome is defined by dolomites of the Campbellrand Subgroup and iron-formation of the Asbestos Hills Subgroup of the Transvaal Supergroup dipping gently at less than 10° in an arc to the north, east and south (Beukes, 1978). Only the eastern half of this dome is exposed (Fig. 1.7). To the west the Transvaal succession is overlain along the Mapedi/ Gamagara erosional unconformity by clastic red beds of the Mapedi/ Gamagara Formation of the Olifantshoek Group (Fig. 1.7). Further to the west, some rocks of the Transvaal Supergroup, including Koegas iron-formation, Makganyene diamictite, and andesitic Ongeluk lavas, are thrust over the Mapedi/ Gamagara Formation along the north-south striking, westerly dipping, low-angle Black Ridge thrust fault (Beukes and Smit, 1987).

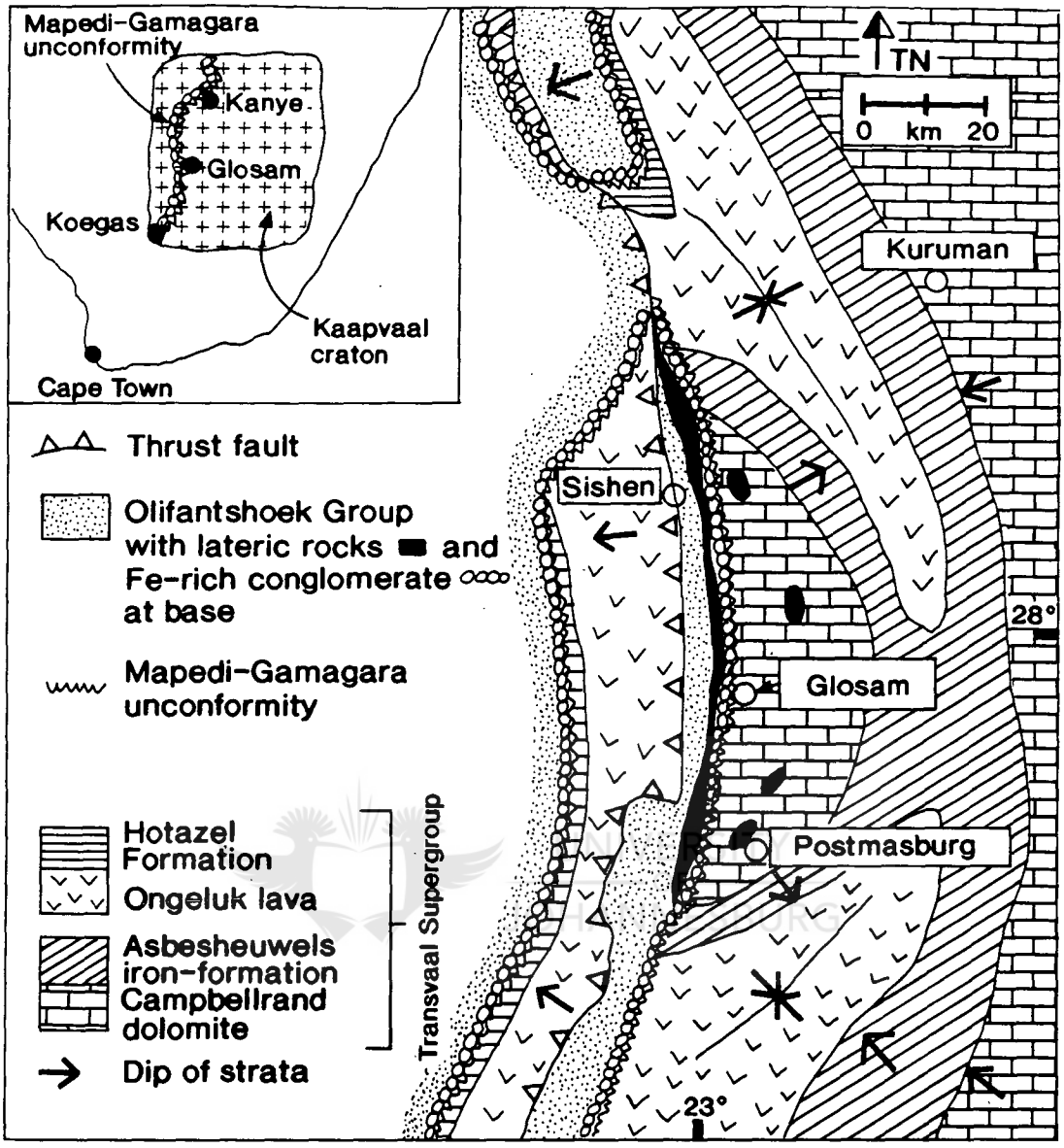

Fig. 1.7 Regional geological map of the Maremane dome showing the location of iron and manganese ore deposits in relation to the underlying dolomite of the Campbell Subgroup and the overlying sediments of the Gamagara Formation. Indicated is the position of thrust faults to the west of the Gamagara Ridge.

Iron and manganese ore deposits occur immediately below or above the Mapedi/ Gamagara unconformity where it separates karstified dolomite and iron-formations of the Transvaal Supergroup from overlying clastic sediments of the Mapedi/ Gamagara Formation (Fig. 1.8). Depressions and sinkholes in the paleokarst surface of the Campbellrand dolomites provided traps for the accumulation of manganese and iron ores and the rocks of the overlying Mapedi/ Gamagara Formation. Large deposits of high-grade iron ores, mined at Sishen and Beeshoek (Fig. 1.7), are composed of hematitic Manganore iron-formation and reworked conglomeratic

equivalents that form fluvial floodplain deposits at the base of the Mapedi/ Gamagara Formation (Van Schalkwyk and Beukes, 1986). Alteration (hematitization and desilification) and erosion of the Manganore Iron Formation is ascribed to a period of intensive chemical weathering prior to deposition of the Mapedi/ Gamagara Formation (Van Schalkwyk and Beukes, 1986; Strauss, 1964).Van Wyk (1980) and Van Wyk and Beukes (1982) showed that the Manganore Iron Formation is a lateral, intensively oxidized equivalent of the Kuruman and Griquatown Iron Formations of the Transvaal Supergroup, slumped into and preserved in large paleosinkholes and paleocaves.

Sinkholes filled with ferruginized Manganore iron formation are only known down into the Fairfield Member of the Campbellrand dolomite (Beukes, 1978). The unconformable contact between Manganore Iron Formation and the underlying dolomite is marked by the occurrence of manganiferous Wolhaarkop chert breccia. This chaotic residual breccia is composed of angular fragments of chert fragments derived from underlying cherty dolomite. The breccia hosts small high-grade braunite orebodies (Boardman, 1964) (Fig. 1.9A).The siliceous manganese ore of the Eastern Belt occurs only, where the ferruginized and desilicified Manganore iron-formation slumped into graben-like sinkhole structures which are aligned parallel to chert-rich dolomite units, belonging either to the Klippan or the Klipfontein Hill Formations of the of the Campbellrand Subgroup (Grobbelaar and Beukes, 1986) (Fig. 1.7). Minable orebodies are restricted to the basal part of the Wolhaarkop breccia (Boardman, 1964), especially well developed orebodies have been found in steep cul-de-sac structures in the karstic dolomite surface (De Villiers, 1958). Orebodies higher up in the Wolhaarkop breccia are smaller, less well

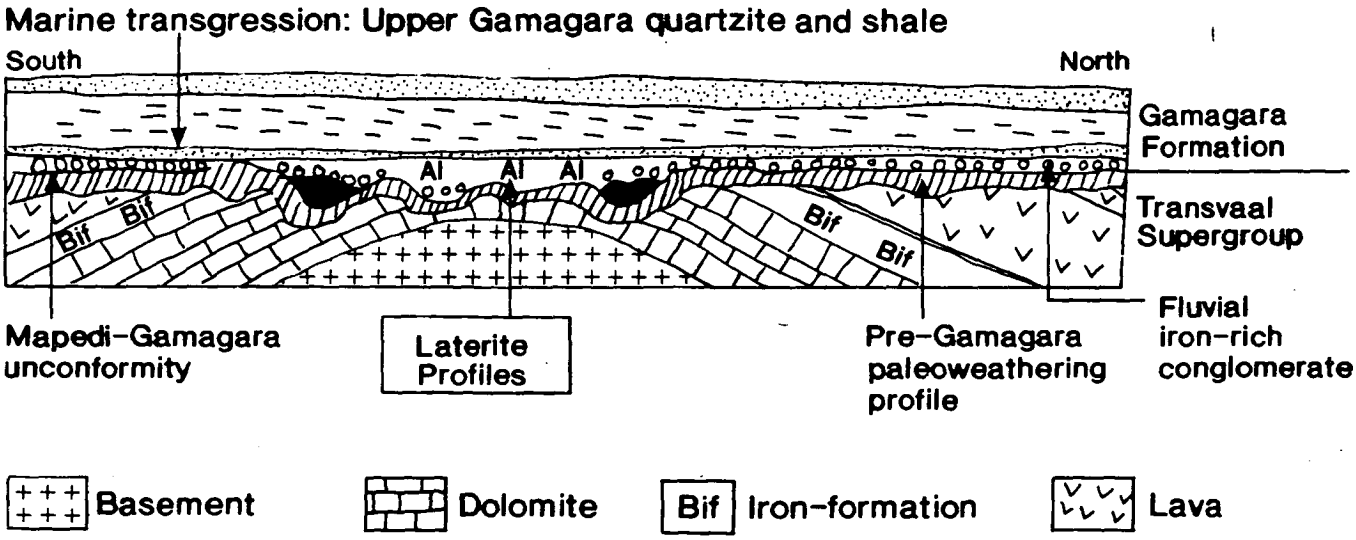

Fig. 1.8 Schematic cross section through the Maremane dome, showing the location of high-grade ore deposits of Manganore Iron Formation, manganese ores of the Eastern and Western Belt, and lateritic paleosols of the Gamagara Formation.

defined and of lower grade (Boardman, 1964), as the matrix of the surrounding breccia becomes gradually more ferruginous and siliceous towards the top. The exact distribution, size and shape of the orebodies is non-predictable; lenses, pods, and sheet-like bodies are predominantly composed of massive braunite. The size of individual orebodies ranges between a few and 5000 t (De Villiers, 1960). The ores are massive, fine to medium crystalline and dense.

A mixed ore-type, combining features of siliceous and ferruginous types of ore, has been described from the Aucampsrust area towards the SW of Postmasburg (Boardman, 1940; De Villiers, 1960; Plehwe-Leisen, 1985) and from the areas, where the Eastern and Western Belt merge e.g. from Rust-en-Vrede and King in the North (De Villiers, 1960), and Beeshoek and Doornfontein in the South of the Gamagara Ridge (Fig. 1.7).Thin, minable units of manganiferous shale and shaly braunite-rich orebodies occur that overly transitional ore type. Orebodies of the mixed type are generally small and irregular in shape (De Villiers, 1960), mining exposures of this ore-type are thus rather poor.

Along the central part of the Gamagara Ridge, the Mapedi/ Gamagara Formation comes to rest directly on manganese- and iron-rich but silica-poor dolomite of the Reivilo Formation (Figs. 1.7, 1.9B). Ferruginous manganese ore occurs in orebodies of highly irregular shape, confined by the intensively karstified floor of dolomite that has closely spaced, up to 20 m high pinnacles and deep solution cavities (Fig. 1.10). Medium to coarse crystalline ferruginous ore of massive to vuggy texture is composed of subhedral bixbyite idioblasts, associated with diaspore and ephesite. It is found in intergrown with fine to medium crystalline ore with abundant sedimentary structures. The interbedding of fine crystalline, shaly laminae with oxide-rich beds has been modified by epigenetic recrystallisation. The transition of the manganese orebody into the overlying clastic sediments of the Mapedi/ Gamagara Formation, either into a hematite pebble conglomerate or into lateritic Al-shales is generally rapid and conformable (Fig. 1.7B).

Thick accumulations of ferruginous ore in deep sinkholes are of secondary origin. Reactivation of the paleokarst during an erosional cycle post-dating the lithification and metamorphic alteration of the manganese ores led to slumping and brecciation of the manganese ore and the overlying Mapedi/ Gamagara sediments.

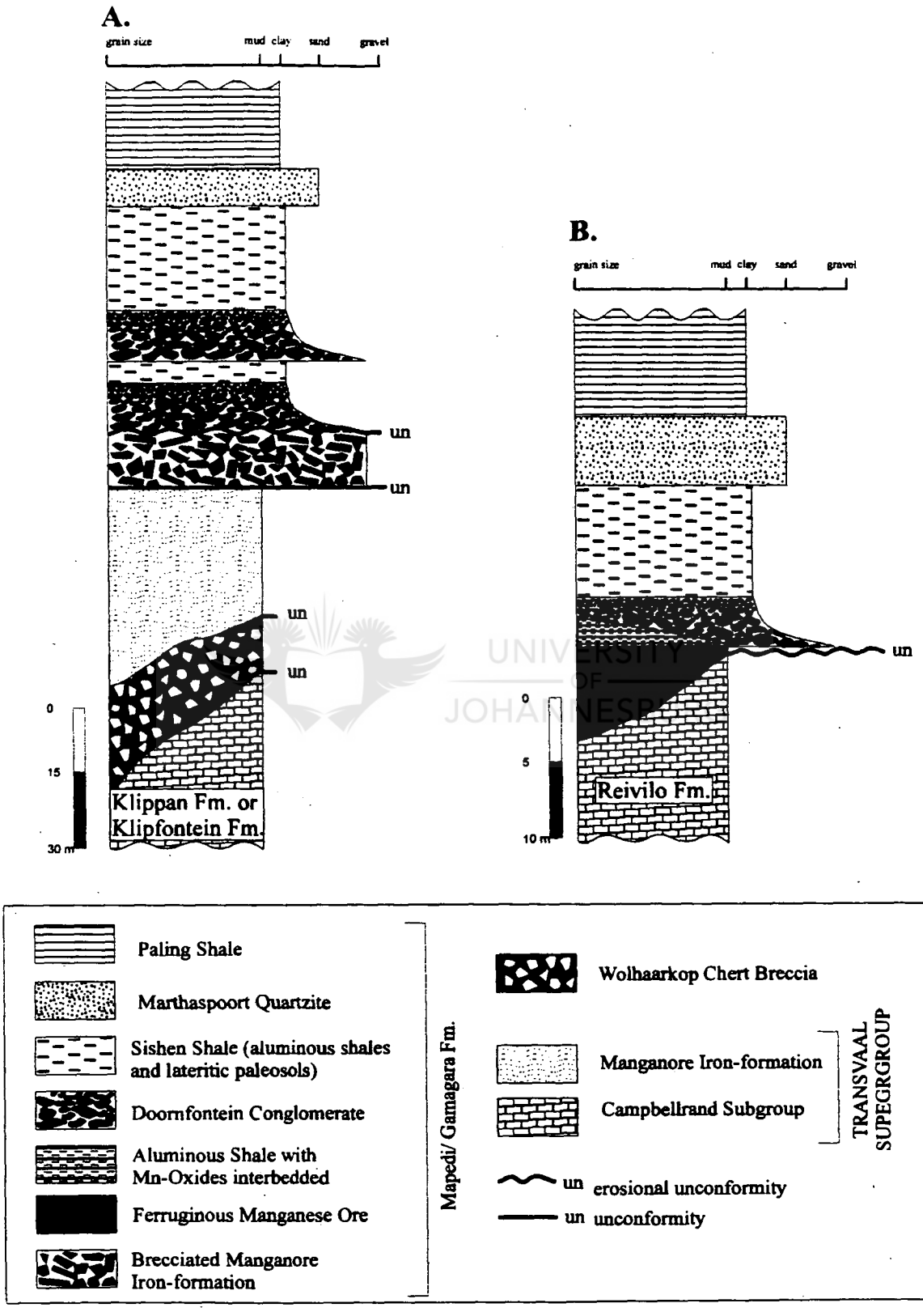

Figure 1.9 Stratigraphic columns illustrating the setting of the manganiferous Wolhaarkop Breccia (and associated siliceous manganese ore) (A) and of ferruginous manganese ore at the base of the Gamagara Formation (B).

Related to this event of renewed karstification is probably the formation of barite lenses surrounded by Ba-rich wad, pyrolusite nodules and botryoidal crusts and cauliflower aggregates of romanechite (Grobbelaar and Beukes, 1986) as well as the replacement of the metamorphic manganese oxides by romanechite.

The Doornfontein hematite pebble conglomerate at the base of the Mapedi/ Gamagara Formation (Fig. 1.9) fines upward into a laterally variable succession of siliciclastics, composed of black arbonaceous, white and red coloured shale or mudstone and occasionally interbedded chert pebble conglomerates. These shales, composed predominantly of pyrophyllite, diaspore, kaolinite, hematite, and minor illite, have been tentatively identified by Reimer (1986) as transported and redeposited lateritic soils. The aluminous Sishen Shale Member is overlain by the Marthaspoort Quartzite Member and red or cream-coloured illitic shales or siltstone of the Paling Shale Member of the Mapedi/ Gamagara Formation.

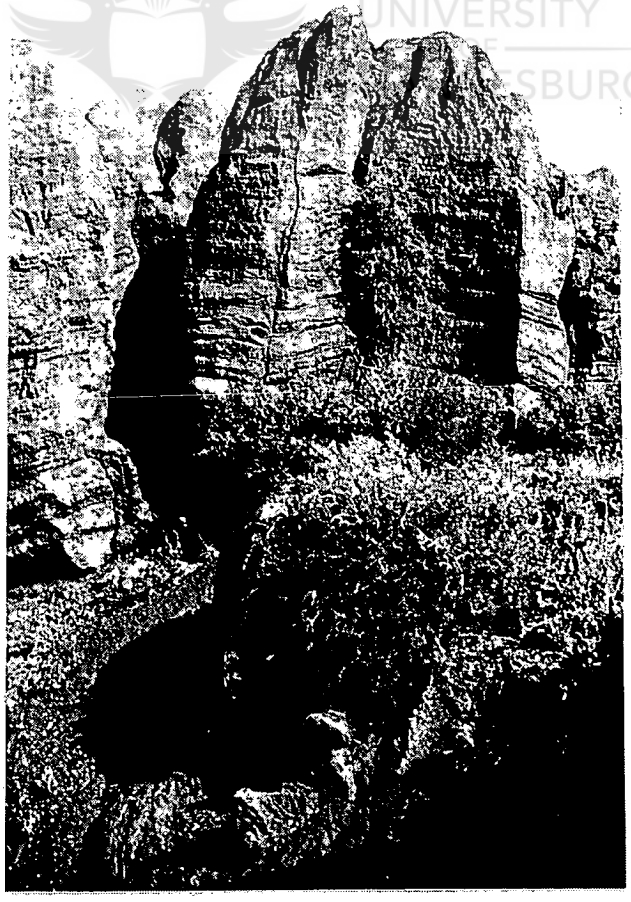

Fig. 1.10 Karst pinnacles exposed by mining operations at Glosam mine.

Strata of the Transvaal-Olifantshoek succession are only locally covered by clays, calcrete and eolian sands of the Cenozoic Kalahari Formation. Well rounded pebbles of manganese and iron ore form alluvial canga deposits along the slopes of the Gamagara Ridge and the Klipfontein Hills.

References

Armbruster, T., Oberhaensli, R., Bermanec, V., and Dixon, R.D. (1993). Hennomartinite and kornite, two new Mn^{3+}-rich silicates from the Wessels Mine, Kalahari, South Africa. Schweiz. Mineral. Petrog. Mit., 73, 349-355.

Armstrong, R.A. (1987). Geochronological studies on Archean and Proterozoic formations of the foreland of the Namaqualand front and possible correlates on the Kaapvaal craton. Unpubl. Ph.D. thesis , Univ. of the Witwatersrand, Johannesburg, 274 pp.

Barton, E.S., Altermann, W., Williams, I. S., and Smith, C.B. (1994). A U-Pb zircon age for a tuff in the Campbell Group, Griqualand West Sequence, South Africa: Implications for Early Proterozoic rock accumulation rates. Geology, 22, 343-346.

Beukes, N.J. (1978). Die Karbonaatgesteentes en Ysterformasies van die Ghaap-Groep van die Transvaal-Supergroup in Noord-Kaapland. Unpubl. Ph.D. thesis, RAU, 580 pp.

Beukes, N.J. (1983). Palaeoenvironmental setting of iron formations in the depositional basin of the Transvaal Supergroup, South Africa. In: Trendall, A.F., and Morris, R.C. (eds.). Iron formations, facts and problems, Elsevier, Amsterdam, 131-209.

Beukes, N.J. (1986). The Transvaal Sequence in Griqualand West. In: Annhaeusser C.R., Maske S., (eds.), Mineral deposits of Southern Africa. Geol. Soc. S. Afr., Johannesburg, 1, 819-828.

Beukes, N.J., Burger, A.M., and Gutzmer, J. (1995). Fault controlled hydrothermal alteration of Palaeoproterozoic manganese ore in Wessels mine, Kalahari manganese field. S. Afr. J. Geol., 98, 430-451.

Beukes, N.J., Kleyenstüber, A.S.E., and Nel, C.J. (1982). Volcanogenic-sedimentary cycles in the Kalahari manganese field. Sedimentology '82, Geol. Soc. S. Afr., Extended Abstracts, 93-97.

Beukes, N.J., and Smit, C. A., (1987). New evidence for thrust faulting in Griqualand West, South Africa: Implications for stratigraphy and the age of red beds. Trans. Geol. Soc. S. Afr., 90, 378-394.

Boardman, L.G. (1940). The geology of the manganese deposits on Aucampsrust, Postmasburg. Trans. Geol. Soc. S. Afr. , 43, 26-37.

Boardman, L.G. (1941). The Black Rock manganese deposit in the South Eastern Kalahari. Trans. Geol. Soc. S. Afr., 44, 51-60.

Boardman, L.G. (1961). Manganese in the Union of South Africa. 7th Commonwealth Min. Metal. Congress, S. Afr. Inst. Mining. Metal., Johannesburg, 1, 200-215.

Boardman, L.G. (1964). Further geological data on the Postmasburg and Kuruman manganese ore deposits, Northern Cape Province. In: Haughton, S.H.(ed.): Geology of some ore deposits in Southern Africa; Geol. Soc. S. Afr., Johannesburg, 415-440.

Borchert, H. (1970). On the ore-deposition and geochemistry of manganese. Mineral. Depos., 5, 300-314.

Burger, A.M. (1994). Fault controlled hydrothermal alteration of Palaeoproterozoic manganese ore in Wessels mine, Kalahari manganese field. Unpubl. MSc. thesis, RAU, Johannesburg, 138 pp.

Button, A. (1976). Transvaal and Hamersley basins - review of basin development and mineral deposits. Mineral Sci. Eng., 8, 262-293.

Chudoba, K. (1929). Über 'Mangandiaspor' und Manganophyll von Postmasburg (Griqualand West, Südafrika). Centralblatt Mineralogie etc., A, 11-18.

Coles-Phillips, F.C. (1931). Ephesite (soda-margarite) from the Postmasburg district, South Africa. Min. Mag., 22, 482-485.

Cornell, D.H., and Schütte, S.S. (1995). A volcanic-exhalative origin for the world's largest (Kalahari)-manganese field. Mineral. Depos., 30, 146-151.

Dai, Y., and Harlow, G.E. (1992). Description and crystal structure of Vonbezingite, a new Ca-Cu-SO_4-H_2O mineral from the Kalahari manganese field, South Africa. Amer. Mineral., 77, 1292-1300.

Dai, Y., Harlow, G.E., McGhie, A.R. (1993). Poldervaartite, $Ca(Ca_{0.5}Mn_{0.5})(SiO_3OH)(OH)$, a new acid nesosilicate from the Kalahari manganese field, South Africa: Crystal structure and description. Amer. Mineral., 78, 1082-1087.

De Villiers, J. (1956). The manganese deposits of the Union of South Africa. Int. Geol. Congr., Mexico, 34-72.

De Villiers, J. (1960). Manganese deposits of the Union of South Africa. Handbook 2, Geol. Surv. S. Afr., Pretoria, 280 pp.

De Villiers, J.E. (1943a). A preliminary description of the new mineral partridgeite. Amer. Mineral., 28, 336-338.

De Villiers, J.E. (1943b). Gamagarite, a new vanadium mineral from the Postmasburg manganese deposits. Amer. Mineral., 28, 329-335.

De Villiers, J.E. (1944). The origin of the iron and manganese deposits in the Postmasburg and Thabazimbi areas. Trans. Geol. Soc. S. Afr., 47, 123-135.

De Villiers, J.E. (1945a). Some minerals occurring in South African manganese deposits. Trans. Geol. Soc. S. Afr., 48, 17-25.

De Villiers, J.E. (1945b). Lithiophorite from the Postmasburg manganese deposits. Amer. Mineral., 30, 629-634.

De Villiers, J.E. (1983). The manganese deposits of Griqualand West, South Africa: Some mineralogic aspects. Econ. Geol., 78, 1108-1118.

De Villiers, J.E. (1986). The mineralogy of the manganese bearing Hotazel Formation of the Proterozoic Transvaal Sequence in Griqualand West, South Africa. - Discussion of a paper by A. S. E. Kleyenstüber (and reply of author). Trans. Geol. Soc. S. Afr., 89, 421-425.

UNIVERSITY OF JOHANNESBURG

De Villiers, J.E. (1992). On the origin of the Griqualand West manganese and iron deposits. S. Afr. J. Sci., 88, 12-15.

De Villiers, J.P.R. (1980). The crystal structure of braunite II and its relation to bixbyite and braunite. Amer. Mineral., 65, 756-765.

De Villiers, P.R., and Herbstein, F.H. (1967). Distinction between two members of the braunit group. Amer. Mineral., 52, 20-30.

De Villiers, P.R. (1970). The geology and mineralogy of the Kalahari manganese-field north of Sishen, Cape Province. Geol. Surv. S. Afr., Memoir 59, Pretoria, 84 pp.

Dixon, R.D. (1985). Sugilite and associated minerals from Wessels mine, Kalahari manganese field. Trans. Geol. Soc. S. Afr., 88, 11-17.

Dixon, R. D. (1989). Sugilite and associated metamorphic silicate minerals from Wessels mine, Kalahari manganese field. Geol. Surv. S. Afr., Bulletin 93, Pretoria, 47 pp.

Du Toit, A.L. (1933). The manganese deposits of Postmasburg, South Africa. Econ. Geol., 28, 95-122.

Frankel, J.J. (1958). Manganese ores from the Kuruman district, Cape Province, South Africa. Econ. Geol., 53, 577-597.

Giester, G., and Rieck, B. (1994). Effenbergerite, $BaCu[Si_4O_{10}]$, a new mineral from the Kalahari manganese field, South Africa: description and crystal structure. Min. Mag., 58, 663-670.

Grobbelaar, W.S. (1985). The Nchwaning manganese mine of the Kalahari manganese field. Geobulletin, Geol. Soc. S. Afr., 31, 34-35.

Grobbelaar, W.S., Burger, M.A., Pretorius, A.I., Marais, W., and van Niekerk, I.J.M. (1995). Stratigraphic and structural setting of the Griqualand West ant the Olifantshoek Sequences at Black Rock, Beeshoek and Rooinekke mines, Griqualand West, South Africa. Mineral. Depos., 30, 152-161.

Grobbelaar, W.S., and Beukes, N.J. (1986). The Bishop and Glosam manganese mines and Beeshoek iron ore mine of the Postmasburg area. In: Annhaeusser, C.R., and Maske, S. (eds.): Mineral deposits of Southern Africa; Geol. Soc. S. Afr., Johannesburg, 957-961.

Gutzmer, J. (1993). Hydrothermale Alteration von Manganerzen der Nchwaning-Mine, Kalahari-Manganerzfeld, Südafrika. Unpubl. Diplom thesis, Technische Universität Clausthal, 161 pp.

Gutzmer, J., and Beukes, N.J. (1995). Hydrothermal alteration and ferruginization of sedimentary manganese ore at the Nchwaning mine, Kalahari manganese field, Early Proterozoic Transvaal Supergroup, South Africa. Econ. Geol., 90, 823-844.

Gutzmer, J., and Kleyenstüber, A.S.E., Beukes, N.J. & Burger, A.M. (1995). Magnetic hausmannite from hydrothermally altered manganese ore in the Palaeoproterozoic Kalahari manganese deposit, Transvaal Supergroup, South Africa. Min. Mag., 59, 703 - 716.

Gruner, J.W. (1943). Massive bixbyite $(Mn,Fe)_2O_3$ of low iron content. Amer. Mineral., 28, 174.

UNIVERSITY OF JOHANNESBURG

Hall, A.L. (1926). The manganese deposits near Postmasburg, West of Kimberley, Trans. Geol. Soc. S. Afr., 29, 17-66.

Jansen, E. (1983). Die Stratigrafie en Sedimentologie van die Volop-Groep, Olifantshoekopeenvolging. Unpubl. MSc. Thesis, RAU, 138 pp.

Jennings, M. (1986). The Middelplaats manganese ore deposit, Griqualand West. In: Annhaeusser, C.R., Maske, S., (eds.), Mineral deposits of Southern Africa. Geol. Soc. S. Afr., Johannesburg, 1, 979-983.

Kaiser, E. (1927). Report on South African manganese company. S. Afr. Min. Eng. J., 1884, 235-236.

Kaiser, E. (1931). Zur Entstehung der Manganerzlagerstätten von Postmasburg in Griqualand West, Südafrika. N. Jb. Mineral., Beilagen Band 64a, 727-737.

Kleyenstüber , A. S. E. (1984). The mineralogy of the manganese bearing Hotazel Formation of the Proterozoic Transvaal Sequence in Griqualand West, South Africa. Trans. Geol. Soc. S. Afr., 87, 257-272.

Kleyenstüber , A. S. E. (1985). A regional mineralogical study of the manganese bearing Voëlwater Subgroup in the northern Cape Province. Unpubl. PhD thesis, RAU, Johannesburg, 328 pp.

Kleyenstüber A.S.E. (1993). Some significant characteristics of the manganese ores and some of the minerals occurring in the Proterozoic Kalahari maganese field, South Africa. Resource Geology,17, 2-11.

Kupferburger, W., Boardman, L.G., Bosch, P.R. (1956). New considerations concerning the manganese ore deposits in the Postmasburg and Kuruman areas, Northern Cape Province, Union of South Africa. Int. Geol. Congr., Mexico, 2, 73-87.

Laznicka, P. (1992). Manganese deposits in the global lithogenetic system: Quantitative approach. Ore Geol. Rev., 7, 279-356.

Leisen, H. (1987). Geologisch-tektonische Kartierung der Griqualand West und Olifantshoek Sequenzen in der nördlichen Kapprovinz, Republik Südafika, auf der Grundlage von LANDSAT-MSS-daten und terrestrisch-photogrammetrischen Aufnahmen. Unpubl. thesis, Ludwig-Maximilians Univ. München, 118 pp.

Miyano, T., and Beukes, N.J. (1987). Physicochemical environments for the formation of quartz-free manganese oxide ores from the Early Proterozoic Hotazel Formation, Kalahari manganese field, South Africa. Econ. Geol., 82, 706-718.

Miyano, T., and Beukes, N.J. (1988). Estimation of carbon dioxide fugacity and braunite II stability in quartz-free manganese oxide ores from the Kalahari manganese field, South Africa. S. Afr. J. Sci., 84, 244-246.

Nel, C.J. (1984). Die mineralogie en geochemie van die Mamatwanertsliggam, Kalaharimangaanveld, Transvaal-Supergroup. Unpubl. MSc. thesis, RAU, 119 pp.

Nel C.J., Beukes N.J., De Villiers J.P.R. (1986). The Mamatwan manganese mine of the Kalahari manganese field. In: Annhaeusser, C.R., Maske, S., (eds.), Mineral deposits of Southern Africa. Geol. Soc. S. Afr., Johannesburg, 1, 963-978.

Nel, L.T. (1929). The geology of the Postmasburg manganese deposits and the surrounding country. Explanation of the geological map. Geol. Surv. S. Afr., Pretoria, 109 pp.

UNIVERSITY OF JOHANNESBURG

Nel, L.T. (1930). A new occurrence of zunyite near Postmasburg, South Africa. Min. Mag., 22, 132-135.

Nyfeler, D., Armbruster, T., Dixon, R.D., and Bermanec, V. (1995). Nchwaningite, $Mn^{2+}_2SiO_3(OH)_2*H_2O$, a new pyroxene-related chain silicate from the Nchwaning mine, Kalahari manganese field, South Africa. Amer. Mineral., 80, 377-386.

Peacor, D.R., Dunn, P.J., and Duggan, M. (1983). Sturmanite, a ferric iron, boron analogue of ettringite. Can. Mineral., 21, 705-709.

Peacor, D.R., Dunn, P.J., and Nelen, J.A. (1990). Orlymanite, $Ca_4Mn_3Si_8O_{20}(OH)_6*2H_2O$, a new mineral from South Africa: A link between gyrolite-family and concentional phyllosilicate minerals ? Amer. Mineral., 75, 923-927.

Plehwe-Leisen, E. von (1985). Geologische und erzpetrographische Untersuchungen der Manganerze des Postmasburgfeldes, Noerdliche Kapprovinz, Südafrika. Unpubl. thesis, Ludwig-Maximilians Univ. München, 129 pp.

Reimer, T.O. (1986). Alumina-rich rocks from the Early Precambrian of the Kaapvaal Craton as indicators of paleosols and as products of other decompositional reactions. Prec. Res., 32, 155-179.

Richter, M. (1933). Geologie der Umgebung von Postmasburg (Westgriqualand) in Südafrika. N. Jb. Mineral., Beilagen Band 69B, 397-449.

Rogers, A.W. (1905). Geological Surveys of parts of Hay and Prieska: Annual rep. geol. Comm. Cape of Good Hope.

Rogers, A.W. (1906). Geological Survey of parts of Bechuanaland and Griqualand West. Annual rep. Comm. Cape of Good Hope.

Rogers, A.W. (1907). Geological Survey of parts of Vryburg, Kuruman, Hay and Gordonia. Annual rep. Comm. Cape of Good Hope.

SACS (1980). Stratigraphy of South Africa. Geol. Surv.S.Afr., Pretoria, 690 pp.

Schalkwyk, J.F. van, and Beukes, N.J.(1986). The Sishen iron ore deposit, Griqualand West. In: Annhaeusser, C.R. and Maske, S. (eds.): Mineral deposits of Southern Africa; Geol. Soc. S. Afr., Johannesburg, 931-956.

Schneiderhöhn, H. (1931). Mineralbestand und Gefüge der Manganerze von Postmasburg, Griqualand West, Südafrika, N. Jb. Mineral., Beilagen Band 64 A, 701-726.

Schütte, S.S. (1992). Ongeluk volcanism in relation to the Kalahar Mn-deposits. Unpubl. PhD. thesis, Natal Univ., 262 pp.

Söhnge, P.G. (1977). Timing aspects of the manganese deposits of the Northern Cape Province (South Africa). In: Klemm, D.D., and Schneider, H.J. (eds.): Time and strata-bound ore deposits. 115-122.

Stow, G.W. (1874). Geological notes upon Griqualand West. Quarterly Journal of the Geological Society, London, 30.

Stowe, C. W. (1986). Synthesis and interpretation of structures along the north-eastern boundary of the Namaqua tectonic province, South Africa. Trans. Geol. Soc. S. Afr., 89, 185-198.

UNIVERSITY OF JOHANNESBURG

Strauss, C.A. (1964). The iron ore deposits in the Sishen area, Cape Province. In: Haughton, S.H. (ed.): The geology of some ore deposits in Southern Africa. Geol. Soc. S. Afr., Johannesburg, 393-403.

Sumner, D.Y. (1995). Facies, paleogeography, and carbonate precipitation on the Archean (2520 Ma) Campbellrand-Malmani Platform, Transvaal Supergroup, South Africa. Unpubl. PhD. thesis, MIT, 514 pp.

Taljaardt, J.J. (1982). Major manganese ore fields, Republic of South Africa. Unpubl. report, SAMANCOR, Johannesburg, 7 pp.

Thomas, R.J., Agenbacht, A.L.D., Cornell, D.H., and Moore, J.M. (1994a). The Kibaran of southern Africa: Tectonic evolution and metallogeny. Ore Geol. Rev., 9, 131-160.

Thomas, R.J., Cornell, D.H., Moore, J.M., and Jacobs, J. (1994). Crustal evolution of the Namaqua-Natal metamorphic province, Southern Africa. S.Afr. J. Geol., 97, 8-14.

Trendall, A.F., and 11 others (1990). Precise zircon U-Pb chronological comparison of the volcano-sedimentary sequences of the Kaapvaal and Pilbara cratons between about 3.1 and 2.4 Ga. 3'rd International Archean Symposium, Perth, Australia, Extended Abstracts, 81-83.

Truter, F.C., Wasserstein, B., Botha, P.R., Visser, D.J.L., Boardman, L.G., and Paver, G.L.(1938). The geology and mineral deposits of the Olifantshoek area, Cape Province. An explanation to Sheet No. 174 Oliphants Hoek. Geol. Surv. S. Afr., Pretoria, 107 pp.

Van Wyk, J.P.(1980). Die geologie van die gebied Rooinekke-Matsap-Wolhaarkop in Noord-Kaapland met spesiale verwysing na die Koegas -Subgroep, Transvaal-Supergroep. Unpubl. MSc. thesis, RAU, 159 pp.

Van Wyk, and Beukes, N.J. (1982). The geology of the Sishen iron ore deposit. In: Glen, H.W. (ed.): Proceedings, 12th CMMI Congress. Geol. Soc. S. Afr., Johannesburg, 203-211.

Visser, D.J.L. (1944). Stratigraphic features and tectonics of portions of Bechuanaland and Griqualand West. Trans. Geol. Soc. S. Afr., 47, 61-74.

UNIVERSITY OF JOHANNESBURG

Chapter Two

Metasomatic and supergene alteration of Early Proterozoic sedimentary manganese ore at Mamatwan Mine, Kalahari manganese field, South Africa

Abstract

The Kalahari manganese field is situated some 60 km northwest of Kuruman in the Northern Cape Province. It is the largest known land-based manganese deposit. Low-grade sedimentary Mamatwan-type ore (containing up to 38 mass % Mn) dominates and constitutes about 97 % of the ore reserves estimated of approximately 13500 Mt. The ore is composed of finely intergrown braunite and Mn-rich carbonates such as kutnahorite and Mn-calcite. Four distinct alteration events which affected the braunite lutite since its deposition can be observed at Mamatwan mine. Relative age relationships between these events are established, but the absolute timing of the events remains unknown. These four alteration events are: a) Low-grade metamorphism associated with metasomatism along specific stratigraphic horizons within the orebody; b) Reduction of ore along veins and joints with hematite-calcite-sulphide mineralization caused by epithermal fluids; c) Intensive brecciation along faults associated with the introduction of groundwater-related fluids; d) Supergene weathering along the suboutcrop of the orebody beneath the Kalahari unconformity by descending meteoric fluids.

Introduction

The Early Proterozoic (2300-2100 Ma) Kalahari manganese field, situated 60 km to the northwest of Kuruman in the Northern Cape Province, contains two major types of manganese ore, namely primary low-grade sedimentary Mamatwan-type ore and high-grade hydrothermally altered Wessels-type ore (Kleyenstüber, 1984, 1985; Nel et al., 1986). Transformation of Mamatwan-type ore to Wessels-type ore by infiltration by hydrothermal fluids took place along a system of mainly north-south striking normal faults in the northwestern part of the Kalahari manganese field (Fig. 2.1). This process of alteration has been well documented and involves ferruginization of manganese ores along fault zones and transformation of carbonate-rich

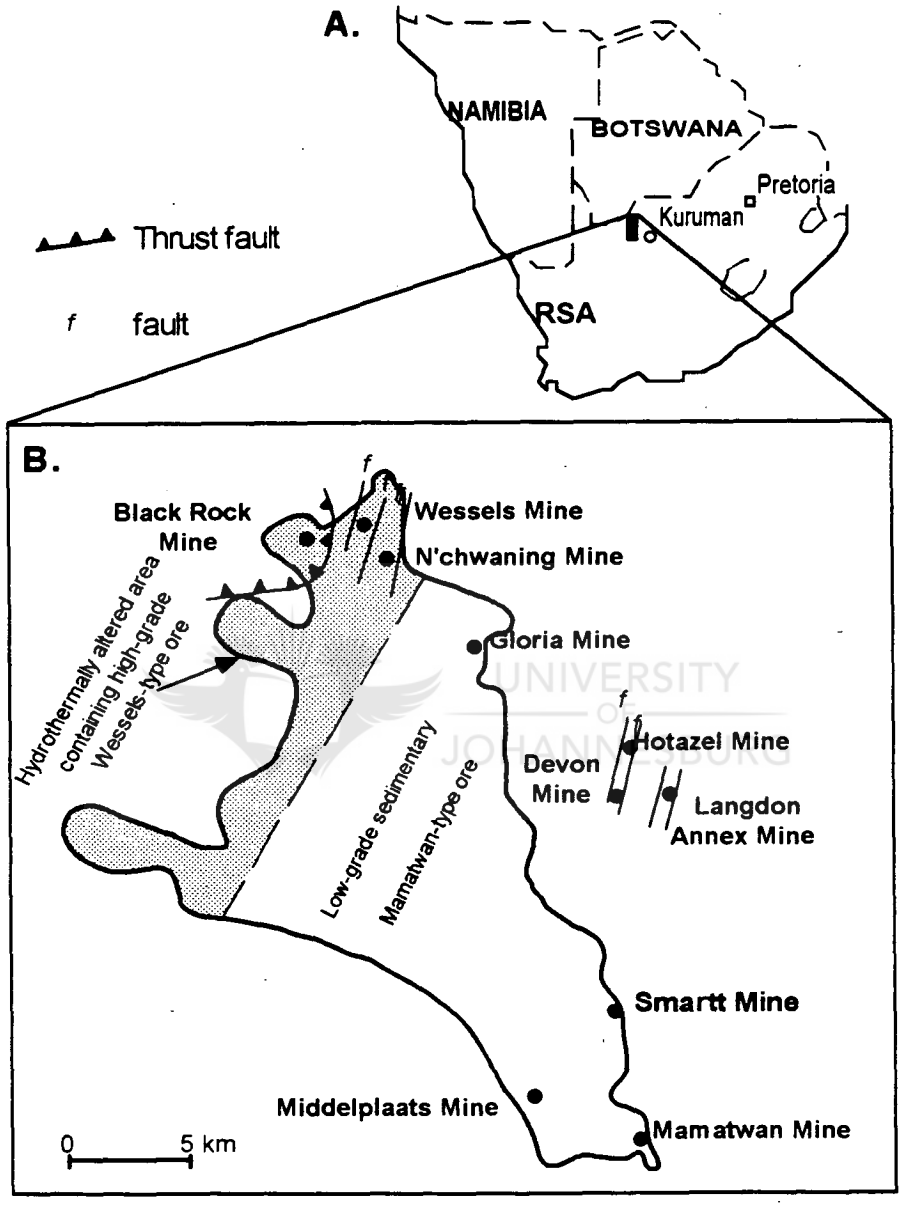

Fig. 2.1 Locality map of the Kalahari manganese field (A) showing the distribution of thrusting, major normal faulting, ore-types and location of mines (B).

braunite-kutnahorite Mamatwan-type ore into carbonate-poor high-grade ore rich in hausmannite, braunite II, bixbyite and gangue minerals such as andradite and clinochlore alongside faults (Gutzmer and Beukes, 1995; Beukes et al., 1995). In contrast to Wessels-type ore, the Mamatwan-type ore is virtually unaltered displaying excellent preservation of primary sedimentary and diagenetic features.

However, at Mamatwan mine the manganese ore bed has been displaced by two east-west striking normal faults and alteration of the ore took place in the fault zones and immediately adjacent to them. The ore has also locally been affected by alteration alongside a set of widely spaced joints transecting the ore bed. Nel et al. (1986) give a detailed account of the geology of Mamatwan mine and the petrography and geochemistry of the orebody. However, the alteration along faults and joint has not been described in any detail. It is the purpose of this paper to document this alteration and to compare it with that of the major Wessels hydrothermal alteration event (Gutzmer and Beukes, 1996) in the northwestern part of the Kalahari manganese field.

At Mamatwan mine the ore bed is unconformably overlain by calcretized sediments of the Cenozoic Kalahari Formation. Supergene alteration of the ore bed took place below this unconformity and the nature of this alteration is described here; especially because ground water apparently preferentially infiltrated the two faults causing supergene alteration to at least 30 m below the unconformity.

UNIVERSITY OF JOHANNESBURG

Geological setting

The open pit Mamatwan manganese mine is situated at the southernmost tip of the Kalahari deposit (Fig. 2.1). Only the lower part of the Hotazel Formation, up to the top of the lower manganese ore bed is preserved at Mamatwan below the unconformity at the base of the Kalahari Formation (Fig. 2.2). This lower manganese ore bed reaches a thickness of 45.2 m within the mine lease area (Fig. 2.2) and was subdivided into eleven texturally, mineralogically and chemically distinct zones by Nel et al. (1986) (Fig. 2.2).

Two normal faults displace the ore bed at Mamatwan. These faults are present in the central part of the mine and strike almost E - W (Fig. 2.3). The southern fault has a displacement of 2 m to the south. The ore bed is discoloured red by hematite alongside the fault making it uneconomic to mine. The northern of the two faults has a displacement of 4.5 m and intensive brecciation is observed in its central part. It is this fault that was sampled for this study. Samples were taken at two levels across the fault in faces of the bottom cut (traverse L1) and middle cut (traverse L2) (Fig. 2.3) in ore zones H and M respectively (Fig. 2.3).

In addition to alteration along the fault, white and red zones of discolouration are observed around widely spaced joints, which strike preferentially parallel or perpendicular to the major

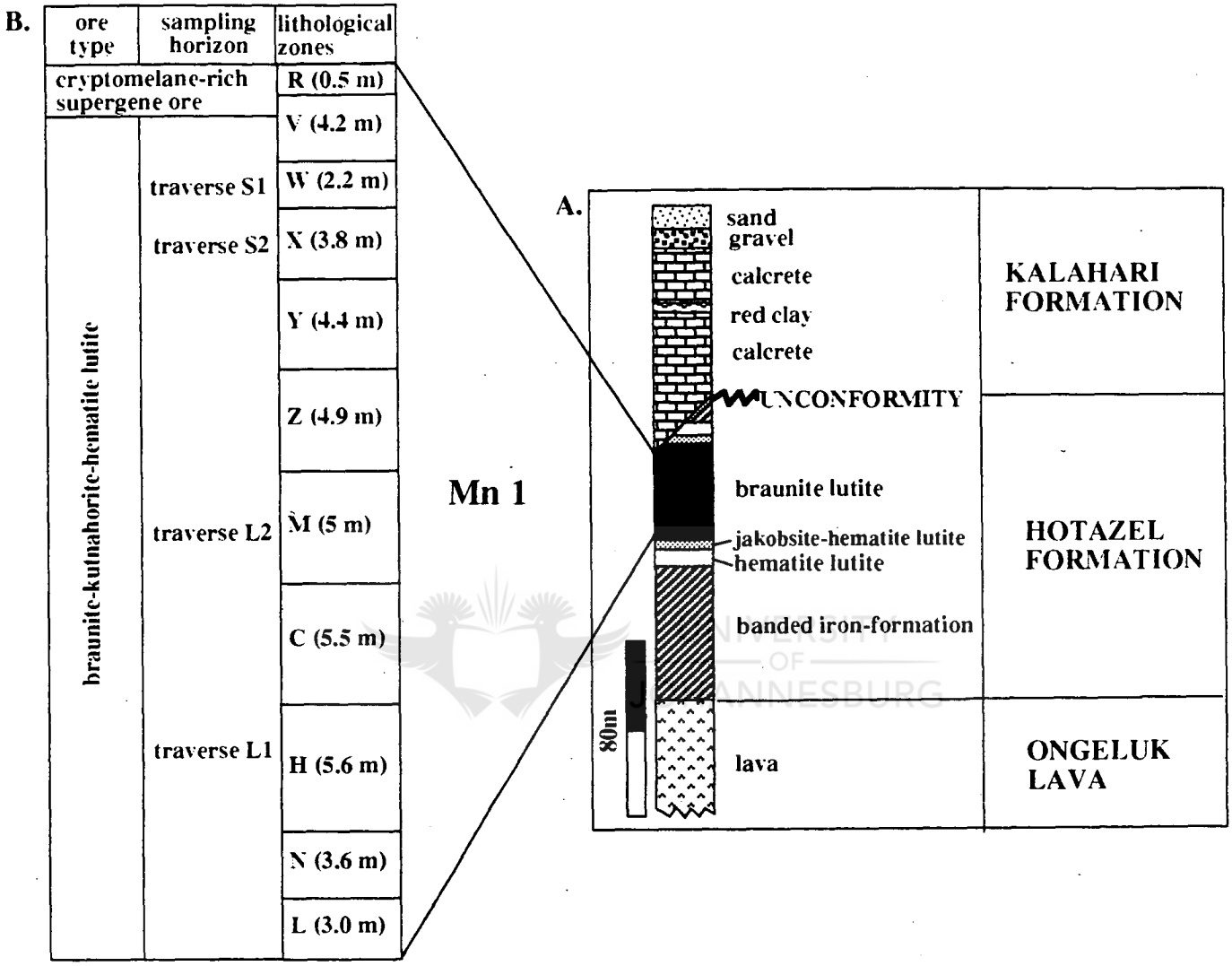

Fig. 2.2 Stratigraphic succession at Mamatwan mine (A) and the subdivision of the orebody into lithological zones (B). The approximate stratigraphic positions of the traverses L1, L2, S1 and S2 are indicated.

fault zones (Fig. 2.3). A detailed study of the alteration along joints was conducted on a set of samples traversing a ferruginized joint in the northwestern corner of the open pit (traverse S1) in the face of the upper cut (Fig. 2.3) in ore zone W. This veinlet, dipping 75 °S, strikes approximately parallel to the normal faults. A 30 cm wide vein hosted by a WNW-ESE striking joint was exposed by mining activities in November 1995. Results of mineralogical studies around this vein in zone X of the orebody are included in this paper traverse S2).

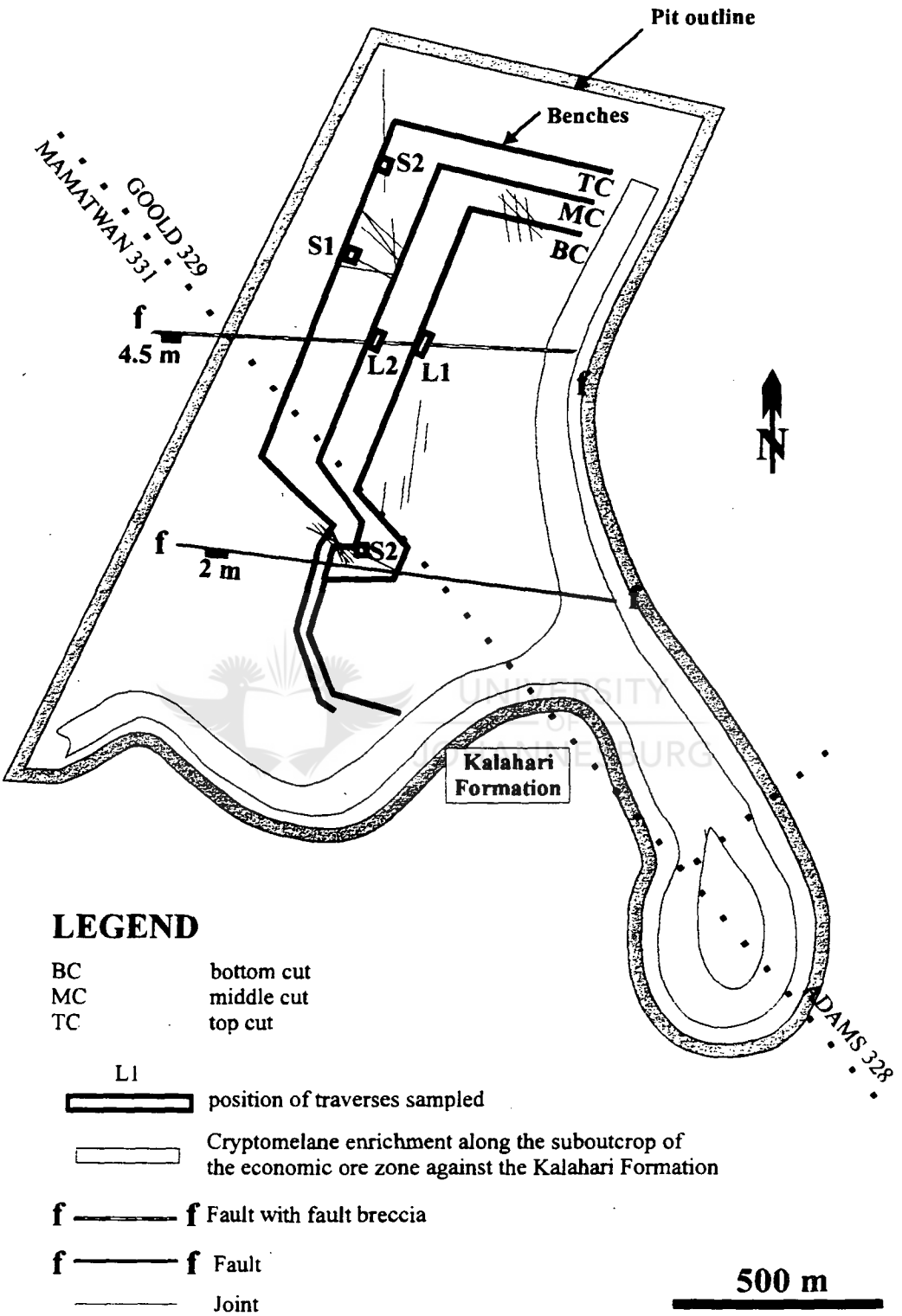

Fig. 2.3 Map of the outline of the Mamatwan open pit and its position in relation to the suboutcrop of the Hotazel Formation against the Kalahari unconformity. Faults and areas of intensive jointing are marked and the locations of the traverses L1, L2, S1 and S2 are indicated.

Supergene alteration of the ore bed below the Kalahari unconformity is characterized by the development of cryptomelane (Nel et al., 1986, Kleyenstüber, 1993) (Figs. 2 and 3). Calcrete-filled fractures, cementing a breccia of weathered ore fragments and aggregates of botryoidal cryptomelane, occur along the suboutcrop of the orebody. Along the faults, truncated by the Kalahari unconformity, this supergene alteration has penetrated the ore bed much deeper than the usual 5 m described by Kleyenstüber (1993).

Analytical techniques

All samples were subjected to X-ray powder diffraction, followed by petrographic studies in reflected light on polished thin sections. X-ray powder diffraction was carried out on a Philips PW 1710 based automated diffractometre with a vertical PW 1050 vertical goniometre. FeK_{α}-radiation (wavelength 1.937 Å) at 40 kV and 40 mA. Patterns were acquired in the range of 5° to 90° 2Θ at a scan speed of 50 sec/ 1° and a step width of 0.02 °. Semiautomatic phase identification was based on the Philips PC-APD 3.6 software.

UNIVERSITY OF JOHANNESBURG

EDS-electron microprobe analysis of phase compositions was performed on a Camebax 355 microprobe with an attached Link EDS spectrometre. Analysis were carried out at 15 kV acceleration voltage and 10 nA adsorbed current (on brass).

A selected set of samples was analysed by XRF on a Philips 1480 X-ray spectrometre on pressed powder pellets. The total carbon content was analysed by coulometric titration with a Stroehlein Coulomat. Loss on ignition determinations were carried out in air at 1100 °C, H_2O^- determinations at 110 °C in air, following the descriptions by Heinrichs and Herrmann (1990). All chemical analyses were carried out at the Institut für Mineralogie und mineralische Rohstoffe at the Technische Universität Clausthal (Germany).

Stable isotopes $\delta^{18}O$ and δ^{3} C of carbonates were determined at the Department of Earth Sciences, Academia Sinica, Taiwan, on a VG SIRA-10 mass spectrometre. Whole rock samples and mineral separates were reacted at 50 °C with anhydrous phosphoric acid. Reaction times ranged between 30 minutes for calcite to up to 5 hours for Mn-rich carbonates. Kutnahorite and calcite were analysed separately in whole-rock samples by selective dissolution using diluted phosphoric acid.

Lateral macroscopic zonation in ore composition

Unaltered Mamatwan-type ore is represented by microcrystalline, grey to brownish-grey, finely laminated braunite lutite. Lamination is accentuated by the presence of elongated, white, red and pink, somewhat coarser-grained carbonate laminae and millimetre-sized, early diagenetic carbonate ovoids of brown and white colour. This ore is affected by four phases of epigenetic alteration, namely:

a) Low-grade regional metamorphism expressed by bedding-parallel metasomatic alteration of kutnahorite and Mn-calcite laminae and ovoids to coarse crystalline hausmannite with submetallic lustre (Fig. 2.4A). The metasomatic alteration predates the alteration that took place along faults and joints.

b) Discolouration and reduction of manganese ore in association with pyrite-carbonate veins (Fig's. 2.4B, 2.4C).

c) Brecciation and veining in reactivated fault zones with associated sparitic calcite-dolomite mineralization and oxidation of the surrounding manganese ore (Fig's 4D, 4E, 4F).

d) Supergene alteration characterized by goethite formation in faults and calcretization along the Kalahari unconformity.

Alteration along faults

The two traverses (L1 and L2) that were sampled across the fault in the central part of the mine (Fig. 2.3) display very similar lateral macroscopic zonation. Macroscopically least altered ore in traverse L1 is only present in sample MMT-111 (Fig. 2.5A). The dark grey ore is characterized by fine, lenticular lamination with abundant greyish-white carbonate ovoids and up to 5 mm thick reddish-white carbonate layers. Coarse recrystallised Mn-oxides replace some of the carbonate ovoids. In traverse L2 (samples 91 and 110) (Fig. 2.5B) least altered ore is represented by finely laminated grey braunite lutite with brownish coloured carbonate laminae and ovoids. Ovoids and carbonate layers are in many cases partially replaced by coarse hausmannite.

Dusty clouds of earthy, greenish-brown or dark grey manganese oxides are the first visible indications of alteration, appearing in both sections as much as 15 to 18 m away from the fault zone. These earthy oxides (manganomelane, todorokite) occur preferentially along carbonate laminae and in ovoids close to microfractures (samples MMT-92 and 105-109 in L2, MMT-112,

124 and 125 in L1). The amount of earthy material increases gradually, forming discrete seams, until the matrix of original Mamatwan-type ore is completely replaced.

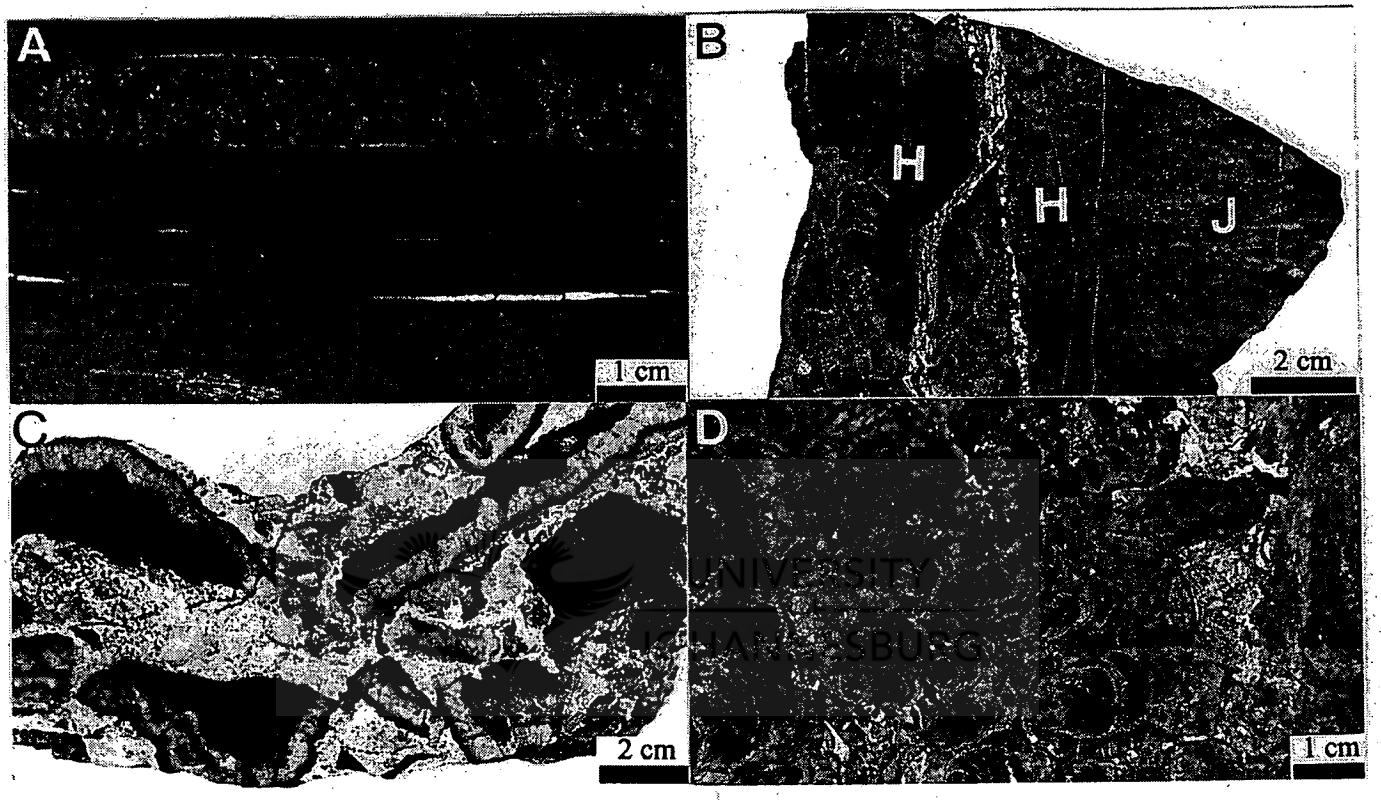

Fig. 2.4 (A) stratiform layers of late diagenetic/ metamorphic hausmannite in braunite lutite; (B) Cross section through reduction zone (H) adjacent to thin veinlet, surrounded by a jacobsite-rich halo (J); (C) Brecciated vein composed of hematitized and pyritized wallrock fragments and clasts of an older banded pyrite-kutnahorite assemblage in a dense talc and calcspar matrix (traverse S2); (D) Manganomelane dendrites transecting dense chalcedony-goethite fault rock (traverse L1).

The manganese ore in close proximity to the fault zone is dark greyish-green in colour with a dense splintery and in places siliceous character. Irregular pockets of earthy manganomelane (see Table 1 for definition of the term manganomelane as a mineral group name) occur enclosed in the splintery matrix (Fig. 2.4F). Aggregates of botryoidal manganomelane occur parallel and perpendicular to the primary sedimentary bedding. Veinlets filled with sparitic calcite increase in abundance in direction of the fault zone (Fig. 2.4E).

The fault zone is 5.7 m wide in section L1 (Fig. 5A), and 6.5 m wide in section L2 (Fig. 2.5B).Two stages of brecciation and veining are present in the fault zone. The southern segment of the fault zone is composed of a goethite-chalcedony fault rock representing an earlier stage

of alteration. The northern segment of a sparitic carbonate-cemented manganese ore breccia, representing a second, younger alteration event (Fig. 2.5A). The carbonate cement of this breccia is composed of sparitic calcite, dolomite and minor amounts of chalcedony and quartz (Fig. 2.5A).

In traverse L1 the ferruginous and siliceous segment of the fault zone is represented by a vein filled with hematitized ore fragments cemented by dense, fine crystalline hematite and dark chalcedony (Fig. 2.5B). A large lens of massive chalcopyrite was developed in this vein (N. Bleeker, pers. comm., 1994). In traverse L2 this ferruginous breccia is absent.

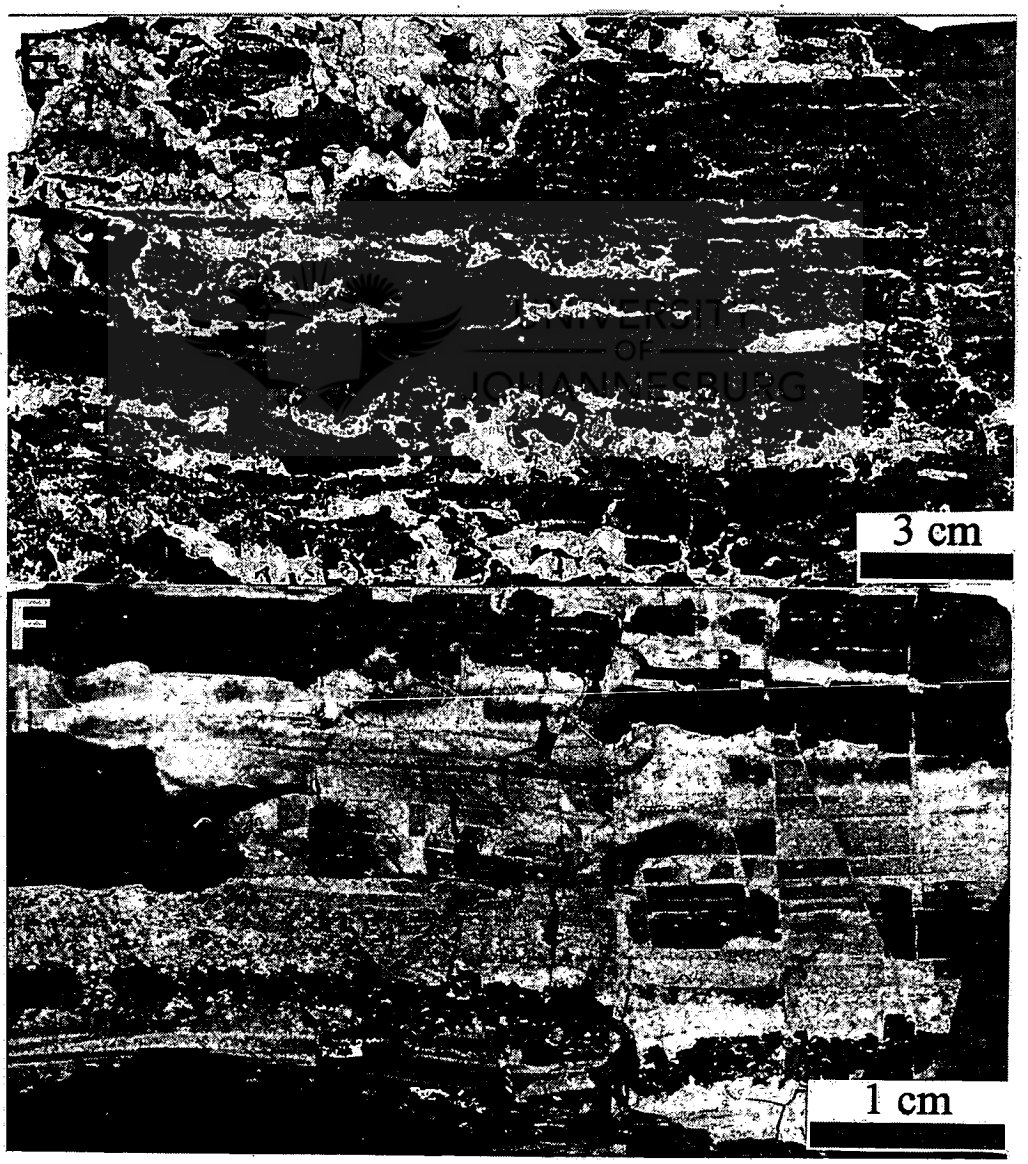

Fig. 2.4 (con.) (E) Bedding parallel calcite veins and vugs and manganomelane dendrites in strongly altered braunite lutite (traverse L2); (F) Pockets of earthy wad in highly altered, siliceous manganese ore close to the fault (traverse L2).

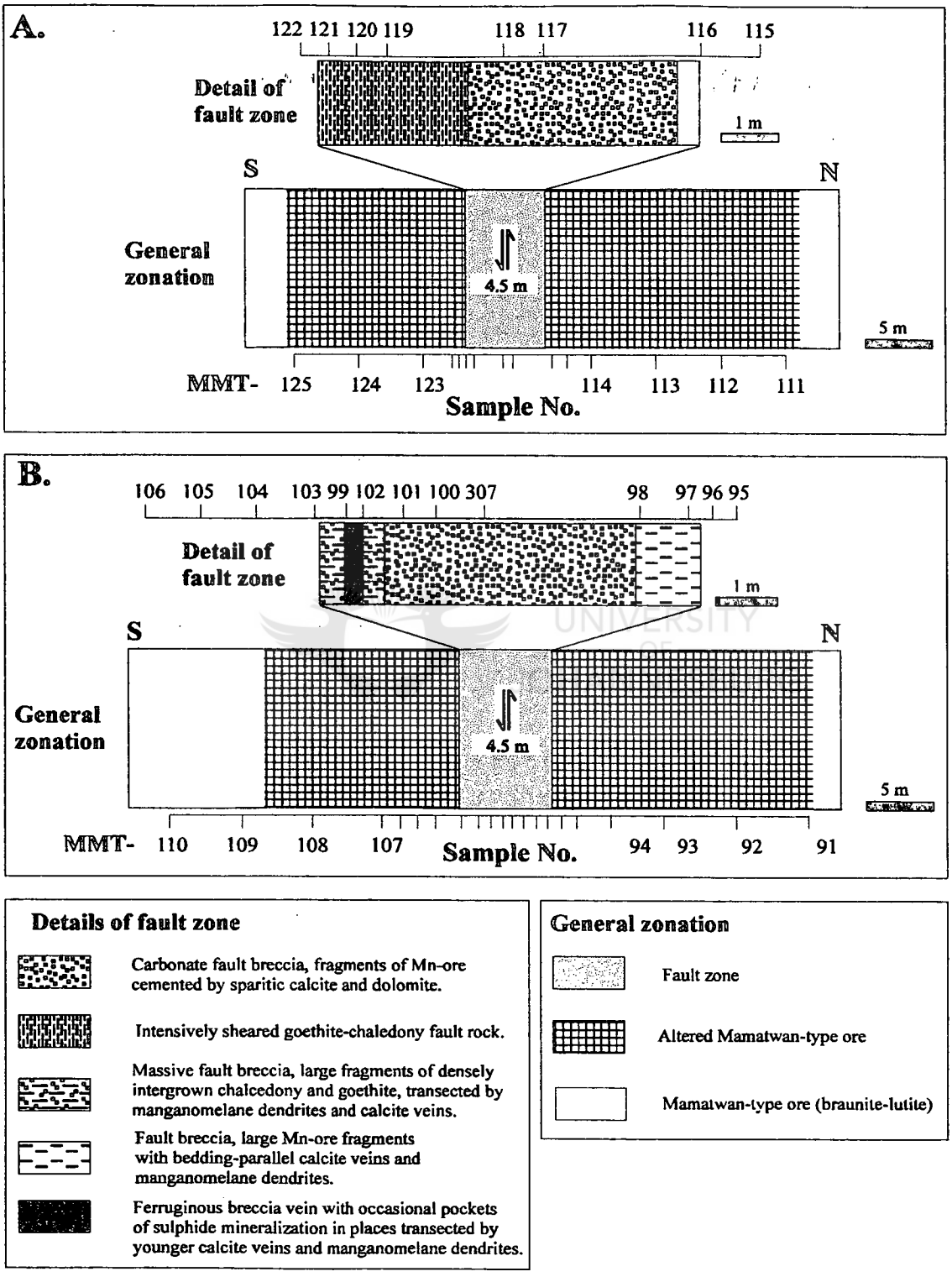

Fig. 2.5 Sections of traverses L1 (A) and L2 (B), indicating the lateral extent of macroscopically visible wallrock alteration and the internal structure of the fault zone relative to sample positions.

The central part of the of the fault zone is in traverse L2 is composed of a carbonate-cemented fault breccia with millimetre to decimetre sized, subangular to subrounded fragments of manganese ore, floating in a vuggy carbonate cement. The manganese ore fragments are greenish-black with an earthy texture. Fragments of iron-formation and hematite lutite are present. Vugs within the fault breccia are lined by calcite or small quartz crystals representing the latest phase of minerals known in the fault zone.

Alteration along joints and veins

In traverse S1 a clearly defined reduction halo is developed adjacent to a central, 5 mm wide veinlet filled by sparitic calcite and chalcedony (Fig. 2.6A). This veinlet pinches out about 1.5

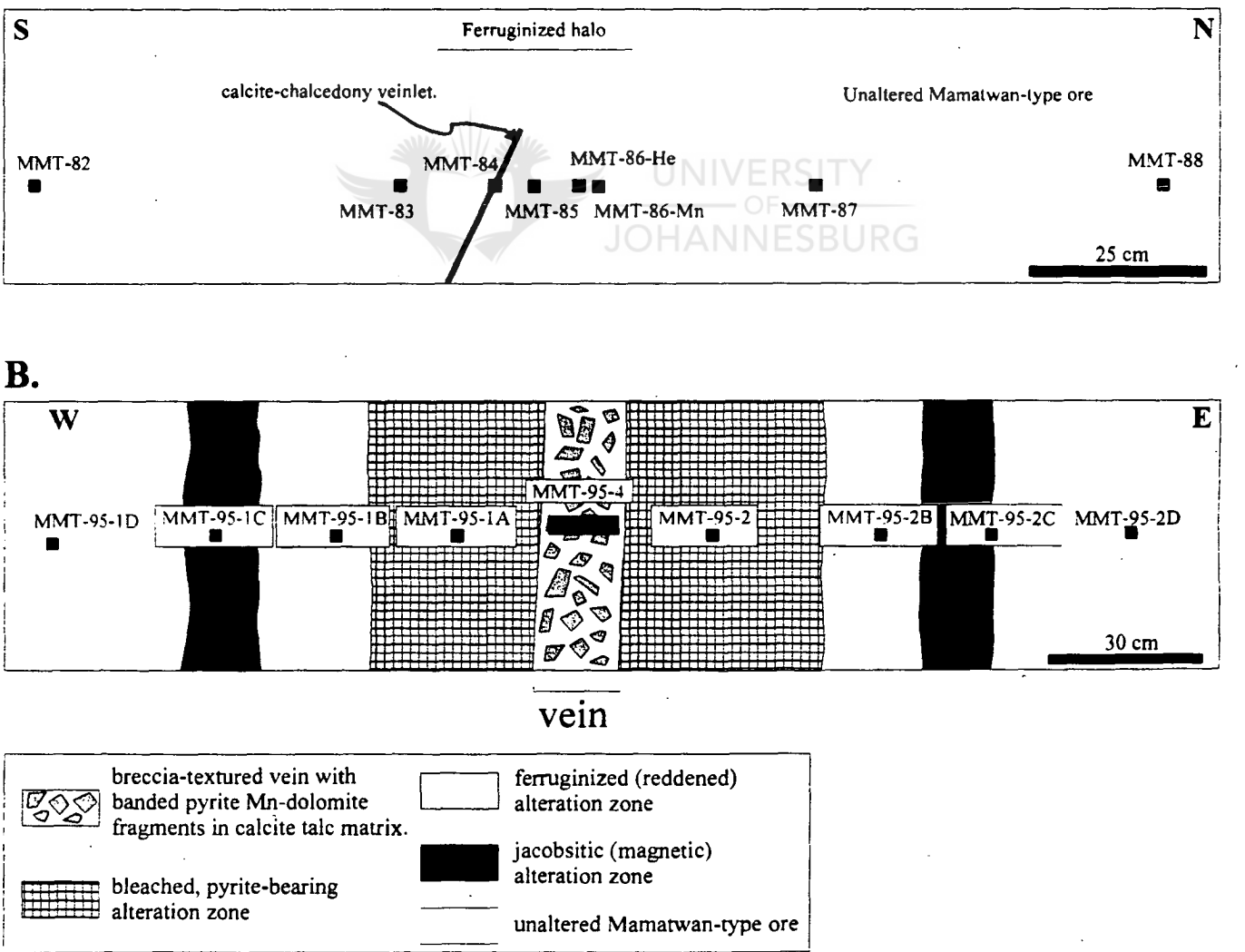

Fig. 2.6 Sections of traverses S1 (A) and S2 (B), indicating sample positions relative to zones of alteration around veins.

m below the contact of the manganese ore with the overlying Kalahari Formation (Fig. 2.6A). Altered manganese ore within the reduction halo is brick-red in colour, in contrast to the surrounding dark grey braunite lutite. The red colouration decreases gradually away from the vein. Sedimentary textures appear very well preserved in the reduction halo.

Alteration along traverse S2 is characterized by white bleaching of the Mn-ore (Fig. 2.6B) immediately adjacent to a central vein with a brecciated texture. Angular fragments of wallrock and a kutnahorite-pyrite vein fill (Fig. 2.4C), are recemented and coated by dense talc and sparitic calcite. The innermost bleached zone of alteration is characterized by the occurrence of few thin streaks and seams of hematite and irregular pods of fine crystalline pyrite in a light coloured carbonate matrix. This up to 30 cm wide bleached zone grades outwards into an about 15 to 25 cm wide zone of red discolouration (Fig. 2.6B). The latter grades through a transitional jacobsite-rich zone into unaltered braunite.

Lateral mineralogical variation

UNIVERSITY
JOHANNESBURG

The results of X-ray diffraction and ore microscopic studies define systematic mineralogical variations along the four traverses. Table 2.1 contains a list of minerals mentioned in the text and their chemical composition. Concentrations of minerals and mineral assemblages differ slightly on opposing sides of the fault in a single traverse because slightly different stratigraphic levels were sampled in the ore bed due to the fault displacement.

Alteration along faults

Least altered Mamatwan-type ore in traverses L1 and L2 contains abundant kutnahorite and Mn-calcite (samples MMT-91, 92, 107 to 110 in L2, and MMT-111, 112, 113 in L1, Fig. 2.7) in association with braunite and hematite. These Mn-bearing carbonates are the first to be replaced during the alteration process (samples MMT-93 and 106 in L2, MMT-113 and 125 in L1) followed by hausmannite, partridgeite and manganite (samples MMT-106 and 105 in L2, MMT-113 and 114 in L1). Braunite is the last mineral to disappear in areas of most intense alteration. Calcite occurs as micritic Mn-calcite in unaltered braunite lutite and as secondary sparitic calcite in altered ore. The amount of hematite increases towards the fault, especially in traverse L1 (Fig. 2.7A).

Table 2.1 Minerals encountered in the manganese ores or their altered equivalents during petrographic and powder diffraction studies.

Mineral	Ideal composition	Group
Hausmannite	Mn_3O_4	Oxides + Hydroxides
Partridgeite[a)]	Mn_2O_3	
Braunite	Mn_7SiO_{12}	
Manganite	α-MnOOH	
Jacobsite	$MnFe_2O_4$	
Pyrolusite	β-MnO_2	
Todorokite	$(Mn^{2+},Ca, Mg,)Mn^{4+}{}_3O_7 \cdot xH_2O$	
Manganomelane[b)]	$(K,Na,Ba)_{2-z}(Mn^{4+},Mn^{2+},Fe^{3+})_{8-z}O_{16-x}(OH)_x$	
Cryptomelane	$K_{2-z}(Mn^{4+},Mn^{2+},Fe^{3+})_{8-z}O_{16-x}(OH)_x$	
Hematite	Fe_2O_3	
Goethite	FeOOH	
Chalcedony	SiO_2	
Quartz	SiO_2	
Calcite	$CaCO_3$	Carbonates
Mn-calcite	$(Ca,Mn)CO_3$	
Dolomite	$CaMg(CO_3)_2$	
Kutnahorite	$Ca(Mn,Mg,Fe^{2+})(CO_3)_2$	
Clinochlore	$(Mg,Fe^{3+})_5Al[(OH)_8/(Si,Al)_4O_{10}]$	Silicates
Nontronite	$Na_{0.3}Fe^{3+}{}_2[(OH)_2/Si_4O_{10}] \cdot H_2O$	
Talc	$Mg_3[(OH)_2/Si_4O_{10}]$	

a) Partridgeite was originally described by De Villiers (1943) as a new mineral species, but was never recognized by the IMA (International Mineralogical Association) and is generally regarded as iron-poor bixbyite. Studies to prove the identity of partridgeite as a separate mineral are in progress.

b)The term manganomelane is used to name a whole group of poorly crystalline manganese oxides as suggested by Frenzel (1980). This group includes the end members manjiroite (Na), cryptomelane (K) and romanechite (Ba, H_2O).

UNIVERSITY OF JOHANNESBURG

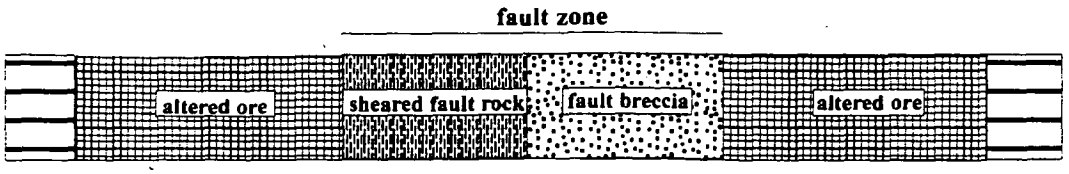

MMT-	125	124	123	122	121	120	119	118	117	116	115	114	113	112	111
hausmannite			/									/	/	X	/
jacobsite									/						
braunite	XXX	XX		/	X	X				X		X	XX	XXX	XXX
partridgeite	-												X	X	X
hematite	X	X	X	XX	XXX	XXX	XXX	X	XXX	X	X	X	X	X	X
manganite				-									X	X	X
pyrolusite				/								/	/		
todorokite	/	X	XX	/	/	/			/	/	X	XX	/	/	/
manganomelane	/	XX	XXX	XX	XX	XX	XX	XX	XX	XX	XXX	XXX	XX	XX	XX
goethite					XX	XX	XX	X	XXX						
chalcedony		/	X	XXX	X	XXX	XXX	XXX	XXX	X	X	/			
calcite				X	X	/	X	X	XXX		X	XX			
Mn-calcite	XXX	XXX											XX	XX	XX
kutnahorite													XX	XXX	XXX
nontronite									X						

Fig. 2.7A Mineralogical composition of ores and fault rocks in traverse L1 as determined by XRD and petrographic studies. (xxx - dominant mineral phase, > 30 Vol. %; xx - important mineral phase, 10 - 30 Vol. %; x - subordinate or minor mineral phase, 1 - 10 Vol. %; / - trace component - < 1 Vol. %).

UNIVERSITY OF JOHANNESBURG

Minerals formed at the expense of the primary phases are manganomelane, todorokite and chalcedony, as well as minor amounts of pyrolusite (Fig's. 2.7A and 2.7B). Manganomelane is present in minor amounts in samples that appear macroscopically unaltered, but it is a major constituent in highly or entirely altered ore close to the fault zone. Todorokite is present in most samples and its content increases with increasing degree of alteration. However, it is rare in samples immediately adjoining the fault and in fragments of altered ore within the fault zone. Chalcedony is present in considerable amounts in highly and entirely altered samples close to, or within, the fault zone, and absent in weakly altered or unaltered samples (Fig's. 2.7A and 2.7B).

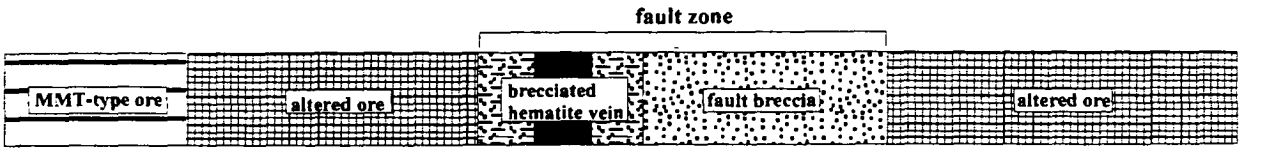

MMT-	110	109	108	107	106	105	104	103	99	102	101	100	98	97	96	95	94	93	92	91
hausmannite	X	/	/	XX	XX															
jacobsite									X											
braunite	XX	XX	XX	XX	XX	X	X										X	X	XX	XXX
partridgeite	XX	XX	/	XX	X	/														
hematite	XX	XX	XX	XX	XX	XX	XX	X	XXX	XX	X	X	X	X	XX	X	X	X	X	X
manganite	X	X	/											X	X					
pyrolusite				/	/									/	X					
todorokite		X				XXX	/		X			X	XX	XX	XXX	XXX	X	X	X	X
manganomelane	/	X	X	X	XX	XX	XXX	XX	X	XX	XXX	XXX	XXX	XXX	XXX	XXX	XXX	XXX	X	X
goethite								XX	X	/			X							
chalcedony						X		XX	X	XX	XX	XX	X	X		X	XX	XX		
calcite					XX	XX	XXX	XXX	X	XX	XXX	XXX		XXX	X					
Mn-calcite	XXX	XXX	XXX	XX															XX	XX
kutnahorite	XX	XX	XX	XX															XX	XX
dolomite													XX							
amesite				/																
nontronite								X												

Fig. 2.7B Mineralogical composition of ores and fault rocks in traverse L2 as determined by XRD and petrographic studies. (xxx - dominant mineral phase, > 30 Vol. %; xx - important mineral phase, 10 - 30 Vol. %; x - subordinate or minor mineral phase, 1 - 10 Vol. %; / - trace component - < 1 Vol. %).

Hematite, jacobsite and chalcedony constitute the ferruginous fault breccia. Minor amounts of todorokite, manganomelane, goethite and calcite are present (sample MMT-99, L2). The massive siliceous matrix surrounding the ferruginous fault breccia consists of dense chalcedony stained by goethite. Manganese ore fragments in the carbonate-cemented fault breccia are composed of manganomelane, with minor todorokite, goethite, chalcedony and sparitic calcite or dolomite. The ore fragments are cemented by sparitic calcite, dolomite, chalcedony, quartz, goethite and nontronite.

Alteration along veins and joints

Kutnahorite and braunite represent major phases in the least-altered braunite lutite along traverse S1 (samples MMT-82 and 86-88). The two minerals are absent from the alteration halo (Fig. 2.8A). Jacobsite occurs only in the transition zone between red discoloured halo and unaltered manganese ore (samples MMT-83 and 86-He). Hematite appears more abundant in the red discoloured halo than in the unaltered ore, but it is absent in the calcite vein which consists of sparitic calcite and chalcedony. Mn-calcite and kutnahorite are apparently not affected by the

alteration. The amount of Mn-bearing carbonates in the hematitized samples appears to increase at the expense of the presence of braunite in the reduction halo (Fig. 2.8A). Todorokite and manganomelane occur in minute amounts in the unaltered braunite lutite.

Alteration along traverse S2 is characterized by the occurrence of pyrite, clinochlore, and quartz (Fig. 2.8B). Kutnahorite and Mn-calcite are apparently not affected by the alteration. Pyrite and minor amounts of hematite, quartz and clinochlore occur with the carbonates in the bleached zone. Hematite and small amounts of clinochlore are associated with the carbonates in the red discoloured zone. The transitional, jacobsite-rich alteration zone is characterized by the occurrence of hausmannite, jacobsite, and minute amounts of clinochlore (Fig. 2.8B).

UNIVERSITY OF JOHANNESBURG

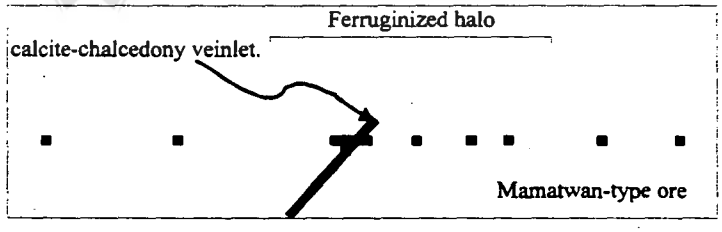

MMT-	82	83	84	84-vein	85	86-He	86-Mn	87	88
jacobsite		XX					XX		
braunite	XX							XX	XX
hematite	X	XX	XX		XX	XX	X	X	XX
manganomelane	/	/							
todorokite	/	/							
chalcedony				XX					
calcite				XXX					
Mn-calcite	XXX	XXX	XXX		XXX	XXX	XXX	XXX	XXX
kutnahorite	XXX	XXX	XXX		XXX	XXX	XXX	XXX	XXX

Fig. 2.8A Mineralogical composition of ores and fault rocks in traverse S1 as determined by XRD and petrographic studies. (xxx - dominant mineral phase, > 30 Vol. %; xx - important mineral phase, 10 - 30 Vol. %; x - subordinate or minor mineral phase, 1 - 10 Vol. %; / - trace component - < 1 Vol. %).

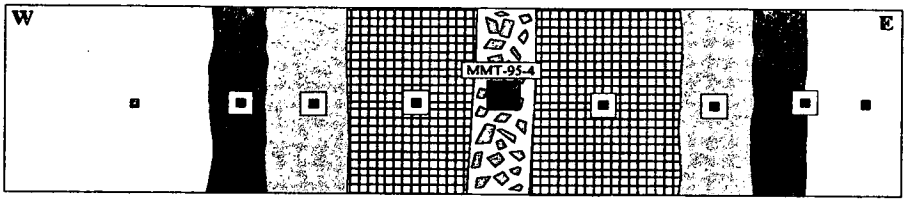

MMT- 95	1D	1C	1B	1A	4	2A	2B	2C	2D
pyrite				XX	XXX	XX			
hausmannite	X	XX						XX	XX
braunite	XXX								XXX
jacobsite		X						X	
hematite	X	X	X	/			X	X	X
Mn-calcite	X	X	X	X	XX	X	X	X	X
kutnahorite	XXX	XXX	XXX	XXX	XX	XXX	XXX	XXX	XXX
clinochlore		/	/	X		/	/	/	
talc					XX				
quartz				X		X			

Fig. 2.8B Mineralogical composition of ores and fault rocks in traverse S2 as determined by XRD and petrographic studies. (xxx - dominant mineral phase, > 30 Vol. %; xx - important mineral phase, 10 - 30 Vol. %; x - subordinate or minor mineral phase, 1 - 10 Vol. %; / - trace component - < 1 Vol. %).

Petrographic zonation and paragenetic relationships

Alteration along faults

The mineral paragenesis for traverses L1 and L2 appears identical. In both traverses least altered Mamatwan-type ore is composed of a finely laminated, microcrystalline matrix consisting of kutnahorite, Mn-calcite, braunite and minor hematite (Fig. 2.9A). Ovoids and seams of carbonate are abundant. Carbonate phases in the ore matrix display different in textures to those in carbonate ovoids and seams. Carbonate grains in the matrix are anhedral, 1-15 μm in diameter and densely intergrown. The grains are associated with 1-5 μm sized subspherical grains of braunite and hematite.

Fig. 2.9 Reflected light photomicrographs. (A) Finely laminated braunite lutite with abundant kutnahorite ovoids in a matrix of micritic kutnahorite (dark grey) with braunite and hematite (both light grey); (B) Massive partridgeite (white) that apparently replace earlier kutnahorite ovoids; (C) Replacement of braunite lutite by cryptocrystalline manganomelane (light-grey) and large grains of hematite (white). Residual kutnahorite appears dark-grey and secondary pores appear black (MMT-93); (D) Highly altered braunite lutite with well preserved sedimentary lamination. Original carbonate ovoids are replaced by massive manganomelane and the matrix displays abundant secondary porosity (MMT-94).

Carbonates in ovoids and also in some carbonate laminae appear recrystallised, they have rhombohedral to subspherical grain shapes and grain sizes ranging between 5 and 300 μm. Subhedral hematite and braunite occur in some of the ovoids as central lenticels or dispersed inclusions.

The formation of hausmannite, manganite and partridgeite that replace the primary braunite lutite assemblage is apparently independent of alteration related to the fault zone. Kleyenstüber (1984, 1985) and Nel et al. (1986) describe hausmannite as a minor constituent of Mamatwan-type ore. De Villiers (1983) mentioned the occurrence of partridgeite. Manganite has previously not been noted in the Mamatwan-type ore. Hausmannite, partridgeite and manganite replace former kutnahorite and Mn-calcite seams and ovoids. Manganite forms massive aggregates of anhedral, 10-30 μm large grains, that replace carbonate ovoids. It occurs next to, but never intermixed, with partridgeite. Partridgeite is present as anhedral grains between 50 and 200 μm in diameter. Small aggregates of partridgeite replace carbonate ovoids and also matrix carbonates (Fig. 2.9B). Hausmannite forms small, isolated subhedral crystals of up to 50 μm size in recrystallised carbonate laminae and ovoids. Primary braunite and hematite are preserved as inclusions in partridgeite and hausmannite grains.

UNIVERSITY OF JOHANNESBURG

Fig. 2.9E Aggregate of todorokite (white) that replaced a kutnahorite ovoid. Note residual kutnahorite inclusions (dark grey).

Todorokite and manganomelane are present in minor amounts in ore that appears macroscopically unaltered distal to the fault zone (Fig. 2.9C), but become become predominant as the fault zone is approached and the degree of alteration increases (Fig. 2.9D). The term manganomelane is used here for a group of tetravalent manganese oxides with broad X-ray diffraction peaks at 6.9 - 7 Å and at 2.1 - 2.2 Å which include the minerals cryptomelane, manjiroite and romanechite (Table 1). Electron microprobe analysis of manganomelane from Mamatwan mine further indicated that most examples have an intermediate composition that cannot be assigned to any of the compositional end members.

In the altered ore primary manganese oxides and carbonates are replaced by intimately interegrown todorokite and manganomelane (for example MMT- 95 and 96). Todorokite aggregates, composed of minute fibers, replace carbonate ovoids. The aggregates enclose abundant residual carbonate inclusions (Fig. 2.9E). Manganomelane forms cryptocrystalline dense masses replacing carbonate crystals along grain boundaries and cleavage plains. It also replaces all other manganese oxides, including todorokite. Hausmannite and the carbonates seem to be most susceptible to replacement by manganomelane. In the altered ore hematite is finely intergrown with manganomelane and its distinction from the former is very difficult by optical methods. Some of the hematite may represent relicts of the primary braunite lutite, but most of it is of secondary origin and occurs as minute recrystallised subhedral laths in the manganomelane. Chalcedony occurs as extremely fine crystalline and dense accumulations in intensively altered ores close to the fault zone. Pyrolusite replaces manganite immediately adjacent to the fault zone (for example samples MMT-113 and MMT-96).

Fragments of manganese ore in the carbonate cemented fault breccia (Fig. 2.5) are most intesely altered. They are composed of massive aggregates of manganomelane intergrown with hematite. The fragments are coated by chalcedony and cemented by white sparitic calcite and dolomite (in sample MMT-98). The sparitic cement is extremely vuggy and openings are lined by white prismatic to scalenohedral calcite and dolomite crystals. These crystals are overgrown by a distinct phase of yellowish calcspar which occurs as very coarse rhombohedral crystals which in turn may be coated by mm-sized quartz crystals.

Angular fragments of hematitized manganese ore in the ferruginous breccia (Fig. 2.5) are composed of 1-100 μm long specularite needles, with interstitial aggregates of collophorm jacobsite in a matrix of chalcedony. The black chalcedony cement of the fragments encloses some needles of specularite and cauliflower-shaped aggregates of jacobsite up to 100 μm in diameter. Small amounts of goethite replace jacobsite and specularite. Veinlets of sparitic calcite and dendritic aggregates of manganomelane crosscut the hematite-rich assemblage. Associated

sulphide mineralization tis composed of anhedral chalcopyrite grains up to 100 μm in size with inclusions of hematite laths, corroded pyrite cubes and minute euhedral bornite grains. The sulphide assemblage displays two distinct stages of oxidation. The first is represented by chalcocite replacing chalcopyrite and bornite along grain boundaries and microfractures. The second stage of oxidation is represented by replacement of sulfides by a complex goethite-malachite-(azurite)-chalcedony-calcite mineral assemblage along fractures that crosscut the sulphide matrix. The massive chalcedony-goethite fault rock (Fig. 2.5) immediately adjacent to the ferruginous breccia is composed of banded chalcedony stained by goethite. Manganomelane aggregates that originate on fracture planes form dendritic structures with crude concentric texture (Fig. 2.4D).

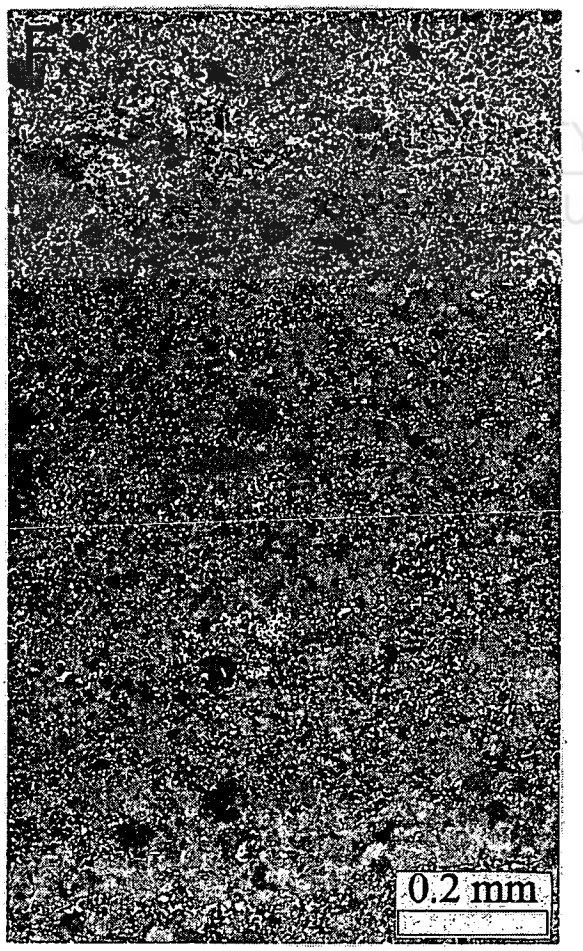

Fig. 2.9F Secondary hematite in recrystallized carbonate matrix.

Alteration along veins and joints

The paragenetic succession along traverses S1 and S2 is similar to that of the central ferruginous breccia described above. Unaltered braunite lutite is similar in composition to that of traverses L1 and L2. However, partridgeite, hausmannite and manganite are absent and only small amounts of manganomelane and todorokite occur.

The transition from grey unaltered ore into the red discoloured halo in traverse S1 is characterized by the occurrence of jacobsite in place of braunite. The jacobsite grains are 1-3 μm in size and intergrown with hematite, kutnahorite and Mn-calcite. Manganomelane occurs only in minute amounts. Jacobsite disappears closer to the central vein. Hematite, intergrown with carbonates, becomes more abundant and accounts for approximately 20 vol% in discoloured samples, as compared to 5-10 % in unaltered braunite lutite. The carbonate matrix in the red discoloured samples is coarser-grained than in the Mamatwan-type ore and secondary pores, developed by leaching of carbonate, are abundant in the recrystallized carbonate matrix (Fig. 2.9F). The vein in the centre of the alteration halo is filled by sparitic calcite with inclusions of hematite.

UNIVERSITY OF JOHANNESBURG

A rather similar paragenetic succession is present in traverse S2. Braunite is replaced by fine crystalline hausmannite, jacobsite and small amounts of clinochlore in the outer part of the alteration zone. The contact between the jacobsite-rich zone and the red discoloured zone (Fig. 2.8B) is marked by the appearance of small amounts of quartz at the expense of kutnahorite and manganese oxides. Dusty hematite, together with increasing amounts of clinochlore appear intergrown with kutnahorite and Mn-calcite. Pyrite predominates and hematite is virtually absent in the inner, bleached zone. The pyrite occurs as minute euhedral grains densely intergrown with kutnahorite and Mn-calcite or as coarse crystalline, irregular pods that apparently replace the carbonate matrix. The carbonate matrix appears barely altered with the presence of secondary pores being the only indication of leaching.

Mineral chemistry

The chemical composition of individual minerals does not appear to vary significantly from one traverse to the other allowing discussion irrespective of their position.

Table 2.2 Average composition of several Mn-oxides from Mamatwan mine (all data in mass %).
N - number of analyses. LLD-less than limit of detection; n.a.-not analysed.

Mine	MMT	MMT	MMT	MMT	MMT	MMT	MMT	MMT	MMT
S. No.	107	93	125	127.3	107	109	99.1	99.2	reference[a)]
Mineral	hausmannite	braunite			partridgeite		jacobsite		
N	3	5	4	5	8	8	5	3	
SiO_2	0.10	10.2	10.3	9.71	0.14	0.19	0.95	1.44	0.35
TiO_2	0.03	0.02	0.03	0.02	0.01	0.03	0.02	0.07	n.a.
Al_2O_3	0.20	0.12	0.03	0.61	0.16	0.31	0.06	0.13	0.74
Fe_2O_3[b)]	1.47	4.62	6.48	4.00	1.52	1.53	65.2	65.2	63.6
Mn_2O_3[c)]	64.6	72.9	72.9	76.5	97.8	97.8			
MnO	33.5	11.6	8.77	7.72			32.7	32.4	33.7
MgO	LLD	0.17	0.33	0.45	0.05	0.08	0.47	0.84	0.92
CaO	LLD	0.20	1.13	1.08	0.06	0.16	0.44	LLD	0.6
BaO	0.03	0.06	0.03	0.06	0.03	0.04	0.06	LLD	LLD
Na_2O	0.10	0.19	0.10	0.06	0.09	0.10	0.30	0.23	0.05
K_2O	LLD	LLD	0.05	LLD	LLD	0.01	LLD	LLD	LLD
TOTAL	100.0	100.1	100.1	100.3	99.9	100.2	100.2	100.3	100.0

a) Reference value for jacobsite from Kleyenstüber (1985).
b) $Fe_{(total)}$ expressed as Fe_2O_3.
c) A Mn_2O_3-MnO balance was calculated for hausmannite and braunite, $Mn_{(total)}$ is expressed as Mn_2O_3 for jacobsite and partridgeite.

Table 2.3 Average composition of manganomelane and todorokite from Mamatwan mine (all data in mass %).
N - number of analyses; LLD- lower than limit of detection.

Mine	MMT	MMT	MMT	MMT	MMT	MMT	MMT	MMT	MMT	MMT	MMT
S. No.	90.1	90.2	98	104	108	118	119.1	119.2	87	92	105
Mineral	manganomelane								todorokite		
N	5	3	10	5	5	5	7	5	5	6	5
SiO_2	0.26	0.23	0.51	0.45	0.32	1.18	0.55	0.66	0.46	0.63	0.30
TiO_2	0.08	0.03	0.05	0.02	0.02	LLD	0.06	LLD	LLD	LLD	0.02
Al_2O_3	0.08	0.13	0.19	0.10	0.14	0.21	0.09	0.15	0.16	0.07	0.42
Fe_2O_3[a)]	1.10	0.37	1.78	1.55	0.63	1.09	4.50	4.56	1.13	1.28	1.12
MnO_2[b)]	84.7	82.5	87.2	88.9	84.1	87.9	84.0	85.7	80.2	83.1	81.3
MgO	0.73	1.16	0.84	0.52	1.27	0.76	1.50	0.84	2.33	1.17	2.89
CaO	0.96	1.37	1.60	1.11	2.04	1.45	1.38	1.31	2.95	1.92	2.25
BaO	0.18	0.43	0.05	LLD	2.22	0.13	0.04	0.10	0.04	1.83	0.06
Na_2O	0.48	0.56	0.85	0.45	1.09	0.76	0.93	0.73	1.17	0.79	1.34
K_2O	5.10	3.19	0.36	0.34	0.32	0.70	0.82	0.45	0.84	0.30	0.34
TOTAL	93.7	90.0	93.5	93.4	92.1	94.2	93.9	94.5	89.2	91.1	90.1

a) -$Fe_{(total)}$ expressed as Fe_2O_3.
b) -$Mn_{(total)}$ is expressed as MnO_2.

Sample descriptions: MMT-90: Botryoidal manganomelane aggregates which form in calcrete-filled cracks along the suboutcrop against the Kalahari Formation; MMT-98: Ore fragments composed of manganomelane; 104: Dendritic manganomelane; 108: Dense manganomelane replacing manganite; 118: Dendritic manganomelane in massive goethite-chalcedony matrix; 119: Dendritic manganomelane closely associated with hematite; MMT- 87: Todorokite aggregate replacing kutnahorite ovoid; 92: Large todorokite fibers in thin Mn-calcite veinlet; 105: Todorokite replacing matrix carbonate.

UNIVERSITY OF JOHANNESBURG

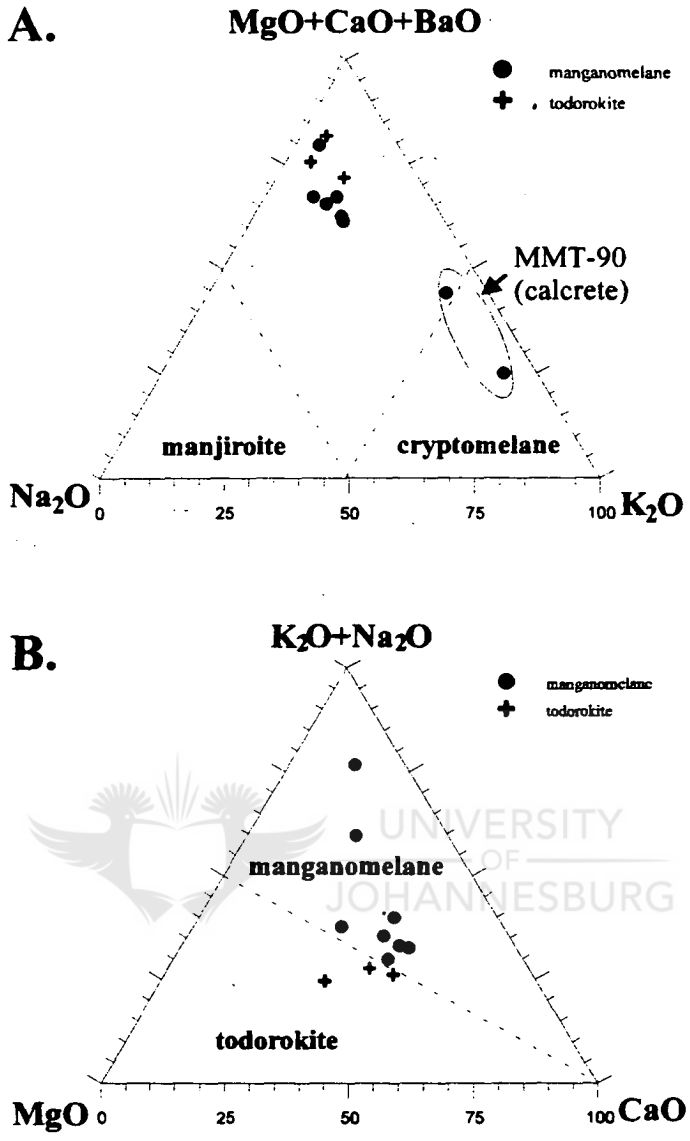

Fig. 2.10 Triangular plots of (MgO+CaO+BaO) - Na_2O - K_2O (A) and of (K_2O+ Na_2O) - MgO - CaO (B) for discrimination of manganomelane from todorokite.

The composition of hausmannite was studied in sample MMT-107 (Table 2.2). The Fe_2O_3 content of 1.47 mass % agrees well with the range of 0.24 to 4.34 mass % Fe_2O_3 reported for hausmannite from Mamatwan-type ore by Nel et al. (1986). Braunite contains between 4.0 and 6.48 mass % Fe_2O_3, up to 1.13 mass % CaO, MgO concentrations below 0.5 mass% and an SiO_2 content of close to 10 mass% (Table 2.2). This is similar to results of Nel et al. (1986). Partridgeite has a very similar composition to hausmannite with Fe_2O_3 contents in the order of 1.5 mass %. Jacobsite, found in assemblage with specularite and chalcedony in the hematite breccia vein in L1 (sample MMT-99, Table 2.2), compares very well with the stoichiometric composition of $MnFe_2O_4$ (30.8 mass% MnO, 69.2 mass% Fe_2O_3), but also with the composition of jacobsite from the hematite-lutite (Kleyenstüber, 1985) overlying the manganese ore bed.

Todorokite and manganomelane have rather similar chemical composition (Table 2.3). Both are characterized by low iron contents of 1 mass% Fe_2O_3 or less. An exception is manganomelane present in dendrites of sample 119 which contains about 4.5 mass% Fe_2O_3. The manganese content varies between 82.5 and 89 mass% MnO_2 for manganomelane and between 78.7 and 83.1 mass% MnO_2 for todorokite.

SiO_2, TiO_2 and Al_2O_3 contents are well below 1 mass% in both minerals. Both todorokite and manganomelane contain small amounts (1-3 mass%) Na, K, Mg, Ca and Ba (Table 2.3). Only botryoidal manganomelane developed along the contact of the lower manganese orebody with calcrete of the Kalahari Formation at Mamatwan Mine (Nel et al. 1986; Kleyenstüber, 1993) (sample MMT-90.1 and MMT-90.2, Table 2.3) contains enough K_2O to be classified as cryptonelane. Tiangular plots of (MgO+CaO+BaO), NaO and K_2O do not discriminate between manganomelane and todorokite (Fig. 2.10A) Incontrast the plot (K_2O+Na_2O) - MgO - CaO (Fig. 2.10B) enables discrimination of todorokite from manganomelane. In todorokite the MgO/ (K_2O + Na_2O) ratio is above and in manganomelane it is below one.

UNIVERSITY OF JOHANNESBURG

Table 2.4 Average composition of calcite and dolomite from Mamatwan mine (all data in mass %).

N - number of analyses. LLD-lower than limit of detection.

Mine	MMT	MMT	MMT	MMT	MMT	MMT	MMT	MMT	MMT	MMT	MMT	MMT
S. No.	107	84	90[c)]	118	98	99	105	92	108.1	108.2	109	125
Mineral	dolomite	sparitic calcite							micritic calcite			
N	2	5	3	5	4	4	3	3	5	5	5	8
SiO_2	0.15	LLD	0.15	0.15	0.15	0.16	0.14	0.17	0.15	0.16	0.14	0.17
FeO[a)]	LLD	LLD	LLD	0.08	LLD	0.15	0.06	LLD	LLD	0.08	0.1	0.12
MnO[b)]	LLD	2.05	0.18	0.05	LLD	0.05	0.2	6.46	4.94	2.56	5.29	2.38
MgO	20.2	0.49	0.39	0.72	1.65	0.58	0.53	0.27	0.34	0.28	0.62	0.43
CaO	33.7	51.9	52.6	53.8	55.1	51.5	53.6	46	49	49.8	48.7	50.3
SrO	LLD	LLD	LLD	LLD	LLD	LLD	LLD	LLD	LLD	LLD	0.02	LLD
BaO	LLD	0.06	LLD	0.08	0.1	0.14	LLD	0.07	0.09	0.1	0.06	LLD
TOTAL	54.1	55.5	56.3	55.0	57.0	55.6	55.6	55.0	54.5	55.0	55.0	56.4

a) -$Fe_{(total)}$ expressed as FeO.

b) -$Mn_{(total)}$ is expressed as MnO.

c) - massive calcrete.

Table 2.5 Average composition of kutnahorite (data in mass %).
N - number of analyses; LLD -lower than limit of detection.

Mine	MMT	MMT	MMT	MMT	MMT
S. No.	83.1	83.2	83.3	84	87
Mineral			kutnahorite		
N	3	5	4	11	6
SiO_2	0.58	0.11	0.27	0.27	0.30
FeO[a)]	1.25	0.05	1.12	3.37	0.29
MnO[b)]	10.0	11.2	6.84	8.41	12.7
MgO	1.00	0.23	1.63	8.79	1.42
CaO	39.6	42.7	43.5	34.8	42.7
SrO	0.20	LLD	0.07	0.03	0.13
BaO	0.03	0.03	0.08	0.02	0.05
TOTAL	55.6	56.3	55.6	55.6	57.6

a) - $Fe_{(total)}$ expressed as FeO.
b) - $Mn_{(total)}$ is expressed as MnO.

Mn-calcite in layers and ovoids of the unaltered braunite lutite contains up to 13 mass% MnO, less than 2 mass% MgO and a maximum of 1.25 mass% FeO (Table 5). The composition of kutnahorite is highly variable and ranges from the ideal composition of $CaMn(CO_3)_2$ towards ankeritic and dolomitic compositions (Table 5). Secondary, sparitic carbonates are either Mn-poor calcite or dolomite (Table 4).

Geochemistry

Sections L2 and S1 were selected to study the lateral geochemical variations related to the increasing degree of alteration (major element data are listed in Tables 2.6 A and 2.6B, trace element data are compiled in Tables 2.7A and 2.7B). Concentrations of many major elements along traverse L2 differ on the two sides of the fault due to displacement of the orebody.

Table 2.6A Major element composition, traverse L2 (all data in mass %). LLD - lower than limit of detection.

Sample No.	type	SiO_2 [a]	TiO_2	Al_2O_3	Fe_2O_3	Mn_3O_4	MgO	CaO	Na O	K_2O	P_2O_5	SO_3	H_2O^-	H_2O^+[b]	CO_2	LOI	SUM	Mn/Fe
MMT-91	TM	3.44	0.05	0.07	7.01	70.2	1.74	4.69	0.41	0.08	0.01	LLD	0.72	7.51	3.87	12.1	99.8	10.5
MMT-93	TM	4.65	0.05	0.03	6.88	66.5	2.79	1.41	0.48	0.87	0.02	LLD	0.66	15.2	0.11	16.0	99.7	10.1
MMT-94	TM	1.21	0.05	LLD	6.07	73.5	1.58	2.12	0.82	0.56	0.02	LLD	0.71	13.6	0.13	14.4	100.3	12.7
MMT-95	TM	6.99	0.05	LLD	6.75	67.1	1.18	2.07	0.82	1.08	0.02	LLD	1.03	13.1	0.11	14.1	100.2	10.4
MMT-96	TM	15.9	0.05	0.01	6.74	59.1	0.55	2.73	0.68	1.04	0.03	LLD	0.95	10.9	0.52	12.4	99.3	9.2
MMT-97	FB	50.4	0.04	0.09	7.44	30.9	0.39	1.12	0.53	0.65	0.02	LLD	0.66	7.22	0.22	8.1	99.6	4.4
MMT-98	FB	42.1	0.04	0.17	5.35	39.2	0.64	1.01	0.48	1.53	0.05	LLD	0.52	8.57	0.21	9.3	99.8	7.7
MMT-99	FHe	15.1	0.04	0.34	64.8	10.3	0.69	4.27	0.12	0.04	LLD	LLD	0.21	1.63	2.76	4.6	100.2	0.2
MMT-100	FGoe	61.5	0.05	0.22	17.8	5.95	0.46	6.23	LLD	0.03	0.09	LLD	0.44	3.49	3.47	7.4	99.7	0.4
MMT-102	FGoe	60.1	0.04	0.33	13.6	3.51	0.41	12.7	LLD	0.08	0.09	0.01	0.31	2.82	6.17	9.3	100.1	0.3
MMT-103	FGoe	63.7	0.05	1.03	10.2	7.16	0.67	8.82	0.07	0.22	0.07	0.03	1.41	4.59	2.01	8.0	100.0	0.7
MMT-104	TM	14.2	0.05	0.11	6.77	50.1	1.41	12.7	0.79	1.14	0.01	LLD	0.85	10.9	1.71	13.5	100.7	7.8
MMT-105	TM	5.31	0.05	0.17	5.54	50.2	1.47	15.2	0.79	1.49	0.01	0.01	0.82	10.9	8.6	20.3	100.6	9.5
MMT-106	TM	1.61	0.05	0.21	5.63	36.4	1.11	27.4	0.45	0.21	0.01	0.03	0.58	4.82	19.8	25.2	98.2	6.8
MMT-107	TM	2.86	0.05	0.36	6.18	52.6	1.36	16.7	0.64	0.11	0.01	0.01	0.89	8.61	9.8	19.3	100.2	8.9
MMT-108	TM	3.11	0.05	0.18	4.96	51.4	3.41	17.7	0.33	0.05	0.02	LLD	0.45	4.15	14.5	19.1	100.2	10.9
MMT-109	MMT	0.67	0.05	0.09	3.78	57.6	1.04	17.2	0.92	0.09	LLD	0.07	0.45	8.65	10.6	19.7	101.1	16.0
MMT-110	MMT	3.55	0.05	0.16	5.11	45.7	5.04	19.3	0.04	LLD	0.01	LLD	0.08	0.00	20.1	20.1	99.0	9.4

a) Ore types defined: MMT - braunite lutite (Mamatwan-type ore); TM- braunite lutite partially or completely altered to todorokite-manganomelane; FB - altered manganese ore fragments in fault breccia; FHe-fault-hosted hematite vein; FGoe- fault-hosted goethite-chalcedony assemblage,
b) H_2O^+ calculated as difference L.O.I. - (CO_2+H_2O^-)

JOHANNESBURG UNIVERSITY OF

Table 2.6B Major element composition, traverse S1(all data in mass %). LLD - lower than limit of detection.

Sample No.	type [a]	SiO_2	TiO_2	Al_2O_3	Fe_2O_3	Mn_3O_4	MgO	CaO	Na O	K_2O	P_2O_5	SO_3	H_2O^-	H_2O^{+b}	CO_2	LOI	SUM	Mn/Fe
MMT-82	MMT	2.01	0.05	0.31	6.61	27.1	2.31	29.3	0.34	0.16	0.02	0.01	0.45	1.55	28.2	30.2	98.4	4.3
MMT-83	Jb	0.83	0.04	0.22	17.6	4.04	3.05	38.3	0.03	LLD	0.01	0.02	0.05	0.45	35.7	36.2	100.4	0.2
MMT-84	He	4.09	0.05	0.36	24.2	8.71	9.14	21.4	0.04	0.04	0.01	LLD	0.21	0.49	31.8	32.5	100.6	0.4
MMT-85	He	1.43	0.05	0.31	17.8	3.06	1.18	40.7	0.05	0.01	0.01	0.02	0.11	0.69	34.5	35.3	99.9	0.2
MMT-86-He	He	1.78	0.05	0.34	17.9	2.88	2.25	39.3	0.14	0.02	0.01	0.02	0.19	0.61	34.5	35.3	100.0	0.2
MMT-86-Mn	Jb	3.46	0.05	0.38	7.42	30.4	2.37	26.6	0.37	0.37	0.03	0.04	0.62	2.98	24.5	28.1	99.5	4.3
MMT-87	MMT	2.62	0.05	0.34	7.62	32.5	2.61	26.1	0.34	0.25	0.02	0.01	0.65	2.15	25.1	27.9	100.2	4.5
MMT-88	MMT	2.66	0.05	0.32	7.28	34.4	2.21	25.1	0.28	0.34	0.02	0.01	0.57	2.03	24.2	26.8	99.4	5.0

a) Ore types: MMT- unaltered braunite lutite (Mamatwan-type ore); Jb - jacobsite-rich ore; He - ferruginized, hematite-rich ore.
b) H_2O^+ calculated as difference L.O.I. - (CO_2+H_2O^-)

UNIVERSITY OF JOHANNESBURG

Table 2.7A Trace element composition, traverse L2 (data in ppm).

Sample No.	type [a)]	V	Cr	Co	Ni	Cu	Zn	Rb	Sr	Ba	Pb
MMT-91	TM	20	17	51	< 1	< 1	57	5	125	896	5
MMT-93	TM	22	14	49	1	< 1	129	4	111	85	< 1
MMT-94	TM	12	26	34	< 1	< 1	332	3	144	1472	8
MMT-95	TM	11	3	38	6	< 1	273	5	125	367	< 1
MMT-96	TM	11	35	46	19	< 1	655	6	186	80	8
MMT-97	FB	14	43	41	18	< 1	964	< 1	180	41	19
MMT-98	FB	12	16	57	8	1	557	< 1	341	18	2
MMT-99/2	FHe	46	59	24	15	< 1	227	5	66	44	< 1
MMT-100	FGoe	23	73	68	21	4013	4	1	75	3937	16
MMT-102	FGoe	27	116	16	9	788	3	4	106	401	< 1
MMT-103	FGoe	32	55	52	20	65	26	4	256	1105	6
MMT-104	TM	19	16	60	11	< 1	75	6	259	518	9
MMT-105	TM	17	< 1	62	< 1	< 1	65	9	480	527	< 1
MMT-106	TM	7	11	27	< 1	23	66	4	263	566	< 1
MMT-107	TM	23	22	35	< 1	< 1	73	< 1	238	175	< 1
MMT-108	TM	18	20	47	2	< 1	23	2	191	907	< 1
MMT-109	MMT	12	4	20	2	< 1	< 1	3	283	2563	< 1
MMT-110	MMT	12	18	33	5	< 1	24	2	121	242	LLD

a) Ore types defined as in Table 2.6A.

Chemical composition on the southern side of the fault correspond very well with the composition of zone H of the orebody as given by Nel (1984). On the northern side of the fault compositions appear more closely related to the downfaulted zone C (Nel, 1984). Mn_3O_4 and Fe_2O_3 concentrations are negatively correlated along traverse L2 (Fig. 2.11A). Mn_3O_4 and Fe_2O_3 concentrations are negatively correlated along traverse L2 (Fig. 2.11A). The Mn_3O_4 content decreases slightly from unaltered braunite lutite into the altered ore, but strongly in samples adjacent or within the fault zone. The Fe_2O_3 content remains constant in samples outside the fault zone, but increases considerably in samples from within the fault zone. The Mn/Fe ratio decreases sharply from values of 10 or more in the braunite lutite to values of as low as 0.17 in the ferruginous breccia vein (Fig. 2.11B). The SiO_2 content in unaltered ore is 3-5 mass%, similar to the mean concentration published by Nel et al. (1986), but increases to up to 63.7 mass% in highly altered samples (Table 2.7A).

CO_2 contents decrease from 20.1 mass% in MMT-110 to less than 10 mass% in altered samples indicating the leaching of carbonate from the ores during alteration. MgO and CaO concentrations are positively correlated with CO_2 in unaltered or weakly altered samples. The CaO concentration decreases from unaltered sample MMT-110 (19.3 mass%) to thoroughly altered sample MMT-98 (1 mass%) and increases again towards sample MMT-91 (4.69 mass%). High CaO contents in altered samples are related to the abundance of secondary calcite. Highest concentrations of MgO (5.04 mass% in MMT-110 and 2.79 mass% in sample MMT-93) are present in least altered samples, whereas concentrations of less than 1 mass% are related to high degrees of alteration. Al_2O_3, Na_2O and K_2O concentrations increase in altered samples close to the fault zone (Table 2.7A). In highly altered samples within the fault zone trace elements Ba, Cr, Ni and Cu appear enriched, and Sr and Zn depleted (Table 2.7A).

Table 2.7B Trace element composition, traverse S1 (data in ppm).

Sample No.	type [a)]	V	Cr	Co	Ni	Cu	Zn	Rb	Sr	Ba	Pb
MMT-82	MMT	14	11	30	9	< 1	4	7	897	222	< 1
MMT-83	Jb	16	13	< 1	4	< 1	< 1	4	198	78	< 1
MMT-84	He	21	19	10	14	< 1	< 1	2	113	83	< 1
MMT-85	He	11	23	3	1	< 1	< 1	1	268	142	1
MMT-86-He	He	13	< 1	3	< 1	< 1	< 1	3	175	137	2
MMT-86-Mn	Jb	22	14	24	9	< 1	19	3	670	145	< 1
MMT-87	MMT	14	9	47	8	< 1	< 1	6	737	170	< 1
MMT-88	MMT	12	20	42	< 1	< 1	< 1	5	722	201	< 1

a) Ore types defined as in Table 2.6B.

The lateral variation of the major elements along traverse S1 is rather similar to that along L2. The Mn_3O_4 content decreases from 34.4 mass% in unaltered ore to as low as 2.88 mass% in the red discoloured halo (sample MMT-86) (Fig. 2.12A, Table 2.6B). Fe_2O_3 and CO_2 concentrations are negatively correlated with Mn_3O_4 and the Mn/Fe ratio decreases in the ferruginous halo (Fig. 2.12B). Ba and Sr are positively correlated with Mn_3O_4 (Fig. 2.12B). The Fe_2O_3 content increases from 6.6 mass% in the unaltered ore (MMT-82) to up to 17.9 mass% in the centre of the hematitized zone (Fig. 2.12A). K_2O and Na_2O concentrations decrease with increasing degree of alteration.

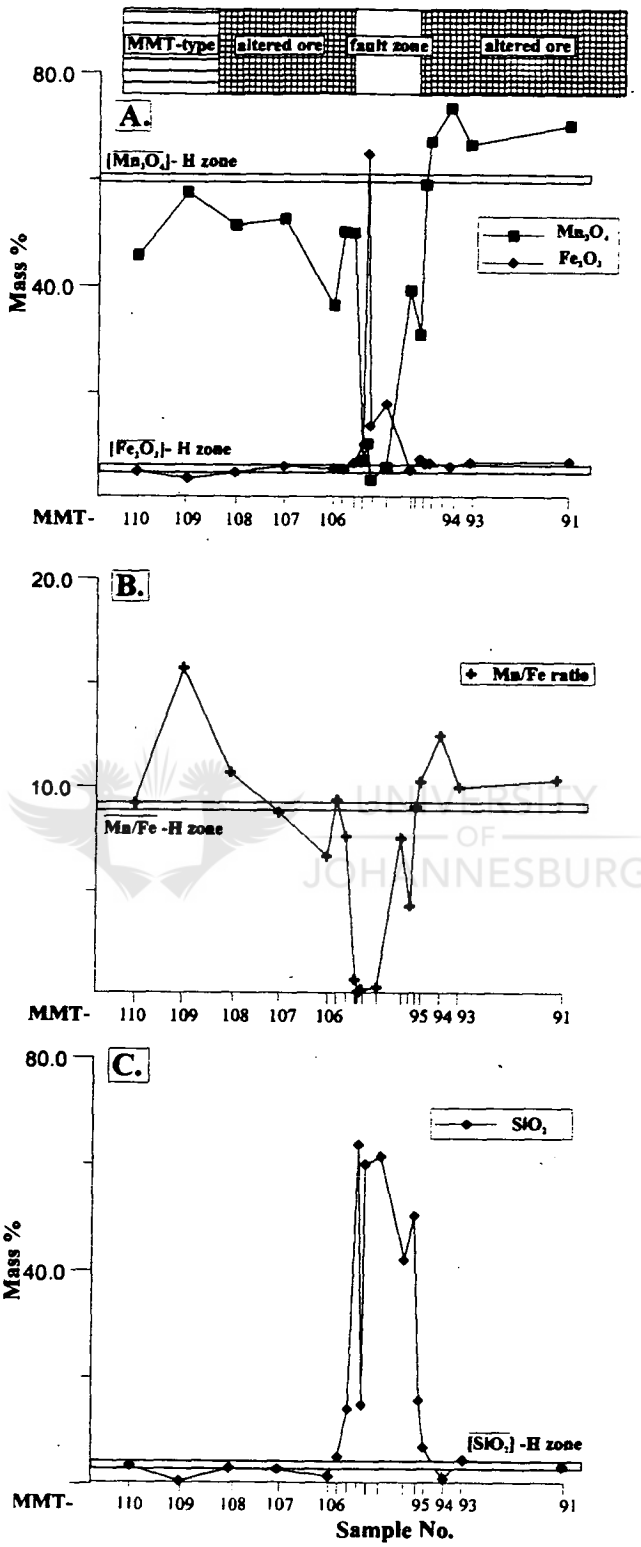

Fig. 2.11 Geochemical trends along traverse L2 illustrated in relation to rock types and degrees of alteration. Mean contents and values for the unaltered braunite lutite in the lithological zone H (Nel et al., 1986) are indicated. Diagrams display lateral variation of Mn_3O_4 and Fe_2O_3 (A), Mn/Fe ratio (B) and SiO_2 (C).

Stable isotope geochemistry

Results of stable-isotope analyses of carbonate-bearing samples from traverses L2 and S1 are listed in Table 2.8 for whole rock samples, and Table 2.9 for pure sparitic carbonate mineral separates. Analyses of four samples of unaltered braunite lutite from drill core M2 at Mamatwan (central economic zone of the lower orebody) (Table 2.8), and also of two calcrete samples MMT-90-1 and MMT-90-2 (Table 2.9) were included for comparison.

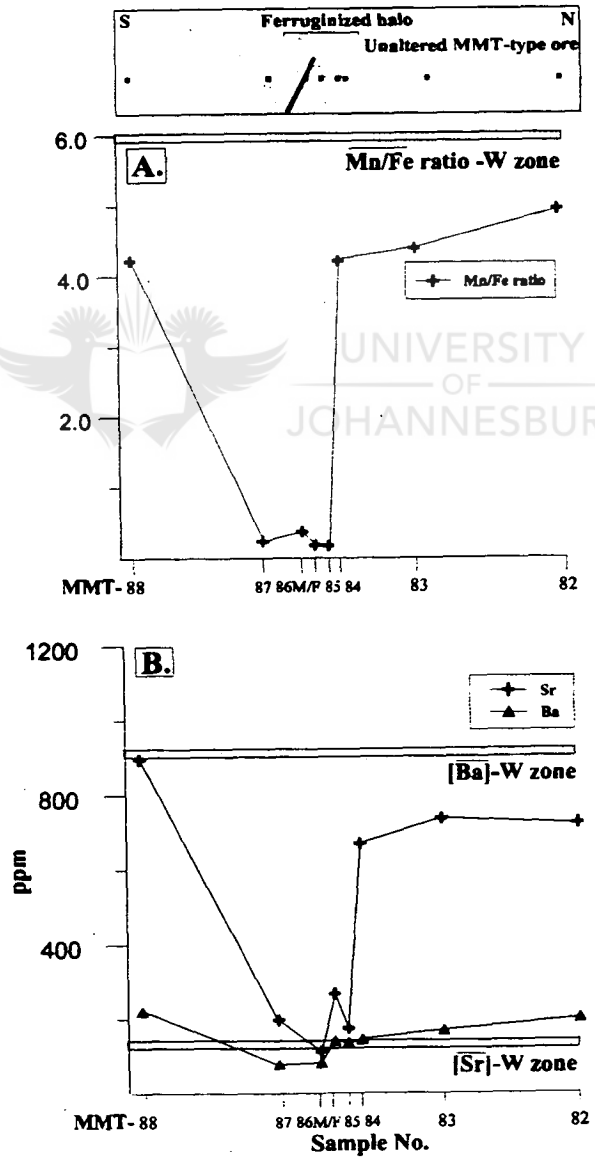

Fig. 2.12 Geochemical trends along traverse S1 illustrated in relation to alteration along the central vein. Diagrams display variations of the Mn/Fe ratio (A), and of Ba and Sr concentrations (B).

Unaltered braunite lutite samples from drill core M2 show $\delta^{18}O_{PDB}$ and $\delta^{13}C_{PDB}$ ratios very similar to those in the least altered samples of sections L1 and S1. $\delta^{18}O_{PDB}$ and $\delta^{13}C_{PDB}$ show close covariation along traverse L2 (Fig. 2.13A). Both oxygen and carbon become isotopically heavier with increasing degree of alteration. Primary Mamatwan-type carbonate has the lightest isotopic composition with values of -12.1 ‰ and -11.0 ‰ $\delta^{18}O_{PDB}$ and -10.8 ‰ and -13.9 ‰ $\delta^{13}C_{PDB}$. The isotopic composition of sparitic carbonates in the calcspar fault breccia are -4.2 ‰ to -6.0 ‰ for $\delta^{18}O_{PDB}$ and -5.7 ‰ to -9.0 ‰ for $\delta^{13}C_{PDB}$.

Along traverse S1 $\delta^{13}C_{PDB}$ and $\delta^{18}O_{PDB}$ appear only weakly correlated (Fig. 2.13B). $\delta^{18}O_{PDB}$ decreases first to -13.5 ‰ and -14 ‰ in the jacobsite-bearing transition zone to increase to a maximum of -8.1 ‰ in the hematitized zone. The vein-filling calcite is characterized by a considerably lower value of -11.1 ‰. $\delta^{18}O_{PDB}$. $\delta^{13}C_{PDB}$ increases continuously from -8.2 ‰ in Mamatwan-type ore to -4.0 ‰ and -4.5 ‰ (vein calcite) in the hematitized zone.

Two calcrete samples (MMT-90-1, MMT-90-2, Table 2.9) from the overlying Kalahari Formation contain the isotopically heaviest oxygen and carbon with - 0.8‰ and -3.1‰ $\delta^{18}O_{PDB}$, and -4.3 ‰ to -6.0 ‰ $\delta^{13}C_{PDB}$ (Table 2.9). These values are very similar to those reported by Netterberg and Talma (1985) for calcretes in South Africa. A distinct linear trend is defined by carbonates in unaltered braunite lutite samples, carbonate in altered ore, sparitic calcite and dolomite in the carbonate fault breccia and possibly also the calcrete (Fig. 2.13C). A disitnct linear trend is also defined by vein calcite, altered braunite lutite and unaltered braunite lutite in traverse S1 (Fig. 2.13D). Linear trends of this kind are usually taken as indication of isotope exchange between rock and an infiltrating fluid (Zheng and Hoefs, 1993).

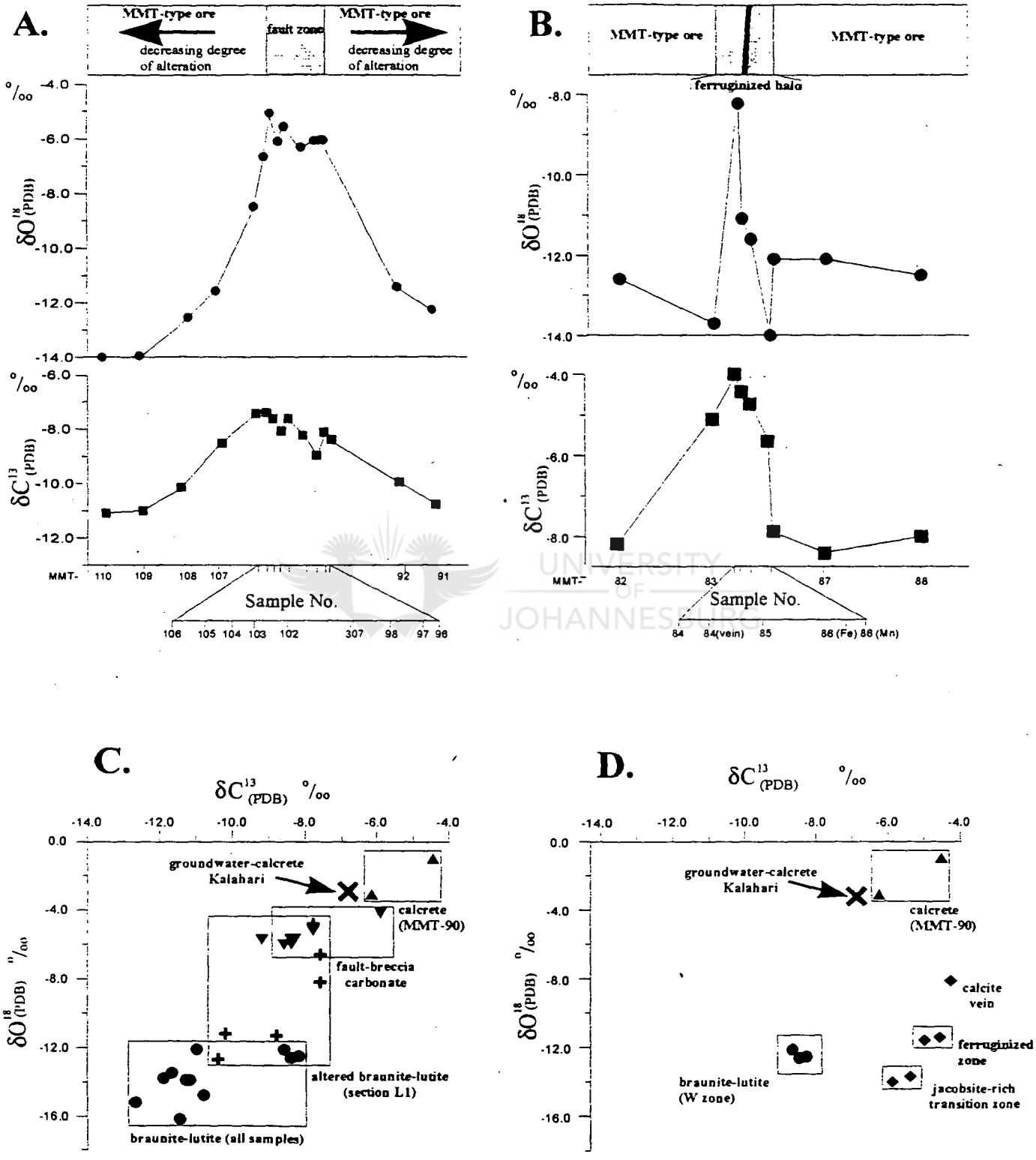

Fig. 2.13 Variations instable isotope signatures of carbonates in relation to alteration along the central fault in traverse L2 (A) and along the central veinlet in traverse S1 (B). Stable isotopes are compared with that of quarternary ground water calcrete from the Kalahari (data from Netterberg and Talma, 1985) and a calcrete sample (MMT-90) from the Kalahari Formation at Mamatwan mine in (C) for L2 and (D) for S1.

Table 2.8 $\delta^{13}C$ and $\delta^{18}O$ isotopes of carbonates in whole rock samples. All values expressed in ‰ relative to PDB.

Sample No.	type[a)]	Carbonate	$\delta^{13}C_{(PDB)}$ (‰)	$\delta^{18}O_{(PDB)}$ (‰)	Carbonate	$\delta^{13}C_{(PDB)}$ (‰)	$\delta^{18}O_{(PDB)}$ (‰)
MMT-82	MMT	calcite	-8.1	-12.8	kutnahorite	-8.3	-12.3
MMT-83	Jb	calcite	-5.2	-14.2	kutnahorite	-5	-13.2
MMT-84	He	calcite	-4.4	-8.6	kutnahorite	-3.6	-7.6
MMT-85	He	calcite	-4.8	-13.2	kutnahorite	-4.5	-9.9
MMT-86-He	He	calcite	-5.5	-14.4	kutnahorite	-5.7	-13.6
MMT-86-Mn	Jb	calcite	-7.9	-12.1	kutnahorite	-8.1	-11.4
MMT-87	MMT	calcite	-8	-12.5	kutnahorite	-8.7	-11.8
MMT-88	MMT	calcite	-7.8	-13.1	kutnahorite	-8.2	-11.8
MMT-91	TM				kutnahorite	-10.8	-12.1
MMT-92	TM				kutnahorite	-10	-11.2
MMT-104	TM	calcite	-7.6	-4.8			
MMT-105	TM	calcite	-7.4	-6.6			
MMT-106	TM	calcite	-7.4	-8.2			
MMT-107	TM	calcite	-8.6	-11.3			
MMT-108	TM	calcite	-9.6	-11.7	kutnahorite	-10.7	-13.6
MMT-109	MMT	calcite	-11	-13.9			
MMT-110	MMT	calcite	-11.1	-14.1	kutnahorite	-11	-13.6
Drill core M2 (Mamatwan, lower, unaltered orebody)							
M2/47B/1	MMT				Mn-calcite	-11.5	-13.5
M2/47B/2	MMT				Mn-calcite	-11.7	-13.8
M2/47B/3	MMT				kutnahorite	-12.5	-15.2
M2/49B/1	MMT				Mn-calcite	-11.3	-16.2

a) Ore types as defined in Tables 2.6A and 2.6B.

UNIVERSITY OF JOHANNESBURG

Discussion

The postulated sequence of events that affected the primary sedimentary braunite-kutnahorite ore at Mamatwan mine is illustrated in figure 2.14. The primary sedimentary braunite lutite ore was first subjected to stratabound metasomatism related to lowest greenschist facies metamorphism (Kleyenstüber, 1984) (Fig. 2.14B). The effect of metasomatism is restricted to oxidation of Mn-bearing carbonates to form hausmannite, partridgeite, manganite and calcite along specific beds and laminae. Kleyenstüber (1984, 1985) and Nel et al. (1986) describe the replacement of kutnahorite ovoids by hausmannite and calcite and interpret this observation as

late diagenetic or metamorphic oxidation of kutnahorite $CaMn^{2+}(CO_3)_2$ to hausmannite $Mn^{2+}Mn^{3+}{}_2O_4$ and calcite. The occurrence of partridgeite at Mamatwan was noted by De Villiers (1983). He considered partridgeite as a primary phase of 'low' temperature origin. This qualitative result is in good agreement with a low-grade metamorphic origin of partridgeite proposed here. Manganite (MnOOH) has not been previously identified at Mamatwan mine. The metasomatic replacement of Mn-bearing carbonates by hausmannite, partridgeite and manganite involves oxidation of Mn^{2+} to Mn^{3+}, but, as in the case of manganite, also hydration. This, together with the observed stratigraphic control, suggests that the metamorphic alteration was related to stratabound fluid movement or to selective loss of CO_2 from certain laminae or ovoids (Fig. 2.14B).

Table 2.9 $\delta^{13}C$ and $\delta^{18}O$ isotope ratios of secondary carbonates. All values expressed in ‰ relative to PDB standard.

Sample No.	Carbonate	$\delta^{13}C_{(PDB)}$ (‰)	$\delta^{18}O_{(PDB)}$ (‰)
MMT-84-vein	calcite	-4.5	-11.1
MMT-96	calcite	-8.4	-6.0
MMT-97	calcite	-8.2	-5.7
MMT-98	dolomite	-9.0	-5.7
MMT-102	calcite	-7.6	-5.2
MMT-103	calcite	-8.1	-5.7
MMT-307-I	calcite	-5.7	-4.2
MMT-307-II	calcite	-8.2	-6.0
MMT-90-1[a)]	calcrete-calcite	-6.0	-3.1
MMT-90-2[b)]	calcrete-calcite	-4.3	-0.8

a) MMT-90-1: Massive calcrete hosting cryptomelane aggregate.
b) MMT-90-2: calcite rhombohedrons lining vugs within cryptomelane aggregate.

Metamorphism is succeeded by two events of structurally controlled hydrothermal-metasomatic alteration along faults and veins (Fig. 2.14). Reduction and bleaching (Fig. 2.14C) along joints and veins are typical for the first (older) structurally controlled alteration event at Mamatwan. Least altered ore is characterized by the formation of jacobsite, hausmannite and clinochlore at the expense of braunite. Selective reduction and dissolution of manganese results in apparent hematitization (reddening) of ores (Fig. 2.14C). Reduction of iron to form pyrite and formation of quartz are associated with bleaching of the wallrock immediately adjacent to joints and veins that acted as fluid feeders during the alteration event (Fig. 2.14C). The central veins and joints

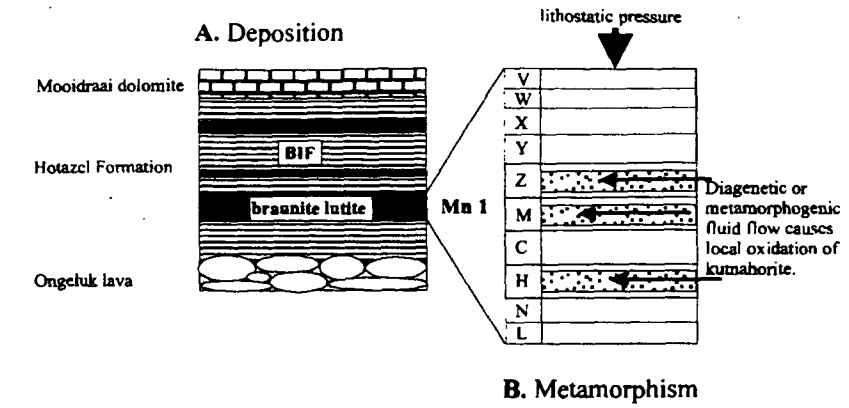

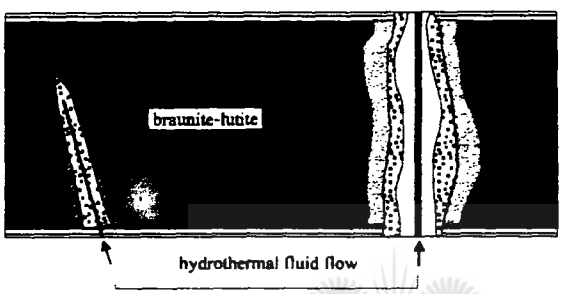

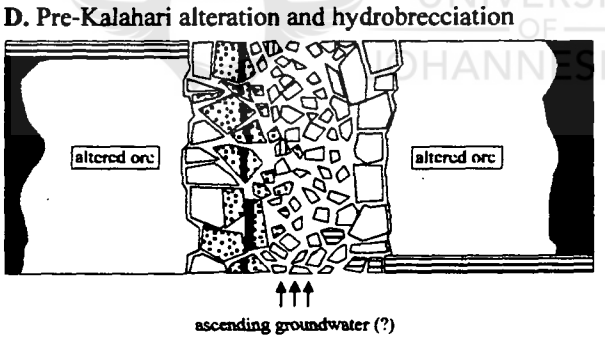

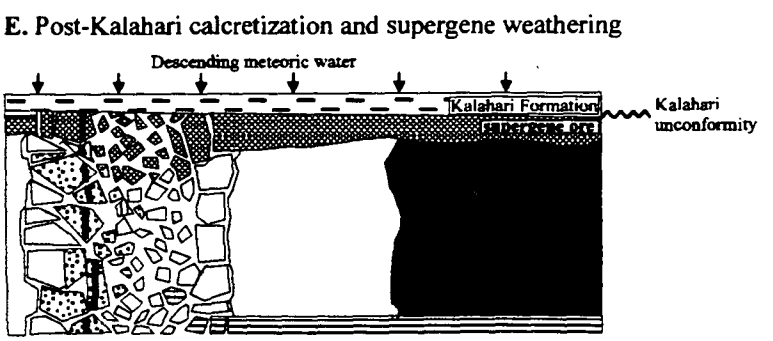

Fig. 2.14 Illustration of events that affected the manganese ores at Mamatwan mine. (A) Deposition of braunite lutite as part of the succession of chemogenic sediments of the Hotazel Formation. (B) Metamorphic overprint; Stratabound fluid flow results in local oxidation of Mn-carbonates to hausmannite, maganite and partridgeite. (C) Ferruginization and bleaching of ores along joints and faults by hydrothermal fluids that deposit hematite, pyrite, chalcopyrite, calcite, kutnahorite, chalcedony and talc. (D) Over pressured ground water ascends along reactivated faults, leading to intensive brecciation and oxidation of manganese ore along faults. (E) Post-Kalahari supergene alteration.

are filled by a complex assemblage of kutnahorite, Mn-calcite, pyrite, and talc. Breccia textures in veins are evidence for syntectonic hydrothermal activity.

The formation of pyrite, recrystallization of carbonates during alteration and the depletion of Ba are strong evidence that alteration proceeded under reducing conditions with considerable amounts of H_2S and CO_2 present. Braunite was first transformed into jacobsite and hausmannite, but further alteration resulted in the leaching of manganese in its highly soluble, divalent form. Ferric iron (hematite) was stable at moderate or low degrees of wallrock alteration, but was reduced to form pyrite at highest degrees of alteration. Alteration was caused and controlled by hydrothermal fluids of unknown origin that were introduced along fractures and joints and that infiltrated the Mamatwan-type ore. Recrystallisation of primary carbonates and increase of intergranular porosity eased the process of infiltration. The vein-hosted mineral assemblage and the relatively light $\delta^{18}O_{PDB}$ signature of the recrystallized carbonates are indicative of epithermal fluid temperatures. This simple and qualitative characterization of the hydrothermal fluid is only tentative and it fails to explain the decrease of $\delta^{18}O$ in the jacobsite-bearing transition zone of the alteration halo.

UNIVERSITY
JOHANNESBURG

Reactivation of the main fault induced the second alteration event (Fig. 2.14D). High fluid pressure and rapid fluid flow are indicated by intensive brecciation of the ore in the up to 6.5 m wide carbonate fault breccia (Fig. 2.14D). Fragments of altered braunite lutite and other rocks belonging to the Hotazel Formation float in a coarse crystalline matrix composed predominantly of calcite and dolomite. The textures of this fault breccia are very similarvery similar to hydrothermal breccias related to carbonate hosted epithermal MVT-type Pb-Zn deposits, as for example known at other localities in Griqualand West (Pering, Bushy Park, see for reference Martini et al., 1995). A similar fluid flow model may therefore be envisaged for the formation of the fault breccia at Mamatwan mine. Infiltration of the hydrothermal fluid into the braunite lutite caused intensive alteration characterized by oxidation of the primary manganese oxides and carbonates (Fig. 2.14D), the removal of CO_2 and the formation of todorokite and manganomelane. Increasing volumes of secondary porosity allowed the infiltration of the hydrothermal fluid far into the orebody. The abundance of todorokite and manganomelane, two Mn^{4+}-dominated oxides, indicates high oxygen fugacities and low temperatures during this alteration event (Frenzel, 1980). The alkali-poor and Ca-Mg-rich composition of todorokite and manganomelane is distinctively different from the K-dominated composition of cryptomelane formed by Post-Kalahari supergene weathering along the Kalahari unconformity (Kleyenstüber, 1993). However, it relates closely to the chemistry of the primary Ca-Mg-Mn-carbonates in the Mamatwan-type ore. The observed transformation of todorokite to manganomelane indicates

progressive leaching of Mg. Alteration involved thus oxidation of Mn^{2+} and Mn^{3+} to Mn^{4+}, the leaching of large amounts of carbonate-derived Ca, Mg and CO_2 and introduction of H_2O and SiO_2.

The covariance of carbon and oxygen isotopes in primary and secondary carbonates are further evidence for intensive fluid-wallrock interaction. The apparent relationship between the isotope composition of carbonates in the fault breccia and groundwater calcrete samples from the overlying Kalahari Formation may indicate a groundwater-related source of the hydrothermal fluid. Fluid-wallrock isotope exchange is generally restricted by small reaction rates at temperatures below 80 °C (Zheng and Hoefs, 1993). This lower temperature restriction may, however, be invalid as the primary carbonates become chemically dissolved and secondary carbonates, with an isotope signature intermediate between that of braunite lutite and fluid, are precipitated. Alteration may therefore have been caused by low temperature water discharging through the fault breccia. Over-pressured ground water ascending through reactivated faults may have well been the cause for hydro-brecciation and the observed alteration effects (Fig. 2.14D). The ground water causing the alteration was probably similar in character to recent groundwater, being highly oxidizing and under saturated with respect to CO_2 but it introduced only small amounts of alkalies, thus indicating low salinities of the ground water.

The two structurally controlled alteration events observed at Mamatwan mine are distinctively different from the alteration event that led to formation of Wessels-type ores in the northwestern part of the Kalahari manganese field (Gutzmer and Beukes, 1995; Beukes et al., 1995). This resulted in leaching of CO_2, Ca, Mg and SiO_2 from the primary Mamatwan-type ore, intensive ferruginization of manganese ore around faults and recrystallization of braunite lutite to coarse crystalline ores rich in hausmannite, braunite II, bixbyite and andradite (Gutzmer and Beukes, 1995; Beukes et al., 1995). The relative age of the earlier alteration event at Mmamatwan mine is also provided by the fact that pyrite-chalcopyrite-calcite vein mineralization, similar to that at Mamatwan, are known from the Wessels, Hotazel, and Gloria mines and crosscut Wessels-type ore. The Wessels event has tentatively been dated at 1250 My (Dixon, 1989).

The mineralogical effects of the two structurally controlled alteration events are also distinct from alteration related to supergene weathering along the Kalahari unconformity (Fig. 2.14E). Weathering caused oxidation of primary ore minerals to cryptomelane, pyrolusite and goethite. Alkali elements were apparently introduced during the weathering process as indicated by the presence of botryoidal cryptomelane (De Villiers, 1970; Kleyenstüber, 1993) and manjiroite (Kleyenstüber, 1993). Kleyenstüber (1993) suggested that K_2O, scavenged by cryptomelane, may be derived from clays and marls in the overlying Kalahari Formation (Fig. 2.14E). It is interesting

to note that supergene cryptomelane related to the weathering event is alkali-enriched compared to manganomelane and todorokite of the earlier structurally-controlled low-temperature hydrothermal alteration event.

Conclusions

Four postdepositional alteration events affected the Early Proterozoic manganese ore at Mamatwan mine. Primary braunite lutite, consisting of Mn-bearing carbonates, braunite and hematite, was first subjected to stratabound metasomatic fluid infiltration during low-grade metamorphism (Fig. 2.14B) which affected manganese ores throughout the Kalahari manganese field. Stratabound metasomatism was succeeded by two periods of structurally controlled metasomatic alteration along faults and joints. The first of these, observed locally throughout the Kalahari manganese field, involved introduction of epithermal fluids along faults, veins and joints, causing locally reduction and bleaching of the manganese ore (Fig. 2.14C). It was followed by an event which involved introduction of low temperature, oxidizing ground water that ascended along reactivated faults and caused intensive oxidation and carbonate leaching of the adjacent manganese ore (Fig. 2.14D). At last supergene alteration by descending ground water took place along the Kalahari unconformity leading to the formation of cryptomelane, pyrolusite and goethite (Fig. 2.14E).

UNIVERSITY OF JOHANNESBURG

Acknowledgements

We would like to thank the management of SAMANCOR for permission to undertake the present study at Mamatwan mine. The staff of the Geology Department at Hotazel is thanked for their generous help during many stays at Hotazel. Special thanks to N. Bleeker for his assistance during sampling and mapping at the mine.

References

Beukes, N.J., Burger, A.M., and Gutzmer, J. (1995). Fault controlled hydrothermal alteration of Palaeoproterozoic manganese ore in Wessels mine, Kalahari manganese field, South Africa. S. Afr. J. Geol., 98, 435-451.

De Villiers, J.E. (143). A preliminary description of the new mineral partridgeite. Amer Mineral., 28, 336-338.

De Villiers, J.E. (1983). The manganese deposits of Griqualand West, South Africa: Some mineralogic aspects. Econ.Geol., 78, 1108-1118.

De Villiers, P.R. (1970). The geology and mineralogy of the Kalahari-manganese field, north of Sishen, Cape Province. Geol. Surv. S. Afr., Memoir 59 , Pretoria, 84 pp.

Dixon, R.D. (1989). Sugilite and associated metamorphic silicate minerals from Wessels mine, Kalahari manganese field. Geol. Surv. S. Afr., Memoir 93, Pretoria, 47 pp.

Frenzel, G. (1980). The manganese ore minerals. In: Varentsov, I.M., Grasselly, G. (eds.): Geology and geochemistry of manganese, Vol. 1, Schweizerbart'sche Verlagsbuchhandlung, Stuttgart, 25-157.

Gutzmer J., Beukes N.J. (1995). Fault controlled metasomatic alteration of Early Proterozoic sedimentary manganese ores in the Kalahari manganese field, South Africa. Econ. Geol., 90, 823-844.

Heinrichs, H., and Herrmann, A.G. (1990). Praktikum der analytischen Geochemie. Springer Verlag, Berlin, 669 pp.

Kleyenstüber, A.S.E. (1984). The mineralogy of the manganese-bearing Hotazel Formation, of the Proterozoic Transvaal Sequence in Griqualand West, South Africa. Trans. Geol. Soc. S. Afr., 87, 257-272.

Kleyenstüber, A.S.E. (1985). A regional mineralogical study of the manganese-bearing Voelwater Subgroup in the Northern Cape Province. Unpubl. PhD thesis, RAU, 328 pp.

Kleyenstüber, A.S.E. (1993). Some significant characteristics of the manganese ores and some of the minerals occurring in the Proterozoic Kalahari maganese field, South Africa. Resource Geology,17, 2-11.

Martini, J.E.J., Eriksson, P.G., and Snyman, C.P. (1995). The Early Proterozoic Mississippi Valley-type Pb-Zn-F deposits of the Campbellrand and Malmani Subgroups, South Africa. Mineral. Depos., 30, 135-145.

Nel, C.J. (1984). Die mineralogie en geochemie van die Mamatwanertsliggam, Kalaharimangaanveld, Transvaal-Supergroup. Unpubl. MSc thesis, RAU, 119 pp.

Nel, C.J., Beukes, N.J., De Villiers, J.P.R. (1986). The Mamatwan manganese mine of the Kalahari manganese field. In: Annhaeusser C.R., Maske S. (eds): Mineral deposits of Southern Africa. Geol. Soc. S. Afr., Johannesburg, 1, 963-978.

Netterberg, T., and Talma, S. (1985). Stable isotope bundances in calcretes. In: Wilson, B.C.L., (ed.): Residual deposits. Geol. Soc. London sp. publ., No. 11, Blackwell, Oxford, 221-233.

Zheng, Y.F., and Hoefs, J. (1993). Carbon and oxygen isotopic covariations in hydrothermal calcites. Mineral Depos., 28, 79-89.

UNIVERSITY OF JOHANNESBURG

Chapter Three

Minerogenesis of the Kalahari manganese field, South Africa

Abstract

The mineralogy of the manganese ores of the giant Paleoproterozoic Kalahari manganese deposit of the Transvaal Supergroup has been subject of many studies and up to now 135 different ore and gangue minerals have been described, of which eight represent new mineral species. In this paper an attempt is made to construct a paragenetic sequence for this complex mineral assemblage. This is done through correlation of different mineral assemblages with specific geological events or structural features and by determining relative ages of minerals in outcrop, hand specimen and under the microscope.

Sedimentation and early diagenesis of the Hotazel Formation, composed of interbedded iron-formation and braunite lutite, was followed by low grade metamorphism and associated stratabound metasomatism. Braunite-lutite of sedimentary origin, comprising 97 % of the total ore reserve of 13500 Mt and contains between 20 and 39 percent Mn. It is composed of braunite, hematite and kutnahorite, and abundant early diagenetic kutnahorite and manganoan calcite forming laminae and ovoids. Fluid flow during late diagenesis or lower greenschist facies metamorphism led to stratabound metasomatic oxidation of Mn-bearing carbonates to hausmannite and Mn-poor calcite.

Three structurally controlled hydrothermal alteration events succeed metamorphism. These events are referred to as Wessels, Mamatwan and Smartt events. The Wessels alteration event is the oldest of the three events and it is of great economic importance because virtually all of the high-grade (> 42 percent Mn) formed during this event through alteration of carbonate-rich low-grade Mamatwan-type manganese ore (braunite-lutite) to high-grade, carbonate-poor Wessels-type manganese ore is related to this event. This Wessels hydrothermal event took place in the northwestern part of the Kalahari deposit, associated with a system of major north-south and minor east-west striking normal faults. The Mamatwan alteration event is observed throughout the Kalahari manganese deposit but alteration is very localized. Reduction halos and discolouration of braunite-lutite around fracture or joint-hosted sulphide-carbonate mineralization are typical features of the Mamatwan alteration event. In contrast, the Smartt alteration event is characterized by oxidation of braunite-lutite and the formation of todorokite and manganomelane.

Syn- and Post-Kalahari supergene alteration took place below the suboutcrop of the Hotazel Formation against the calcretized sediments of the Cenozoic Kalahari Formation. Cryptomelane and pyrolusite are the predominant minerals of this supergene alteration event.

Introduction

The Kalahari manganese field, situated some 60 km to the northwest of Kuruman in the Northern Cape Province of South Africa (Fig. 3.1), represents the worlds largest manganese deposit with some 13500 Mt of Mn ore at >20 percent Mn (Taljaardt, 1982), and its wealth of beautiful and rare mineral specimens are sought after by mineral collectors (von Bezing et al., 1991). Its mineralogical diversity is unique and matched only by the much smaller and geologically complex manganese deposits of Franklin/ New Jersey (Frondel and Baum, 1974) and Långban/ Sweden (Moore, 1971; Boström et al., 1979).

Many scientific publications have dealt with the systematic mineralogy of the manganese ore (Kleyenstüber, 1984, 1985; Nel, 1985; Nel et al., 1986) and with the geological processes that led to the formation of different ore types (Boardman, 1964; De Villiers, 1960; De Villiers, 1970; De Villiers, 1983; Beukes, 1983; Miyano and Beukes, 1987; Kleyenstüber, 1993; Gutzmer, 1993; Cornell and Schütte, 1995; Grobbelaar et al., 1995; Beukes et al., 1995; Gutzmer and Beukes, 1995). Others describe the chemical and crystallographic properties of specific rare (or new) minerals (De Waal and Hiemstra, 1968; Dunn et al., 1980; Pienaar, 1982; Peacor et al., 1983; Dixon, 1989; Peacor et al., 1990; Dai and Harlow, 1992; Von Bezing, 1992; Beukes et al., 1993; Gutzmer and Cairncross, 1993; Armbruster et al., 1993a and b; Dai et al., 1993; De Bruiyn et al., 1994; Giester and Rieck, 1994; Gutzmer et al., 1995; Hoffmann and Armbruster, 1995; Nyfeler et al., 1995) or document the occurrence of attractive mineral specimens of interest for mineral collectors (Wilson, 1978; Von Bezing et al., 1991; Gutzmer and Cairncross, 1993; Von Bezing, 1992; Von Bezing and Gutzmer, 1994a and b). However, no attempt has ever been made to place all, or even some of the minerals into the context of a paragenetic sequence. Kleyenstüber (1984) distinguished only between minerals of primary and secondary (metamorphic and hydrothermal) origin and stated that 'the

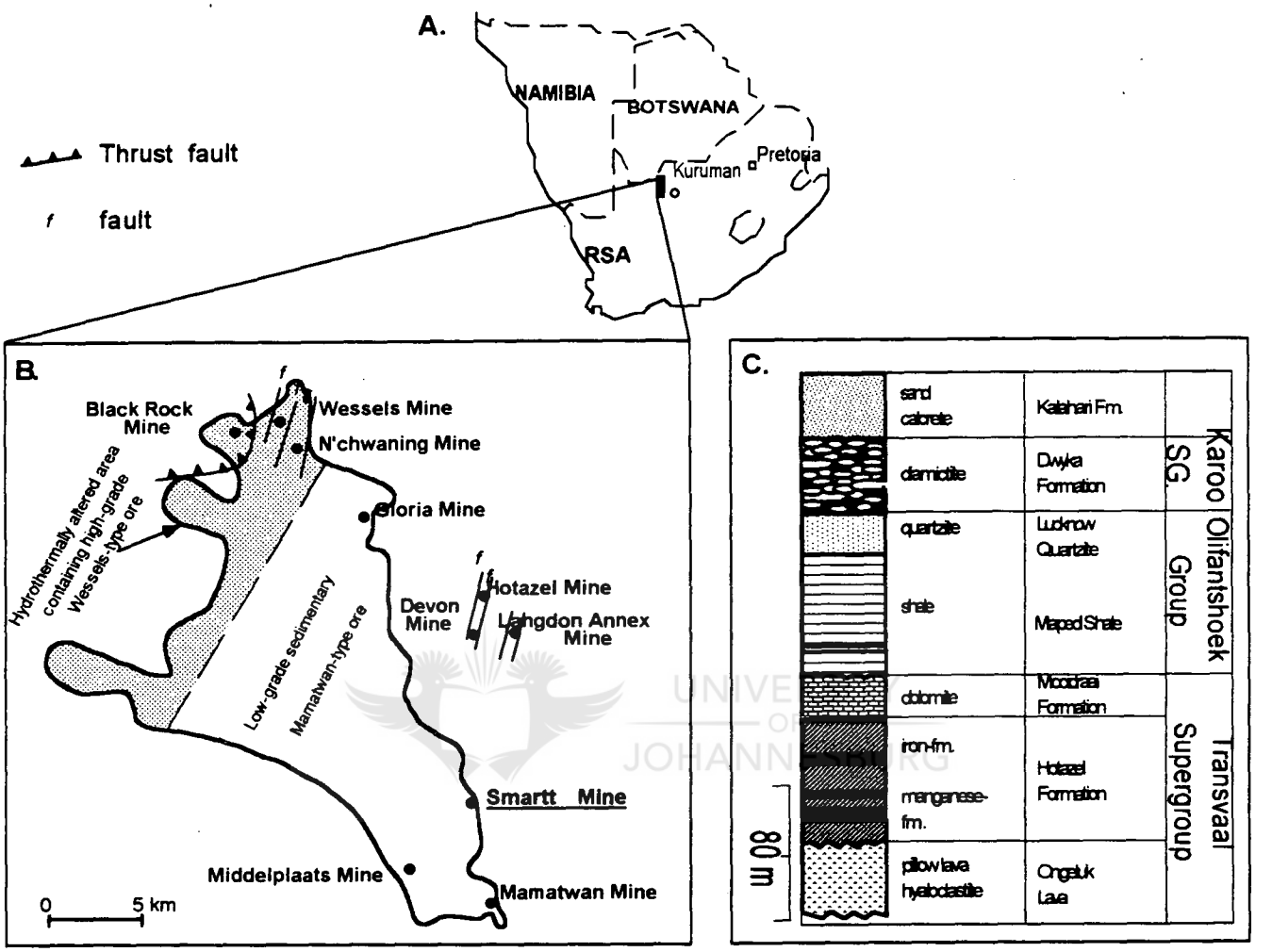

Fig. 3.1 Locality map of the Kalahari manganese deposit (A) showing the distribution of thrusting, major normal faulting, ore-types and location of mines (B) and the generalized stratigraphy of the area (C).

proposal of any precise mineralogical paragenetic setting is difficult, since certain minerals are present as various generations depending on whether they are diagenetic, metamorphic or hydrothermal in origin'. Understanding mineral paragenesis and the relationship of specific mineral assemblages to certain geological processes or structures is, however, fundamental to understanding the origin and geological evolution of the Kalahari manganese field (Gutzmer and Beukes, 1995; Beukes et al., 1995) and if neglected places serious doubt on certain interpretations about the deposit (Beukes and Gutzmer, 1996). This paper is an attempt to overcome this shortcoming. Paragenetic sequences of minerals are identified and related to specific geological events or structures.

The paper is based on systematic field observations and petrographic analyses of several hundred manganese ore samples. However, many of the rare minerals in the Kalahari manganese deposit represent unique finds and their parageneses could only be defined in hand specimen that are preserved in mineral collections. It is especially due to the courtesy of Dr. L. von Bezing from Kimberley that one of the most complete and systematic collection of minerals from the Kalahari manganese field was accessible for study. The existing mineralogical literature about the Kalahari manganese deposit was consulted in cases where sample material was not available for a specific mineral. It must be stressed that the study is confined to minerals occurring in the manganese ore beds and that those of associated iron-formations, basaltic lavas and intrusive bostonite dykes are not considered.

The exact meaning of the terms mineral assemblage, mineral association, mineral paragenesis and paragenetic sequence are often confused. In this study these important terms are defined following the definitions by Bates and Jackson (1984). Groups of minerals that form contemporaneously as products of one geological event are referred to as a mineral paragenesis. The terms mineral assemblage and mineral association bear no genetic significance, but refer to the total number of mineral phases in a rock or ore sample irrespective of their mode of formation and their relationship towards each other. The paragenetic sequence is the sequential order of mineral deposition, either as individual phases or mineral assemblages.

Previous mineralogical work

De Villiers (1970) conducted the first systematic study of the mineralogy of the manganese ores of the Kalahari manganese field. Kleyenstüber (1984) made a considerable contribution in studying the mineralogy of the manganese ore and its country-rocks. Nel et al. (1986) and De Villiers (1983) performed local studies of the occurrence and distribution of economically important minerals. Dixon (1989) presented a detailed mineralogical study of the peculiar occurrence of sugilite in calc-silicate bodies in the Wessels-type ore. Von Bezing (1992) recorded 127 identified mineral species from the Kalahari manganese deposit (including some minerals occurring only in the iron-formation and in the bostonite dykes), of which the following three had been described as new mineral species: sturmanite (Peacor et al., 1983), orlymanite (Peacor et al., 1990), and vonbezingite (Dai and Harlow, 1992). Following Von Bezings (1992) publication five new mineral species have been described, namely, poldervaartite (Dai et al., 1993), hennomartinite and kornite (Armbruster et al., 1993), effenbergerite (Giester and Rieck, 1994),

and nchwaningite (Nyfeler et al., 1995). A fair number of rare minerals could also be added to the list of identified minerals, such as taikanite (Armbruster et al. 1993), shigaite, mozartite and 11Å tobermorite (Gutzmer and Cairncross, 1993). Up to the present a total of 135 minerals have been identified in the Kalahari manganese deposit (Appendix 1) and several unknown mineral species are awaiting identification.

Geological setting

The primary manganese ore of the Kalahari manganese deposit is of sedimentary origin and interbedded with iron-formation of the Hotazel Formation of the Paleoproterozoic Transvaal Supergroup (Fig. 3.1C). Three manganese beds are present in the Hotazel Formation (Fig. 3.1C), but only the lower one is extensively mined. The Hotazel Formation is conformably underlain by andesitic lava, pillow lava and hyaloclastite of the Ongeluk Formation and conformably overlain by stromatolitic dolomite of the Mooidraai Formation. The strata are gently folded and dip regionally at about 8° to the west.

UNIVERSITY OF JOHANNESBURG

The sedimentary rocks of the Hotazel Formation were affected by a number of postdepositional geological events (Fig. 3.2) (Beukes et al., 1995). Deposition of the sediments of the Hotazel Formation took place approximately at 2.2-2.3 Ga (Beukes et al., 1995). Contact metamorphism must have affected the ore around NE-SW and NNE-SSW striking bostonite dykes that intruded after diagenetic lithification of the Hotazel Formation (Fig. 3.2B), but prior to erosion and paleooxidation of the Hotazel Formation (Fig. 3.2C) and the deposition of the Late Paleoproterozoic Olifantshoek red bed sequence (Fig. 3.2D). The origin of major N-S striking and normal faults in the northwestern part of the Kalahari manganese appears to coincide with the deposition of this red bed sequence at about 1.95 Ga (Beukes and Smit, 1987). Regional metamorphism of lower greenschist facies (Kleyenstüber, 1984) affected the Olifantshoek sequence as well as the underlying rocks of the Transvaal Supergroup and was most probably related to thrusting and crustal thickening from the west during the Kheis orogenetic event at 1.8-1.9 Ga (Fig. 3.2E) (Beukes and Smit, 1987).

Hydrothermal alteration and upgrading of low-grade Mamatwan-type ore to high-grade Wessels-type ore next to major N-S and minor E-W striking normal faults (Gutzmer and

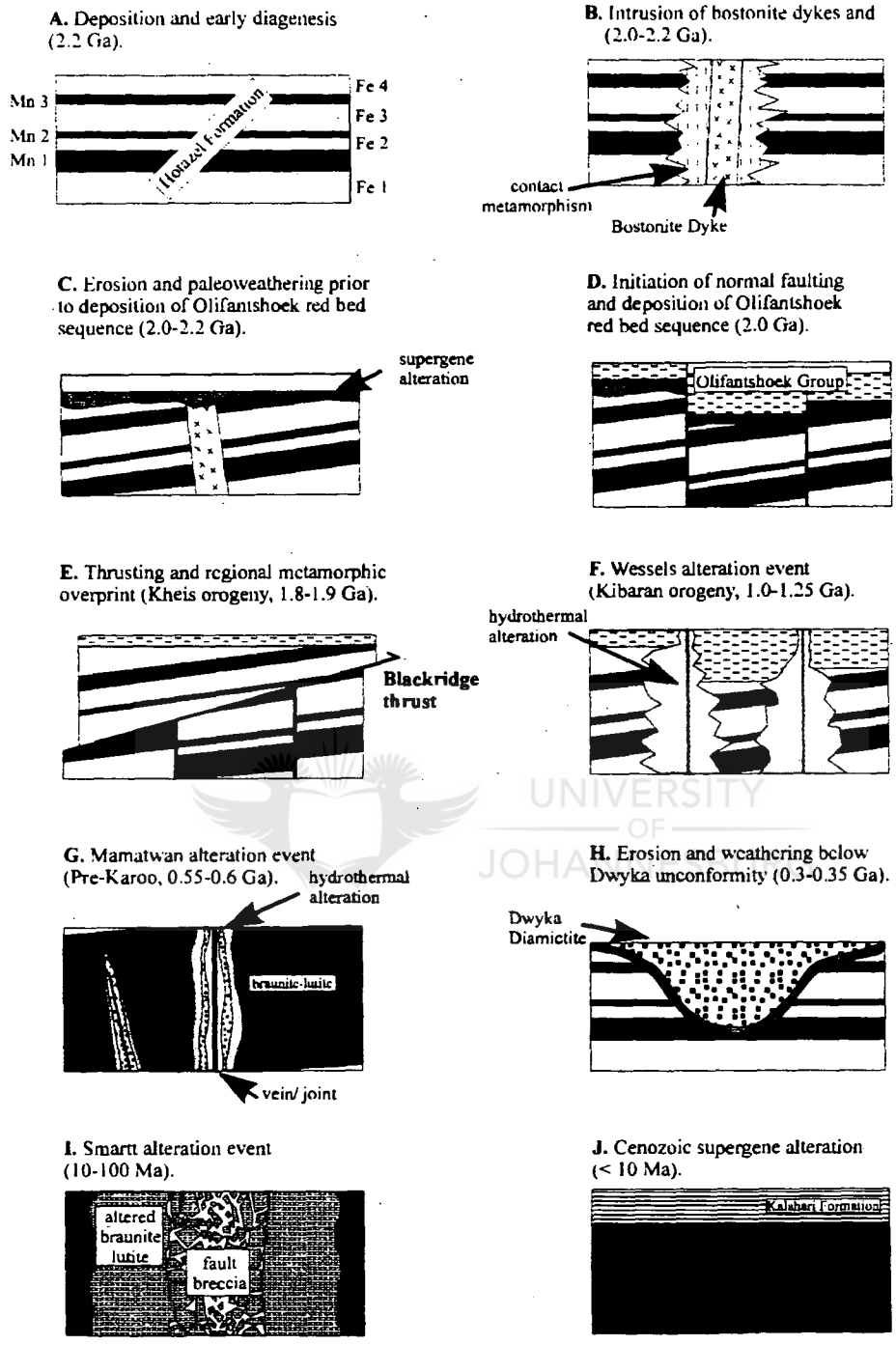

Fig. 3.2 Relative geochronological framework of important geological and structural events in the Kalahari manganese field. (A) Deposition of iron- and manganese-formations of the Hotazel Formation (Transvaal Supergroup); (B) Intrusion of bostonite dykes into the Hotazel Formation; (C) Paleoweathering of the Hotazel Formation along the Mapedi unconformity, and associated N-S orientated normal faulting in the NW part of the Kalahari deposit (D); (E) Thrusting from the west and associated crustal thickening induces lower greenschist facies metamorphism; (F) Hydrothermal alteration along normal faults in the NW part of the Kalahari manganese deposit (Wessels alteration event); (G) Syntectonic sulphide-carbonate mineralization in joints and veins and associated wallrock alteration (Mamatwan alteration event); (H) Paleoweathering associated with the Late Devonian-Early Carboniferous Dwyka glaciation; (I) Smartt alteration event, oxidation of ores around fault breccias induced by Pre-Kalahari ground water; (J) Recent supergene oxidation along the Kalahari unconformity.

Beukes, 1995; Beukes et al., 1995) (Fig. 3.2F) is apparently related to the Kibaran orogenetic event (Beukes et al., 1995) as preliminary dating of the hydrothermal mineral assemblage associated with this 'Wessels alteration event' indicates an age of about 1.0-1.25 Ga (Dixon, 1989; Frey, pers. comm., 1995). The Wessels alteration event is succeeded by a second event of structurally controlled hydrothermal alteration. Reduction and bleaching of braunite-lutite along joints and secondary normal faults are characterize the alteration known as the Mamatwan alteration event (Fig. 3.2G). Carbonate-sulphide vein mineralization associated with this alteration event occurs sporadically across the entire Kalahari manganese deposit and appears to be related to a period of tectonic activity and the formation of WSW - ENE and ESE-WSW striking faults and joints. These structures possibly predate the deposition of the Early Permian Karoo Supergroup.

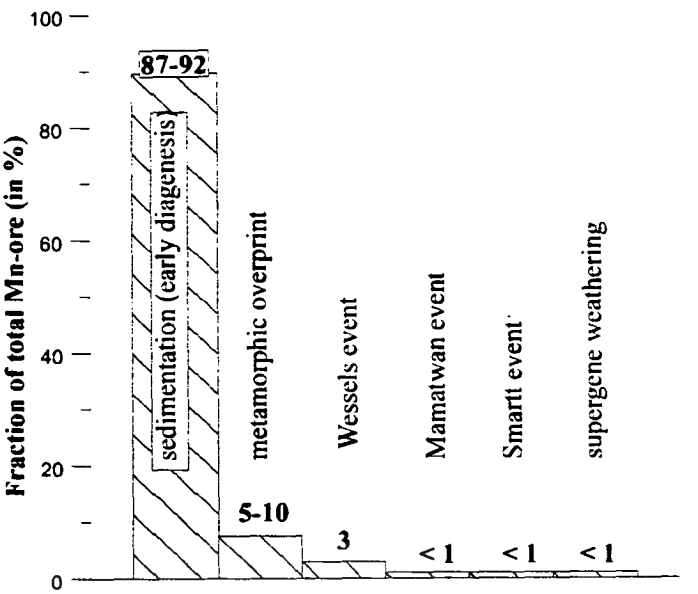

Fig. 3.3A Quantitative importance of the different alteration assemblages as compared to the primary sedimentary braunite lutite mineral assemblage.

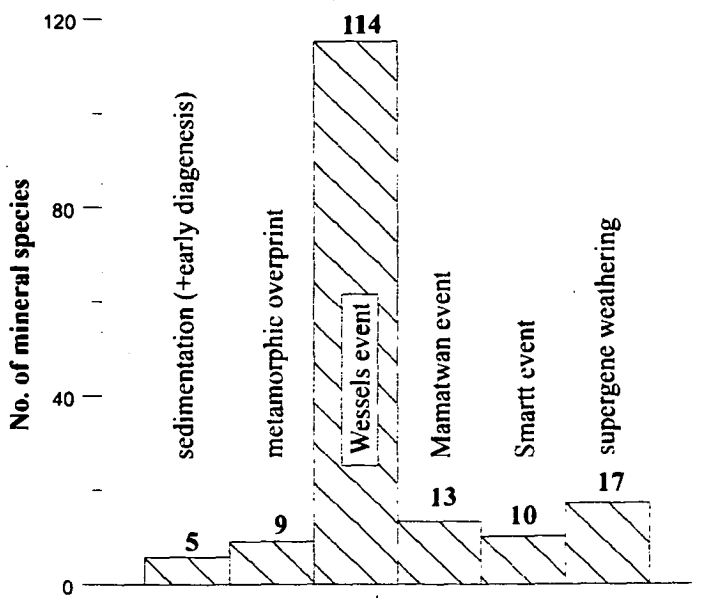

Fig. 3.3B Mineralogical diversity of specific geological events. Note the unusual mineralogical diversity associated with the Wessels alteration event.

A third and apparently final event of fluid influx and alteration of manganese ore along faults is evident only in the southern and eastern parts of the Kalahari manganese deposit, where the Hotazel Formation was exposed by erosion prior to the deposition of the Kalahari Formation . It is known as the Smartt event and characterized by infiltration of

low temperature fluids causing brecciation and hydrofracturing along faults and oxidation and upgrading of braunite-lutite adjacent to the feeder structures.

Recent (Syn- to Post-Kalahari, < 10 Ma) supergene alteration of manganese ores by descending meteoric water is restricted to the eastern suboutcrop of the Hotazel Formation below the unconsolidated and calcretized sediments of the Kalahari Formation (Fig. 3.2J). Supergene alteration represents the only event that today affects the mineralogy of the manganese ores of the Kalahari manganese deposit (De Villiers, 1970; Kleyenstüber, 1993). The absolute ages of the Mamatwan and Smartt events are unknown. Tentatively the Mamatwan event is considered pre-Karoo in age. The Smartt event is definitely pre-Kalahari in age and possibly post-Karoo.

Only the characteristics of six of these nine geological events are well enough understood to allow reliable identification of the associated mineral paragenesis. The three remaining geological events, e.g. contact metamorphism next to bostonite dykes and paleoweathering of the ore below unconformities at the base of the Late Paleoproterozoic Olifantshoek red beds and the Permian Dwyka Formation of the Karoo Supergroup have not been studied in detail and shall only receive cursory comment in this paper. Ore formed during the Mamatwan and Smartt events and the supergene alteration event constitute a fraction of a percent of the total

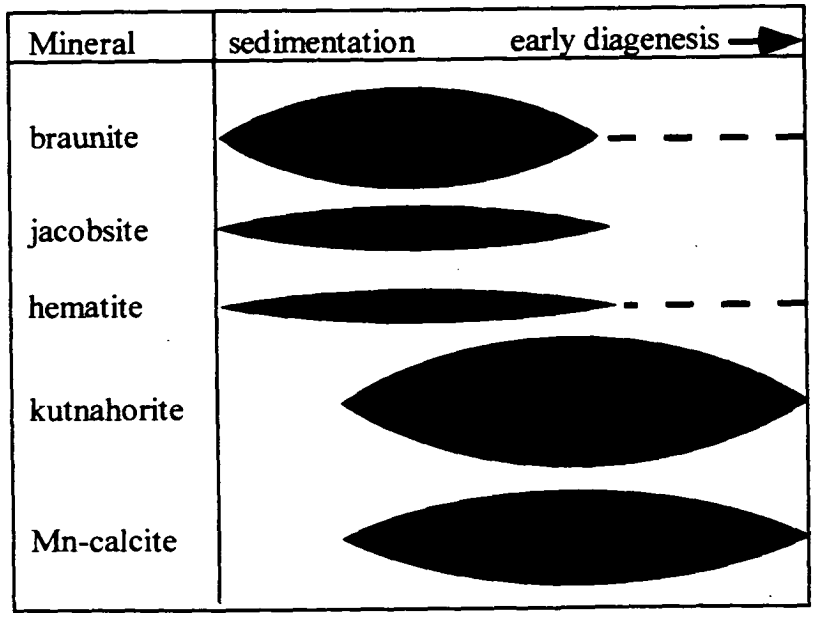

Fig. 3.4A Paragenetic sequence for the sedimentary and early diagenetic braunite lutite mineral assemblage.

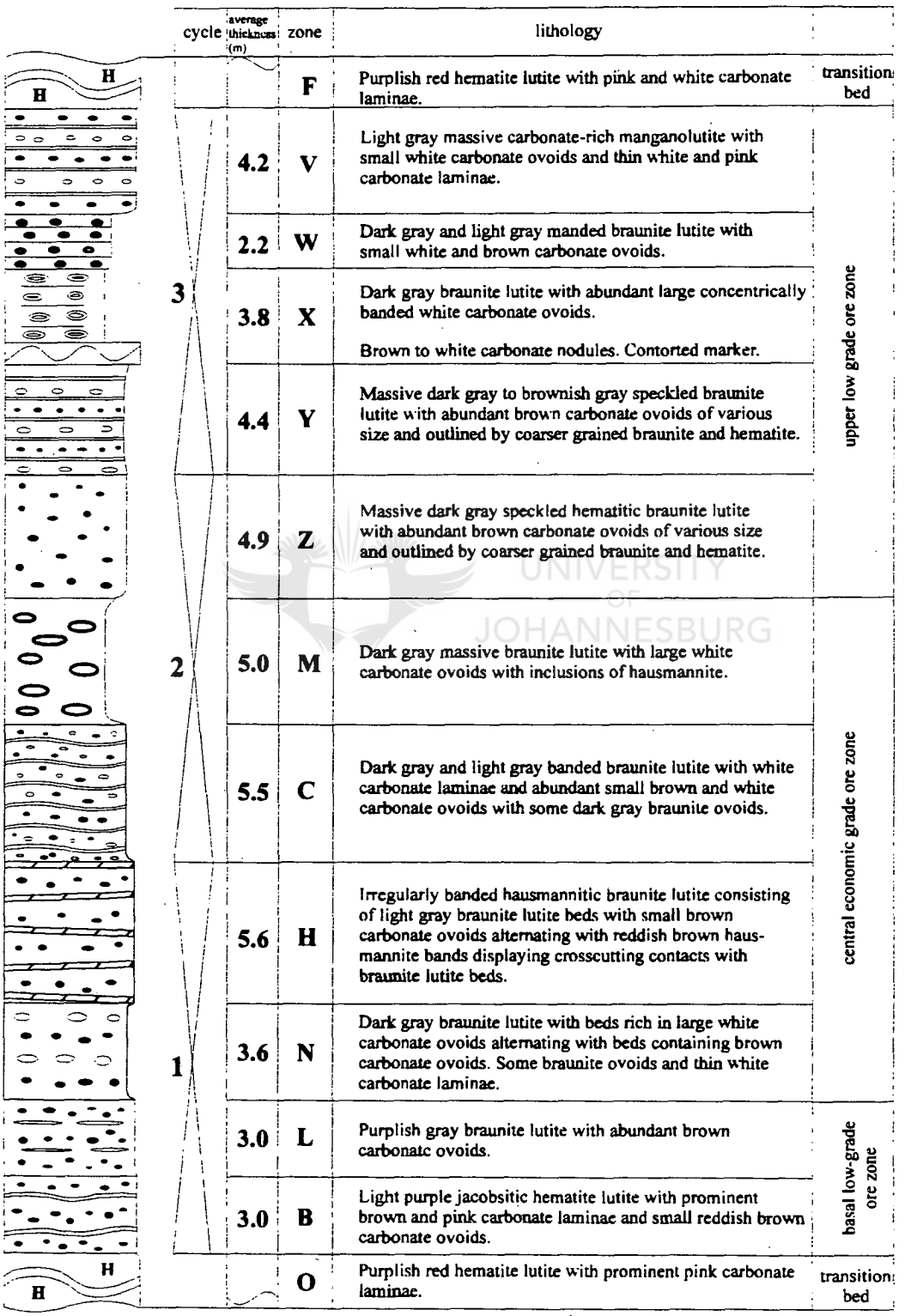

Fig. 3.4B Detailed lithostratigraphic subdivision of the lower manganese ore bed at Mamatwan mine (modified after Nel et al., 1986).

ore reserve (Fig. 3A). Sedimentary ores and their low-grade metamorphosed equivalent account for 97 percent of the ore reserve, and Wessels-type ore constitutes the remaining 3 percent of the reserve (Fig. 3.3A).

It is interesting to note that of all the minerals present in the Kalahari manganese field some 114 are known to be associated with the Wessels alteration event (Fig. 3.3B). Diagenesis and low-grade metamorphic alteration are represented by 13 minerals, the Mamatwan event by 13 minerals, the Smartt event by 10 minerals and supergene weathering by 17 minerals (Fig. 3.3B).

Paragenesis of the chemosedimentary braunite-lutite mineral association

The primary sedimentary braunite-lutite is finely laminated and microcrystalline consisting of finely intergrown braunite, hematite and manganese-bearing carbonate (Fig. 3.4A) with compositions ranging from Mn-calcite to Mg-kutnahorite (Kleyenstüber, 1984; Nel et al., 1986). The braunite-lutite is typically of grey to dark brownish-grey colour, and without any microscopically visible porosity. A characteristic feature is the occurrence of numerous early diagenetic kutnahorite and Mn-calcite ovoids and laminae of brownish or reddish-white colour. In some cases compaction is visible around the ovoids in the braunite-lutite matrix. Braunite and dusty hematite are finely intergrown with the matrix carbonate.

Based on textural, petrographical and quantitative mineralogical data the basal manganese orebody, exposed by mining activities at Mamatwan and Middelplaats mines, was subdivided into three sedimentary cycles composed of 11 texturally distinct zones (Nel et al., 1986) (Fig. 3.4B). The transition of the manganese orebody into the over- and underlying iron-formation is characterized by the occurrence of hematite-lutite with minor jacobsite (Fig. 3.4B).

Late diagenetic/ lower greenschist facies metamorphic mineral association

The metamorphic mineral assemblage is characterized by the occurrence of hausmannite and calcite as replacement products of early diagenetic kutnahorite and Mn-calcite ovoids and laminae (Fig's. 3.5A, 3.5B). Kleyenstüber (1984) suggested that hausmannite which replaces Mn-bearing carbonate ovoids (Fig. 3.5C) formed earlier than hausmannite which replaces carbonate laminae (Fig. 3.5B). However, our evidence suggests that the hausmannite in carbonate ovoids and laminae is of similar character and composition and formed during the same alteration event. The hausmannite occurs along specific laminae (Fig. 3.5B). It forms relatively coarse

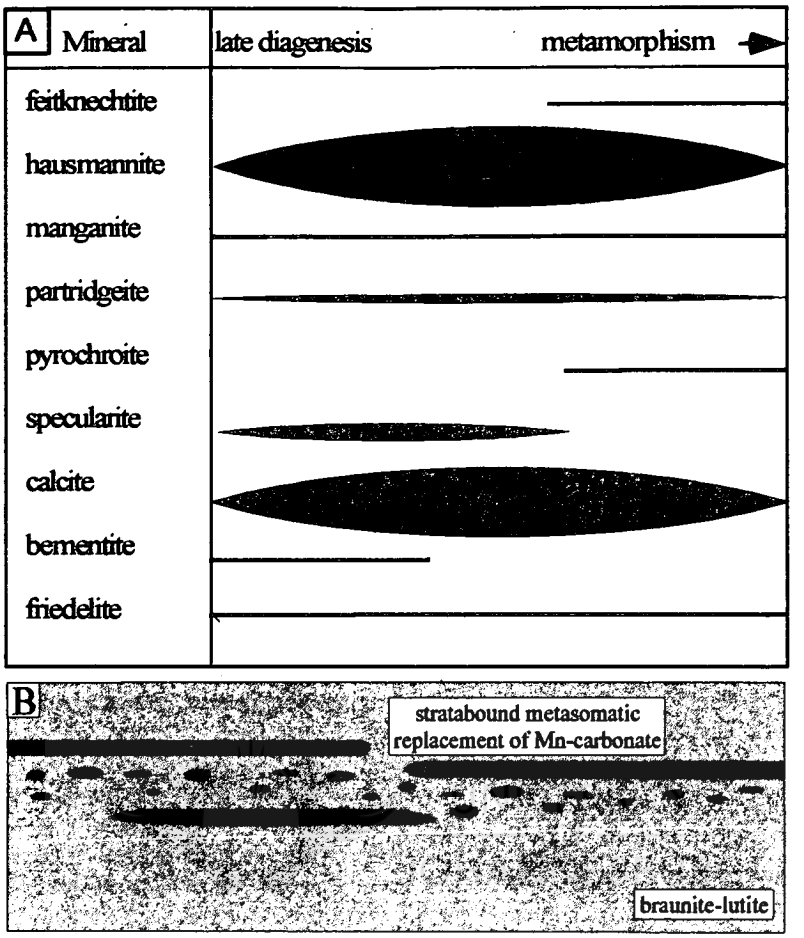

Fig. 3.5 Metamorphic/ metasomatic mineral paragenesis. (A) Paragenetic sequence for minerals of late diagenetic or greenschist facies metamorphic origin. (B) Sketch illustrating the occurrence of minerals of metasomatic origin as replacement product of Mn-bearing carbonates.

crystals and is closely associated with calcite which contains no more than about 5 wt % MnO in contrast to early-diagenetic Mn-calcite containing 10-17 wt % MnO. The occurrence of partridgeite, manganite, bementite, feitknechtite, friedelite, pyrochroite and platy, recrystallised hematite is very similar to that of hausmannite (Fig. 3.5C) (Pienaar, 1982; Kleyenstüber, 1985). It is important to note that this metamorphic overprint is not absolutely penetrative and restricted to certain lamina or zones in the Mamatwan-type ore (Fig. 3.5B) (Nel et al., 1986). This suggests fluid movement and the importance of metasomatism during the low-grade metamorphic event.

Fig. 3.5C Photomicrograph showing metasomatic hausmannite (light gray) replacing kutnahorite ovoids in fine crystalline braunite lutite matrix composed of braunite and hematite (white) and kutnahorite (gray) (reflected light).

Wessels-event of hydrothermal alteration

Hydrothermal alteration affected Mamatwan-type ore (braunite-lutite) along major N-S striking and minor E-W striking faults and transformed the primary braunite-lutite into oxide-rich, carbonate-poor high-grade Wessels-type manganese ore (Gutzmer and Beukes, 1995; Beukes et al., 1995). The transformation of Mamatwan-type ore to Wessels-type ore involved removal of the sedimentary carbonate, considerable leaching of Si, Ca and Mg and local redistribution of Fe and Mn. Fe and minor amounts of Na and K were introduced by the hydrothermal fluid (Gutzmer and Beukes, 1995; Beukes et al., 1995). The degree of alteration is highest immediately adjacent to faults and diminishes towards the centre of fault blocks, where relatively unaltered Mamatwan-

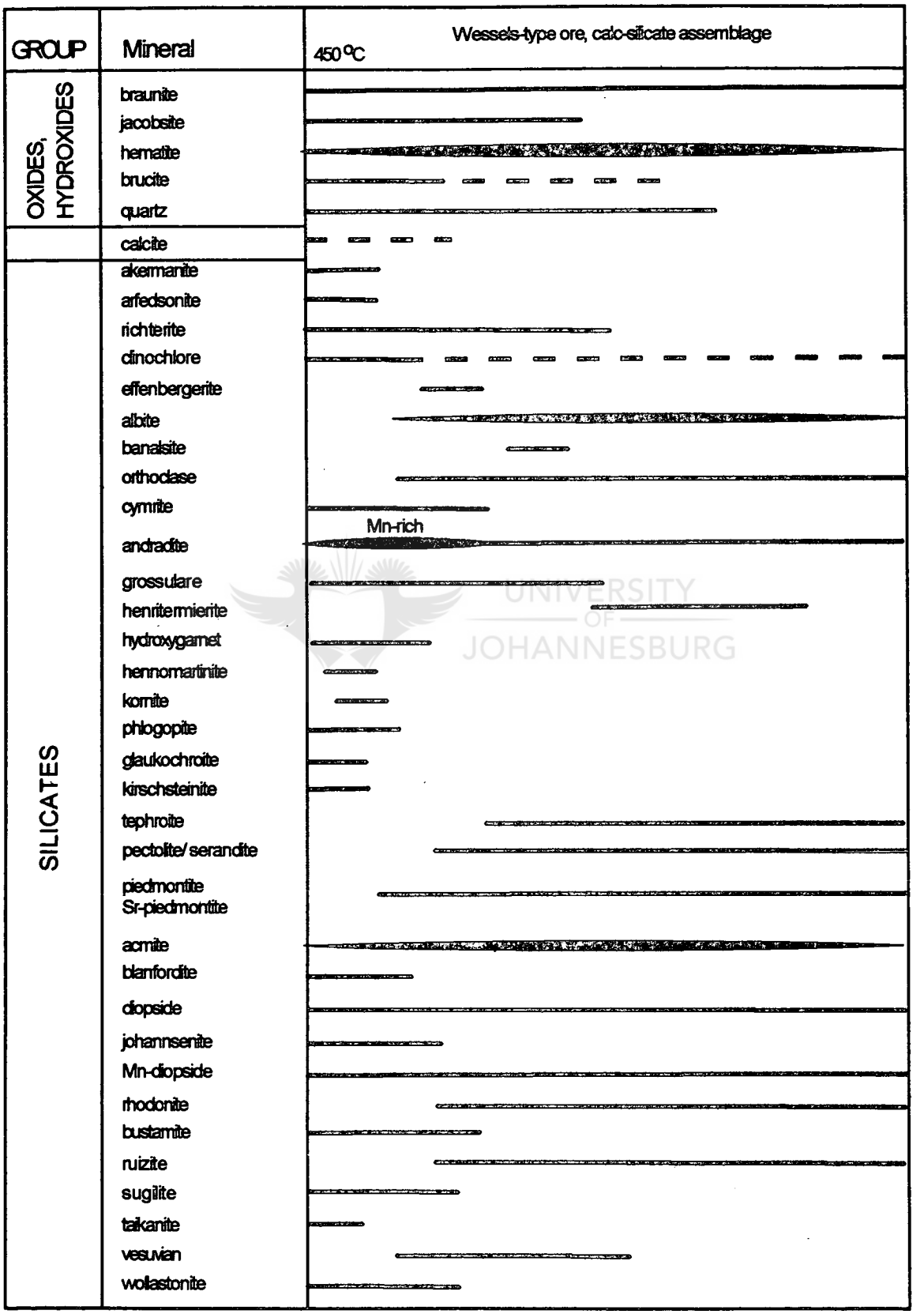

Fig. 3.6A Suggested paragenetic succession for the sugilite calc-silicate assemblage.

type ore is preserved (Fig. 3.7B). The Wessels-type ore is either coarse-crystalline and massive with abundant secondary porosity and small vugs lined by euhedral crystals of ore and gangue minerals, or fine-grained and dense (Fig. 3.7D). The ore is typically black or brownish-black with submetallic shine.Kleyenstüber (1984, 1993) used the terms Wessels-type ore, Hotazel-Supergrade ore and Black Rock-type ore to name high-grade manganese ores of different mineralogy and chemistry. However, they all appear to be part of the Wessels mineralizing event, defining different styles and degrees of hydrothermal alteration. Hotazel-Supergrade ore, consisting merely of hausmannite and hematite, represents the highest degree of alteration, in contrast to Black Rock type ore Black Rock type ore, consistingg of braunite II, hausmannite, hematite, and andradite, which would represent a relatively low degree of alteration. Typical Wessels-type ore, composed of hausmannite, bixbyite, braunite-group minerals, hematite and many other minor phases, represents and intermediate degree of alteration.

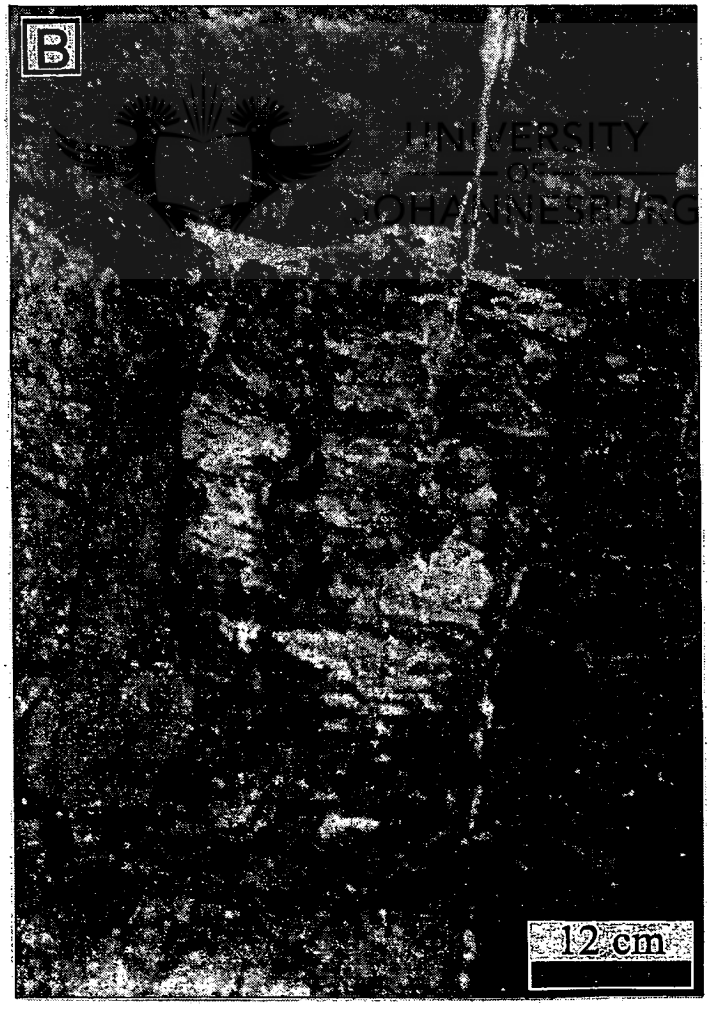

Fig. 3.6B Massive, dense manganese calc-silicate lens in Wessels-type ore at Wessels mine. The lens is composed of andradite, brucite, clinochlore, ruizite and hematite.

Most minerals that were formed during the Wessels event are composed of a combination of the following elements (in order of decreasing abundance): Mn^{2+} - Mn^{3+} - Fe^{3+} - Ca - Mg - Na- K - Ba - Sr -Al (cations) and O^{2-} - SiO_4^{4-} - CO_3^{2-} - SO_4^{2-} - BO_3^{3-} (anions). The number and abundance of Ca-Mn-hydroxy-silicates, Ca-hydroxy-silicates and of minerals containing boron are extraordinary. It is also interesting to note that there are a number of mineral species that contain considerable amounts of Cu (native Cu, vonbezingite, effenbergerite) and Pb (kentrolite, galena). Only one Zn-rich mineral (sphalerite) has been reported from one mineral specimen (Von Bezing and Gutzmer, 1994a). It is interesting to note that the chemistry of the minerals formed during the Wessels alteration event display a very close relationship to the composition of the precursor braunite-lutite which is a Mn-Fe-Ca-Mg-Si-CO_3^{2-} -bearing rock containing about 0.2 wt% B (in braunite), small amounts of SO_4^{2-}, Ba and Sr, and low contents of all other elements, including Ti, Al, Na and K.

Three distinct styles of mineralization are thought to represent different stages of the Wessels alteration event, namely,

1) Massive and dense sugilite-silicate accumulations in and around faults and veins and as isolated lenses within the manganese ore bed (Fig. 3.6A). The occurrence of sugilite is characteristic of this style of mineralization.

2) High-grade hausmannite-rich Wessels-type ore with clear lateral zonation relative to normal faults (Fig. 3.7A). Hausmannite-rich associations represent the bulk of the high-grade ores mined.
3) Vein and vug-hosted mineral associations in Wessels-type ore (Fig. 3.8A).

The mineralization styles are very distinctive and it is seldomly difficult to discriminate between the Wessels event and later overprints.

Sugilite calc-silicate association

This association was well documented by Dixon (1989) who states that the largest of the calc-silicate bodies occur along veins. It is also described by Gutzmer (1993) from next to a xonotlite-calcite vein at Nchwaning mine. Burger (1995) reported similar mineralization as cement of a fault breccia in which fragments of banded iron-formation are replaced by acmite and recrystallised hematite. Most commonly the calc-silicates are developed as dense fine-grained lenticular bodies along the footwall and/ or hanging wall contact of the lower manganese ore bed

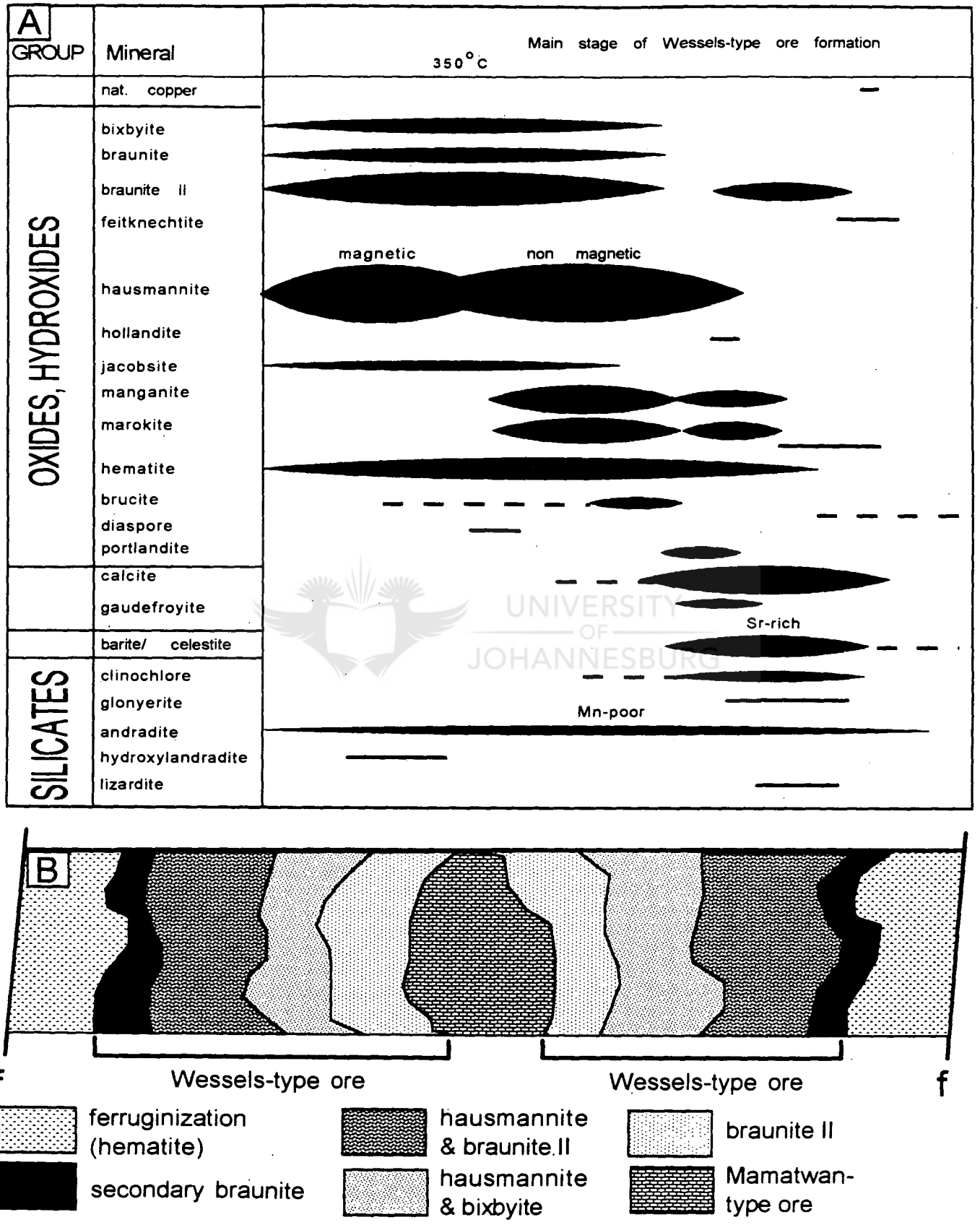

Fig. 7 Wessels-type ore mineral assemblage. (A) Paragenetic succession suggested for Wessels-type ore. (B) Sketch illustrating the distribution of mineralogically distinct types of Wessels-type ores around normal faults acting as fluid feeder (modified after Gutzmer and Beukes, 1995).

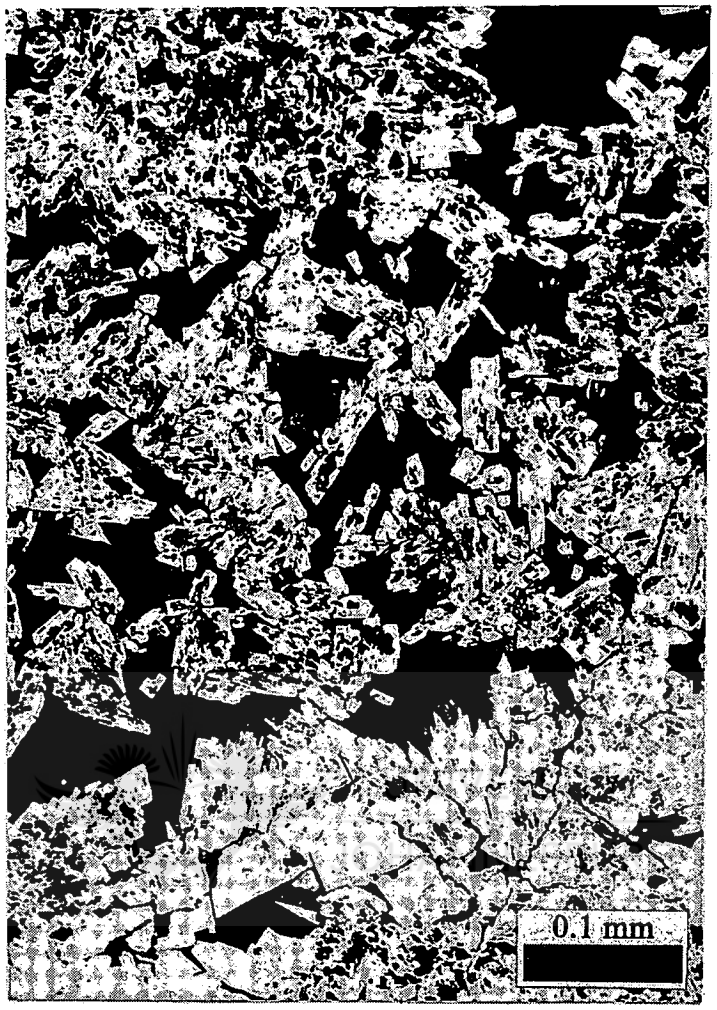

Fig. 3.7C Photomicrograph. Skeletal prisms of braunite (new) defining a typically porous texture observed in Wessels-type ore (reflected light, oil immersion).

different ores types relative to normal faults that acted as feeder channels for the hydrothermal fluids during the Wessels event (Fig's. 7A, B). From this work it is known

that hausmannite and hematite are the most common minerals formed during the alteration process. Iron-rich magnetic hausmannite (Fig. 3.7A) (Gutzmer et al., 1995) forms prior to ordinary hausmannite (from here on only referred to as hausmannite). Bixbyite, braunite II (Fig. 3.7C), braunite, marokite and manganite form penecontemporaneously with the hausmannite, but are also replaced by a later phase of hausmannite. The latter phase may be related to hausmannite filling late stage veinlets and vugs in the ore and it therefore postdates the main phase of oxide formation. Andradite, calcite and clinochlore are the most common gangue minerals

to over- and underlying hematite-lutite (altered to massive hematite) at Wessels and Nchwaning mines. However, in some cases the calc-silicates occur as isolated lenticular bodies in the central part of the ore bed (Fig. 3.6B). Many of the calc-silicate bodies are characterized by detailed preservation of the sedimentary textures of the braunite-lutite precursor (Fig. 3.6C), indicating a metasomatic origin by pari passu replacement. The occurrence of these calc-silicate bodies is restricted to Wessels-type ore with highest degree of alteration. They show a transitional contact towards the high-grade hausmannite-rich manganese ore but are crosscut by vein- and vug-hosted mineral assemblages (Fig. 3.6C) related to the final stages of the Wessels alteration event.

Paragenetic relationships can be established within this assemblage, as younger minerals appear in cross-cutting veins or as interstitial fillings between older minerals (Fig. 3.6A). The most striking and one of the first minerals to have formed in this mineral assemblage is deep purple to violet coloured sugilite described by Dunn et al. (1980) and Dixon (1989). Dixon (1989) identified braunite, hematite, amphibole (arfedsonite, richterite, and potassium-richterite), clinochlore, garnet (Mn-bearing andradite, henritermierite and hydrox-grossular), phlogopite, Mn-rich olivine (glaucochroite, kirschsteinite), akermanite, minerals of the pectolite-serandite group, wollastonite, pyroxene (acmite, diopside) (Fig. 3.6A), vesuvianite and quartz in association with sugilite. Armbruster et al. (1992, 1993) identified taikanite in the sugilite paragenesis, and described hennomartinite and kornite as new mineral species. Our studies revealed the presence of orthoclase, brucite, ruizite, tephroite and johannsenite in silicate bodies devoid of sugilite (Fig. 3.6A). Effenbergerite occurs on fracture planes within sugilite-rich calc-silicate bodies.

An interesting occurrence of a manganese-rich calc-silicate assemblage is present in the 'chilled margins' of the intrusive bostonite dykes. The chilled margins are represented by a fine crystalline, dense rose-coloured siliceous rock composed of pseudomorphs after feldspar and pyroxene grains consisting of silicates such as tephroite, Mn-diopside, Mn-rich clinochlore, hematite, calcite, and several unidentified mineral phases. De Villiers (1970) reports the occurrence of cymrite and Kleyenstüber (1985) that of banalsite, pyrophanite and bustamite from hydrothermally altered bostonite dykes.

Hausmannite-rich association (Wessels-type ore)

The mineralogy of the hausmannite-rich assemblage of the Wessels-type ore was first studied by Kleyenstüber (1984, 1985). More recently Gutzmer and Beukes (1995) and Beukes et al. (1995) indicated that hydrothermal alteration led to a systematic lateral zonation of mineralogically

Fig. 3.7D Photomicrograph. Andradite (dark gray) in large, rounded blastic grains with an euhedral core and a round, anhedral rim. The rim contains abundant poikilitic inclusions of surrounding fine crystalline hausmannite and braunite. This association is typical for fine crystalline hausmannite-rich Wessels-type ore (reflected light, oil immersion).

intergrown with the manganese oxides (Fig. 3.7D). They may also fill later stage veins and vugs in the ore. Other common minerals such as barite and gaudefroyite occur mainly as vug fillings and in veinlets that postdate the formation of the oxides (Fig. 3.7A).

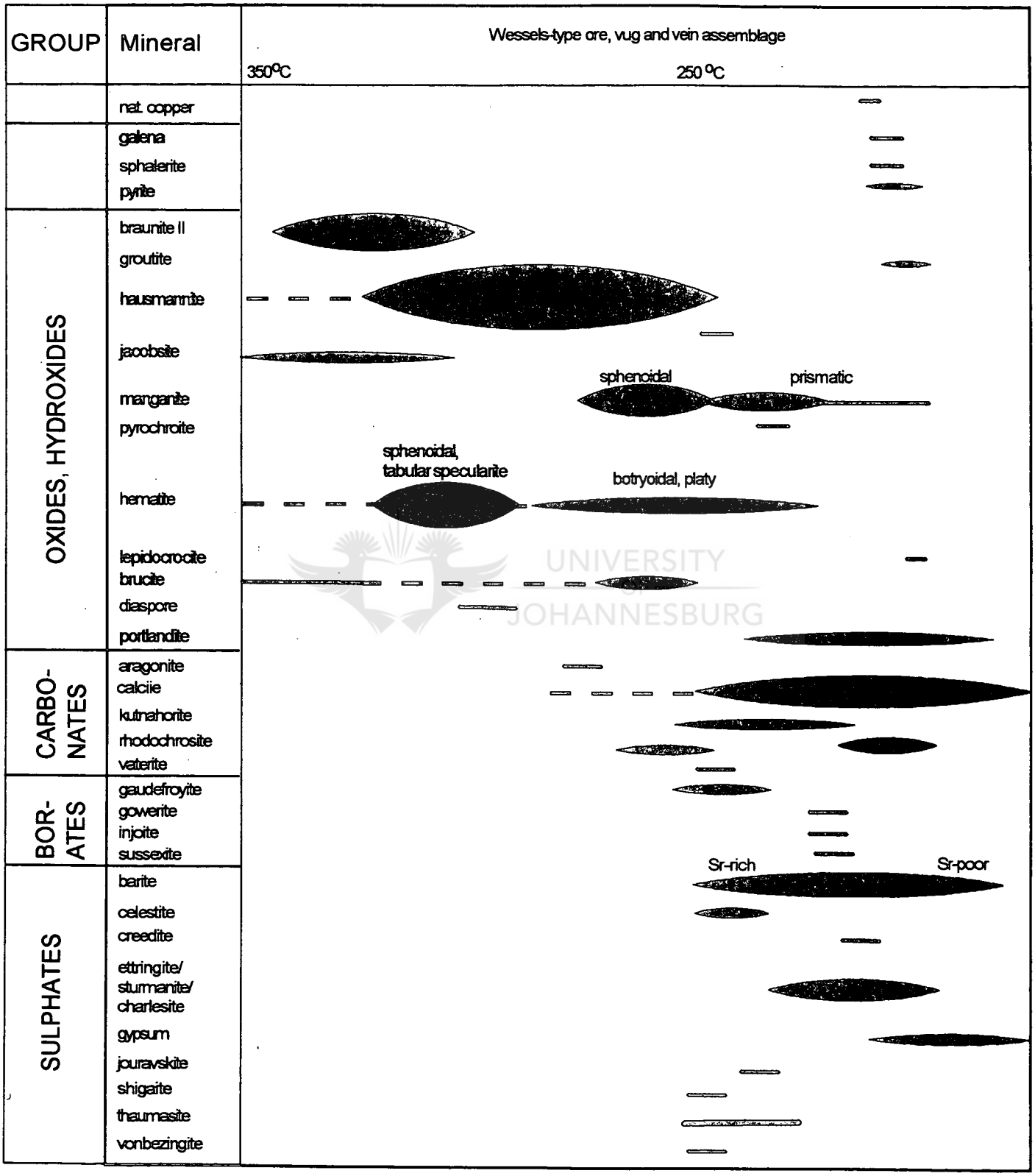

Fig. 3.8A Association of minerals hosted in vugs and veins in Wessels-type ore. Paragenetic succession suggested for minerals in vugs and veins.

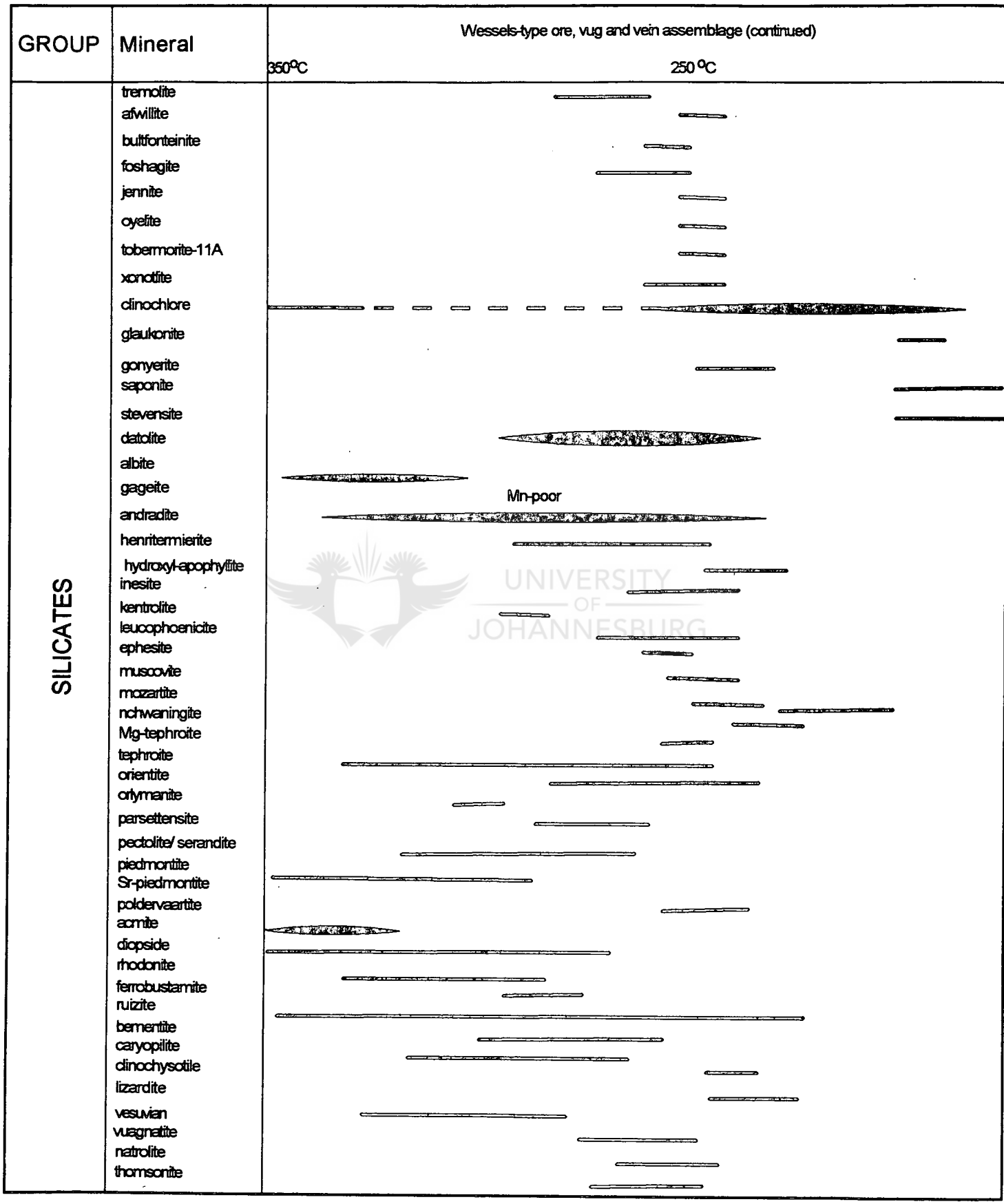

Fig. 3.8A continued.

Vein and vug-hosted association

The largest variety of minerals in the Kalahari manganese deposit is encountered in veins and vugs in Wessels-type ore. A total of about 84 minerals are known from the vein and vug association, and five new minerals, sturmanite, orlymannite, vonbezingite, poldervaartite, and nchwaningite, have been described from this association (Fig. 3.8A). Numerous rare minerals species occur in abundance and in unusually large and well developed crystals, such as rhodochrosite (Von Bezing et al., 1991), inesite (Gutzmer and Cairncross, 1993), xonotlite, and thaumasite. Other very rare minerals are also occasionally found as large well developed crystals include mozartite, 11Å tobermorite, shigaite, and bultfonteinite.

Four textural types of vein- and vug-hosted mineralization are present in Wessels-type ore, namely 1) small vugs and veinlets, 2) veins and fractures (Fig. 3.8B), 3) fault-hosted silicate veins, and 4) large isolated vugs or 'pockets'.

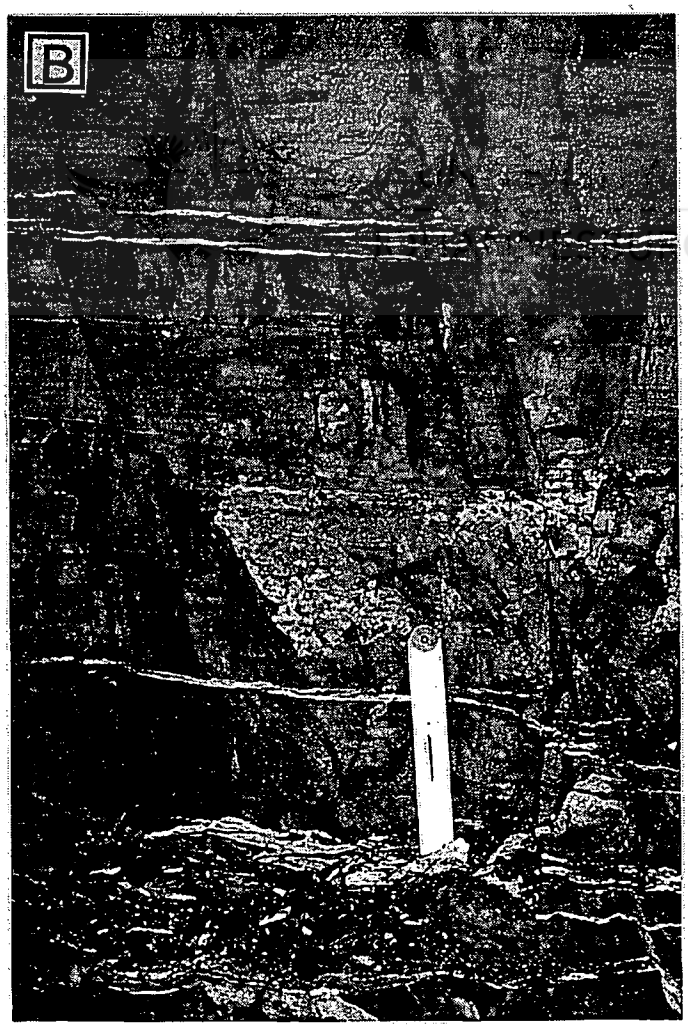

Fig. 3.8B Sets of thin, stratiform portlandite veins in an underground exposure of high-grade Wessels-type ore at Wessels mine. Scale is 20 cm long.

Tiny vugs or veinlets, which are merely part of the secondary porosity that developed during the main stage of formation of hausmannite-rich Wessels-type ore, are filled by either one or several of the following minerals: specularite, hausmannite, braunite II, andradite, gaudefroyite, calcite, clinochlore, and Sr-barite (Fig. 3.8A). Specularite, andradite and braunite II appear to be the earliest phases in this association. Hausmannite replaces braunite II, indicating a paragenetic sequence identical to that observed in the hausmannite-rich association (Fig. 3.8A). Braunite II, hausmannite and specularite may in turn be coated by a younger generation of andradite. Gaudefroyite coats and encloses oxide minerals and andradite, and is in turn overgrown by Sr-barite, calcite and/or clinochlore. Many vugs are entirely filled with Sr-barite, calcite or manganoan calcite (Fig. 3.8A). The Sr-barite is interesting in that its composition may range from strontio-barite to barian celestite (Gutzmer, 1993).

Veins and fractures, crosscutting earlier pores and vugs, are lined or filled by a coarse-crystalline association of Mn- and Fe-oxides, carbonates, sulphates, borates and silicates. These veins display no wallrock alteration. The veins are generally less than 25 cm wide, dip subvertical and crosscut ores of high to medium degree of alteration. Others are orientated subparallel to the original bedding in the ore (Fig. 3.8B). Mineral assemblages in the veins are highly variable, consisting of the following minerals (to name but a few): native copper; hausmannite, jacobsite, hematite (specularite, pseudocubic hematite crystals), and groutite; portlandite (Fig. 3.8B), brucite, and pyrochroite; calcite, Mn-calcite, and rhodochrosite; Sr-barite, celestine, the sturmanite-group of minerals, gypsum, and shigaite; gaudefroyite; caryopilite, leucophoenicite, clinochlore, and lizardite (Fig. 3.8A). Common associations are (for example): gaudefroyite covered by calcite or Sr-barite; caryopilite and leucophoenicite associated with andradite and rhodochrosite or calcite, sturmanite and gypsum; portlandite associated with minor hausmannite occurs in bedding parallel veins (Fig. 3.8B). The silicate minerals, together with hausmannite, are generally early phases (Fig. 3.8A), followed by gaudefroyite, rhodochrosite, Sr-barite or celestite, the minerals of the sturmanite group, and gaudefroyite (Fig. 3.8A). Calcite occurs throughout generally speaking gypsum, clinochlore, lizardite and groutite appear to be the youngest phases in this association (Fig. 3.8A). Minor amounts of sulphide (pyrite, galena) are locally associated with calcite.

A second type of vein fill is present in fault zones and display wallrock alteration. They are generally enveloped by a zone of ferruginization and/ or silicification (Gutzmer and Beukes, 1995; Beukes et al., 1995). These veins vary in width from below 1 cm to 50 cm. They are in some cases filled by massive fine crystalline silicates. Hematite, acmite and andradite are always present, associated with amphiboles (arfedsonite, richterite), rhodonite or bustamite, albite and/

or orthoclase, grossulare, and serandite-pectolite. Clasts of manganese ore in these veins are typically ferruginized and consist of massive, fine crystalline hematite. Vugs remaining in this dense silicate assemblage are filled by coarse crystalline calcite, gypsum or gageite. The mineral association and their intergrowth is very similar to that of the calc-silicate bodies.

Vugs (called 'pockets' by the miners) occur in a setting very similar to that of the calc-silicate bodies, either in groups of lensoidal dissolution hollows concentrated along the hanging wall or the footwall contact of the orebody or, in rare cases, as large irregular vugs within the orebody. The size of these vugs ranges in volume from a few cubic millimeter to several cubic meter in volume. The pockets are host to some of the most beautiful and rare mineral specimens coming from the Kalahari manganese field. Although highly variable, a crude concentric mineralogical zonation is observable in most vugs. The walls are characteristically lined by a thin selvage of massive hematite or jacobsite. An outer lining along the wallrock is composed of a fine crystalline, massive mixture of densely intergrown andradite, tephroite, jacobsite, clinochlore, datolite and caryopilite a.o. (Fig. 3.8A). This fine crystalline assemblage is overgrown by a coarser grained mineral association often containing euhedral crystals of a multitude of mineral species ranging from andradite and hausmannite to xonotlite, tobermorite, datolite, inesite and many more (Gutzmer and Cairncross, 1993) (Fig. 3.8A). The central part of the vugs is either empty and dry, or filled by water, or filled with a wet clayey material composed of serpentine (lizardite), clinochlore, xonotlite, stevensite or loose masses of granular thaumasite. The best developed and largest crystal specimens occur extending from the coarse crystalline walls of the pockets into the soft clay infill. In some cases these crystals are found broken loose in the clay matrix, because of underground blasting operations. The presence of water and soft, clayey material in the pockets indicate that alterations of the mineral assemblage may even be taking place today. However, the original pockets and their characteristic mineral assemblage, which bears close similarities to that of veins and pores, most probably formed during the Wessels event of alteration.

The Mamatwan event of hydrothermal alteration

This alteration event is characterized by the development of carbonate-sulphide-hematite mineral associations along joints and minor faults in the Kalahari manganese deposit. Chalcopyrite,

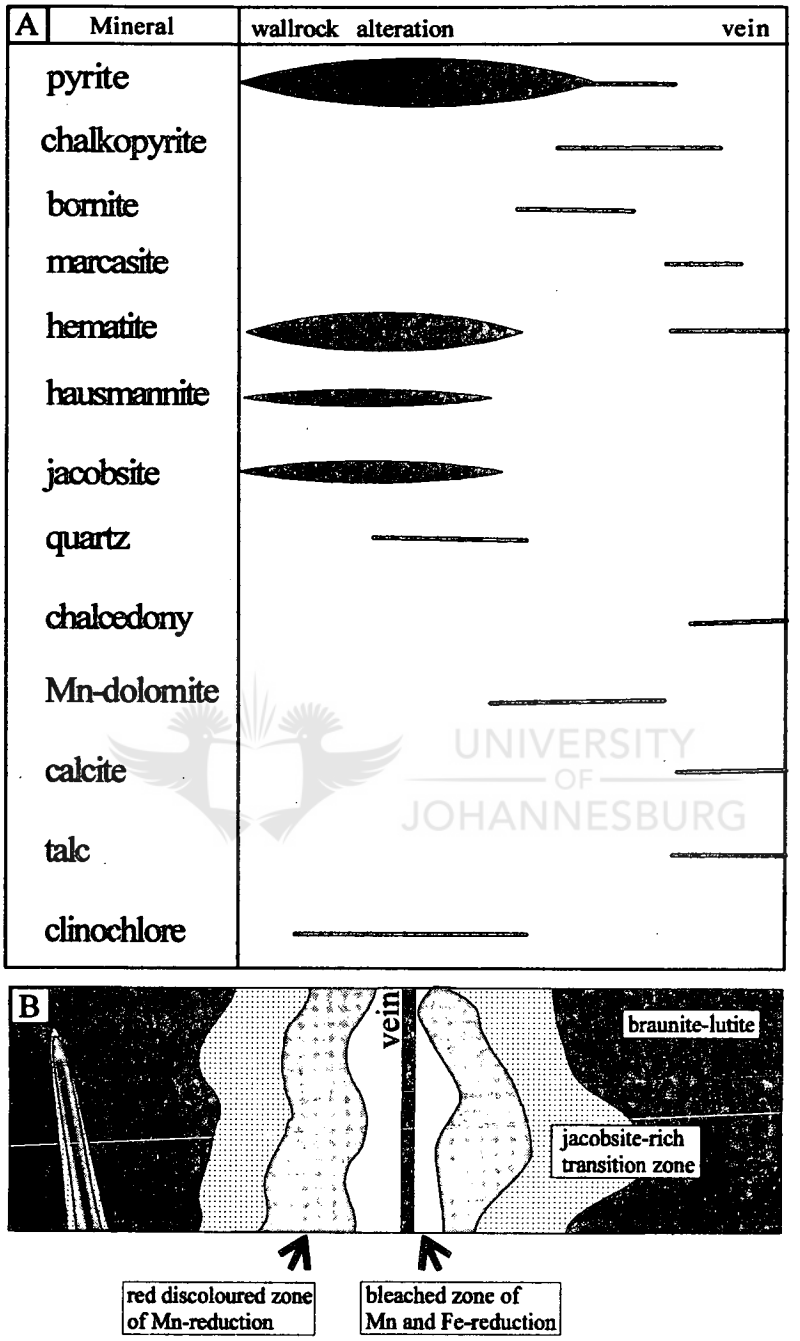

Fig. 3.9 The Mamatwan alteration event. (A) Suggested paragenetic succession. (B) Sketch illustrating the alteration of braunite-lutite adjacent to carbonate-sulphide veins during the Mamatwan alteration event.

bornite, pyrite, marcasite, ankerite, calcite, hematite, chalcedony, tridymite and talc were found at Mamatwan mine (Fig. 3.9A). Alteration of carbonate-rich braunite-lutite along such veins is represented by reduction of manganese and iron oxides and the formation of jacobsite, pyrite, and quartz at the expense of braunite and hematite (Fig. 3.9B). A symmetrical array of different zones

zones of alteration illustrates decreasing degrees of wallrock alteration (Fig. 3.9B). Bleaching of the originally dark brown or gray manganese ore and the formation of quartz and pyrite represents the highest degree of alteration (Fig. 3.9C).

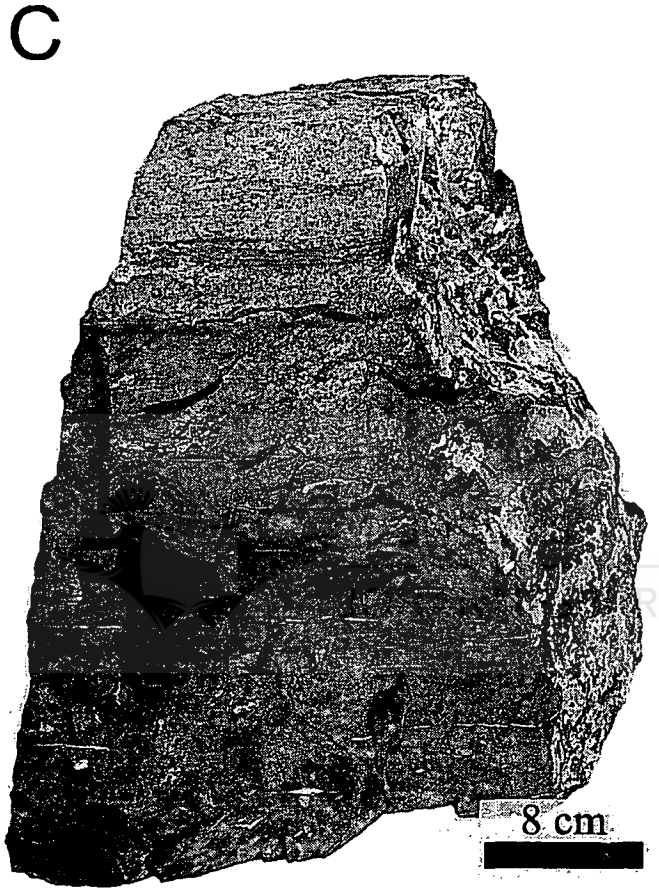

Fig. 3.9C Alteration of braunite lutite during the Mamatwan alteration event. The white (bleached) zone, immediately adjoining a sulphide-carbonate veinlet, grades into a red discoloured zone (light gray), which in turn grades into a jacobsite-rich transition zone (dark gray) and finally into unaltered braunite lutite. Note the detailed preservation of sedimentary bedding at all degrees of alteration.

Red discolouration of the manganese ore is due to reduction and leaching of manganese (Fig. 3.9C). The transition of this red discoloured zone into the surrounding Mamatwan-type ore is characterized by the replacement of braunite by jacobsite (Fig. 3.9B). Recrystallization of the sedimentary carbonates in the braunite-lutite and the dissolution of braunite result in the formation of small amounts of clinochlore and quartz (Fig. 3.9B).

Sedimentary textures of the braunite-lutite are preserved in microscopic detail. Breccia-textured veins at Mamatwan mine suggest a syntectonic nature of hydrothermal fluid flow and wallrock alteration. At Wessels, Nchwaning and Gloria mines, veins in fault zones are filled by a brecciated assemblage of coarse crystalline botryoidal hematite and sparitic calcite associated with small amounts of pyrite. Calcite crystals of this assemblage are generally scalenohedral or rhombohedral (or flat rhombohedral, lensoidal) with pyrite forming large complex cubes, up to 3 cm in diameter.

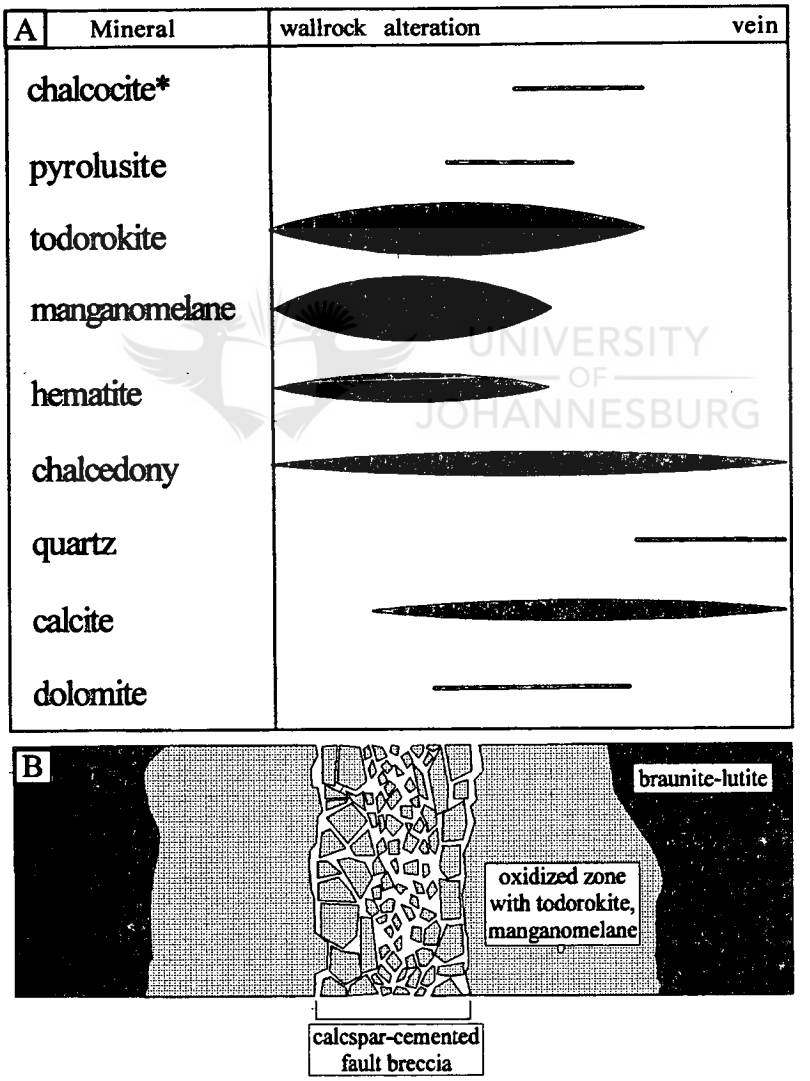

Fig. 3.10 The Smartt alteration event. (A) Suggested paragenetic succession. Chalcocite (*) was only noted once as alteration product of a chalcopyrite-rich fault-hosted sulphide lens at Mamatwan mine. Its relation to the Smartt event has to be confirmed. (B) Sketch illustrating the alteration of braunite lutite around a fault-hosted hydrothermal breccia (at Mamatwan mine) that acted as fluid conduit during the Smartt alteration event.

The Smartt event of hydrothermal alteration

At Mamatwan mine the Smartt event of hydrothermal alteration (Fig. 3.10A) is represented by todorokite and manganomelane replacing Mn-bearing carbonates, braunite and hausmannite (Fig. 3.10B) in a 15 to 18 m wide zone next to an intensely brecciated normal fault zone (Fig. 3.10B). Sedimentary textures are obscured by the alteration process. Altered ores are greenish to brownish black, and either dense splintery and massive, or earthy in appearance. The fault breccia consists of altered manganese ore and iron-formation fragments cemented by a vuggy matrix of chalcedony, calcite (in places dolomite) and some quartz (Fig. 3.10A). Calcite crystals range in habit from simply rhombohedral and complex rhombohedral or lens-shaped to scalenohedral.

Fig. 3.10C Bedding parallel asbestiform cryptomelane/ todorokite associated with calcite (white) from Smartt mine. These veins are thought to have formed during the Smartt alteration event.

A very similar paragenesis is observed in association with up to 7 cm wide bedding parallel veins of fibrous manganomelane/ todorokite at Smartt mine (Fig. 3.10C). Several generations of asbestiform manganese oxides occur in successive bands in some of these seams. Todorokite is also a major component in altered braunite-lutite surrounding these veins. Calcite and rose-coloured chalcedony, associated with the manganomelane/ todorokite fibers appear somewhat younger than the todorokite (Fig. 3.10C). Coarse crystalline calcspar fills vugs between fiber bundles (Fig. 3.10C). Massive sparitic calcite fills fractures in the todorokite seams or encloses

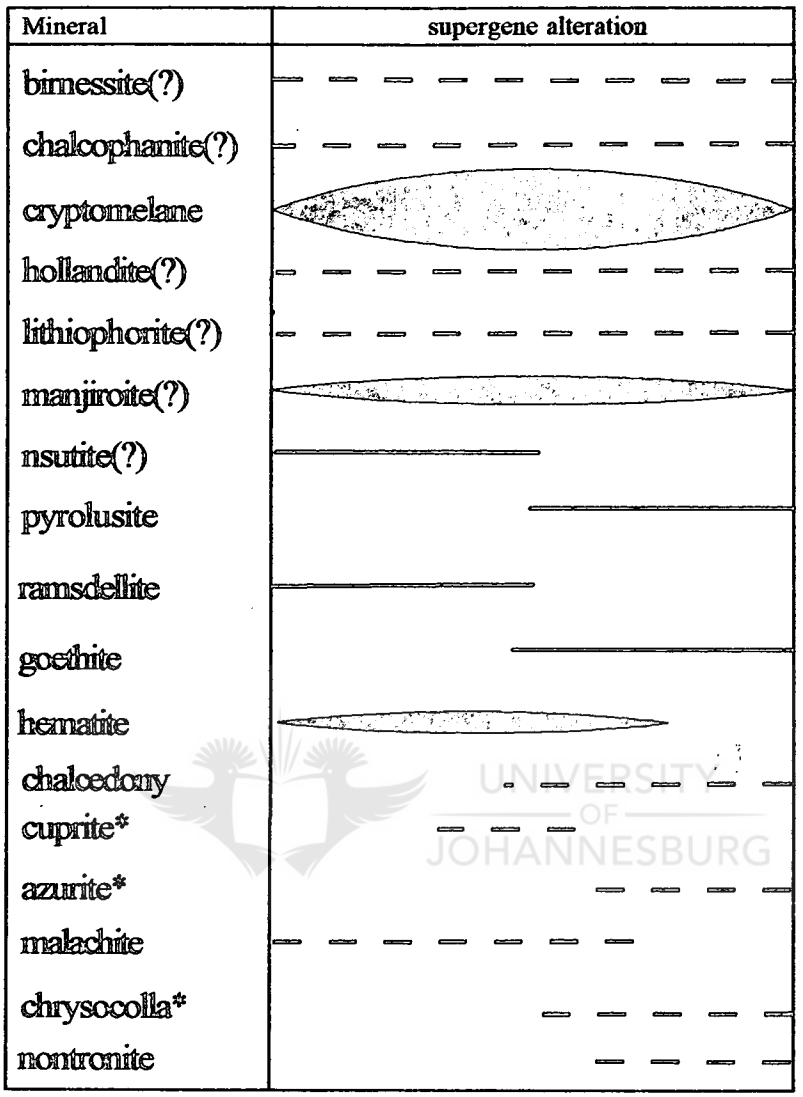

Fig. 3.11A Syn- and Post-Kalahari supergene alteration. Suggested paragenetic succession. The identity of minerals marked with a (?)-symbol has to be regarded as questionable. Minerals marked by a *-symbol represent unique finds and the constructed relation to supergene alteration processes has to be confirmed.

fragments of todorokite/ manganomelane fibers, indicating renewed opening of the bedding parallel fractures. Similar occurrences of todorokite are also known to occur in Wessels-type ore at Hotazel and Langdon mines.

Supergene weathering along the Kalahari unconformity

De Villiers (1970), Nel et al. (1986), and Kleyenstüber (1993) describe the effects of recent supergene weathering (Fig. 3.11A) on the manganese ore along the eastern suboutcrop of the Hotazel Formation below the calcretized sediments of the Kalahari Formation (Fig. 3.11B). These supergene alteration processes are apparently ongoing today. Recent weathering of manganese ores produces tetravalent hydrated Mn-oxides and goethite. Cryptomelane and pyrolusite seem to be the most stable among the manganese oxides (Fig. 3.11A). Goethite replaces hematite where open fractures allow free access of water.

High-grade Wessels-type ore was exposed to weathering at Hotazel mine suboutcropping below

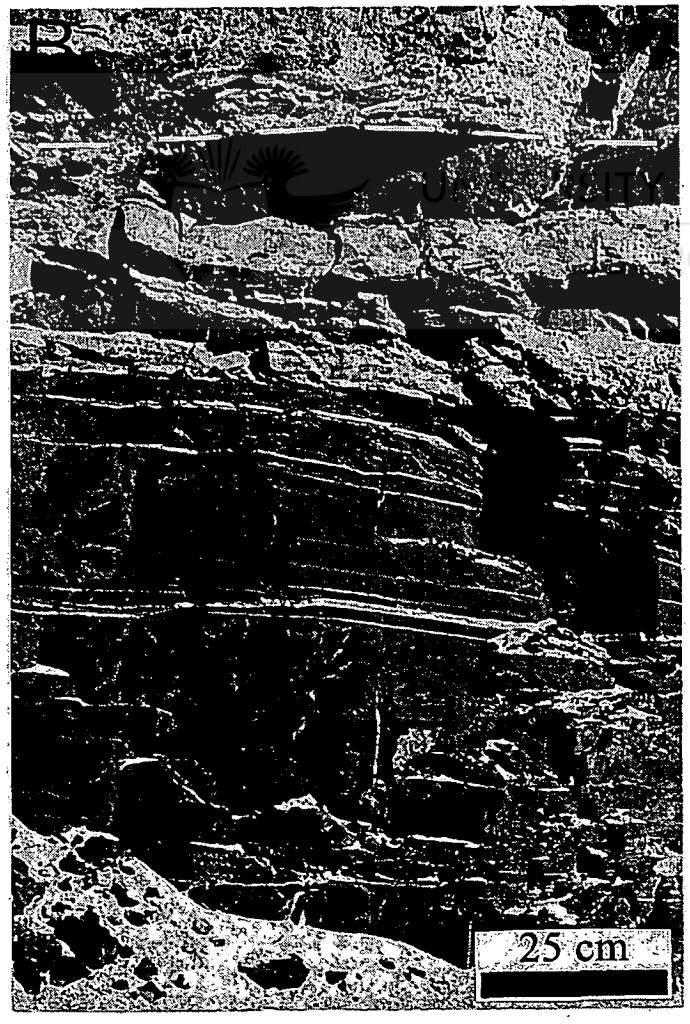

Fig. 3.11B Partly weathered braunite-lutite of the lower manganese orebody at Mamatwan mine is cut by the Kalahari unconformity (white line) and covered by Cenozoic calcrete of the Kalahari Formation.

the Kalahari Formation and exposed subaerially at Black Rock (incidentally the only known natural outcrop of the Kalahari deposit; Boardman, 1944). The distribution of supergene minerals in high-grade ores is generally disperse, concentrated along grain boundaries or microfractures and the degree of supergene alteration can often only be established under the microscope. Coarse crystalline vuggy hausmannite-rich ores close to the main graben faults at Hotazel appear matt black with increasing degrees of replacement of hausmannite by cryptomelane. De Waal and Hiemstra (1960) identified supergene ramsdellite from the Hotazel mine (Fig. 3.11A). De Villiers (1970) described cryptomelane associated with small amounts of birnessite, chalkophanite, hollandite, goethite, lithiophorite, nontronite, nsutite, pyrolusite, and todorokite as products of weathering at Black Rock and Hotazel (Fig. 3.11A). The validity of the identification of some of the rare mineral species by De Villiers (1970) remains doubtful, as they were based only on the optical properties of the minerals. This is especially true for birnessite, chalkophanite, hollandite, lithiophorite, and nsutite (Fig. 3.11A).

Supergene weathering of Mamatwan-type ore was studied by Nel et al. (1986) and Kleyenstüber (1993) at Mamatwan mine. Cryptomelane predominates as a product of weathering in an up to 5 m thick zone where braunite-lutite crops out against the Kalahari unconformity (Fig. 3.11B). The ores are matt black and dense with slight earthy appearance, sedimentary textures of the braunite-lutite precursor are often well preserved. Manjiroite, pyrolusite, todorokite and chalcedony are associated with cryptomelane (Kleyenstüber, 1993). Weathering of the fault-hosted carbonate-sulphide mineralization at Mamatwan (formed during the Mamatwan alteration event) produced azurite, malachite, goethite, hematite and nontronite (Fig. 3.11A).

Discussion

The deposition of the 2.2 - 2.3 Ga old Hotazel Formation of the Paleoproterozoic Transvaal Supergroup was explained by Beukes (1983) by transgressive-regressive events relative to the site of deposition. Beukes (1983) suggested a distant submarine volcanic source for iron, manganese and silica. The manganese-formation, originally probably a mixed precipitate composed of carbonates and oxides, would represent the more distal sedimentary facies, as compared to the more proximal iron-formation. Braunite, hematite and the matrix carbonates are thought to have formed during very early diagenesis, soon followed by kutnahorite and Mn-calcite present in ovoids and laminae.

Stratabound oxidation of manganese-rich carbonates to oxides such as hausmannite, partridgeite and manganite, or silicates such as bementite or friedelite, are attributed to metasomatism during

lower greenschist facies metamorphism related to thrusting and crustal thickening during the Kheis orogeny some 1.8-1.9 Ga ago (Fig. 3.2E). Formational waters may represent a possible source for fluids during late diagenetic/ metamorphic alteration.

Coarse crystalline, high-grade Wessels-type ore was derived from precursor Mamatwan-type ore by removal of CO_2, and leaching of Si, Ca, and Mg. Fe, Na and K were introduced locally (Gutzmer and Beukes, 1995; Beukes et al., 1995). The microcrystalline carbonate-rich braunite-lutite was transformed into coarse-grained oxidic Wessels-type ore during this alteration process. The fluid source for this alteration event remains unknown. However, the timing of the alteration event appears to be constrained to 1.0-1.25 Ga, the Namaqua-Natal (Kibaran-) orogeny (Thomas et al. 1994; Dixon, 1989). Interesting to note is that almost the entire mineral paragenesis of the Wessels event constitutes merely a recombination of major elements present in the braunite-lutite precursor. Miyano and Beukes (1987) and Gutzmer (1993) modelled the pT-conditions and fluid compositions for the formation of Wessels-type ore based on the thermodynamic stability of observed mineral assemblages. The results indicate alteration between 300 and 400° C at a maximum lithological pressure of 0.5 to 1 kbar, oxygen fugacities as low as 10^{-11} bar, CO_2 fugacities of $10^{-0.7}$ bar, and a dissolved SiO_2 activity of 10^{-3} to 10^{-4} mol/l. These values indicate, that the hydrothermal fluid had an alkaline character after equilibration with the braunite-lutite host rock. An alkaline, hydrothermal environment at low fCO_2 are known preconditions for the formation of minerals such as portlandite, tobermorite, xonotlite and ettringite (Eitel, 1966).

The considerable secondary porosity of the altered ores may have enabled the effective removal of a low density CO_2-rich volatile phase from the hydrous hydrothermal fluid system. Preferential fluid movement along normal faults and lithological contacts led to the formation of dense sugilite-bearing calc-silicate assemblages during the progressive stage of alteration. These may have formed by pari passu replacement of the braunite-lutite by fine crystalline silicates at temperatures of up to 450 °C at low CO_2 fugacities as envisaged by Dixon (1989). Coarse crystalline minerals in veins and dissolution vugs were precipitated from residual solutions trapped in veins, vugs and pores in the Wessels-type ore during waning stages of hydrothermal alteration. Cooling of the hydrothermal fluid during the waning stages of hydrothermal alteration resulted in supersaturation of the fluids and the precipitation of the large number of Mn^{3+}-Mn^{2+}-Fe-Ca-Mg-oxides, hydroxides, -sulphates, -silicates and minor amounts of carbonates. The observed cogenetic formation of 11Å tobermorite and xonotlite in vug-hosted assemblages, for example, indicates a temperature of formation of between 250° and 270 °C (Gutzmer, 1993).

environment, are regarded as important factors for the mineralogical diversity developed during the Wessels event (Fig. 3.3B). More than 100 of the 135 minerals present in the Kalahari manganese field (Appendix 1) formed during the Wessels alteration event (Fig. 3.3B).

Only qualitative information is available about fluids that were introduced along faults, joints and fractures during the Mamatwan (Fig. 3.2G) and the Smartt (Fig. 3.2I) hydrothermal alteration events. Reduction of manganese and iron oxides, preservation of a micritic carbonate matrix and the presence of sulphides indicate low fO_2, but considerable fCO_2 and the predominance of reduced sulphur species in the hydrothermal fluid wallrock alteration during the Mamatwan alteration event. The alteration assemblage, consisting of clinochlore, carbonate and quartz, in association with the vein-hosted mineralization with chalcopyrite, pyrite, ankerite, calcite and talc indicates an epithermal temperature for the fluids introduced (Evans, 1992; Guilbert and Park, 1989).

The influx of low-temperature, oxidizing solutions is invoked by the oxidation of carbonates and the formation of todorokite and manganomelane during the Smartt alteration event (Nicholson, 1992). No absolute ages can be assigned to the latter two hydrothermal alteration events, but they have tentatively been correlated with periods predating the onset of deposition of the Phanerozoic Karoo Supergroup (0.55-0.6 Ga) and the deposition of the Cenozoic Kalahari Formation (10-100 Ma).

UNIVERSITY OF JOHANNESBURG

Supergene alteration along the erosional Kalahari unconformity is related to the influx of descending meteoric water along the Cenozoic Kalahari unconformity. Supergene alteration is clearly distinguished from the preceding alteration events by the associated influx of Na and K into the manganese ore.

Conclusions

The paragenetic sequence suggested in this study represents a first attempt to point out mineralogical characteristics of specific geological events in the Kalahari manganese deposit and to place them in a relative geochronological framework. The paragenetic sequence of a mineral assemblage as complex as that of the Kalahari deposit will probably never be complete and shall in future probably be continually modified as new information becomes available. However, it is believed that the basic parameters of the paragenetic sequence has been correctly laid down in this paper.

Acknowledgements

The authors are very grateful to Dr. L. von Bezing (Kimberley) for his continuous interest and support during this study. Dr. B. Cairncross (RAU) and C. Queit are acknowledged for supplying interesting mineral samples. We are also grateful to the staff of the geology departments at Hotazel (SAMANCOR), especially D. McIyver, N. Bleeker and P. Naidoo, and A. Pretorius at Black Rock (AMMOSAL) as they gave considerable support to perform the necessary underground studies.

References

Armbruster, T., Oberhaensli, R., Bermanec, V., and Dixon, R.D. (1993). Hennomartinite and kornite, two new Mn^{3+}-rich silicates from the Wessels Mine, Kalahari, South Africa. Schweiz. Mineral. Petrog. Mit., 73, 349-355.

Armbruster, T., Oberhaensli, R., and Kunz, M. (1993). Taikanite, $BaSr_2Mn_2^{3+}O_2[Si_4O_{12}]$, from the Wessels Mine, South Africa: A chain silicate related to synthetic $Ca_3Mn_2^{3+}O_2[Si_4O_{10}]$. Amer. Mineral., 78, 1088-1093.

Bates, R.L., and Jackson, J.A. (1984). Directory of geological terms. Anchor Books, New York, 3'rd ed., 571 pp.

Beukes, G., De Bruiyn, H., and Van der Westhuizen, W. (1993). Gaudefroyite from the Kalahari manganese field, South Africa. N. Jb. Min., Monatshefte, 385-392.

Beukes, N.J. (1983). Palaeoenvironmental setting of iron formations in the depositional basin of the Transvaal Supergroup, South Africa. In: Trendall, A.F. and Morris, R.C. (Eds.): Iron formations: Facts and problems. Elsevier, Amsterdam, 131-209.

Beukes, N.J., Burger, A.M., and Gutzmer, J. (1995). Fault controlled hydrothermal alteration of Palaeoproterozoic manganese ore in Wessels mine, Kalahari manganese field. S. Afr. J. Geol., 98, 430-451.

Beukes, N.J., and Gutzmer, J. (1996). A volcanic-exhalative origin for the world's largest (Kalahari) manganese field, A discussion of a paper by Cornell and Schütte. Mineral. Depos, 31, 342-345.

Beukes, N.J., and Smit, A. (1987). New evidence for thrust faulting in Griqualand West, South Africa: Implications for stratigraphy and the age of red beds. Trans. Geol. Soc. S. Afr., 90, 378-394.

Bezing, L. von (1992). The rare minerals of the Kalahari manganese field. SA mineral collectors symposium, RAU, 32.

Bezing, L. von, Dixon, R.D., Pohl, D., and Cavallo, G. (1991). The Kalahari manganese field: An Update. Mineral. Rec., 24: 10-27.

Bezing, L. von, and Gutzmer, J. (1994a). Das Kalahari Manganerzfeld und seine Mineralien (Teil 1) Mineralien Welt, 4, 4, 24-46.

Bezing, L. von, and Gutzmer, J. (1994b). Das Kalahari Manganerzfeld und seine Mineralien (Teil 2) Mineralien Welt, 4, 5, 41-59.

UNIVERSITY OF JOHANNESBURG

Boström, K., Rydell, H., Joensuu, O. (1979). Långban - an exhalative sedimentary deposit ? Econ. Geol., 74, 1002-1011.

Burger, A.M. (1994). Fault controlled hydrothermal alteration of Palaeoproterozoic manganese ore in Wessels mine, Kalahari manganese field. Unpubl. MSc. thesis, RAU, Johannesburg, 138 pp.

Dai, Y., and Harlow, G.E. (1992). Description and crystal structure of Vonbezingite, a new Ca-Cu-SO_4-H_2O mineral from the Kalahari manganese field, South Africa. Amer. Mineral., 77, 1292-1300.

Dai, Y., Harlow, G.E., McGhie, A.R. (1993). Poldervaartite, $Ca(Ca_{0.5}Mn_{0.5})(SiO_3OH)(OH)$, a new acid nesosilicate from the Kalahari manganese field, South Africa: Crystal structure and description. Amer. Mineral., 78, 1082-1087.

De Bruiyn, H., Van der Westhuizen, W., Beukes, G. (1994). Gageite from the Kalahari manganese field, South Africa. N. Jb. Min., Monatshefte, 193-204.

De Villiers, P.R. (1970). The geology and mineralogy of the Kalahari-manganese field, north of Sishen, Cape Province. Geol. Surv. S. Afr., Memoir 59, Pretoria, 84 pp.

De Villiers, J.E. (1983). The manganese deposits of Griqualand West, South Africa: Some mineralogic aspects. Econ.Geol., 78, 1108-1118.

De Waal, S.A. and Hiemstra, S.A. (1968). Ramsdellite from the Hotazel mine, Northern Cape Province. NIM, Johannesburg, Report 288, 9 pp.

Dixon, R.D. (1989). Sugilite and associated metamorphic silicate minerals from Wessels mine, Kalahari manganese field. Geol. Surv. S. Afr., Pretoria, Bulletin 93, 47 pp.

Dunn, P.J., Brummer, J.J., and Belsky, H. (1980). Sugilite, a second occurrence: Wessels Mine, Kalahari manganese field, Republic of South Africa. Can. Mineral., 18, 37-39.

Eitel, W. (1966). Silicate Science. Vol. IV: Hydrothermal silicate systems. Academic Press, New York, 617 pp.

Evans, A.M. (1992). Erzlagerstättenkunde. Enkel Verlag, Stuttgart, 2'nd ed., 356 pp.

Frondel, C., and Baum, J.L. (1974). Structure and mineralogy of the Franklin Zinc-Iron-manganese deposit, New Jersey. Econ. Geol., 69, 157-180.

Giester, G., and Rieck, B. (1994). Effenbergerite, $BaCu[Si_4O_{10}]$, a new mineral from the Kalahari manganese field, South Africa: description and crystal structure. Min. Mag., 58, 663-670.

Grobbelaar, W.S., Burger, M.A., Pretorius, A.I., Marais, W., and van Niekerk, I.J.M. (1995). Stratigraphic and structural setting of the Griqualand West ant the Olifantshoek Sequences at Black Rock, Beeshoek and Rooinekke mines, Griqualand West, South Africa. Mineral. Depos., 30, 152-161.

Guilbert, J.M., and Park, C.F. Jr. (1989). The geology of ore deposits. Freeman, New York, 985 pp.

Gutzmer, J.(1993). Hydrothermale Alteration von Manganerzen der Nchwaning Mine, Kalahari Manganerzfeld, Südafrika. Unpubl. Diplom-thesis, TU Clausthal, 161 pp.

Gutzmer, J., and Beukes, N.J. (1995). Fault controlled metasomatic alteration of Early Proterozoic sedimentary manganese ores in the Kalahari manganese field, South Africa. Econ. Geol., 90, 823-844.

UNIVERSITY OF JOHANNESBURG

Gutzmer, J., and Cairncross, B. (1993). Recent mineral discoveries from the Wessels mine, Kalahari manganese field, South Africa. Mineral. Record, 23, 365-368.

Gutzmer, J., Kleyenstüber, A.S.E., Beukes, N.J., and Burger, A.M. (1995). Magnetic hausmannite from hydrothermally altered manganese ore in the Palaeoproterozoic Kalahari manganese deposit, Transvaal Supergroup, South Africa. Min. Mag, 59, 703-716.

Hoffmann, C., and Armbruster, T. (1995). Crystal structure of a (001) twinned sussexite $Mn_2B_2O_4(OH)_2$ from the Kalahari manganese field, South Africa. Schweiz. Mineral. Petrog. Mit., 75, 123-133.

Kleyenstüber, A.S.E. (1984). The mineralogy of the manganese-bearing Hotazel Formation, of the Proterozoic Transvaal Sequence in Griqualand West, South Africa. Trans. Geol. Soc. S. Afr., 87, 257-272.

Kleyenstüber, A.S.E.(1985). A regional mineralogical study of the manganese-bearing Voelwater Subgroup in the Northern Cape Province. Unpubl. PhD. thesis, RAU, Johannesburg, 328 pp.

Kleyenstüber, A.S.E. (1993). Some significant characteristics of the manganese ores and some of the minerals occurring in the Proterozoic Kalahari maganese field, South Africa. Resource Geology, 17, 2-11.

Miyano, T., and Beukes, N.J. (1987). Physicochemical environments for the formation of quartz-free manganese oxide ores from the Early Proterozoic Hotazel Formation, Kalahari manganese field, South Africa. Econ. Geol., 82, 706-718.

Moore, P.B. (1971). Mineralogy & chemistry of Långban-type deposits in Bergslagen, Sweden. Mineral. Record, 4, 154-172.

Nel, C.J., Beukes, N.J., and De Villiers, J.P.R. (1986). The Mamatwan manganese mine of the Kalahari manganese field. In: Annhaeusser, C.R., and Maske, S. (Eds.): Mineral deposits of Southern Africa. Geol. Soc. S. Afr., Johannesburg, 1, 963-978.

Nicholson, K. (1992). Contrasting mineralogical-geochemical signatures of manganese oxides: Guides to metallogenesis. Econ. Geol., 87, 1253-1264.

Nyfeler, D., Armbruster, T., Dixon, R.D., and Bermanec, V. (1995). Nchwaningite, $Mn^{2+}{}_2SiO_3(OH)_2{}^*H_2O$, a new pyroxene-related chain silicate from the Nchwaning mine, Kalahari manganese field, South Africa. Amer. Mineral., 80, 377-386.

Peacor, D.R., Dunn, P.J., and Duggan, M. (1983). Sturmanite, a ferric iron, boron analogue of ettringite. Can. Mineral., 21, 705-709.

Peacor, D.R., Dunn, P.J., and Nelen, J.A. (1990). Orlymanite, $Ca_4Mn_3Si_8O_{20}(OH)_6{}^*2H_2O$, a new mineral from South Africa: A link between gyrolite-family and concentional phyllosilicate minerals ? Amer. Mineral., 75, 923-927.

Pienaar, H.S. (1982). Gem-quality friedelite from the Kalahari manganese field near Kuruman, South Africa. Gems and Gemmology, 18, 221-224.

Taljaardt, J.J. (1982). Major manganese ore fields, Republic of South Africa. Unpubl. report, SAMANCOR, Johannesburg, 11 pp.

UNIVERSITY OF JOHANNESBURG

Thomas, R.J., Agenbacht, A.L.D., Cornell, D.H., and Moore, J.M. (1994). The Kibaran of southern Africa: Tectonic evolution and metallogeny. Ore Geol. Rev., 9. 131-160.

Wilson, W.E., Dunn, P.J. (1978). Famous mineral localities: The Kalahari manganese field Mineral. Record, 22, 137-153.

UNIVERSITY OF JOHANNESBURG

Appendix 1

Minerals of the Kalahari manganese field

Elements

nat. copper	Cu

Sulphides

bornite	Cu_4FeS_5
chalcopyrite	$CuFeS_2$
chalcocite	Cu_2S
galena	PbS
marcasite	FeS_2
pyrite	FeS_2

Oxides and Hydroxides

birnessite (?)	$Na_4Mn_{14}O_{27} \cdot 9H_2O$
bixbyite #	$(Mn^{3+},Fe^{3+})_2O_3$
braunite #	$Mn^{2+}Mn^{3+}{}_6SiO_{12}$
braunite II *,#	$Ca(Mn^{3+},Fe^{3+})_{14}SiO_{24}$
brucite	$Mg(OH)_2$
chalkophanite (?)	$(Zn,Fe^{2+},Mn^{2+})Mn^{3+}{}_4O_7 \cdot 3H_2O$
cryptomelane	$K(Mn^{4+},Mn^{2+})_8O_{16}$
cuprite	Cu_2O
diaspore	AlO(OH)
feitknechtite	β-$Mn^{3+}O(OH)$
goethite	α-$Fe^{3+}O(OH)$
groutite	$Mn^{3+}O(OH)$
hausmannite #	$Mn^{2+}Mn^{3+}{}_2O_4$
hematite #	α-Fe_2O_3
hollandite	$Ba(Mn^{4+},Mn^{2+})_8O_{16}$
jacobsite #	$(Mn^{2+},Fe^{2+},Mg)(Fe^{3+},Mn^{3+})_2O_4$
lepidocrocite	γ-$Fe^{3+}O(OH)$
lithiophorite (?)	$(Al,Li)Mn^{4+}O_2(OH)_2$
manganite #	$Mn^{3+}O(OH)$
manganomelane	$(Na, K, Ba)_{2-y}(Mn^{4+}, Mn^{2+},Fe^{3+})_{8-z}O_{16-x}(OH)_x$
manjiroite	$(Na,K)(Mn^{4+},Mn^{2+})_8O_{16} \cdot nH_2O$
marokite	$CaMn^{3+}{}_2O_4$
nsutite	$(Mn^{4+}O_2)Mn^{3+}Mn^{4+}{}_{1-x}O_{2-2x}(OH)_{2x}$
opal/ chalcedony	$SiO_2 \cdot nH_2O$

UNIVERSITY OF JOHANNESBURG

portlandite	$Ca(OH)_2$
pyrochroite	$Mn^{2+}(OH)_2$
pyrolusite	$Mn^{4+}O_2$
quartz	SiO_2
ramsdellite	$Mn^{4+}O_2$
rancieite (?)	$Ca_2Mn^{4+}{}_{1-x}O_2 \cdot H_2O$
todorokite	$(Ca, Na, K)(Mg, Mn^{2+})Mn^{4+}{}_5O_{12} \cdot xH_2O$
tridymite	SiO_2

Carbonates

aragonite	$CaCO_3$
azurite	$Cu_3(CO_3)_2(OH)_2$
calcite #	$CaCO_3$
dolomite	$CaMg(CO)_3$
gaudefroyite	$Ca_4Mn^{3+}{}_{3-x}(BO_3)_3(CO_3)(O,OH)_3$
kutnahorite #	$Ca(Mn^{2+},Mg,Fe^{2+})(CO_3)_2$
malachite	$Cu_2(CO_3)(OH)_2$
rhodochrosite #	$Mn^{2+}CO_3$
thaumasite	$Ca_6Si_2(CO_3)_2(SO_4)_2(OH)_{12} \cdot 24H_2O$
vaterite	$CaCO_3$

Borates

gowerite	$CaB_6O_{10} \cdot 5H_2O$
inyoite	$Ca_2B_6O_{11} \cdot 13H_2O$
sussexite	$Mn^{2+}BO_2(OH)$

Sulphates

barite	$BaSO_4$
celestite	$SrSO_4$
charlesite	$Ca_6(Al,Si)_2(SO_4)_2B(OH)(OH,O)_{12} \cdot 26H_2O$
creedite	$Ca_3Al_2(SO_4)(F,OH)_{10} \cdot 2H_2O$
ettringite	$Ca_6Al_2(SO_4)_3(OH)_{12} \cdot 26H_2O$
gypsum	$CaSO_4 \cdot 2H_2O$
jouravskite	$Ca_6Mn^{4+}{}_2(SO_4,CO_3)_4(OH)_{12} \cdot 26H_2O$
shigaite	$Al_4Mn^{2+}{}_7(SO_4)_2(OH)_{22} \cdot 8H_2O$
sturmanite *	$Ca_6(Fe^{3+},Al,Mn^{2+})_2(SO_4)_2[B(OH)_4](OH)_{12} \cdot 25H_2O$
thaumasite	$Ca_6Si_2(CO_3)_2(SO_4)_2(OH)_{12} \cdot 24H_2O$
vonbezingite *	$Ca_6Cu_3(SO_4)_3(OH)_{12} \cdot H_2O$

UNIVERSITY OF JOHANNESBURG

Silicates

aegirine (acmite)	$NaFe^{3+}Si_2O_6$
afwillite	$Ca_3Si_2O_4(OH)_6$
akermanite	$Ca_2MgSi_2O_7$
albite	$NaAlSi_3O_8$
andradite #	$Ca_3Fe^{3+}2(SiO_4)_3$
banalsite	$BaNa_2Al_4Si_4O_{16}$
bementite	$Mn^{2+}{}_8Si_6O_{15}(OH)_{10}$
blanfordite	$(Na,Ca)(Fe^{3+},Mg,Mn^{3+})Si_2O_6$
bultfonteinite	$Ca_2SiO_2(OH,F)_4$
bustamite	$(Mn^{2+},Ca)_3Si_3O_9$
caryopilite	$(Mn^{2+},Mg)_3Si_2O_5(OH)_5$
chrysocolla	$(Cu,Al)_2H_2Si_2O_5(OH)_4 \cdot nH_2O$
clinochlor #	$(Mg,Fe^{2+})_5Al(Si_3Al)O_{10}(OH)_8$
clinochrysotil	$Mg_3Si_2O_5(OH)_4$
cymrite	$BaAl_2Si_2(O,OH)_8 \cdot H_2O$
datolite	$CaBSiO_4(OH)$
diopside	$CaMgSi_2O_6$
effenbergerite *	$BaCu(Si_4O_{10})$
ephesite	$NaLiAl_2(Al_2Si_2)O_{10}(OH)_2$
ferrobustamite	$Ca(Fe^{2+},Ca,Mn^{2+})Si_2O_6$
foshagite	$Ca_4Si_3O_9(OH)_2$
friedelite	$(Mn^{2+},Fe^{2+})_8Si_6O_{15}(OH,Cl)_{10}$
gageite	$(Mn^{2+},Mg,Zn)_{42}Si_{16}O_{54}(OH)_{40}$
glaucochroite	$CaMn^{2+}SiO_4$
glauconite	$(K,Na)(Fe^{3+},Al,Mg)_2(Si,Al)_4O_{10}(OH)_2$
grossular	$Ca_3Al_2(SiO_4)_3$
hennomartinite *	$SrMn^{3+}{}_2(Si_2O_7)(OH)_2 \cdot H_2O$
henritermierite	$Ca_3(Mn,Al)_2(SiO_4)_2(OH)_4$
hydroxyandradite	$Ca_3Fe_2(SiO_4)_{3-x}(OH)_{4x}$
hydroxygrossular	$Ca_3Al_2(SiO_4)_{3-x}(OH)_{4x}$
hydroxyl-apophyllite	$KCa_4Si_8O_{20}(OH,F) \cdot 8H_2O$
inesite	$Ca_2Mn^{2+}{}_7Si_{10}O_{28}(OH)_2 \cdot 5H_2O$
jennite	$Ca_9H_2Si_6O_{18}(OH)_6 \cdot 6H_2O$
johannsenite	$CaMn^{2+}Si_2O_6$
kentrolite	$Pb_2Mn^{3+}2Si_2O_9$
kirschsteinite	$CaFe^{2+}SiO_4$
kornite *	$(K,Na)(Na,Li)_2(Mg,Mn^{3+},Fe^{3+},Li)_5Si_8O_{22}(OH)_2$
leucophoenicite	$Mn^{2+}{}_7(SiO_4)_3(OH)_2$
lizardite	$Mg_3Si_2O_5(OH)_4$
Mg-arfedsonite	$Na_3(Mg,Fe^{2+})_4Fe^{3+}Si_8O_{22}(OH)_2$
Mn-diopside	$(Ca,Mn^{2+})MgSi_2O_6$
mozartite	$CaMn(OH)SiO_4$
natrolite	$Na_2[Al_2Si_3O_{10}] \cdot 2H_2O$
nontronite	$(Fe^{2+},Mg)_3Si_4O_{10}(OH)_2$

UNIVERSITY OF JOHANNESBURG

nchwaningite *	$Mn^{2+}_2SiO_3(OH)_2 \cdot H_2O$
orientite	$Ca_2Mn^{2+}Mn^{3+}_2Si_3O_{10}(OH)_4$
orlymanite *	$Ca_4Mn^{2+}_3Si_8O_{20}(OH)_6 \cdot 2H_2O$
oyelite	$Ca_{10}Si_8B_2O_{29} \cdot 12.5H_2O$
pargasite	$NaCa_2(Mg,Fe^{2+})_4Al(Si_6Al_2)O_{22}(OH)_2$
parsettensite	$(K,Na,Ca)(Mn,Al)_7Si_8O_{20}(OH)_8 \cdot 2H_2O$
pectolite	$NaCa_2Si_3O_8(OH)$
phlogopite	$KMg_3Si_3AlO_{10}(F,OH)_2$
piemontite/ Sr-piemontite	$(Ca,Sr)_2(Al,Mn^{3+},Fe^{3+})_3(SiO_4)_3(OH)$
poldervaartite *	$Ca(Ca_{0.5}Mn_{0.5})(SiO_3OH)(OH)$
rhodonite	$(Mn^{2+},Fe^{2+},Mg,Ca)SiO_3$
richterite	$Na_2Ca(Mg,Fe^{2+})_5Si_8O_{22}(OH)_2$
ruizite	$CaMn^{3+}Si_2O_6(OH) \cdot 2H_2O$
saponite	$(Ca,Na)_{0.3}(Mg,Fe^{2+})_3(Si,Al)_4O_{10}(OH)_2 \cdot 2H_2O$
serandite	$Na,(Mn^{2+},Ca)_2Si_3O_8(OH)$
sugilite	$KNa_2(Fe^{2+},Mn^{2+},Al)_2Li_3Si_{12}O_{30}$
taikanite	$Sr_3BaMn^{2+}_2Si_4O_{14}$
talc	$Mg_3[(OH)_2/Si_4O_{10}]$
tephroite/Mg-tephroite	$(Mn^{2+},Mg)_2SiO_4$
thaumasite	$Ca_6Si_2(CO_3)_2(SO_4)_2(OH)_{12} \cdot 24H_2O$
thomsonite	$NaCa_2[Al_2(Al,Si)Si_2O_{10}]_2 \cdot 6H_2O$
titanite	$CaTiSiO_5$
tobermorite-11Å	$Ca_9Si_{12}O_{30}(OH)_6 \cdot 4H_2O$
tremolite	$Ca_2(Mg,Fe^{2+})_5Si_8O_{22}(OH)_2$
vesuvianite	$Ca_{10}Mg_2Al_4(SiO_4)_5(Si_2O_7)_2(OH)_4$
vuagnatite	$CaAlSiO_4(OH)$
wollastonite	$CaSiO_3$
xonotlite	$Ca_6Si_6O_{17}(OH)_2$

Labels:
(?) - identification questionable
- important ore-forming mineral
* - new minerals (type locality)

UNIVERSITY OF JOHANNESBURG

Chapter Four

Effects of mass transfer, compaction and secondary porosity on hydrothermal upgrading of Paleoproterozoic sedimentary manganese ore in the Kalahari manganese field, South Africa.

Abstract

Hydrothermal alteration of Paleoproterozoic sedimentary manganese ore in the Kalahari manganese field, South Africa, has been described in considerable detail with regards to its mineralogical and petrographical characteristics. Low-grade carbonate-rich Mamatwan-type ore is altered to high-grade oxide-rich Wessels-type ore in association with normal faults in the northwestern part of the Kalahari manganese deposit. Mass balance calculations, based on the assumption that manganese behaved geochemically immobile, suggest that upgrading of the manganese ore can be attributed to leaching of Mg, Ca, CO_2 and SiO_2 from the sedimentary ore and residual enrichment of Mn. No lateral introduction of manganese has to be invoked. Two styles of hydrothermal alteration are present namely a) a ferruginous style of alteration, associated with coarse crystalline, mineralogically complex ores, and characterized by the introduction of considerable amounts of Fe_2O_3 and intense leaching of SiO_2 and b) a siliceous alteration style, typically associated with dense ores composed of variable amounts of hausmannite, andradite, braunite and hematite, and characterized by moderate losses of SiO_2 and no introduction of Fe_2O_3. Hydrothermal alteration resulted in development of between 10 % and 20 % of secondary porosity in the ores and the orebed was compacted to two thirds of its original stratigraphic thickness.

UNIVERSITY OF JOHANNESBURG

Introduction

The Kalahari manganese field (Fig. 4.1A) is situated some 60 km to the northwest of Kuruman in the Northern Cape Province of South Africa (Fig. 4.1A). The manganese field consists of five known, structurally preserved, erosional relics of the manganese-bearing Hotazel Formation (Nel et al., 1986), of which the Kalahari deposit is by far the largest (Fig. 4.1B). Manganese ores are of sedimentary origin and interbedded with iron-formation of the Hotazel Formation of the Paleoproterozoic Postmasburg Group of the Transvaal Supergroup (Fig. 4.1C). Two main ore types are present in the Kalahari deposit, namely low-grade primary sedimentary carbonate-rich

braunitic Mamatwan-type ore, with Mn contents of 20-38 wt %, and secondary carbonate-poor hausmannite-rich Wessels-type ore containing 45-60 wt % Mn (Kleyenstüber, 1984). The high-grade ores constitute about 3 percent of the total ore reserve of 13500 Mt at > 20 wt % manganese content.

High-grade Wessels-type ore formed as a product of hydrothermal metasomatic alteration of low-grade sedimentary Mamatwan-type ore along a series of normal faults in the Wessels-Nchwaning and Hotazel areas of the Kalahari manganese field (Fig. 4.1B). The petrography of the transformation of low-grade sedimentary to high-grade metasomatic ores has been documented in detail (Kleyenstüber, 1985; Gutzmer and Beukes, 1995; Beukes et al., 1995). However, the exact mechanism of upgrading of the manganese content from values in the order of 35-38 wt % in original sedimentary braunite lutite to values of 45 - 60 wt % in carbonate-poor

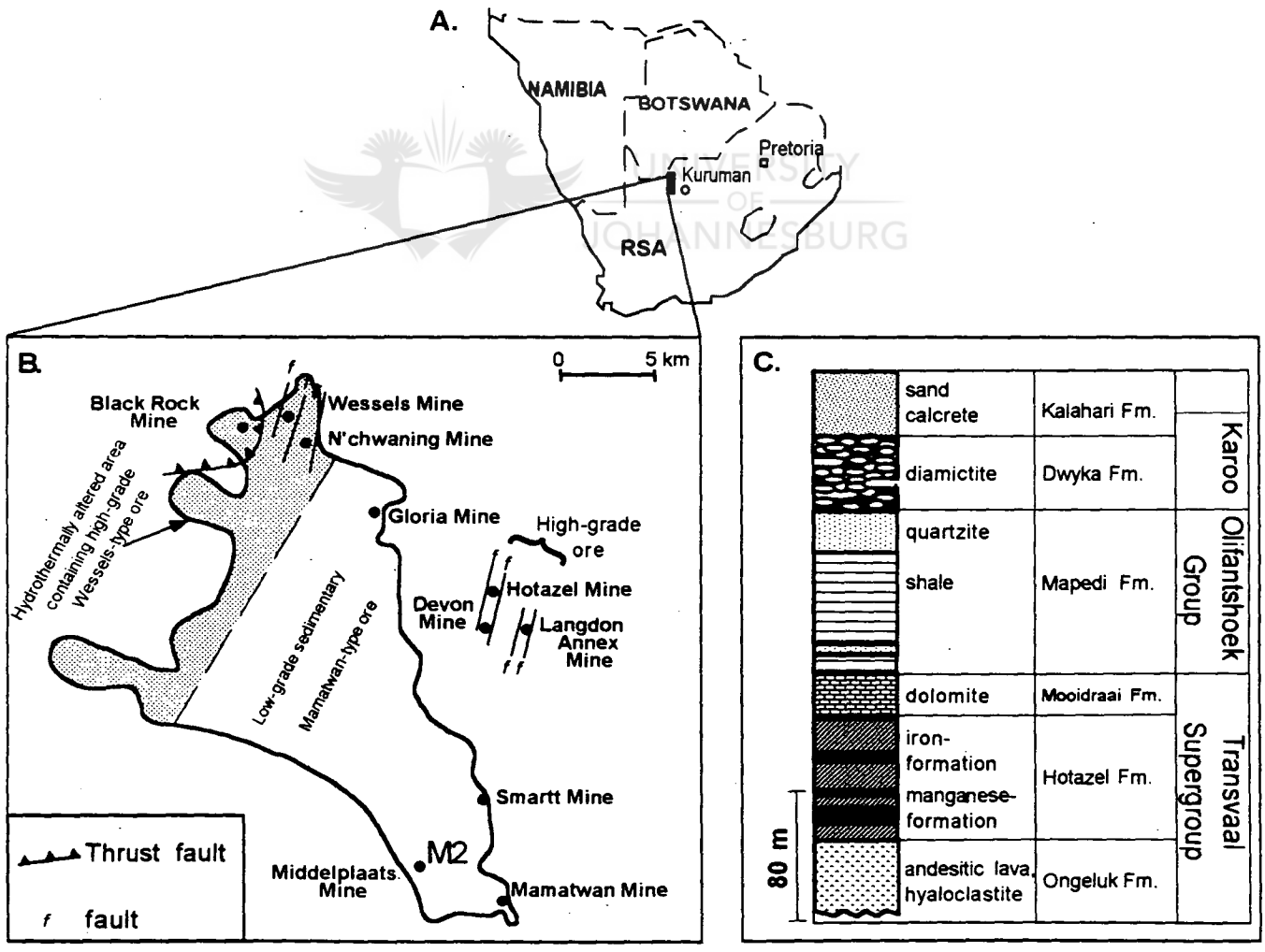

Fig. 4.1 Locality map of the Kalahari manganese deposit (A) showing the distribution of thrusting, major normal faulting, ore-types and location of mines (B) and the generalized stratigraphy of the area (C).

hausmannite-rich ores remains uncertain. Part of the upgrading may be related to the loss of CO_2 from the system during metasomatic transformation of manganese carbonates to manganese oxides (Kleyenstüber, 1985) with development of secondary porosity (Gutzmer and Beukes, 1995) and/or to compaction associated with metasomatic alteration. In addition it is possible that some manganese was introduced by hydrothermal (metasomatic) fluids, or that manganese was mobilized and reconcentrated during the Wessels alteration event (Beukes et al., 1995; Gutzmer and Beukes, 1995).

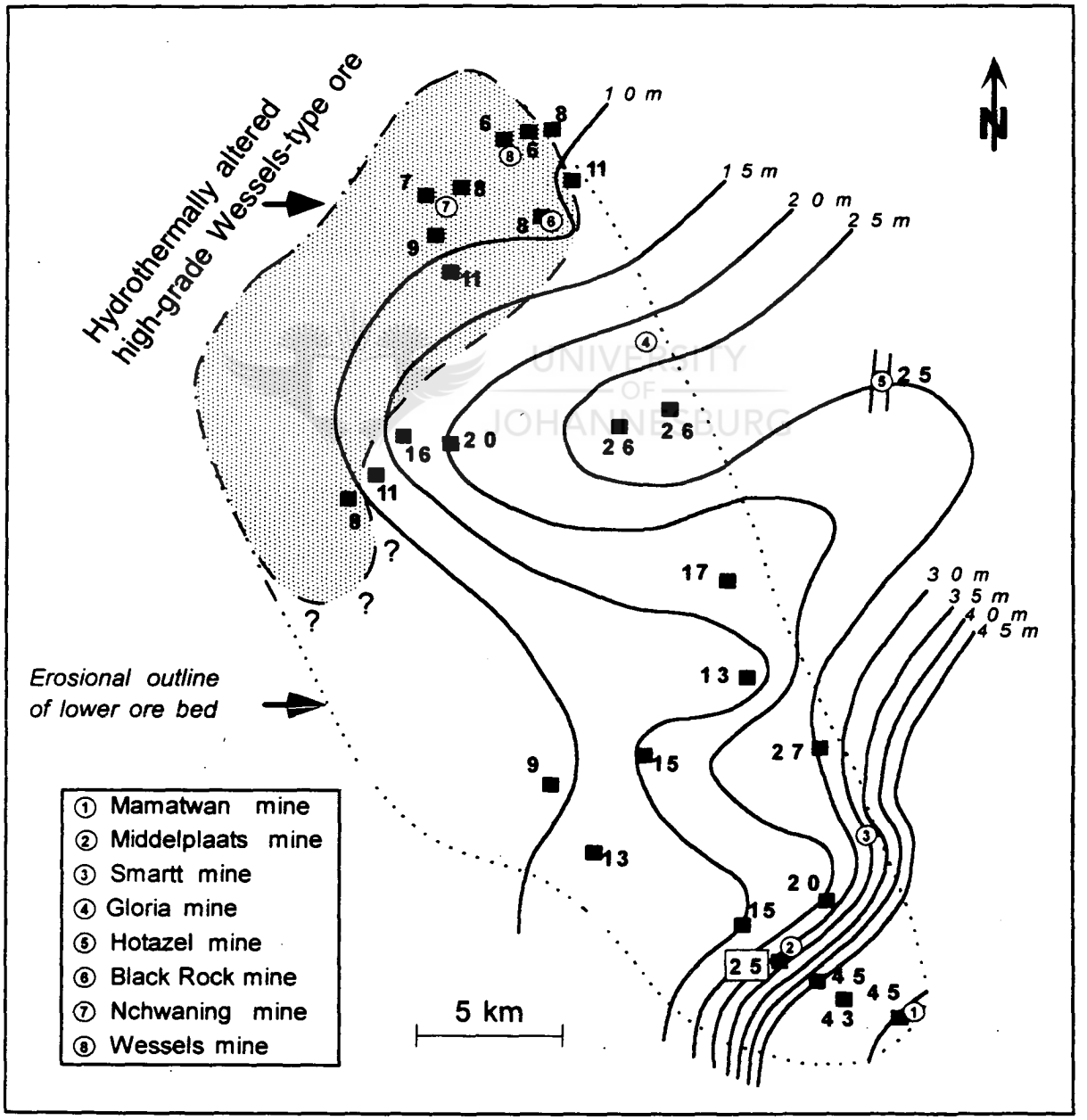

Fig. 4.2 Sketch map illustrating thickness variations of the lower manganese orebody in the Hotazel Formation in the Kalahari manganese field.

It is the purpose of this paper to address the questions surrounding the transformation of low-grade sedimentary Mamatwan-type manganese ore to high-grade Wessels-type ore very specifically. An attempt is made to quantify the contributions of decarbonatization, development of secondary porosity, compaction and metasomatic introduction or mobilization of manganese in the process of upgrading of the manganese ore. The deposit lends itself ideally for such studies because strata are virtually undeformed dipping gently at 4-10 ° to the west and zonation of low-grade Mamatwan-type ore to high-grade Wessels-type ore with associated normal faults is very well defined because of numerous exploration drill holes and excellent exposures in underground and opencast mines.

Geology

The manganese-bearing Hotazel Formation is preserved below a younger cover of late Paleoproterozoic Olifantshoek red beds, late Carboniferous-early Permian Dwyka diamictite of the Karoo Supergroup and Tertiary Kalahari beds (Fig. 4.1C). It is conformably underlain by pillow lava, hyaloclastite and jaspilite of the Ongeluk Formation and overlain by Mooidraai dolomite of the Postmasburg Group of the Transvaal Supergroup (Fig. 4.1C). Three manganese beds are present in the Hotazel Formation, each forming the centre of three symmetrical iron-formation ↔ hematite lutite ↔ braunite lutite sedimentary cycles. Virtually all manganese ore reserves and production come from the lower manganese bed which reaches a maximum known thickness of about 45 m at Mamatwan mine but ranges between 4 - 8 m in the Wessels and Nchwaning mining areas (Fig. 4.2).

Near the western margin of the Kalahari deposit, Ongeluk lava and Hotazel Formation have been duplicated by thrusting from the west (Fig. 4.1B) (Boardman, 1941; Beukes and Smit, 1987). Here the sequence has also been displaced by a series of north-trending normal faults which postdate the deposition of the Olifantshoek red beds but predate the thrust event (Beukes and Smit, 1987). It is along these normal faults that low-grade primary sedimentary Mamatwan-type ore has been upgraded by metasomatic alteration to high-grade Wessels-type ore (Fig's 4.3A and B).

The metasomatic hydrothermal alteration event apparently took place long after normal and thrust faulting. U-Pb dating by Dixon (1989) suggest Wessels ore to have formed at 1.25 Ga. Thrusting is known to be associated with the 1.8 Ga. old Kheis deformation event along the western margin of the Kaapvaal craton, whereas deposition of the red beds took place at 2.0-2.3

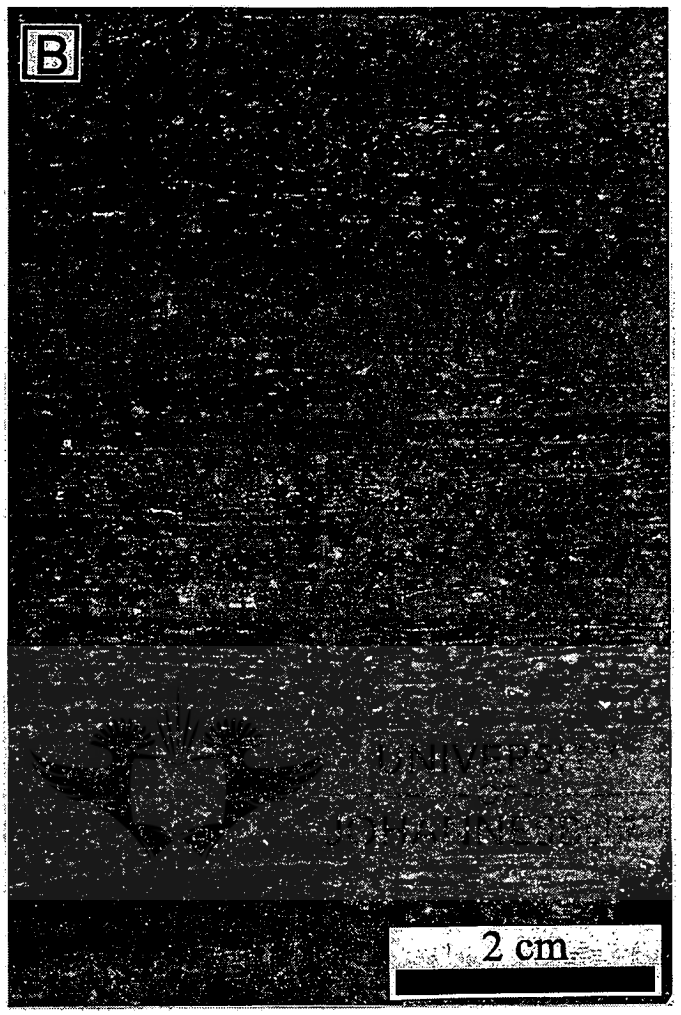

Fig. 4.4B Typical ore textures developed in hausmannite-rich ores affected by the siliceous style of alteration. Note that fine sedimentary lamination and outline of carbonate ovoids are recognizable in the ore affected by the siliceous alteration.

ore, except for in zones of very intense alteration where SiO_2 contents may be as low as 1.0 wt %. The occurrence of fine crystalline andradite, densely intergrown with hausmannite, is typical for the siliceous style of alteration.

In case of the ferruginous style of alteration, most common in the Wessels and Nchwaning mines, sedimentary Mamatwan-type ore, developed most distal from ferruginized normal fault zones (Fig. 4.3A), is composed of slightly porous, fine to medium crystalline, braunite-calcite-hausmannite ore associated with hematite. Towards the fault zone there is a marked increase in porosity and a decrease in preservation of original sedimentary lamination. The mineralogical composition of the ore changes from braunite II-hausmannite and hausmannite-bixbyite-braunite II to hausmannite-rich ore (Fig. 4.3A). The hausmannite-rich ore represents the highest-grade ore with least preservation of sedimentary structures. Immediately adjacent to the ferruginized fault

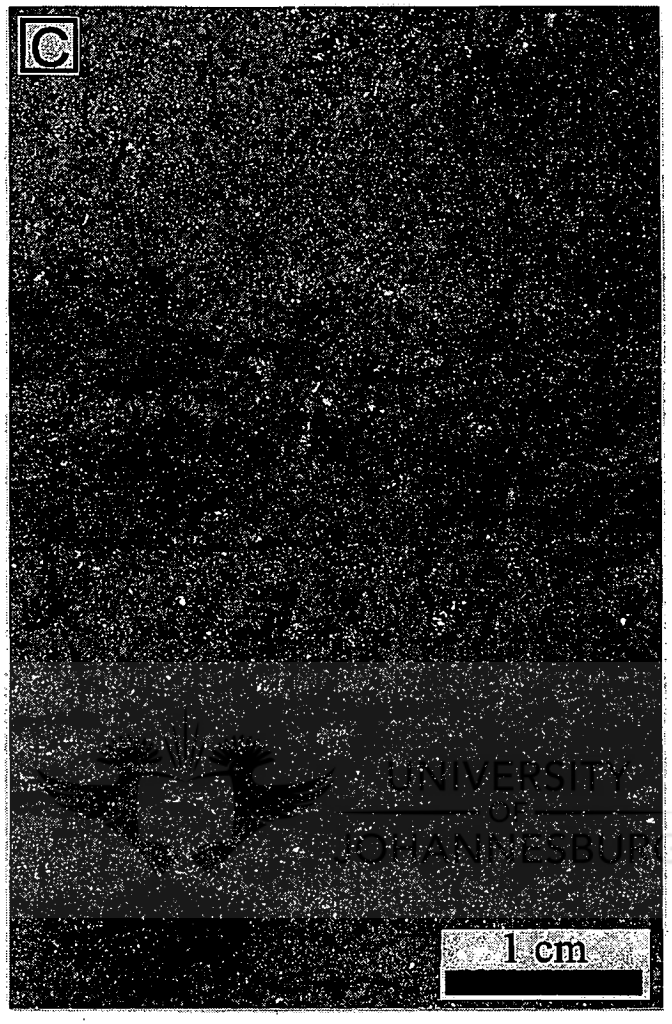

Fig. 4.4C Typical ore textures developed in hausmannite-rich ores affected by the ferruginous style of alteration. Note that sedimentary textures are completely obscured in the coarse crystalline vuggy ore typical for the ferruginous style of alteration.

zone a very dense secondary braunite-rich ore is developed, containing abundant metasomatic hematite with some andradite. In case of the siliceous style of alteration, most typically developed in the Hotazel mine, but also present in the Wessels-Nchwaning area, least altered ore is composed of braunite, hausmannite and andradite (Fig. 4.3B). In direction of zones of ferruginization next to normal faults, the ore mineral assemblage changes to that of hausmannite-andradite which may be of very high grade (+60 wt % Mn). Immediately adjacent to normal faults a relatively narrow zone of hausmannite-rich ore, with associated jacobsite and hematite (Fig. 4.3B), is developed. High-grade ores of the siliceous style of alteration appears less porous and more dense (Fig. 4.4B) than equivalent high-grade ores of the ferruginous style of alteration (Fig. 4.4C). Original sedimentary lamination and concretionary ovoids also appear better

Ga (Holland and Beukes, 1990). Normal faulting took place before the thrust event and after or during the deposition of the Olifantshoek red beds (Beukes and Smit, 1987).

Highest grade Wessels-type ore is developed immediately adjacent to ferruginized normal faults and low-grade Mamatwan-type ore is preserved in the centre of fault blocks (Fig. 4.3). Gradual and very systematic lateral transitions take place from Mamatwan to high-grade Wessels-type ore

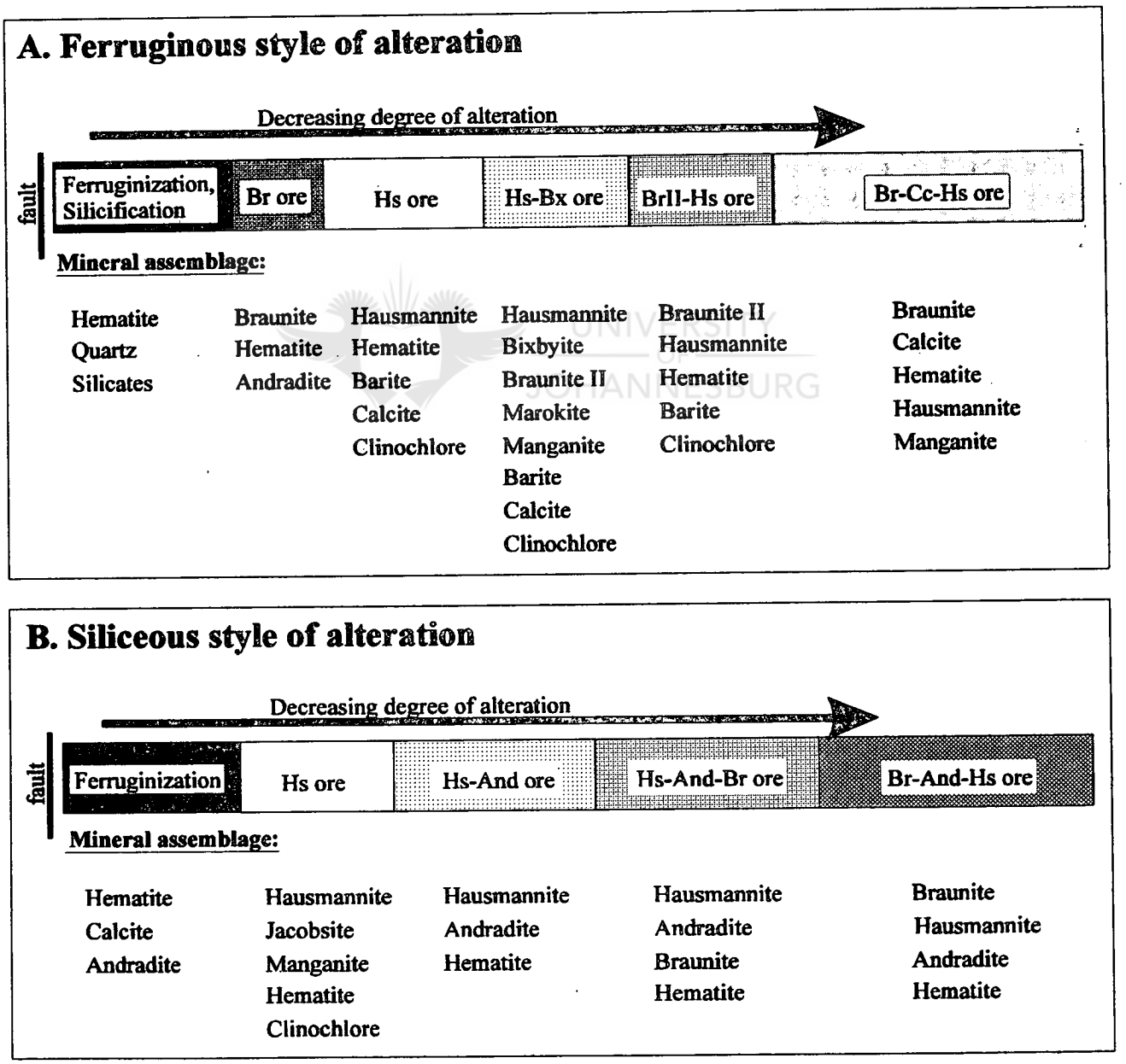

Fig. 4.3 Systematic mineralogical zonation developed along fault zones that acted as fluid feeder during ferruginous (A) and siliceous (B) styles of alteration.

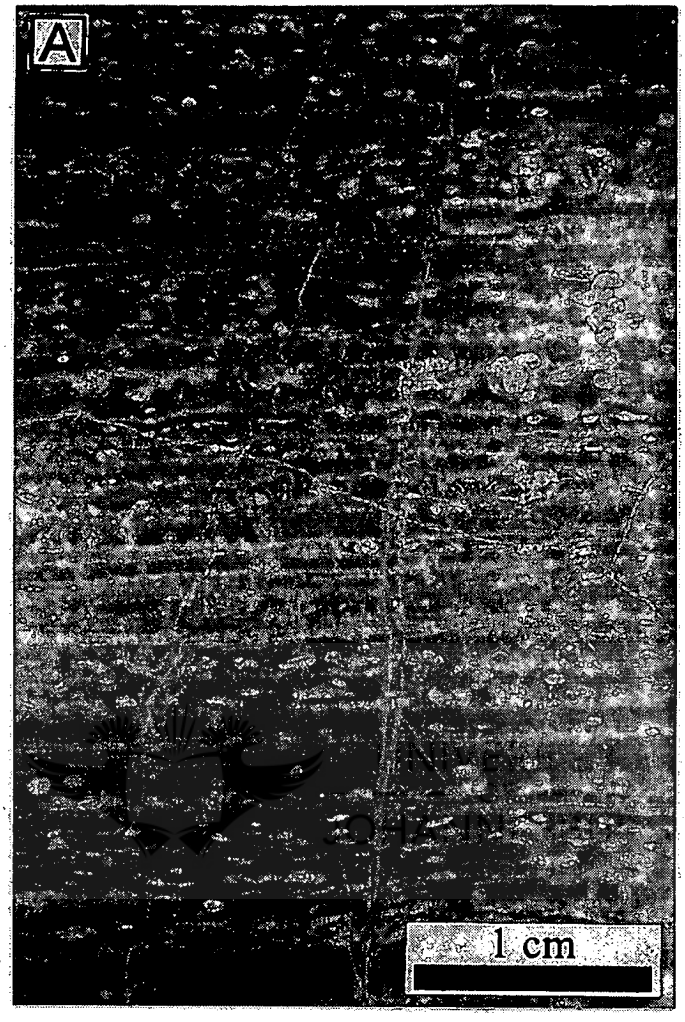

Fig. 4.4A Primary sedimentary carbonate rich Mamatwan-type ore. Note fine lamination and carbonate ovoids.

(Fig. 4.3). Mamatwan-type ore is typically microcrystalline and laminated and composed of finely intergrown braunite, hematite, kutnahorite, Mn-calcite and hausmannite with small concretionary ovoids of kutnahorite and Mn-calcite (Fig. 4.4A). In contrast Wessels-type ore appears rather porous, it is carbonate-poor, hausmannite-rich, coarse crystalline and massive to poorly laminated. Two styles of alteration, ferruginous and siliceous, are present in Wessels-type ore. The ferruginous style of alteration is characterized by a very variable mineralogy and lowering of the Mn:Fe ratio from approximately 10 in primary sedimentary Mamatwan-type ore to values in the order of about 6 in Wessels-type ore. There is also a marked decrease in the average silica content of the ore from about 6 wt % SiO_2 in Mamatwan-type ore to values below 1 wt % in hausmannite-rich Wessels-type ore. In the siliceous style of alteration the Mn:Fe ratio and the SiO_2 contents of altered ores are in general not much different to that in Mamatwan-type

preserved in ore of the siliceous style of alteration (Fig. 4.4B) than in ores of the ferruginous style of alteration (Fig. 4.4C).

If only low-grade sedimentary Mamatwan-type ore is taken into consideration the thickness of the lower manganese ore bed decreases from about 45 m at Mamatwan mine to between 12 and 8 m in the Wessels-Nchwaning area (Fig. 4.2). This decrease in thickness is considered to be of primary sedimentary origin. However, if thickness data are taken into consideration at localities where the lower ore bed has been altered to high-grade Wessels-type ore, the thickness may be

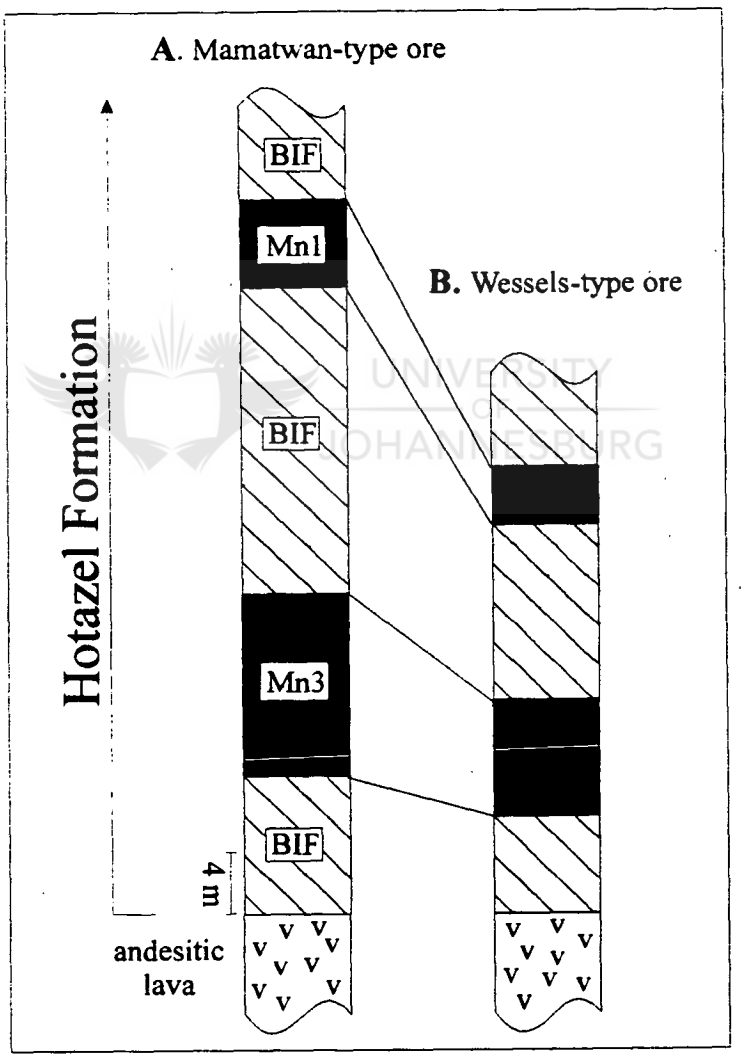

Fig. 4.5 Two closely associated drill core intersections through low-grade, unaltered manganese ore (A) and high-grade, altered manganese ore (B) from the northwestern part of the Kalahari manganese deposit. Note that the stratigraphic thickness of the orebody decreases by about 40 % from the unaltered to the altered orebed. Note thant the middle manganese orebody (Mn2) is not developed.

as little as 4 m. This decrease in thickness may be related to the metasomatic alteration event. This effect is clearly illustrated in closely spaced drill cores where the high-grade lower manganese ore bed is 7.5 m thick in contrast to a thickness of 11 m in adjacent low-grade Mamatwan-type ore (Fig. 4.5).

Sampling and analytical methods

In order to establish density, porosity and chemical mass balances for the ore, samples of unaltered Mamatwan-type ore of the lower manganese orebody were taken from drillcore M2, drilled on the farm Middelplaats in the southern part of the Kalahari deposit (Fig. 4.1B). Hand-sized ore sample of Wessels-type ore were taken from mining exposures at Wessels, Nchwaning and Hotazel mines (Fig. 4.1B). Sampling was restricted to the central part of the 4 - 8 m thick lower manganese ore bed. This central zone of high-grade ores is assumed to be the lateral equivalent of the central economic zone of unaltered Mamatwan-type ore in the lower manganese ore bed at Mamatwan mine (Nel et al., 1986).

Whole rock densities were determined on small, 1 to 4 cm^3 large, blocks of ore that were dried for several hours at 50°C, weighed, coated with paraffinum (density of 0.88 g/cm^3) and weighed again, first in air and then submerged in water. The density of the coated samples was calculated applying the law of Archimedes after correcting for the mass of paraffinum and the ambient temperature of the water. Duplicate analyses were performed and reproducibility of measurements was found to be ± 0.05 g/cm^3. Density values determined in this way are a measure of the density of the sample per unit rock volume, not per unit solid matter, because the paraffinum coating prohibits water entering the sample along fractures and pores (Brimhall and Dietrich, 1987).

Samples used for chemical analyses were cleaned carefully and then crushed with a hammer. About 500 g of sample chips were handpicked, avoiding unusually large vug infills or material from crosscutting veinlets, and milled in a Siebtechnik swingmill. Major and minor element analysis of the samples was performed at the Institut für Mineralogie und mineralische Rohstoffe, Technische Universität Clausthal, by X-ray fluorescence spectrometry. Pressed powder pellets were analysed on a Phillips PW 1480 X-ray spectrometer, equipped with a Rh-X-ray tube. Precision of the results was estimated by analysing certified reference materials to be ± 5 % relative. H_2O^- (adsorbed moisture) was determined at 110 °C and the loss on ignition at 1100 °C following techniques described by Heinrichs and Herrmann (1990). The CO_2 content was determined volumetrically in Wessels-type ore samples and by coulometric titration (Heinrichs

and Herrmann, 1990) in Mamatwan-type ore samples. Concentrations of Ti and trace elements were analysed by the Analytical Science Division, MINTEK, South Africa, using a VG2+ Plasmaquad ICP-MS instrument.

Mineral identification was based on X-ray powder diffraction and ore microscopic studies of polished thin sections. Electron microprobe analysis was used for mineral identification in doubtful cases. The average quantitative mineralogical composition of Mamatwan-type ore (in mass %) was estimated using quantitative X-ray powder diffraction analyses reported by Nel et al. (1986) and our own petrographic observations. The quantitative mineralogical composition of the different types of Wessels-type ore was estimated by careful light microscopic examination of polished thin sections using standard mineral volume estimation charts.

Quantitative mineralogical composition and density of manganese ores

The quantitative mineralogical composition of different ore types, estimated to the nearest 5 vol %, is presented in Table 4.1. It is obvious that Wessels-type ore of both the ferruginous and the siliceous styles of alteration are depleted in carbonates relative to Mamatwan-type ore which contains on average about 45 vol % kutnahorite and 15 vol % Mn-calcite (Table 4.1). In turn Wessels-type ore of the ferruginous style of alteration seldomly contains andradite whereas it is an abundant mineral (5-10 vol %) in ores of the siliceous style of alteration. In both ores of the ferruginous and the siliceous style of alteration highest-grade ores are essentially composed of hausmannite (90-95 vol %, Table 4.1). Zones of ferruginization along fault zones are largely depleted in manganese minerals and in the ferruginous style of alteration ferruginized zones may be composed of as much as 80 vol % quartz and/or silicates and 20 vol % hematite. In the siliceous style of alteration fault ferruginized zones contain little quartz but abundant hematite and minor calcite and andradite (Table 4.1).

Altered manganese ores of the siliceous style of alteration have an on average 0.4 g/cm^3 larger density than ores of the ferruginous style of alteration (Table 4.1). The density of Wessels-type ores of the ferruginous style of alteration vary in a rather narrow range between 3.85 and 3.94 g/cm^3. Sedimentary Mamatwan-type ore has an average density of 3.86 g/cm (Table 4.1). Secondary massive braunite-rich ores immediately adjacent to ferruginized fault zones and very high grade hausmannite-bixbyite ores have largest densities of 3.93 and 3.94 g/cm^3. Manganese ores of the siliceous style of alteration have densities of between 4.05 and 4.23 g/cm^3. Hematite-rich ores in fault zones associated with the siliceous style of alteration have a

Table 4.1 Quantitative mineral composition of different types of manganese ore, measured density and average mineral grain density, porosity and relative density increase.

Ore type	Quantitative mineralogical composition (in Vol %, unless otherwise stated)	ρ (g/cm)	ρ_g [a] (g/cm^3)	D[b] (%)	P[c] (Vol %)
Mamatwan type	45% Ku, 15% Cc, 30% Br, 6% He, 4% Hs	3.86	3.94		negligible
in wt %:	35% Ku, 10% Cc, 40% Br, 10% He, 5% Hs				
Ferruginous alteration					
Br-Cc-Hs type	20% Cc, 55% Br, 15% Hs, 10% He	3.85	4.35	0	11
BrII-Hs type	80% BrII, 15% Hs, 5% He	3.87	4.77	0	19
Hs-Bx type	65% Hs, 15% BrII, 15% Bx, 5% He	3.94	4.77	2	17
in wt %:	64% Hs, 15% BrII, 16% Bx, 5% He				
Hs type	95% Hs, 5% He	3.86	4.73	0	18
Br type	60% Br, 20% Hs, 15% He, 5% And	3.93	4.73	2	17
He type	80% Qz, 20% He	2.79	3.16	-28	12
Siliceous alteration					
Br-And-Hs type	40% Br, 45% Hs, 10% And, 5% He	4.14	4.63	7	11
Hs-And-Br type	75% Hs, 10% Br, 10% And, 5% He	4.23	4.63	10	9
Hs-And type	85% Hs, 10% And, 5% He	4.23	4.63	10	9
in wt %:	86% Hs, 8% And, 6% He				
Hs type	90% Hs, 5% And, 5% He	4.05	4.68	5	13
He type	90% He, 5% Cc, 5% And	4.18	5.00	8	16

[a] - average mineral grain density; [b] whole rock density increase of altered ore relative to Mamatwan-type ore; [c] total porosity.
Abbreviations: And-andradite, Br-braunite, Br II-braunite II, Bx-bixbyite, Cc-calcite, He-hematite, Hs-hausmannite, Ku-kutnahorite.

UNIVERSITY OF JOHANNESBURG

Table 4.2 Important ore-forming minerals.

Mineral	chemical formula	ρ (g/cm^3)
Hausmannite	Mn_3O_4	4.7
Braunite	Mn_7SiO_{12}	4.7
Braunite II	$Ca_{0.5}Mn_7Si_{0.5}O_{12}$	4.75
Bixbyite	$(Mn,Fe)_2O_3$	4.95
Hematite	Fe_2O_3	5.2
Andradite	$Ca_3Fe_2(SiO_4)_3$	3.75
Quartz	SiO_2	2.65
Kutnahorite	$CaMn(CO_3)_2$	3.0
Mn-Calcite	$(Ca,Mn)CO_3$	2.8

density of 4.18 g/cm^3 whereas quartz and silicate-rich ferruginized ores associated with the ferruginous style of alteration have a density of about 2.79 g/cm^3 (Table 4.1).

The simplified stoichiometric chemical compositions and densities of major ore-forming minerals are presented in Table 4.2 (data from Rösler, 1983; De Villiers, 1980). The major manganese ore minerals, hausmannite, braunite II, and braunite, have very similar densities of 4.7 - 4.75 g/cm^3. Bixbyite (4.95 g/cm^3) and hematite (5.2 g/cm^3) have significantly higher and andradite (3.75 g/cm^3), quartz (2.65 g/cm^3) and the carbonates kutnahorite (3.0 g/cm^3) and Mn-calcite (2.8 g/cm^3) significantly lower densities than the major manganese oxide minerals (Table 4.2).

With reference to whole rock minor and trace element composition, it is important to note that Mamatwan-type ore contains virtually no other minerals than those listed in Table 4.1. However, Wessels-type ore contains a wide variety of gangue minerals erratically distributed in small vugs and veinlets. These minerals, which include barite, celestite, gypsum and gaudefroyite, may drastically influence absolute concentrations of trace or minor elements in whole rock Wessels-type ore samples.

Table 4.3A Major and minor element composition of unaltered braunite-lutite from the lower Mn-orebody in the Hotazel Formation. All samples from drillcore M2 (Mamatwan), samples 44 and 45 from the upper subeconomic zone, samples 47B and 49B from the central economic zone, sample 49C from the lower subeconomic zone.

Sample	zone	SiO	TiO_2	Al_2O_3	Fe_2O_3	Mn_3O_4	MgO	CaO	Na O	K_2O	H_2O^-	$_2CO_2$	L.O.I.	TOTAL	Mn:Fe	ρ
M2-44	USE	4.97	0.093	<0.4	7.96	29.8	4.11	24.4	<0.1	0.1	0.11	24.4	26.9	98.3	3.9	3.20
M2-45	USE	6.19	0.058	<0.4	9.77	47.2	3.2	14.6	<0.1	0.1	0.09	15.3	20.7	101.8	5.0	3.81
M2-47B	E	4.61	0.077	<0.4	4.91	49.4	2.14	17.9	<0.1	0.14	0.07	17.7	20.4	99.6	10.3	3.82
M2-49B	E	6.79	0.044	<0.4	5.96	60.9	1.56	11.3	<0.1	0.12	0.05	11.2	11.7	98.4	10.5	3.96
M2-49C	LSE	3.99	0.044	0.45	9.61	30.3	2.59	24.6	<0.1	0.09	0.05	23.7	23.7	95.8	3.2	3.43
Average [a]	E	4.07	0.061[b]	0.19[a]	4.75[a]	53.1[a]	3.17[a]	12.6[a]	0.05[c]	0.13[b]	0.05[a]	15.0[a]			11.5	3.86[b]

[a] data from Kleyenstüber (1993), [b] average calculated from samples M2-47B and M2-49B, [C] Average for Na_2O as suggested by XRF analysis. [#] Average composition of Mamatwan-type ore (central economic part of lower orebody). Abbreviations: E-economic zone, LSE-lower subeconomic zone, USE-upper subeconomic zone.

Table 4.3B Trace element composition of unaltered braunite-lutite from the lower Mn-orebody of the Hotazel Formation. All samples from drillcore M2 (Mamatwan), samples 44 and 45 from the upper subeconomic zone, samples 47B and 49B from the central economic zone, sample 49C from the lower subeconomic zone. All data in ppm.

Sample	zone	B	Co	Ni	Cu	Zn	Rb	Sr	Y	Zr	Sn	Ba	Pb
M2-44	USE	360	23	13	<2	<2	1.1	210	6.5	2.1	1.9	53	<1
M2-45	USE	530	30	264	<2	18	1.4	94	5.2	12	1.7	77	13
M2-47b	E	610	24	25	<2	110	1.3	110	5.1	20	2.6	250	170
M2-49b	E	865	27	15	<2	14	1.2	83	4.2	<2	<2	185	90
M2-49c	LSE	540	23	44	<2	160	1.7	170	10	90	1.9	45	190

Abbreviations as in Table 4.3A.

UNIVERSITY OF JOHANNESBURG

Table 4.4 Composition of altered ores of the ferruginous style of alteration.

Ores	Br-Cc-Hs		BrII-Hs		Hs-Bx		Hs		Br		Fe	
	mean	range	mean	range	mean	range	mean	range	mean	range	mean	range
N		3		4		4		4		4		3
in wt %												
SiO_2	6.91	5.7-7.74	2.71	0.89-4.71	1.03	0.72-1.75	0.20	0.1-0.69	9.32	6.42-12.1	56.8	52.8-60.6
TiO_2	0.03	0.03-0.04	0.04	0.02-0.06	0.06	0.02-0.09	0.02	0.00-0.07	0.04	0.02-0.09	0.02	0.02-0.03
Al_2O_3	0.20	0.03-0.4	0.79	0.00-2.93	0.20	0.03-0.14	0.16	0.00-0.42	0.44	0.1-0.87	0.61	0.45-0.77
Fe_2O_3	8.59	7.20-11.0	9.74	5.9-13.3	12.2	7.38-18.3	12.2	0.74-32.9	11.1	7.4-18.4	28.7	25.1-32.3
Mn_3O_4	58.3	49.8-63.7	76.8	71.5-80.5	78.8	74.3-88.0	87.5	67.3-96.9	71.7	64.4-77.9	3.28	2.70-3.80
MgO	0.53	0.35-0.73	1.68	0.02-6.06	0.67	0.51-1.06	0.18	0.04-0.26	0.55	0.10-1.62	0.30	0.03-0.56
CaO	13.0	8.80-17.8	5.56	2.74-6.45	3.01	0.91-6.54	0.31	0.17-0.49	5.79	4.19-8.01	3.58	3.41-3.74
Na_2O	0.03	0.01-0.05	0.01	0.01-0.02	0.01	0.01-0.03	0.00	0.01	0.03	0.02-0.05	3.90	3.68-4.11
K_2O	0.02	0.01-0.04	0.01	0.01	0.01	0.01	0.04	0.01-0.12	0.02	0.01-0.03	0.60	0.24-0.96
H_2O^-	0.11	0.1-0.12	0.10	0.05-0.21	0.19	0.06-0.35	0.03	0.05-0.1	0.06	0.1-2.1	0.12	0.07-0.17
CO_2	9.13	6.5-13.4	0.27	0.1-0.85	0.79	0.1-2.28	0.12	0.1-0.2	0.78	0.1-2.1	0.09	0.1-0.17
L.O.I.	10.8	7.4-14.4	1.27	-0.5-4.8	3.31	0.6-4.6	-0.39	-1.3-0.0	1.54	0.7-3.1	0.35	0.3-0.4
TOTAL	99.2		99.0		97.6		99.6		98.7		98.1	
Mn/Fe	7.0	4.7-9.1	8.1	6.2-13.9	6.6	5.6-10.3	54.6	8.8-134.2	6.7	4.0-10.2	0.1	0.1
in g/cm^3												
ρ_m	3.85	3.62-4.07	3.87	3.78-4.01	3.94	3.87-3.98	3.86	3.71-3.97	3.93	3.61-4.07	2.79	2.78-2.79
in ppm												
B	421	375-467	238	170-315	330	280-380	155	85-270	1528	935-1850	105	100-110
Co	18	15-21	122	14-270	46	31-60	20	20	23	20-25	7	5.5-9.1
Ni	105	79-130	9	2-17	22	21-23	6	3.3-12	24	17-31	24	17-30
Cu	11	5-16	20	<2-56	12	<2-23	12	<2-36	25	<2-74	1	<2-2.4
Zn	53	45-60	275	7.3-790	55	10-100	89	5.8-210	18	11-29	2	1-2
Rb	<2	<2	<2	<2	<2	<2	<2	<2	<2	<2	<2	<2
Sr	253	205-301	197	3.4-580	158	26-290	18	3.3-40	15	10-18	145	100-190
Y	65	<5-130	7	3.7-12	13	12-14	4	2.2-6.9	6	3.6-8.8	3	2.3-3.8
Zr	<2	<2	9	<2-20	10	<2-20	4	<2-11	20	4.8-45	9	8.5-9
Sn	<2	<2	5	3.5-7.1	1	<1-1.3	2	1.5-2.2	2	<1-3.2	4	4.4-3.6
Ba	14	5-22	5135	4.3-13500	617	33-1200	401	14-980	5394	1.8-16000	78	56-100
Pb	51	46-55	101	3-240	27	23-30	112	16-220	22	29-36	15	10-20

UNIVERSITY OF JOHANNESBURG

Table 4.5 Composition of altered ores of the siliceous style of alteration.

Ores	Br-And-Hs		Hs-And-Br		Hs-And		Hs		Fe	
in wt %	mean	range	mean	range	mean	range	mean	range	mean	range
N	4		6		4		4		3	
in wt %										
SiO_2	6.22	4.16-8.79	4.38	3.62-4.79	4.71	3.00-5.42	1.15	0.44-1.91	4.87	2.35-11.0
TiO_2	0.05	0.04-0.05	0.05	0.04-0.05	0.05	0.04-0.05	0.05	0.04-0.05	0.05	0.04-0.05
Al_2O_3	0.11	0.07-0.28	0.10	0.03-0.18	0.29	0.09-0.51	0.31	0.01-0.85	0.17	0.1-0.26
Fe_2O_3	7.48	7.13-7.86	7.29	6.30-8.80	7.45	4.97-8.73	8.31	5.24-10.5	88.5	71.1-94.6
Mn_3O_4	82.6	78.3-85.4	85.7	83.2-88.8	80.8	74.8-88.0	86.5	82.1-89.8	0.64	0.45-1.08
MgO	0.78	0.42-1.55	0.38	0.27-0.52	0.79	0.39-1.55	0.46	0.18-1.03	1.67	0.23-6.28
CaO	2.10	0.91-7.77	1.17	0.49-1.68	4.02	1.99-5.98	0.28	0.36-0.39	1.46	0.08-5.19
Na_2O	0.02	0.00-0.09	0.06	0.00-0.1	0.05	0.02-0.1	0.08	0.00-0.28	0.04	0.03-0.04
K_2O	0.00	0.00	0.01	0.00-0.03	0.00	0.00	0.02	0.00-0.08	0.02	0.02
H_2O^-	0.14	0.00-0.25	0.07	0.08-0.17	0.09	0.05-0.36	0.21	0.06-0.56	0.18	0.08-0.15
CO_2	0.00	0.00-0.01	0.02	0.00-0.13	0.03	0.00-0.1	0.15	0.00-0.4	1.04	0.00-4.07
L.O.I.	0.82	0.4-1.5	0.83	0.11-1.90	0.64	<0.05-1.0	2.46	0.2-4.1	1.95	0.5-5.5
TOTAL	100.2		99.7		99.8		99.6		99.4	
Mn/Fe	11.4	10.3-12.2	12.1	9.7-14.3	9.8	6.4-18.2	10.7	8.0-17.7	0.0	0.0-0.01
in g/cm^3										
ρ_m	4.14	3.96-4.40	4.23	4.08-4.36	4.23	4.07-4.36	4.05	3.82-4.07	4.18	4.05-4.44
in ppm										
B	542	150-990	455	<2-910	195	<2-390	65	40-90	60	60
V	15	8-24	18	8-20	12	10-14	23	18-32	34	13-49
Cr	54	39-74	69	43-101	44	32-56	36	26-44	54	34-78
Co	27	22-33	8	0.4-24	12	0.8-20	3	0.2-7.1	2	1.6
Ni	10	5.6-13	4	0-9	11	6.5-18	4.7	1-13	7	0-13
Cu	<2	<2	<2	<2	<2	<2	<2	<2	<2	<2
Zn	133	35-320	676	105-2586	135	20-208	1790	24-4700	51	4-131
Rb	<2	<2	<2	<2	<2	<2	<2	<2	<2	<2
Sr	113	19-160	31	24-43	23	10-30	10	3-24	18	7-33
Y	10	8.4-11	7	6.8	6	5.8-6.2	6	6.2-6.5	3	2.8
Zr	<2	<2	<2	<2	2	<2-3.1	4	<2-7.2	8	8.2
Sn	2	1.4-2	<2	<2	2	1.7-2.2	<2	<2	<2	<2
Ba	118	35-180	41	24-80	136	51-326	11	<2-30	98	30-170
Pb	119	73-150	67	30-104	188	41-370	80	15-140	11	0-27

UNIVERSITY OF JOHANNESBURG

Geochemistry

The composition of Mamatwan manganese ore shows considerable variation across the lower manganese orebed as illustrated by five samples from drillcore M2 (Tables 4.3A and B). Major, minor and trace element concentrations vary considerably, a fact already noted by Nel et al. (1986). It is interesting to note that absolute concentrations of manganese and the Mn/Fe ratio increase and MgO, CaO and CO_2 concentrations decrease towards the central economic zone of the ore body, indicating a general increase of the amount of manganese oxides (braunite, hausmannite) at the expense of carbonates. Concentrations of TiO_2, Al_2O_3, Na_2O, K_2O and of most trace elements are very low and show little variation (Tables 4.3A and B).

Wessels-type ores appear considerably enriched in manganese and iron relative to Mamatwan-type ore. Concentrations of Fe_2O_3 increase from an average of 4.75 wt % in Mamatwan-type ore (Table 4.3A) to concentrations of 8.59-12.2 wt % in ores affected by the ferruginous style of alteration (Table 4.4), and to 7.45-8.31 wt % in samples affected by the siliceous style of alteration (Table 4.5). Manganese concentrations increase from an average of 53.1 wt % Mn_3O_4 in Mamatwan-type ore (Table 4.3A) to a maximum of 96.9 wt % Mn_3O_4 in Wessels-type ore (Table 4.4 amd 4.5). Mn/Fe ratios of 11.5 in Mamatwan-type ore remain similar in Wessels-type ore of the siliceous style of alteration (Table 4.4) but decrease to values of between 6 and 8 in ores of the ferruginous style of alteration (Table 4.5). Zones of ferruginization are characterized by exceptional Fe_2O_3 enrichment and depletion of Mn_3O_4.

CaO, MgO, CO_2 appear moderately to strongly depleted in all varieties of Wessels-type ore relative to Mamatwan-type ore. The same is true for SiO_2, with the notable exception of weakly altered braunite-calcite-hausmannite (Br-Cc-Hs) ore (Table 4.4). The depletion of these components in Wessels-type ore may be explained by the leaching of carbonates and the replacement of braunite by braunite II, bixbyite and hausmannite during the Wessels metasomatic alteration event (Gutzmer and Beukes, 1995; Beukes et al., 1995).

The minor elements TiO_2, Na_2O and K_2O occur only in very small concentrations in Wessels-type ore, somewhat below the range of these elements in Mamatwan-type ore. Strong enrichment of the alkali elements is obvious for the ferruginized and silicified ores associated with the ferruginous style of alteration along fault zones. The large spread of concentrations of trace elements such as B, Co, Cu, Zn, Sr, Pb and especially for Ba (Tables 4.4 and 4.5) is explained by the heterogenous distribution of pore-filling trace mineral phases such as barite, celestite, gypsum, gaudefroyite and others, in which these trace elements are concentrated (Gutzmer and Beukes, 1995; Beukes et al., 1995). It is likely that these trace elements are redistributed and

locally concentrated during the alteration event and were not necessarily introduced by hydrothermal fluids. The concentrations for Ba and Sr are good examples. Concentrations of about 100 ppm Sr and 200 ppm Ba are present in the central economic zone of the parent Mamatwan-type ore bed (Table 4.3B). Hydrothermal alteration resulted in concentration of Ba and Sr in barite and/or celestite occurring irregularly distributed in secondary pores and veinlets in Wessels-type ore (Gutzmer and Beukes, 1995). Thus the concentrations of Ba and Sr vary erratically, displaying local enrichment to concentrations of 16000 ppm Ba and 580 ppm Sr (Table 4.4) but also depletion to concentrations less than 10 ppm. The distribution of boron in Wessels-type ores appears similarly controlled by the heterogenous occurrence of minor B-rich mineral phases such as gaudefroyite, datolite and braunite. However, in general boron appears to be depleted in Wessels-type ores, with concentrations ranging between 60 and 550 ppm (Tables 4.4 and 4.5), compared to Mamatwan-type ore which contains on average about 700 ppm B (Table 4.3B, samples M2-47B and M2-49B).

Other trace elements, such as Ni, Rb, Y, Zr, and Sn appear less heterogeneously distributed but occur in very small concentrations (Tables 4.4 and 4.5), that are generally below or within the same range of concentrations in Mamatwan-type ore. Notable exceptions are Cu that is enriched in Wessels-type ore of the ferruginous style of alteration (Table 4.4) and Zn that appears to be enriched in ores of the siliceous style of alteration (Table 4.5).

UNIVERSITY OF JOHANNESBURG

Estimating Compaction and Secondary Porosity

A detailed account on how to relate changes of chemical and physical parameters in metasomatic hydrochemical alteration systems is provided by Brimhall and Dietrich (1987). They show that the porosity P in altered and unaltered rocks can be calculated by relating the measured density of a rock type ρ_m to its average mineral grain density ρ_g

(1)

$$P=(1-\frac{\rho_m}{\rho_g})\cdot 100$$

In this equation ρ_m can be measured (Table 4.5) and ρ_g may be calculated from the quantitative mineralogical composition of the different manganese ore types (Table 4.1) and the known density of the minerals present (Table 4.2).

The average mineral grain density for Mamatwan-type ore is 3.94 g/cm^3 which is very similar to its measured density of 3.86 g/cm^3. It implies negligible porosity in sedimentary Mamatwan-type (Table 4.1). However, calculations indicate porosities of between 11 - 19 vol % in ores of the ferruginous style of alteration and between 9 - 13 vol % in ores of the siliceous style of alteration. These porosities are of secondary origin and related to hydrothermal alteration of primary Mamatwan-type ore to secondary high-grade Wessels-type ore (Table 4.1).

The amount of compaction that affected the orebody as a result of hydrothermal alteration can now be assessed by estimating the total volume of solid mineral phases removed during the alteration process. This estimate is based on the assumption that the volume that is originally occupied by mineral matter that is leached during the hydrothermal alteration process may be preserved as secondary porosity or consumed either by compaction or lateral introduction and precipitation of secondary mineral phases. To exclude the latter it is necessary to show that upgraded Wessels-type manganese ores can form by residual enrichment, e.g. leaching of components, and that lateral introduction of chemical constituents, in particular of manganese, is quantitatively negligible. In order to manifest this assumption, the mineral-chemical transformation of Mamatwan-type ore to Wessels-type ore was simulated for two examples (Tables 4.6 and 4.7). Only the transformation of major phases present in unaltered sedimentary and hydrothermally altered ores was modelled leading to an estimate of maximum compaction. Alteration was modelled for hausmannite-bixbyite (Hs-Bx) ore (Table 4.6) as an example for the ferruginous style of alteration, and for hausmannite-andradite (Hs-And) ore as an example for the siliceous style of alteration (Table 4.7). These two ore types were selected because they represent highly altered ore types but are at the same time situated in a considerable distance from the fluid feeder fault zones alongside which remobilisation of manganese took place (Gutzmer and Beukes, 1995).

The alteration is modelled in two steps. First the mineral assemblage present in Mamatwan-type ore is quantitatively transformed into the mineral assemblage typical for Wessels-type ore. All manganese present in the sedimentary Mamatwan-type ore, is transformed quantitatively into manganese oxides such as hausmannite, bixbyite and braunite II (Tables 4.6 and 4.7). The relative amounts of the different manganese oxides formed were selected to be similar to that observed in the Wessels-type ore under consideration. All iron is transformed into hematite and/or andradite. CaO and SiO_2 are taken up in stoichiometric amounts by braunite II and andradite, excess amounts are removed from the modelled system together with MgO and CO_2. The amounts of the different minerals present in the alteration mineral assemblage $N_{mineral}$ is

expressed in mass % (Tables 4.6 and 4.7) but may be recalculated into vol % by using the following relation

(2)

$$N_{mineral}(vol\%) = \frac{N_{mineral}(mass\%)}{\rho_{mineral}}$$

The free volume created by leaching of mineral phases can be estimated by difference (Tables 4.6 and 4.7). The density of these leached phases (Ca-Mg-carbonate and SiO_2) is set to 2.7 g/cm^3, an average value close to the densities of calcite, dolomite and quartz, mineral phases that are

Table 4.6 Amount of compaction ϵ estimated by modelling the formation of Hs-Bx ore (ferruginous style of alteration)[#].

Mineral	$\rho_{mineral}$	$M_{mineral}^{a}$	$V^{i}_{mineral}^{a,b}$	$V^{c}_{mineral}^{c}$
	(g/cm^3)	(mass %)	(Vol %)	(Vol %)
hausmannite	4.70	34.1	26.2	58.5
bixbyite	4.95	10.0	7.3	16.3
braunite II	4.75	10.0	7.7	17.2
hematite	5.20	5.2	3.6	8.0
leached fraction	2.70	40.7	55.2	
TOTAL		**100.0**	**100.0**	**100.0**
Total free volume created			55.2 %	
secondary porosity P			17.0 %	
compaction ϵ			**38.2 %**	

[#] The following assumptions were introduced to simplify the calculations: A) Only major mineral phases in Mamatwan and Wessels-type ore were taken into consideration. The mineral association present in Mamatwan-type ore is quantitatively transformed into the altered mineral assemblage; B) Average contents of Mn and Fe of kutnahorite (16.2 wt% MnO, 0.3 wt% FeO) and Mn-calcite (10 wt% MnO, 0.3 wt% FeO) in Mamatwan-type ore were reported by Nel et al. (1986); C) Other mineral phases are of pure, stoichiometric composition; D) All CO_2 and MgO are removed during alteration. CaO and SiO_2 are retained in stoichiometric amounts; F) Mass transfer takes place exclusively out of the system.

[a] mass (volume) of primary Mamatwan-type ore equals 100 %; [b] vol% and mass% of mineral phases present are linked with each other through density; [c] normalized to volume of solid phases only, these values are comparable to the average quantitative mineral composition estimated in Table 4.1.

Table 4.7 Amount of compaction ϵ estimated by modelling the formation of Hs-And ore (siliceous style of alteration). #

Mineral	$\rho_{mineral}$	$M_{mineral}$ [a]	$V^{i}_{mineral}$ [a,b]	$V^{c}_{mineral}$ [c]
	(g/cm³)	(mass %)	(Vol %)	(Vol %)
hausmannite	4.70	52.5	31.8	84.5
andradite	3.75	5.0	3.8	10.1
hematite	5.20	3.8	2.0	5.4
leached fraction	2.70	39.0	52.2	0.0
TOTAL		**100.0**	**100.0**	**100.0**
Total free volume created			**52.2 %**	
secondary porosity P			9.0 %	
compaction ϵ			**43.2 %**	

Simplifying assumptions are identical to those outlined in Table 4.6.
[a] mass (volume) of primary Mamatwan-type ore equals 100 %; [b] vol% and mass% of mineral phases present are linked with each other through density; [c] normalized to volume of solid phases only, these values are comparable to the average quantitative mineral composition estimated in Table 4.1.

representative for the chemical constituents leached during the alteration process. As mineral matter is leached from the system, free volume remains behind. This free volume can be preserved as secondary porosity, it may be reoccupied by mineral matter introduced laterally into the system, or it may be consumed by compaction. The amount of secondary porosity in the altered ores has already been calculated (Table 4.1). Results indicate that in order to have form hausmannite-bixbyite ore from Mamatwan-type ore, some 38 vol % compaction must have taken place (Table 4.6). In case of the siliceous style of alteration some 43 vol % of compaction must have taken place during transformation of Mamatwan-type ore to hausmannite-andradite ore (Table 4.7).

To test the validity of these compaction values it is worthwhile to look at thickness data available from drill cores. Generally speaking the thickness of the orebed appears to decrease by about 40 % from low-grade Mamatwan-type ore to high-grade Wessels-type ore, i.e. from 11 m to 7.5 m for the example of two closely spaced drill cores illustrated in Fig. 4.5. Results thus appear to be supported by true measurements. It is thus not necessary to introduce any Mn laterally and relative immobility of manganese may be assumed during the alteration process for certain types of altered ores namely for braunite-calcite-hausmannite, braunite II-hausmannite and hausmannite-bixbyite ores of the ferruginous style of alteration and braunite-andradite-hausmannite, hausmannite-andradite-braunite and hausmannite-andradite ores of the siliceous style of alteration (Table 4.1).

This leads to another test for compaction. It is known that the degree of residual enrichment of an immobile element may be used to estimate the degree of compaction ϵ (called 'strain' by Brimhall and Dietrich, 1987) in a metasomatic alteration system

(3)

$$\epsilon = [\frac{(\rho_m{}^O \cdot c_x{}^O)}{(\rho_m{}^A \cdot c_x{}^A)} - 1] * 100$$

ϵ - compaction (in vol %)

$\rho_m{}^O$ - density of unaltered sample

$\rho_m{}^A$ - density of altered sample

$c_x{}^O$ - concentration of immobile monitor x in unaltered sample

$c_x{}^A$ - concentration of monitor x in altered sample (Brimhall and Dietrich, 1987).

UNIVERSITY OF JOHANNESBURG

Table 4.8 Amount of compaction ϵ estimated for altered ores. Manganese is used as monitor of the alteration process.

style	ferruginous style					siliceous style			
ore-type	Br-Cc-Hs	BrII-Hs	Hs-Bx	Hs	Br	Br-And-Hs	Hs-And-Br	Hs-And	Hs
ϵ	8.7	31.0	34.0	39.3	27.3	40.1	43.5	40.0	41.5

With manganese as the immobile element the equation leads to estimates of compaction of between 8.7 vol % and 39.3 vol % for ores of the ferruginous alteration style. It must be pointed out that the lowest value is obtained for Br-Cc-Hs ore of lowest degree of alteration, and the highest amount of compaction is obtained for highest-grade Hs-type ore very close to the zones of ferruginization, where lateral introduction of manganese appears most likely. An average value of about 33 vol % of compaction appears reasonable for manganese ores altered to a moderate to high degree by the ferruginous style of alteration (Table 4.8). Ores affected by the siliceous style of alteration were apparently compacted by 40 vol % (Table 4.8). These estimates are in very good agreement with the amount of compaction derived by modelling the effects of major alteration reactions (Tables 4.6 and 4.7).

Mass Balance Calculations

Method

The classical approach by Gresens (1967) to estimate composition-volume relationships in metasomatic systems is based on the equation:

(4)

$$\Delta c_i = f_V \cdot \left(\frac{\rho^A}{\rho^O}\right) \cdot c_i^A - c_i^O$$

Δc_i - gain or loss of component (in wt %)

c_i^A - concentration of component I in altered sample (in wt %)

c_i^O - concentration of component I in unaltered precursor (in wt %)

ρ^A - density of altered sample

ρ^O - density of unaltered precursor

f_V - volume factor

UNIVERSITY OF JOHANNESBURG

Gresens (1967) pointed out that measured concentrations in unaltered and altered rocks have to be corrected for the respective density ratio (ρ^A/ρ^O) between altered rock and the precursor material. Brimhall et al. (1985) and Brimhall and Dietrich (1987) further refined this idea by suggesting that the appropriate density for the correction of measured concentrations is in fact the density per unit rock volume and not the density per unit solid matter, especially if porosity changes take place during alteration. The volume factor f_V is the factor by which the volume of altered solids is multiplied in order to obtain the volume occupied by the solids in the unaltered sample. If $f_V = 1$ then volume-for-volume replacement is indicated, if $f_V > 1$ then replacement has taken place under volume gain, if $f_V < 1$, then replacement has taken place under volume loss (Gresens, 1967).

Grant (1986) pointed out, that the term $f_V \cdot (\rho^A/\rho^O)$ can be replaced by the ratio of equivalent concentrations of a geochemically immobile monitor element before (C^O) and after (C) alteration. Grant (1986) consequently modified Gresens equation for situations where immobility of a specific monitor element can be assumed

(5)

$$\Delta c_i = \left(\frac{c_x^O}{c_x^A}\right) \cdot c_i^A - c_i^O$$

Δc_i - gain or loss of component (in wt %)

c_i^A - concentration of component in altered sample (in wt %)

c_i^O - concentration of component I in unaltered precursor (in wt %)

c_x^A - concentration of immobile monitor x in altered sample (in wt %)

c_x^O - concentration of immobile monitor x in unaltered sample (in wt %)

Different techniques were suggested to identify immobile components. Grant (1986) and Olsen and Grant (1991) discussed the use of the so-called isocon diagram. This technique was further refined by Baumgartner and Olsen (1995). MacLean and Kranidiotis (1987) proposed to identify immobile element pairs by correlation plots displaying immobile element pairs.

In the case of the manganese ores of the Kalahari manganese field mass balance calculations appear impeded by the fact that concentrations of most minor and trace elements are very low or show are large erratic spread. Mass balance calculations had thus to be restricted to few components namely SiO_2, Fe_2O_3, Mn_3O_4, MgO, CaO, Na_2O, K_2O, and CO_2. Attempts to identify geochemically immobile components, such as Al, Ti, and Zr using standard techniques (Grant, 1986; Olsen and Grant, 1991; Baumgartner and Olsen, 1995; McLean and Kranidiotis, 1987), were unsuccessful for the same reason. However, if geochemical immobility of manganese during the hydrothermal alteration process can be assumed, than constitutive mass balance calculations may be performed using the predominant chemical constituent manganese itself as a monitor of the alteration process (Babcock, 1973). Immobility of manganese appears to be a reasonable assumption for all ores that occur in considerable distance to zones of ferruginization. These are braunite-calcite-hausmannite, braunite II-hausmannite and hausmannite-bixbyite ores of the ferruginous style of alteration and braunite-andradite-hausmannite, hausmannite-andradite-braunite and hausmannite-andradite ores of the siliceous style of alteration. However, mobility of manganese is indicated for altered ores in close proximity to ferruginized fault zones. Results of mass balance calculations are thus of only restricted value for hausmannite, braunite and

hematite ores of the ferruginous style of alteration and for hausmannite and hematite ores of the siliceous style of alteration (Table 4.1).

Table 4.9A Losses and gains in % (relative to the composition of Mamatwan-type ore) for ores affected by ferruginous alteration.

	Ores				
in %	Br-Cc-Hs	BrII-Hs	Hs-Bx	Hs	Br
SiO_2	54.7	-53.9	-82.9	-97.0	69.5
Fe_2O_3	64.7	41.7	72.6	55.9	72.6
Mn_3O_4	0	0	0	0	0
MgO	-84.9	-63.3	-85.9	-96.6	-87.1
CaO	-6.2	-69.5	-83.9	-98.5	-66.0
Na_2O	-45.3	-93.1	-89.9	-97.0	-63.0
K_2O	-84.3	-97.1	-97.2	-79.8	-89.2
CO_2	-44.6	-98.8	-96.5	-99.5	-96.2

UNIVERSITY OF JOHANNESBURG

Ferruginous style of alteration

Mass balance calculations on major components indicate that, relative to manganese, CO_2, the alkali elements and MgO were the first components to have been leached from Mamatwan-type ore in its transformation to Wessels-type ore (Table 4.9A). Some 85 % of MgO and K_2O and

Table 4.9B Losses and gains in g/100g (relative to the precursor composition of Mamatwan-type ore) to form Wessels-type ore types associated with the ferruginous style of alteration.

	ore type				
	Br-Cc-Hs	BrII-Hs	Hs-Bx	Hs	Br
SiO_2	2.2	-2.2	-3.4	-3.9	2.8
Fe_2O_3	3.1	2.0	3.4	2.7	3.4
Mn_3O_4	0	0	0	0	0
MgO	-2.7	-2.0	-2.7	-3.1	-2.8
CaO	-0.8	-8.8	-10.6	-12.4	-8.3
Na_2O	-0.023	-0.047	-0.045	-0.048	-0.031
K_2O	-0.101	-0.117	-0.117	-0.096	-0.107
CO_2	-6.7	-14.8	-14.5	-14.9	-14.4

about half of the primary CO_2 and Na_2O are leached from the least altered type of ore (Br-Cc-Hs) relative to Mamatwan-type ore (Table 4.9A). Smaller amounts of CaO are lost, whereas gains are observed only for SiO_2 (54.7 %) and Fe_2O_3 (64.8 %) relative to manganese (Table 4.9A). With increasing degree of alteration SiO_2 is leached from the system. More than half of the initial SiO_2 is leached from braunite II-hausmannite ore relative to Mamatwan-type ore. Losses of SiO_2 are greatest for hausmannite ores of highest grade (Table 4.9A). A considerable gain of SiO_2 is indicated for the Br ores close to zones of ferruginization. Fe_2O_3 appears enriched by 41.7 to 72.8 % in all altered ores of the ferruginous style of alteration (Table 4.9A). MgO, CaO, Na_2O, K_2O and CO_2 are invariably lost from the altered ores. CO is almost completely removed in hausmannite-rich ores. Losses of MgO, CaO, Na_2O and K_2O range between 60-100 % (Table 4.9A).

Gains and losses expressed in absolute amounts (Table 4.9B) illustrate that only removal of CO_2, CaO, MgO, SiO_2 and the moderate gains of Fe_2O_3 relative to Mn_3O_4 affect the composition of the high-grade altered ores. Absolute gains/ losses of Na_2O, and K_2O are quantitatively negligible.

UNIVERSITY OF JOHANNESBURG

Siliceous style of alteration

More than two thirds of the initial content of MgO, CaO, K_2O , and CO_2 in Mamatwan-type ore are lost in its transformation to high-grade hausmannite-andradite-type ores (Table 4.10A). Losses of Na_2O appear to be moderate to high ranging between 27.7 and 71.1 %. Highest grade

Table 4.10A Losses and gains in % (relative to the composition of Mamatwan-type ore) for ores associated with the siliceous style of alteration.

	ore type			
in %	Br-And-Hs	Hs-And-Br	Hs-And	Hs
SiO_2	-1.7	-33.3	-24.0	-82.7
Fe_2O_3	1.2	-4.9	3.1	7.4
Mn_3O_4	0	0	0	0
MgO	-84.1	-92.6	-83.6	-91.0
CaO	-89.3	-94.3	-79.0	-98.6
Na_2O	-71.1	-27.7	-40.8	1.3
K_2O	-100.0	-95.7	-100.0	-89.8
CO_2	-100.0	-99.9	-99.9	-99.4

Table 4.10B Losses and gains in g/100g (relative to the precursor composition of Mamatwan-type ore) to form Wessels-type ore types associated with the siliceous style of alteration.

	ore type			
	Br-And-Hs	Hs-And-Br	Hs-And	Hs
SiO_2	-0.1	-1.4	-1.0	-3.4
Fe_2O_3	0.1	-0.2	0.1	0.4
Mn_3O_4	0	0	0	0
MgO	-2.7	-2.9	-2.7	-2.9
CaO	-11.3	-11.9	-10.0	-12.5
Na_2O	-0.036	-0.014	-0.020	0.001
K_2O	-0.120	-0.115	-0.120	-0.108
CO_2	-15.0	-15.0	-15.0	-14.9

hausmannite ore is characterized by an apparent gain in Na_2O. Fe_2O_3 concentrations show only very small, erratic gains and losses of less than 5 % of the initial concentration, indicating a geochemical behaviour closely linked to that of Mn_3O_4 (Table 4.10A).

It is interesting to note that loss of up to 30 % of SiO_2 from ores only took place in andradite-bearing ores containing little or no braunite. Further depletion of SiO_2 is only evident for highest-grade hausmannite ores. Only losses of CO_2, CaO, MgO, and SiO_2 are of quantitative importance for upgrading of the ores during the siliceous style of alteration (Table 4.10B). The siliceous style of alteration is clearly distinguished from the ferruginous style of alteration by the lack of consistent gain of Fe_2O_3 and the only moderate losses of SiO_2 at low and moderate degrees of alteration (Tables 4.9 and 4.10).

Conclusions

Metasomatic alteration and hydrothermal upgrading of the manganese ores can be attributed to residual enrichment of manganese in a system from which components such as MgO, CaO, CO_2 and SiO_2 were removed. Three physical parameters namely compaction, secondary porosity and whole rock density changed as a result of metasomatic alteration of the manganese ores.

Mass balance calculations allow quantification of mass transfer of major elements at low and moderate degrees of alteration. Results indicate that hydrothermal upgrading of manganese ores during the Wessels hydrothermal alteration event is a result of intense leaching and removal of MgO, CaO, Na_2O, K_2O, CO_2, and SiO_2. Minor and trace elements such as Ba, Sr, and B, were locally redistributed and effectively concentrated in vug-filling trace mineral phases. Introduction of chemical constituents appears to be restricted to zones of ferruginization developed along fluid feeder structures. Laterally extensive introduction of Fe is characteristic for the ferruginous style of alteration. Manganese behaved immobile with the notable exception of zones of ferruginization along which manganese was replaced by iron, and highest-grade manganese ores surrounding the zones of ferruginization where manganese was apparently reprecipitated.

The two mineralogically and petrographically defined styles of alteration show distinct features. The ferruginous style of alteration is characterized by a higher amount of secondary porosity accompanied by a negligible whole rock density increase. The ferruginous style of alteration resulted in compaction of the orebody to about 66 vol % of its original thickness. The siliceous style of alteration is characterized by a smaller contribution of secondary porosity and a considerable increase of the whole rock density. The amount of compaction (40 vol %) is larger than for the ferruginous style of alteration.

UNIVERSITY OF JOHANNESBURG

Compaction of the orebody to 60 to 66 Vol % of its original thickness is in good agreement with available geological information from core intersections of the orebody (Fig. 4.5). However, compaction is not immediately obvious on a mesoscopic or microscopic scale in the altered

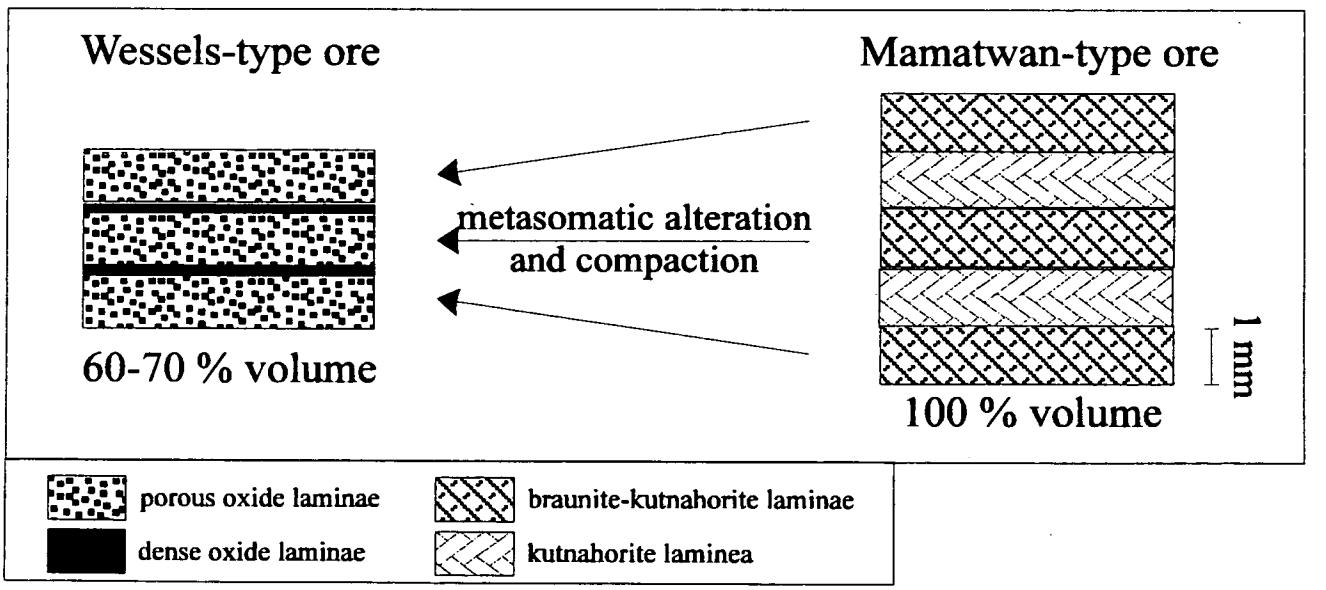

Fig. 4.6 Simplified model for bedding-parallel compaction of the manganese orebody during hydrothermal alteration. Most of the compaction is accommodated by carbonate-rich layers, oxide-rich layers are recrystallized and form beds of variable porosity.

manganese ore. Detailed preservation of sedimentary lamination and outlines of diagenetic carbonate ovoids invoke a peculiar process of differential compaction along the bedding planes. It is suggested that carbonate-rich laminae were dissolved during the hydrothermal alteration process and compaction may have consequently concentrated along these laminae (Fig. 4.6). Manganese present in the dissolved carbonates may have reprecipitated to form thin and dense manganese oxide laminae (Fig. 4.6). Alternatively carbonate laminae may have been cannibalized by reprecipitation of their manganese content in neighbouring oxide-rich laminae that recrystallized to form laminae of variable porosity. This interpretation is apparently supported by the observation that outlines of carbonate ovoids that occur in oxide-rich laminae of Mamatwan-type ore are preserved during the alteration process. The ovoids are often massively replaced by hausmannite and do not show any visible flattening suggesting lateral transport of manganese into the oxide-rich laminae took place during the alteration process.

The results presented here suggest that hydrothermal upgrading of manganese ores in the Kalahari manganese field is a result of residual enrichment rather than lateral introduction of manganese. Mass transfer of mobile components appears thus to be directed predominantly out of the alteration system. Hydrothermal decomposition and leaching of carbonates from the sedimentary Mamatwan-type ore created abundant free volume some of which was preserved as secondary porosity. However, most of it was consumed by compaction of the stratiform orebody to about two thirds of its original thickness. This thickness decrease should distinctively overprint primary sedimentary thickness changes and these thickness changes could be used as a local exploration tool for high-grade ores in the Kalahari manganese deposit. High grade ores should be associated with considerably smaller stratigraphic thicknesses of the manganese orebody (and the entire ore-bearing Hotazel Formation) as compared to residual patches of low-grade ore that were not affected by hydrothermal alteration.

Acknowledgements

The authors are grateful to Mrs. C. Pohland-Watson and J.P.R. de Villiers of MINTEK to provide us with the opportunity to obtain ICP-MS trace element data. A.G. Herrmann, K. Herrmann, M.G. Siemann, A. Stascheit and especially Bernd Knipping of the Institut für Mineralogie und mineralische Rohstoffe, TU Clausthal, are gratefully acknowledged for their hospitality and help while performing XRF analysis in 1993 and 1994. Special thanks also to the staff of ASSMANG and SAMANCOR at Black Rock and Hotazel in the Kalahari manganese field for their support of the necessary field work.

References

Babcock, R.S. (1973). Computational models of metasomatic processes. Lithos, 6, 279-290.

Baumgartner, L. P., and Olsen, S. N. (1995). A least-squares approach to mass transport calculations using the isocon method. Econ. Geol., 89, 1261-1270.

Beukes N.J., Burger A.M., and Gutzmer J. (1995). Fault controlled hydrothermal alteration of Palaeoproterozoic manganese ore in Wessels mine, Kalahari manganese field. S. Afr. J. Geol., 98, 430-451.

Beukes, N.J., and Smit, C.A. (1987). New evidence for thrust faulting in Griqualand West, South Africa: Implications for stratigraphy and the age of red beds, Trans. Geol. Soc. S. Afr., 90, 378-394.

Boardman, L.G. (1941). The Black Rock manganese deposit in the South-Eastern Kalahari, Transa. Geol. Soc. S. Afr., 44, 51-62.

Brimhall, G.H., Alpers, C.N., and Cunningham, A.B. (1985). Analysis of supergene ore-forming processes and ground-water solute transport using mass balance principles. Econ. Geol., 80, 1227-1256.

Brimhall, G.H., and Dietrich, W.E. (1987). Constitutive mass balance relations between chemical composition, volume, density, porosity, and strain in metasomatic hydrochemical systems: Results on weathering and pedogenesis. Geochim. Cosmochim. Acta, 51, 567-587.

De Villiers, J.P.R. (1980). The crystal structure of braunite II and its relationship to bixbyite and braunite. Amer. Mineral., 65, 756-765.

Dixon, R.D. (1989). Sugilite and associated metamorphic silicate minerals from Wessels mine, Kalahari manganese field. Geol. Surv. S. Afr., Bulletin, 93, 47 pp.

Grant, J.A. (1986). The isocon diagram - a simple solution to Gresens equation for metasomatic alteration. Econ. Geol., 81, 1976-1982.

Gresens, R.L. (1967). Composition-volume relationships of metasomatism, Chem. Geol., 2, 47-65.

Gutzmer J., and Beukes N.J. (1995). Fault controlled metasomatic alteration of Early Proterozoic sedimentary manganese ores in the Kalahari manganese field, South Africa. Econ. Geol., 90, 823-844..

Heinrichs, H., and Herrmann, A.G. (1990). Praktikum der analytischen Geochemie. Springer, Berlin, 669 pp.

Holland, H.D., and Beukes, N.J. (1990). A paleoweathering profile from Griqualand West, South Africa: Evidence for a dramatic rise in atmospheric oxygen between 2.2 and 1.9 BYBP. Amer. J. Sci., 290-A, 1-34.

Kleyenstüber, A.S.E. (1984). The mineralogy of the manganese-bearing Hotazel Formation, of the Proterozoic Transvaal Sequence in Griqualand West, South Africa, Trans. Geol. Soc. S. Afr., 87, 257-272.

Kleyenstüber, A.S.E. (1985). A regional mineralogical study of the manganese-bearing Vöelwater Subgroup in the Northern Cape Province. Unpubl. PhD thesis, RAU, 328 pp.

Kleyenstüber, A.S.E. (1993). Some significant characteristics of the manganese ores and some of the minerals occurring in the Proterozoic Kalahari manganese field, South Africa. Resource Geology, 17, 2-11.

UNIVERSITY OF JOHANNESBURG

MacLean, W.H., and Kranidiotis, P. (1987). Immobile elements as monitors of mass transfer in hydrothermal alteration: Phelps Dodge massive sulfide deposit, Matagami, Quebec, Econ. Geol., 82, 951-962.

Nel C.J., Beukes N.J., and De Villiers J.P.R. (1986). The Mamatwan manganese mine of the Kalahari manganese field. In: Annhaeusser C.R., Maske S. (eds.), Mineral deposits of Southern Africa. Geol. Soc. S. Afr., Johannesburg, 963-978.

Olsen, S.N., and Grant, J.A. (1991). Isocon analysis of migmatitization in the Front Range, Colorado, USA. J. Metam. Geol., 9, 151-164.

Rösler, H.J. (1983). Lehrbuch der Mineralogie. VEB Verlag, Leipzig, 833 pp.

UNIVERSITY OF JOHANNESBURG

Chapter Five

Tropical Terrestrial Weathering and Vegetation in the Paleoproterozoic: Evidence from a Pisolithic Paleolaterite from South Africa

Abstract

Paleosols or 'fossil soil profiles' preserve information about the composition of the atmosphere and paleoclimatic conditions [1]. They are a particular important source of information for the early evolution of the Earth's atmosphere [2]. Here we report the discovery of the first pisolitic laterite paleosols from the Precambrian. The paleolaterite profiles are located in the basal part of the late Paleoproterozoic Gamagara Formation associated with paleokarst depressions in dolomite of the Transvaal Supergroup on the Kaapvaal craton. The profiles are very well preserved with zonality, relict soil structures and chemical composition similar to that of modern laterites. The discovery of pisolitic laterites provides not only evidence for a highly oxygenated atmosphere and tropical climatic conditions in late Paleoproterozoic times, but also strongly suggest the presence of terrestrial life on the Kaapvaal craton some 2.0 to 2.2 billion years ago.

Introduction

Precambrian paleosols may provide valuable information about early climatic conditions and evolution of the ancient atmosphere [1,2,3]. They may also hold the key to understanding when and how subaerial land surfaces became colonized by organisms [1,4,5]. A fair number of Precambrian paleosols are already known and some have been studied in considerable detail [6,7,8,9,10,11,12]. Results indicate that the oxygen content of the atmosphere increased dramatically in the period 2.0 - 2.2 Ga from less than about 0.02 PAL (present atmospheric level) to at least 0.15 PAL [11]; a result consistent with the rapid decline in iron-formation deposition at the time and the development of the first major red bed successions [2,11]. This conclusion is largely based on the ferruginized and oxidized paleoweathering profile developed in strata of the late Archean to early Paleoproterozoic Transvaal Supergroup below the Mapedi-Gamagara

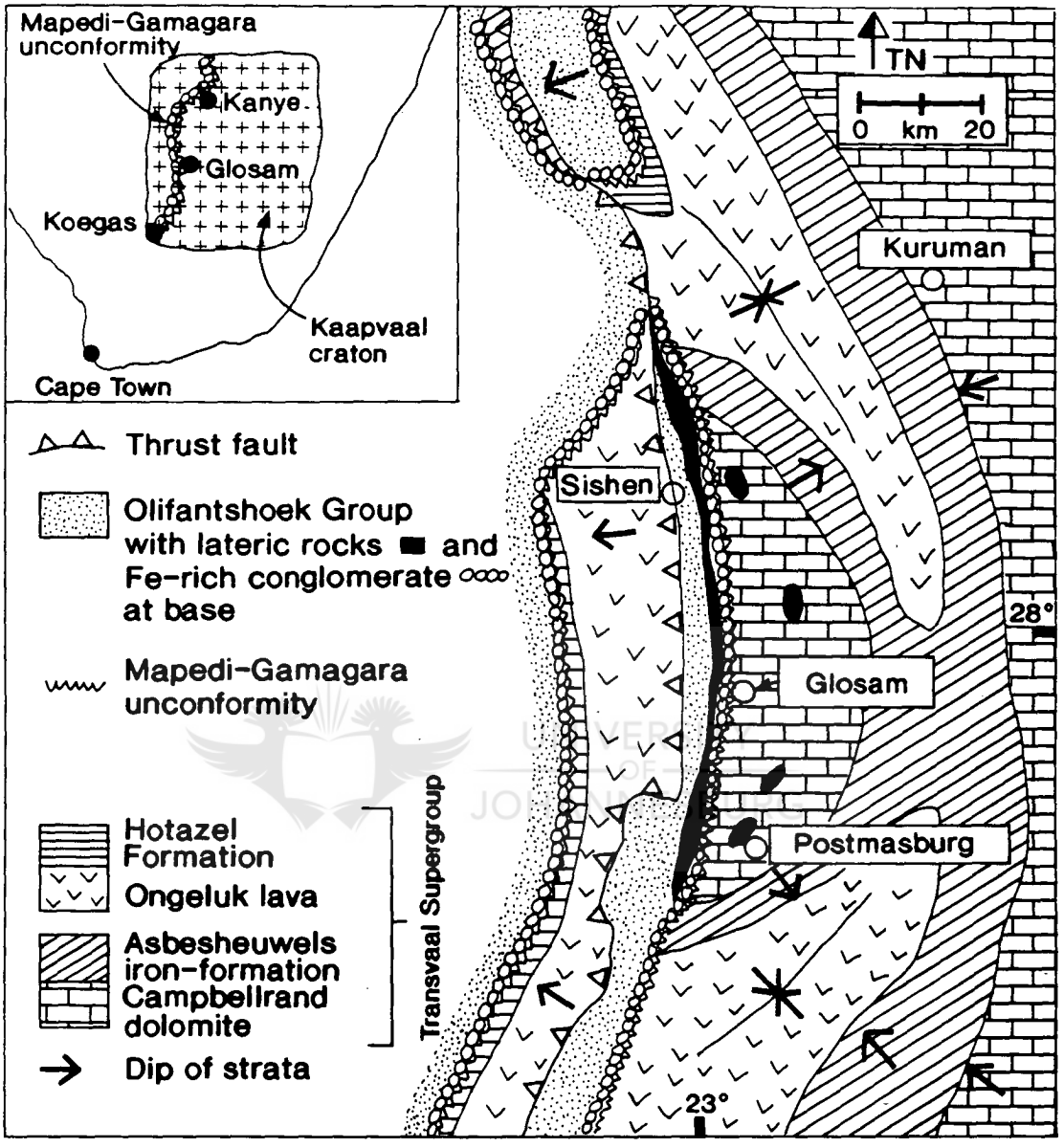

Fig. 5.1 Simplified geological map of the Maremane dome showing the location of the Glosam paleolaterites associated with the Mapedi-Gamagara unconformity. Inset map shows the outcrop trace of the Mapedi-Gamagara unconformity from Koegas in the Northern Cape Province of South Africa to Kanye in Botswana.

paleoerosion surface (unconformity) at the base of overlying red beds of the late Paleoproterozoic Olifantshoek Group in South Africa (Fig. 5.1). This paper focuses on the occurrence of extraordinary well preserved karst-hosted pisolitic paleolaterite profiles immediately above the Mapedi-Gamagara unconformity. The paleolaterite profiles are of special interest not only because they extend the fossil record of pisolitic laterites back some 1 billion years from the oldest known previously in the Phanerozoic [13], but also because they

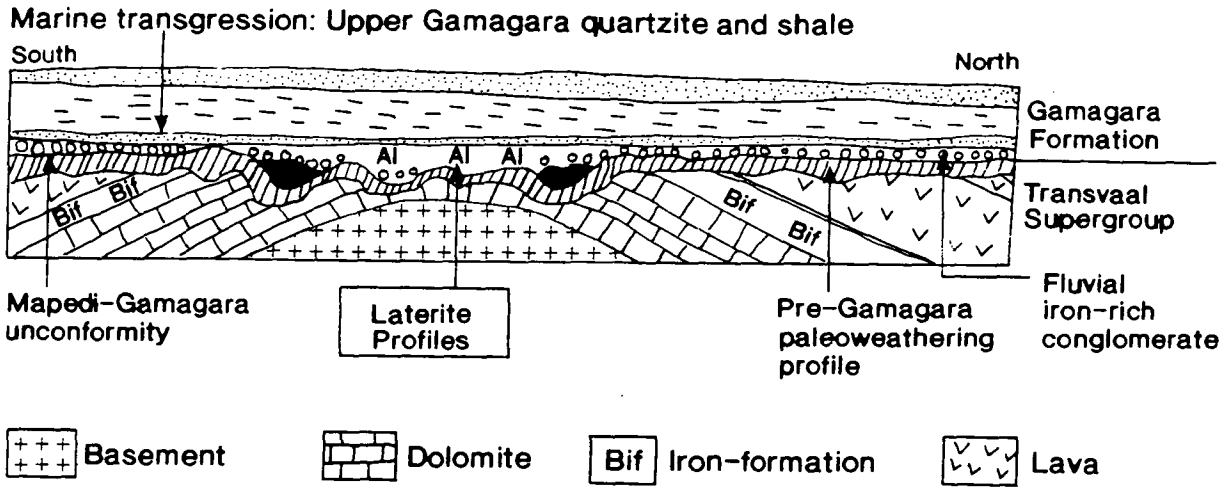

Fig. 5.2 Simplified north-south cross section through the Maremane dome indicating the geological position of the paleolaterite profiles in relation to the underlying rocks of the Transvaal Supergroup, pre-Gamagara weathering profiles, fluvial hematite pebble conglomerates and the overlying red beds of the Gamagara Formation.

(a) confirm the existence of an oxygenated atmosphere at the time, (b) provide evidence for tropical climatic conditions, and (c) contain indirect evidence for presence of microbial vegetation at 2-2.2 Ga.

UNIVERSITY OF JOHANNESBURG

Description of the paleolaterite profiles

The paleolaterite profiles are located in a succession of aluminous and ferruginous mudstone in the lower part of the Gamagara Formation which forms the basal rock unit of the Olifantshoek red bed succession. The aluminous mudstone are confined to paleokarstic depressions on Campbellrand dolomite of the Transvaal Supergroup on the Maremane dome between Sishen and Postmasburg (Fig's. 5.1 and 5.2) [14,15,16]. At Glosam manganese mine (Fig. 5.1), where the pisolitic laterites are well exposed, the succession comprises a basal layer of manganese ore, thought to represent a fossil manganese wad that was derived from the underlying manganese-bearing dolomite [15], overlain by a poorly sorted conglomerate composed of hematitized iron-formation clasts and pebbles in a hematite-rich matrix (Fig. 5.3). The conglomerate fines upward into a succession of aluminous and ferruginous mudstone with interbeds of hematite-rich granulestone and mudclast conglomerate. The pisolitic laterites are developed in the latter succession thought to represent fluvial floodplain deposits overlying fluvial channel conglomerates [16] (Fig. 5.3).

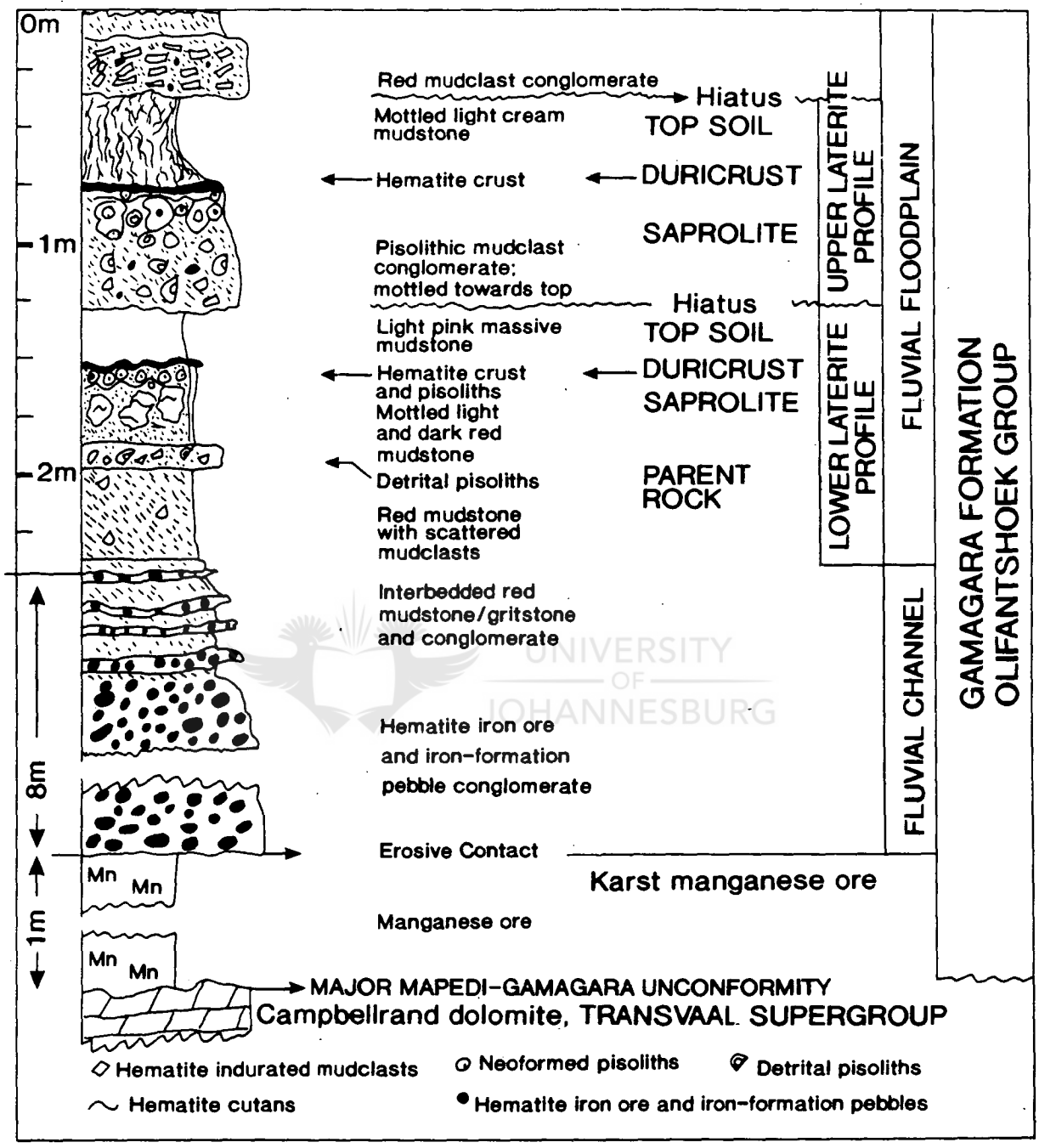

Fig. 5.3 Stratigraphic and sedimentological setting of the paleolaterite profiles at the base of the Gamagara Formation in Glosam Mine.

The detailed stratigraphy of the paleolaterite profiles varies from one locality to another, a feature typical of laterites deposited in a karst environment [13,17]. An example from the Glosam open pit manganese mine indicates the presence of two closely stacked pisolitic laterite profiles (Fig. 5.3). Both profiles show the zonal succession common for some modern

laterites [18,19] with a leached light coloured top soil zone, a ferric duricrust zone, and a lower pisolitic mottled saprolite zone grading down into parent material (Fig. 5.3). Both laterite profiles are overlain with sharp erosional contact by mudclast conglomerate beds. The mudclasts are angular in shape and are indurated by fine dusty hematite. The lower mudclast conglomerate in actual fact forms part of the parent material of the upper laterite profile and contains abundant detrital compound pisoliths (Fig. 5.3).

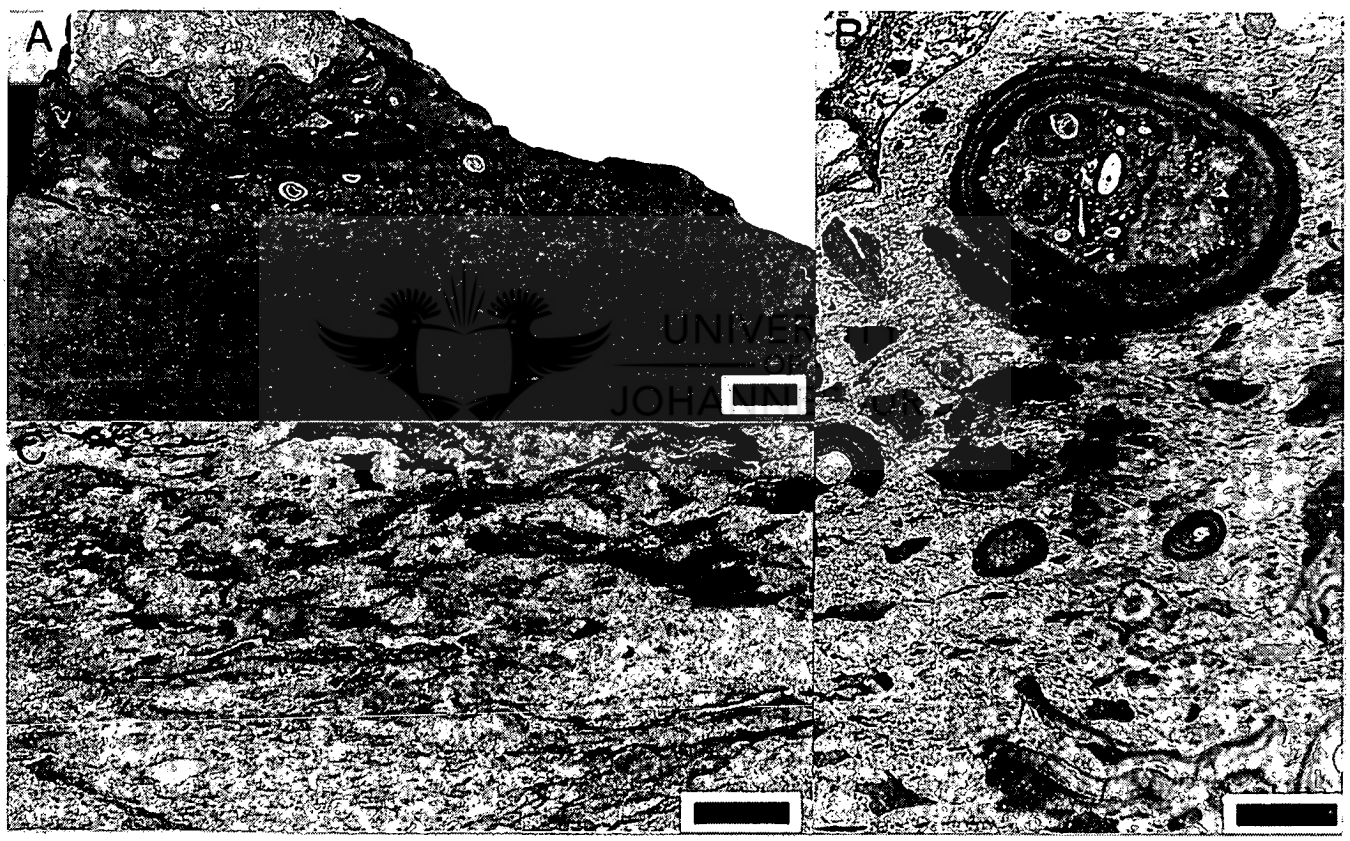

Fig. 5.4 Photographs of paleolaterite profiles. (A) Finely laminated hematite duricrust and pisolitic layer separate the leached top soil horizon from hematite-rich lateroid saprolite in the lower paleolaterite profile. Note ferric cutans in saprolite and cores of detrital pisoliths composed of leached mudclasts; (B) Lateroid saprolite of upper laterite profile composed of large, complex detrital pisoliths, fragments of pisoliths and duricrust, neoformed hematite mottles and abundant hematite-indurated mudclasts in a hematite-bearing matrix; (C) Leached top soil horizon of upper paleosoil profile with possible relics of blocky clay peds (the contrast has been enhanced in this photograph to illustrate small scale structures). All samples in original orientation, scale bars equivalent to 1 cm length.

One of the most striking features in both laterite profiles is the sharply defined undulating hematite duricrust separating the upper leached soil zone from the lower saprolite zone. In the lower profile the duricrust is 2 - 5 mm thick and very finely laminated. It overlies a band of hematite pisoliths developed in top part of the underlying saprolite (Fig. 5.4A). Both

neoformed (in situ) and detrital pisoliths are present in the band which is two to three centimetres thick. The pisolitic band grades down into a light and dark red mottled hematite-rich mudstone representing the lower part of the saprolite zone which in turn grades down into dark red mudstone parent material (Fig. 5.3). Discontinuous wavy films of hematite in the mottled mudstone may represent ancient ferric cutans (Fig. 5.4A).

In the upper laterite profile the hematite duricrust is 0.5 - 5 cm thick and has a heterogeneous texture. Certain parts are finely laminated whereas others consists of small clayclasts and hematite pisoliths cemented by wavy hematite crusts. Below the duricrust, in the saprolite zone, modification of the pisolitic mudclast conglomerate parent material is represented by the presence of hematite cutans around small mudclasts, neoformed pisoliths and hematite crusts around older detrital pisoliths, and large diffuse hematite mottles (Fig. 5.4B). The neoformed pisoliths often incorporate several small mudclasts as nuclei or a combination of mudclasts and detrital pisoliths. Detrital pisoliths, up to 6 cm in diameter, show signs for physical transport in that they are abraded, broken and/or fractured (Fig. 5.4B). Dense hematite with grain size in order of one micron is the main component of duricrusts and cortexes of pisoliths.

UNIVERSITY OF JOHANNESBURG

The top soil zones of the two paleolaterite profiles are composed of light coloured mudstone with an irregular blockey mottled appearance (Fig. 5.4C). which may represent blockey clay peds of the original soil. The parent mudstone of the laterite profiles must have been derived from an iron-rich aluminous lateroid mud as indicated by its mineralogical composition of pyrophyllite with abundant finely dispersed hematite, small amounts of diaspore and minor anatase. In contrast the light coloured mudstone of the top soil zone is composed of pyrophyllite associated with up to about 30 volume percent diaspore, 2 volume percent anatase and traces of hematite. The top soil zone thus appears to be enriched in alumina and titanium, and depleted in hematite relative to parent material; a feature common of modern lateritic profiles [13,19]. This is confirmed by chemical analyses of the upper laterite profile which indicate much lower Fe_2O_3 concentrations, and higher TiO_2/SiO_2 and Al_2O_3/SiO_2 ratios in the top soil zone relative to that in the parent mudstone (Table 5.1). Components such as MgO, CaO, Na_2O and K_2O are present in very small amounts in all zones of the laterite profiles resulting in a chemical index of alteration [20] of virtually 100 percent. This is evidence for extremely effective chemical weathering in the source area with reference to the origin of the parent mudstone of the laterite profiles [20].

Table 5.1 Chemical composition of upper paleosol.

	SiO_2	TiO_2	Al_2O_3	Fe_2O_3	MnO	$\sum$*	P_2O_5	SiO_2/Al_2O_3	CIA**
top soil	45.9	2.28	42.1	0.22	0.00	0.20	0.05	1.09	99.2
duricrust	14.7	0.50	10.9	68.0	0.04	0.10	0.13	1.35	98.5
pisolith	15.6	0.68	13.1	65.1	0.05	0.16	0.04	1.19	98.0
saprolite	32.3	1.38	26.3	33.9	0.08	0.16	0.06	1.22	99.0

* $\sum (Na_2O+K_2O+CaO)$
** Chemical index of alteration: $Al_2O_3/(Al_2O_3+Na_2O+K_2O+CaO) \cdot 100$ [20]

The mineral assemblage pyrophyllite, diaspore and hematite could have been derived under greenschist facies metamorphism from the products of lateritic weathering i.e. kaolinite with variable hematite and/or goethite content. The reaction of kaolinite to form pyrophyllite and diaspore takes place at 300 - 320 °C and 1-2 kbar [21].

The abundance of hematite indurated lateroid clayclasts, reworked hematite duricrust fragments and detrital pisoliths indicates that the paleolaterite profiles developed in an environment where multiple cycles of erosion, transport, deposition and soil formation took place. The preservation potential of soil profiles in such an environment is low and accumulation in karstic depressions may have been a prerequisite for preservation. Stacking of soil profiles in close succession suggest active aggradation of the host fluvial floodplain sediments so that time available for soil formation could not have been long; from there perhaps the thin nature of the top soil zones and duricrusts. The sharp contact of the duricrust with the overlying soil zone and downward gradation into the saprolite zone characterize them as ground water paleolaterite profiles [18,19].

Conclusions

Generally speaking accumulations of ferric laterites have little paleogeographic and paleoclimatic significance and can form in a variety of environments by numerous mechanisms [22]. However, such accumulations do become environmentally sensitive if associated with alumina-rich kaolinite or bauxite deposits on regional unconformities such as in case of the Gamagara paleolaterites (Fig's 1 and 2). Most probably the whole process of lateritic weathering at that time started during development of the thick ferruginized

paleoweathering profile preserved below the Mapedi-Gamagara unconformity [10,11] and continued through formation of the karst-hosted Postmasburg-type manganese [15] and Sishen-type iron ore deposits [16] to deposition of the fluvial succession in which the laterite profiles are developed (Fig. 5.2). The regional extend of the ferric lateroid successions on both sides of the Mapedi-Gamagara unconformity implies a mature landscape [13,18,19] with widespread lateritization on the Kaapvaal craton at about 2-2.2 Ga. Such lateritization events are well documented to form under humid warm tropical to subtropical settings; normally within 30 degrees latitude of the equator in areas with minimum average annual air temperature above 22 °C and annual rainfall above 1000 mm [13,18,21]. We have no reasons to believe that geographic setting and climatic conditions were much different during formation of the Gamagara paleolaterite profiles; especially in light of strong indications that the composition of the atmosphere at the time may have been rather similar to that of today [2,12,23].

This brings us to indications for possible terrestrial microbial vegetation in warm humid tropical to subtropical environments of the earth at about 2 Ga. Clearly the hematite indurated laterites at the base of the Olifantshoek red bed sequence formed under oxidizing conditions with all iron present in ferric form. The question then becomes what was the reducing agent for leaching ferric iron from the iron-depleted top soil zones of the paleolaterite profiles. With reference to modern soils a logical candidate would have been organic matter derived from organisms that lived in the soil and/or vegetated the surface. However, it is important to realize that the highly leached top soil zone must have been extremely depleted in nutrients making it difficult to believe that it could have sustained a purely soil-confined microbial community and whether nutrients would have been leached from the soil rather than have been recycled in it. Rather the comparison seems much more compatible with that of modern soil environments in the tropics where a lush vegetation covers a thin highly leached and nutrient deficient organic poor top soil (immediately underlain by a ferric duricrust and or pisolith zone) and cycling of nutrients is effectively maintained in the cover of organic matter. In case of the Gamagara soil profiles this organic cover could have been removed by erosion during deposition of overlying clayclast conglomerate beds and/ or it may have been destroyed by aerobic degradation.

If life was present on subaerial land surfaces at 2.0-2.2 Ga the question becomes when and how it developed. It is also good to be reminded that this idea of life on land is not absolutely new. It is speculated on by Retallack [1,4] and has also been offered as an explanation for extensive gold-bearing organic carbon accumulations along disconformities in the Archean

Witwatersrand Supergroup of South Africa [24]. In light of the conclusion of this paper these suggestions for life on land during the Archean deserve perhaps more serious attention than what they have received up to now.

References

[1] Retallack, G.J (1990). Soils of the past. Unwin Hyman, Boston, 520 pp.

[2] Holland, H.D. (1984). The chemical evolution of the atmosphere and oceans. Princeton Univ. Press, Princeton, 351 pp.

[3] Holland, H.D., Lazar, B., and McCaffrey , M. (1986). The evolution of the atmosphere and oceans. Nature, 320, 27-33.

[4] Retallack, G. (1992). How to find a Precambrian paleosol. In: Schidlowski, M. (Ed.): Early organic evolution: Implications for Mineral energy resources. Springer Verlag, New York, 13-30.

[5] Horodyski, R.J. and Knauth, L.P. (1994). Life on land in the Precambrian. Science, 263, 494-498.

[6] Gay, A.L. and Grandstaff, D.E. (1980). Chemistry and mineralogy of Precambrian paleosols at Elliot Lake, Ontario, Canada. Prec. Res., 12, 349-373.

[7] Grandstaff, D.E., Edelman, M.J., Foster, R.W., Zbinden, E., and Kimberley, M.M. (1986). Chemistry and mineralogy of Precambrian paleosols at the base of the Dominion and Pongola Groups (Transvaal, South Africa). Prec. Res., 32, 97-131.

[8] Farrow, C.E.G. and Mossman, D.J. (1988). Geology of Precambrian paleosols at the base of the Huronian Supergroup, Elliot Lake, Ontario, Canada. Prec. Res., 42, 107-139.

[9] Holland, H.D., Feakes, C.R., and Zbinden, E.A. (1989). The Flin-Flon paleosol and the composition of the atmosphere 1.8 bybp. Am. J. Sci., 289, 362-389.

[10] Wiggering, H. and Beukes, N.J. (1990). Petrography and geochemistry of a 2100-2200 m.y. old hematitic paleoalteration profile on Ongeluk basalt of the Transvaal Supergroup, Griqualand West, South Africa. Prec. Res., 46, 241-258.

[11] Holland, H.D. and Beukes, N.J. (1990). A paleoweathering profile from Griqualand West, South Africa: Evidence for a dramatic rise in atmospheric oxygen between 2.2 and 1.9 bybp. Am. J. Sci. 290-A, 1-34.

[12] Driese, S.G., Simpson, E.L., and Eriksson, K.A. (1995). Redoximorphic paleosols in alluvial and lacustrine deposits, 1.8 Ga Lochness Formation, Mount Isa, Australia: Pedogenic processes and implications for paleoclimate. J. Sed. Research, A65, 675-689

[13] Bárdossy, G. and Aleva, G.J.J. (1990). Lateritic Bauxites. Elsevier, Amsterdam, 624 pp.

UNIVERSITY OF JOHANNESBURG

[14] Nel, L.T. (1929). The geology of the Postmasburg manganese deposits and the surrounding country. Government Printer, Pretoria, 104 pp.

[15] Grobbelaar, W.S. and Beukes, N.J. (1986). The Bishop and Glosam manganese mines and the Beeshoek iron ore mine of the Postmasburg area. In: Annhaeusser, C.R. & Maske, S.S. (eds.): Mineral deposits of Southern Africa. Geol. Soc. S. Afr., Johannesburg, 957-961.

[16] Van Schalkwyk, J. and Beukes, N.J. (1986). The Sishen iron ore deposit, Griqualand West. In: Annhaeusser, C.R. and Maske, S.S. (eds.): Mineral deposits of Southern Africa. Geol. Soc. S. Afr., Johannesburg, 931-956.

[17] Bárdossy, G. (1982). Karst Bauxites. Elsevier, Amsterdam, 441 pp.

[18] McFarlane, M.J. (1976). Laterite and Landscape. Academic Press, London, 151 pp.

[19] Aleva, G.J.J. (1995). Laterites. Intern. Soil Ref. Ctr., Wageningen, 159 pp.

[20] Maynard, J.B. (1992). Chemistry of modern soils as a guide to interpreting Precambrian paleosols. J. Geol., 100, 279-289.

[21] Anovitz, L.M., Perkins, D., and Essene, E.J. (1991). Metastability in near-surface rocks of minerals in the system Al_2O_3-SiO_2-H_2O. Clays Clay Min., 39, 225-233.

[22] Bourman, R.P. (1993). Perennial problems in the study of laterite - A review. Austr. J. Earth . Sci., 40, 387-401.

[23] Rye, R., Kuo, P.H., and Holland, H.D. (1995). Atmospheric carbon dioxide concentrations before 2.2 billion years ago. Nature, 378, 603-605.

[24] Button, A. (1979). Algal concentration in the Sabi River, Rhodesia: Depositional model for Witwatersrand Carbon ? Econ. Geol., 74, 1876-1889.

UNIVERSITY OF JOHANNESBURG

Chapter Six

Petrography and geochemistry of the karst-hosted manganese deposits in the Postmasburg manganese field, Northern Cape Province, South Africa.

Abstract

The Postmasburg manganese field, situated in the Northern Cape Province of South Africa, provides an excellent example of karst-controlled manganese ore deposition. Two distinct types of ore are present, namely ferruginous ores composed of partridgeite, bixbyite and braunite and siliceous ores composed of braunite and quartz. Ores of the siliceous type are present as small pods and lenses in the Wolhaarkop chert breccia which is a subsurface solution collapse breccia that accumulated in a paleokarst cave system which developed in the dolomites of the Fairfield Formation of the Campbell Subgroup of the Late-Archean/Early-Proterozoic Transvaal Supergroup. Ferruginous manganese orebodies are highly irregularly shaped and are confined by the intensively karstified floor of the Reivilo Formation of the Campbellrand Subgroup. They formed as infill of karst depressions and are conformably overlain by a hematite pebble conglomerate and/or aluminous shales of the Gamagara Formation of the Late Paleoproterozoic Olifantshoek Group. Sedimentary structures are abundant in the ferruginous ores and indicate accumulation of wad intermixed with aluminous clays in a terrestrial surficial paleokarst environment. Accumulation of siliceous and ferruginous manganese ores in a freshwater terrestrial environment is confirmed by their geochemical character suggesting poor separation of manganese from iron, low and highly variable concentrations of Cu, Ni, Co, and Zn and low contents of Na and Mg.

The ores underwent diagenetic compaction and lower greenschist facies metamorphism. Metamorphism resulted in recrystallization of the manganese wad to braunite, partridgeite, hematite and bixbyite. Textural and geochemical similarities with unmetamorphosed karst-hosted manganese deposits suggest that the manganese ores in the Postmasburg manganese field were deposited as residual Mn^{4+} - Fe^{3+} oxide wad. This wad accumulated during a period of erosion and intensive terrestrial weathering during the Late Paleoproterozoic on Mn and Fe-rich dolomites of the Transvaal Supergroup. The ores represent the oldest known oxidized terrestrial sediments and provide evidence for the presence of a highly oxidizing atmosphere in the Paleoproterozoic at 2 - 2.25 Ga.

Introduction

The Postmasburg manganese field, situated in the Northern Cape Province, South Africa, extends along strike for some 60 km in two distinct belts of deposits, the so-called Western and Eastern Belts, from Sishen in the north to Postmasburg in the south (Fig. 6.1). Mining of the manganese ores commenced soon after discovery by Cpt. L.T. Shone in 1922 (Truter et al., 1938) and was discontinued in 1989, despite considerable remaining ore reserves (Grobbelaar and Beukes, 1986) because of the more favourable composition and availability of high-grade manganese ores from the giant Kalahari manganese field situated some 45 km to the north of the PMF. Recently, an attempt was made to revive mining of high-grade ores on a small scale (Anonymous, 1993). The manganese ores are closely associated with high-grade iron ore deposits currently mined at Sishen (Van Schalkwyk and Beukes, 1986) and Beeshoek (Grobbelaar and Beukes, 1986).

The manganese ores of the Postmasburg field are subdivided into ferruginous and siliceous types (Nel, 1929). The ferruginous type is typical of the Western Belt manganese deposits located along the central part of the Gamagara ridge. Siliceous ore types occur in the Eastern Belt along the Klipfontein Hills and along the northern and southern extremities of the Gamagara ridge (Fig. 6.1) (Hall, 1926; Nel, 1929; De Villiers, 1960; Plehwe-Leisen, 1985). Ferruginous manganese ore formed the bulk of the ore reserves and was mined at the Bishop, Lohatlha, Gloucester, and Paling open cast mines with siliceous ores having been mined at the Beeshoek, Kapstewel, Pensfontein, and Klipfontein (Fig. 6.1).

The origin of the deposits remains enigmatic. De Villiers (1944, 1983) suggested a magmatic-hydrothermal origin whereas others thought that the deposits originated from metasomatic replacement of the country rock by Mn-rich meteoric solutions (Hall, 1926; Nel, 1929; Du Toit, 1933; Truter et al., 1938; De Villiers, 1960; Boardman, 1940, 1964; Borchert, 1970). In contrast Schneiderhöhn (1931) suggested a sedimentary origin; an idea supported by Plehwe-Leisen (1985) and Grobbelaar and Beukes (1986).

Schneiderhöhn (1931) and Plehwe-Leisen (1985) based their work on systematic petrographic studies of the deposits whereas De Villiers (1943, 1944, 1945a and b, 1983) concentrated on

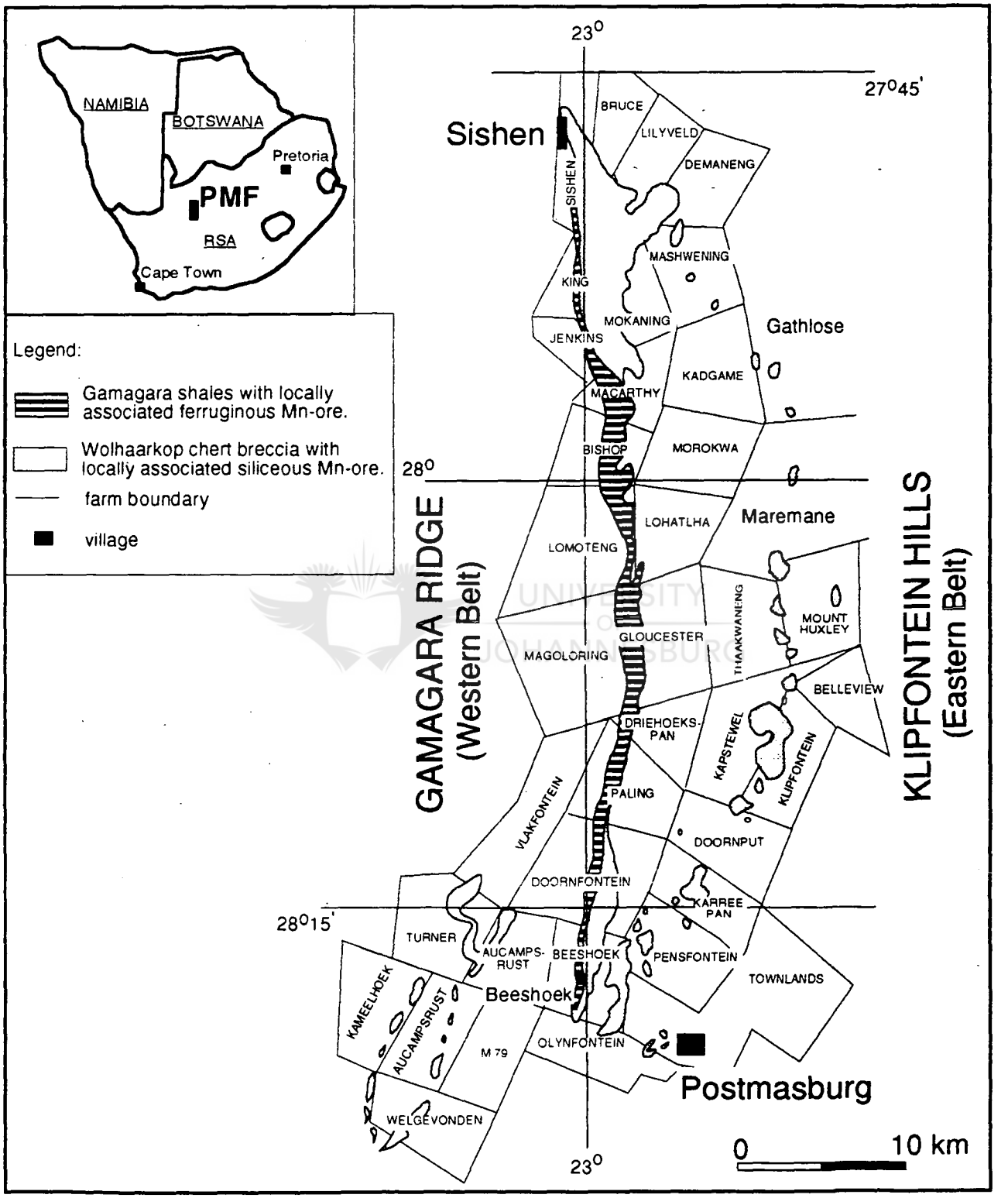

Fig. 6.1 Regional map of the Postmasburg manganese field showing the location of the deposits of ferruginous manganese ore along the Gamagara Ridge (Western Belt) and the occurrence of Wolhaarkop Breccia (and associated manganese ores of the siliceous type) in the Klipfontein Hills (Eastern Belt), the Gamagara Ridge and in the Aucampsrust area.

mineralogical studies. However, surprisingly little is known about the geochemistry of the deposits with only Hall (1926), Nel (1929), and De Villiers (1960) presenting a few major element analyses.

This paper presents a detailed description of the mineralogy, petrography and geochemistry of the manganese ores of the Postmasburg manganese field and provides evidence that the ores originated as karst-hosted wad deposits. These were then subjected to lower greenschist facies metamorphism before supergene alteration strongly modified the mineralogy and geochemistry of the ores.

Analytical techniques

The mineralogy and petrography of approximately 100 manganese ore samples, covering all macroscopically distinct ore types, was investigated using powder X-ray diffractometry, ore petrography, and electron microprobe analyses. Electron microprobe analysis was carried out on a CAMECA CAMEBAX 355 microprobe with an attached LINK ExLII energy dispersive spectrometer system operated at 15kV and 10nA sample current. Data acquisition time for each analytical spot was 80 sec. A pure cobalt metal standard was used for routine calibration of the spectrometer. All results were ZAF corrected. Several spot analyses were performed for each mineral in one or several small pre-selected areas on the samples. Only average compositions are reported.

Samples for whole rock chemical analyses were first cleaned with a plastic brush and then fragmented into centimeter-sized chips. Approximately 500 g of these chips, visually devoid of weathering crusts, large vein or vug infills, were handpicked. The chips were cleaned in an air stream and crushed for 3 minutes in a Cr-steel SiebTechnik swing mill. X-ray fluorescence analyses for major and trace elements were performed at the Institut für Mineralogie und mineralische Rohstoffe at the Technische Universität Clausthal (Germany) using a Philips PW 1480 X-ray spectrometer, equipped with a Rh X-ray tube. Duplicates of every tenth sample were prepared to test the reproducibility of results. Analyses of major and minor elements were performed on pressed powder pellets. Reproducibility of the results was found to be within 3 % relative deviation for major and trace elements. The accuracy, based on the repeated analysis of international geochemical reference materials SARM-16 and SARM-17 (manganese ores), was estimated to be 5% (relative) for most major elements and 10 % for

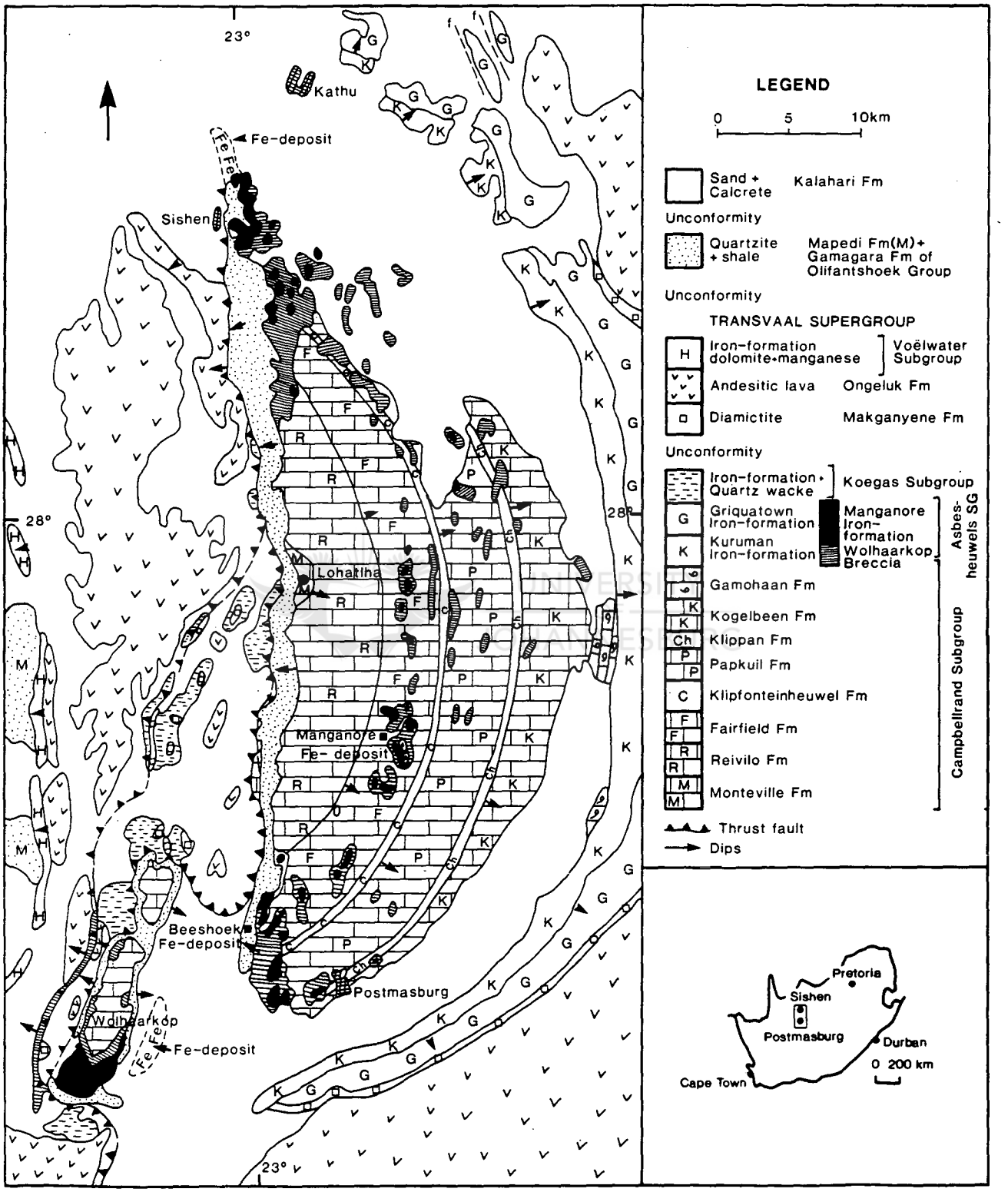

Fig. 6.2 Regional geological map of the Maremane dome showing the location of iron and manganese ore deposits in relation to the underlying dolomite of the Campbellrand Subgroup and the overlying sediments of the Gamagara Formation. Note the position of thrust faults to the West of the Gamagara Ridge.

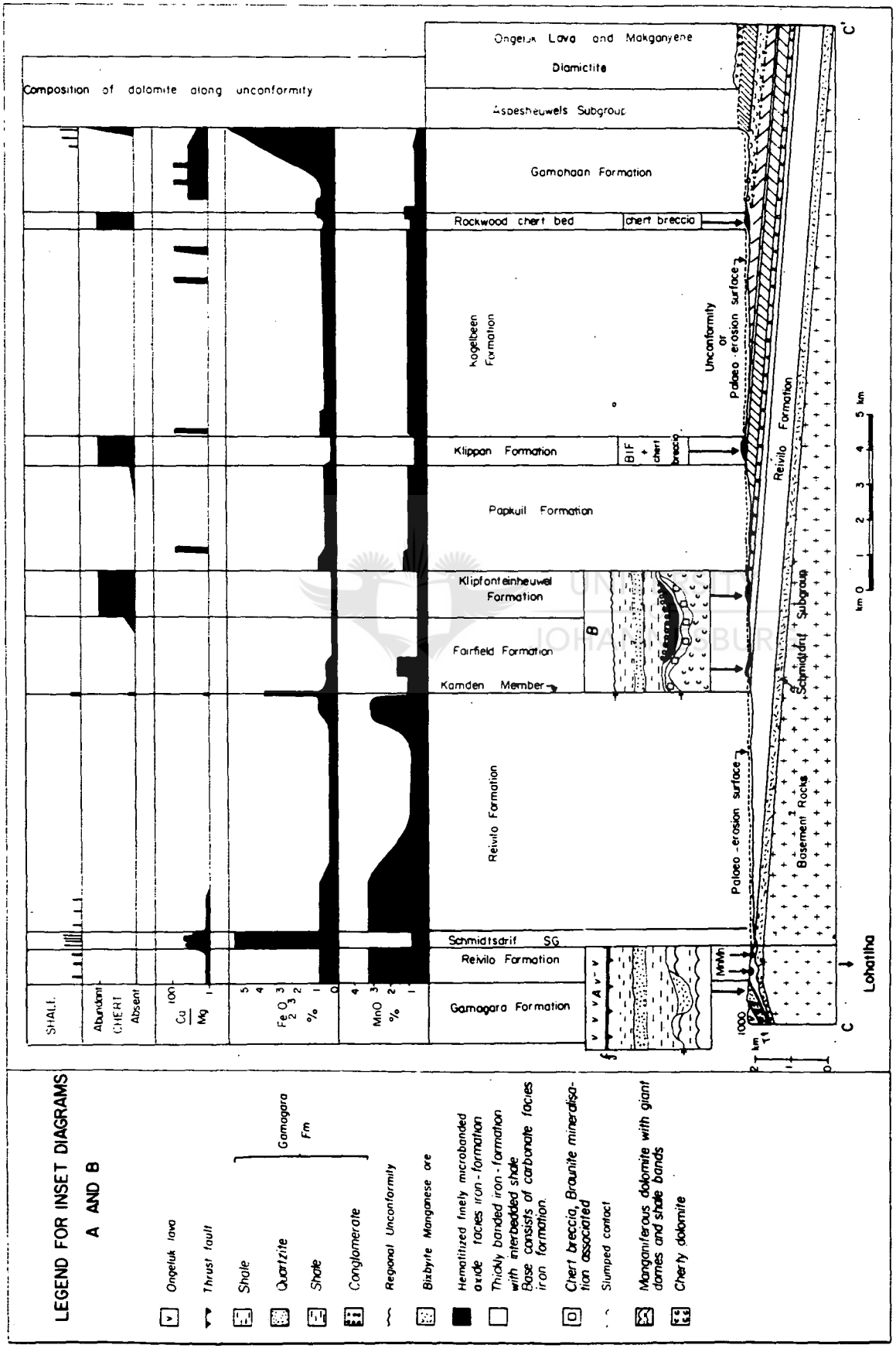

Fig. 6.3 North-facing, west-east stratigraphic section through the Maremane dome. The section illustrates the apparent geochemical control that manganiferous dolomites imposed on the distribution and character of manganese ores in the Postmasburg manganese field. The composition of the carbonate units cut by the Mapedi/ Gamagara unconformity is shown schematically along the top of the section. Also shown is the character of the the iron-ore deposits associated with the Manganore Iron-Formation which slumped into paleosinkholes in proximity to chert-bearing dolomite formations (modified after Beukes, 1986).

trace elements and Na_2O. Two samples of dolomite of the Reivilo Formation were submitted for analysis at the Analytical Science Division of MINTEK (Randburg, South Africa).

Whole rock densities were determined on small, 1 to 4 cm^3 large blocks of ore that were dried for several hours at 50°C, weighed dry, coated with paraffin (density of 0.88 g/cm^3) and weighed again, first in air and then submerged in water. The density of the coated samples was calculated applying the law of Archimedes after correcting for the mass of paraffin and the density of water at the ambient temperature. Duplicate analyses were performed and reproducibility of measurements was found to be ± 0.05 g/cm^3. Because the paraffin coating prohibits water entering the sample along fractures and pores the measured densities are a measure of the density of the sample per unit rock volume, not per unit solid matter

Regional Geological Setting

The manganese and iron ore deposits of the Postmasburg manganese field are situated on the Maremane dome which is composed of dolomite of the Campbellrand Subgroup and iron-formation of the Asbestos Hills Subgroup of the Ghaap Group of the Paleoproterozoic Transvaal Supergroup (2.5-2.7 Ga). These dip gently less than 10° in an arc to the north, east and south (Beukes, 1986). Only the eastern half of this dome is exposed because to the west the Transvaal strata are overlain with low-angle unconformity by Late Paleoproterozoic (1.9-2.2 Ga) red beds of the Mapedi/Gamagara Formation of the Olifantshoek Group (Fig. 6.2). Further to the west, older rocks belonging to the Transvaal Supergroup, including Koegas Iron Formation, Makganyene diamictite, and andesitic Ongeluk lavas are thrust over the Gamagara Formation along the north-south striking westerly dipping Black Ridge thrust. Total displacement from west to east along this thrust is at least 35 km (Beukes and Smit, 1987).

The manganese and iron ore deposits of the Postmasburg area are directly related to the angular unconformity that separates dolomite and iron-formation of the Transvaal Supergroup from red beds of the Mapedi/Gamagara Formation of the Olifantshoek Group. The ores of the Eastern belt and Western belt have different geological settings. Along the Eastern belt iron and manganese ores occur below the Mapedi/Gamagara unconformity. Here, pockets of siliceous braunite-rich manganese ore are developed in the Wolhaarkop chert breccia which disconformably separates the Campbellrand carbonates from the overlying Manganore iron-formation containing giant high-grade hematite ore deposits of the Sishen-type (Strauss, 1964; Van Wyk, 1980; Van Wyk and Beukes, 1982; Van Schalkwyk and Beukes, 1986; Grobbelaar and Beukes, 1986). The

Manganore Iron Formation represents portions of the Asbestos Hills iron-formation which slumped into sinkholes in the Campbellrand dolomite during development of the pre-Mapedi/Gamagara erosion surface. Solution collapse and slumping of the iron-formation was accompanied by leaching of silica and oxidation of iron-silicate and carbonate minerals to high-grade hematite-rich iron ore of the Sishen-type (Van Schalkwyk and Beukes, 1986).

The unconformable contact between the Manganore Iron Formation and the underlying Campbellrand dolomite is marked by the occurrence of the Wolhaarkop chert breccia which contains angular chert fragments derived from chert-bearing dolomites. The Wolhaarkop chert breccia hosts the small high-grade braunite-rich siliceous manganese orebodies of the Eastern Belt. It is important to note that the "unconformity" between the Manganore Iron Formation and the Campbellrand Subgroup originated by solution collapse and that the Wolhaarkop Breccia represents a subsurface solution collapse breccia along this surface. The Wolhaarkop breccia is hosted by cherty dolomites of the Fairfield Formation, and the occurrence of high-grade siliceous manganese ores is closely associated to the manganiferous and chert-poor beds within this formation (Fig. 6.3).

UNIVERSITY OF JOHANNESBURG

In contrast to the manganese ores of the Eastern belt, those of the Western belt occur in direct contact with the Campbellrand dolomites intimately associated with highly aluminous shales in the basal part of the Gamagara Formation. The development of the ferruginous ores appears to be geochemically controlled by the composition of the underlying dolomites of the Reivilo Formation of the Campbellrand dolomites (Fig. 6.3). Large deposits at Glosam, Lohatlha, and Bishop (Fig. 6.1) are associated only with the basal portion of the Reivilo Formation which is composed of manganese-rich dolomites (Fig. 6.3).

The deposition of the Gamagara Formation, following development of the superficial and subsurface supergene iron- and manganese deposits, started with the development of the Doornfontein conglomerate member disconformably overlying the Manganore iron-formation and Wolhaarkop chert breccia of the Eastern Belt and bixbyite-rich manganese ores of the Western Belt. Pebbles and granules in this conglomerate are composed of reworked fragments of Manganore iron-formation and associated hematite iron ore. Thick beds of conglomerates are present at Sishen and Beeshoek in the northern and southern extremities of the Maremane dome where they constitute part of the iron ore reserve. This conglomerate is interpreted as an alluvial-fan deposit that accumulated on a paleokarstic surface at the base of the Gamagara Formation (Van Schalkwyk and Beukes, 1986).

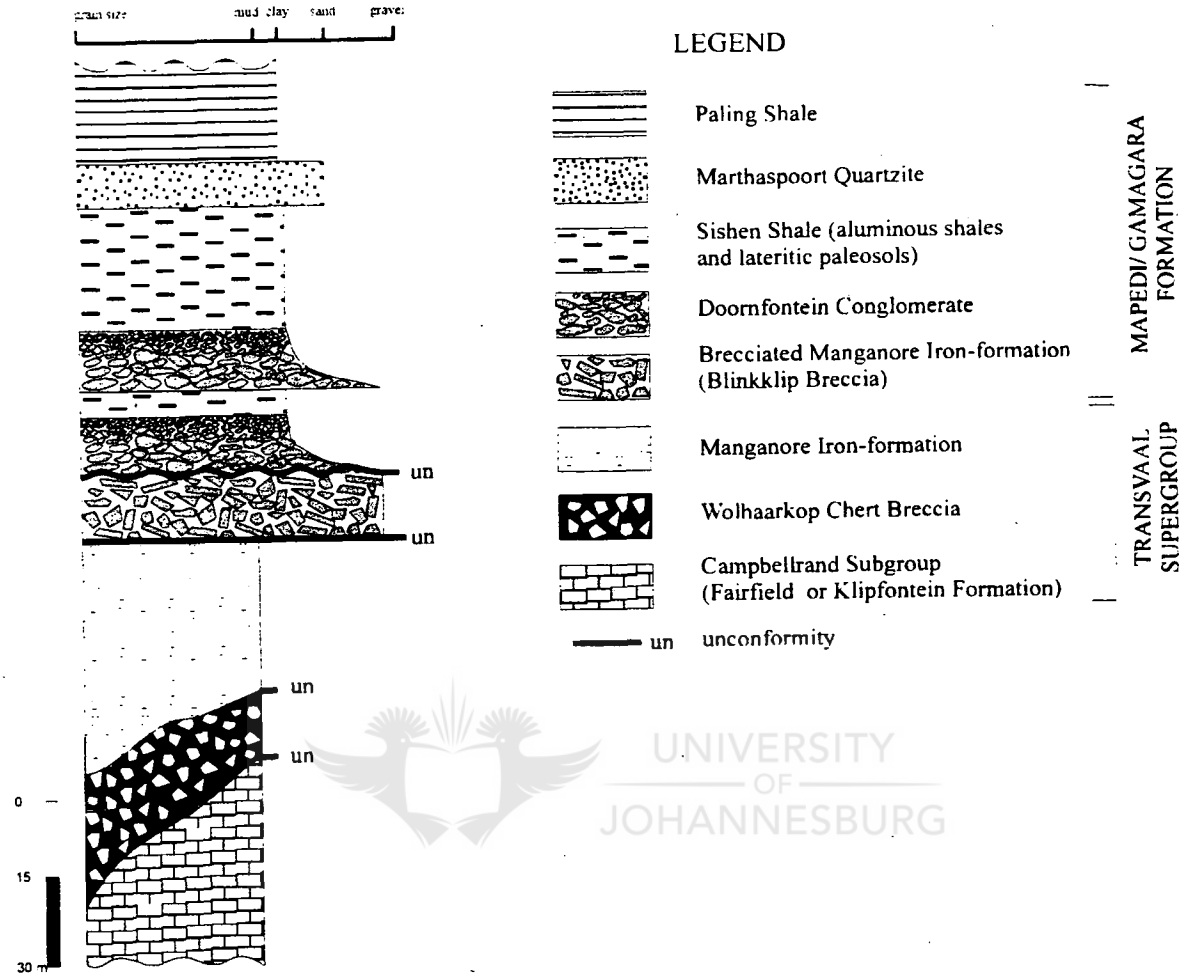

UNIVERSITY OF JOHANNESBURG

Fig. 6.4 Schematic profile illustrating the geological setting of the Wolhaarkop Breccia (and associated siliceous manganese ores) unconformably below slumped and hematitized Manganore Iron-formation.

The Doornfontein conglomerate fines upwards into a laterally highly variable succession of black, white and red aluminous shales and mudstones and occasionally interbedded chert- pebble conglomerates. Reimer (1986) tentatively identified these aluminous shales as transported residues of lateritic weathering. Well preserved karst laterite paleosol profiles developed on reworked lateroid parent rock have been discovered at Glosam mine (see Chapter 6, this thesis). These aluminous shales grade upwards into red and cream coloured banded shales and quartzites forming the upper part of the Gamagara Formation.

The Proterozoic succession is in places covered by clays, calcrete and eolian sands of the Cenozoic Kalahari Formation. Well-rounded pebbles of manganese and iron ore form recent alluvial canga deposits along the slope of the Gamagara Ridge and the Klipfontein Hills.

Detailed Geological Setting

Eastern Belt

The siliceous Wolhaarkop chert breccia and associated siliceous manganese ores occur only where ferruginized and desilicified Manganore iron-formation slumped into graben-like sinkhole structures which are aligned parallel to chert-rich dolomite units, of the Fairfield Formation of the Campbellrand Subgroup (Grobbelaar and Beukes, 1986) (Fig. 6.4). The breccia is composed of chert fragments set in a matrix of fine crystalline quartz, hematite and braunite. The matrix becomes siliceous and iron-rich towards the top and more manganiferous towards the base in contact with the Campbellrand dolomite. Minable braunitic manganese orebodies seem to be concentrated along the specific contact of the breccia with the underlying dolomites (Boardman, 1964); especially well developed orebodies appear in steep cul-de-sac structures along the karstic dolomite surface (De Villiers, 1956). Orebodies located higher up in the Wolhaarkop breccia are smaller, less well defined and lower grade (Boardman, 1964). Lenses, pods, and sheet-like bodies of massive braunite occur. The size of individual siliceous manganese orebodies ranges from a few tons to up to 5000 tons (De Villiers, 1960). Some thin beds of hematite-rich illitic shale may be present. Transitions between chert breccia and orebodies are gradual (Fig. 6.5), characterized by a rapid increase in the amount of manganiferous matrix at the expense of the amount of chert fragments present in the breccia. The ores are dense and massive, fine to medium crystalline, occasionally containing small vugs lined by euhedral braunite crystals and filled by earthy supergene cryptomelane or goethite.

Ore and chert appear massive but locally some crude bedding is developed. Zones of intensive shearing and mylonitization in the breccia were noted by Boardman (1964), who also observed that the siliceous breccia below the surface is less dense and compact than in outcrop. At depth it is commonly friable and porous. This observation is confirmed by recent exposures in the Sishen and Beeshoek iron ore mines, where the matrix of the Wolhaarkop breccia is decomposed to earthy, poorly crystalline supergene manganese oxides. Veins of coarse crystalline barite, botryoidal hematite and pyrolusite crosscut the Manganore iron-formation, the Wolhaarkop breccia and penetrate into the underlying dolomite (Du Toit, 1931). In some places the chert fragments are replaced by coarse crystalline barite (De Villiers, 1944; De Villiers, 1960).

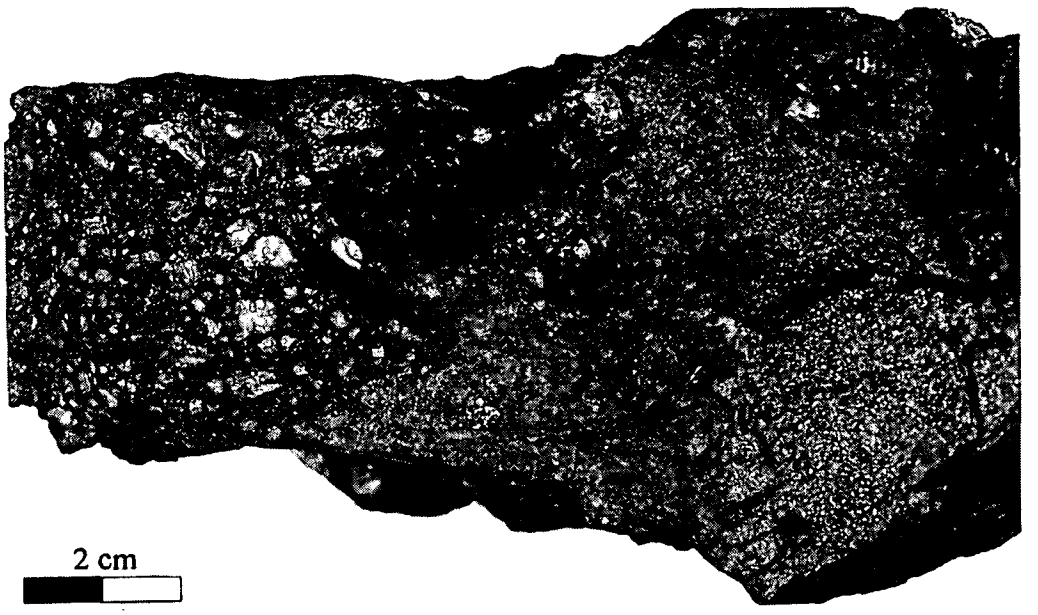

Fig. 6.5 Wolhaarkop chert breccia grading into massive, braunitic manganese ore (sample from Kapstevel mine).

UNIVERSITY OF JOHANNESBURG

A transitional ore-type, combining features of siliceous and ferruginous ores, has been described from Aucampsrust (Boardman, 1940; De Villiers, 1960; Plehwe-Leisen, 1985) and from areas where the Eastern and Western belt merge, e.g. from Rust-en-Vrede and King in the north (De Villiers, 1960), and Beeshoek and Doornfontein in the south of the Maremane Dome. Orebodies of the mixed type are generally small and irregular in shape (De Villiers, 1960). Mining exposures of this ore-type are thus rather poor. In the existing exposures, it would appear as if Wolhaarkop chert breccia grades upwards into a variable succession of immature quartzite, interbedded with breccia beds, manganiferous shale and massive, braunitic manganese ore. Quartzites, composed of angular to subrounded quartz grains, are interbedded with manganiferous shales. Manganese orebodies are associated with shale beds and the chert breccia (De Villiers, 1960). The petrography and mineralogy of the transitional ore-type turned out to be similar to that of the siliceous-type of ore and no separate discussion of the characteristics of the transitional ore type is necessary.

An enigmatic occurrence of high-grade manganese ore in small stratiform lenses, hosted by the Marthaspoort quartzite member in the upper part of the Gamagara Formation, was

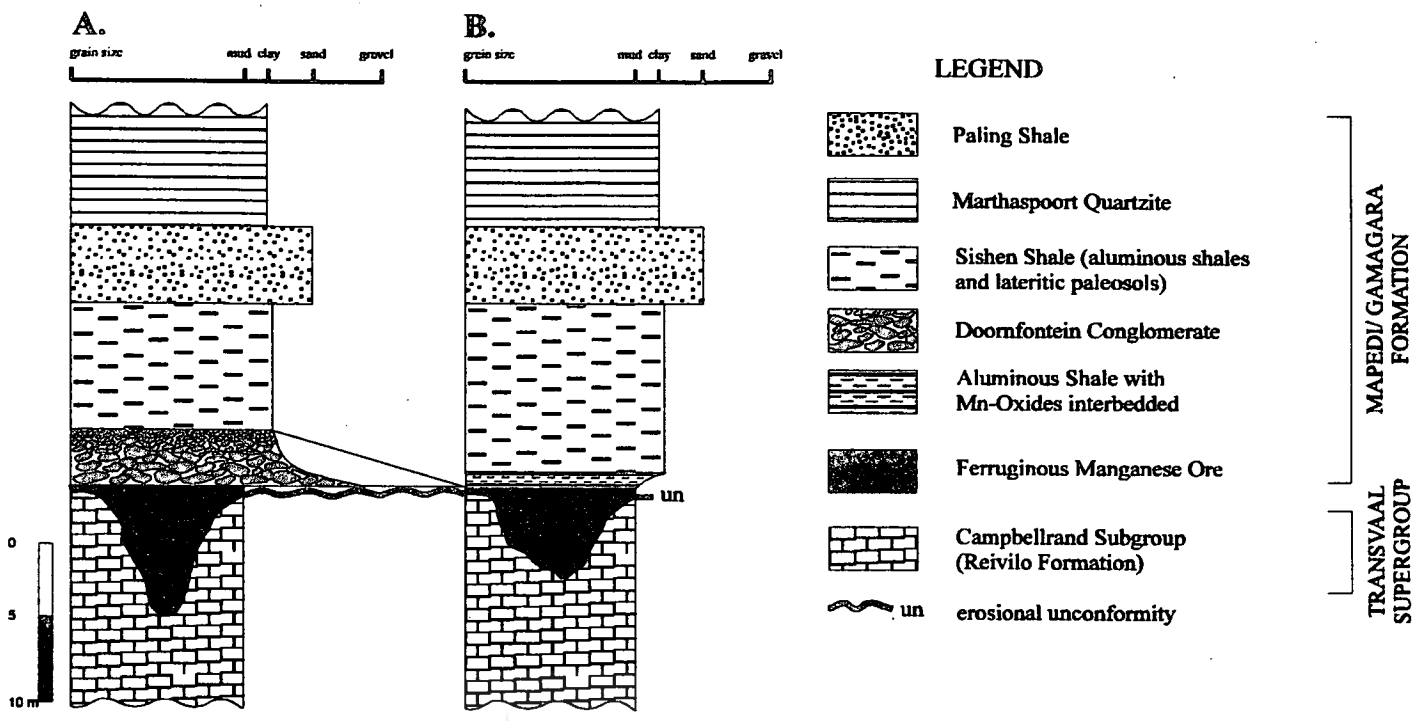

Fig. 6.6 Schematic profiles illustrating the typical geological setting of the ferruginous manganese orebodies filling in karst depressions in the Fairfield dolomite (A) overlain by Doornfontein hematite pebble conglomerate and (B) grading into aluminous and ferruginous Sishen Shale.

described by De Villiers (1960) from the farm Aucampsrust. It bears some similarities to the quartzite-hosted ores of the mixed type described above. However, exposure of this type of manganese ore is too poor to allow proper characterization.

Western Belt

Along the central part of the Gamagara ridge, the Doornfontein conglomerate member of the Gamagara Formation rests directly on chert-free manganiferous and ferruginous dolomite of the Reivilo Formation (Fig's. 6.6A and 6.6B). Ferruginous manganese orebodies are developed below the conglomerate in paleokarst depressions in the dolomite. Manganese accumulations are thickest within deep depressions, reaching a maximum thickness of approximately 17 m at Lohatlha, in the central part of the Gamagara Ridge. Reactivation of the paleokarst during an erosional cycle post-dating the lithification of the manganese ores led

Fig. 6.7 A. Massive fine crystalline lithiophorite bed with irregular pods and fracture infills of braunite and partridgeite; B. Faintly laminated lithiophorite-rich aluminous ore. Dark laminae consist of lithiophorite, lighter layers of braunite, partridgeite and romanechite (sample from Bishop). C. Finely laminated ore with apparent soft sediment deformation. Lamination partly obliterated by massive recrystallization of interbedded laminae of diaspore (gray) and braunite-partridgeite (lighter gray) (sample from Glosam).

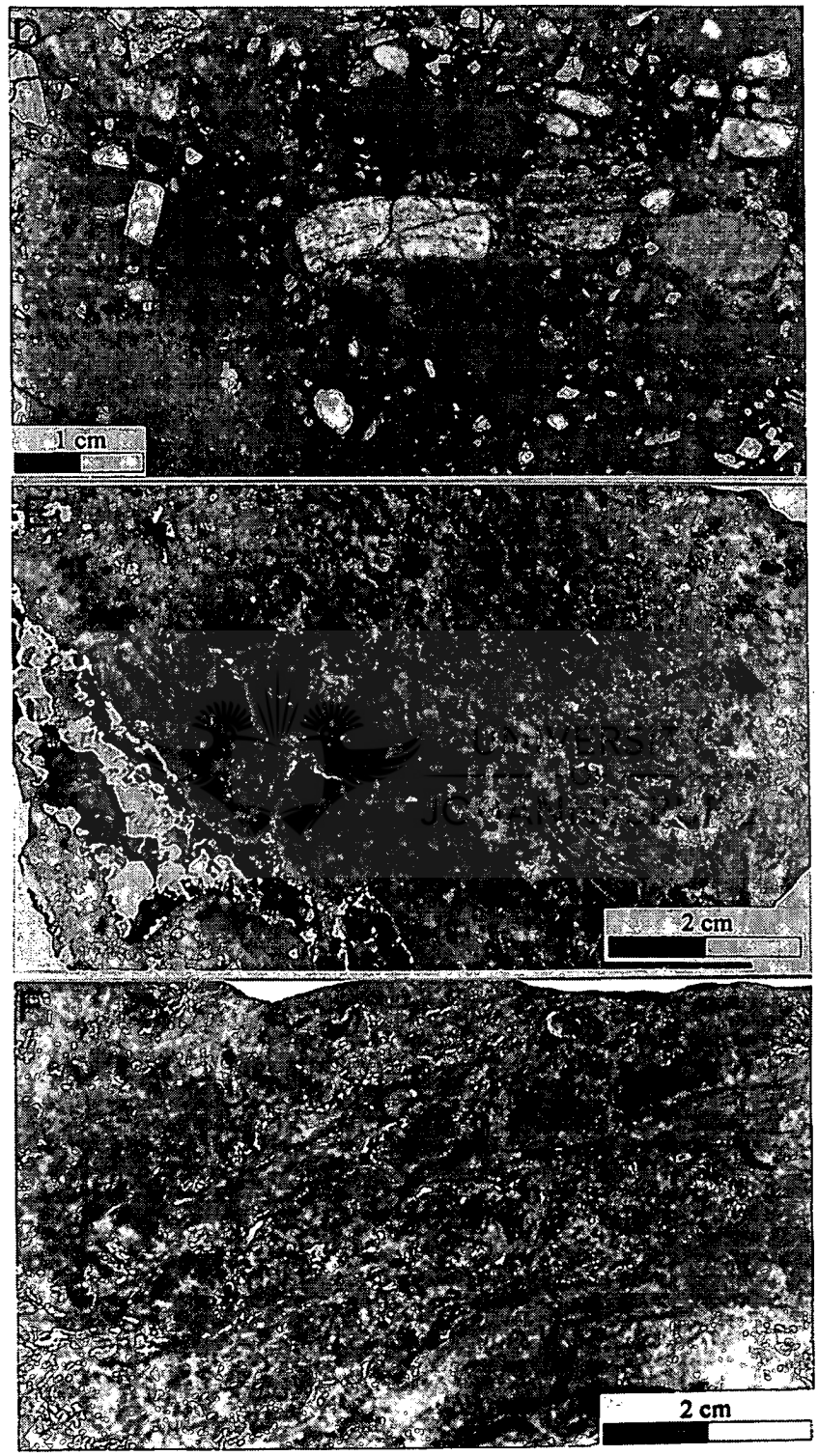

Fig. 6.7 (cont.) D. Pebbles of hematitized iron-formation, massive hematite and ferruginous shale (dull) with braunite matrix (sample from Aucampsrust); E. Coarse crystalline idioblastic and vuggy bixbyite ore with vug infills of ephesite (white plates) and small, irregular patches of supergene romanechite (light grey) (sample from Bishop); F. Subspherical braunite-partridgeite aggregates (darker gray) in ferruginous Paling shale (white and light gray) (sample from Glosam).

to slumping and brecciation of the ore and the overlying Mapedi/ Gamagara sediments (Grobbelaar and Beukes, 1986). Thick accumulations of brecciated manganese ore in deep sinkholes are therefore of secondary origin, with red clayey soil forming the interstitial fillbetween angular fragments of manganese ore of widely varying size and shape.

Three major varieties of ferruginous manganese ore are distinguished. The first is represented by fine to medium crystalline sedimentary ores with well preserved sedimentary lamination and bedding. The ore is composed of partridgeite and braunite. Coarse crystalline, massive to extremely vuggy bixbyite-rich ores form the second group. A third, minor group of ores is of supergene origin. Pyrolusite nodules, botryoidal crusts and cauliflower aggregates of romanechite occur as well as boxwork-textured aggregates of romanechite and cryptomelane that replace aluminous shale. The formation of a thin layer of amorphous wad separating the manganese ores from the underlying dolomite is ascribed to recent weathering.

Two types of fine to medium crystalline sedimentary ores are present. Aluminous ores, characterized by the abundance of supergene lithiophorite, appear in massive beds of 5 cm to more than 50 cm thick. These beds are typically massive, with lenses, pods and veins of recrystallized braunite and/or partridgeite crosscutting the bedding (Fig. 6.7A). Faint discontinuous wavy nonparallel or wavy parallel to discontinuous wavy nonparallel lamination are rarely observed (Fig. 6.7B). Beds of manganese-rich ore, on the other hand, are characterized by interbedding of oxide-rich laminae composed of braunite or partridgeite with thin, discontinuous shale laminae rich in diaspore and ephesite (Fig.6.7C). Well developed bedding and soft sediment deformation structures are common features in these manganese-rich ores (Fig. 6.7C). At some localities coarse clastic interbeds a few millimeter to 10 cm thick are present. These beds are composed of well rounded to subangular hematite (Fig. 6.7D) and manganese oxide clasts set in a muddy manganiferous or ferruginous matrix. The amount of hematite and shaly gangue in the fine crystalline ores increases towards the top of the orebodies where hematite-rich aluminous shale occurs as thin streaks and interbeds.

Irregular pods of coarse crystalline bixbyite-rich ores occur intimately associated with the fine crystalline, bedded ores. It is important to note that the coarse crystalline and fine crystalline ore originated penecontemporaneously, as there is no replacement of the one by the other. Sedimentary bedding commonly observed in the bedded ores is entirely obscured by the coarse grained idioblastic texture of the coarse crystalline ores. The ore is predominantly composed of subhedral bixbyite idioblasts (Schneiderhöhn, 1931), diaspore and ephesite (Fig. 6.7E). Fractures filled by ephesite are especially common in the upper part of the manganese orebodies. They show characteristic breccia textures and may protrude into the overlying ferruginous shales where

they pinch out. The ephesite appears in plates up to 4 cm in diameter and also as unusual bipyramidal crystals. Diaspore occurs as elongated platy brownish-red crystals which may be up to 10 cm long. These large crystals form either scaffold or parallel intergrowths.

The transition of the manganese orebodies into the overlying Doornfontein conglomerate member is generally conformable and gradual. In the transition zone abundant hematite pebbles may be present in the manganese ore (Fig. 6.6A and 6.6B). Considerable amounts of braunite, partridgeite and lithiophorite may in turn be present in the lower part of the Doornfontein hematite pebble conglomerate. At localities where the Doornfontein conglomerate is absent manganese ore beds grade upward into hematite-rich aluminous shale or mudstone. Here, shale interbeds become more common towards the top of the manganese orebodies. Round concretionary aggregates of braunite and partridgeite, up to 1 cm in diameter, are dispersed in ferruginous mudstone directly above the orebody at Glosam and Paling (Fig. 6.7F) whereas at Lohatlha lenticular bodies of braunite may be present in the shale overlying the orebody. Sharp contacts between manganese ore and overlying shale have been observed at Bishop.

Barite veins and lenses, often with a Ba-rich wad selvage, occur along the contact of the manganese orebodies with the underlying dolomite. Veins of very coarse crystalline fine tabular specularite (with plate diameters of up to 10 cm) and of dense and fine crystalline botryoidal hematite have been observed at Glosam and Paling. The specularite veins may contain minor amounts of quartz and braunite.

The supergene manganese ores display a highly variable texture comprising botryoidal and cauliflower aggregates of romanechite encrusting fragments of fine crystalline bedded and coarse crystalline bixbyite-rich ferruginous manganese ore. It is also common to find boxworks of dense romanechite or cryptomelane developed along bedding planes and joints in aluminous shales of the Gamagara Formation. Supergene alteration tends to obscure sedimentary and metamorphic textures. The final product of supergene alteration is the complete disintegration of the ore

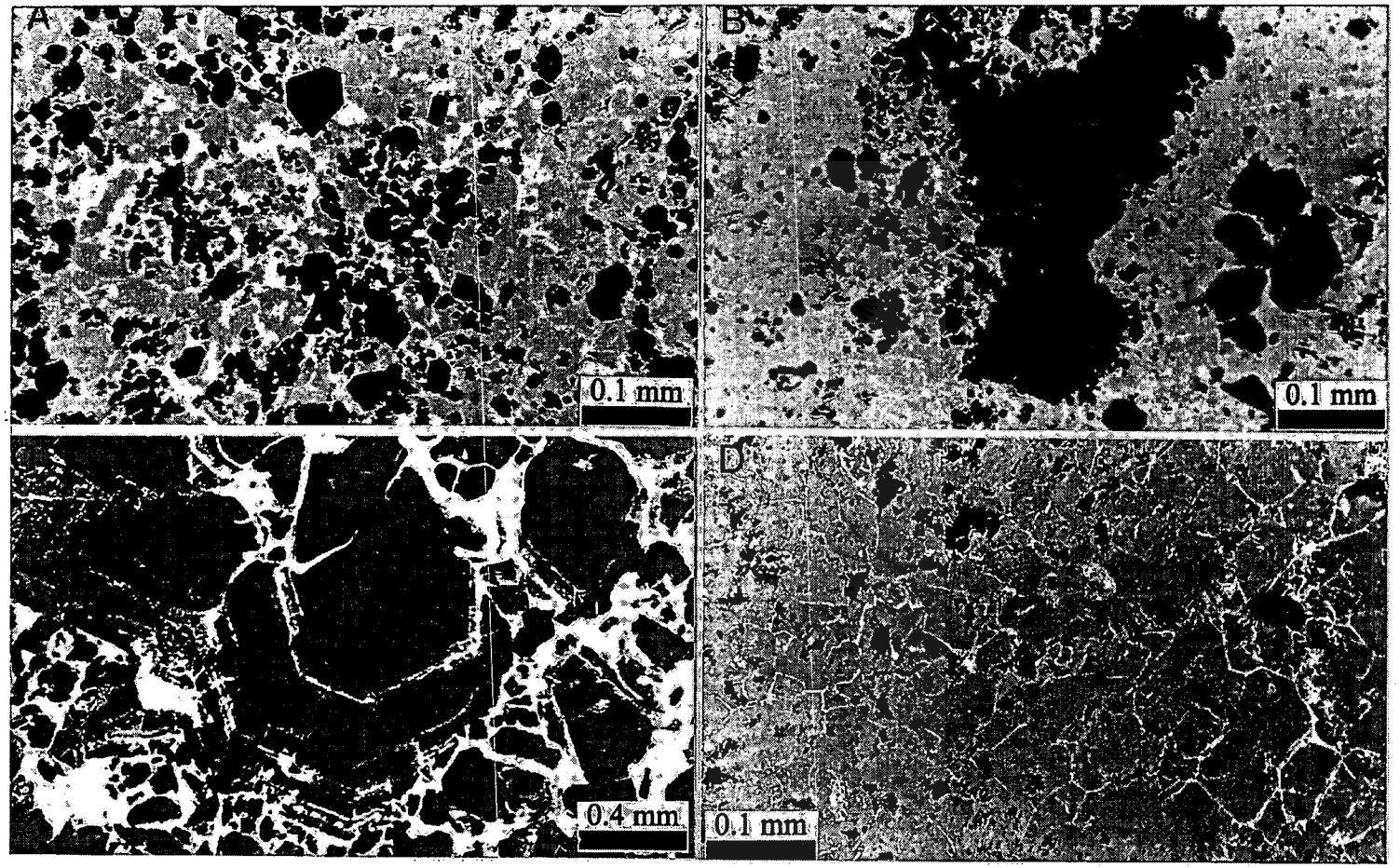

Fig. 6.8 Reflected light photomicrographs. A. Small, euhedral, authigenic quartz crystals in mosaic textured braunite matrix, braunite replaced by manganomelane (white) along grain boundaries (200x, oil immersion, sample MAN-238); B. Shredded outline of quartz clast (dark gray) replaced by braunite matrix (gray). Greyish-white manganomelane replaces braunite along grain boundaries (200x, sample MAN-236); C. Large quartz crystal with pseudohexagonal cross section, replaced by braunite along concentric growth zones of authigenic origin. Braunite is in turn replaced by fine crystalline manganomelane(white) (50x, sample MAN-238); D. Typical braunite mosaic texture, enhanced by replacement of braunite by romanechite along grain boundaries (200x, oil immersion, sample BEE-208).

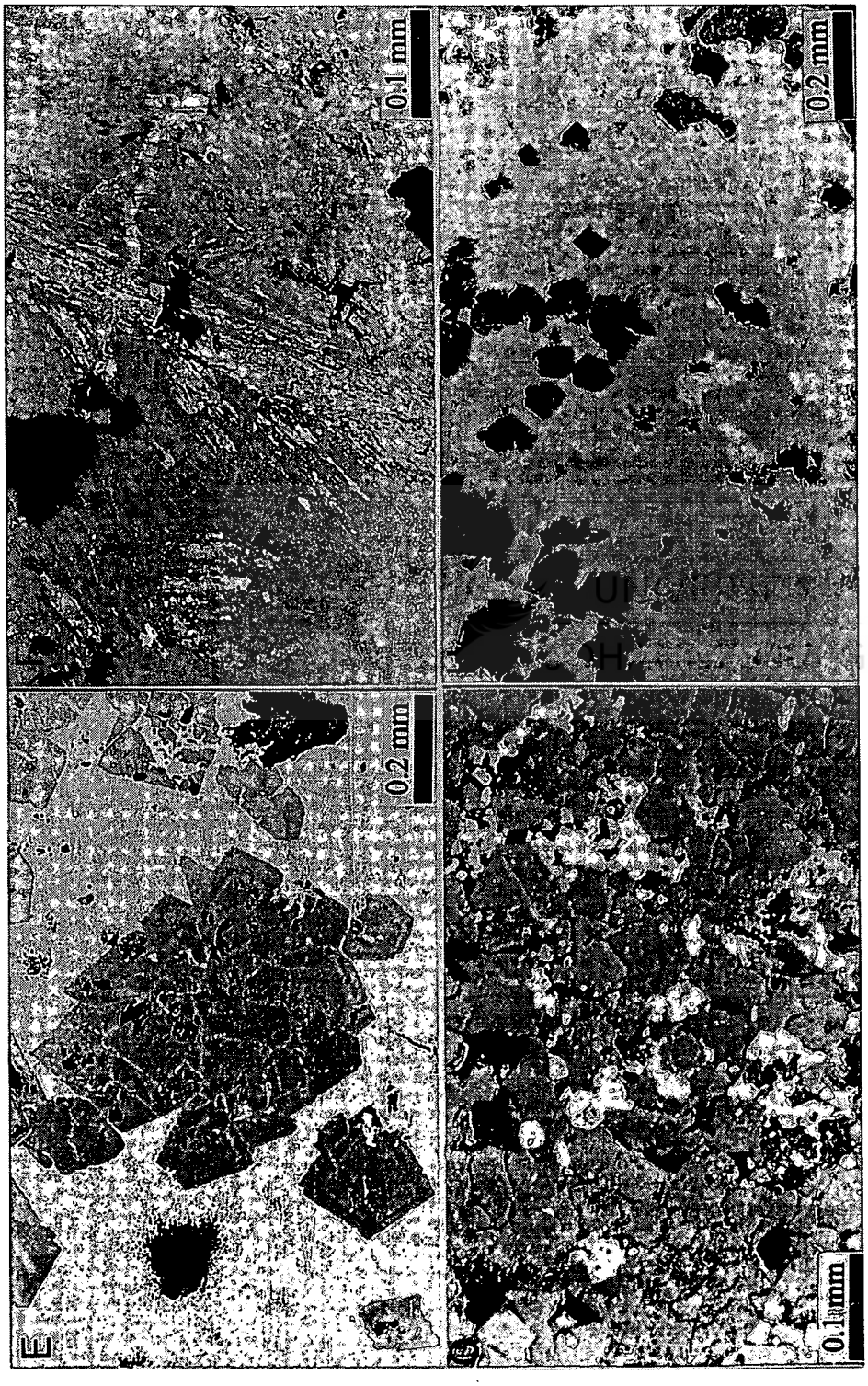

Fig. 6.8 (cont.) Reflected light photomicrographs. E. Cluster of concentrically zoned euhedral braunite crystals in vug filled by supergene romanechite (white) (320x, oil immersion, sample BEE-208). F. Laminar intergrowth of braunite (gray) and partridgeite (light gray), replacement by romanechite (white) (200x, oil immersion, DO-168); G. Braunite in association with subhedral, pseudohexagonal-rounded hematite grains (200x, oil immersion, sample PAL-221); H. Apatite grains (dark gray) with euhedral, hexagonal cross-section, replaced by braunite (gray), in turn replaced by manganomelane, romanechite vug infills (white) (200x, sample DO-169).

to friable wad. Supergene alteration is especially prominent along the contact of the orebodies with underlying dolomite.

Mineralogy and Petrography

Siliceous ores of the Eastern Belt

Chert clasts in the Wolhaarkop Breccia are generally recrystallized to polygonal quartz. In the upper part of the breccia the clasts are set in a fine crystalline matrix of hematite and polyhedral quartz. Towards the base of the breccia the matrix becomes manganiferous and may consist almost entirely of braunite, with minor amounts of partridgeite, hematite and authigenic quartz. Many of the recrystallized chert clasts are overgrown by authigenic euhedral quartz and parallel-fibrous chalcedony. Doubly terminated authigenic quartz crystals occur locally in abundance in the matrix of the breccia (Fig. 6.8A), as well as in the interbedded shales. Braunite may replace chert clasts but not the small, authigenic quartz crystals (Fig. 6.8B, C). Radial fibrous spherical aggregates of microcrystalline braunite replace fibrous chalcedony.Siliceous high-grade braunite ore-bodies occur as isolated bodies in the manganiferous chert breccia. They are composed of tightly interlocking subhedral braunite with grain sizes varying between 5 to 1000 μm (Fig. 6.8D). Euhedral braunite crystals line small vugs and fracture planes (Fig. 8E). Many of the braunite crystals are distinctly zoned (Fig. 6.8E) a feature discovered by Plehwe-Leisen (1985). Tiny crystals of partridgeite, less than 20 μm in diameter, are very intimately intergrown with braunite. In rare cases large millimeter-sized grains, composed of parallel intergrown lamellae of braunite and partridgeite, occur (Fig. 6.8F). Hematite occurs only as trace amounts in the high-grade braunite ores. Needle-shaped crystals are enclosed in braunite, whereas platy anhedral grains fill interstices in the braunite matrix (Fig. 6.8G). Small euhedral apatite crystals, partly replaced by braunite, were found in a massive braunite ore sample from Doornfontein (Fig. 6.8H). In another sample of strongly weathered braunite ore from Doornfontein, some sheaf-like aggregates of Ba-muscovite are present. The muscovite is partly replaced by romanechite. De Villiers (1945) described aggregates of acmite and compact crystalline masses of coarse

crystalline albite ($Ab_{94}An_6$) in braunitic ores from Sishen and Mokaning. Barite is quite common in the ore and distinctly associated with coarse recrystallized braunite. The barite appears to have formed cogenetically with the braunite. Veinlets filled with barite may also crosscut coarse recrystallized braunite ore.

The siliceous ores display various degrees of supergene alteration. Romanechite and cryptocrystalline cryptomelane are the most common products of supergene alteration. Romanechite occurs as a finely dispersed dusty alteration product in braunite crystals or as replacive seams along grain boundaries of braunite and partridgeite. Botryoidal aggregates, with a rim of microcrystalline cryptomelane and a core of fibrous romanechite, are common. Pyrolusite and ramsdellite are also products of supergene alteration and occur as well developed crystals (20-150 μm large) and crystal aggregates in vugs in braunite-rich ore. However, both ramsdellite and pyrolusite are replaced by romanechite and cryptomelane. Pyrolusite needles, up to 1 cm long, are common in veins crosscutting the Wolhaarkop breccia and orebodies. Needles of lithiophorite, 10 to 50 μm long, are associated with the pyrolusite. Relics of tiny hematite grains are preserved in cryptomelane-romanechite aggregates. In rare cases goethite occurs in association with cryptomelane.

UNIVERSITY OF JOHANNESBURG

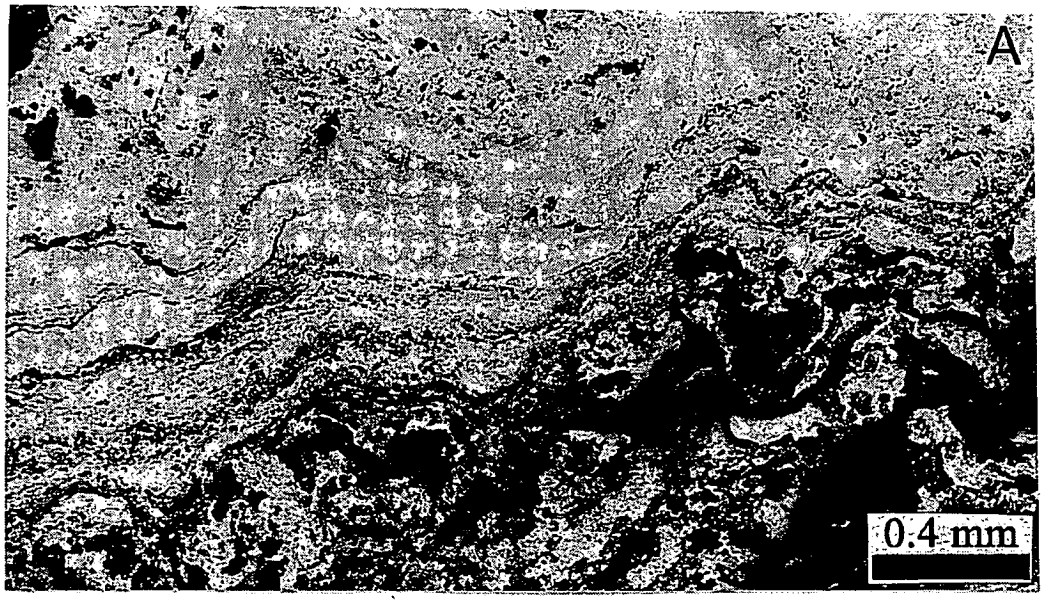

Fig. 6.9A. Reflected light microphotograph. Soft-sediment deformation in finely laminated ore, interbedded oxide-rich laminae of romanechite (white) and braunite (light-gray) with ephesite laminae (dark gray) (50x, sample GLO-187)

Fig. 6.9 (cont.) Reflected light microphotographs. B. Round partridgeite microconcretions (light gray), partly replaced by romanechite (white) in massive braunite matrix (gray), diaspore and vugs appear black (200x, oil immersion, sample GLO-187); C. Botryoidal crust composed of finely intergrown braunite (gray) and partridgeite (light gray), associated with hematite fibres (bright white), diffuse replacement by romanechite (white) (200x, oil immersion, sample DO-167-2); D. Layered botryoidal crust with separate layers composed of braunite (gray) and partridgeite (light gray), alteration to romanechite (white) (200x, oil immersion, sample BIS-246).

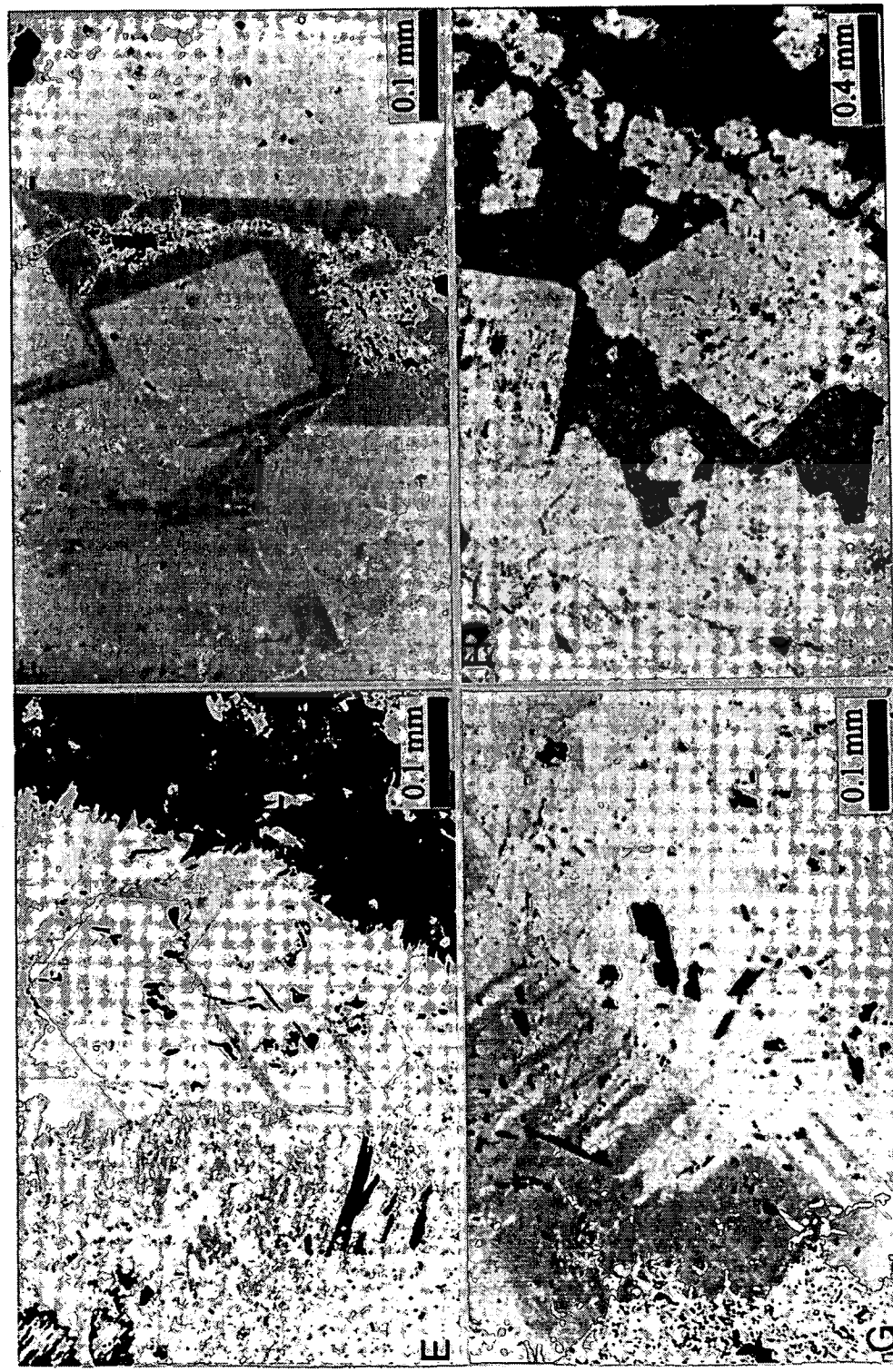

Fig. 6.9 (cont.) Reflected light microphotographs. E. Braunite lamellae (gray) intersect large Partridgeite idioblast (light-gray), diaspore laths and aggregate (black) to the right of partridgeite idioblast, cryptic intergrowth of partridgeite, braunite and hematite (bright white) in the left half of the picture, replacement of partridgeite along cracks by romanechite (white) (200x, oil immersion, sample GLO-187); F. Growth zone of braunite (gray) around partridgeite idioblast (light gray), supergene romanechite (white) (200x, oil immersion, sample LOH-179); G. Orientated flames of silica-depleted braunite penetrate from partridgeite (light gray) idioblast into surrounding braunite (gray); hematite is white, diaspore appears black (200x, oil immersion, sample GLO-187); H. Idioblastic bixbyite cubes (light gray) with small hematite inclusions (white) lining vug and enclosed in gamagarite (dark gray with small hematite inclusions) and diaspore (porous, dark gray) (50x, sample Mn10-63).

Fine crystalline bedded ferruginous manganese ores

Manganese-rich beds in the fine to medium crystalline bedded ores are composed of alternating laminae of braunite-partridgeite and ephesite-diaspore. Lamination and bedding is irregular, wavy and discontinuous (Fig. 6.9A). Various degrees of recrystallization and supergene alteration are present in these ores obscuring original sedimentary textures and structures. The less altered dense manganese oxide beds are composed of microcrystalline braunite-partridgeite laminae parted by irregular, often discontinuous, veneers of diaspore-ephesite (Fig. 6.9A). Supergene alteration of braunite-partridgeite to romanechite typically takes place in an irregular fashion from outside to inside of laminae. Similarly, diaspore-ephesite veneers are preferentially replaced by lithiophorite.

A characteristic feature of many of the fine crystalline braunite-partridgeite laminae is the presence of spheroidal to ellipsoidal microconcretions, 50 - 350 μm in diameter, composed of partridgeite and/or braunite (Fig. 6.9B). Flattening of the concretions parallel to bedding suggest an early diagenetic origin prior to compaction of the sediment. Internal textures of the microconcretions range from radial fibrous to granular. In case of the latter the concretions often have a massive core of granular interlocking partridgeite rimmed by subhedral braunite crystals protruding into the concretion (Plehwe-Leisen, 1985).

UNIVERSITY JOHANNESBURG

Complex botryoidal laminated structures, composed of braunite and partridgeite, appear closely associated with the diagenetic microconcretions (Fig. 6.9C,D). Braunite and partridgeite form an extremely fine crystalline parallel fibrous or cryptic intergrowth (Fig. 6.9C). In one case a botryoidal crust was found to be composed of separate laminae of microcrystalline partridgeite and braunite (Fig. 6.9D). Also of diagenetic origin are anastomosing veinlets filled by partridgeite or braunite and hematite. These veinlets are usually highly contorted normal to bedding suggesting that they were deformed by compaction of the sediment. Shaly laminae in the manganese-rich beds are composed of fine crystalline flaky diaspore and ephesite. A distinct type of microconcretion occurs in these shaly laminae. The concretions have rims of hematite, braunite or partridgeite that surround 50 to 200 μm large cores of diaspore or lithiophorite.

Table 6.1 Composition of members of the braunite-bixbyite group of minerals (selected analyses, all data in wt %).

Sample No.	AUC198.2	BEE214	DO169	GLO185.3	LOH179	GLO185.3	PAL219.4	GLO185.3	LOH79.1	BIS247	BIS289.3	GLO10-63
Mineral			Braunite			Si-Braunite		Partridgeite			Bixbyite	
N	4	10	3	5	10	10	2	5	5	3	10	5
SiO_2	10.3	10.3	10.8	10.4	10.0	4.07	0.65	0.28	0.32	LLD	0.20	1.39
TiO_2	0.05	0.04	LLD	0.06	0.09	0.05	0.05	0.02	0.12	0.07	0.06	0.41
Al_2O_3	0.35	1.27	0.80	1.30	0.58	3.03	1.25	0.61	2.25	2.30	2.18	1.41
Fe_2O_3	0.34	2.51	1.80	2.21	0.42	3.54	1.90	0.67	4.59	20.0	14.5	16.6
Mn_2O_3*	78.6	75.4	75.7	78.7	76.7	89.8	96.7	98.6	92.7	76.9	83.0	79.0
MnO*	8.58	9.07	9.80	4.41	11.8							
MgO	LLD	LLD	0.10	0.12	0.15	LLD	0.20	LLD	0.18	0.10	LLD	LLD
CaO	1.52	1.24	1.20	2.95	0.15	1.16	LLD	LLD	0.10	LLD	LLD	0.65
BaO	0.24	0.12	0.10	0.13	0.05	0.07	0.10	0.04	LLD	0.10	0.10	0.09
Na_2O	LLD	0.17	0.10	0.12	0.15	0.10	LLD	LLD	0.12	0.23	0.12	LLD
K_2O	LLD	LLD	LLD	LLD	LLD	LLD	LLD	LLD	LLD	LLD	LLD	LLD
TOTAL	100.1	100.2	100.4	100.5	100.1	101.9	100.9	100.5	100.4	99.9	100.3	99.7

Abbreviations: N - number of analyses; LLD - Lower than detection limit; n.a. - not analysed; PAL-Paling, GLO-Glosam, LOH-Lohatla, BIS-Bishop, AUC-Aucampsrust, BEE-Beeshoek, DO-Doornfontein. * Mn^{2+}-Mn^{3+} charge balance calculated

UNIVERSITY OF JOHANNESBURG

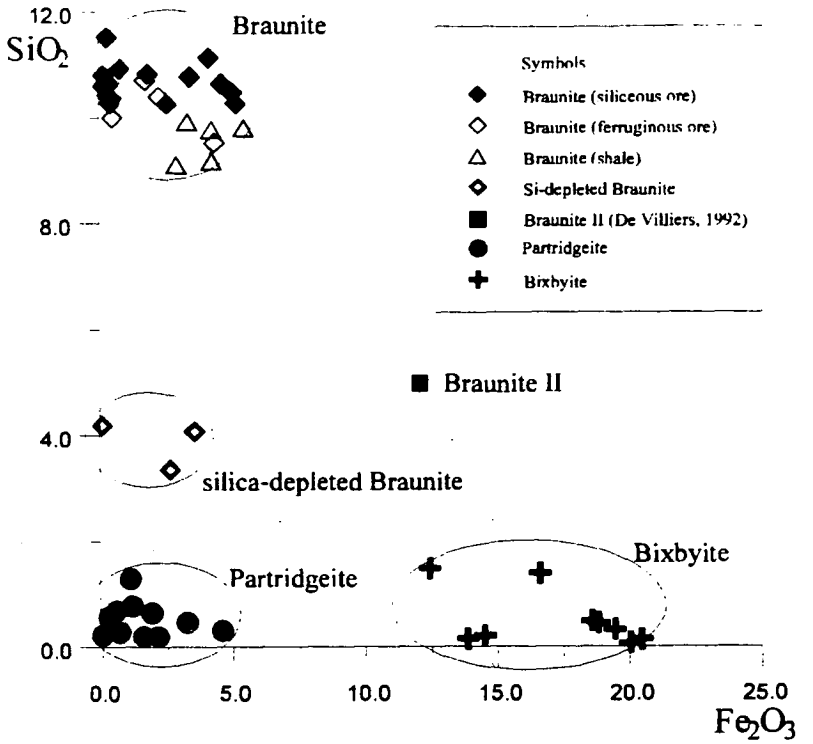

Fig. 6.10 Plot SiO_2 - Fe_2O_3 illustrating compositional differences between different members of the braunite-bixbyite group.

Massive beds of aluminous manganese ore in the fine to medium crystalline bedded ores are composed of 1 to 30 μm densely intergrown anhedral lithiophorite flakes of supergene origin. Advanced supergene alteration obscures sedimentary textures in most of these beds. Anastomosing veinlets of fine crystalline partridgeite and braunite, dispersed euhedral braunite crystals and hematite needles, up to 200 μm long, are remnants of earlier mineral assemblages preserved in some of the lithiophorite beds.

The first signs of recrystallization of the sedimentary ores are provided by the presence of mosaic-textured aggregates of braunite and cryptic and lamellar intergrowths of braunite and partridgeite. Further recrystallization produced medium-grained braunite-partridgeite laminae with a granular texture. In these recrystallized ores braunite-rich laminae are composed of equigranular braunite, with grain sizes between 100 and 500 μm, intimately intergrown with minor hematite, ephesite and diaspore. Hematite is either included in braunite or fills interstitial pores. In some cases distinct hematite-rich laminae are present. The hematite typically occurs as 10 - 30 μm platelets. Partridgeite is relatively common as small inclusions or laminae in braunite. Small anhedral hausmannite grains are rather rare constituents of medium-grained braunite-rich laminae. Ephesite forms subhedral micaceous plates, up to 100 μm long, that occur concentrated along distinct laminae, but also fill tiny vugs.

In contrast recrystallized, medium-grained partridgeite-rich laminae, pods and lenses are characterized by graphic to cryptic intergrowth of partridgeite and braunite (Fig. 6.9F). Pseudocubic partridgeite idioblasts are overgrown by rims of braunite (Fig. 6.9G). Pods of mosaic-textured braunite and subhedral hematite plates occur between these partridgeite idioblasts and clusters of diaspore laths are enclosed or transect the partridgeite-braunite intergrowths. Partridgeite idioblasts may be replaced by 5-100 μm large anhedral hausmannite grains or by fine crystalline braunite. In one sample from Glosam mine (Fig's. 6.9F and 6.9G) flames of silica-depleted braunite protrude from partridgeite idioblasts into the surrounding braunite matrix (Fig. 6.9G).

The braunite, silica-depleted braunite and partridgeite is characterized by the presence of low concentrations of Fe_2O_3, CaO and Al_2O_3. (Table 6.1, Fig. 6.10). Braunite contains about 10 wt % SiO_2, partridgeite generally less than 1 wt % SiO_2 and silica-depleted braunite about 3-5 wt % SiO_2.

Coarse crystalline ferruginous manganese ores

The coarse crystalline manganese orebodies of the Western belt are composed of pseudocubic bixbyite idioblasts, up to 30 mm in diameter, in an open framework intergrowth with subhedral plates of hematite and small aggregates of mosaic-textured braunite. Interstitial pores and vugs are filled by coarse crystalline diaspore, ephesite, and amesite (Fig. 6.9H) or by supergene romanechite, pyrolusite and lithiophorite. The bixbyite contains between 10 and 22 wt % Fe_2O_3 (Table 6.1, Fig. 6.10). Crystals are characterized by pseudosymmetric, lamellar twinning (Schneiderhöhn, 1931; Ramdohr, 1960) and concentric growth zonation along the {100} planes. Orientated intergrowth inclusions (Ramdohr, 1960) of thin braunite lamellae (10 to 100 μm long) and up to 100 μm long diaspore laths appear along the {100} and {111} planes. Non-orientated clusters of diaspore inclusions and dispersed minute rounded hematite inclusions are common in the bixbyite. Similar hematite inclusions are present in ephesite and diaspore. The hematite inclusions often define primary sedimentary laminae which are now transected by the large bixbyite crystals (Schneiderhöhn, 1931). A late phase of braunite replaces the bixbyite crystals along microfractures.

Diaspore laths and ephesite plates penetrate from the interior of bixbyite crystals into vugs and pores. Amesite occurs in pseudohexagonal slender prisms, up to several centimeter long, intimately intergrown with diaspore and ephesite. Coarse crystalline barite, often with inclusions of hematite or euhedral braunite, occurs intimately associated with diaspore at Paling and

Glosam. Gamagarite, a unusual Ba-Mn-Fe-vanadate, was discovered as a new mineral species by De Villiers (1943) in some bixbyite-rich ore samples from Glosam mine. The gamagarite forms dark-brown to red clusters of needle-like crystals, up to 1 cm long, densely intergrown with ephesite, diaspore and amesite.

Masses of coarse crystalline hausmannite ores and fine-crystalline massive jacobsite-rich ore were described from the Western Belt by De Villiers (1945a) and De Villiers (1960). Hausmannite occurs in massive aggregates of anhedral grains with diameters up to several millimeter, altered along grain boundaries and twinning lamellae to romanechite. Fine crystalline jakobsite is associated with hematite and hausmannite in bedded ores or as microscopic veinlets that crosscut and replace hausmannite (De Villiers, 1960).

Supergene ores

Cauliflower aggregates, botryoidal crusts and boxworks of supergene ore are composed of parallel or massively intergrown romanechite fibres, less than 10 μm long, with minute inclusions of hematite. Small amounts of illite and quartz are enclosed in the romanechite. Earthy wad layers along the contact between dolomite and manganese ore and between barite lenses and manganese ore are respectively composed of X-ray amorphous manganese oxides, hematite and traces of goethite. Friable aggregates of pyrolusite needles are present in the wad.

Supergene weathering affected the manganese ores to a highly variable degree. The various minerals of diagenetic or metamorphic origin show different susceptibilities to weathering. Most strongly affected is hausmannite, followed in order of less alteration by partridgeite, braunite, bixbyite, diaspore, ephesite, and quartz. Replacement of manganese oxides and gangue minerals is most intense along grain or aggregate boundaries, fractures or compositional heterogenities (growth zones, solid inclusions), often enhancing textures of ores in weakly weathered samples (Fig. 6.8D). However, intense weathering almost totally obscures all sedimentary and metamorphic textures. Microcrystalline cryptomelane and romanechite are the most common products of supergene alteration. Botryoidal aggregates along grain boundaries or fractures are commonly zoned with a diffuse outer zone of cryptomelane and a core of massive romanechite or cryptomelane. It should be noted that the optical differentiation between different members of the manganomelane group is very difficult (Frenzel, 1980). Electron microprobe analysis was employed to distinguish between romanechite and cryptomelane.

In contrast to the supergene assemblage formed by replacement of manganese oxides, lithiophorite prevails in the aluminous ore beds of the ferruginous ore type. Lithiophorite is generally regarded to be of supergene origin, but in the Postmasburg manganese field it is most difficult to place into the mineral paragenesis. It apparently formed in multiple generations, ranging from coarse crystalline vug linings described by De Villiers (1945), to coatings of minute lithiophorite needles on romanechite, and massive aggregates of fine crystalline lithiophorite replacing aluminous shale.

Less abundant phases of supergene origin include manganite, pyrolusite and ramsdellite. Manganite is regarded by Plehwe-Leisen (1985) as the earliest mineral phase of supergene origin. De Villiers (1960) and Schneiderhöhn (1931) also noted its rare occurrence. Pyrolusite is present as coarsely developed anhedral to subhedral prismatic crystals, up to 300 μm in diameter, filling vugs and fractures in the ore, but also forming fine crystalline, irregular granular masses in supergene altered ore. Ramsdellite, first identified by Plehwe-Leisen (1985), could be easily confused with pyrolusite. It forms rhomb-shaped crystals, 10 to 150 μm in diameter, with a typical fish-scale cleavage pattern (Frenzel, 1980).

UNIVERSITY OF JOHANNESBURG

Shales

Shale beds present in the upper part of orebodies and in the transition zone to the overlying Gamagara shales are composed of ephesite, diaspore, hematite and finely dispersed braunite. A very similar assemblage is observed in aluminous shales of the Mapedi/ Gamagara Formation where these are in direct contact with manganese ore. Higher up in the succession shales of the Gamagara Formation are composed of pyrophyllite, diaspore, and kaolinite with variable amounts of muscovite/illite and hematite. Idioblastic diaspore laths or grains, up to several millimetres long, crosscut the fine crystalline matrix of the shales composed of pyrophyllite, kaolinite, muscovite/illite and dusty hematite. Tiny grains of detrital rutile and tourmaline are present in the shales. Microcrystalline anatase appears in small neoformed accumulations.

Conglomerates

Conglomerates interbedded with the ferruginous manganese ore and those of the overlying Doornfontein member are composed of well rounded pebbles of hematititized iron-formation, botryoidal hematite, hematitic shale or massive hematite. Pores within these clasts are filled by shaly material or by fine crystalline braunite and partridgeite. In rare cases small manganese-rich

clasts are present in the conglomerate. Cryptic intergrowth of fine crystalline braunite and partridgeite and mosaic-textured braunite is present in these manganese-rich clasts. The matrix of the conglomerate beds is composed of fine crystalline hematite, ephesite and braunite when interbedded with manganese ore, but of pyrophyllite and kaolinite in the Doornfontein member overlying the ferruginous manganese orebodies.

Geochemistry

Siliceous ores and Wolhaarkop breccia of the Eastern Belt

Table 6.2 Composition of siliceous manganese ore and Wolhaarkop chert breccia.

Type	siliceous ore									Wolhaarkop Breccia			
Mine	BEE	BEE	BEE	MAN	KAP	KAP	KAP	DO	DO	AUC	MAN	KAP	KAP
No.	212	213	214	238	225	230	231	167/1	168	204	239	228	229
major elements (wt.%)													
SiO_2	4.56	4.11	8.22	8.76	5.50	8.79	10.7	4.84	1.70	21.2	43.9	14.6	57.0
TiO_2	0.07	0.13	0.11	0.04	0.14	0.05	0.16	0.11	0.07	0.05	0.04	0.05	0.05
Al_2O_3	0.28	1.53	2.68	0.09	1.73	1.69	4.37	2.92	0.47	0.98	0.28	1.08	0.35
Fe_2O_3	5.13	10.6	8.75	1.24	5.27	1.93	4.39	4.93	1.85	0.99	2.88	1.40	0.99
Mn_3O_4	80.4	72.9	69.5	78.3	78.6	72.4	63.7	79.1	82.0	62.2	44.6	75.6	35.8
MgO	0.14	0.25	0.09	0.15	0.28	0.23	0.59	0.24	0.10	0.61	0.21	0.24	0.23
CaO	0.73	0.74	0.95	0.17	0.90	0.20	0.24	1.00	0.13	0.54	0.18	0.93	0.35
Na_2O	0.12	0.06	0.02	0.23	0.35	0.37	0.18	0.00	0.08	0.37	0.43	0.08	0.10
K_2O	0.25	0.85	0.74	0.51	0.65	2.26	2.40	0.62	0.22	1.53	0.40	0.50	0.17
P_2O_5	0.07	0.21	0.32	0.04	0.10	0.01	0.03	0.03	0.02	0.02	0.04	0.06	0.00
SO_3	1.10	0.00	0.17	0.00	0.00	0.14	0.00	0.00	1.25	0.00	0.00	0.03	0.56
H_2O^-	0.14	0.22	0.21	0.23	0.30	0.23	0.43	0.15	0.18	0.77	0.23	0.16	0.09
LOI	4.2	5.5	5.2	10.4	6.1	10.5	9.5	4.5	8.7	9.3	5.9	3.7	2.4
Ba	2.80	1.83	2.70	0.12	0.28	1.50	3.17	1.62	2.94	1.82	0.47	1.17	0.93
trace elements (in ppm)													
Co	107	159	156	88	119	113	131	51	49	45	120	83	42
Cr	144	243	131	237	144	100	92	156	134	66	246	167	251
Cu	223	225	221	30	87	294	202	201	328	288	79	303	147
Ni	65	214	191	149	238	284	662	77	86	214	112	219	50
Pb	11	122	127	15	16	58	446	265	<5	27	27	148	30
Rb	1	5	2	5	14	12	28	8	2	21	4	2	1
Sr	129	133	173	56	103	159	247	97	127	347	77	86	57
Th	<1	<1	1	<1	<1	3	13	3	<1	LLD	2	0	3
V	70	67	92	30	39	127	93	96	68	64	25	97	21
Zn	4	89	74	29	29	35	109	56	<3	50	18	28	17
Zr	LLD	20	3	LLD	11	3	23	5	<1	9	<1	<1	<1
TOTAL	**100**	**98.8**	**99.6**	**100.1**	**100.1**	**100.3**	**100**	**100.1**	**100.6**	**100.5**	**99.7**	**99.6**	**99.1**
Mn/Fe	16.1	7.1	8.2	65	15.4	38.6	15	16.5	45.6	64.7	16.0	55.6	37.2
Si/Al	14.4	2.4	2.7	97.3	2.8	4.6	2.2	1.5	3.2	19.1	139	12.0	144
Ba/Sr	217	137	156	21	27	94	128	167	310	52	61	136	169
$\rho(g/cm^3)$	4.33	4.42	3.95	3.57	4.34	3.91	4.12	4.28	4.35	3.41	2.99	3.55	3.24

Abbreviations: BEE-Beeshoek, MAN-Manganore, KAP-Kapstevel, DO-Doornfontein

The siliceous braunite-rich ores hosted by the manganiferous Wolhaarkop chert breccia are characterized by Mn_3O_4 concentrations between 63.7 and 82.0 wt %, low iron contents and Mn/Fe ratios of between 7 and 65 (Table 6.2). The Mn/Fe ratio in the manganiferous Wolhaarkop chert breccia (Table 6.2) are similar to that of the ore, but with lower absolute concentrations of Mn and Fe as SiO_2 contents increase. SiO_2 contents in the braunitic ores vary between about 1.70 and about 10 wt % (Table 6.2), whereas samples of Wolhaarkop breccia contain more than 50 wt % SiO_2. The ores contain between 0.28 - 4.37 wt % and the chert breccia about 1 wt % Al_2O_3. Concentrations of CaO (0.13 to 1 wt %), MgO (0.09-0.61 wt %) and Na_2O (< 0.01 to 0.43 wt %) are equally low in chert breccia and braunitic ore. K_2O concentrations are highly variable and greater in ore samples (0.22-2.40 wt %) than in the chert breccia (0.17-1.53 wt %). The same applies to the P_2O_5 content, which is less than 0.1 wt % in the chert breccia and up to 0.32 wt % in the braunitic ore (Table 6.2). Ba concentrations of 1-4 wt % are common in ore and breccia samples. Trace elements such as Sr (21-310 ppm), Co (39-159 ppm), Cr (52-251 ppm), Cu (30-328 ppm), Ni (50-662 ppm), Pb (11-446 ppm),V (21-318 ppm) and Zn (4-109) have similar concentrations in chert breccia and braunitic ore (Table 6.2) and variations appear to be unrelated to the Mn concentration. Rb (1-28 ppm), Th (<1-13 ppm), and Zr (<1 - 23 ppm) concentrations are very low.

UNIVERSITY OF JOHANNESBURG

Ferruginous ores of the Western Belt

Fine crystalline bedded ores and coarse crystalline bixbyite-rich ores are geochemically very similar (Table 6.3). Mn_3O_4 concentrations vary between 44.9 and 77.1 wt % and Fe_2O_3 contents range between 10 and 30 wt %, with an exceptionally low concentration of 3.65 wt % in a partridgeite-rich sample from Lohatlha (LOH-179) (Table 6.3). Mn/Fe ratios are relatively constant between 1.5 and 5.8, with an average of 3.8 (excluding the unusual sample LOH-179) (Table 6.3) which is considerably lower than in the siliceous ores of the Eastern belt. SiO_2 contents of between 0.35 and 5.51 wt % are lower than the concentrations of Al_2O_3 which range between 3.02 and 30 wt % (Table 6.3). Si/Al ratios are thus always below one which is in contrast to that in ores of the Eastern belt in which the ratio is always greater than one (Table 6.1). Ba ranges between 0.07 and 4.86 wt %, and Ba/Sr ratios are between 1.74 in the extremely Ba-poor sample PAL-221 (Table 6.3) and 244 in Ba-rich samples. Some minor and trace elements are present in greater amounts in the ferruginous ores than in the siliceous ores. These include TiO_2 (0.08-0.54 wt %), MgO (0.15-1.38 wt%), Na_2O (0.01-2.35 wt%),

Table 6.3 Composition of ferruginous manganese ore.

Type	fine crystalline, bedded ores									coarse crystalline bixbyite-rich ores						
Mine	PAL	PAL	PAL	PAL	GLO	GLO	LOH	BIS	BIS	GLO	GLO	LOH	LOH	BIS	BIS	BIS
No.	216	217	220	221	186	187	179	245	246	185	197	178	180	241	248	250
major elements (in wt.%)																
SiO_2	2.77	5.51	2.11	2.96	1.52	6.35	2.63	0.35	3.62	2.50	4.01	2.55	0.71	2.14	3.07	4.00
TiO_2	0.30	0.15	0.16	0.24	0.54	0.42	0.14	0.32	0.23	0.22	0.31	0.08	0.11	0.38	0.23	0.15
Al_2O_3	11.7	16.1	3.02	10.5	9.87	12.7	4.34	3.32	18.5	14.1	6.09	5.75	4.42	29.6	5.81	4.44
Fe_2O_3	31.4	13.0	25.1	12.0	16.4	23.1	3.65	19.9	11.4	15.2	13.7	12.6	30.1	9.38	17.4	18.0
Mn_3O_4	44.9	55.7	58.3	63.0	57.8	46.7	77.1	57.9	56.6	58.6	63.9	70.4	57.3	49.9	66.7	67.3
MgO	0.85	1.38	0.26	0.41	0.94	0.35	0.27	0.24	0.87	0.28	1.87	0.16	0.22	1.19	0.25	0.15
CaO	0.53	0.54	0.55	0.80	0.20	0.17	0.80	0.15	0.04	0.61	0.68	0.14	0.13	0.00	0.22	0.47
Na_2O	0.11	0.05	0.10	0.08	0.01	2.35	0.13	0.11	1.20	0.17	0.11	0.66	0.00	0.00	0.01	0.04
K_2O	0.31	0.12	0.49	0.82	0.83	0.76	1.08	2.55	0.44	0.37	0.78	0.60	0.77	0.06	0.11	0.65
P_2O_5	0.04	0.08	0.10	0.06	0.02	0.02	0.09	0.01	0.00	0.05	0.04	0.09	0.04	0.00	0.36	0.02
SO_3	0.00	0.00	0.00	0.00	0.00	0.00	0.00	0.00	0.00	0.00	0.00	0.00	0.00	0.00	0.00	0.00
H_2O^-	0.28	0.32	0.20	0.37	0.14	0.21	0.13	0.08	0.07	0.06	0.35	0.09	0.08	<0.05	0.08	0.08
LOI	7.4	7.8	6.0	9.1	10.7	7.2	7.5	8.7	6.6	6.5	8.4	5.7	6.3	7.4	5.3	5.1
Ba	0.86	1.06	3.05	0.07	2.51	0.69	1.94	4.86	0.42	0.69	0.58	1.40	0.14	0.17	0.91	0.34
trace elements (in ppm)																
Co	84	141	36	199	158	69	37	42	226	69	14	285	52	149	157	59
Cr	206	116	93	118	174	117	116	57	189	156	132	164	179	212	178	157
Cu	28	167	69	55	<5	14	73	<5	159	85	13	1451	105	45	23	106
Ni	259	214	36	199	253	239	213	64	375	125	49	566	84	345	344	41
Pb	352	102	326	28	1249	538	<5	4212	9	31	5	4	52	22	88	33
Rb	3	<1	6	6	12	2	17	36	5	3	13	3	6	3	7	<1
Sr	114	72	216	419	103	204	469	421	93	55	340	112	210	33	67	41
Th	9	<1	8	1	24	11	1	72	<1	2	<1	3	<1	1	1	<1
V	94	164	79	58	66	314	413	83	64	111	56	248	141	22	12	63
Zn	177	180	43	103	70	36	29	64	16	47	33	703	14	42	4	5
Zr	48	29	23	156	33	76	38	56	23	71	108	109	38	47	7	16
TOTAL	**101.5**	**101.9**	**99.5**	**100.5**	**101.7**	**101.2**	**100.0**	**99.0**	**100.1**	**99.4**	**100.9**	**100.6**	**100.3**	**100.3**	**100.5**	**100.8**
Mn/Fe	1.5	4.4	2.4	5.4	3.6	2.1	21.8	3.0	5.1	4.0	4.8	5.8	2.0	5.5	4.0	3.9
Si/Al	0.21	0.30	0.62	0.25	0.14	0.44	0.54	0.09	0.17	0.21	0.30	0.62	0.25	0.14	0.44	0.80
Ba/Sr	75	148	141	1.74	244	34	41	115	45	125	17	125	7	51	135	83
$\rho(g/cm^3)$	3.91	3.74	3.96	3.89	3.67	3.86	3.32	4.21	3.51	4.48	3.89	3.91	4.35	4.04	4.10	4.35

Abbreviations: PAL-Paling, GLO-Gloucester, LOH-Lohatlha, BIS-Bishop

Zr (7-156 ppm), Pb and Th. Contents of Pb (4 - 4212 ppm) and Th (<1 - 72 ppm) (Table 6.3) are considerably higher than in the siliceous ores. Exceptionally high values of 1249 and 4212 ppm Pb were detected in two fine crystalline, bedded samples from Glosam (GLO-186) and Bishop (BIS-245) (Table 6.3). Coarse crystalline bixbyite-rich ores have distinctively lower Pb (4 - 88 ppm) and Th (<1 - 3 ppm) contents than the fine crystalline bedded ores.

Table 6.4 Composition of botryoidal romanechite and Ba-rich wad, Fe-Mn-bearing dolomite of the Reivilo Formation and wad formed from dolomite of the Reivilo Fm.

Mine	GLO	BIS	GLO	LOH	BOETSAP*	LOH	LOH
No.	192/2	242	291	294		309/1*	182
Description	romanechite	romanechite	Ba-rich wad	Ba-rich wad	dolomite	dolomite	wad
major elements (in wt.%)							
SiO_2	6.22	2.19	20.7	6.48	<0.20	0.33	7.24
TiO_2	0.24	0.13	0.37	0.21	<0.04	<0.04	0.19
Al_2O_3	6.8	1.60	7.21	3.44	0.27	0.40	4.59
Fe_2O_3	8.09	0.57	12.5	21.4	0.52	0.50	6.93
Mn_3O_4	54.4	68.8	34.3	36.5	2.53	2.85	50.7
MgO	0.57	0.23	1.16	0.98	19.3	19.3	2.28
CaO	0.10	0.20	1.07	1.24	30.6	30.4	5.77
Na_2O	0.12	0.19	0.05	0.18	0.02	0.02	0.00
K_2O	1.23	0.20	1.49	0.87	0.02	0.05	1.31
P_2O_5	0.22	0.47	0.00	0.26	0.00	0.00	0.00
SO_3	0.00	0.00	0.08	0.04	0.00	0.00	0.05
H_2O	0.54	0.47	0.80	4.77	0.30	0.20	2.88
LOI	11.8	12.0	12.5	20.8	45.9	45.4	21.7
Ba	10.1	14.1	7.92	8.17			
trace elements (in ppm)							
Ba					32	<5	781
Co	78	510	26	29	<1	<1	27
Cr	71	22	42	26	<5	<5	80
Cu	<5	7	45	<5	2	14	<5
Ni	29	198	72	286	<3	<3	16
Pb	<5	<5	<5	<5	<1	<1	16
Rb	19	3	27	15	<1	<1	31
Sr	131	119	237	104	16	11	324
Th	<1	<1	<1	1	<1	<1	2
V	134	155	75	305	58	<5	48
Zn	89	317	5	75	6	5	32
Zr	19	<1	45	2	<5	4	24
TOTAL	**99.8**	**100.7**	**99.4**	**100.6**	**99.5**	**99.4**	**100.8**
Mn/Fe	6.9	124.3	2.8	1.8	5.1	5.9	7.5
Si/Al	0.8	1.2	2.5	1.7	<1	0.7	1.4
Ba/Sr	768	1185	334	785	2.0	0.7	2.4
ρ(g/cm3)	3.81	3.66	1.65	1.16	2.79	2.79	0.38

Abbreviations: GLO-Gloucester, LOH-Lohatla, BIS-Bishop, BOETSAP- Dolomite sample from Reivilo Fm. at Boetsap, about 130 km West of the Gamagara Ridge (Beukes, 1978). *ICP-MS analyses (MINTEK).

Supergene ores

Botryoidal romanechite aggregates and Ba-rich wad selvages around barite lenses contain considerable amounts of SiO_2 and Al_2O_3, with Si/Al ratios between 0.8 and 2.5 (Table 6.4). Mn/Fe ratios are much higher in the compact botryoidal aggregates (greater than 5) than in the wad (1.8 and 2.8), with Fe_2O_3 contents considerably greater in the Ba-rich wad samples (Table 6.4). Botryoidal aggregates and Ba-rich wad are anomalously Ba-rich, with Ba contents in the botryoidal aggregates ranging between 10.1 - 14.1 wt % which are distinctively higher than in the wad where it is between 7.92 and 8.17 wt %. Ba/Sr ratios are greater than 350 with Sr contents of between 104 - 237 ppm. K_2O and P_2O_5 occur in both sample types in variable concentrations up to 1.49 and 0.47 wt % respectively. The absolute concentrations of Co, Ni, Rb, Sr, V, and Zn in wad and botryoidal aggregates are very similar to those in the adjacent

Table 6.5 Enrichment/ depletion of components in Ba-poor wad formed from dolomite of the Reivilo Fm.*.

element	enrichment
SiO_2	22x
TiO_2	>5x
Al_2O_3	12x
Fe_2O_3	14x
Mn_3O_4	18x
MgO	0.12x
CaO	0.19x
Na_2O	<1x
K_2O	26x
Ba	>156x
Co	>27x
Cr	>16x
Cu	<0.35x
Ni	>16x
Pb	>16x
Rb	>31x
Sr	29x
Th	>2x
V	>10x
Zn	6x
Zr	6x
Mn/Fe	1.27x
Si/Al	2x
Ba/Sr	3.43x
ρ	0.14x

* Based on the compositions of samples LOH-309/1 (dolomite) and LOH-182 (wad).

UNIVERSITY OF JOHANNESBURG

Table 6.6A Correlation coefficients for element (element-group) pairs calculated for 17 samples of siliceous manganese ores and Wolhaarkop Breccia from the Eastern Belt.

Element (-group) pair	correlation coefficient	Element (-group) pair	correlation coefficient
SiO_2 ⇔ Mn_3O_4	-0.91	K_2O ⇔ Ni	0.70
SiO_2 ⇔ (Mn_3O_4+Fe_2O_3)	-0.97	K_2O ⇔ Rb	0.81
TiO_2 ⇔ Al_2O_3	0.74	K_2O ⇔ Th	0.71
(Mn_3O_4+Fe_2O_3) ⇔ (Al_2O_3+SiO_2+TiO_2)	-0.97	Pb ⇔ Th	0.76
Al_2O_3 ⇔ Ni	0.64	Rb ⇔ Th	0.94
Al_2O_3 ⇔ Pb	0.80	Rb ⇔ Sr	0.67
Al_2O_3 ⇔ Th	0.72	Sr ⇔ Th	0.75
Al_2O_3 ⇔ Zn	0.83	Sr ⇔ V	0.74
Fe_2O_3 ⇔ Co	0.82	Th ⇔ Zr	0.99
MgO ⇔ Rb	0.82	Cr ⇔ Sr	-0.79
MgO ⇔ Sr	0.69	Ni ⇔ Rb	0.71
MgO ⇔ Th	0.91	Ni ⇔ Th	0.81
SO_3 ⇔ Ba	0.78		

UNIVERSITY OF JOHANNESBURG

ferruginous manganese ore. However, the concentrations of Cr, Pb, Th, and Zr are much lower in the ferruginous manganese ore than in the supergene ores.

Dolomite of the Reivilo Formation and wad

Two samples of fresh, unweathered Mn-Fe-rich dolomite of the Reivilo Formation of the Campbellrand Subgroup, the unit immediately underlying the ferruginous manganese ores of the Western Belt, and one of a greenish-gray wad sample formed from Reivilo dolomite in recent times, have been analysed for comparative purposes.

The dolomite contains between 2.53 and 2.85 wt % Mn_3O_4 and about 0.5 wt % Fe_2O_3. The Mn/Fe ratio ranges between 5 and 6, a result in accordance with that of Beukes (1978). SiO_2 and Al_2O_3 contents are very low and the Si/Al ratio is below 1. Similarly concentrations of Ba and Sr are very low and the Ba/Sr ratio is close to 1. All other trace elements are present in negligible

amounts with only Cu (2 and 14 ppm), V (58 ppm in the Boetsap sample), Zn (6 and 5 ppm) and Zr (4 ppm in LOH-309/1) present in amounts above the detection limit.

The wad sample is very depleted in CaO and MgO relative to the dolomite precursor. If the dolomite sample LOH-309/1 is taken as a reference, then 81 % of the original amount of CaO and 90 % of MgO were removed (Table 6.5). This decrease is matched by enrichment factors of between 6 and 22 for Mn_3O_4, Fe_2O_3, SiO_2, TiO_2, Al_2O_3, and Zr from dolomite to wad (Table 6.5). All other trace elements follow this enrichment trend, except Cu, which is depleted below the detection limit of 5 ppm in the wad sample (Table 6.4). Particularly strongly enriched are K_2O (enrichment factor 26), Ba (enrichment factor >156) and Sr (enrichment factor 29) (Table 6.5). The density decreases from 2.79 g/cm^3 in the fresh dolomite to 0.38 g/cm^3 in the wad sample (Table 6.4).

A comparison of the composition of the wad with that of the ferruginous manganese ore reveals higher concentrations of SiO_2, MgO, CaO, and K_2O in the wad relative to ferruginous ore (Table 6.2). The contents of Fe_2O_3, P_2O_5, Na_2O are distinctively lower in the wad sample than in the ferruginous ores. The same is true for the trace elements Ba, Co, Cr, Cu, Ni, and Pb. Concentrations of Sr, Th, V, Zn, and Zr in wad and ferruginous manganese ores are very similar.

UNIVERSITY OF JOHANNESBURG

Table 6.6B Correlation coefficients for element (element-group) pairs calculated for 15 samples of ferruginous manganese ore from the Western Belt.

Element (-group) pair	**correlation coefficient**	**Element (-group) pair**	**correlation coefficient**
$(Al_2O_3+TiO_2)$ ⇔ $(Mn_3O_4+Fe_2O_3)$	-0.93	K_2O ⇔ Th	0.88
Al_2O_3 ⇔ $(Mn_3O_4+Fe_2O_3)$	-0.92	K_2O ⇔ Rb	0.91
Co ⇔ Cu	0.64	Ba ⇔ Pb	0.85
Co ⇔ Ni	0.86	Ba ⇔ Rb	0.78
Cu ⇔ Ni	0.65	Ba ⇔ Th	0.83
Cu ⇔ Zn	0.95	Pb ⇔ Rb	0.92
Ni ⇔ Zn	0.64	Pb ⇔ Th	1.00
Zn ⇔ (Cu+Ni+Co)	0.91	Rb ⇔ Sr	0.64
K_2O ⇔ Pb	0.89	Rb ⇔ Th	0.87

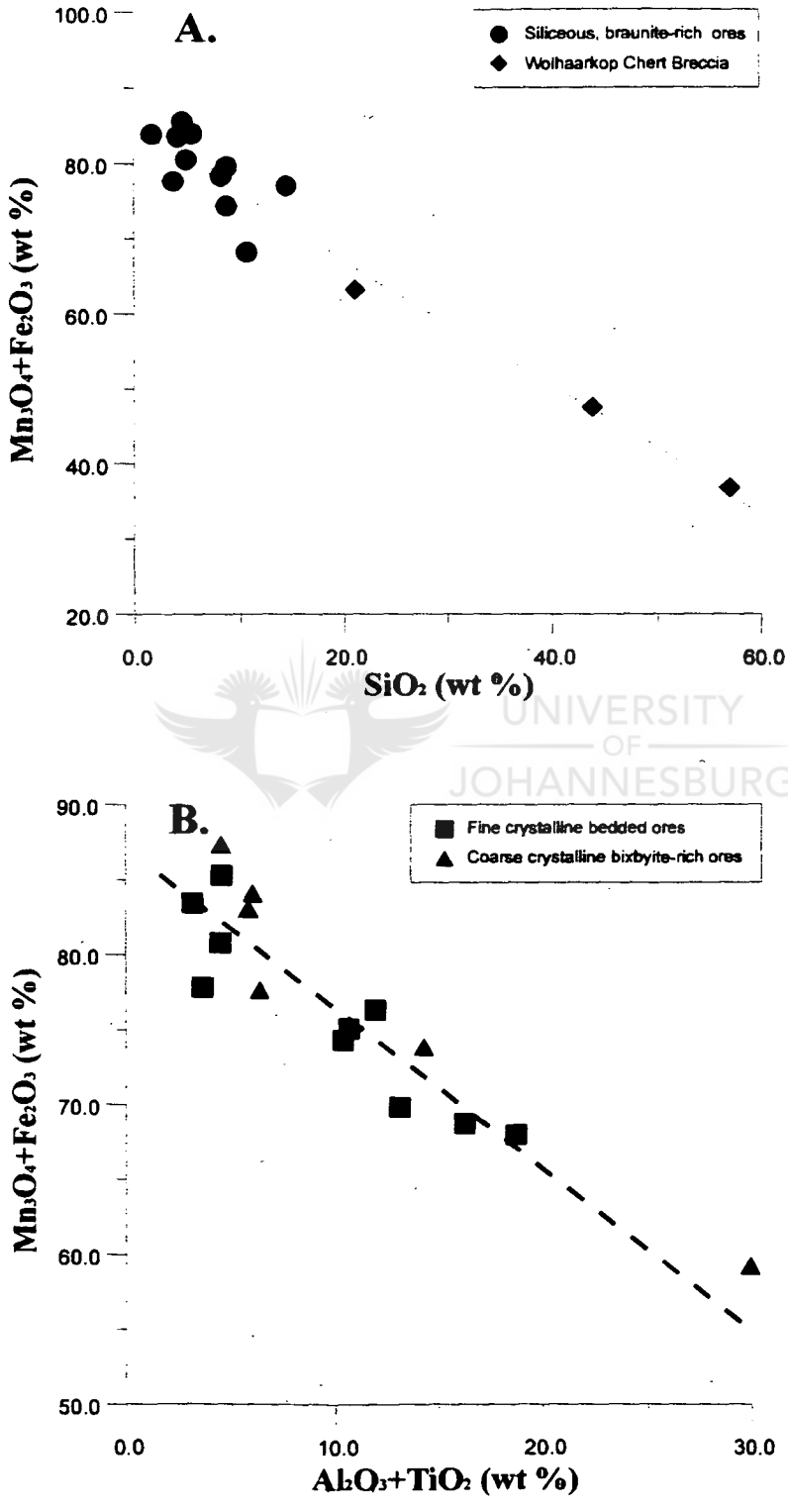

UNIVERSITY OF JOHANNESBURG

Fig. 6.11 Diagrams illustrating the strong negative correlation between the major chemical and clastic components in the siliceous (A) and ferruginous (B) manganese ores.

Geochemical associations

A strong negative correlation of SiO_2 and (SiO_2+Al_2O_3+TiO_2) with (Mn_3O_4+Fe_2O_3) is obvious for the siliceous ores (Table 6.6A, Fig. 6.11A). Al_2O_3 and TiO_2 are positively correlated and so are Al_2O_3, Pb and Zn. Fe_2O_3 displays strong positive correlation with Co. Positive correlation also exists between MgO and Rb, Sr and Th (Table 6.6A). The following geochemical associations can be distinguished from the obtained correlation coefficients for the siliceous ores: 1) Si, Al, Ti; 2) Al, Ti, Mg, Zn, Pb, (Ni, Th); 3) Mn, Fe; 4) Fe, Co; 5) K_2O, Rb, Sr, Pb, Th, (V, Zr); 6) Ba, SO_3.

A similar set of inter-element correlations is obtained for the ferruginous manganese ores (Table 6.6B). The concentrations of Al_2O_3 and (Mn_3O_4+Fe_2O_3) are negatively correlated (Fig. 6.11B). The group of Cu, Ni, Co and Zn shows strong positive correlation (Table 6.6B). Another distinct group of associated elements is represented by K_2O, Pb, Rb, Sr, Th and Ba.

Depositional environment and evolution of the manganese ore deposits

Manganese ores of both the Eastern or Western Belts of the Postmasburg manganese field apparently accumulated in a paleokarst environment which developed on Campbellrand dolomite during the period of erosion that preceeded deposition of the Olifantshoek red beds. However, the depositional setting of the ores in the two belts are completely different with those of the Eastern Belt representing subsurface solution collapse cave deposits (Fig. 6.12) and those of the Western Belt surficial wad accumulations in paleokarst depressions (Fig. 6.14).

Wolhaarkop breccia and siliceous manganese ore

A basic fact to understanding the depositional environment of the Wolhaarkop chert breccia and associated siliceous ores of the Eastern belt is that the hematitized Manganore Iron Formation overlying the Wolhaarkop chert breccia, is a lateral equivalent of the Asbestos Hills Subgroup (Kuruman and Griquatown Iron Formations) normally overlying the Campbellrand carbonates with a conformable contact (Beukes, 1986) (Fig. 6.12A). Alteration and slumping of the iron-formations of the Asbestos Hills Subgroup into large paleokarst sinkholes took place prior to the deposition of the overlying Olifantshoek red beds on the Maremane dome. This correlation suggests that the Wolhaarkop chert breccia accumulated as residual sediment

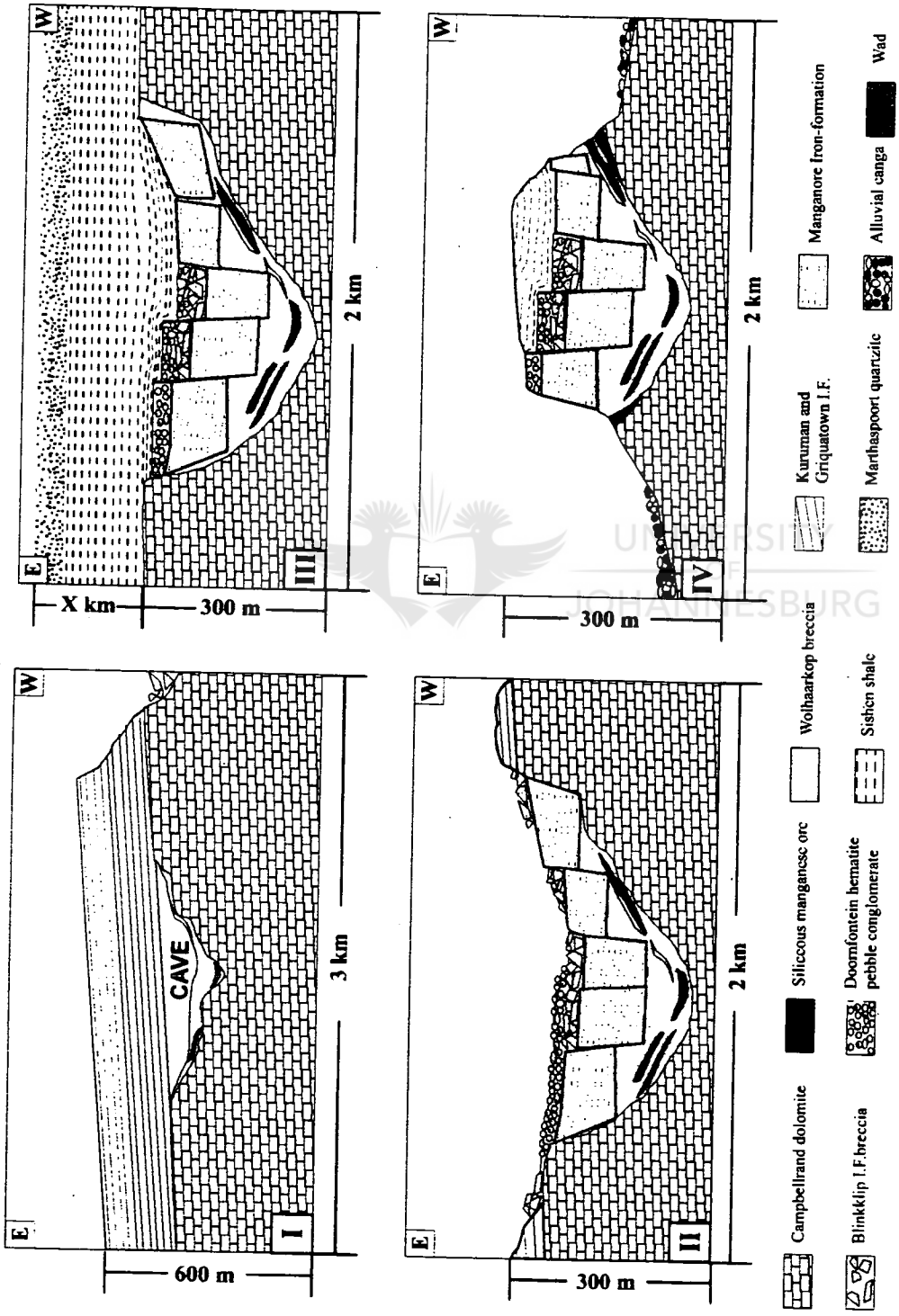

Fig. 6.12 The model envisaged for the origin of the Wolhaarkop Breccia and siliceous manganese ores of the Eastern Belt. I. Karst cave formation and accumulation of breccia as residual sediment during a period of intense weathering in the Late Paleoproterozoic, contemporaneous hematitization and enrichment of the overlying Kuruman and Griquatown Iron-formations to form Manganore Iron-formation. II. Collapse of caves under the load of the overlying Manganore Iron-formation, slumping of blocks of iron-formations into the caves. Iron-formation breccia and fluvial conglomerates of reworked iron-formation are deposited on top of the slumped blocks. III. After further karstification and slumping, the erosion surface is buried by aluminous, lateritic Sishen shale and a transgressive sequence of Marthaspoort quartzite and Paling shales and younger rocks. Manganese wad is recrystallized to braunite. IV. Renewed terrestrial exposure and erosion lead to the formation of inselberg-type hills (Klipfontein Hills) composed of weathering resistant Wolhaarkop Breccia and Manganore Iron-formation overlooking the less resistant Campbellrand dolomite plain. Formation of alluvial canga deposits along the footslope of the hills.

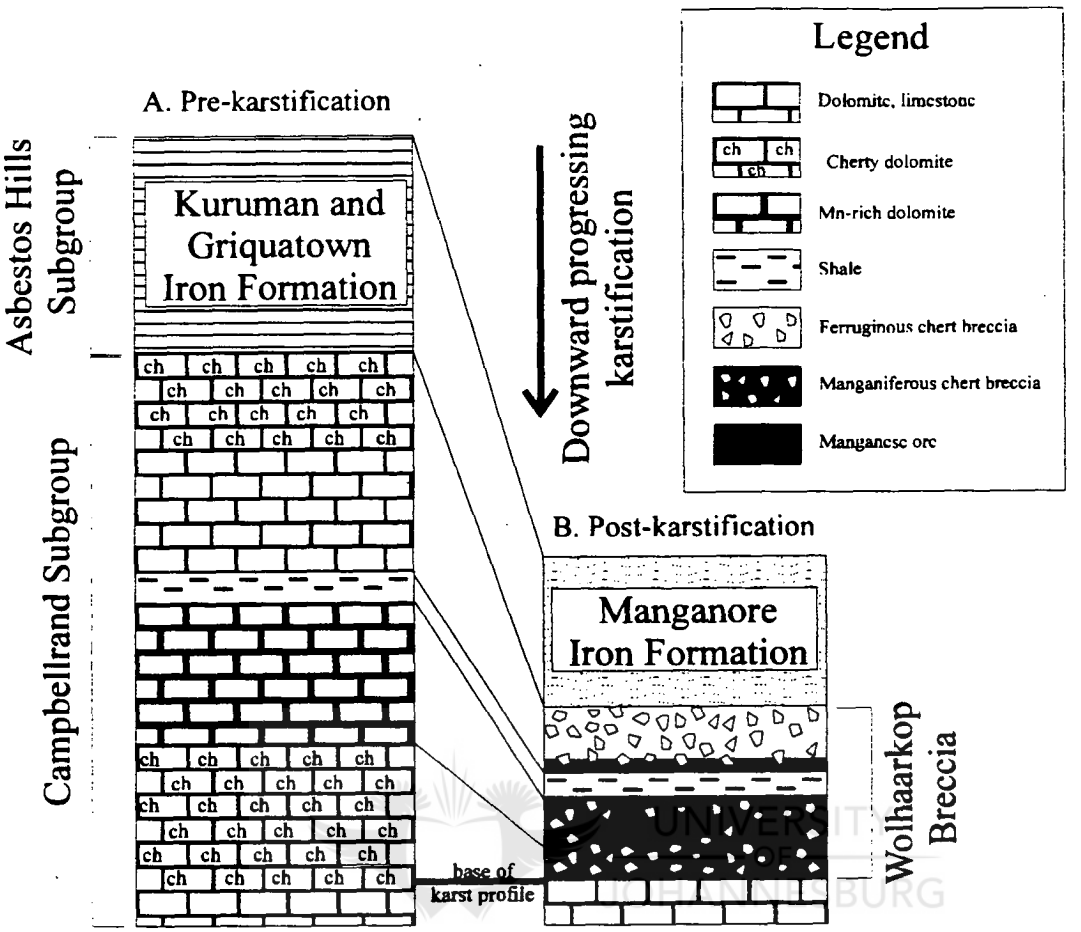

Fig. 6.13 The development of an inverted stratigraphic column during karstification and deposition of the residual Wolhaarkop chert breccia.

during karstification of the Campbellrand dolomites in paleokarst caves capped by iron-formations of the Asbestos Hills Subgroup (Fig. 6.12.I). The breccia developed only at the base of large sinkholes in the Campbellrand dolomites and overlain by slumped Manganore Iron Formation. As karstification advanced, progressively older dolomite beds decomposed into a chaotic mixture of chert fragments and wad. Relative abundances of wad and chert were controlled *in-situ* by the composition of the dissolved dolomite, resulting in the observed crude bedding of the Wolhaarkop breccia. The processes of downward progressing dolomite dissolution, residual subsurface sediment accumulation and slumping of altered iron-formation into the paleokarst caves (Fig. 6.12.II) resulted in an inverted stratigraphy, e.g. older Manganore iron-formation covers younger Wolhaarkop breccia and newly formed breccia beds accumulate below existing ones (Fig. 6.13).Dolomite-derived chert fragments and hematite clasts from the Manganore iron-formation are the only visible mineralogical remnants of the primary residual sediment (Fig. 6.15A). Diagenesis and low-grade metamorphism (Fig. 6.12.III) resulted in complete recrystallization of the wad matrix. Authigenic quartz overgrowth and apatite formed

during early diagenesis in the unconsolidated sediment. They are replaced by braunite and can thus be distinguished from minerals that formed cogenetic with braunite, such as small authigenic quartz crystals, Ba-muscovite, acmite and albite. The fine concentric zonation of many braunite crystals are evidence for variations in the availability of chemical constituents during their growth. This indicates the importance of fluid flow during recrystallization of the wad. Chert clasts replaced by barite are difficult to place in the paragenetic sequence; they may be of metamorphic or post-metamorphic hydrothermal origin as suggested by the presence of braunite inclusions in the barite.

Barite veins are evidence for localized postmetamorphic hydrothermal fluid flow. Veins filled by pyrolusite and botryoidal hematite are thought to be related to the percolation of meteoric water and recent supergene alteration. Subrecent erosion processes resulted in the exhumation of the sinkholes that are filled by weathering-resistant Manganore Iron Formation and Wolhaarkop chert breccia that weather positive against the surrounding dolomite host (Fig. 6.12.IV). Canga deposits of iron ore, manganese ore and Wolhaarkop breccia accumulate along the slopes of these hills. The introduction of Ba and K during chemical weathering of the siliceous ores by meteoric and/or ground water resulted in a considerable enrichment of these two elements, and the replacement of the metamorphic braunite assemblage by romanechite and cryptomelane (Fig. 6.15A).

UNIVERSITY OF JOHANNESBURG

Ferruginous manganese ores

The ferruginous ores of the Western Belt accumulated in karst depressions in the most manganese-rich and chert-deficient basal part of the Reivilo Formation of the Campbellrand Subgroup (Fig. 6.14.I). Well developed sedimentary bedding in the ferruginous manganese orebodies, the presence of interbeds of aluminous shale and hematite pebble conglomerate and the conformable and gradual contact of the manganese ores with the overlying sediments of the Gamagara Formation (Fig. 6.14.II) strongly suggest accumulation of the ores in a surficial paleokarst environment. The sedimentary and early diagenetic structures, such as early diagenetic microconcretions and soft sediment deformation structures, are very similar to those described from the unmetamorphosed Miocene karst-hosted Fe-Mn wad deposits if the Lindener Mark-type in Hesse, Germany (Schneiderhöhn, 1962; Bottke, 1969; Borchert, 1970; Brannath and Smykatz-Kloss, 1992). These ores are composed of poorly crystalline Na-K-Ca-Mg-bearing manganese oxides such as cryptomelane, todorokite, birnessite,

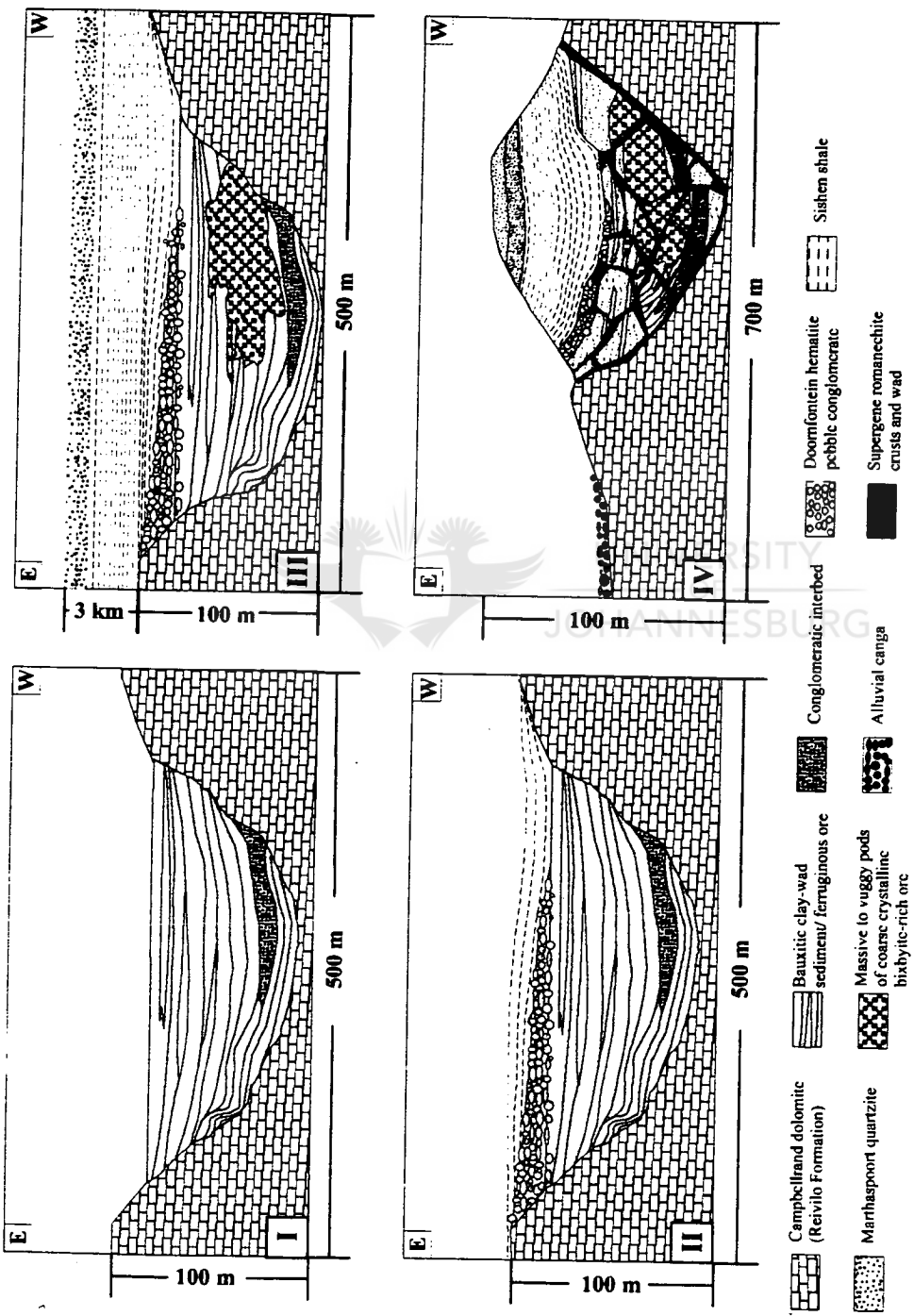

Fig. 6.14 The model envisaged for the origin of the ferruginous manganese ores of the Western Belt. I. Deposition of a layered succession of mixed bauxitic clay-ferromanganiferous wad with interbedded clay lenses and conglomeratic beds in open karst depressions of the Reivilo Formation. II. Doornfontein hematite pebble conglomerate and aluminous Sishen shales are deposited conformably overlying the clay-wad sediment. Burial metamorphism (formation of bedded braunite-partridgeite-diaspore-ephesite ore) leads to hydrothermal remobilization and formation of irregular pods of coarse crystalline bixbyite, ephesite and diaspore that crosscut the stratigraphy). IV. Recent terrestrial exposure and erosion results in renewed karstification, brecciation of the manganese orebody and formation of romanechite crusts and botryoidal aggregates, manganese wad and alluvial canga deposits.

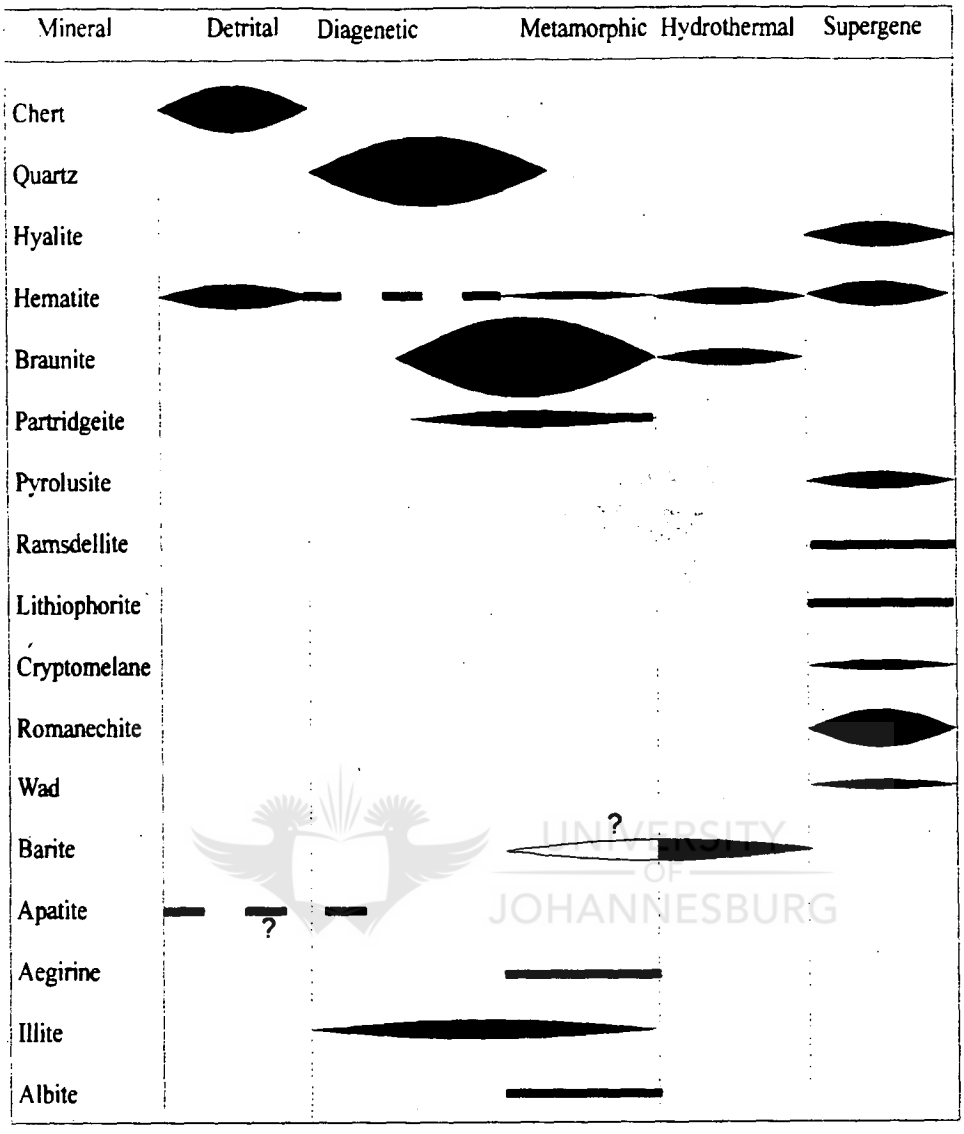

Fig. 6.15A Paragenetic table for the siliceous manganese ores of the Eastern Belt.

rancieite, lithiophorite, associated with kaolinite, goethite, lepidocrocite and hematite (Brannath and Smykatz-Kloss, 1992). The ores occur as soft, earthy, poorly crystalline wad or as hard, botryoidal banded aggregates of early diagenetic origin. This is very similar to textures observed in the ferruginous ores of the Postmasburg manganese field suggesting that these ores may also have accumulated as hydrous Mn^{4+}-Fe^{3+} oxides in a wad interbedded with fine clastic aluminous clays. A lateritic character of these clays is indicated by the positive correlation of Al_2O_3 with TiO_2 and their clastic character is confirmed by the negative correlation of (Al_2O_3+TiO_2) vs. the chemically precipitated (Mn+Fe).

The close association of the ores with aluminous, lateritic shales (Chapter 5, this thesis) and hematite pebble conglomerates deposited in a fluvial environment (Van Schalkwyk and Beukes,

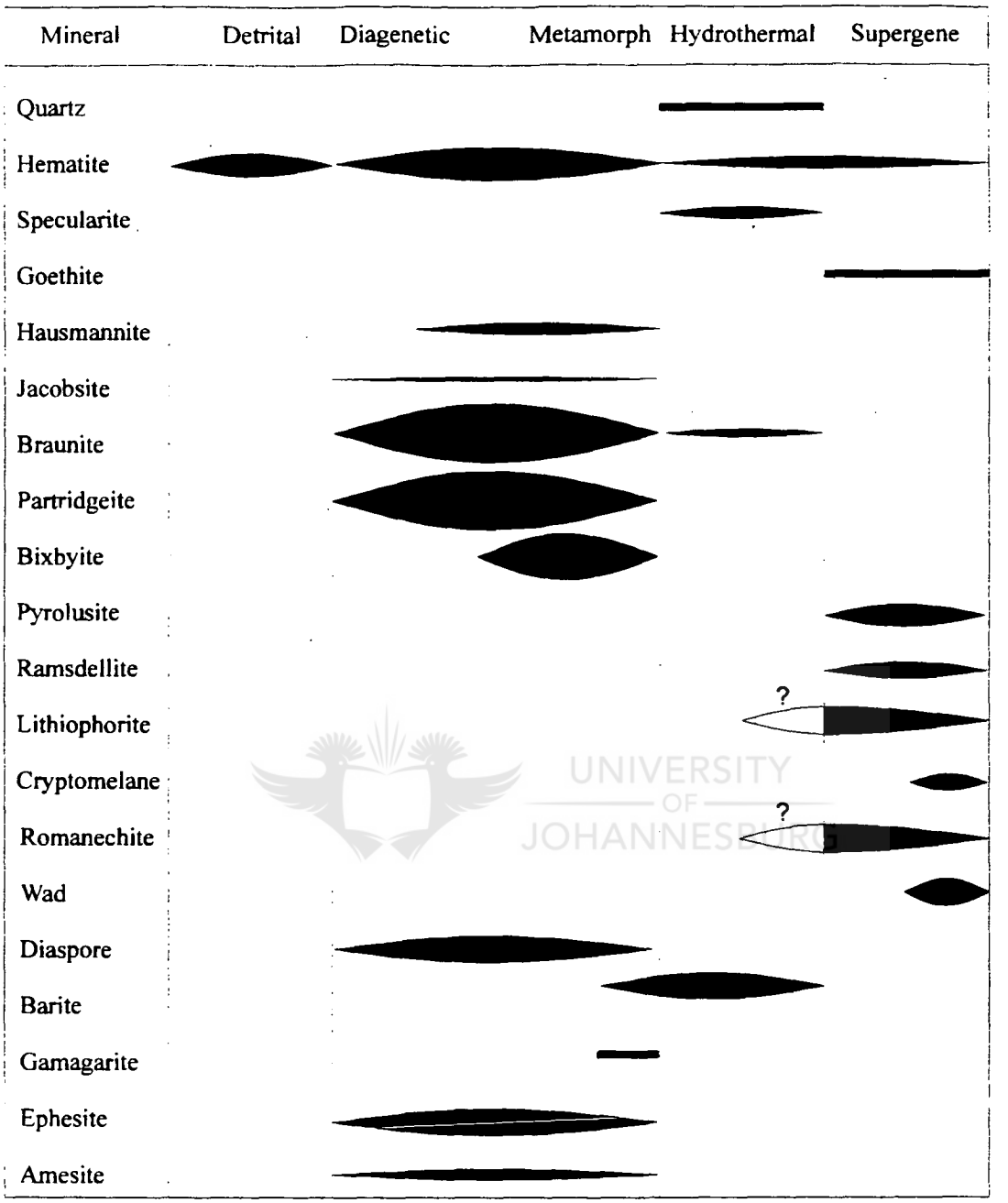

Fig. 6.15B Paragenetic table for the ferruginous manganese ores of the Western Belt.

1986) confirms a terrestrial depositional environment. Further evidence is supplied by the Na- and Mg-poor composition of the ores typical for manganese accumulations of freshwater origin (Fig. 6.16). Other geochemical arguments for a freshwater origin include the apparent lack of Fe-Mn separation as well as the low range of the concentrations of Cu, Ni, Co and Zn and the lack of covariation of these trace elements with Mn or Fe contents (Callender and Bowser, 1976; Calvert and Price, 1977). This freshwater geochemical signature is not surprising as karstification normally proceeds under the influence of meteoric or ground water in terrestrial environments

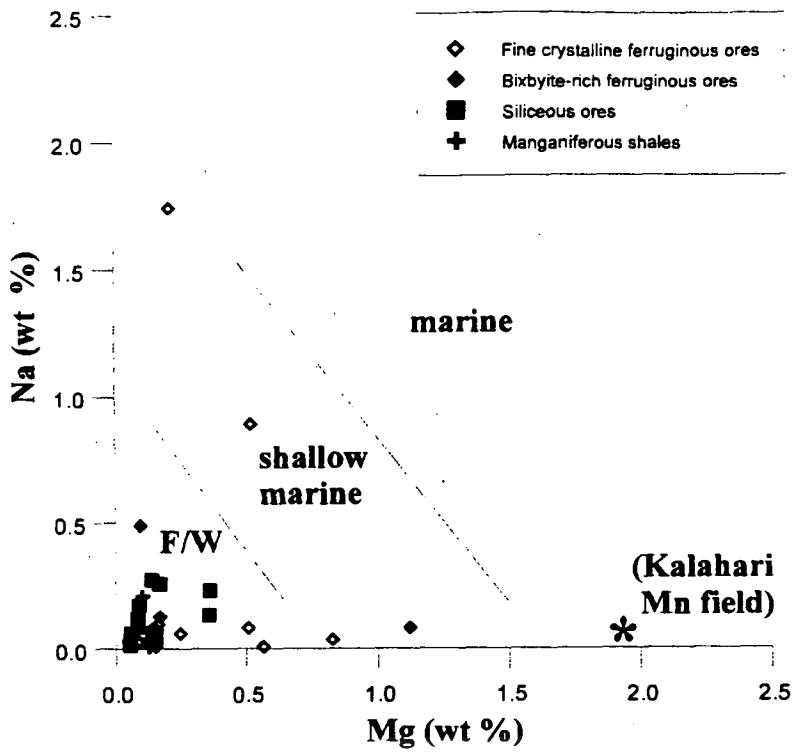

Fig. 6.16 Diagnostic Na-Mg plot to differentiate manganese deposits of marine, shallow marine and freshwater (f/w) origin (Nicholson, 1992). For comparison the composition of average low-grade Mamatwan-type ore (of marine origin) from the Kalahari manganese field is indicated.

(James and Choquette, 1987). Hematite grains present in the ore are of detrital origin. Diagenesis and low-grade metamorphism (Fig. 6.13.III) caused complete recrystallization of the original sediment into the observed assemblage of braunite, partridgeite, bixbyite, diaspore and ephesite. Products of diagenetic recrystallization can only be distinguished texturally (and thus tentatively) from products of metamorphic origin (Fig. 6.15B). Fine-grained, cryptic or fibrous braunite-partridgeite intergrowths in microconcretions and botryoidal crusts are considered early diagenetic in origin. Medium-crystalline, granular aggregates of braunite and partridgeite or pods of coarse crystalline bixbyite are possibly of late diagenetic or metamorphic origin (Fig. 6.14.III). Diagenetic/metamorphic formation of these Mn^{3+}-bearing manganese oxides from poorly crystalline Mn^{4+} precursor sediments is not unusual and is observed in many metamorphosed manganese deposits (Roy et al., 1990).

Multiple generations of veinlets and pods of recrystallized material suggest fluid mobilization from the hydrous wad during diagenetic and metamorphic recrystallization. The development of large pods of coarse crystalline bixbyite-rich ores is also related to fluid release during dehydration of the wad (Fig. 6.14.III). Formation of these coarse crystalline ores by postmetamorphic introduction of hydrothermal fluids cannot be entirely ruled out but appears

unlikely as bixbyite-rich ores are geochemically and mineralogically very similar to the fine crystalline-bedded ores and both types of ore appear to have formed penecontemporaneously. The occurrence of ephesite veins that originate in the coarse crystalline ores and extend into the overlying shales indicate focussed fluid flow associated with the origin of this ore type. Conversely, massive metasomatic replacement of aluminous shales by ephesite suggest pervasive release of Na-Ca rich fluids from the fine crystalline bedded manganese ores.

Veins of specularite and quartz crosscut the manganese orebodies together with lenses of barite and provide ample evidence for post-metamorphic hydrothermal fluid flow (Fig. 6.15B). Circumstances of hydrothermal fluid flow are, however, very poorly constrained.

Erosion and secondary karstification resulted in renewed surficial exposure of the manganese ores in geologically recent times (Fig. 6.14.IV). Slumping and *in-situ* accumulation of thick brecciated orebodies and the formation of extensive canga deposits are related to this erosional event. The metamorphic mineral assemblage is replaced by a characteristic suite of supergene minerals (Fig. 6.15B). Lithiophorite predominates in beds rich in aluminous shale. The formation of abundant romanechite and cryptomelane at the expense of braunite, partridgeite and bixbyite provides evidence for the introduction of Ba and K by oxidizing meteoric fluids identical to those altering the siliceous ores of the Eastern Belt.

UNIVERSITY JOHANNESBURG

Metamorphism

The timing of metamorphism is unknown at present but it may be related to thrusting and crustal thickening during the 1.8-1.9 Ga Kheis orogeny (Beukes and Smit, 1987). Peak metamorphic temperatures can be estimated fairly accurately. The pyrophyllite-diaspore association in the basal Gamagara shales overlying the manganese orebodies in the Western belt and the Manganore Iron Formation in the Eastern belt, is indicative of dehydration of kaolinitic clays under lower greenschist facies conditions at 300 to 350 °C (Anovitz et al., 1991). This temperature would correspond to a lithostatic pressure of 3-4 kbar. This result is in excellent agreement with

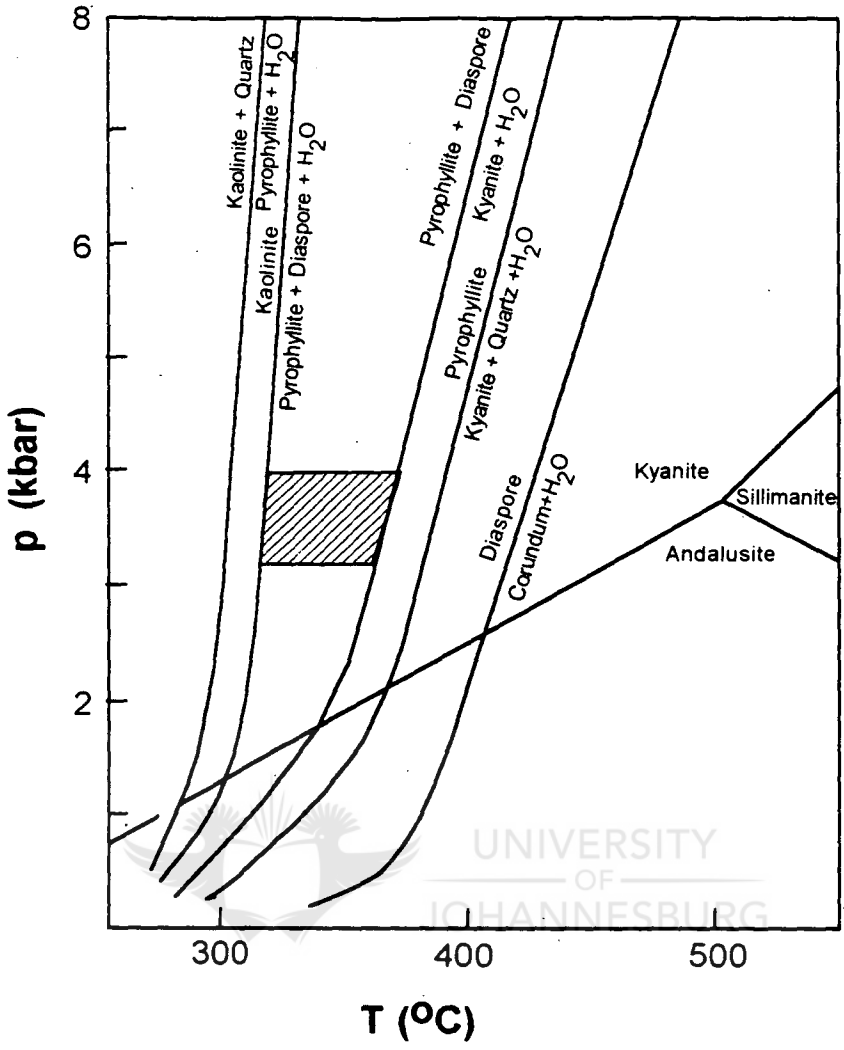

Fig. 6.17 Phase diagram showing stable equilibria in the system Al_2O_3-SiO_2-H_2O. Hatched area outlines peak metamorphic conditions suggested for the manganese ores and associated sediments of the Olifantshoek Group in the Postmasburg manganese field (from Anovitz et al., 1991).

metamorphic pT estimates by Plehwe-Leisen (1985) (T < 370 °C, p < 4 kbar). It also coincides with the temperature of formation of bixbyite determined by Nell et al. (1994) at between 315-370 °C. Nell et al. (1994) used a newly devised bixbyite-geothermometer based on the site distribution of Fe in the bixbyite structure. In contrast De Villiers (1983) derived temperatures of formation of below 300 °C for partridgeite and up to 470 °C for bixbyite. This is in obvious disagreement with all other above-mentioned estimates. De Villiers (1983) used the bixbyite thermometer proposed by Mason (1943) which is based on the observation that the amount of iron substituted into bixbyite increases with increasing temperature of formation. This bixbyite geothermometer (Mason, 1943) is thus only applicable, where an excess of iron was available during the formation of bixbyite. It should thus be applied with caution and in situations where bixbyite formed cogenetic with hematite.

Conclusions

Manganese ores in the Postmasburg manganese field represent weakly metamorphosed residual wad deposits that accumulated between 2.0-2.25 Ga during a period of extensive karstification and erosion of manganiferous dolomites of the Campbellrand Group of the Early Proterozoic-Late Archean Transvaal Supergroup. This period of erosion coincides with the development of the Mapedi/ Gamagara unconformity at the base of the Olifantshoek red bed sequence. Accumulation of Mn^{4+}-Fe^{3+} precipitates in this environment suggest the presence of an oxygenated atmosphere during the Early Proterozoic. This result coincides with supporting evidence from paleoweathering profiles developed below the Mapedi/ Gamagara erosion surface (Wiggering and Beukes, 1990; Holland and Beukes, 1990), the presence of lateritic paleosol profiles overlying the manganese ore deposits of the Postmasburg manganese field (Chapter 5, this thesis), and the occurrence of the first red bed sediments in the Mapedi Formation of the Olifantshoek Group. As the manganese deposits mark the very base of the Olifantshoek Group, they represent the presently oldest known oxidized terrestrial sediments that provide evidence for the presence of an oxygenated atmosphere in the Early Proterozoic.

UNIVERSITY OF JOHANNESBURG

Acknowledgements

The authors are greatly indebted to the geological staff of ASSMANG (Beeshoek), ISCOR (Sishen), SAMANCOR (Hotazel) and Rio Tinto Exploration for granting permission to visit their properties in the Postmasburg manganese field. Special thanks to Willem Grobbelaar (ASSMANG), Technical Manager at Beeshoek iron ore mine, for his generous support and many interesting discussions during field-work in 1993 and 1994 by one of us (J.G.). We also want to thank the team of the Arbeitsgruppe Salzlagerstätten und Untergrunddeponien at the Institut für Mineralogie und mineralische Rohstoffe, TU Clausthal (Germany), for the use of their analytical equipment. We are grateful to Arno Kleyenstüber and Tina Pohlandt-Watson (MINTEK) for ICP-MS analyses of two dolomite samples. We also want to express special thanks to Andreas "Hasselblad"-Pack, who gave us excellent advice on how to obtain high quality black and white photographs and photomicrographs and to Bruce Cairncross for improving the English of the manuscript.

References

Anonymous (1993). Union tin mines Ltd to be new miner of manganese. Mining Mirror, 32-33.

Anovitz, L.M., Perkins, D., and Essene, E.J. (1991). Metastability in near-surface rocks of minerals in the system Al_2O_3-SiO_2-H_2O. Clays Clay Min., 39, 225-233.

Bardossy, G. (1982). Karst bauxites, bauxite deposits on carbonate rocks. Elsevier, Amsterdam, 441 pp.

Beukes, N.J. (1978). Die Karbonaatgesteentes en Ysterformasies van die Ghaap-Groep van die Transvaal-Supergroup in Noord-Kaapland. Ph.D. thesis (unpubl.), RAU, 580 pp.

Beukes, N.J. (1986). The Transvaal Sequence in Griqualand West. In: Annhaeusser, C.R. and Maske, S. (eds.): Mineral deposits of Southern Africa; Geol. Soc. S. Afr., Johannesburg, 819-828.

Beukes, N.J., and Smit, C.A. (1987). New evidence for thrust faulting in Griqualand West, South Africa: Implications for stratigraphy and the age of red beds, Trans. Geol. Soc. S. Afr., 90, 378-394.

Boardman, L.G. (1940). The geology of the manganese deposits on Aucampsrust, Postmasburg, Trans. Geol. Soc. S. Afr., 43, 26-37.

Boardman, L.G. (1964). Further geological data on the Postmasburg and Kuruman manganese ore deposits, Northern Cape Province. In: Haughton, S.H.(ed.): Geology of some ore deposits in Southern Africa; Geol. Soc. S. Afr., Johannesburg, 415-440.

Borchert, H. (1970). On the ore-deposition and geochemistry of manganese, Mineral. Depos., 5, 300-314.

Bottke, H. (1969). Die Eisenmanganerze der Grube Dr. Geier bei Bingen/ Rhein als Verwitterungsbildungen des Mangans vom Typ Lindener Mark. Mineral. Depos., 4, 355-367.

Brannath, A., and Smykatz-Kloss, W. (1992). Mineralogische Untersuchungen an einigen hessischen Mangan-Eisenerzvorkommen. Chemie der Erde, 52, 3-31.

Callender, E., and Bowser, C.J. (1976). Freshwater ferromanganese deposits. In: Wolf, K.H. (ed.): Handbook of strata-bound and stratiform ore deposits, Vol. 7, Regional studies and specific deposits. Elsevier, Amsterdam, 341-394.

Calvert, S.E., and Price, N.B. (1977). Shallow water, continental margin and lacustrine nodules: Distribution and geochemistry. In: Glasby, G.P. (ed.): Marine manganese deposits. Elsevier, Amsterdam, 45-86.

De Villiers, J. (1956). The manganese deposits of the Union of South Africa. In: Symposium del Manganeso, XX Congreso Geologico International, Mexico City, 40-52.

De Villiers, J. (1960). Manganese deposits of the Union of South Africa. Handbook 2, Geol. Surv. S. Afr., Pretoria, 280.

De Villiers, J.E. (1943). A preliminary description of the new mineral partridgeite, Amer. Mineral., 28, 336-338.

De Villiers, J.E. (1943). Gamagarite, a new vanadium mineral from the Postmasburg manganese deposits, Amer. Mineral., 28, 329-335.

UNIVERSITY OF JOHANNESBURG

De Villiers, J.E. (1944). The origin of the iron and manganese deposits in the Postmasburg and Thabazimbi areas, Trans. Geol. Soc. S. Afr., 47, 123-135.

De Villiers, J.E. (1945a). Some minerals occurring in South African manganese deposits, Trans. Geol. Soc. S. Afr., 48, 17-25.

De Villiers, J.E. (1945b). Lithiophorite from the Postmasburg manganese deposits, Amer. Mineral., 30, 629-634.

De Villiers, J.E. (1983). The manganese deposits of Griqualand West, South Africa: Some mineralogic aspects, Econ. Geol., 78, 1108-1118.

De Villiers, J.P.R., and Buseck, P.R. (1989). Stacking variations and nonstoichiometry in the bixbyite-braunite polysomatic mineral group. Amer. Mineral., 74, 1325-1336.

Du Toit, A.L. (1933). The manganese deposits of Postmasburg, South Africa, Econ. Geol., 28, 95-122.

Frenzel, G. (1980). The manganese ore minerals. In:Varentsov, I.G., and Grasselly, Gy. (Eds.): Geology and geochemistry of manganese, Schweizerbart, Stuttgart, 1, 25-157.

Grobbelaar, W.S., and Beukes, N.J. (1986). The Bishop and Glosam manganese mines and Beeshoek iron ore mine of the Postmasburg area. In: Annhaeusser, C.R., and Maske, S. (eds.): Mineral deposits of Southern Africa; Geol. Soc. S. Afr., Johannesburg, 957-961.

Hall, A.L. (1926). The manganese deposits near Postmasburg, West of Kimberley, Trans. Geol. Soc. S. Afr., 29, 17-66.

Holland, H.D., and Beukes, N.J. (1990). A palaeoweathering profile from Griqualand West, South Africa: Evidence for a dramatic rise in atmospheric oxygen between 2.2 and 1.9 BYBP. Amer. J. Sci., 290-A, 1-34.

James, N.P., and Choquette, P.W. (1988). Paleokarst. Springer Verlag, New York, 416 pp.

Nel, L.T. (1929). The geology of the Postmasburg manganese deposits and the surrounding country. Explanation of the geological map. Geol. Surv. S. Afr., Pretoria, 109 pp.

Nicholson, K. (1992). Contrasting mineralogical-geochemical signatures of manganese oxides: Guides to metallogenesis. Econ. Geol., 87, 1253-1264.

Plehwe-Leisen, E. von (1985). Geologische und erzpetrographische Untersuchungen der Manganerze des Postmasburgfeldes, Noerdliche Kapprovinz, Südafrika. Ludwig-Maximilians Universität München, 129 pp.

Ramdohr, P. (1960). Die Ermineralien und ihre Verwachsungen. Akademie Verlag, Berlin, 1089 pp.

Reimer, T.O. (1986). Alumina-rich rocks from the Early Precambrian of the Kaapvaal Craton as indicators of paleosols and as prooducts of other decompositional reactions. Prec. Res., 32, 155-179.

Roy, S., Bandopadhyay, P.C., Perseil, E.A., And Fukuoka, M. (1990). Late diagenetic changes in manganese ores of the Upper Proterozoic Penganga Group, India. Ore Geol. Rev., 5, 341-357.

Schneiderhöhn, H. (1931). Mineralbestand und Gefüge der Manganerze von Postmasburg, Griqualand West, Südafrika, N.Jb.Min., Beilagen, 64 A, 701-726.

Schneiderhöhn, H. (1962). Erzlagerstätten-Kurzvorlesungen. G. Fischer Verlag, Jena, 371 pp.

UNIVERSITY OF JOHANNESBURG

Strauss, C.A. (1964). The iron ore deposits in the Sishen area, Cape Province. In: Haughton, S.H. (ed.): The geology of some ore deposits in Southern Africa. Geol. Soc. S. Afr., Johannesburg, 393-403.

Truter, F.C., Wasserstein, B., Botha, P.R., Visser, D.J.L., Boardman, L.G., and Paver, G.L.(1938). The geology and mineral deposits of the Olifantshoek area, Cape Province. An explanation to Sheet No. 174 Oliphants Hoek. Geol. Surv. S. Afr., Pretoria, 107 pp.

Van Schalkwyk, J.F., and Beukes, N.J.(1986). The Sishen iron ore deposit, Griqualand West. In: Annhaeusser C.R. and Maske S. (eds.): Mineral deposits of Southern Africa; Geol. Soc. S. Afr., Johannesburg, 931-956.

Van Wyk, J.P.(1980). Die geologie van die gebied Rooinekke-Matsap-Wolhaarkop in Noord-Kaapland met spesiale verwysing na die Koegas -Subgroep, Transvaal-Supergroep. Unpubl. MSc. thesis, RAU, 159 pp.

Van Wyk, and Beukes, N.J. (1982). The geology of the Sishen iron ore deposit. In: Glen, H.W. (ed.): Proceedings, 12th CMMI Congress. Geol. Soc. S. Afr., Johannesburg, 203-211.

Wiggering, H., and Beukes, N.J. (1990). Petrography and geochemistry of a 2000-2200-Ma-year-old hematitic Paleo-alteration profile on Ongeluk Basalt of the Transvaal Supergroup, Griqualand West, South Africa. Prec. Res., 46, 241-258.

UNIVERSITY OF JOHANNESBURG

Chapter Seven

Mineralogy and mineral chemistry of manganese ores of the Postmasburg manganese field, Northern Cape Province, South Africa

Abstract

The diagenetic to very low-grade metamorphic manganese ores of the Postmasburg manganese field provide a unique example of oxide-facies manganese ores in a Paleoproterozoic paleokarst setting. The ores are composed mainly of braunite group minerals, including braunite, partridgeite and bixbyite, with rare braunite II and Ca-poor silica-depleted braunite. Iron-poor partridgeite is distinguished from iron-rich bixbyite and the occurrence of Ca-poor silica-depleted braunite is reported for the first time. Braunite and partridgeite formed during early diagenesis but remained stable under greenschist metamorphic conditions. In contrast, bixbyite is apparently a product of metasomatic remobilisation under peak metamorphic conditions. It is suggested that local variation of the metamorphic mineral association reflect variations of the host rock composition and that they are not related to changing pT-conditions of metamorphic alteration, a model promoted by previous authors. The phase chemistry of braunite, braunite II and bixbyite is explained by the existing polysomatic stacking model for the braunite group. However, the chemical composition of partridgeite and Ca-poor silica-depleted braunite can only be explained by adding a distinct new module layer with partridgeite composition to the polysomatic stacking model.

UNIVERSITY JOHANNESBURG

Introduction

Manganese deposits of the Postmasburg manganese field occur along the so-called Eastern and Western Belts between Sishen in the north and Postmasburg in the south in the Northern Cape Province of South Africa (Fig. 7.1). Mining of manganese ores commenced in 1922 and was discontinued in 1989, despite considerable remaining ore reserves (Grobbelaar and Beukes, 1986), a decision based on the more favourable composition and availability of high-grade manganese ores from the giant Kalahari manganese field only 45 km to the north of the Postmasburg manganese field.

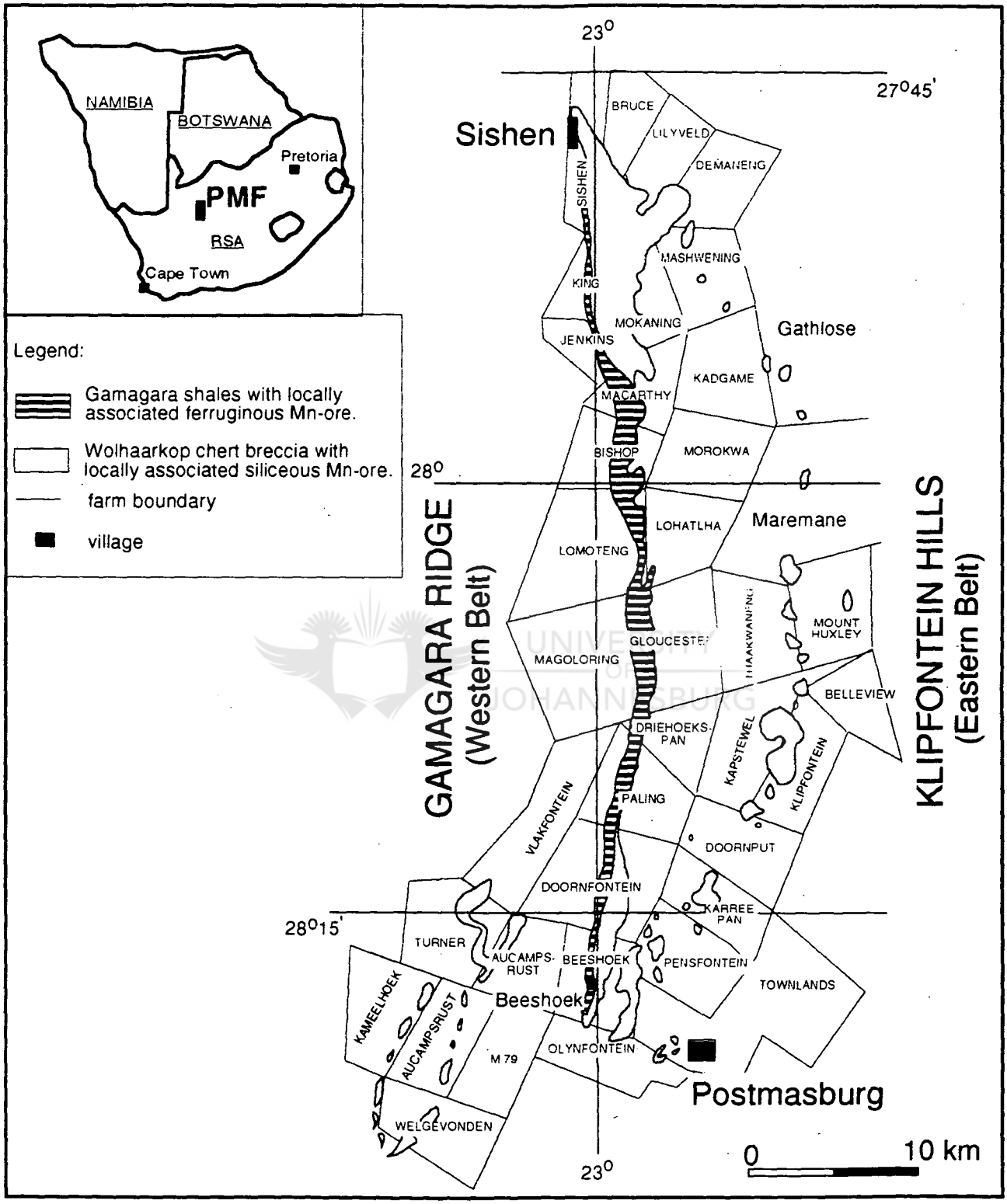

Fig. 7.1 Regional map of the Postmasburg manganese field showing the location of the deposits of ferruginous manganese ore along the Gamagara Ridge (Western Belt) and the occurrence of Wolhaarkop Breccia (and associated manganese ores of the siliceous type) in the Klipfontein Hills (Eastern Belt), the Gamagara Ridge and in the Aucampsrust area.

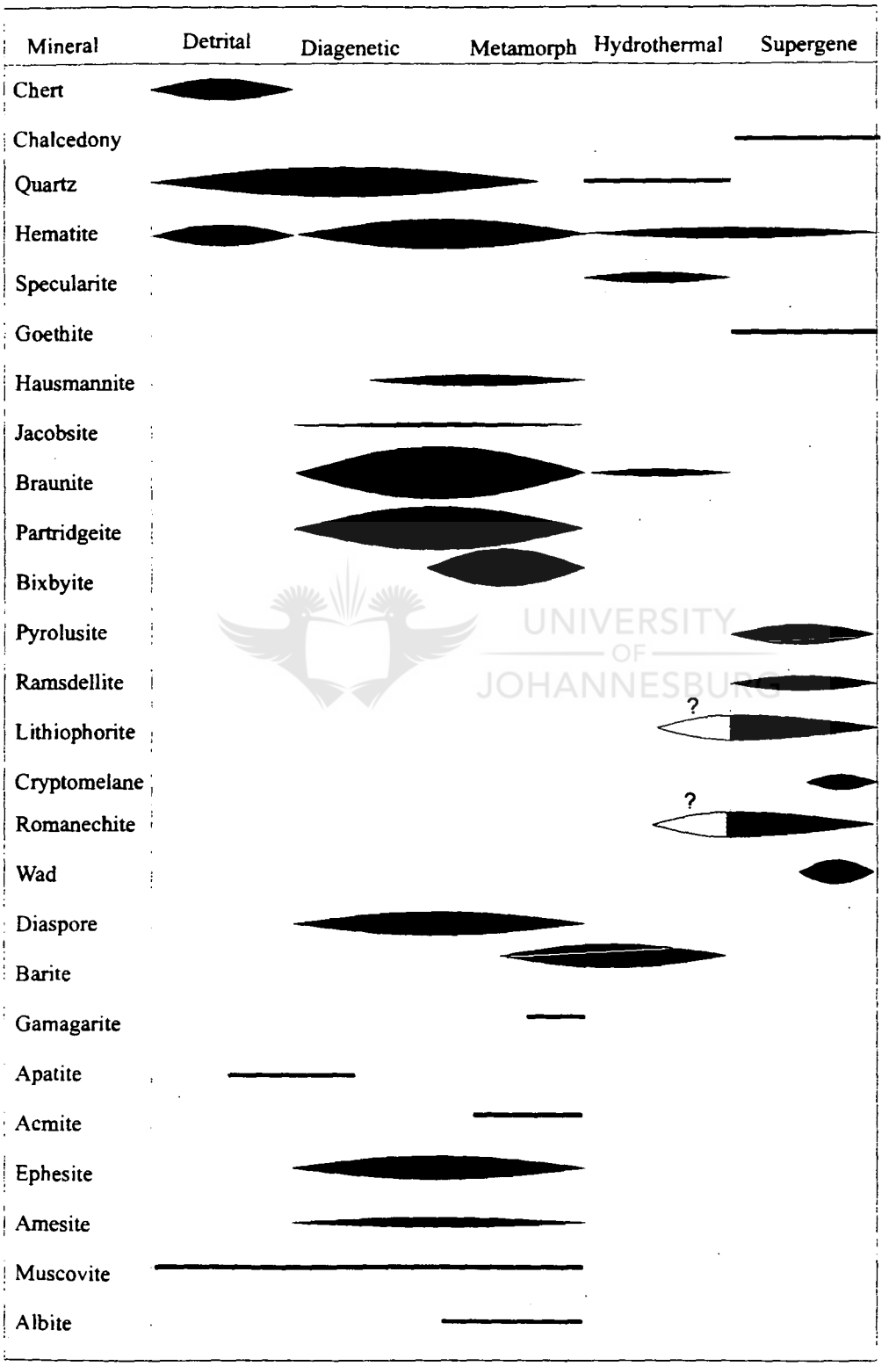

Fig. 7.2 Mineral paragenetic table for the manganese ores of the Postmasburg manganese field.

Table 1 List of minerals encountered in the Postmasburg manganese field.

Mineral Name	Formula
jacobsite	$Mn^{2+}Fe_2O_4$
hausmannite	$Mn^{2+}Mn^{3+}{}_2O_4$
braunite	$Mn^{2+}Mn^{3+}{}_6SiO_{12}$
partridgeite*	Mn_2O_3
bixbyite	α-$(Mn,Fe)_2O_3$
manganite	γ-MnOOH
romanechite	$Ba_{1\text{-}2}Mn^{4+}{}_8O_{16} \cdot xH_2O$
cryptomelane	$K_{1\text{-}2}Mn^{4+}{}_8O_{16} \cdot xH_2O$
manganomelane	$(Na, K, Ba)_{1\text{-}2}Mn^{4+}{}_8O_{16} \cdot xH_2O$
lithiophorite	$Li_2Mn^{2+}Mn_5{}^{4+}Al_4O_{18} \cdot 6H_2O$
pyrolusite	β-MnO_2
ramsdellite	MnO_2
hematite	α-Fe_2O_3
goethite	α-FeOOH
diaspore	α-AlOOH
barite	$BaSO_4$
apatite	$Ca_5[(OH,F,Cl)/(PO_4)_3]$
gamagarite	$Ba_2(Fe^{3+},Mn)[(OH,H_2O)/(VO_4)_2]$
ephesite	$(Na,Ca)Al_2[(OH)_2/Al(Al,Si)Si_2O_{10}]$
muscovite	$KAl_2[(OH)_2/AlSi_3O_{10}]$
amesite	$(Mg,Fe)_2Al_2[(OH)_8/(Si_2,Al_2)O_{10}]$

* Partridgeite is not a mineral recognized by the IMA (International Mineralogical Association), see further discussion in text.

UNIVERSITY OF JOHANNESBURG

The manganese ores of the Postmasburg manganese field can be subdivided into three geologically, mineralogically and petrographically distinct types, namely ferruginous, siliceous and supergene types. Ferruginous manganese ore was of greatest economic importance and occurs along the central part of the Gamagara ridge or Western Belt of manganese deposits (Fig. 7.1). Siliceous manganese ores were mined from small deposits along the Klipfontein Hills or Eastern Belt and the northern and southern extremities of the Gamagara Ridge (Fig. 7.1) (Hall, 1926; Nel, 1929; De Villiers, 1960). Supergene ores occur where manganese was remobilised from ferruginous or siliceous manganese ores during supergene alteration processes. The supergene ores occur locally as pyrolusite veins and nodules, and as boxwork or cauliflower-shaped aggregates and botryoidal laminated crusts of romanechite and cryptomelane.

The rather complex ore mineral assemblage, composed of a variety of manganese oxides and gangue minerals of diagenetic, metamorphic, hydrothermal, and supergene origin (Table 7.1, Fig. 7.2) has been subject of several detailed mineralogical and ore petrographic studies (Schneiderhöhn, 1931; De Villiers, 1960, 1983; Plehwe-Leisen, 1985). All these studies relied largely on the optical identification of ore and gangue minerals, a procedure unreliable for manganese oxides (Ramdohr and Frenzel, 1956; Frenzel, 1980), especially for optically very similar minerals such as the braunite group (Kleyenstüber, 1985) and the manganomelane group of minerals (Frenzel, 1980). Very little is known about the chemical composition of the various ore-forming and gangue minerals. In this study an attempt is made to characterize the occurring minerals in greater detail and to relate the major and minor element composition of the minerals to their paragenetic and geological setting. Special attention is given to the crystal chemistry of the braunite group of manganese oxides.

Analytical techniques

Identification of ore and gangue minerals was based on a combination of X-ray powder diffraction analysis carried out on whole rock samples and mineral separates and ore petrographic studies. Electron microprobe analysis were then carried out on a CAMECA CAMEBAX 355 microprobe with an attached LINK ExLII energy dispersive spectrometer operated at 15kV and 10 nA sample current. Data acquisition was 80 sec per spot analysis. A pure cobalt metal standard was used for calibration of the spectrometer. All results were ZAF corrected. Several spot analyses were performed for each mineral in one or several small preselected areas on the samples. Only average compositions are reported in this study to ensure the representative

character of the results. Mineral formulas were calculated using the program Minfile, version 3-88 (Afifi and Essene, 1988).

Geological setting

The manganese ore deposits of the Postmasburg manganese field are situated on the Maremane dome defined by dolomites of the Campbellrand Subgroup and iron-formation of the Asbestos Hills Subgroup of the Ghaap Group of the Late Archean to Paleoproterozoic Transvaal Supergroup (2.5-2.7 Ga) dipping gently at less than 10° in an arc to the north, east and south (Beukes, 1978). Only the eastern half of this dome is exposed (Fig. 7.3). To the west the Transvaal strata are overlain along the Mapedi/ Gamagara erosional unconformity by Late Paleoproterozoic (2.2-1.9 Ga) siliciclastic sediments of the Olifantshoek Group (Fig. 7.3). Further to the west older rocks belonging to the Transvaal Supergroup, including iron-formation, diamictite, and andesitic lavas, are thrust over the Gamagara Formation along the north-south striking, westerly dipping, low-angle Black Ridge thrust fault (Beukes and Smit, 1987).

Manganese ores, and closely associated hematitic iron ores (Grobbelaar and Beukes, 1986; Van Schalkwyk and Beukes, 1986) occur along or immediately below the Mapedi/ Gamagara unconformity. The hematitized Manganore Iron Formation and its reworked equivalents, the alluvial Doornfontein hematite pebble conglomerate and the Blinkklip iron formation breccia, are preserved as infills of large karstic sinkhole structures. Van Wyk (1980) and Van Wyk and Beukes (1982) showed that the Manganore Iron Formation is a lateral equivalent of the Kuruman and Griquatown Iron Formations of the Asbestos Hills Subgroup of the Transvaal Supergroup. High-grade iron ores are currently mined from the Manganore Iron Formation at the Sishen and Beeshoek iron ore mines to the north and south of the Maremane dome (Fig. 7.1). Siliceous ores of the Eastern Belt are developed in the Wolhaarkop chert breccia which is considered to be a subsurface solution collapse breccia that accumulated as the iron formations of the Asbestos Hills Subgroup slumped into the dolomites of the Campbellrand Subgroup to form the ferruginized Manganore Iron Formation (Fig. 7.4). Karstification and alteration of the iron formations took place during a period of intense karstification on the Maremane dome some 2.0 - 2.25 Ga ago (Van Schalkwyk and Beukes, 1986).

Minable bodies of high-grade, siliceous manganese ore occur only in the lower part of the Wolhaarkop breccia near the contact with the underlying dolomite (Fig. 7.4).

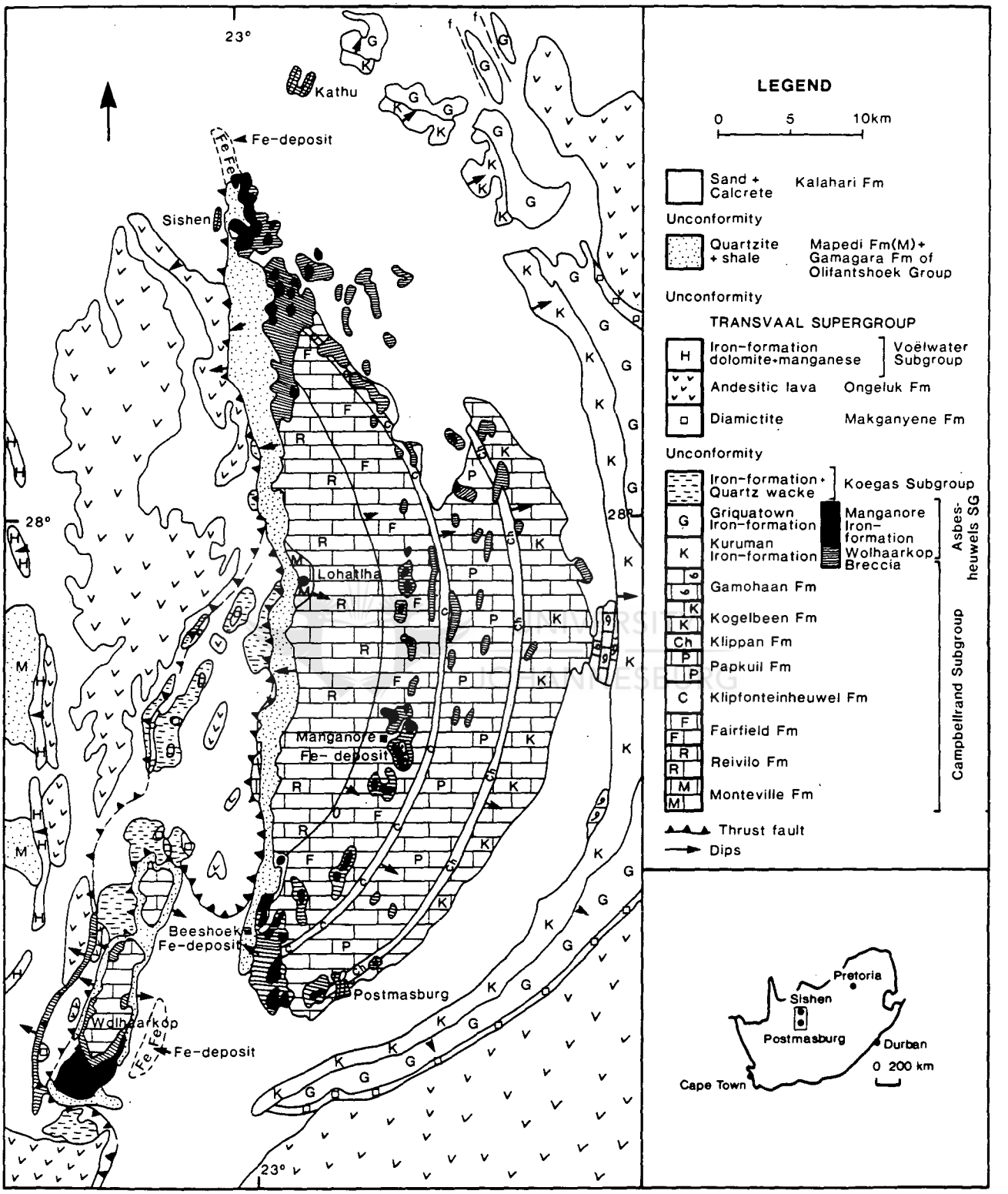

Fig. 7.3 Regional geological map of the Maremane dome showing the location of iron and manganese ore deposits in relation to the underlying dolomite of the Campbellrand Subgroup and the overlying sediments of the Gamagara Formation. Note the position of thrust faults to the West of the Gamagara Ridge (modified after Beukes, 1986).

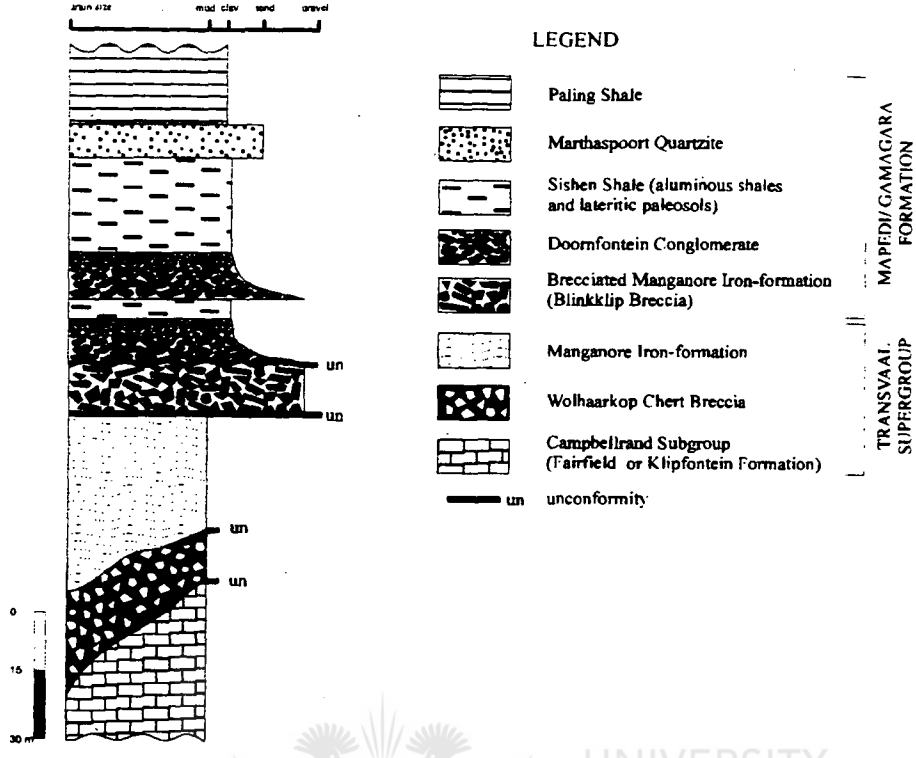

UNIVERSITY OF JOHANNESBURG

Fig. 7.4 Schematic section illustrating the geological setting of the Wolhaarkop Breccia (and siliceous manganese ores) unconformably below slumped and hematitized Manganore Iron Formation.

Orebodies are small and their distribution unpredictable. Lenses, pods, and sheet-like bodies have been mined (De Villiers, 1960).The ores are massive, fine to medium crystalline and dense. Coarse crystalline barite occurs in irregular patches within the Wolhaarkop breccia (De Villiers, 1944; De Villiers, 1960) where it replaces chert fragments. Siliceous manganese ores and the manganiferous matrix of the Wolhaarkop breccia are composed of braunite, associated with variable amounts of authigenic quartz, and small amounts of partridgeite, and hematite. Apatite, acmite (De Villiers, 1960) and Ba-muscovite are rare. Romanechite, cryptomelane, pyrolusite, ramsdellite, and lithiophorite occur as products of supergene alteration.

Ferruginous ores of the Western belt form the base of the Gamagara Formation in the central part of the Gamagara ridge where the succession unconformably overlies Mn-rich dolomites of the Reivilo Formation (Fig. 7.5). Aluminous shales or hematite pebble gritstones/ conglomerates of the Mapedi/ Gamagara Formation rest directly on irregular bodies of ferruginous manganese ore

that are confined by the intensively karstified floor of dolomite with closely spaced pinnacles and deep solution cavities (Fig. 7.6). The transition of the manganese ores into the overlying siliciclastic sediments of the Mapedi/ Gamagara Formation is conformable. Small pods or mudclasts of manganese oxides occur in the immediately overlying aluminous shales and hematitic gritstones. The locally variable basal portion of the Mapedi/ Gamagara Formation, composed of ferruginous manganese ores, Doornfontein hematite pebble conglomerate and aluminous shales were deposited an alluvial floodplain environment (Van Schalkwyk and Beukes, 1986). The Doornfontein hematite pebble conglomerate of the Gamagara Formation fines upward into a laterally variable succession of aluminous shales and mudstones composed of pyrophyllite, diaspore, kaolinite, variable amounts of hematite (Fig. 7.5). Illite, anatase and

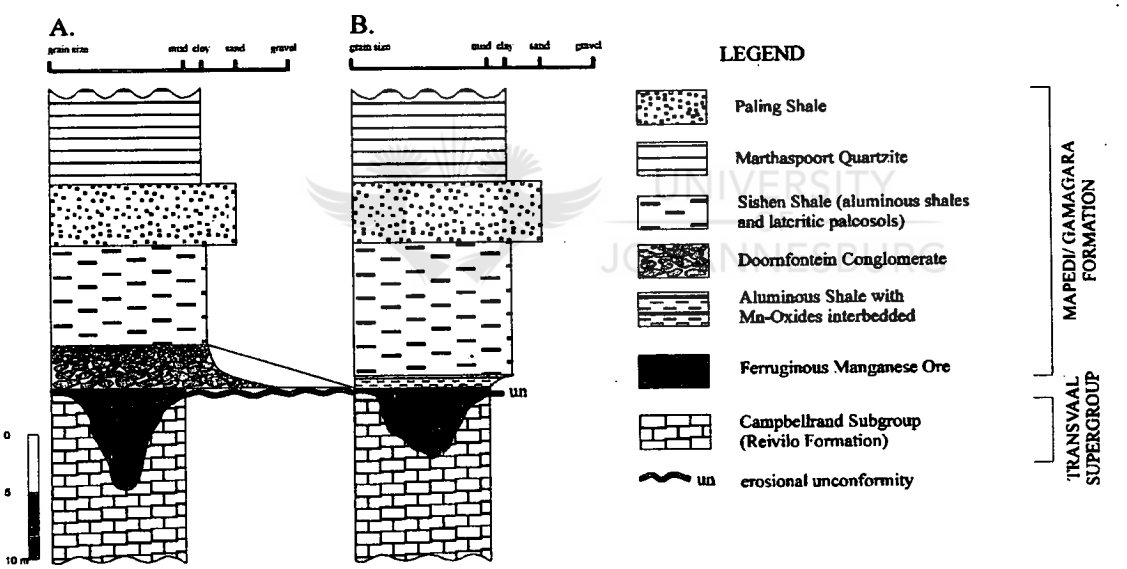

Fig. 7.5 Schematic sections illustrating the typical geological setting of the ferruginous manganese orebodies filling in karst depressions in the Fairfield dolomite (A) overlain by Doornfontein hematite pebble conglomerate and (B) grading into aluminous and ferruginous Sishen Shale.

rutile occur as minor constituents in the aluminous shales that grade into a thick, monotonous succession of quartzites and siltstones interbedded with red- and cream-coloured muscovite-rich shales.

Two varieties of ferruginous manganese ores can be distinguished macroscopically. Fine crystalline bedded ores are characterized by abundant sedimentary and diagenetic structures such as fine bedding, interbeds of shale or hematite pebble conglomerate and soft sediment deformation structures. These ores are composed of an intimate association of braunite,

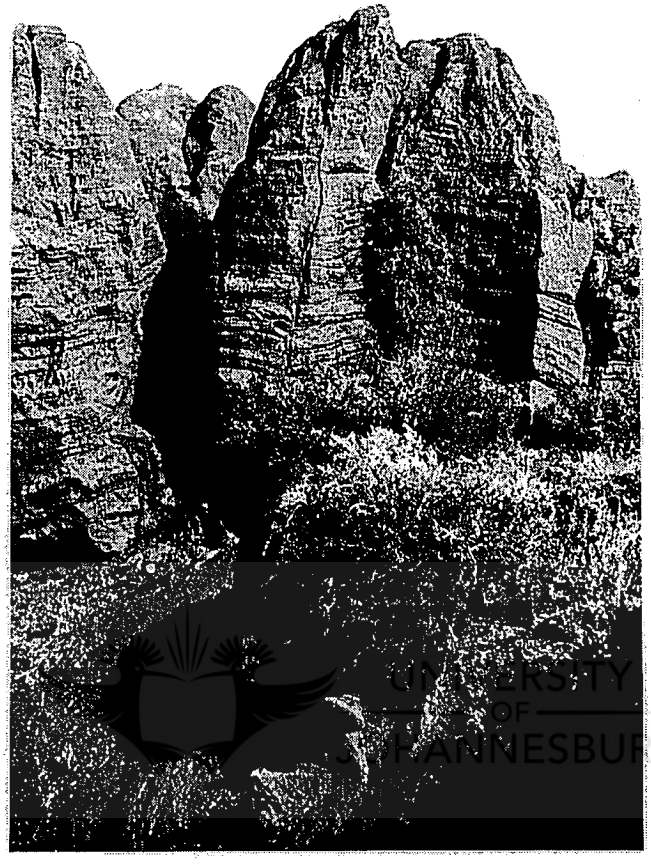

Fig. 7.6 Tall dolomite pinnacles at Glosam mine that are exposed due to mining operations.

partridgeite, hematite, diaspore and ephesite. Romanechite, cryptomelane, pyrolusite and lithiophorite are of supergene origin.

Coarse crystalline ores in contrast are characterized by their massive idioblastic appearance with typical textures such as veining, brecciation and vug infill. The coarse crystalline ores form irregular pods and appear to have formed penecontemporaneously with the fine crystalline bedded ores. The mineral assemblage in the coarse crystalline ferruginous manganese ores is characterized by the abundance of Fe-rich bixbyite associated with very coarse crystalline diaspore, ephesite and little barite. Braunite and hematite occur locally. The supergene mineral association is identical to that observed in the fine crystalline bedded ferruginous manganese ores.

The formation of lenses and veins of barite and coarse crystalline specularite that crosscut the Wolhaarkop breccia as well as the ferruginous manganese ore bodies is related to the postmetamorphic influx of hydrothermal fluids. Veins filled by botryoidal hematite and pyrolusite may have formed by descending ground or meteoric water. The formation of supergene ores is related to geologically recent oxidation processes induced by the introduction of meteoric or ground water.

Petrographical and geochemical evidence indicate that siliceous and ferruginous manganese ores of the Postmasburg manganese field accumulated as residual paleokarst sediments in distinct geological settings during the period of intensive chemical weathering and erosion that preceeded the deposition of the siliciclastic sediments of the Olifantshoek Group. Mn^{4+}-Fe^{3+}-oxide wad

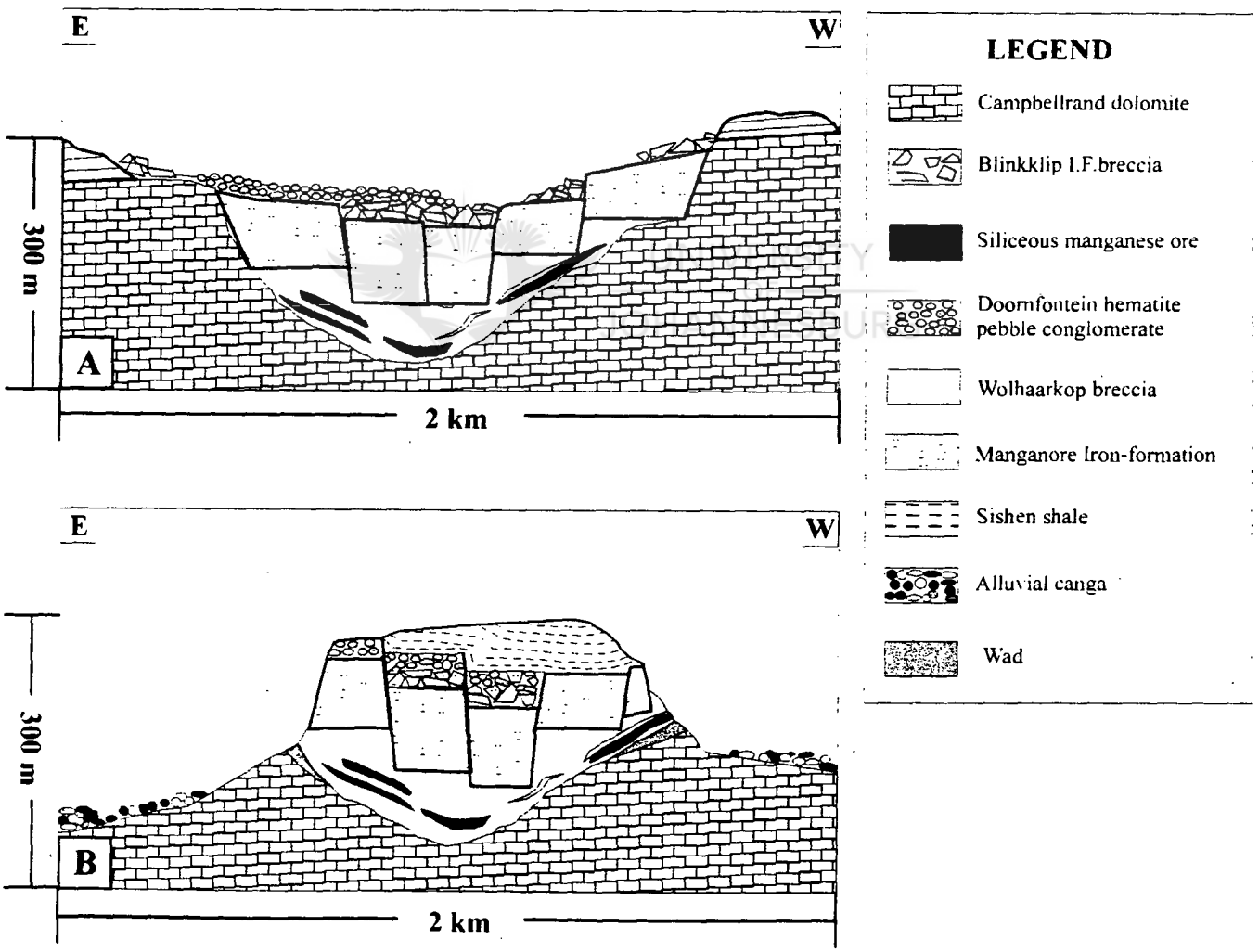

Fig. 7.7 Simplified model for the origin of the Wolhaarkop Breccia and siliceous manganese ores of the Eastern Belt. A. Wolhaarkop chert breccia accumulates as residual sediment in karst caves into which subsequently portions of hematitized Manganore Iron-Formation slump. Fluvial conglomerates of reworked iron-formation cover the slumped iron-formation. B. Following burial and greenschist facies metamorphism, renewed terrestrial exposure and erosion lead to relief inversion. The sinkhole infills are positively exposed against the surrounding dolomite host. Alluvial canga deposits accumulate along the footslope of the hills.

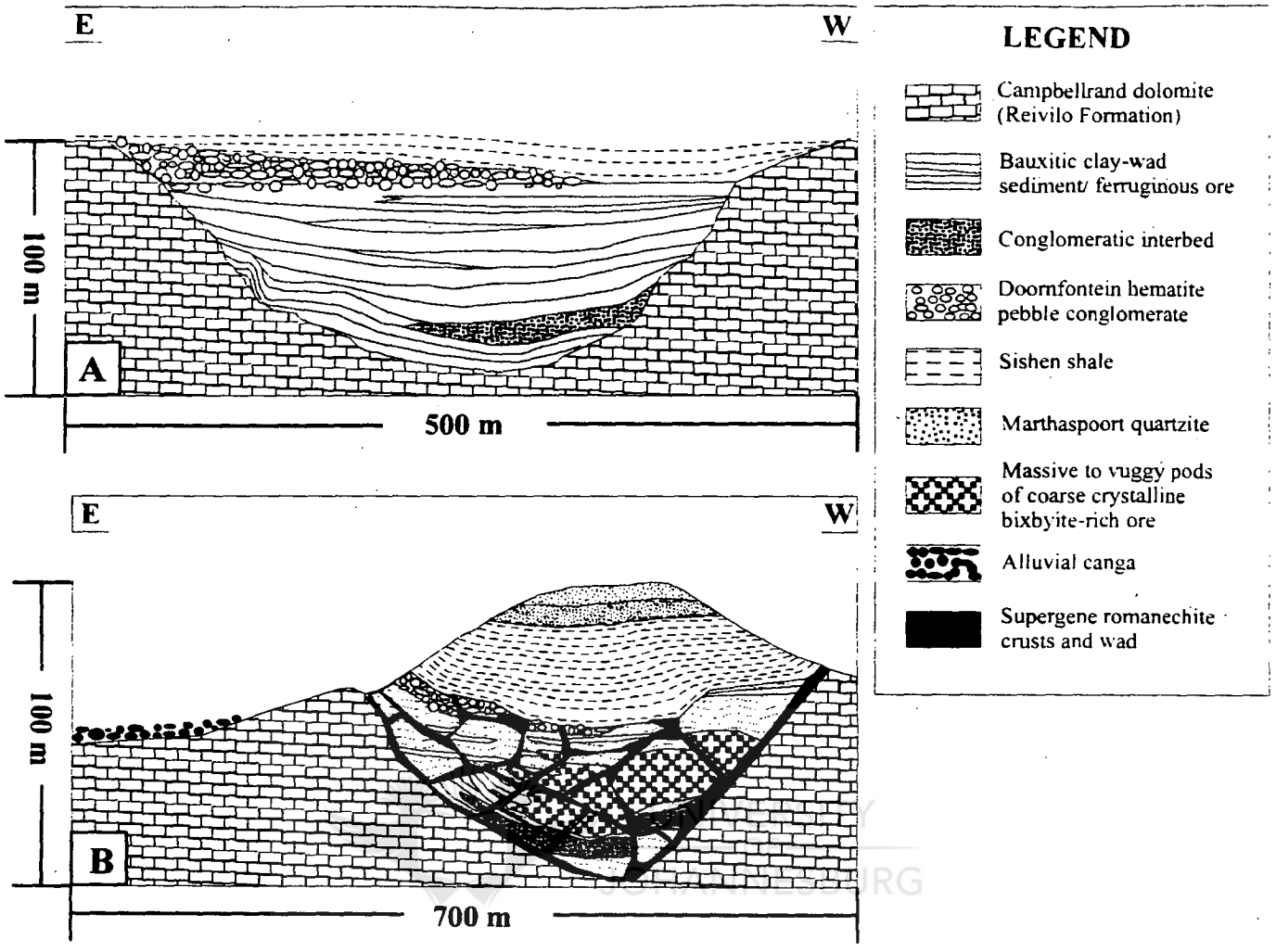

Fig. 7.8 Simplified model for the origin of the ferruginous manganese ores of the Western Belt. A. A layered succession of mixed bauxitic clay-ferromanganiferous wad with interbedded clay lenses and conglomeratic beds is deposited in open karst depressions of the Reivilo Formation and buried below hematite conglomerates and lateritic clays of the Gamagara Formation. B. Greenschist facies metamorphism is succeeded by terrestrial exposure and erosion resulting in renewed karstification, brecciation of the manganese orebody, formation of romanechite crusts and manganese wad and accumulation of alluvial canga deposits.

accumulated in karst caves intimately associated with the Wolhaarkop subsurface solution collapse breccia to form the siliceous type of ore (Fig. 7.7), and in open sinkholes intermixed with lateritic clays to form the ferruginous type of ore (Fig. 7.8). The karstified Fe- and Mn-bearing Paleoproterozoic dolomites of the Campbellrand Subgroup represent not only the host for the manganese ore bodies, are also regarded as source for the iron and manganese accumulation. Alteration of the iron-formations of the Asbestos Hills Subgroup, preserved as the hematitized and slumped Manganore iron formation are attributed to the same period of intensive chemical weathering (Fig. 7.7) (Van Schalkwyk and Beukes, 1986; Strauss, 1964).

The ores were subjected to diagenetic compaction and low grade regional metamorphism. A second period of subaerial exposure resulted in relief inversion (Fig. 7.7). Renewed karstification of the Campbellrand dolomites caused slumping and brecciation of the

Fig. 7.9 Reflected light photomicrographs. A. Small, euhedral, authigenic quartz crystals in mosaic textured braunite matrix, braunite replaced by manganomelane (white) along grain boundaries (200x, oil immersion, sample MAN-238); B. Concentrically zoned euhedral braunite crystals in vug filled by supergene romanechite (white) (320x, oil immersion, sample BEE-208). The profile analysed by electron microprobe is marked (arrow, compare Fig. 12) (200x, oil immersion, sample BEE-208); C. Round partridgeite microconcretions (light gray), partly replaced by romanechite (white) in massive braunite matrix (gray) (200x, oil immersion, sample GLO-187).

ferruginous manganese ores into secondary karst depressions (Fig. 7.8). Intense chemical weathering and remobilization of manganese resulted locally in the origin of supergene manganese ores. Associated with the chemical weathering are mechanical erosion and the formation of canga deposits along the footslope of the hills.

Petrography of siliceous ores of the Eastern Belt

The Wolhaarkop breccia, host to the siliceous ores of the Eastern Belt is composed of recrystallized chert clasts set in a fine crystalline matrix of braunite, hematite and authigenic quartz. Many of the recrystallized chert fragments show overgrowths of authigenic quartz which are replaced by fine crystalline braunite. Small authigenic quartz crystals show no indication of replacement (Fig. 7.9A). Braunite becomes more abundant towards the basal contact of the Wolhaarkop breccia with the the underlying dolomite. Small high-grade orebodies occur in this lower, manganiferous part of the breccia and are composed of braunite associated with minor amounts of partridgeite and hematite. The braunite occurs as equigranular mosaic-textured aggregates composed of subhedral grains 5 to 1000 μm in diameter. Braunite crystals are often distinctly zoned (Fig. 7.9B). The zonation is characterized by different zones of variable brown to brownish-gray colour shades. Lamellar and spotty intergrowth of different braunite varieties and of braunite with partridgeite are present. Small amounts of partridgeite are very intimately intergrown with the braunite. Up to millimeter-sized, poorly defined grains of parallel intergrown braunite and partridgeite lamellae have been observed.

Needle-shaped and platy, anhedral grains of hematite occur and become more common where the matrix of the breccia is ferruginous. Euhedral apatite prisms with a diameter of up to 250 μm are present occasionally as already been described by De Villiers (1945). The apatite is replaced by diagenetic/ metamorphic braunite and also by supergene romanechite. Sheaf-like aggregates of Ba-muscovite were found in strongly weathered siliceous ore. Coarse crystalline, white barite occurs in irregular patches in the Wolhaarkop Breccia, intimately intergrown with braunite. Aggregates of divergent needles of acmite and compact crystalline masses of coarse crystalline albite ($Ab_{94}An_6$), have been described to occur in braunitic ores from Sishen and Mokaning by De Villiers (1945). These minerals were not found during this study.

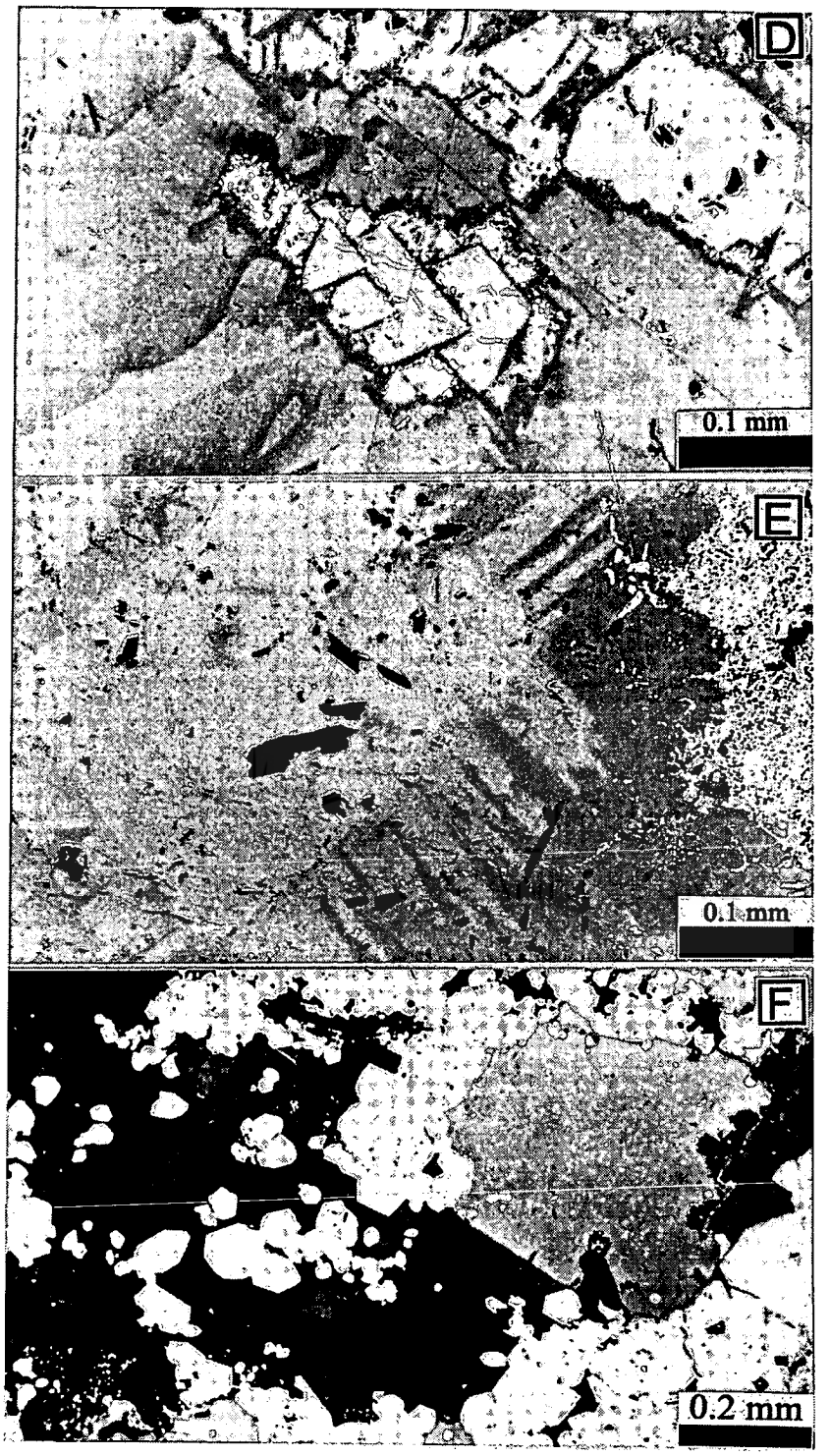

Fig. 7.9 (cont.) Reflected light photomicrographs. D. Braunite lamellae (gray) intersect partridgeite blasts (light-gray), in a matrix of finely intergrown Si-depleted braunite and braunite, replacement of partridgeite and Si-depleted braunite by romanechite (white) (200x, oil immersion, sample GLO-187); E. Flames of Si-depleted braunite (medium gray) originate on the surface of a large partridgeite idioblast (light gray) and project into braunite (gray). Romanechite appears white, diaspore black (200x, oil immersion, sample GLO-187); F. Idioblastic bixbyite cubes (light gray) with small hematite inclusions (white) surrounded by hematite (white), lithiophorite (dark gray) and diaspore (black, short laths) (50x, oil immersion, sample LOH-79).

Petrography of ferruginous ores of the Western Belt

Fine crystalline bedded ores are composed of braunite, partridgeite, and diaspore associated with variable amounts of hematite, ephesite and amesite. Up to 50 cm thick manganese-rich braunite-partridgeite beds are interbedded with equally thick aluminous, shale-rich beds. Braunite predominates in shale interbeds rich in alumosilicates, partridgeite is more abundant in oxide- and diaspore-rich beds. Different laminae within these beds are characterized by different mineral assemblages, different internal textures or variable degrees of supergene alteration. Sedimentary and diagenetic structures are abundant: Irregular pinch and swell structures, fine lamination, and lensoidal bedding are common. Early diagenetic structures include soft sediment deformation structures and the formation of ovoidal microconcretions (Fig. 7.9C), botryoidal layered crusts and anastomosing veinlets composed of braunite and partridgeite. Ovoid-shaped microconcretions and botryoidal layered crusts composed of braunite and partridgeite are characterized by extremely fine crystalline fibrous, cryptic or layered braunite-partridgeite intergrowths.

Aggregates of braunite with well developed equigranular mosaic texture and grain sizes between 10 and 500 μm and massive to idioblastic partridgeite are of late diagenetic or low-grade metamorphic origin. Orientated intergrowths of braunite with partridgeite are common (Fig. 7.9B). In one sample from Glosam mine flames of silica-depleted braunite were found to protrude from partridgeite-braunite grain boundaries into the surrounding braunite and are also present as isolated flames (Fig. 7.9E) in braunite grains. These flames appear very similar to those of pentlandite in pyrrhotite (Ramdohr, 1969). 5-100 μm large, anhedral hausmannite grains are a rare constituent of the partridgeite-braunite assemblage and appear to replace only partridgeite. Ephesite forms subhedral micaceous plates, up to 100 μm long, that occur concentrated along distinct laminae or in clusters, together with diaspore in up to 500 μm long laths.

Coarse crystalline ores are composed of cubic bixbyite idioblasts that are up to 30 mm in diameter and intergrown with coarse crystalline diaspore, ephesite, and amesite (Fig. 7.9F), as well as mosaic-textured aggregates of braunite and pseudohexagonal plates of hematite. Gamagarite, a Ba-vanadate, was discovered as new mineral species by De Villiers (1943) in bixbyite-rich ore from Glosam mine. It forms clusters of up to 1 cm long brownish red needles intergrown with bixbyite, ephesite, diaspore and amesite. Bixbyite cubes are characterized by pseudosymmetric, lamellar twinning (Schneiderhöhn, 1931; Ramdohr, 1969) and concentric growth zonation along the {100} planes. Orientated intergrowth inclusions (Ramdohr, 1969) of

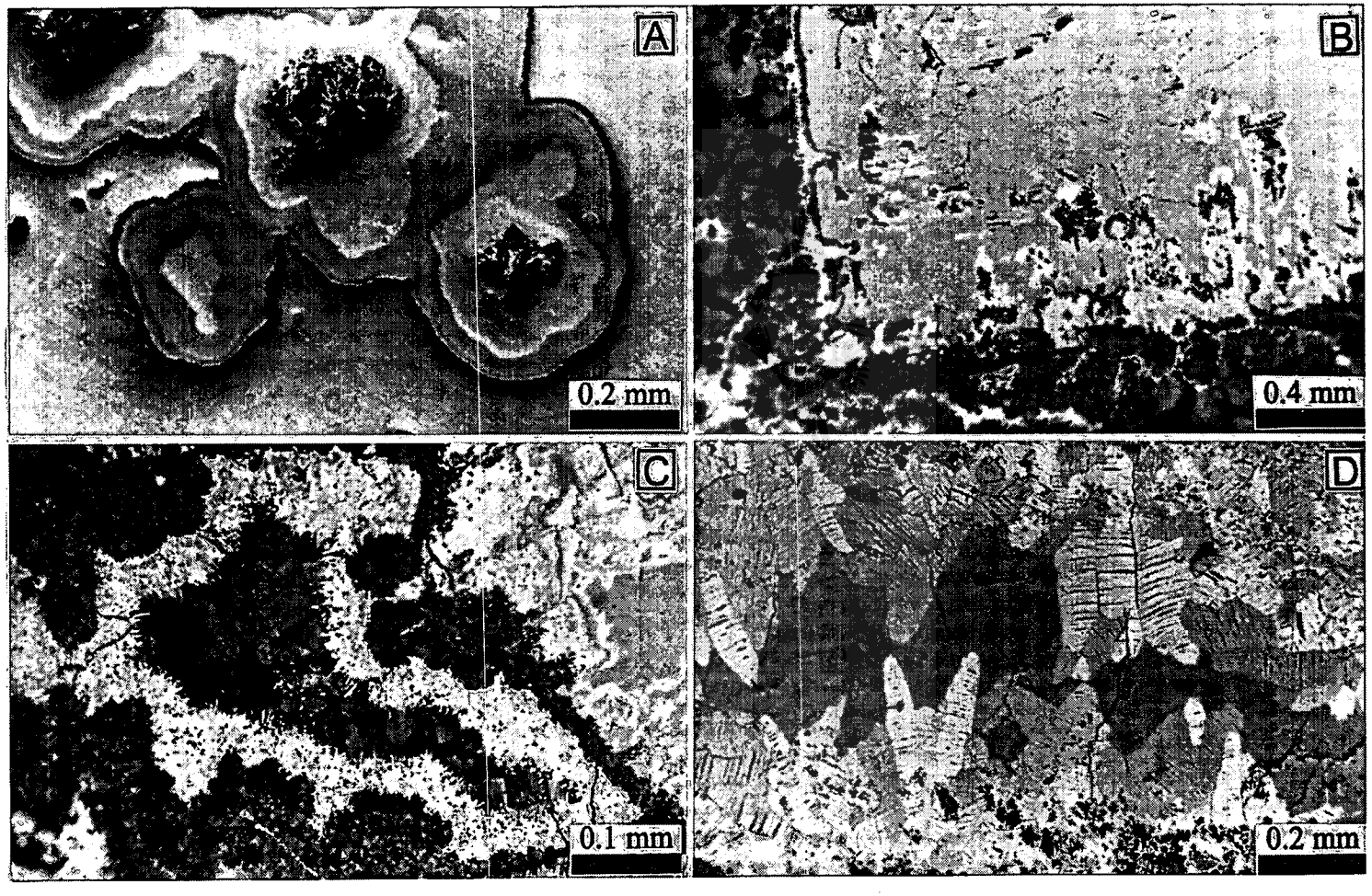

Fig. 7.10 Reflected light microphotographs A. Botryoidal romanechite (100x, sample BIS-244). B. Large bixbyite cube is replaced by fine crystalline romanechite (white) and lithiophorite (dark gray) (50x, LOH-79); C. Close up of previous photograph. Note that different generations of manganomelane/ romanechite are characterized by different colour shades. Note polishing scratches and strong bireflectivity of coarse crystalline lithiophorite (200x, oil immersion); D. Coarse crystalline euhedral pyrolusite fills in vug in siliceous manganese ore (100x, BEE-210).

thin braunite and braunite II (De Villiers, 1992) lamellae (10 to 100 μm long) and up to 100 μm long diaspore laths appear along the {100} and {111} planes.

Petrography of supergene ores

The supergene mineral assemblage of both the Eastern and Western Belts is composed of romanechite and cryptomelane, with minor amounts of manganite, pyrolusite, ramsdellite, goethite, and X-ray amorphous wad. Lithiophorite is abundant only in the aluminous ore beds of the Western Belt. Only romanechite and pyrolusite form accumulations large enough to be considered as distinct ore type. In the Western Belt cauliflower aggregates and botryoidal crusts and boxwork-structured remains of aluminous Mapedi/ Gamagara shale are composed of fine crystalline fibrous romanechite (Fig. 7.10A). In the Eastern Belt coarse crystalline pyrolusite veins that crosscut the Wolhaarkop breccia and penetrate into the underlying dolomite were mined locally (De Villiers, 1960). Pyrolusite and romanechite, associated with other minerals of supergene origin, occur in highly variable amounts in siliceous and ferruginous manganese ores. Manganomelane, cryptomelane and romanechite occur as finely dispersed dust and replacive seams along grain boundaries and between different laminae or zones of braunite, partridgeite and bixbyite. Diaspore and ephesite are most often replaced by lithiophorite or romanechite (Fig. 7.10B, 10C). Manganite was noted as a rare phase of possibly supergene origin by Schneiderhöhn (1931), De Villiers (1960), and Plehwe-Leisen (1985) but it was not identified during this study. Pyrolusite occurs generally as coarsely developed anhedral to subhedral prismatic crystals of up to 300 μm size tapering vugs and fractures in the ore, but also as relatively fine crystalline, granular masses (Fig. 7.10D). Ramsdellite, first identified by Plehwe-Leisen (1985) is rare and easily mistaken with pyrolusite. It was identified in 10 to 150 μm large, typical rhomb-shaped crystals with fish-scale fracture patterns (Frenzel, 1980).

Mineral Chemistry

Braunite

Three varieties of braunite are present namely braunite, braunite II, and newly discovered silica-depleted braunite. Major element electron microprobe analyses of braunite (Tables 7.2A and 7.2B) indicates a generally Fe-poor composition and a near stoichiometric SiO_2 concentration of 10 wt %. Several concentrically zoned braunite grains from siliceous ores were studied, but no systematic differences in composition between zones of different colouration could be

Table 7.2A Composition of braunite in siliceous manganese ores (selected analyses, data in wt %).

Sample No.	AUC198.2	AUC201.1	AUC204.3	BEE208	BEE213	BEE214	DO169	DO171	KAP228.2	KAP229	KAP230	MAN238
Mineral	Br	Br	Br	Br	Br	Br	Br	Br	Br	Br	Br	Br
Paragenesis	Ptr	He, illite	Qz		He	Ptr, He	Ptr, apatite	Ptr, barite	He, Qz	Qz	Qz	Qz
Texture	poor mosaic	poor mosaic, He-Cgl.	good mosaic	good mosaic	good mosaic	good mosaic	good mosaic	good mosaic	poor mosaic	poor mosaic	poor mosaic lamellar aggregates	good mosaic
Structure/ Zoning		lamellar, cryptic	concentric	concentric		Ptr-Br intergr.: lamellar, cryptic	complex zoning	Ptr-Br-interowth: cryptic		concentric	lamellar, spotty	
N	4	8	5	20	5	10	3	5	5	5	7	6
SiO_2	10.3	10.3	10.4	10.8	10.5	10.3	10.8	11.5	11.1	10.9	10.6	10.7
TiO_2	0.05	0.10	0.04	LLD	0.1	0.04	LLD	0.06	0.02	0.10	LLD	0.02
Al_2O_3	0.35	1.52	0.55	1.10	0.50	1.27	0.80	0.63	1.14	1.06	1.41	0.51
Fe_2O_3	0.34	5.10	0.21	0.07	5.00	2.51	1.80	0.22	4.11	0.70	0.16	4.58
Mn_2O_3	78.6	72.8	78.0	76.7	72.4	75.4	75.7	77.8	72.7	75.8	76.9	72.7
MnO	8.58	8.90	9.15	10.0	11.1	9.07	9.80	7.22	9.27	9.77	9.38	10.5
MgO	LLD	0.10	LLD	0.11	LLD	LLD	0.10	0.20	LLD	LLD	0.13	LLD
CaO	1.52	1.30	1.50	1.20	0.70	1.24	1.20	2.36	1.62	1.47	1.30	0.96
BaO	0.24	0.22	LLD	0.21	0.06	0.12	0.10	0.04	0.08	0.14	0.13	0.05
Na_2O	LLD	LLD	LLD	LLD	LLD	0.17	0.10	0.14	0.12	0.12	LLD	0.15
K_2O	LLD	0.11	LLD	LLD	LLD	LLD	LLD	LLD	LLD	LLD	LLD	LLD
TOTAL	100.1	100.4	100.1	100.3	100.4	100.2	100.4	100.3	100.3	100.1	100.1	100.2
Mn/(Mn+Fe)	1.00	0.94	1.00	1.00	0.94	0.97	0.98	1.00	0.95	0.99	1.00	0.95

Abbreviations: N - number of analyses; LLD - Lower than detection limit; n.a. - not analysed; Br-braunite; He-hematite; Ptr-partridgeite; qz- Quartz
* Mn^{2+}-Mn^{3+} charge balance calculated

JOHANNESBURG

Table 7.2B Composition of braunite and silica-depleted braunite, ferruginous ores and shales (selected analyses, all data in wt %).

Sample No.	PAL219	GLO185.1	GLO185.2	GLO185.3	LOH179	GLO185.1	GLO185.3	GLO185.4	GLO187	LOH176	PAL216.1	PAL216.2
Mineral	Br	Br	Br	Br	Br	Si-Br	Si-Br	Si-Br	Br	Br	Br	Br
Host	ferruginous manganese ore								shale			
Paragenesis	Ptr, Hs, He	Si-Br,Ptr, Mn-Di	Si-Br, Ptr, Mn-Di	Si-Br, Ptr, Mn-Di	Ptr, He	Ptr, Br, Mn-Di	Ptr, Br, Mn-Di	Ptr,Br, Mn-Di	He, Ptr, ephesite, Mn-Di	Ptr, He, ephesite	He, Ptr, ephesite, Mn-Di	He, Ptr, ephesite, Mn-Di
Texture	orientated intergrowth idioblasts of ptr-br	good mosaic, massive with flamelike Br II intergrowth.	good mosaic, massive with flamelike Br II intergrowth.	good mosaic, massive with flamelike Br II intergrowth.	orientated overgrowth on and with ptr idioblasts	good mosaic, massive with flamelike Br II intergrowth.	good mosaic, massive with flamelike Br II intergrowth.	good mosaic, massive with flamelike Br II intergrowth.	Br-Ptr ooids in shale	Br-lenses interbedded with shale, partly ooidal	blastic aggregates in shale, good mosaic	blastic aggregates in shale, good mosaic
Structure	Br-Ptr intergrowth: lamellar, cryptic,	Br-Ptr intergrowth: cryptic	Br-Ptr intergrowth: cryptic	Br-Ptr intergrowth: cryptic	Br-Ptr intergrowth: lamellar	flamelike bodies with Br	flamelike bodies with Br	flamelike bodies with Br	Br-Ptr intergrowth: cryptic	subhedral, disperse	Ptr-Br intergrowth: cryptic	Ptr-Br intergrowth: cryptic
N	3	8	10	5	10	10	10	10	3	5	5	5
SiO_2	9.52	10.6	10.7	10.4	10.0	4.19	4.07	3.36	9.78	9.10	9.81	9.18
TiO_2	0.08	0.01	0.03	0.06	0.09	0.04	0.05	0.08	0.98	1.05	0.41	0.47
Al_2O_3	1.64	1.27	1.67	1.30	0.58	3.99	3.03	2.71	1.06	1.28	1.14	1.08
Fe_2O_3	4.32	0.06	1.67	2.21	0.42	LLD	3.54	2.61	4.19	2.87	5.42	4.20
Mn_2O_3	76.1	78.4	78.3	78.7	76.7	92.2	89.8	90.7	71.4	73.0	70.6	73.8
MnO*	6.14	7.98	4.56	4.41	11.8	n.c.	n.c.	n.c.	10.8	12.4	12.6	10.7
MgO	0.14	LLD	0.11	0.12	0.15	0.10	LLD	LLD	0.20	LLD	LLD	0.13
CaO	1.89	1.85	3.08	2.95	0.15	1.21	1.16	1.18	0.54	0.30	LLD	0.50
BaO	0.16	0.06	0.07	0.13	0.05	0.06	0.07	0.04	0.27	0.04	0.08	LLD
Na_2O	0.12	LLD	0.10	0.12	0.15	0.13	0.10	LLD	0.17	LLD	LLD	0.10
K_2O	LLD	LLD	LLD	LLD	LLD	LLD	LLD	LLD	0.59	LLD	LLD	LLD
TOTAL	100.2	100.4	100.3	100.5	100.1	102.0	101.9	100.8	100.0	100.2	100.3	100.2
Mn/(Mn+Fe)	0.95	1.00	0.98	0.97	1.00	1.00	0.96	0.97	0.95	0.97	0.94	0.95

Abbreviations: N - number of analyses; LLD - Lower than detection limit; Br-braunite; He-hematite; Ptr-partridgeite; Mn-Di -diaspore; Hs-hausmannite; Si-Br- silica-depleted braunite; *Mn^{2+}-Mn^{3+} charge balance calculated; n.c. - charge balance not calculated.

UNIVERSITY OF JOHANNESBURG

established (Fig's. 7.9B and 7.12). Braunite in close association with hematite in the ferruginous and siliceous manganese ores contain 2.51 and 5.41 wt % Fe_2O_3 whereas braunite in assemblages devoid of hematite contain between 0.1 to 2.21 wt % Fe_2O_3 (Tables 7.2A and 7.2B). Concentrations of TiO_2 in the braunites vary also systematically between different paragenetic settings (Fig. 7.11). Braunites in aluminous shales contain 0.41 to 1.05 wt % TiO_2 with that in ferruginous and siliceous manganese ores containing less than 0.1 wt % TiO_2 (Tables 7.2A and 7.2B, Fig. 7.11).

SiO_2 contents decrease with increasing TiO_2 contents indicating substitution of Si by Ti (Table 7.2B, Fig. 7.11). Another distinct chemical trend is displayed by CaO. Braunites in aluminous shales contain as little as 0.3 to 0.54 wt % CaO (Table 7.2A), compared to 0.70 to 1.62 wt % in braunite samples from the siliceous manganese ores (Table 7.2A), and 1.85-3.09 wt % in the ferruginous manganese ores (with one exceptionally low value of 0.15 wt % in sample LOH179) (Table 7.2B). Baudracco-Gritti (1985) indicated that Ca substitutes for Mn^{2+} in the braunite structure.

Al_2O_3 contents of braunite appear to be independent of the paragenetic setting. There appears to be no consistent relation between SiO_2 and Al_2O_3 concentrations in braunite and it is thus likely that Al substitutes for Mn^{3+} in the braunite structure rather than for Si^{4+}. The generalized formula for braunites from the Postmasburg manganese field is $(Mn^{2+}_{0.7\text{-}1}\ Ca^{2+}_{0\text{-}0.2})\ (Mn^{3+}_{5.5\text{-}5.9}\ Al^{3+}_{0\text{-}0.2}\ Fe^{3+}_{0\text{-}0.4})\ (Si_{0.9\text{-}1.1}\ Ti_{0\text{-}0.1})O_{12}$.

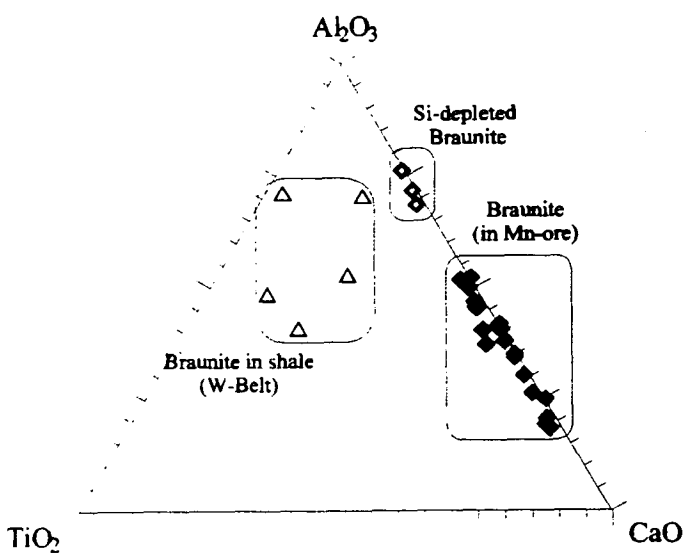

Fig. 7.11 Triangular diagram Al_2O_3-TiO_2-CaO to distinguish braunite formed in different geological environments.

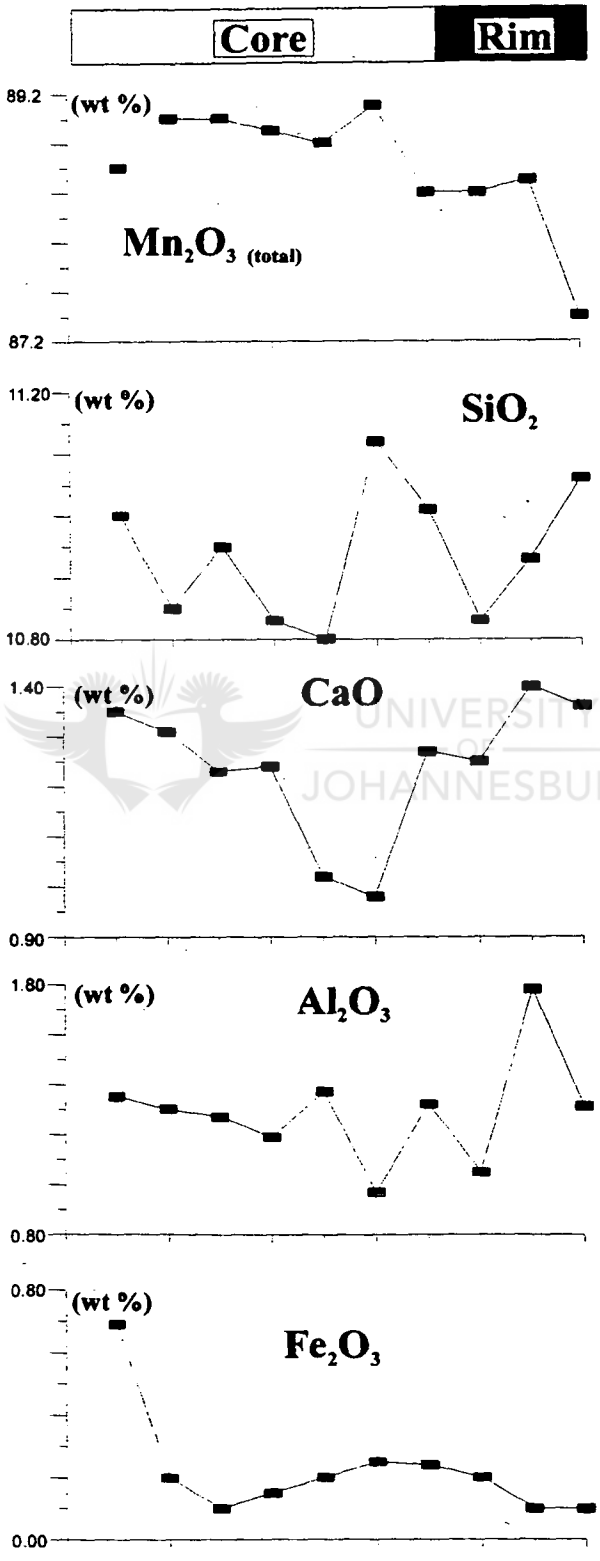

Fig. 7.12 Composition of zoned braunite along cross section displayed in Fig. 9B. Composition and optical zonation appear unrelated to each other.

A Ca-bearing silica-depleted variety of braunite was first described from the Kalahari manganese field by De Villiers (1945) as 'ferrian braunite'. De Villiers and Herbstein (1967) studied this phase in detail and named it braunite II. Braunite II from its type locality contains 3-5 wt % SiO_2, approximately the same amount of CaO and about 20 wt % Fe_2O_3. A second occurrence of braunite II was reported only recently by De Villiers (1992) from the Glosam mine in the Postmasburg manganese field. He described lamellar braunite II inclusions in bixbyite with contents of 4.8 wt % SiO_2, 12 % Fe_2O_3 and 4.64 wt % CaO. This phase was not encountered during this study and is apparently very rare.

In addition to braunite II, a different variety of silica-depleted braunite was identified during this study in a sample from the Glosam mine. It occurs intricately intergrown with partridgeite and braunite (Fig's 9D and E). Silica-depleted braunite (Sample No. GLO185.1, .3 and .4 in Table 7.2B) contains about 1.1 wt % CaO, 3.36 to 4.19 wt % SiO_2, high concentrations of Al_2O_3 (2.71 to 3.99 wt %), but low concentrations of Fe_2O_3 (0 - 3.54 wt %) (Table 7.2B). Analytical totals add up to somewhat more than 100 wt % (Table 7.2B) suggesting that some of the manganese may be present as MnO and not as Mn_2O_3, dissimilar to braunite II in which the divalent cation position is occupied only by Ca (De Villiers and Buseck, 1989). The compositional data of the Ca-poor silica-depleted braunite lead to the chemical formula $Ca_{0.1}Mn^{3+}_{6.8}Fe^{3+}_{0.1}Al_{0.5}Si_{0.4}O_{12}$.

Bixbyite

Two distinct varieties of bixbyite are present namely iron-poor bixbyite with generally less than 4 wt % Fe_2O_3 and iron-rich bixbyite with between 10 and 22 wt % Fe_2O_3. The iron poor bixbyite was described by De Villiers (1943a) as the new mineral species partridgeite from the Glosam mine. De Villiers (1943a) suggested that three minerals of the general composition $(Mn,Fe)_2O_3$ should be distinguished namely partridgeite with an iron content of less than 10 wt % Fe_2O_3, sitaparite containing between 10 and 30 wt % Fe_2O_3 and bixbyite containing more than 30 wt % Fe_2O_3. The name sitaparite was soon dropped in favour of bixbyite as both minerals were found to be cubic and isostructural (Mason, 1944). Mason (1944) and Roy (1981) challenged the necessity to distinguish a mineral with the name partridgeite from bixbyite so that many authors refer to it as iron-poor bixbyite (Plehwe-Leisen, 1985; Roy et al. 1990). However, Geller (1971) showed that synthetic α-Mn_2O_3 with less than 0.75 wt % Fe_2O_3 has an orthorhombic structure in contrast to Mn_2O_3 with higher iron content that has a cubic structure. Huebner (1976) questioned the natural existence of orthorhombic α-Mn_2O_3, e.g. partridgeite, although no crystallographic study was ever performed on the type material described by De Villiers (1943a). Therefore it may be wise to retain the name partridgeite for naturally occurring Fe-poor Mn_2O_3, if it proves to have

Table 7.3A Composition of partridgeite (selected analyses, all data in wt %).

Sample No.	AUC198	BEE214.1	BEE214.2	DO161	PAL219.3	PAL219.4	GLO185.2	GLO185.3	GLO193	LOH79.1	LOH178.2	LOH179
Mineral	Ptr	Ptr	Ptr	Ptr	Ptr	Ptr	Ptr	Ptr	Ptr	Ptr	Ptr	Ptr
Assemblage	Br	Br, He	Br	Br	Br, Hs, He, Bx	Br, Hs, He, Bx	Br, Si-Br, Mn-Di	Br, Si-Br, Mn-Di	Br, He, Li	He, Br, Mn-Di	Br, He, ephesite	Br, He
Texture	poor Br-mosaic, fine crystalline aggregates of Ptr	good Br mosaic	good Br mosaic	poor Br mosaic, fine crystalline aggregates of Ptr	medium grained, Ptr-Br in orientated intergrowth	medium grained, Ptr-Br in orientated intergrowth	medium grained aggregates around Mn-Di	medium grained aggregates around Mn-Di	aggregates and dispersed in Li bed	medium grained idioblastic	large ptr idioblast in massive bed	large Ptr idoblasts, massive bed, Br-overgrowth
Structure	massive, spotty	Ptr-Br intergrowth: cryptic	Ptr-Br intergrowth: cryptic	cryptic to spotty	Bx and Ptr zones in idioblasts, Br intergrowth: lamellar, cryptic	Bx and Ptr zones in idioblasts, Br intergrowth: lamellar, cryptic	Br-Ptr intergrowth: cryptic, orientated lamellar	Br-Ptr intergrowth: cryptic, orientated lamellar	euhedral, homogenous	euhedral, homogenous	Ptr-Br intergrowth: lamellar, orientated cryptic	Ptr-Br intergrowth: orientated, lamellar
N	1	5	5	3	5	2	10	5	3	5	3	10
SiO_2	0.30	0.95	0.50	0.57	1.30	0.65	0.22	0.28	0.69	0.32	0.20	0.78
TiO_2	LLD	LLD	0.04	0.05	0.04	0.05	0.04	0.02	0.13	0.12	LLD	0.09
Al_2O_3	0.54	0.54	0.99	0.45	1.62	1.25	1.42	0.61	1.12	2.25	2.80	1.55
Fe_2O_3	0.00	0.40	0.04	0.24	1.08	1.90	0.00	0.67	0.54	4.59	2.15	1.15
Mn_2O_3*	99.0	98.0	98.5	98.7	95.4	96.7	98.4	98.6	97.5	92.7	95.3	95.3
MgO	LLD	0.06	0.04	LLD	0.12	0.20	0.10	LLD	LLD	0.18	0.13	LLD
CaO	0.10	0.12	0.10	0.13	0.39	LLD	LLD	LLD	0.20	0.10	LLD	0.91
BaO	0.50	0.04	0.10	0.05	0.08	0.10	0.04	0.04	0.03	LLD	0.03	0.10
Na_2O	0.10	0.08	0.06	0.15	0.12	LLD	LLD	LLD	LLD	0.12	LLD	0.12
K_2O	LLD	LLD	LLD	LLD	LLD	LLD	LLD	LLD	LLD	LLD	LLD	LLD
TOTAL	100.5	100.2	100.4	100.4	100.2	100.9	100.4	100.5	100.3	100.4	100.7	100.0
Mn/(Mn+Fe)	1.00	1.00	1.00	1.00	0.99	0.98	1.00	1.00	0.99	0.95	0.98	0.99

Abbreviations: N - number of analyses; LLD - Lower than detection limit; n.a. - not analysed; Br-braunite; He-hematite; Ptr-partridgeite; Bx-bixbyite; Hs-hausmannite; Si-Br - silica-depleted braunite; Li-lithiophorite; Mn-Di -diaspore. * $Mn_{(total)}$ expressed as Mn_2O_3

UNIVERSITY OF JOHANNESBURG

Table 7.3B Composition of bixbyite and hausmannite (all data in wt %).

Sample No.	BIS241	BIS243	BIS247	BIS289.3	GLO10-63	PAL219.3	PAL224	PAL228.1	PAL228.2	PAL219
Mineral	Bx	Bx	Bx	Bx	Bx	Bx	Bx	Bx	Bx	Hs
Paragenesis	Mn-Di, He amesite	He, Br, Mn-Di	Mn-Di	Mn-Di	Mn-Di, ephesite, amesite,	Hs, He, Ptr, Br	Mn-Di	ephesite, amesite, Mn-Di, He	ephesite, amesite, Mn-Di, He	Ptr, Br, He
Texture	coarse grained, massive	medium grained, massive	very coarse grained, vuggy	coarse crystalline, vuggy	medium grained, massive to vuggy	medium grained Ptr-Bx idioblasts	coarse crystalline, vuggy	coarse crystalline, vuggy	coarse crystalline, vuggy	Ptr-idioblast replaced by Hs
Structure	idioblastic, Mn-Di and He inclusions	idioblastic	idioblastic	idioblastic	idioblastic, with He inclusions	Concentric zoned Ptr-Br blasts	idioblastic, twinning	idioblastic	idioblastic	anhedral, twinned
N	10	3	3	10	5	5	5	9	4	9
SiO_2	0.14	0.13	LLD	0.20	1.39	1.48	0.32	0.48	0.45	0.25
TiO_2	0.45	0.37	0.07	0.06	0.41	0.16	0.68	0.55	0.58	0.07
Al_2O_3	2.89	1.88	2.30	2.18	1.41	1.97	1.77	1.58	1.80	1.51
Fe_2O_3	13.9	20.5	20.0	14.5	16.6	12.4	19.5	18.6	18.8	1.07
Mn_2O_3*	82.6	76.4	76.9	83.0	79.0	84.0	78.0	78.6	78.4	63.34
MnO										33.43
MgO	LLD	LLD	0.10	LLD	LLD	0.14	0.12	0.07	LLD	0.25
CaO	LLD	LLD	LLD	LLD	0.65	0.43	LLD	0.10	LLD	LLD
BaO	0.03	0.07	0.10	0.10	0.09	LLD	0.04	0.06	0.03	0.07
Na_2O	LLD	LLD	0.23	0.12	LLD	0.10	LLD	0.11	0.18	LLD
K_2O	LLD	LLD	LLD	LLD	LLD	LLD	LLD	LLD	LLD	LLD
TOTAL	100.2	99.5	99.9	100.3	99.7	100.7	100.6	100.1	100.3	100.1
Mn/(Mn+Fe)	0.86	0.79	0.79	0.85	0.83	0.87	0.80	0.81	0.81	0.99

Abbreviations: N - number of analyses; LLD - Lower than detection limit; n.a. - not analysed; Br-braunite; He-hematite; Ptr-partridgeite; Hs-hausmannite; Si-Br-silica depleted braunite; Bx-bixbyite; Mn-Di -diaspore;

* for bixbyite $Mn_{(total)}$ expressed as Mn_2O_3, for hausmannite Mn^{2+}-Mn^{3+} charge balance calculated

UNIVERSITY OF JOHANNESBURG

an orthorhombic structure, and to apply the name bixbyite to all naturally occurring cubic α-Mn_2O_3, regardless of its iron content.

During this study abundant partridgeite was examined microscopically and compared to the associated bixbyite. The two phases are easily distinguished. Partridgeite is notably anisotropic and bixbyite appears isotropic, a distinctive feature already described by De Villiers (1943a) and De Villiers (1960). Microprobe analysis confirmed that those examples identified optically as partridgeite are in fact iron-poor and contain between 0 and 4.6 wt % Fe_2O_3 (Table 7.3A). Isotropic examples identified as bixbyite proved to contain more than 10 wt % Fe_2O_3 (Table 7.3B). The mineral name partridgeite is therefore retained in this study to distinguish Fe-poor, anisotropic α-Mn_2O_3 from Fe-rich, isotropic bixbyite. The studies necessary to properly characterize partridgeite from its type locality is an ongoing project.

The minor element contents in partridgeite and bixbyite are very similar. Contents of MgO, CaO, BaO and alkalies are well below 0.5 wt % (Tables 7.3A and 7.3B). Al_2O_3 concentrations vary between 0.45 and 2.80 wt % in partridgeite (Table 7.3A) but appear somewhat higher in bixbyite (1.41 - 2.90 wt %) (Table 7.3B). This is also true for TiO_2 with partridgeite containing less than 0.15 wt % TiO_2 and bixbyite containin between 0.06 and 0.68 wt % TiO_2. The microprobe data correspond to chemical formulas of $(Mn^{3+}_{1.90\text{-}1.96}\ Al_{0.02\text{-}0.05}\ Fe^{3+}_{0.01\text{-}0.04})O_3$ for partridgeite and $(Mn^{3+}_{1.52\text{-}1.64}\ Fe^{3+}_{0.24\text{-}0.37}\ Al_{0.05\text{-}0.09})O_3$ for bixbyite.

Hausmannite

Microprobe analysis of hausmannite is impeded by the fact that it is most easily weathered to manganomelane. Only one sample (PAL219) with sufficiently fresh hausmannite was encountered to do microprobe work on. The hausmannite occurs as replacement product of partridgeite (Table 7.4B). It is interesting to note that the replaced partridgeite and the replacing hausmannite contain are of very similar major and minor element composition (Table 7.3B, compare with partridgeite sample PAL219.3 in Table 7.3A).The average Fe_2O_3 content of 1.07 wt % in the hausmannite is low and within the range usually reported for hausmannite (Frenzel, 1980, Roy, 1981). The Al_2O_3 content of 1.51 wt %, however, appears to be unusually high. No descriptions of such Al-rich hausmannite are present in the literature. It is suggested that Al^{3+} and Fe^{3+} substitute for Mn^{3+} in hausmannite, leading to a generalized formula $Mn^{2+}_{1.05}(Mn^{3+}_{1.8}\ Al^{3+}_{0.1}\ Fe^{3+}_{0.05})O_4$.

Table 7.4A Composition of cryptomelane, manganomelane, and romanechite (selected analyses, all data in wt %).

Sample No.	BIS247	DO171	LOH79	AUC198	MAN238	GLO185	KAP229	BEE211	DO169	GLO185	LOH179	BIS244
Mineral	Crypt	Crypt	Crypt	Mang	Mang	Mang	Rom	Rom	Rom	Rom	Rom	Rom
N	3	6	5	5	5	3	3	5	3	5	3	5
SiO_2	0.83	0.52	0.88	0.40	0.80	1.12	0.20	0.34	0.47	0.51	0.45	0.36
TiO_2	LLD	0.12	0.02	0.06	0.04	0.07	LLD	LLD	0.03	0.38	0.03	LLD
Al_2O_3	3.74	1.33	3.50	1.21	0.98	2.01	0.20	0.42	0.23	1.99	1.06	0.38
Fe_2O_3	6.16	LLD	0.93	0.89	2.90	LLD	0.07	0.65	LLD	1.65	0.35	LLD
MnO_2*	76.8	87.8	82.8	86.5	85.5	89.1	80.5	78.8	82.0	79.8	78.7	77.2
MgO	0.30	0.27	0.72	0.12	0.12	0.03	LLD	0.22	LLD	0.12	0.03	0.20
CaO	0.23	0.17	LLD	0.20	0.14	0.84	LLD	0.10	0.27	0.18	0.23	0.24
BaO	0.76	0.43	1.99	3.67	0.91	0.07	15.4	13.3	13.2	9.01	15.7	14.3
Na_2O	0.27	0.45	0.18	1.12	1.61	1.58	0.30	0.39	0.23	0.59	0.37	0.36
K_2O	5.34	5.42	4.92	3.06	1.55	0.23	LLD	0.86	0.17	1.38	LLD	0.25
TOTAL	94.5	96.5	96.0	97.2	94.6	95.0	96.7	95.1	96.7	95.6	96.9	93.3

Abbreviations: N - number of analyses; LLD - Lower than detection limit; n.a. - not analysed; Crypt-crptomelane; Mang-manganomelane; Rom-romanechite; * $Mn_{(total)}$ expressed as MnO_2.

Manganomelane group of minerals and pyrolusite

Following the suggestion by Frenzel (1980) the complex group of minerals with the generalized formula $A_{1-2}Mn^{4+}{}_8O_{16} \cdot xH_2O$ (A=Na, K, Pb, Ba) is to be referred to as the manganomelane group. Several compositional end-members are distinguished in this group namely manjiroite (Na-rich), cryptomelane (K-rich), coronadite (Pb-rich) and romanechite (Ba-rich). Compounds of intermediate composition may simply be referred to as manganomelane. In the Postmasburg manganese field, manganomelane, cryptomelane and romanechite have been identified (Table 7.4A). The triangular diagram Na_2O-K_2O-BaO (Fig. 7.13) discriminates clearly between the compositional end members romanechite and cryptomelane that are of rather restricted composition, and a much larger central field occupied by manganomelane. Among the phases of the manganomelane group of minerals, romanechite is most common in the Postmasburg manganese field.

The romanechite from the Postmasburg manganese field contains 7 to 16 wt % BaO (Table 7.4A), less than 1 wt % Na_2O and K_2O and less than 0.5 wt % MgO, CaO and SiO_2(Table 7.4A). Contents of Fe_2O_3 and Al_2O_3 are below 2 wt %. The cryptomelane contains more K_2O (4.92-5.42 wt %) than BaO (0.43-1.99 wt %) or Na_2O (0.18-0.45 wt %). Highly variable Fe_2O_3 contents in cryptomelane (up to 6.16 wt %), may be related to the presence of small amounts of fine crystalline hematite that is optically indistinguishable from the cryptomelane. Al_2O_3 concentrations range between 1.33 and 3.50 wt %, and MgO and CaO contents are below 1 wt % in cryptomelane. None of the large cations Na-K-Ba is predominant in manganomelane (Table 7.4A). Concentrations of minor elements vary considerably between 0.07-3.67 wt % BaO, 1.12-

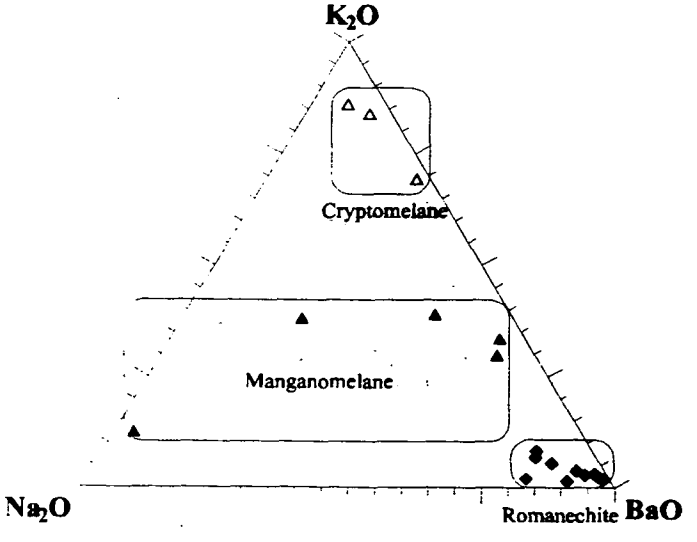

Fig. 7.13 Triangular diagram K_2O-Na_2O-BaO to distinguish different members of the manganomelane-group of minerals.

Table 7.4B Composition of lithiophorite and pyrolusite (all data in wt %).

Sample No.	GLO-Li01	LOH79	De Villiers	AUC198	KAP229	AUC199.2	BIS243	DO169	PAL216
Mineral	Lithio	Lithio	Lithio	Pyro	Pyro	Pyro	Pyro	Pyro	Pyro
N	5	3		2	5	6	2	3	3
SiO_2	LLD	LLD	0.30	0.35	0.78	0.63	0.52	2.28	0.88
TiO_2	0.41	0.20	n.a.	0.10	0.06	0.03	0.05	0.07	0.03
Al_2O_3	26.8	25.9	23.8	0.67	0.85	0.77	0.25	0.30	0.50
Fe_2O_3	0.63	2.16	0.96	0.83	LLD	0.13	LLD	LLD	LLD
MnO_2[a]	58.4	56.1	58.9	92.8	95.9	95.8	95.4	94.6	93.9
MgO	1.61	2.48	n.a.	0.10	LLD	LLD	LLD	LLD	LLD
CaO	0.02	0.20	LLD	0.50	LLD	0.10	LLD	0.20	0.41
BaO	0.10	0.07	n.a.	0.35	0.08	0.17	0.41	0.50	0.10
Na_2O	0.10	LLD	LLD	0.20	0.12	0.22	0.20	0.13	0.13
K_2O	LLD	0.10	LLD	0.30	LLD	0.17	0.30	0.10	0.10
Li_2O[b]	3.31	n.a.	3.30	n.a.	n.a.	n.a.	n.a.	n.a.	n.a.
TOTAL	88.2	87.3	100.2[c]	96.2	97.9	98.0	97.2	98.2	96.1

Abbreviations: N - number of analyses; LLD - Lower than detection limit; n.a. - not analysed; Lithio - lithiophorite; Pyro - pyrolusite; [a] $Mn_{(total)}$ as MnO_2; [b] Li_2O determined by AAS (I. Finnegan, written comm.); [c] includes 13.2 wt % H_2O^+ and 1.45 wt % H_2O^-.

1.68 wt % Na_2O, 0.23-3.06 wt % K_2O, up to 2.90 wt % Fe_2O_3, and 0.98 - 2.01 wt% Al_2O_3; contents of SiO_2, MgO and CaO are, however, generally below 1 wt %. Totals of the manganomelane group minerals range between 93.3 and 97.2 wt % indicate the presence of variable amounts of absorbed and structural water (Frenzel, 1980).

Coarse crystalline pyrolusite was found to be almost pure MnO_2, with only negligible amounts of impurities (Table 7.4B). The presence of absorbed water in the pyrolusite is indicated by analytical totals below 100 wt % (Frenzel, 1980).

Lithiophorite

Lithiophorite is an especially abundant supergene phase in the ferruginous type of ores. Its occurrence in the Postmasburg manganese field was first noted by Gruner (1943). De Villiers (1945b) described the occurrence of coarse botryoids, composed of up to 1 cm large lithiophorite plates from the Glosam mine. A small fragment of the type material analysed by De Villiers (1945b) was used for microprobe analysis and atomic absorption spectrometry for Li_2O (sample GLO-Li01, Table 7.4B) in order to compare it with fine crystalline lihiophorite that is abundant in the ferruginous manganese ore. The results for coarse crystalline lithiophorite (sample GLO-Li01) and fine crystalline lithiophorite (LOH79) (Table 7.4B) are very similar. They illustrate the predominance of Al_2O_3 (26.8 wt % and 25.9 wt %) and Mn (58.4 wt % and 56.1 wt % MnO_2) in

Table 7.5A Composition of barite, apatite, and gamagarite (all data in wt %).

Mine	GLO	GLO	GLO	DO	KAP	LAH	BEE	GLO	LOH
S. No.	Mn10-63	De Villiers	Harlow et al.	169	297	166	211	290	293
Mineral	gamag	gamag	gamag	apatite	barite	barite	barite	barite	barite
Paragenesis	Bx, He amesite ephesite			Br	Br	He	Br		He
N	5			8	5	5	5	5	5
SiO_2	0.17	n.a.	n.a.	0.18	LLD	LLD	LLD	LLD	LLD
TiO_2	LLD	n.a.	n.a.	0.06	n.a.	n.a.	n.a.	n.a.	n.a.
Al_2O_3	0.19	LLD	0.8	LLD	n.a.	n.a.	n.a.	n.a.	n.a.
Fe_2O_3	7.13	7.6	8.1	LLD	n.a.	n.a.	n.a.	n.a.	n.a.
Mn_2O_3	5.93			0.67	n.a.	n.a.	n.a.	n.a.	n.a.
MgO	0.11	5.5	5.7	LLD	LLD	LLD	LLD	LLD	LLD
CaO	LLD	n.a.	n.a.	57.3	LLD	LLD	LLD	LLD	LLD
SrO	n.a.	n.a.	n.a.	LLD	1.16	0.28	0.77	1.20	1.45
BaO	51.5	52.4	53.5	LLD	64.4	65.0	64.7	64.6	64.7
SO_3	LLD	n.a.	n.a.	LLD	34.4	34.2	34.1	34.4	34.4
V_2O_5	32.1	31.9	31.9	n.a.	n.a.	n.a.	n.a.	n.a.	n.a.
P_2O_5	n.a.	n.a.	n.a.	40.6	n.a.	n.a.	n.a.	n.a.	n.a.
TOTAL	97.1	99.3[a]	101.9[b]	98.8	98.8	99.2	98.8	99.0	99.1

Abbreviations: N-number of analyses; LLD-below detection limit; n.a.-not analysed; Br-braunite; He-hematite; Bx-bixbyite; Mn-Di - diaspore; gamag - gamagarite; [a] includes 1.06 wt % H_2O; [b] includes 1.91 wt % H_2O.

UNIVERSITY OF JOHANNESBURG

lithiophorite. Small amounts of Fe_2O_3, MgO (1.61 wt % and 2.48 wt %) and Li_2O (about 3 wt %) were detected. The results obtained in this study are in very good agreement with the original wet chemical analysis of coarse crystalline lithiophorite by De Villiers (1945b), which included unkown amounts of impurities such as braunite, partridgeite and romanechite. The formula $Li_2Mn^{2+}Mn_5^{4+}Al_4O_{18}\cdot 6H_2O$ suggested by De Villiers (1945b) for lithiophorite from the Postmasburg manganese field is thus essentially correct. This formula is further confirmed by the results of Giovanoli et al. (1973) who were able to synthesize and study lithiophorite of very similar composition.

Gamagarite, apatite and barite

The rare Ba-vanadate gamagarite has only been reported from two localities, the type locality at Glosam Mine (De Villiers, 1943b) and from the Molinello manganese mine in Eastern Liguria, Italy (Basso et al., 1987). Microprobe analyses during this study were performed on a small piece of the type material of gamagarite (sample Mn10-63) described by De Villiers (1943b). The average of 5 point analyses, reported in Table 7.5A, is very similar to the original wet chemical

analyses by De Villiers (1943b) and also the composition reported by Harlow et al. (1984) (Table 7.5A) who suggested the idealized formula $Ba_2(Fe^{+3}Mn)[(OH, H_2O)/(VO_4)_2]$.

Table 7.5B Composition of Mn-diaspore, ephesite, and amesite (all data in wt %).

Sample No.	PAL228	GLO289	BIS241	AUC202	BIS241	GLO197	GLO187	LOH176
Mineral	Mn-Di	Mn-Di	Mn-Di	Ba-Mu	amesite	amesite	ephesite	ephesite
Paragenesis	Bx	Bx	amesite, Bx	Br	Bx, Mn-Di	Bx	Bx	He
N	9	10	10	5	5	5	3	3
SiO_2	LLD	LLD	LLD	32.7	22.2	23.7	32.3	32.1
TiO_2	0.04	0.02	0.13	0.10	0.08	0.01	0.01	0.13
Al_2O_3	84.7	84.6	84.2	39.6	35.7	35.3	52.1	52.6
Fe_2O_3	0.34	0.31	0.54					
FeO				0.45	0.16	0.40	1.68	1.24
Mn_2O_3	0.21	0.21	0.60					
MnO				0.89	0.42	1.07	1.60	1.33
MgO	LLD	LLD	0.10	0.22	26.6	28.5	0.34	0.24
CaO	LLD	LLD	LLD	LLD	LLD	LLD	LLD	0.07
BaO	LLD	LLD	LLD	20.5	LLD	LLD	n.a.	n.a.
Na_2O	LLD	LLD	LLD	0.37	LLD	LLD	7.75	7.35
K_2O	LLD	LLD	LLD	3.37	LLD	LLD	0.13	0.10
Li_2O^a	n.a.	n.a.	<0.01	n.a.	n.a.	n.a.	n.a.	1.80
H_2O	14.5	14.9	14.6	n.a.	n.a.	n.a.	n.a.	n.a.
TOTAL	99.9	100.1	100.2	98.2	85.1	89.0	95.9	97.0

Abbreviations: N - number of analyses; LLD - Lower than detection limit; Br-braunite; He-hematite; Ba-Mu - barian-muscovite; Mn-Di -diaspore; Bx-bixbyite; Br-braunite; [a] Li_2O analysed by atomic absorption (I.Finnegan, written comm.)

The occurrence of apatite in the Postmasburg manganese field was reported first by De Villiers (1960). He described disseminated grains in a single ore specimen from the farm Lomoteng, central Gamagara Ridge. During this study, apatite was identified in association with braunite in a sample of siliceous manganese ore from the farm Doornfontein. Microprobe analysis indicate a composition similar to hydroxyapatite (Table 7.5A), as neither the presence of Cl nor of F could be detected.

Barite is a widespread gangue mineral associated with the manganese ores. The composition of barite in the siliceous ore and small lenses or veins crosscutting the manganese ore bodies is fairly uniform, with 0-1.5 wt % SrO substituting for BaO (Table 7.5A).

Diaspore, ephesite, and Ba-Al muscovite

The three Al-rich minerals diaspore, amesite and ephesite are the most common gangue minerals in the ferruginous manganese ore and their unusually coarse crystalline occurrence has attracted the attention of several previous workers (Chudoba, 1929; Hall, 1929; Coles-Phillips 1931).

Probably unique is the occurrence of up to 10 cm long Mn and Fe-bearing diaspore crystals of a distinct whisky brown to brownish red colour. The crystals are elongated along [001] and tabular developed along (010).The diaspore, first mistaken with rhodonite (Hall, 1926), was identified by Chudoba (1929) who reported concentrations of 1.96 wt % Fe_2O_3 and 4.32 wt% Mn_2O_3 by wet chemical analysis. Nel (1929) reported similar Fe_2O_3 concentrations of 1.32 to 1.47 wt %, but Mn_2O_3 contents of only 0.11-0.5 wt %. Large diaspore crystals, associated with bixbyite, were analysed during this study in order to resolve the obvious disagreement between the results of these two previous studies. Results of electron microprobe analysis are listed in Table 7.5B. Concentrations range between 0.3-0.54 wt % Fe_2O_3 and 0.2-0.6 wt % Mn_2O_3. Both elements are present in approximately equal amounts. The much lower concentrations obtained for Fe_2O_3, as compared to the results of Chudoba (1929) and Nel (1929), is best explained by the presence of minute hematite inclusions in the diaspore crystals, which were probably included during wet chemical analysis performed during previou studies. Unit cell constants calculated for the diaspore from Guinier camera exposure of a single crystal fragment are 4.40052±0.0015Å, b=9.42824±0.00170Å, c=2.84505±0.00140Å (D. Nyfeler, written communication 1994), in very good agreement with unit cell constants of diaspore reported in the ICDD (International Centre fro Diffraction Data) database record 5-355 (a=4.396Å, b=9.426Å, c=2.844Å) (ICDD, 1994). X-ray and backscattered electron images of single crystal fragments orientated into different crystallographic orientations indicated an entirely homogenous distribution of Mn and Fe. The available data suggest that small amounts of Fe^{3+} and Mn^{3+} are substituting for Al in the diaspore lattice. The presence of small amounts of Mn may explain the unusual whisky-brown to brownish-red colour.

Ephesite is the Na-rich analogue of margarite with the idealized formula $(Na,Ca)Al_2[(OH)_2/Al(Al,Si)Si_2O_{10}]$ (Rösler, 1984). This mineral was first identified by Chudoba (1929) as manganophyll but later correctly identified Coles-Phillips (1931). Several samples of ephesite were examined during this study, and results for two samples are listed in Table 7.5B. Ephesite was found to contain 1.80 wt % of Li_2O The formula $(Na_{0.92}Li_{0.47})(Al_{2.04},Fe_{0.13},Mn_{0.14},Mg_{0.05})[(OH)_2/Al(Al_{0.92}Si_{0.08})Si_2O_{10}]$ was calculated for sample LOH176.

Amesite is an aluminous serpentine (Rösler, 1984). Its occurrence in the PMF was noted by De Villiers (1945), who described its close association with bixbyite, ephesite and diaspore. Two samples of amesite, one in paragenesis with ephesite and the other with diaspore are included in Table 7.5B. The calculated formula for sample BIS241 is and for sample GLO197 are $Mg_{3.96}Al_{1.97}Mn^{+2}_{0.03}Fe^{+3}_{0.01}Ti_{0.01}[(OH)_8/(Si_{2.06},Al_{1.94})O_{10}]$ and

$Mg_{3.87}Al_{1.95}Mn_{0.08}Fe_{0.03}[(OH)_8/(Si_{2.16}Al_{1.84})O_{10}]$ respectively.

Ba-Al-muscovite, a mineral previously unknown in the PMF, was identified by microprobe analysis (Table 7.5B). The formula calculated for this mineral (assuming a stoichiometric water content) is $(Ba_{0.6}K_{0.32}Na_{0.06}Mn^{2+}_{0.05}Fe^{2+}_{0.03})Al_{1.92}[(OH)_2\(Si_{2.44}Al_{1.56})O_{10}]$.

Discussion

The crystal chemistry of the braunite group

The mineral chemistry of the braunite group of minerals in the Postmasburg manganese field deserves special attention. The members of this group of minerals are characterized by a crystal structure that can be perceived as a derivative of the fluorite lattice (Moore and Araki, 1976; De Villiers, 1980; De Villiers and Buseck, 1989). An attempt was made by De Villiers and Buseck (1989) to explain the crystal chemistry of the braunite group in terms of a polysomatic stacking model with distinct layer modules for braunite, bixbyite and braunite II. Compositional data to back up the the proposed model were then only available from Tachgagalt (Morocco) (Baudracco-Gritti, 1985) and the Kalahari manganese field (Kleyenstüber, 1985). Another occurrence of silica-depleted braunites with about 8 wt % SiO_2 (7-module polysome), 4 wt % SiO_2 (5 module polysome) and 3 wt % SiO_2 (7 module polysome) was only recently described by Ostwald and Nayak (1993) from the Kajlidongri Mine, Madhya Pradesh, India. Observations made during this study may thus be very valuable to test the polysomatic model proposed by De Villiers and Buseck (1989).

Braunite, silica-depleted braunite, braunite II, partridgeite and bixbyite from the Postmasburg manganese field occupy distinct, non-overlapping fields in the SiO_2-Fe_2O_3 diagram (Fig. 7.14). The crystal chemistry of three of the five members of the braunite group in the Postmasburg manganese field, namely braunite, braunite II and bixbyite, can be explained by the polysomatic stacking model of De Villiers and Buseck (1989). However, the chemical composition of the

other two minerals of the braunite group, namely iron-poor partridgeite, and Ca-poor and silica-depleted braunite cannot be explained without adding a new partridgeite layer module to the existing model. The partridgeite module, expressed here as $Mn_{16}O_{24}$, most probably has lower symmetry than the iron-rich bixbyite module as is indicated by the optical anisotropy of partridgeite in the manganese ore. Partridgeite in the Postmasburg manganese field is thought to be essentially composed of this newly suggested module. The composition of Ca-poor silica-depleted braunite could then be explained by stacking three layers of the partridgeite with two layers of the braunite module.

UNIVERSITY OF JOHANNESBURG

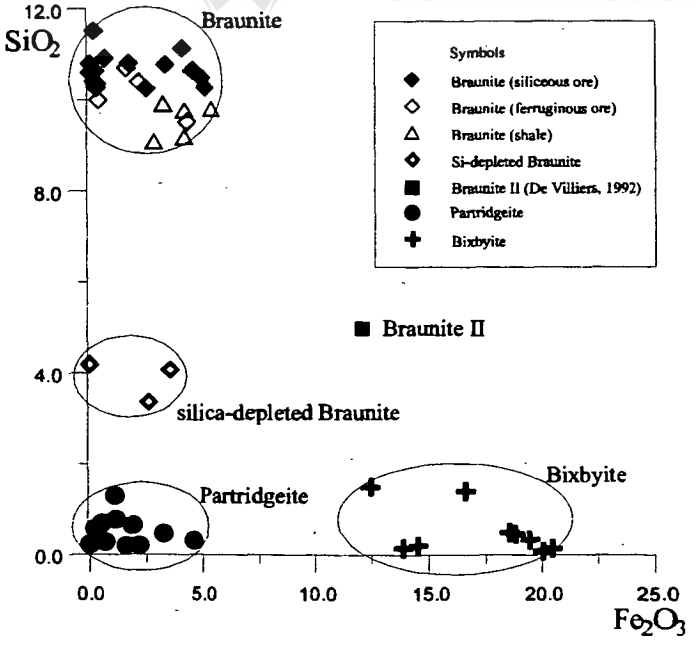

Fig. 7.14 SiO_2-Fe_2O_3 diagram to discriminate different members of the braunite group of minerals. Note clear separation between partridgeite and braunite.

The polysomatic model of De Villiers and Buseck (1989) is also supported by the unique light microscopic observation of coherent intergrowth of silica-depleted braunite with braunite with apparently gradual boundaries (Fig. 7.9B and 7.9C).

Paragenetically controlled enrichments of TiO_2, Al_2O_3, Fe_2O_3, and CaO in braunite group minerals have already been described (Fig. 7.14). Systematic differences in the minor element

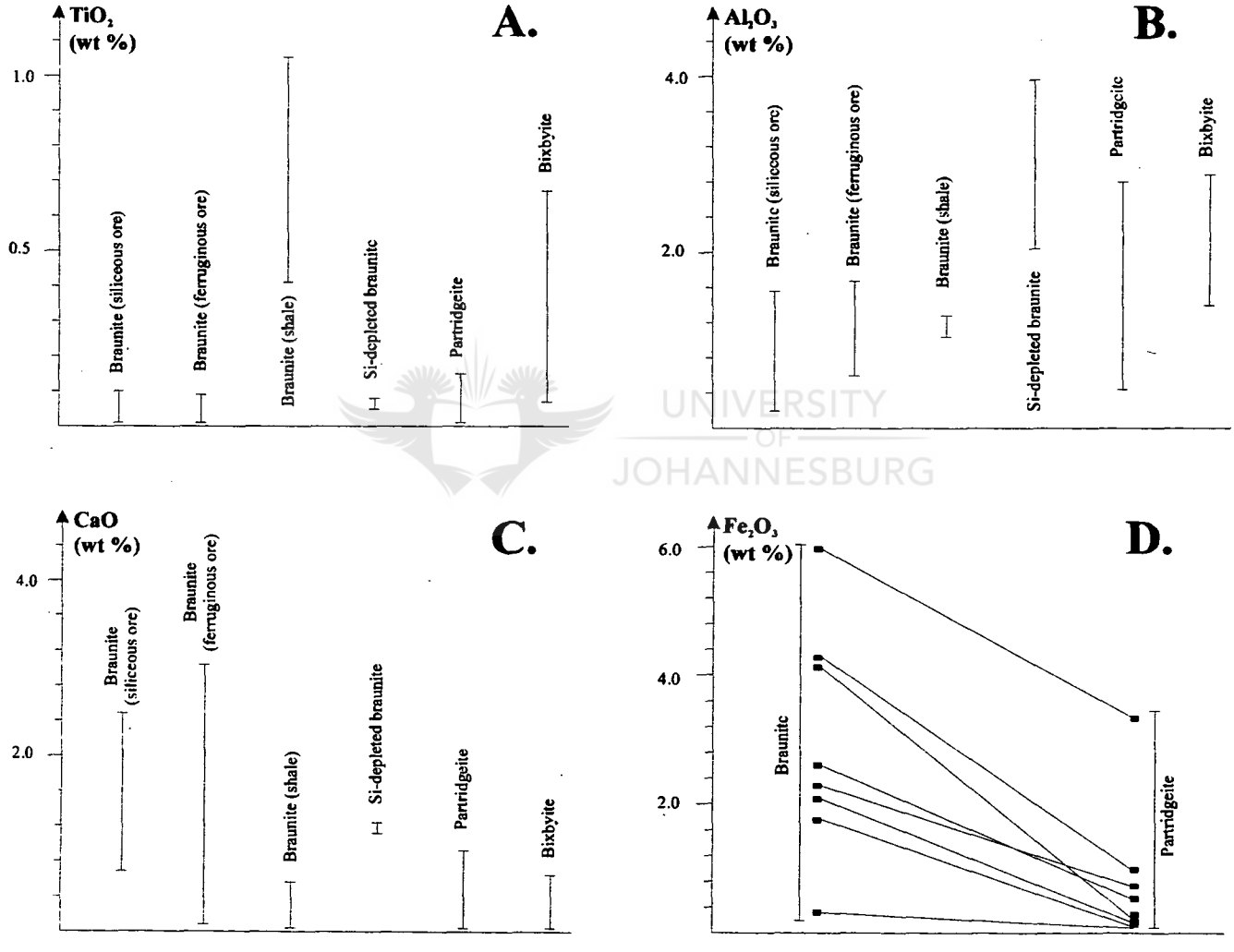

Fig. 7.15 Concentrations of TiO_2 (A), Al_2O_3 (B), and CaO in the different members of the braunite group of minerals. (D) Fe_2O_3 content of braunite and partridgeite. Coexisting pairs are connected by tie lines.

composition of braunite, partridgeite, Si-depleted braunite and bixbyite (Tables 7.2A and 7.2B, 7.3A and 7.3B), however, appear to be crystal-chemically controlled. Shale-hosted braunites are unusually enriched in TiO_2, even if compared to other members of the braunite group (Fig. 7.15A). Few bixbyite samples show concentrations greater than 0.5 wt %, but TiO_2 contents remain well below 0.2 wt % in other examples (Fig. 7.15A). Partridgeite and Si-depleted braunite

contain generally less than 0.1 wt % TiO_2. It is likely that the absence of a specific tetrahedrally coordinated lattice site in the structure of partridgeite and bixbyite, e.g. the absence of Si, impedes the incorporation of the Ti cation.

Highest concentrations of CaO (Fig. 7.15C) are present in braunite II (4.64 wt % De Villiers, 1992). Concnetrations of CaO in braunite, Ca-poor silica-depleted braunite are significantly lower and Ti-rich braunite, bixbyite, and partridgeite are virtually devoid of CaO (Fig. 7.15C). These results confirm the presence of a distinct Ca-bearing module layer in braunite II as suggested by De Villiers and Buseck (1989) but its absence in the silica-depleted braunite. In braunite and silica-depleted braunite, Ca may substitute in small amounts for Mn^{2+}. The absence of this divalent cation position in partridgeite and bixbyite restricts the amount of Ca incorporated into these minerals. Al_2O_3 (Fig. 7.15B) appears in highest concentrations in silica-depleted braunite, followed by bixbyite, partridgeite and braunite. The significance of this trend is at present not fully understood.

The formation of partridgeite vs. braunite appears to be controlled locally by the availability of SiO_2 as indicated by the predominance of braunite in the siliceous manganese ores. Partridgeite is much more abundant in the SiO_2-deficient ferruginous manganese ores. Another interesting observation is that iron is preferentially incorporated into braunite in cogenetic braunite-partridgeite pairs (Fig. 7.15D). A similar observation was made by Dasgupta et al. (1990) in braunite-bixbyite pairs in manganese ores of higher metamorphic grade.

Other minerals

In the siliceous manganese ore quartz is the predominant gangue mineral. Rare gangue minerals such as albite, acmite, apatite, barite, illite and Ba-muscovite are of early diagenetic or metamorphic origin. The presence of Ba-muscovite, barite, albite and acmite suggests that considerable amounts of Ba and Na were present in the manganese ores prior to supergene alteration. The unusual set of gangue minerals in the ferruginous manganese ores including diaspore, ephesite, and amesite is certainly indicative of a highly aluminous character of the precursor sediment of this type of ore. Of special interest are the enrichment of Na, Ca and Li in ephesite and Mg in amesite. It is speculated that these elements were present in the original wad-bauxitic clay sediment, possibly incorporated in compounds such as birnessite (Ca, Mg, Na), todorokite (Ca, Mg, Na), or lithiophorite (Li). The unique occurrence of gamagarite may be related to local enrichment of vanadium in the precursor wad.

Metamorphism

Members of the braunite group are known to be stable in various geological settings. Braunite and bixbyite form under metamorphic conditions ranging from lowest greenschist facies to granulite facies (Roy, 1981). Several authors ahve presented convincing evidence for the early diagenetic formation of braunite as a reaction product of poorly crystalline Mn^{4+} oxihydroxides and quartz (Ostwald and Bolton, 1990; Roy et al., 1990; Ostwald, 1992). Others have advocated its sedimentary (Serdyuchenko, 1980; Hou, 1994) or even supergene origin. Partridgeite, or iron-poor bixbyite, is only known from lower greenschist facies metamorphic assemblages (Roy et al., 1990), although experimental studies suggest the stability of the association braunite-partridgeite at high temperatures and pressures of up to 600 °C and 7 kbar at oxygen fugacities controlled by the MnO_2/Mn_2O_3 buffer (Abs-Wurmbach et al., 1983). Apart from its occurrence in the Postmasburg manganese field, silica-depleted braunite has as yet only been recognized in the lower-greenschist metamorphic oxide ores of the Kaljidongri mine, India (Ostwald and Nayak, 1993), and as a major constituent of hydrothermally altered Wessels-type ore of the Kalahari manganese field (Gutzmer and Beukes, 1995).

UNIVERSITY OF JOHANNESBURG

Petrographic evidence suggests that braunite, partridgeite and Ca-poor silica-depleted braunite formed diagenetically in the manganese ores of the Postmasburg manganese field and were locally recrystallized during greenschist facies metamorphism. The occurrence of bixbyite is restricted to isolated pods of very coarsely recrystallized ferruginous manganese ores. Textures such as veiining, brecciation and the abundance of vugs indicate that bixbyite-rich ores formed as a result of localized metasomatism with hydrothermal fluids most probably expelled from the immediate host rocks.

Peak metamorphic temperatures can be deduced fairly accurately from the aluminous Gamagara shales that cover the Mn-ores. Pyrophyllite and diaspore form during lower greenschist facies metamorphic dehydration of kaolinitic clays at temperatures ranging between 300 and 350 °C (Fig. 7.16) (Anovitz et al., 1993) suggesting a corresponding pressure range of between 3 and 4 kbar. This result is in very good agreement with peak metamorphic temperatures of below 370 °C and pressures below 4 kbar proposed by Plehwe-Leisen (1985) who studied the crystallinity of illite in shales of the Olifantshoek Group. It is also in consensus with the results of Nell et al. (1994) who derived a temperature of formation between 315 and 375 °C for the iron-rich bixbyites in the ferruginous manganese ores by applying an experimentally calibrated bixbyite geothemometer. This new geothermometer is based on the fractionation of Fe^{3+} ions between the

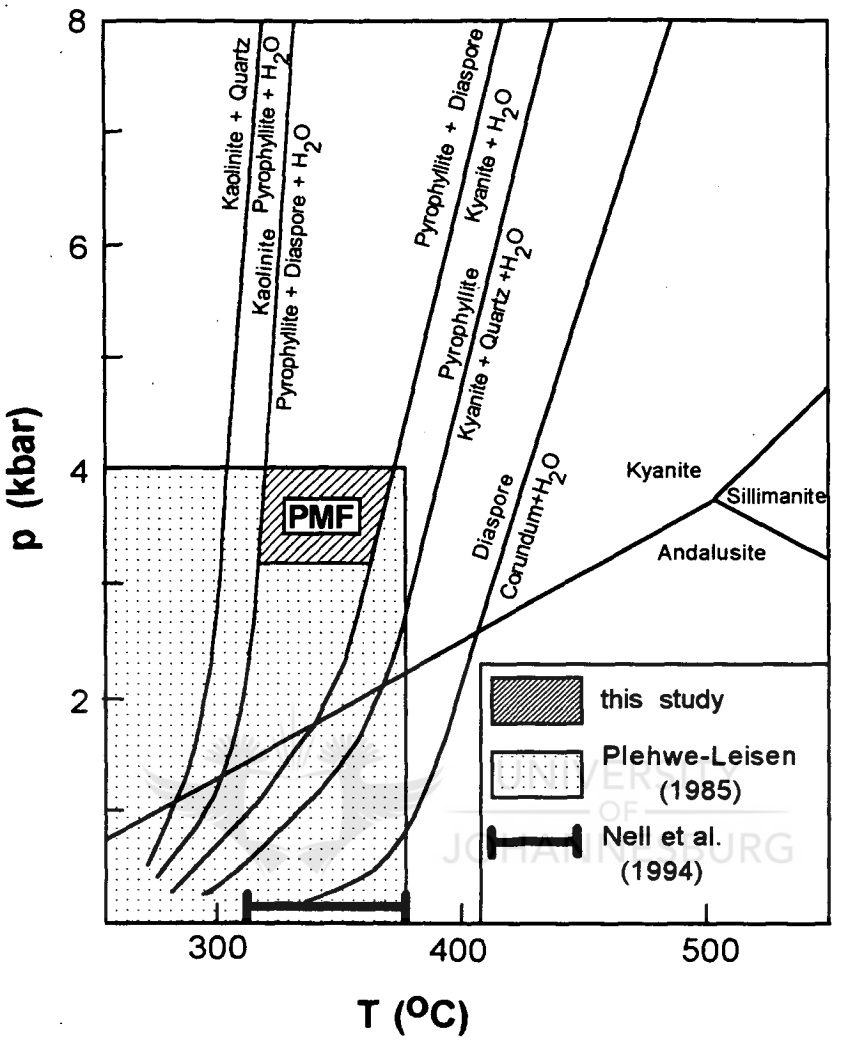

Fig. 7.16 Stable equilibria in the system Al_2O_3-SiO_2-H_2O. Hatched area outlines peak metamorphic conditions suggested for the manganese ores and associated sediments of the Olifantshoek Group in the Postmasburg manganese field. Lower greenschist metamorphic conditions are in agreement with the temperature of formation of bixbyite (Nel et al., 1994) and metamorphic conditions estimated by Plehwe-Leisen (1985) for the Postmasburg manganese field.

different cation sites in the bixbyite structure. This fractionation appears to be only dependent on the temperature of formation (or reequilibration) of bixbyite but independent of its absolute iron content (Nell et al., 1994).

The classical bixbyite geothermometer established by Mason (1943) was based on the absolute iron content in bixbyite, a variable that must dependend on the availabiity of iron during the formation of bixbyite. Restricted availability or mobility of iron during metamorphism may be reason for the formation of partridgeite and bixbyite during metamorphism in the Postmasburg

formation of bixbyite. Restricted availability or mobility of iron during metamorphism may be reason for the formation of partridgeite and bixbyite during metamorphism in the Postmasburg manganese field. It may also explain why De Villiers (1983) arrived at divergent temperatures of formation of below 300 °C for partridgeite and up to 470 °C for bixbyite by applying Masons bixbyite geothermometer to the ores of the Postmasburg manganese field. Masons bixbyite geothermometer should thus be used with great caution and only in assemblages where the presence of cogenetic hematite is evidence for the free availability of iron during the formation of bixbyite.

Supergene alteration

Secondary karstification, pervasive oxidation of the manganese ores and local remobilization of manganese form small amounts of supergene ores that are evidence for the introduction of meteoric fluids. The predominance of romanechite and cryptomelane in the supergene mineral assemblage indicates that considerable amounts of barium and potassium were introduced by oxidizing, sulphate-deficient meteoric water. The supergene formation of abundant lithiophorite in the ferruginous ores is apparently controlled by the local availability of manganese, alumina and lithium in the ferruginous manganese ores.

UNIVERSITY OF JOHANNESBURG

Conclusions

The braunite group minerals that occur in the oxide facies manganese ores of the Postmasburg manganese field formed during diagenesis and low-grade metamorphism at the expense of poorly crystalline Mn^{4+}-Fe^{3+} oxihydroxides. The metamorphic oxide assemblage reflects a regionally uniform lower greenschist facies metamorphic overprint for the Postmasburg manganese field unlike suggested by Schneiderhöhn (1931), De Villiers (1960) and De Villiers (1983). Local variations of the metamorphic oxide association are explained by differences in the host rock composition.

Five members of the braunite group are present in the Postmasburg manganese ore, namely braunite, braunite II, Ca-poor silica-depleted braunite, partridgeite and bixbyite. Iron-poor partridgeite is a distinct phase that is chemically and optically easily distinguished from iron-rich bixbyite. The phase chemistry of braunite, braunite II and bixbyite is in agreement with the polysomatic stacking model for the braunite group suggested by De Villiers and Buseck (1989). However, the composition of partridgeite and Ca-poor silica-depleted braunite can only be

explained in terms of this polysomatic stacking model if a module layer with partridgeite composition ($Mn_{16}O_{24}$) is introduced.

Acknowledgements

The authors are greatly indebted to the geological staff of ASSMANG (Beeshoek), ISCOR (Sishen), SAMANCOR (Hotazel) and Rio Tinto Exploration for their permission to visit their properties in the Postmasburg manganese field. Special thanks to Willem Grobbelaar (ASSMANG), Technical Manager at Beeshoek Iron Ore Mine, for logistical support and many interesting discussions during field-work in 1993 and 1994 by J.G. We want to express special thanks to Andreas "Hasselblad"-Pack, for his expert advice on how to obtain high quality black and white photomicrographs and to Daniel Nyfeler (Bern) for information on the manganese diaspore.

UNIVERSITY OF JOHANNESBURG

References

Abs-Wurmbach, I, Peters, Tj., Langer, K., and Schreyer, W. (1983. Phase relations in the system Mn-Si-O an experimental and petrological study. N. Jb. Mineral. Abh., 146, 258-279.

Afifi, A.M., and Essene, E.J. (1988). Minfile Version 3-88.

Anovitz, L.M., Perkins, D., and Essene, E.J. (1991). Metastability in near-surface rocks of minerals in the system Al_2O_3-SiO_2-H_2O. Clays Clay Min., 39, 225-233.

Baudracco-Gritti, C. (1985). Substitution du manganese bivalent par du calcium dans les minéraux du groupe: Braunite, neltnerite, braunite II. Bulletin de Minéralogie, 108, 437-445.

Beukes, N.J. (1978). Die Karbonaatgesteentes en Ysterformasies van die Ghaap-Groep van die Transvaal-Supergroup in Noord-Kaapland. Ph.D. thesis (unpubl.), RAU, 580 pp.

Beukes, N.J., and Smit, C.A. (1987). New evidence for thrust faulting in Griqualand West, South Africa: Implications for stratigraphy and the age of red beds, Trans. Geol. Soc. S. Afr., 90, 378-394.

Coles-Phillips, F.C. (1931). Ephesite (soda-margarite) from the Postmasburg district, South Africa, Min. Mag., 22, 482-485.

Chudoba, K. (1929). Über 'Mangandiaspor' und Manganophyll von Postmasburg (Griqualand West, Südafrika), Centralblatt Mineralogie etc., Beilagen Band A, 11-18.

Dasgupta, S. Bannerjee, H., Fukuoka, M., Bhattacharya, P.K., and Roy, S. (1990). Petrogenesis of metamorphosed manganese deposits and the nature of the precursor sediments. Ore Geol. Rev., 5, 359-384.

De Villiers, J. (1960). Manganese deposits of the Union of South Africa. Handbook 2, Geol. Surv. S. Afr., Pretoria, 280 pp.

De Villiers, J.E. (1943a). A preliminary description of the new mineral partridgeite, Amer. Mineral., 28, 336-338.

De Villiers, J.E. (1943b). Gamagarite, a new vanadium mineral from the Postmasburg manganese deposits, Amer. Mineral., 28, 329-335.

De Villiers, J.E. (1944). The origin of the iron and manganese deposits in the Postmasburg and Thabazimbi areas, Trans. Geol. Soc. S. Afr., 47, 123-135.

De Villiers, J.E. (1945b). Some minerals occurring in South African manganese deposits, Trans. Geol. Soc. S. Afr., 48, 17-25.

De Villiers, J.E. (1945b). Lithiophorite from the Postmasburg manganese deposits, Amer. Mineral., 30, 629-634.

De Villiers, J.E. (1983). The manganese deposits of Griqualand West, South Africa: Some mineralogic aspects, Econ. Geol., 78, 1108-1118.

De Villiers, J.E. (1992). On the origin of the Griqualand West manganese and iron deposits, S. Afr. J. Sci., 88, 12-15.

De Villiers, J.P.R. (1980). The crystal structure of braunite II and its relation to bixbyie and braunite. Amer. Mineral., 65, 756-765.

De Villiers, J.P.R., and Buseck, P.R. (1989). Stacking variations and nonstoichiometry in the bixbyite-braunite polysomatic mineral group. Amer. Mineral., 74, 1325-1336.

De Villiers, P.R., and Herbstein, F.H. (1967). Distinction between two members of the braunite group. Amer. Mineral., 52, 20-30.

Frenzel, G. (1980). The manganese ore minerals. In: Anhaeusser, C.R., and Maske, S.S. (eds.): Geology and geochemistry of manganese, Vol 1, Schweizerbart, Stuttgart, 25-157.

Geller, S. (1971). Structures of α-Mn_2O_3, $(Mn_{0.983}Fe_{0.017})_2O_3$ and $(Mn_{0.37}Fe_{0.63})_2O_3$ and relationship to magnetic ordering. Acta Cryst., B27, 821-828.

Giovanoli, R., Bühler, H., and Sokolowska, K. (1973). Synthetic lithiophorite: electron microscopy and X-ray diffraction. Journal Microscopy, 18, 271-284.

Grobbelaar, W.S., and Beukes, N.J. (1986). The Bishop and Glosam manganese mines and Beeshoek iron ore mine of the Postmasburg area. In: Annhaeusser C.R., and Maske S. (eds.): Mineral deposits of Southern Africa; Geol. Soc. S. Afr., Johannesburg, 957-961.

Gruner, J.W. (1943). Massive bixbyite $(Mn,Fe)_2O_3$ of low iron content. Amer. Mineral., 28, 174.

Gutzmer, J., and Beukes, N.J. (1995). Fault-controleld metasomatic alteration of Early Proterozoic sedimentary manganese ores in the Kalahari manganese field, South Africa. Econ. Geol, 90, 833-844.

Hall, A.L. (1926). The manganese deposits near Postmasburg, West of Kimberley, Trans. Geol. Soc. S. Afr., 29, 17-66.

UNIVERSITY OF JOHANNESBURG

Harlow, G.E., Dunn, P.J., and Rossman, G.R. (1984). Gamagarite: A reexamination and comparison with brackebuschite-like minerals, Amer. Mineral., 69, 803-806.

Hou, B. (1994). Primary braunite in Triassic sedimentary manganese deposits of Dounanm Yunnan, China. Ore Geol. Rev., 9, 219-239.

Huebner, S. (1976). The manganese oxides - A bibliographic commentary. In: Ribbe, P.H. (Ed.): Oxide minerals. Reviews in Mineralogy, Washington, 7, SH1 - SH17.

Kleyenstüber, A.S.E.(1985). A regional mineralogical study of the manganese-bearing Voelwater Subgroup in the Northern Cape Province. Ph.D. thesis (unpubl.), RAU, 328 pp.

Mason, B. (1943). Mineralogical aspects of the system FeO-Fe_2O_3-MnO-Mn_2O_3 . Geol. För. Förhandl., 65, 97-180.

Mason, B. (1944). The system Mn_2O_3-Fe_2O_3: Some comments on the names bixbyite, sitaparite and partridgeite. Amer. Mineral., 29, 66-69.

Moore, P.B., and Araki, T. (1976). Braunite: Its structure and relationship to bixbyite and some insights on the genealogy of fluorite-derivative structures. Amer. Mineral., 61, 1228-1240.

Nel, L.T. (1929). The geology of the Postmasburg manganese deposits and the surrounding country. Explanation of the geological map. Geol. Surv. S. Afr., Pretoria, 109 pp.

Nell, J., Pollak, H., and Lodya, J.A. (1994). Intersite partitioning in natural and synthetic alpha-$(Fe, Mn)_2O_3$ (bixbyite) solid solutions determined from ^{57}Fe Mössbauer spectroscopy. Hyperfine Interactions, 91, 601-605.

Ostwald, J. (1992). Diagenetic and supergene braunites in the Proterozoic Manganese Group, Western Australia. Min. Mag., 56, 611-616.

Ostwald, J., and Bolton, B.R. (1990). Diagenetic braunite in sedimentary rocks of the Proterozoic Manganese Group, Western Australia. Ore Geol. Rev., 5, 315-323.

Ostwald, J., and Nayak, V.K. (1993). Braunite mineralogy and paragenesis from the Kajlidongri mine, Madhya Pradesh, India. Mineral. Depos., 28, 153-156.

Plehwe-Leisen, E. von (1985). Geologische und erzpetrographische Untersuchungen der Manganerze des Postmasburgfeldes, Noerdliche Kapprovinz, Südafrika. Ludwig-Maximilians Universität München, 129 pp.

Ramdohr, P. (1969). The ore minerals and their intergrowths. Pergamon Press, Oxford, 1174 pp.

Ramdohr, P., and Frenzel, G. (1956). Die Manganerze. In: Symposium sobre yacimentos de manganeso. XX. International Geological Congress, Mexico, 19-73.

Rösler, H.J. (1984). Lehrbuch der Mineralogie. VEB Verlag, Leipzig, 3. edition, 833 pp.

Roy, S. (1980). Manganese deposits. Academic Press, London, 458 pp.

Roy, S., Bandopadhyay, P.C., Perseil, E.A., and Fukuoka, M. (1990). Late diagenetic changes in manganese ores of the Upper Proterozoic Penganga Group, India. Ore Geol. Rev., 5, 341-357.

Serdyuchenko, D.P. (1980). Precambrian biogenic sedimentary manganese deposits. In: Varentsov, I.M., and Grasselly, G., (eds.): Geology and Geochemistry of manganese, 2, 61-88.

UNIVERSITY OF JOHANNESBURG

Schneiderhöhn, H. (1931). Mineralbestand und Gefüge der Manganerze von Postmasburg, Griqualand West, Südafrika, N.Jb.Min., Beilagen, 64 A, 701-726.

Strauss, C.A. (1964). The iron ore deposits in the Sishen area, Cape Province. In: Haughton, S.H. (ed.): The geology of some ore deposits in Southern Africa. Geol. Soc. S. Afr., Johannesburg, 393-403.

Van Schalkwyk, J.F., and Beukes, N.J.(1986). The Sishen iron ore deposit, Griqualand West. In: Annhaeusser C.R. and Maske S. (eds.): Mineral deposits of Southern Africa; Geol. Soc. S. Afr., Johannesburg, 931-956.

Van Wyk, J.P.(1980). Die geologie van die gebied Rooinekke-Matsap-Wolhaarkop in Noord-Kaapland met spesiale verwysing na die Koegas -Subgroep, Transvaal-Supergroep. Unpubl. MSc. thesis, RAU, 159 pp.

Van Wyk, and Beukes, N.J. (1982). The geology of the Sishen iron ore deposit. In: Glen, H.W. (ed.): Proceedings, 12th CMMI Congress. Geol. Soc. S. Afr., Johannesburg, 203-211.

UNIVERSITY OF JOHANNESBURG

Chapter Eight

Conclusions

This chapter provides a summary and discussion of the results presented in the previous chapters. Genetic models for manganese deposits of the Kalahari and Postmasburg manganese fields are compared and evaluated to point out similarities and differences. Remaining problems are outlined that may be solved by future research projects.

Genesis and alteration of manganese ores in the Kalahari manganese field

Several geological characteristics are important for the understanding of the sedimentary origin of the Kalahari manganese field. The most striking one is the presence of three symmetrical sedimentary cycles in the manganese-bearing Hotazel Formation, each composed of a succession of jaspilitic iron-formation → hematite lutite → braunite lutite (Fig. 8.1A).The stratigraphic setting of the Hotazel Formation between the underlying Ongeluk lavas and the transition of the Hotazel Formation into the stromatolitic dolomites of the Mooidraai Formation are evidence for deposition of the Hotazel Formation in a shallow marine sedimentary environment (Beukes, 1983). The gradational contacts between the beds and the lack of detrital sediments are indicative of a stable, low energy depositional system. The depositional environment is thus very similar to that commonly envisaged for Superior-type iron formations (Trendall, 1973; Beukes, 1973, 1983; Lougheed, 1983; Garrels, 1987). The Hotazel Formation, however, is unique as it is the only example of an Early Proterozoic Superior-type iron-formation interbedded with manganese-formation. Similar deposits are known to be of Late Proterozoic age and include the Chuos Formation at Otjosondu in Namibia (Bühn et al., 1991, 1992, 1993), the Jacadigo Group at Urucum in Brazil (Schneider, 1984; Schreck, 1984; Urban et al., 1992) and the Penganga Group close to Adilabad, Andhra Pradesh, India (Roy, 1981; Roy et al., 1990).

The mechanisms that controlled separation and selective precipitation of manganese and iron in these deposits are still poorly understood but may well be based on physicochemical variations as response to marine transgression-regression cycles as suggested by Beukes (1983) and Bühn et al. (1991). The

REE geochemistry of iron-formations suggests a large contribution of iron and manganese from hydrothermal sources during the Archean and Early Proterozoic and a considerably smaller influence of hydrothermal fluids to the formation of Late Proterozoic iron-formations (Klein and Beukes, 1993). However, the absolute size of the hydrothermal contribution remains speculation (see for different opinions see for example: Mel'nik, 1982; Holland, 1973, 1984; Simonson, 1985; Klein and Beukes, 1989; Kimberley, 1989). The rare occurrence of volcanoclastic material in the Hotazel Formation (Kleyenstüber, 1985) is strong evidence for the concept that a volcanic source, if present, was situated a considerable distance from the depositional site of the Hotazel Formation (Beukes, 1983), and not proximal as suggested by Cornell and Schütte (1995).

Mineralogy and petrography of the braunite-lutite suggest that the manganese ores of the Hotazel Formation precipitated as a finely bedded mud composed of manganese-rich carbonates, braunite and hematite. This interpretation would favour the formation of braunite in the sedimentary environment, a suggestion previously made by Hou (1994). However it is more likely that a poorly crystalline silica-bearing Mn^{4+} - phase was precipitated and diagenetically transformed into braunite (Ostwald and Bolton 1990; Ostwald 1992). Carbonate remobilization and formation of kutnahorite-Mn-calcite ovoids are other visible effects of early diagenesis (Fig. 8.1A). The replacement of carbonate ovoids by hausmannite, partridgeite, manganite and calcite is attributed to late diagenetic or metamorphic oxidation associated stratabound fluid flow (Fig. 8.1E). Metamorphic alteration of the Hotazel Formation did not exceed lower greenschist facies (Kleyenstüber, 1985). Early diagenesis and regional metamorphism affected the entire Hotazel Formation. Low-grade Mamatwan-type ore is thus composed of mineral phases of sedimentary, early diagenetic and metamorphic origin. The metamorphic event can be tentatively correlated with thrusting and crustal thickening during the Kheis orogeny (Fig. 8.1F).

The intrusion of bostonite dykes and the onset of normal faulting (8.1D) in the northern part of the Kalahari deposit and the graben structures of Hotazel and Langdon-Devon predate the metamorphic overprint (Fig. 8.1B). The deposition of the Olifantshoek Group between 2.2 and 2.0 Ga apparently coincides with the origin of normal faults (Fig. 8.1D) (Beukes and Smit, 1987). Three distinct structurally controlled episodes of hydrothermal-metasomatic alteration are observed in the Kalahari manganese field. The oldest of these three events is the Wessels alteration event. Intensive

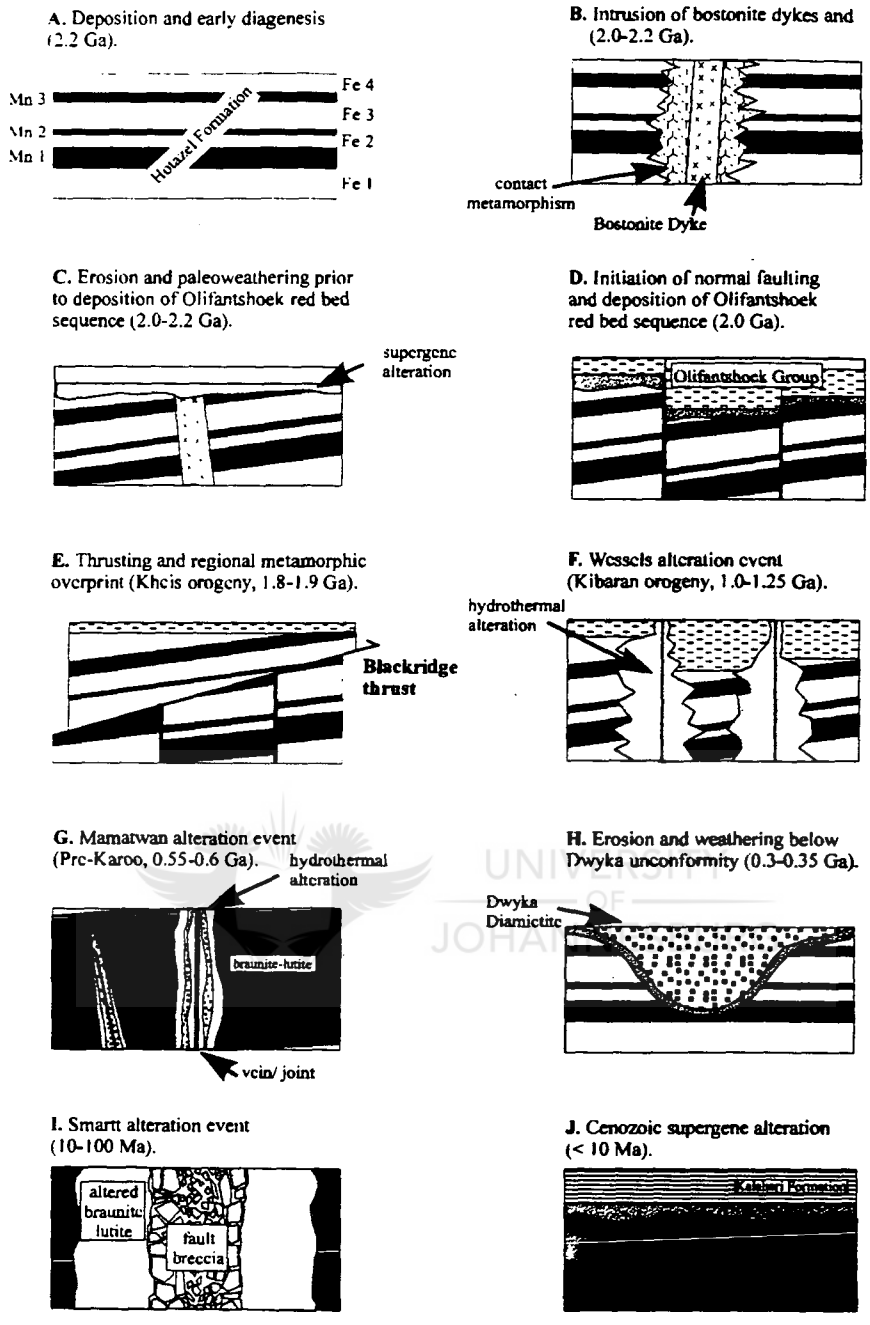

Fig. 8.1 Geological evolution of the Kalahari manganese field. (A) Cyclic deposition of iron- and manganese-formations of the Hotazel Formation; (B) Intrusion of bostonite dykes into the Hotazel Formation; (C) Erosion and paleooxidation below the Mapedi unconformity; (D) Deposition of the red bed sediments of the Late Paleoproterozoic Olifantshoek Group and N-S orientated normal faulting in the NW part of the Kalahari deposit; (E) Low angle thrusting from the west along the Blackridge thrust induces lowest greenschist facies metamorphism; (F) Hydrothermal alteration along reactivated normal faults in the NW part of the deposit (Wessels alteration event) during the Kibaran orogenetic event; (G) Syntectonic sulphide-carbonate mineralization in joints and veins and localized wallrock alteration (Mamatwan alteration event); (H) Erosion and paleoweathering associated with the Late Devonian-Early Carboniferous Dwyka glaciation; (I) Smartt alteration event, oxidation of ores around fault breccias induced by ascending Pre-Kalahari groundwater; (J) Subrecent and recent supergene oxidation of manganese ores below the Kalahari unconformity.

hydrothermal metasomatic alteration affected the ores around reactivated normal faults in the northern portion of the Kalahari manganese deposit.

Ongeluk lavas, intrusive bostonite dykes, iron-formation interbedded with the manganese ore and shales belonging to the Olifantshoek Group were also affected by this hydrothermal metasomatic alteration event. The timing of the Wessels event, based on radiometric dating of alteration minerals (Dixon, 1989; R. Frey, pers. comm., 1995), indicate that alteration took place at 1.0-1.25 Ga. Normal faults acted as fluid feeders for hydrothermal fluids entering into the manganese orebody having a temperature of about 350-400 °C, 0.5-1.5 kbar pressure, low fO_2 and extremely low fCO_2 (Miyano and Beukes, 1987).

Two distinct styles of alteration may be distinguished by virtue of different metasomatic zoning patterns around faults acting as fluid feeders. The ferruginous style of alteration, encountered at Wessels and Nchwaning mines, is characterized by a narrow zone of massive braunite ore around a zone of intensive ferruginization immediately adjacent to fluid feeder faults. With decreasing degree of alteration the massive braunite ore grades into zones of porous, coarse crystalline hausmannite-rich ore, then into massive, medium grained hausmannite-rich ore, in turn grading into bixbyite-braunite II-hausmannite rich ore and finally into braunite II-braunite (new)-rich ore. The latter envelops portions of residual Mamatwan-type ore preserved in the centre of fault blocks. The siliceous-type of alteration that is especially well developed at Hotazel Mine is characterized by the development of a zone of extremely high-grade, coarse crystalline hausmannite-rich ore immediately adjacent to zones of ferruginization adjacent to fluid feeder faults. Grain size and amount of hausmannite decrease with decreasing degree of alteration away from faults. The association of andradite and hausmannite is characteristic for a moderate degree of alteration. The amount of residual primary braunite increases with decreasing degree of alteration.

Manganese ores were upgraded considerably during the Wessels alteration event. Upgrading is achieved by leaching of the primary carbonates (CO_2, Ca, Mg) and SiO_2 from the Mamatwan-type precursor and residual enrichment of manganese. A large amount of secondary porosity remained as primary carbonates were removed. A large part of this porosity was consumed by compaction of the orebed by about one third of its entire original thickness. Minor and trace elements were redistributed and concentrated in pore-filling trace mineral phases. Only Fe and Cu (ferruginous style

of alteration) and Fe and Zn (siliceous style of alteration) were apparently introduced by the hydrothermal fluid.

Hydrothermal fluids turned alkaline on reaction with the carbonate-rich braunite-lutite. The high alkalinity of the hydrothermal system is clearly illustrated by the occurrence of calcium-hydroxy-silicates such as tobermorite and xonotlite. The unusual combination of highly alkaline hydrothermal fluids with low fO_2 and fCO_2 in an manganese and iron-rich environment are regarded as most important factors for the mineralogical diversity that characterizes the Wessels alteration event.

The Mamatwan alteration event postdates the Wessels alteration event. It is present throughout the Kalahari manganese field, non-penetrative and confined to faults and joints (Fig. 8.1G). Pyrite-chalcopyrite-carbonate mineralization in veins and joints suggest the introduction of epithermal solutions with low fO_2 and high fH_2S along fractures and reactivated faults. Different zones of wallrock alteration around the mineralized veins and joints are representative of different degrees of wallrock alteration. Lowest degree of wallrock alteration is characterized by the transformation of braunite into jacobsite and hausmannite. Leaching of manganese oxides results in apparent hematitization of the ore at moderate degrees of alteration. The formation of pyrite at the expense of hematite is typical for the highest degree of wallrock alteration. Secondary porosity is created by recrystallization of the Mn-bearing carbonates of the Mamatwan-type ore. The Mamatwan alteration event has been tentatively placed in the period pre-dating deposition of the Phanerozoic Karoo Supergroup.

A third hydrothermal alteration event is only evident where the rocks of the Hotazel Formation crop out below the Kalahari unconformity (Fig. 8.1I). The formation of todorokite in stratiform veins and as metasomatic replacement product of Mn-bearing carbonates (especially prominent at Smartt mine) are the most prominent features of the Smartt alteration event. The origin of todorokite is related to the interaction of manganese ore with ground water of low temperature and high fO_2 that entered the Hotazel Formation prior to deposition of the Kalahari Formation.

Supergene alteration must have affected the manganese ore along three erosional unconformities (Kleyenstüber, 1993). These three unconformities are the Late Paleoproterozoic Mapedi unconformity, predating the deposition of the Olifantshoek Group (Fig. 8.1C), the Late Carboniferous-Early Permian Dwyka unconformity (Fig. 8.1H), and the Late Mesozoic/Cenozoic

Kalahari unconformity (Fig. 8.1J). Supergene alteration along the suboutcrop of the Hotazel Formation below the Kalahari unconformity is characterized by oxidation of carbonates and lower manganese oxides (braunite, hausmannite) to cryptomelane, pyrolusite and other Mn^{4+}-oxides. Alteration took place as meteoric water percolated downward through the loose sediment cover of the Kalahari Formation.

Genesis and alteration of manganese ores in the Postmasburg manganese field

Mineralogical and petrographical studies indicate that the manganese ores of the Postmasburg manganese field formed as residual sediments during subaerial exposure, erosion and weathering of the Late Archean Transvaal Supergroup below the Late Paleoproterozoic Mapedi unconformity. Manganese deposition coincided with the onset of deposition of the basal Gamagara Formation of the Late Paleoproterozoic Olifantshoek Group. The manganese ores accumulated along and immediately below the unconformity that separates the Transvaal Supergroup from the Gamagara Formation. The ores developed in karst depressions in the Fe- and Mn-rich dolomite of the Campbellrand Subgroup of the Transvaal Supergroup.

Weathering processes that affected the rocks of the Transvaal Supergroup prior to deposition of the Gamagara Formation appear very similar to modern lateritic weathering. They are characterized by oxidation and retention of Mn and Fe, intensive leaching of SiO_2, Na, K, Ca and Mg, and residual enrichment of Al_2O_3 and TiO . Karstification of underlying dolomites of the Campbellrand Supergroup provided a suitable source for the accumulation of iron and manganese and traps for their *in-situ* accumulation.

The deposition of Mn^{4+}-Fe^{3+} oxide wad and lateritic paleosols in a terrestrial environment requires the presence of a highly oxygenated atmosphere during the Late Paleoproterozoic (2.2-2.0 Ga). This agrees very well with studies of paleoweathering profiles below the Mapedi erosion surface by Wiggering and Beukes (1990) and Holland and Beukes (1990). These weathering profiles show a high degree of iron retention, e.g. iron oxidation, indicating that weathering proceeded under the influence of an atmosphere with a content of O_2 larger than 0.15 PAL (Present Atmospheric Level) (Holland and Beukes, 1990). The stratigraphic setting of the manganese deposits at the very base of

A. Erosion and paleoweathering along Mapedi unconformity (2.2-2.0 Ga)

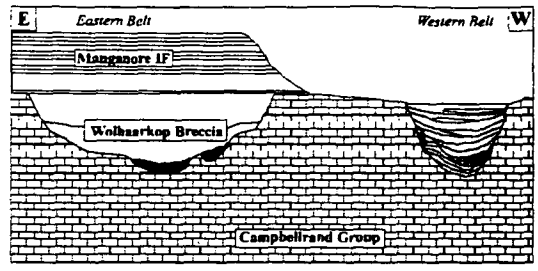

B. Deposition of Olifantshoek Group (2.0 Ga).

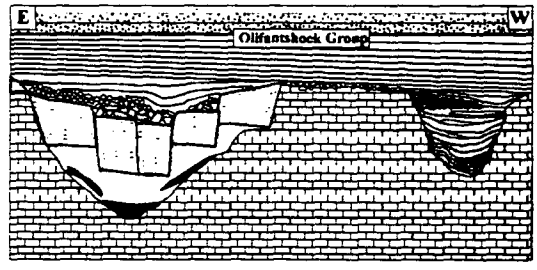

C. Thrusting and regional metamorphic overprint (Kheis orogeny, 1.8-1.9 Ga).

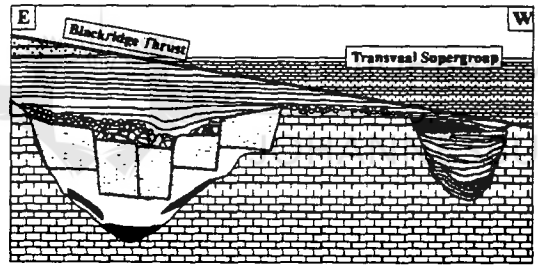

D. Secondary karstification and supergene alteration.

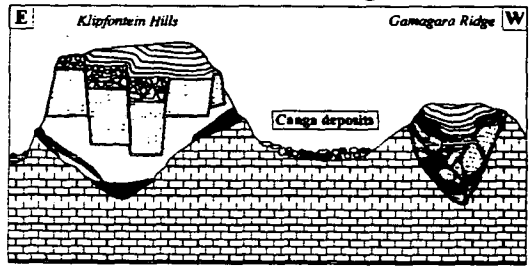

Fig. 8.2 Geologic evolution of the Postmasburg manganese field (A) Erosion and paleoweathering of the Transvaal Supergroup along the Paleoproterozoic Mapedi unconformity. Karstification of the Campbellrand dolomite. Accumulation of Mn-wad and clastic detritus in karst sinkholes and karst caves coincides with hematitization of the Manganore iron-formation. (B) Slumping of the Manganore iron-formation into large sinkholes. Floodplain deposits of the Gamagara Formation (hematite conglomerates, laterites and aluminous shales) are followed by deposition of illitic shale and quartzite of the Olifantshoek Group. (C) Low angle thrusting from the West along the Blackridge and lower greenschist facies metamorphism. (D) Erosion and subaerial exposure result in secondary karstification, oxidation of metamorphic mineral assemblage and formation of alluvial canga deposits.

the Olifantshoek Group leads to the conclusion that the manganese ores of the Postmasburg manganese field represent the oldest known oxidized terrestrial sediments that provide evidence for the presence of a highly oxygenated atmosphere.

Accumulation of minable manganese ores took place in two distinct environments: The siliceous type of manganese ore are an integral part of the residual Wolhaarkop chert breccia that formed as residual subsurface slump breccia in paleokarst caves associated with cherty dolomites of the Fairfield Formation of the Campbellrand Subgroup (Fig. 8.2A). Griquatown and Kuruman iron formations apparently formed the roof of these karst caves. Hematitization and enrichment of these iron-formations coincide with the accumulation of manganese ores. Continued weathering resulted in collapse of the karst caves and slumping of the hematitized Manganore iron-formation into the sinkholes (Fig. 8.2B).

The ferruginous manganese ores of the Western Belt represent equivalents of the Lindener Mark type (Borchert, 1970) of manganese deposits. Ferruginous and aluminous manganese ores formed as intimate mixtures of chemical (wad) and detrital (lateritic clay, hematite pebbles) components in open sinkholes and depressions in the underlying dolomite of the Reivilo Formation of the Campbellrand Group (Fig. 8.2A). Reworked lateritic weathering products of silicate rocks are a likely source for the clay component. Hematite pebbles in conglomeratic interbeds were derived from erosion of parts of the Manganore iron-formation and their deposition in alluvial fan deposits. Accumulation of manganese ores came to an end with the deposition of the shales of the Gamagara Formation of the Olifantshoek Group (Fig. 8.2B).

Lower greenschist facies metamorphism affected the manganese ores of both belts of manganese deposits in the Postmasburg manganese field (Fig. 8.2C). The wide distribution of the intimate association of braunite and partridgeite suggests a low and consistent metamorphic overprint throughout the Postmasburg manganese field. Coarse crystalline bixbyite-rich ferruginous ores of the Western Belt are regarded to be products of synmetamorphic fluid remobilization. Postmetamorphic hydrothermal alteration is restricted to the formation of lenses and veins of barite and specularite. The timing of hydrothermal alteration is only very poorly constrained.

Renewed subaerial exposure of the Campbellrand dolomite sequence led to secondary karstification, and slumping and brecciation of the metamorphosed manganese ores (Fig. 8.2D). Supergene

oxidation of the metamorphic mineral assemblage to romanechite and lithiophorite took place. Oxidation and replacement of the metamorphic mineral assemblage by manganomelane-type minerals, pyrolusite, ramsdellite or lithiophorite (Fig. 8.2D) are a result of supergene alteration. The abundance of Ba-rich romanechite call for influx of Ba-rich low temperature ground water. Recent canga deposits formed as a product of mechanical erosion (Fig. 8.2D).

Two manganese fields - one story ?

At present geochronological evidence provides only a broad time frame for the deposition of the manganese ores of the Kalahari and Postmasburg manganese fields. The 2.22 Ga extrusion age for the andesitic Ongeluk lavas (Cornell et al., reference in Cornell and Schütte, 1995; Armstrong, 1987) represents the lower, and the 1.93 Ga extrusion age for the Hartley basalt of the Olifantshoek Group (Cornell, reference in Schütte, 1992) the upper age limit for the deposition of the manganese ores of the Kalahari manganese field and the Postmasburg manganese field. Stratigraphic relationships suggest that the manganese-bearing Hotazel Formation of the Kalahari manganese field is considerably older than the manganese deposits of the Postmasburg manganese field.

Manganese ores in both manganese fields represent chemical sediments where the accumulation took place in entirely different sedimentary environments. The carbonate-rich braunite lutite of the Kalahari manganese deposit is part of the shallow marine sedimentary sequence of the Hotazel Formation. Marine regression and uplift of the Kapvaal Craton occurred after deposition of the dolomite of the Mooidraai Formation and resulted in extensive subaerial exposure of the rocks of the Transvaal Supergroup, including the Hotazel Formation. Erosion and deep weathering were the consequence of prolonged exposure to an oxidizing atmosphere and 'tropical' climatic conditions. The manganese ores of the Postmasburg manganese field accumulated in karst depressions as residual terrestrial sediments from rapidly dissolving Mn- and Fe-rich dolomites of the Campbellrand Supergroup. Marine transgression and deposition of illitic shales and quartzites of the Olifantshoek Group terminated the processes of weathering and manganese wad accumulation.

Regional geological and tectonic events influenced both manganese fields. Some similarities are apparent in the paragenetic mineral record and can be related to regional geological events. Other alteration events appear unique and restricted to one of the manganese fields. Similarities include:

1) Bostonite dykes are known to intrude the manganese ores in both areas, they have been described from Lohatla and Sishen in the Postmasburg area (De Villiers, 1960), and they also occur in the northern part of the Kalahari deposit. 2) Regional metamorphic overprint is of lower greenschist facies in both manganese fields. This regional metamorphic event is (in this study) tentatively correlated with crustal thickening related to the Kheis orogenetic event (~ 1.8-1.9 Ga), but could similarly be related to the Kibaran orogenetic event (~ 1.1 Ga). 3) Syn- or Post-Kalahari supergene alteration is evident in both manganese fields.

Extensive hydrothermal alteration associated with the Kibaran orogenetic event is apparently restricted to the intensively faulted and structurally complex northern part of the Kalahari manganese deposit and the graben-hosted deposits of Hotazel and Langdon-Devon (Wessels alteration event). The Pre-Karoo Mamatwan and Pre-Kalahari Smartt alteration events seem similarly restricted to the Kalahari manganese field, but they are of only very restricted, local importance.

It is concluded, that the close geographic association of the Kalahari manganese field and the Postmasburg manganese field is coincidental. There is no close direct genetic link between the minable ores present in the two deposits. Similarities in mineralogy and mineral paragenesis are related to regional alteration events that postdate the deposition the manganese ores. However, there is a distinct indirect genetic link. The reservoir of iron and manganese in the Archean and Paleoproterozoic oceans was depleted during the deposition of iron and manganese formations, but also during the deposition of marine carbonates. Studies by Veizer et al. (1989, 1990, 1992) illustrate that marine carbonates of Archean and Paleoproterozoic age are significantly enriched in manganese and iron as compared to their Phanerozoic counterparts. Enrichment of manganese in the Campbellrand dolomite, that constitutes the source for the manganese deposits of the Postmasburg manganese field, and the origin of the Hotazel Formation may thus both be related to the presence of iron and manganese-rich seawater during the Archean and the Paleoproterozoic eras.

UNIVERSITY OF JOHANNESBURG

Suggestions for future work

The purpose of the present study was to understand the mineralogy, petrography and geochemistry of the manganese ores of the Kalahari and Postmasburg manganese fields. Two events of supergene alteration of manganese ore in the Kalahari manganese field were not studied mainly due to the lack of suitable sample material. These events are the supergene alteration along the Late Paleoproterozoic Mapedi/ Gamagara unconformity and weathering associated with the Paleozoic Dwyka unconformity as they affect the manganese ore of the Kalahari manganese field. It was also not possible to reconstruct the mineralogical effects of contact metamorphism around bostonite dykes, because of a penetrative overprint by the Wessels hydrothermal alteration event. These gaps in the mineral paragenetic table should be closed by further mineralogical and petrographical studies from samples that become available from exploration or mining operations.

Results obtained during this study allowed recognition of relative ages or events of ore formation and alteration. However, there is little information available concerning the absolute age of the different events, such as the deposition of the Hotazel Formation, weathering and erosion along the Mapedi unconformity, the exact timing of regional greenschist metamorphism, the Mamatwan and Smartt hydrothermal alteration events in the Kalahari manganese field and secondary karstification in the Postmasburg manganese field. Radiometric dating of at least some of these events should now be possible as the mineralogical composition of the ores and their relation to ore-forming events are better understood.

The sources of hydrothermal fluids that altered the manganese ores also remain unknown. pT-conditions and fluid compositions may be derived from fluid inclusion studies; fluid sources and alteration conditions could be deduced from stable and radiogenic isotope studies. Problems are imposed by the lack of knowledge about the isotope systematics of manganese oxides and the scarce occurrence of minerals suitable for fluid inclusion studies in association with the manganese ore. Results of preliminary stable isotope studies and microthermometry performed on fluid inclusions in gangue minerals associated with the manganese ores are compiled in Appendix 5 and 6. The results are far from complete. Further stable isotope studies should involve $\delta^{18}O$ signatures of different generations of manganese oxides, $\delta^{34}S$ of sulphides and $\delta^{34}S$ and $^{87}Sr/^{86}Sr$ of sulphates and

more detailed studies of the stable isotope composition of the carbonates associated with different alteration events.

References

Armstrong, R.A. (1987). Geochronological studies on Archean and Proterozoic formations of the foreland of the Namaqualand front and possible correlates on the Kaapvaal craton. Unpubl. Ph.D. thesis , Univ. of the Witwatersrand, Johannesburg, 274 pp.

Beukes, N.J. (1973). Precambrian iron-formations of South Africa. Econ. Geol., 68. 960-1004.

Beukes, N.J. (1983). Palaeoenvironmental setting of iron formations in the depositional basin of the Transvaal Supergroup, South Africa. In: Trendall, A.F., and Morris, R.C. (eds.). Iron formations, facts and problems, Elsevier, Amsterdam, 131-209.

Beukes, N.J., and Smit, C. A., (1987). New evidence for thrust faulting in Griqualand West, South Africa: Implications for stratigraphy and the age of red beds. Trans. Geol. Soc. S. Afr., 90, 378-394.

Borchert, H. (1970). On the ore-deposition and geochemistry of manganese, Mineral. Depos., 5, 300-314.

Bühn, B., Stannistreet, I.G., and Okrusch, M. (1991). Genesis of late proterozoic sedimentary manganese deposits at Otjosondu, Damara mobile belt, east central Namibia. EGRU Info. Circ, 234, 26 pp.

Bühn, B., Stannistreet, I.G., and Okrusch, M. (1992). Late Proterozoic outer shelf manganese and iron deposits at Otjosondu (Namibia) related to the Damaran oceanic opening. Econ. Geol., 87, 1393-1411.

Bühn, B., Stannistreet, I.G., and Okrusch, M. (1993). Preservation of sedimentary features in late Proterozoic manganese and iron formations (Namibia) through upper amphibolite facies metamorphism: Protoliths, paleoenvironments and ore genesis. Resource Geology, 17, 12-26.

Cornell, D.H., and Schütte, S.S. (1995). A volcanic-exhalative origin for the world's largest (Kalahari)-manganese field. Mineral. Depos., 30, 146-151.

Dixon, R. D. (1989). Sugilite and associated metamorphic silicate minerals from Wessels mine, Kalahari manganese field. Bull. geol. Surv.. S. Afr., 93, Pretoria, 47 pp.

Garrels, R.M. (1987). A model for the deposition of the microbanded Precambrian iron-formations. Amer. J. Sci., 287, 81-106.

Holland, H.D. (1973). The ocenas: a possible source of iron in iron-formations. Econ. Geol., 68, 1169-1172.

Holland, H.D. (1984). The chemical evolution of the atmosphere and oceans. Princeton Univ. Press, Princeton, 582 pp.

Holland, H.D., and Beukes, N.J. (1990). A paleoweathering profile from Griqualand West, South Africa: Evidence for a dramatic rise in atmospheric oxygen between 2.2 and 1.9 BYBP. Amer. J. Sci., 290-A, 1-34.

Hou, B. (1994). Primary braunite in triassic sedimentary manganese deposits of Dounan, Yunnan, China. Ore Geol. Rev., 9, 219-239.

Kimberley, M.M. (1989). Exhalative origins of iron-formations: Ore Geol. Rev., 5, 13-145.

Klein, C., and Beukes, N.J. (1989). Geochemistry and sedimentology of a facies transition from limestone to iron-formation deposition in the Early Proterozoic Transvaal Supergroup, South Africa. Econ. Geol., 84, 1733-1774.

Klein, C., and Beukes, N.J. (1993). Sedimentology and geochemistry of the glaciogenic Late Proterozoic Rapitan iron-formation in Canada. Econ. Geol., 88, 542-565.

Kleyenstüber , A. S. E. (1984). The mineralogy of the manganese bearing Hotazel Formation of the Proterozoic Transvaal Sequence in Griqualand West, South Africa. Trans. geol. Soc. S. Afr., 87, 257-272.

Kleyenstüber , A. S. E. (1985). A regional mineralogical study of the manganese bearing Voëlwater Subgroup in the northern Cape Province. Unpubl. Ph.D thesis, RAU, Johannesburg, 328 pp.

Lougheed, M.S. (1983). Origin of Precambrian iron-formations in the Lake Superior region. Geol Soc. Am. Bull., 94, 325-340.

Mel'nik, Y.P. (1982). Precambrain banded iron-formations: physicochemical conditions of formation. Elsevier, Amsterdam, 5, 310 pp.

Miyano, T., and Beukes, N.J. (1987). Physicochemical environments for the formation of quartz-free manganese oxide ores from the Early Proterozoic Hotazel Formation, Kalahari manganese field, South Africa. Econ. Geol., 82, 706-718.

Ostwald, J. (1992). Diagenetic and supergene braunites in the Proterozoic manganese group, Western Australia. Min. Mag., 56, 611-616.

Ostwald, J., and Bolton, B. (1990). Diagenetic braunite in sedimentary rocks of the Proterozoic manganese group, Western Australia. Ore Geol. Rev., 5, 315-323.

Roy, S. (1981). Manganese deposits. Academic Press, London, 458 pp.

Roy, S., Bandopadhyay, P.C., Perseil, E.A., And Fukuoka, M. (1990). Late diagenetic changes in manganese ores of the Upper Proterozoic Penganga Group, India. Ore Geol. Rev., 5, 341-357.

Schneider, G. (1984). Zur Mineralogie und Lagerstättenbildung der Mangan- und Eisenerzvorkommen des Urucum-Distriktes. Frankf. Geow. Arb., Serie C, 1, 206 pp.

Schreck, P. (1984). Geochemische Klassifikation und Petrogenese der Manganerze des Urucum-Distriktes bei Corumbá, Mato Grosso do Sul, Brasilien. Frankf. Geow. Arb., Serie C, 3, 205 pp.

Schütte, S.S. (1992). Ongeluk volcanism in relation to the Kalahar Mn-deposits. Unpubl. PhD. thesis, Natal Univ., 262 pp.

Simonson, B.M. (1985). Sedimentological constraints on the origins of Precambrian iron-formations. Geol. Soc. Amer. Bull., 96, 244-252.

Trendall, A.F. (1973). Precambrian iron-formation of Australia. Econ. Geol., 68, 1089-1097.

Urban, H., Stribrny, B., and Lippolt, H.J. (1992). Iron and manganese deposits of the Urucum District, Mato Grosso do Sul, Brazil. Econ. Geol., 87, 1375-1392.

Veizer, J., Clayton, R.N., Hinton, R.W., Brunn, V. von, Mason, T.R., Buck, S.G., and Hoefs, J. (1990). Geochemistry of Precambrian carbonates: 3-shelf seas and non-marine environments of the Archean. Geochim. Cosmochim. Acta, 54, 2717-2729.

Veizer, J., Clayton, R.N., and Hinton, R.W. (1992). Geochemistry of Precambrian carbonates: IV. Early Paleoproterozoic (2.25±0.25 Ga) seawater. Geochim. Cosmochim. Acta, 56, 875-885.

Veizer, J., Hoefs, J., Lowe, D.R., and Thurston, P.C. (1989). Geochemistry of Precambrian carbonates: II. Archean greenstone belts and Archean sea water. Geochim. Cosmochim. Acta, 53, 859-871.

Wiggering, H., and Beukes, N.J. (1990). Petrography and geochemistry of a 200-2200-Ma-old hematitic paleo-alteration profile on Ongeluk basalt of the Transvaal Supergroup, Griqualand West, South Africa. Prec. Res., 46, 241-258.

UNIVERSITY OF JOHANNESBURG

Appendix I

Analytical techniques

I.1 Sample preparation

Preparation of sample material for chemical, isotope or X-ray powder diffraction analysis was done at the Department of Geology, RAU.

The following procedure was followed for the preparation of milled powders from whole rock samples: Hand-sized samples were cleaned of loose material with a plastic brush. Parts of these hand-sized samples were fragmented with a hammer into centimeter-sized chips. Chips devoid of weathering crusts, vein material, large vug infills or other contaminating material were hand-picked. 100 to 500 g of these chips were cleaned in an air stream and subsequently crushed for 3 minutes in a Siebtechnik swing mill, using a hardened steel set and rings. The set and rings were cleaned after each sample by wiping with a clean paper towel and exposing it to an air stream. Glass was milled before and after each sample, to minimise contamination to the samples. The finely crushed samples were then stored in glass viles.

Mineral separates for isotope studies and powder diffraction were separated by crushing the original material with a hammer. The crushed material was sieved and washed with distilled water to remove fine dust. Clean, monomineralic grains of the wanted mineral were handpicked under a binocular after drying. The samples were stored in clean glass viles.

I.2 Analytical Chemistry

Various analytical techniques were applied during this study to perform chemical analysis of manganese ores and associated minerals. These are described in detail in this chapter. Mention is made of the various techniques used and problems that were encountered. The results obtained are reported in Appendix III (whole rock chemical analyses) and in Appendix IV (mineral chemistry, electron micro probe analyses).

I.2.1 X-ray fluorescence spectrometry (XRF)

Whole rock chemical analyses for main and trace elements by X-ray fluorescence spectroscopy was performed at the Institut für Mineralogie und mineralische Rohstoffe at the Technische Universität Clausthal (Germany). Analyses were obtained using a Phillips PW 1480 X-ray spectrometer, equipped with a Rh-X-ray tube. Duplicate analyses for every tenth sample was conducted to demonstrate the reproducibility of the method.

At first an attempt was made to produce fused pellets. 600 mg of dried sample powder were mixed with 3.6 g Li-tetra borate (fusing agent) and 100 mg of ammonium nitrate (oxidising agent). The mixtures were fused in platinum crucibles at a temperature of 1300 °C. This method proved to be unsuitable for samples with very high manganese and iron contents. Some solid sample material remained after fusing of manganese-rich samples and melts of iron-rich samples recrystallized upon cooling. These effects could not be eliminated by reducing the 1:6 ratio of sample and fusing agent to as low as 1:60 or by slowing down the cooling process of the fused material.

As an alternative to fused pellets it was decided to produce pressed powder pellets. 5 g of dried sample powder was mixed with 1 g of wax. Pellets were pressed at 15 t/cm^2 in a hydraulic press. The use of powder pellets has the advantage of a much larger ratio of sample material to analytical agents (5:1 as compared to 1:6 for fused pellets). This decreases the detection limit for trace elements considerably. Using pressed powder pellets has, however, also major disadvantages: differing sample matrix and textures of the pellets may introduce greater analytical errors. These disadvantages can be diminished by careful calibration of the spectrometer with reference materials of similar matrix and composition to that of the samples.

Manganese ores with extremely variable matrices were analysed during this study: supergene, hydrous Mn-ores, carbonate-rich ores and high-grade, oxide-rich ores with low water and CO_2 contents. Matrix effects were indeed found to constitute the most serious problem. A number of international standards and in-house reference materials were available for calibration of the spectrometer (manganese ores: BAM-633, SARM-16, SARM-17, OOPE-401, OOPE-402, OOPE-501, OOPE-601, OOPE-602, OOPE-603, OOPE-604, TUC-Mn-6, TUC-Mn-7, TUC-Mn-8, TUC-Mn-9, TUC-Mn-10, TUC-Mn-16, TUC-Mn-21, TUC-Mn-31, TUC-Mn-32). OOPE standards (submarine manganese nodules and crusts, origin: former USSR) and TUC reference material

(submarine manganese nodules and crusts, origin: in-house reference material, Technische Universität Clausthal) report at least some trace element contents, whereas SARM standards 16 and 17 (Wessels and Mamatwan-type ores, origin: MINTEK, South Africa), and BAM (manganese ore, origin: Bundesantstalt für Materialwissenschaften, Berlin) report only selected major, minor and trace element contents. Unfortunately it was found that trace element contents reported for OOPE standards as well as TUC reference materials were not reproducible, their reliability doubtful. Other international standard materials of manganese ores, especially those certifying trace element contents, seem not to be available (Govindaraju, 1994).

It was therefore necessary to include international standards other than manganese ores to calibrate the spectrometer. These were GXR-1, GXR-3, GPOS-301, GPOS-302, GPOS-303, SO-3, An-G, IF-G, GD-Goe, KK-Goe, JDo-1, JGb-1, Jgb-2, JLs-1, NIM-N, SDC-1-USGS, SDO-1-USGS, An-ZGI, KH-ZGI. All these standards are recognized international geochemical standards, listed and described by Govindaraju (1994) and cover a wide variety of rock and ore-types ranging from sediments such as limestones and iron ore to magmatic rocks such as gabbro and granite. Specific standards were selected for each calibration run to suit different types of matrices of manganese ore. Matrix correction factors (alpha-factors of Williams, 1987), utilized by the analytical software package UniQuant (Omega Data Systems, Netherlands) for inter-element matrix correction calculations, were modified by trial-and-error methods until the best fit between the measured and the certified values for a specific international reference material, selected to match closely the composition of the samples to be analysed, was obtained. These standards were: SARM 16 for Mn^{2+}-Mn^{3+} -oxide ores; SARM-17 for carbonate-rich MMT-type ores; and BAM-633 for hydrous ores composed predominantly of Mn^{4+}-oxides.

SARM-16 and 17 were analysed repeatedly with the samples to check for the accuracy and reproducibility of the analyses. Accuracy for major elements was found to be generally within 5 % relative error for the certified concentrations for these standards. Exceptionally large errors were found for light elements that occur in concentrations below 1 wt % (Na), here deviations of up to more than 100 % relative from the certified values were encountered. Reproducibility was always found to be within 3 % relative deviation. Trace element concentrations for some samples were cross-checked for several samples by ICP-AES and ICP-MS spectrometry. XRF-results compare well with the latter data, as well as with available MINTEK reference data for SARM-16 and

SARM-17. In table I.1 and table I.2, results for selected elements of SARM-16 (Wessels-type ore) and SARM-17, as obtained from different analytical techniques, are compared to MINTEK reference values. Deviations between uncertified reference values from MINTEK and XRF-data are generally within 10 to 15 % relative, a satisfactory result, considering the fact that the calibration of the X-ray fluorescence spectrometer was conducted using reference materials with matrices poor in iron and manganese.

I.2.2 Inductively coupled - atomic emission spectrometry (ICP-AES)

Several samples with highly variable compositions were analysed for selected elements by ICP-AES at the Institut für Mineralogie und mineralische Rohstoffe, TU Clausthal. Analyses were performed on a SPECTROFLAME-ICP spectrometer.

Different sample preparation techniques were assessed for their suitability to decompose and different kinds of Mn-ores. Acid decomposition in open and closed systems (as described by Heinrichs and Herrmann, 1990) were unsuccessful. Incomplete decomposition or reprecipitation of compounds such as $BaSO_4$ occurred Fusion methods utilizing H_2SO_4 or HNO_3 for dissolution of the fused material, led to the same dissatisfactory result. All sample types were successfully prepared using the following fusion method: 0.5 g of finely milled sample was transferred into a Pt-crucible and thoroughly mixed with 5 g of $Na_2B_4O_7$ (sodium-tetra borate).

Table I.1 Comparison of results obtained for SARM-16 from XRF, ICP-AES, AAS and ICP-MS. Results reported for XRF and ICP-AES are mean values of duplicate analyses.

SARM-16		**XRF (Clausthal)**	**ICP-AES (Clausthal)**	**AAS (Othfresen)**	**ICP-MS (MINTEK)**	**Reference (MINTEK)[a]**
SiO_2	wt %	5.29	n.a.[b]	5.14	n.a.	5.04
Al_2O_3	wt %	0.34	n.a.	0.36	n.a.	0.3
Mn_3O_4	wt %	67.9	68.8	68.4	n.a.	68.2
Fe_2O_3	wt %	16.8	16.2	16.2	n.a.	16.4
MgO	wt %	0.87	n.a.	0.76	n.a.	0.76
CaO	wt %	4.69	n.a.	4.75	n.a.	4.7
Na_2O	wt %	0.09	n.a.	0.03	n.a.	0.03
K_2O	wt %	0.01	n.a.	0.02	n.a.	0.02
SO_3	wt %	0.56	n.a.	n.a.	n.a.	0.42
V	ppm	14	44	< 100	n.a.	n.a.
Cr	ppm	26	76	< 100	n.a.	n.a.
Co	ppm	47	93	< 100	21	34
Ni	ppm	19	36	< 100	36	14
Cu	ppm	LLD[c]	60	60	12	4
Zn	ppm	313	368	300	358	364
Sr	ppm	526	505	n.a.	585	602
Pb	ppm	132	nn.a.	300	145	148
Ba	wt %	0.55	0.6	0.66	0.79	0.54

[a] Reference values reported by MINTEK are certified only for SiO_2, Mn_3O_4, Fe_2O_3, MgO, CaO, K_2O, Ba, SO_3, and Zn; concentrations of all other elements are provisional property values.

[b] n.a. - not detected [c] LLD - lower than limit of detection

UNIVERSITY OF JOHANNESBURG

Table I.2 Comparison of results obtained for SARM-16 using XRF, ICP-AES, and AAS. Results reported for XRF and ICP-AES are mean values of duplicate analyses.

SARM-16		XRF (Clausthal)	ICP-AES (Clausthal)	AAS (Othfresen)	Reference (MINTEK)[a]
SiO_2	wt %	4.43	n.a.[b]	4.86	4.69
Al_2O_3	wt %	0.18	n.a.	0.25	0.24
Mn_3O_4	wt %	54.0	55.3	54.1	53.9
Fe_2O_3	wt %	6.14	5.5	6.11	6.10
MgO	wt %	2.90	n.a.	3.20	3.03
CaO	wt %	14.4	n.a.	13.7	14.4
Na_2O	wt %	0.08	n.a.	0.11	0.09
K_2O	wt %	0.13	n.a.	0.11	0.09
SO_3	wt %	LLD[c]	n.a.	n.a.	0.025
V	ppm	12	32	< 100	
Cr	ppm	24	67	< 100	
Co	ppm	41	93	100	
Ni	ppm	8	30	< 100	
Cu	ppm	LLD	6	20	
Zn	ppm	19	64	< 100	43
Sr	ppm	201	174	n.a.	
Pb	ppm	7	n.a.	< 100	
Ba	ppm	739	510	1000	720

[a] Reference values reported by MINTEK are certified only for SiO_2, Al_2O_3, Mn_3O_4, Fe_2O_3, MgO, Na_2O, K_2O, and Zn; concentrations of all other elements are provisional property values.

[b] n.a. - not detected [c] LLD - lower than limit of detection

UNIVERSITY OF JOHANNESBURG

This mixture was fused in the covered crucible for 4 h at 1000 °C in a muffle oven. The samples were agitated by swirling at regular intervals until a clear melt formed. The fused bead in the Pt-crucible was allowed to cool before it was placed into a 250 ml squat beaker. 100 ml of 6.25 mol/l HCl were added. The beaker was placed on a magnetic stirrer and the melt slowly dissolved over several hours at 50 ° C. During the dissolution process 5 ml of concentrated HCl were added to the solution to prevent manganese and iron oxides from precipitating. For trace element determination, the resultant clear solution was transferred into clean 250 ml graduated flask and filled up with diluted HCl (1 n). For the determination of Mn and Fe 25 ml of the solution in the graduated flask were transferred into another clean 250 ml graduated flask and filled up, leading to an additional tenfold dilution. For analyses solutions were drawn directly from the graduated flasks.

Two series of 4 multiple element standards, one for main and one for trace element analysis, were prepared from MERCK single element calibration solutions for spectrometric analyses in the appropriate concentration range (Heinrichs and Herrmann, 1990). Fe and Mn solutions were added to trace element calibration solutions in concentrations of 20 ppm and 50 ppm to simulate the high contents of these elements in the sample solutions.

UNIVERSITY OF JOHANNESBURG

Results obtained for SARM-16 and SARM-17 are listed in table I.1 and I.2. Accurate determination of major elements was easily accomplished. The determination of low trace element concentrations was restricted by the high background signal introduced by high Mn and Fe concentrations resulting in large positive errors for trace element concentrations below 100 ppm (compared to ICP-MS and XRF results). Attempts to overcome this problem by measuring various sectroscopic lines and careful selection of positions for the background measurement were unsuccessful.

I.2.3 *Atomic absorption spectrometry (AAS)*

Few AAS major and trace element analyses of differing sample types, but especially of extremely Fe-rich sampes, were performed at the Studiengesellschaft für Eisenerzaufbereitung, Othfresen, in combination with titrimetric Fe(total) determination (see section 1.2.5).

125 mg of finelly milled sample were weighed into a platinum crucible and thoroughly mixed with 1.5 g of $Li_2B_4O_7$ (lithium-tetraborate). This mixture was, under regular swirling, fused for 4 h at 1100 °C in a muffeloven to produce a clear melt. The cooled bead was dissolved slowly in 100 ml of 1:10 diluted HNO_3 (65 %) at 80 °C on a magnetic stirrer. The clear solution was transferred into a 250 ml graduated flask and filled up with diluted HNO_3. Problems were encountered on dissolution of some samples as incomplete fusing and dissolution occurred.

Measurements were performed in a laminar air-acytelene flame.

Single element solutions for calibration were produced from MERCK standard solutions as described for ICP-AES, but without adapting the standard to the sample matrix. Results for trace elements were therefore regarded to be only semiquantitative. The results reported in table I.1 and I.2 for main elements compares well with results certified for SARM 16 and SARM 17. Results for trace element contents fall in the appropriate range.

I.2.4 Inductively coupled plasma - mass spectrometry (ICP-MS)

Trace element ICP-MS analyses of 40 selected ores from the KMF as well as 11 samples of bostonite dykes were performed by the Analytical Chemistry Division at MINTEK. The procedure employed for sample preparation and analysis is described below (description by Robie, 1995, pers. comm.). For a detailed description of the ICP-MS technique it is referred to Heinrichs and Herrmann (1990).

ICP-MS has got major advantages compared to techniques of instrumental spectroscopy such as ICP-AES and AAS. Analyses by ICP-MS is based on absolute counts by the mass spectrometer. Specific elements are identified by the characteristic mass/ charge ratio of their complex ions, not by the intensity of characteristic lines in the emission or absorption spectrum as the case with any

spectroscopic technique. The high sensitivity of the collector of the mass spectrometer allows accurate analysis at very low trace element concentrations (0.01 - 0.1 ppm in solution) (Heinrichs and Herrmann, 1990). Mass interferences of ions of different elements with similar mass/ charge ratios are numerous and may impose serious problems on the analysis of some elements at extremely low concentrations (Heinrichs and Herrmann, 1990). Due to such mass interferences between ions of the solvent medium and the plasma gas with Cr (overlaps with ionized compounds of ^{40}Ar, ^{35}Cl, ^{16}O and $^{1}H^{+}$) and V (overlaps with ionic compounds of ^{35}Cl and $^{16}O^{1}$) analysis for these two elements by ICP-MS was not possible (probably due to overlap with the ClO^{+} -cation, Robert, 1995, pers. comm.).

Samples for ICP-MS analyses were prepared as follows (Robert, 1995, pers. comm.): Sample portions of approximately 0.2 g were accurrately weighed into 35 ml zirconium crucibles. (For the determination of Zr, nickel crucibles were used). 2g of Na_2O_2 (sodium-peroxide) (A.R. grade) was added to each sample. The samples were fused over an air-entraned bunsen burner, and allowed to cool before being placed in 250 ml squat beakers. The fusion beads were leached with approximately 40 ml distilled water, and then acidified with 20 ml HNO_3 (nitric acid) (Merck 67 %, A.R. grade). The samples were heated on a hotplate to allow hydrogen peroxide to boil oo, After cooling, the samples were transferred to 100ml volumetric flasks and diluted to volume with distilled water. A reagent blank was prepared similarly to the samples. The samples were then diluted further ten times (using 2%(v/v) nitric acid), to decrease the level of dissolved solids to 0.2 % (the upper limit of the ICP-MS).

A range of calibration standards, containing from 100 ppb to 200 ppb of each analyte element (in 2 % (v/v) nitric acid) were prepared. A standard blank solution comprising 2 % (v/v) nitric acid was also prepared.

100 ppb of Sc, In and Re were added to each standard, sample and blank solutions. The latter three elements were used as internal standards during the analyses.

Instrumental parameters were the following (Robie, 1995, pers. comm.): A VG2+ Plasmaquad ICP-MS instrument, with Gilson autosampler attached, was used for all analyses. Ar was used as ICP-plasma gas. Samples were analysed using the 'scanning' mode, and two runs were performed for each

solution analysed. The instrument was flushed with 2 % (v/v) nitric acid for 90 sec between scans. All calculations were performed using the software provided by the instrument supplier.

The results obtained by ICP-MS analyses are reported in Appendix III.

I.2.5 Titrimetric Fe(total) determination

Accurrate determination of the total iron content in iron ore is generaly accomplished by titrimetric analysis (Vogel, 1961). The sample is only subjected to a simple HCl decomposition process, as complete disolution is not necessary. Only few ores, preferentially iron-rich samples, have been analysed with this method. Analyses were performed at the Studiengesellschaft für Eisenerzaufbereitung, Othfresen. Fe_2O_3 concentrations measured for SARM-16 and SAM-17 are reported in table I.1 and I.2 (AAS-column) and compare very well with certified values.

4 g of finelly milled sample were dissolved in 50 ml concentrated HCl (37 %) in an Erlenmeyer flask at 150 °C for 1-3 hours on a magnetic stirrer. Then 1 ml H_2O_2 (30 %) and 1 ml H_2F_2 (40 %) were added and the solution boiled for 10 min at 250 °C. At last 2 ml KSCN solution (10 %) was added. An iron III-thiocyanate $Fe(SCN)_6^{3-}$ complex forms that colours the clear solution bright red.

The solution was titrated in the absence of air (N_2 atmosphere) with $TiCl_3$ solution, until the red color of the Fe III-thiocyanate complex just disappeared. Three titers were determined for each sample and the mean calculated.

I.2.6 CO_2 (total) determination by coulometric titration

A detailed desciption of the determination of the total carbon content by coulometric titration is found in Heinrichs and Herrmann (1990). The analysis is based on volatilization of any carbon contained in the sample (as organic carbon or inorganic carbon) in the form of CO_2. Oxidation is accomplished in an oxygen stream at 1200 °C. The produced CO_2 reacts with barium-perchlorate solution to form a precipitate of barium-carbonate. The original pH of 10 in the original barium-perchlorate solution decreases as result of the precipitation. The pH is reset by elctrolytic titration.

The amount of electrical charge needed during the titration process is equivalent to the amount of $BaCO_3$ precipitate and therefore also equivalent to the total CO_2 in the sample.

A set of selected samples of Mamatwan-type ore was analysed using an automated Ströhlein Coulomat at the Institut für Mineralogie und mineralische Rohstoffe, TU Clausthal. The analytical procedure descibed by Heinrichs and Herrmann (1990) was followed. The amount of sample per analysis used varied with the expected content of CO_2 between 500 and 100 mg. Duplicate analyses were performed for every fifth sample, reproducibility was better than 3 % relative, accurracy within 5 % relative, as estimated from repeated analyses of standard SARM-17.

Certified value (MINTEK) for SARM-17 (Mamatwan-type ore):

15.4 wt % CO_2

Analytical mean of coulometric tritration of CO_2 during this study:

14.9 wt % CO_2 (n = 8; max: 14.9 wt %, min: 14.8 wt %).

Accurrate and reproducible results of total carbon contents of manganese ores are easily accomplished with this technique. Results are reported in Appendix III.

I.2.7 H_2O^- determination by drying

Determinations were performed at the Department of Geology, RAU, following the instructions by Heinrichs and Herrmann (1990). 2 g of sample powder were weighed into a china clay crucible that had been dried to weight constancy at 110 °C. Sample were dried in an oven in the open crucible at 110 °C for 3 h. The dried samples were allowed to cool in a desiccator and then weighed. This procedure was repeated, until weight constancy was reached.

The weight difference between the total of crucible and sample before and after analysis is called the H_2O^- content of the sample and is assumed to be a measure for the amount of water that is adsorbed bound to the sample material (Heinrichs and Herrmann, 1990). Results are reported in Appendix III.

I.2.6 Loss on ignition determination (L.O.I.)

L.O.I. determinations were performed at the Institut für Mineralogie und mineralische Rohstoffe, TU Clausthal, modifying the instructions by Heinrichs and Herrmann (1990). Results are reported in Apppendix III.

1 g of sample powder was weighed into a china clay crucible that had been ignited to weight constancy at 1100 °C prior to analysis. The open crucible with the sample powder was ignited for 4 h at 1100 °C in a muffleoven. Crucible and sample were allowed to cool down in a desiccator and then weighted. This process was repeated until weight constancy was reached.

The L.O.I. determination is generally conducted at about 1000 °C (Heinrichs and Herrmann, 1990). It is a measure of the total of adsorbed and structurally bound volatiles in the sample material. This includes H_2O, CO_2 and SO_3, but also other volatiles. In manganese ores, however, Redox processes and associated phase transformations of the different manganese compounds are observed during the heating process. These Redox-transformation processes were observed in ore samples of different mineralogy and composition, by studying the phases present in samples prior and after ignition with X-ray powder diffraction. Hausmannite and hematite were found to be the dominant Mn-Fe-bearing phases after ignition of hydrous Mn^{4+}-dominated ores (marine nodules and crusts, psilomelane and wad from PMF), carbonaceous Mn^{2+}- Mn^{3+}-ores as well as in oxidic Mn^{2+}-Mn^{3+} ores at 1100 °C. On ignition to only 1000 °C, considerable amounts of braunite and bixbyite were still present in the sample material.

The amount of braunite and bixbyite, as indicated by XRD, was found to decrease considerably in samples that were heated to 1100 °C, a result in agreement with literature data on the thermal behaviour of these phases (Kleyenstüber, 1979). The work of Dressel and Kennworthy (1961) and Muan (1959) showed the stability of braunite in air to up to 1000 °C, but its thermal break down to hausmannite and tephroite above this temperature. Dressel and Kennworthy (1961) described also the thermal reduction of bixbyite to hausmannite. Work by Kleyenstüber (1979) showed bixbyite from the Kalahari manganese field is thermally reduced to jakobsite above 1000 °C. Thermal transformation of tetragonal hausmannite into cubic Mn_3O_4 takes place at 1170 °C (Van Hook and Keith, 1958). It was therefore decided to ignite the manganese ore samples to 1100 °C for the determination of L.O.I. and to report the total manganese content as Mn_3O_4 and the iron content as

Fe_2O_3. (Appendix 3). Mn contents of bostonite dykes and similar hard-rock samples are, however, reported as MnO and Fe_2O_3, as no important thermal transformation affect the low manganese and iron contents.

In this way the analytical total should amount to approximately 100 %. This calculation allows an important first estimate about the quality of a chemical analysis that includes values for all major elements but not specified values for all volatile components (as is the case for most chemical analysis of manganese and iron ores in literature). By expressing manganese and iron concentrations simply as Mn and Fe (as common practice in industry) or as MnO (for example Schütte, 1992) this process of quality control is inhibited.

I.2.7 Electron micro probe analysis (EMPA)

The basic theory of electron micro probe analysis is delineated in great detail by Reed (1994). Extensive EMPA analysis was performed to establish the phase chemistry of all common and some rare phases occurring in the manganese ores studied. To ascertain the representative character of the results reported in Appendix IV, it was decided to do at least 5 spot analyses analysis per phase per sample and to calculate and report only the mean of these analyses.

Analyses were performed on a Cameca CAMEBAX 355 electron micro probe system equipped with 3 wavelength dispersive spectrometers (WDS) and an additional Link energy dispersive spectrometer (EDS), carrying a Li-driven Si-detector, at the Department of Geology, RAU. The system was controlled by the Link ExL II and Lemas software packages. Only the EDS system was utilized for analyses. For the present purpose the rapid but slightly less accurate EDS analysis gave satisfactory results. The use of the more accurate but much slower WDS system was unnecessary. The raw EDS spectra were automatically ZAF-corrected by the ExL II software.

A wide variety of phases was analysed and only a selected set of the setups used for analyses can be listed here. The electron beam was set for all analyses at 15 kV acceleration voltage and 10 nA absorbed beam current on brass. Polished sections and polished thin sections of ore and rock samples, as well as grain mounts of separate minerals were carbon-coated prior to analyses. Orientation on the sample surface was generally done through the optical microscope attached to the

micro probe, the back-scattered electron image was used only in cases of extremely fine-grained samples. Spectra were acquired for 80 sec, decreasing to 50 sec for carbonates and to 25 sec for albite.

Manganese oxides were analysed using the following element list and standard materials:

element list	standard materials
SiO_2	wollastonite $CaSiO_3$
TiO_2	syn. $MnTiO_3$
Al_2O_3	almandine $(Fe,Mg)_3Al_2[SiO_4]_3$
Fe_2O_3	hematite Fe_2O_3
Mn_2O_3	syn. Mn_3O_4
MgO	augite $Ca(Mg,Fe,Al)(Si,Al)_2O_6$
CaO	wollastonite $CaSiO_3$
BaO	barite $BaSO_4$
Na_2O	halite NaCl
K_2O	orthoclase $KAlSi_3O_9$

UNIVERSITY OF JOHANNESBURG

Garnets, pyroxenes, amphiboles, micas, chlorites and serpentine minerals were analysed using the following element list and standard materials:

element list	standard materials
SiO_2	diopside $CaMgSi_2O_6$
TiO_2	syn. $MnTiO_3$
Al_2O_3	almandine $(Fe,Mg)_3Al_2[SiO_4]_3$
Cr_2O_3	chromite $(Mg,Fe)Cr_2O_4$
FeO	hematite Fe_2O_3
MnO	syn. Mn_3O_4
MgO	augite $Ca(Mg,Fe,Al)(Si,Al)_2O_6$
CaO	diopside $CaMgSi_2O_6$
Na2O	halite NaCl
K_2O	orthoclase $KAlSi_3O_9$

Feldspars were analysed using the following element list and standard materials:

SiO_2	wollastonite $CaSiO_3$
Al_2O_3	almandine $(Fe,Mg)_3Al_2[SiO_4]_3$
FeO	hematite Fe_2O_3
MnO	syn. Mn_3O_4
MgO	forsterite Mg_2SiO_4
CaO	diopside $CaMgSi_2O_6$
Na_2O	halite NaCl
K_2O	orthoclase $KAlSi_3O_9$

Calcium-hydroxysilicates and carbonates were analysed using the following setup:

SiO_2	wollastonite $CaSiO_3$
Al_2O_3	almandine$(Fe,Mg)_3Al_2[SiO_4]_3$
Fe_2O_3	almandine $(Fe,Mg)_3Al_2[SiO_4]_3$
Mn_2O_3	syn. Mn_3O_4
MgO	almandine $(Fe,Mg)_3Al_2[SiO_4]_3$
CaO	fluorite CaF_2
Na_2O	halite NaCl
K_2O	orthoclase $KalSi_3O_9$

UNIVERSITY OF JOHANNESBURG

The accuracy of EDS analysis was established to be about 3 % relative error for all elements by repeated analyses of standard materials. The reproducibility of results was generally better than 3 % relative deviation, confirmed by several repeated measurements on the same spot on standard materials. Exceptionally large errors were encountered during the analyses of light elements and phases containing large amounts of volatiles. Satisfactory results for Na were obtained by decreasing the time of data acquisition to 25 sec (feldspars). The difficulties encountered during EMP-analysis of carbonates are well known (Lane and Dalton, 1994). The thermal release of CO_2 from the sample under the electron beam results generally in too high analytical totals. Lane and Dalton (1994) illustrate that relative errors as high as 20 % can occur. During this study, analyses were accepted and included in Appendix IV if the analytical total deviated not more than 5 % relative from the total expected for a carbonate of the composition indicated by cation ratios obtained for the sample.

I.3 Stable ($\delta^{13}C$, $\delta^{18}O$, $\delta^{34}S$) and radiogenic ($^{87}Sr/^{86}Sr$) isotope analysis

Whole rock samples were drawn from the material prepared for chemical analysis (see Chapter I.1). Mineral separates were prepared and at least 0.1 g of optically clean fragments submitted for analysis. Measurements of stable isotope ratios on many carbonate samples ($\delta^{13}C$, $\delta^{18}O$) were conducted by Prof. Hsueh-Wen Yeh at the Institute of Earth Sciences, Academica Sinica, Taipe, Taiwan on a VG SIRA-10 mass spectrometer. Mineral separates were reacted with anhydrous phosphoric acid at 50 °C for 30 minutes (calcite) to 5 hours (Mn-carbonates). 3 to 5 standards were analysed along with the samples and results corrected accordingly. Calcite and Mn-carbonates in whole rock samples were analysed by selective dissolution in diluted phosphoric acid (Yeh, written comm.). Few carbonate samples were analysed by S. Talma at EMATEK at the CSIR, Pretoria and by H. Strauß at the Institut für Geologie, Ruhruniversität Bochum, Germany.

Results are listed in Appendix V. $\delta^{18}O$ and $\delta^{13}C$ isotope ratios are reported relative to PDB (Belemnitella americana, a belemnite from the Peedee Formation (Cretaceous), South Carolina, USA). $^{87}Sr/^{86}Sr$ ratios and $\delta^{34}S$ isotope ratios of a set of 11 samples of barite and celestite were analysed by Dr. H. Strauß at the Institut für Geologie, Ruhruniversität Bochum, Germany. They are listed in Appendix V; $\delta^{34}S$ is reported relative to CDT (FeS from the Canyon Diablo iron meteorite, Mexico).

I.4 Density determination

Densities of all samples submitted to chemical analyses were determined at the Department of Geology, RAU. The measured densities have been used to perform mass balance calculations and are listed, together with whole-rock geochemical data in Appendix III.

Cube- or brick-shaped, regular bodies of 1 to 4 cm length were cut from homogenous parts of the hand specimens. Parts showing supergene alteration or containing veins and anomalous amounts of vug-filling material were avoided or cut off. The resultant bodies were first dried at 50 °C, then weighed. After registering the original, dry weight (ODW) of the bodies, they were submerged for a short while in molten paraffinum, then lifted out and cooled. By doing his this the bodies were coated completely by a layer of paraffinum. The layer of paraffinum sealed the existing surface pores

and cracks of the samples to prohibit water to enter the interior of the sample and fill an unpredictable amount of the existing pore space. The amount of paraffinum (G_{pa}) coating the sample can easily be calculated by:

$$CWA - OPW = G_{pa}$$

The weight of the coated bodies was measured first in air (CWA) and then submerged in water (CWW). The exact temperature of the water was registered with a thermocouple (accuracy ± 0.1 °C). The density of the coated samples was calculated by applying the law of Archimedes, based on the weight of the sample in air and the amount of water of known temperature (and therefore known density) replaced by the sample when submerged. The highly temperature dependent water density was approximated using the equation and parameters listed by Prause (1993)

$$\rho_{°C} = (a_0 + a_1 \cdot t + a_2 \cdot t^2 + a_3 \cdot t^3 + a_4 \cdot t^4 + a_5 \cdot t^5)/ (1+ b \cdot t).$$

$a_0 = 999.86396$ $a_1 = 18.224944$ $a_2 = -7.922210 \cdot 10^3$ $a_4 = -55.44846 \cdot 10^6$

$a_4 = 149.7562 \cdot 10^9$ $a_5 = -393.2952 \cdot 10^{12}$ $b = 18.15973 \cdot 10^3$

UNIVERSITY OF JOHANNESBURG

The density of the coated sample can now be calculated

$$\rho_G = G_G/(G_G - G_W) \cdot \rho_{°C}$$

where ρ_G - density of coated sample

G_G - weight of coated sample in air

G_W - weight of coated sample in water

$\rho_{°C}$ - density of water

This results has still to be corrected for the contribution of the paraffinum coat to the measured density. The density of a block of pure block of paraffinum was measured at 0.88 g/cm^3. The following formula was derived to calculate the true density of the samples.

$$\rho_{pr} = \rho_G \cdot G_G/G_{pr} - \rho_{pa} \cdot (G_G - G_{pr})/G_{pr}$$

where ρ_{pr} - corrected density of sample

G_G - weight of coated sample in air

ρ_G - uncorrected density of sample

G_{pr} - weight of sample without paraffinum coat in air

ρ_{pa} - density of paraffinum (0.88 g/cm^3)

Duplicate analyses of approximately every 10th sample were performed and the reproducibility of the measurements was found to be ± 0.05 g/cm^3 (absolute error).

As the paraffinum coating prohibited the filling of any pore spaces and cracks by water, the now corrected density of sample ρ_{pr} is a measure for the density of the sample material per unit rock volume, not per unit solid matter. Especially for samples with large porosities, density per unit rock volume may be considerably lower than measurements of the density per unit solid matter. The latter involves the infill of an unknown volume of pore space by water during the submerged measurement. This volume does consequently not contribute to the amount of water replaced by the sample, thus leading to an increase in the resultant density.

UNIVERSITY OF JOHANNESBURG

Mass balance calculations in metasomatic processes are based either on the presumption of constant volume during metasomatism or on immobile behaviour of one ore several elements is assumed (Gresens, 1967; Grant, 1986). Gresens (1967) pointed out, that measured concentrations in unaltered and altered rocks have to be corrected with the respective density of the rock before mass balance calculations may be performed. The idea of Brimhall and Dietrich (1987) is introduced here, that the appropriate density for the correction of measured concentrations is in fact the density per unit rock volume and not the density per unit solid matter. The validity of this idea may be visualized by imagining an alteration process that increases the porosity of a rock, for example by devolatilisation. The information about this process is kept partly preserved by increasing porosities. The density per unit rock volume may therefore remain the same in altered and unaltered rock, whereas the density per unit solid matter may be expected to increase, as the light volatile component is released from the solid state during the alteration reaction.

I.4 X-ray powder diffraction analysis (XRD)

All mineral, ore and rock samples studied have been subjected to qualitative XRD-analysis prior to any petrographical work. This simplified the otherwise very difficult optical identification of very fine-grained phases and the distinction between manganese oxides of very similar optical appearance under the microscope.

Very good general introductions into the technique of phase identification with X-ray powder diffraction are provided by Klug and Alexander (1974), Jenkins (1993) and Allmann (1994).

Samples were prepared either as side-loaded loose powder pellets or as back-loaded pressed powder pellets following the instructions by Kleyenstüber (1985). Side-loading of loose powder pellets was accomplished by filling a sample holder open to one side and to the front. The front is covered with a glass slide during the infill of 2 - 3 g of finely milled sample powder from the side into the sample holder. The glass slide is carefully removed after the filling process, leaving behind a smooth, straight surface ready for analysis. This preparation technique allows recovery of the examined sample material and decreases the effects of preferred orientation (Allmann, 1994). The process of producing back-loaded and pressed pellets as described by Kleyenstüber (1985) involves the thorough mixing of 1 g of the milled sample material with 0.3 g of instant coffee powder as a binding agent. This mixture is filled from the back into a sample holder and pressed for 10 sec in a hydraulic press at about 10 ton/cm^2 pressure. The resultant pellet shows strong preferred orientation of any tabular or needle-shaped phase and the sample material is lost due to contamination with the binder. However, smoother surfaces with higher particle densities result in higher peak/ background ratios in the XRD pattern, simplifying the phase identification..

Comparison between the number and distribution of phases identified during petrographic studies of polished thin sections and those identified by XRD show, that phases are reliably identified by XRD, if they are present in more than 5 vol. % in the sample material. Phases present in amounts lower than this generally escape identification. In favourable cases contents as low as 1 vol. % may be enough to lead to the recognition of a specific phase in the XRD-pattern.

XRD patterns were obtained on a Philips PW 1710 based automated diffractometer with a vertical PW 1050 vertical goniometer. Co-K_α radiation (wavelength 1.791 Å) was used, generated at 40 kV and 30 mA. Patterns were generally acquired in the range of 5 to 80 °2Θ using a scan speed of 50

sec/ 1° at a step width of 0.02 °. The range of data acquisition was extended to 3 to 140 °2Θ for difficult mineral identifications. Data collection, pattern treatment and semiautomatic phase identification were controlled by the version 3.6 of the APD (automated powder diffraction) software package by Philips. The diffractometer was calibrated monthly with an external standard (NBS 640b, silicon) to an accuracy of ≤ 0.01°2Θ deviation in the range of data acquisition.

Phase identification was based on reference patterns of the powder diffraction file (PDF) database of the International Centre for Diffraction Data (ICDD). These were retrieved from the TOTAL ACCESS DIFFRACTION DATA (TADD) CD-ROM database provided by PHILIPS until 1994 (Philips, 1992), later from the PC-PDFWIN CD-ROM database system provided by the ICDD (Jenkins and Holomay, 1987). Both database systems are yearly updated to include new data files of the PDF.

Semiautomatic phase identification by the APD software package uses the fuzzy-data set search-match technique described by Blaffert (1987, in Philips, 1992). The peak positions and intensities of the measured pattern are mathematically matched with a range of reference patterns selected by the user. The result of the match procedure is a so-called match-score for each reference pattern/ phase, with higher match-scores signalling a higher probability for the presence of the specific phase in the sample. The software creates a list of the phases most probably present and the user has to visually compare the experimental pattern to the listed reference patterns to decide which phases are present.

During this study it was found that by following this procedure of combining automated search-match techniques with a final manual decision by the user led to effective and very accurate qualitative phase identifications even in very complex mixtures of more than 5 phases.

I.5 Petrography and ore petrography

More than 300 polished thin sections and polished sections and 50 thin sections were examined and described during this study. A Leitz ORTHOPLAN microscope was used to study polished thin sections and polished sections in reflected and transmitted light. A NIKON Optiphot microscope was used for petrographic studies of thin sections in transmitted light. All of the photomicrographs in this

study were produced using the ORTHOMAT camera equipment attached to the ORTHOPLAN microscope. Optical mineral identification was based on Ramdohr (1960) and Frenzel (1980) for the opaque phases, and on Tröger (1959a, b) for the transparent minerals.

I.6 Fluid inclusion studies

The techniques used to study fluid inclusions is described in many recent publications, so by Roedder (1984) and Shepherd et al. (1985).

Approximately 60 samples of gangue minerals from the Kalahari manganese field (KMF) (carbonates, sulphates, silicates) and the Postmasburg manganese field (PMF) (barite) were examined for the presence of fluid inclusions. Only 15 of these contained any fluid inclusions of the size necessary (larger than 3 μm) to allow micro thermometric observations. However, in some of the samples studied, only very small numbers of suitable inclusions were present, and few measurements were possible.

UNIVERSITY OF JOHANNESBURG

50 - 250 μm thick, doubly polished wafers were cut of these 15 samples. The location, size and distribution of fluid inclusions was mapped and described for each sample under a petrographic microscope prior to micro thermometric measurements. The fluid inclusions were classified into primary, pseudo secondary and secondary inclusions on the basis of textural arguments listed by Shepherd et al. (1985). The thermal behaviour of primary and pseudo secondary fluid inclusions was observed in single heating-freezing cycles in a temperature range between -100 °C and 300 °C with a U.S.G.S. stage described by Werre et al. (1979).

Calibration of the thermocouple on the U.S.G.S. stage was accomplished by accurately determining two points on the voltage-temperature curve, following the instructions by Reynolds (1982). The melting point of water inclusions in synthetic quartz at (-) 0.0 °C was used to determine the zero point of the temperature scale and the triple point of CO_2 inclusions in synthetic quartz at -56.6 °C was used to determine the negative slope of the voltage-temperature curve. No additional calibration point included to determine the positive slope of the voltage-temperature curve. This calibration technique relies on the assumption that the voltage-temperature curve approximates a straight line over the entire temperature range of measurement.

Initial melting (eutectic temperature), final melting and homogenization temperatures, but also temperatures for additional observable phase transitions were determined in about 30 fluid inclusions per sample wherever possible. The characteristics of the respective phase transitions have been described. A data sheet was prepared for each sample measured, listing not only the individual temperature measurements, but also the statistical evaluation of the distribution of final melting and homogenization temperatures and short description of distinct fluid inclusion populations and the characteristics of the observed phase transitions (Appendix VI).

References

Allmann, R. (1994). Röntgen-Pulver-Diffraktometrie. Verlag Sven von Loga, Cologne, 228 pp.

Blaffert, T. (1984). Computer assisted multi-component spectra analysis with fuzzy data sets, Analyt. Chim. Acta, 161, 135-148.

Brimhall (1987). Constitutive mass balance relations between chemical composition, volume, density, porosity, and strain in metasomatic hydrochemical systems: Results on weathering and pedogenesis. Geochim. Cosmochim. Acta, 51, 567-587.

Dressel, W.M., and Kennworthy, H. (1961). Thermal behaviour of manganese minerals in controlled atmospheres. U.S. Bureau of Mines Report, 5761, 35 pp.

Frenzel G. (1980). The manganese ore minerals. In: Varentsov IM, Grasselly G (eds.): Geology and geochemistry of manganese. Vol. 1, Schweizerbarth, Stuttgart, 25-157.

Govindaraju (1994). Compilation of working values and sample descriptions for 383 geostandards. Geostandards Newsletters, special issue, 18, 98 pp.

Grant, J.A. (1986). The isocon diagram - a simple solution to Gresens equation for metasomatic alteration. Economic Geology, 81, 1976-1982.

Gresens, R.L. (1967). Composition-volume relationships of metasomatism, Chemical Geology, 2, 47-65.

Heinrichs, H., and Herrmann, A.G. (1990). Praktikum der Analytischen Geochemie. Springer Verlag, Berlin, 669 pp.

Jenkins, R. (1993). Methods and practices (in X-ray powder diffraction). International Center for Diffraction Data, Pennsylvania.

Jenkins, R., and Holomay, M. (1987). PC-PDF: A search-display system utilizing the CD-ROM and the complete Powder Diffraction File, P.Diffr., 2, 215-219.

UNIVERSITY OF JOHANNESBURG

Kleyenstüber, A.S.E. (1979). 'N mineralogiese ondersoek van hoë-temperatuur-reduksieprodukte van mangaanerts vanuit die Mamatwanmyn, Kalaharimangaanveld. Unpubl. MSc-thesis, RAU, 125 pp.

Kleyenstüber, A.S.E. (1985). A regional mineralogical study of the manganese bearing Vöelwater Subggroup in the northern Cape Province. Unpubl. PhD thesis, RAU, 328 pp.

Klug, H.P., and Alexander, L.E. (1974). X-ray diffraction procedures. John Wiley & Sons, New York, 966 pp.

Lane, S.J., and Dalton, J.A. (1994). Electron microprobe analysis of geological carbonates, Amer. Mineral., 79, 745-749.

Muan, A. (1959). Stability relations among some manganese minerals. Amer. Mineral., 44, 946-960.

Philips. (1992). Total Access Diffraction Database - User's guide. 2nd ed., Philips, Almelo.

Philips. (1994). PC-APD Version 3.6 - Software Operation Manual. 5th ed., Philips, Almelo.

Prause, B. (1993). Archimedes. Unpubl. Software manual, TU Clausthal, 18 pp.

Ramdohr, P. (1960). Die Ermineralien und ihre Verwachsungen. 3rd ed., Akademie Verlag, Berlin, 1089 pp.

Reed, S.J.B. (1993). Electron microprobe analysis. 2'nd ed., Cambridge University Press, Cambridge, 326 pp.

Roedder (1984). Fluid inclusions. Reviews in Mineralogy (ed. Ribbe, P.H.), Amer. Mineral. Soc., Chlesea, 12 , 644 pp.

Shepherd, T.J., Rankin, A.H., and Alderton, D.H. (1985). A practical guide to fluid inclusion studies. Blackie and sons, Glasgow, 239 pp.

Schütte, S.S. (1992). Ongeluk volcanism in relation to the Kalahari manganese deposits. Unpubl. PhD-thesis, University of Natal, 262 pp.

Tröger, W.E. (1959a). Optische Bestimmung der gesteinsbildenden Minerale, Textband. 4'th ed., Schweizerbarth, Stuttgart, 822 pp.

Tröger, W.E. (1959b). Optische Bestimmung der gesteinsbildenden Minerale: Bestimmungstabellen. 4'th ed., Schweizerbarth, Stuttgart, 147 pp.

Van Hook and Keith (1958). The system Fe_3O_4-Mn_3O_4. Amer. Mineral., 43, 69-83.

Vogel. J. (1961). A textbook of quantitative inorganic analysis. Longmans, London, 3'rd ed., 1216 pp.

Werre, R.W., Bodnar, R.J., Bethke, P.M., and Barton, P.M. (1979) A novel gas-flow fluid inclusion heating/freezing stage [abs.]. Geological Society of America Abstracts and Program, 11, 539.

Williams, K.L. (1987). Introduction to X-ray spectrometry. Allen & Unwin, London, 370 pp.

Appendix II

Sample Descriptions

This appendix contains detailed descriptions of samples and sample profiles studied. Samples derived from the Postmasburg manganese field are described in section II.1. Macroscopic characteristics and the semi quantitative mineralogical composition (major: more than 10 vol %; minor: 1-10 vol%; trace: less than 1 vol %) are described briefly, the relation of the sampling location to the surrounding geology is mentioned. Samples submitted for chemical analysis are marked (results are listed in Appendix III). The samples are listed in two tables, table II.1 contains samples from the Western Belt, table II.2 samples derived from the Eastern Belt and Aucampsrust. Samples from specific mines/ farms are further grouped together. The sampled mines/ farms are listed in their geographic succession from S to N.

Groups of samples from the KMF that logically belong together as they have been collected along profiles are specified in section II.2.

The following abbreviations are used in this appendix:

Mineral names:

haus-te:	hausmannite
lithio-te:	lithiophorite
Mn-m.:	manganomelane
partrid-te:	partridgeite
psi-m.:	romanechite (psilomelane)
gamaga-te:	gamagarite
pyro-ite:	pyrophyllite

Other abbreviations:

Analysis (Y/N): Chemical analysis (present/ not present)

UNIVERSITY OF JOHANNESBURG

II.1 Samples from the Postmasburg manganese field

Table II.1 Western Belt, PMF (including mines at Paling, Glosam, Lohatla and Bishop)

Mine	S. No.	Appearance	Analysis	Mineral constituents		
			(Y/N)	Major	Minor	Trace
Paling						
PAL	215	Earthy wad developed along basal dolomite - orebody contact. Wad contains small remains of braunitic ore.	Y	hematite crypto-m.	haus-te braunite	
PAL	216	Fine crystalline ore with distinct convolute lamination and abundant shaly material enclosing cm-sized lenses of drusy, recrystallized ore. Base of orebody.	Y	braunite hematite diaspore	psi-m.	pyrolusite
PAL	217	Fine crystalline, shaly ore with wavy nonparallel lamination. Contact of ore to interlayer of red shale.	Y	braunite diaspore hematite lithio-te	psi-m.	pyrolusite
PAL	218	Top of orebody, irregular contact of fine crystalline ore with discontinuous wavy nonparallel lamination to conglomeratic gritstone with clay-hematite matrix, flat hematitized BIF clasts and Mn-ore clasts.	Y	braunite diaspore hematite	lithio-te	pyrolusite psi-m.
PAL	219	Lenses of massive, coarse crystalline ore interbedded with thin evenly laminated brownish weathered shale beds.	Y	braunite haus-te partrid-te	hematite Mn-m.	ephesite pyrolusite lithio-te psi-m.
PAL	220	Medium crystalline ore with wavy nonparallel lamination.	Y	braunite partrid-te hausman nite Mn-m.	hematite	lithio-te psi-m. pyrolusite
PAL	221	Fine crystalline ore with visible discontinuous nonparallel wavy lamination interbedded with layers and lenses of massive, medium crystalline ore. Cm-large patches and flat lenses of diaspore weathering to brownish, earthy wad.	Y	braunite hematite psi-m.	lithio-te	partrid-te haus-te pyrolusite
PAL	222	Top of orebody, gradual, diffuse contact of fine crystalline ore with chaotic texture with rare hematitic BIF clasts into hematitic gritstone with shaly matrix and hematite fragments (BIF and other types of fragments).	Y	hematite diaspore	Mn-m. Mn-m.	lithio-te pyrolusite goethite braunite

UNIVERSITY OF JOHANNESBURG

Mine	S. No.	Appearance	**Analysis**	Mineral constituents		
			(Y/N)	Major	Minor	Trace
PAL	223	Fracture filling of botryoidal specularite, crosscutting the contact of ore to overlying hematitic conglomerate.	**N**	spec-te	braunite	diaspore Mn-m. pyrolusite lithio-te
PAL	224	Coarse crystalline ore with cm-large euhedral bixbyite crystals and large vugs filled by scaffold-type intergrowth of large diaspore laths. Centre of orebody.	**N**	bixbyite diaspore		haus-te hematite Mn-m. lithio-te
Glosam						
GLO	184	Top of orebody. Massive matrix of fine crystalline hematitic shale with minor amounts of Mn-oxides, enclosing numerous badly defined mud clasts of hematite and lithiophorite.	**Y**	hematite ephesite	lithio-te braunite psi-m.	pyrolusite Mn-m.
GLO	185	Coarse crystalline, massive bixbyite-rich ore with rare vug-fillings of scaffold-textured diaspore. Centre of orebody.	**Y**	bixbyite braunite ephesite	psi-m. lithio-te Mn-m. hematite	
GLO	186	Massively textured, fine crystalline ore with few small irregular open vugs. Crosscut by veins of coarse crystalline bixbyite and ephesite.	**Y**	ephesite hematite braunite Mn-m. psi-m.	lithio-te pyrolusite	
GLO	187	Convolute interbedding of laminae of red shale with layers of ore. The latter is coarse recrystallised and massive, partly fine crystalline and laminated. Upper part of orebody.	**Y**	braunite partrid-te ephesite Mn-m.	psi-m. pyrolusite	lithio-te
GLO	188	Top of orebody. Fine crystalline ore with discontinuous wavy nonparallel bedding enclosing small irregular lenses and patches of red shale. Abundant mm-large diaspore laths are concentrated along discrete layers and in patches.	**N**	braunite Mn-m. ephesite diaspore		partrid-te lithio-te
GLO	189	Massive, dense lens of hematite with vugs lined by quartz crystals. Overlain by coarse crystalline ore, underlain by wad.	**Y**	hematite	quartz	
GLO	190	Coarse crystalline, specularitic hematite with botryoidal texture, from within hematite lens (as 189).	**Y**	hematite	quartz	

UNIVERSITY OF JOHANNESBURG

Mine	S. No.	Appearance	Analysis (Y/N)	Mineral constituents Major	Minor	Trace
GLO	191	Botryoidal textured hematite from within hematite lens (as 189).	N	psi-m.	illite quartz	
GLO	192/1	Cauliflower aggregates of psilomelane, found in loose shaly material filling interstices between large ore fragments.	Y	psi-m.		hematite illite
GLO	192/2	'Spider-web' ore, dense psilomelane replacing evenly laminated weathered red shale covering the orebodies.	N	psi-m.		hematite illite quartz
GLO	194	Lens of massive, dense hematite hosted in red Gamagara shale.	Y	hematite	illite	
GLO	195	Top of orebody. Conglomeratic texture, abundant hematite pebbles of up to 15 cm size and smaller braunite-partridgeite mudclasts. Matrix consists of densely intergrown hematite, diaspore and lithiophorite.	N	hematite lithio-te	braunite partrid-te ephesite	Mn-m. psi-m.
GLO	196	Coarse recrystallized vuggy ore with euhedral bixbyite crystals lining irregular, often horizontally elongated tube-like vugs. Smaller vugs filled by amesite, dense diaspore occurs in irregular, diffuse patches in the matrix.	Y	bixbyite hematite ephesite	braunite	Psi-m. lithio-m. Mn-m.
GLO	197	Coarse recrystallized bixbyite-rich ore with numerous, up to 10 cm large round clasts of massive white clayey material.	Y	braunite partrid-te lithio-te Mn-m. hematite	ephesite	pyrolusite psi-m.
GLO	291	Ba-rich wad forming a selvage between a massive barite lens and a dolomite pillar.	Y	psi-m.		quartz
GLO	Mn-10-63	Massively textured, medium grained bixbyite-rich ore with up to 5 mm large sprays of gamagarite prisms, associated with minor diaspore, amesite and ephesite.	N	bixbyite diaspore	ephesite amesite gamaga-te hematite	
GLO	391	Doornfontein hematite gritstone with shaly matrix, directly overlying finely bedded manganese ore. Gritstone fines upward into red, lateritic mudstone.	Y	hematite ephesite	kaolinite braunite	
GLO	392	Lower laterite paleosol. Thin hematite duricrust separates upper, light-red coloured mudstone from deep red, hematite-rich mudstone with pisoliths below the duricrust.	N	hematite pyro-ite kaolinite		

UNIVERSITY OF JOHANNESBURG

Mine	S. No.	Appearance	**Analysis**	Mineral constituents		
			(Y/N)	Major	Minor	Trace
GLO	393	Hematite-rich lateritic mudstone with abundant transported pisoliths from upper laterite profile.	**N**	hematite pyro-ite diaspore	kaolinite	
GLO	394	Lateritic mudstone with large transported compound pisoliths, hematite mottles and hematite indurated clay fragments in red, hematitic mudstone matrix. Upper paleosol profile.	**Y**	hematite pyro-ite diaspore	kaolinite	tourmalin e zircon
GLO	395	Leached top soil horizon of upper paleosol profile. Light coloured, slightly greenish-cream coloured mudstone with blockey clay ped structures.	**Y**	pyro-ite diaspore	kaolinite anatase	rutile hematite tourmalin e zircon
GLO	398	Finely bedded lateritic shale composed of compacted clay clasts of read and cream colour and few rounded hematite pebbles.	**Y**	pyro-ite diaspore hematite	illite	tourmalin e zircon
Lohatla						
LOH	79	Coarse crystalline, massive bixbyite-rich ore with visible pore fillings of diaspore.	**N**	bibyite spec-te lithio-te	diaspore Mn-m. psi-m.	pyrolusite
LOH	175	Fine crystalline shaly ore with fine continuous wavy lamination interbedded with several cm-thick beds of massive, coarse crystalline bixbyite-rich ore.	**N**	bixbyite diaspore psi-m.	braunite	
LOH	176	Top of orebody, contact to overlying shales. Lenses of fine crystalline ore with discontinuous wavy lamination showing convolution, interbedded with red shale with small scale non parallel wavy bedding.	**Y**	braunite ephesite hematite	partrid-te psi-m.	lithio-te
LOH	177	Contact of orebody to overlying shale. Densely packed cm-small 'nodules' or clasts of massive Mn-oxides in a matrix of red shale.	**Y**	braunite psi-m. Mn-m.	partrid-te ephesite psi-m.	lithio-te hematite
LOH	178	Massive, coarse crystalline bixbyite-rich ore with numerous small vugs. Crosscut by vein filled by coarse crystalline ephesite.	**Y**	bixbyite braunite hematite	Mn-m.	lithio-te psi-m.
LOH	179	Vuggy, medium crystalline ore as occurring in irregular within fine crystalline, bedded ore.	**Y**	partrid-te braunite	hematite psi-m. pyrolusite	lithio-te

UNIVERSITY OF JOHANNESBURG

Mine	S. No.	Appearance	Analysis	Mineral constituents		
			(Y/N)	Major	Minor	Trace
LOH	180	Massive, very dense manganese ore, fine to medium crystalline, typical for base of orebody. Poor non continuous wavy bedding.	Y	bixbyite Mn-m.	hematite	braunite ephesite psi-m. pyrolusite
LOH	181	Hematitized shale crosscut by numerous ephesite veins. Immediately overlying the orebody.	N	ephesite hematite		
LOH	182	Greenish earthy wad typically present along the basal contact of the orebody to the underlying dolomite.	Y	birnessite		illite
LOH	294	Ba-rich wad selvage along the contact of a massive barite-hematite lens with the surrounding dolomite.	Y	psi-m.		quartz
Bishop						
BIS	240	Dense, fine crystalline ore with discontinuous non parallel wavy lamination . Upper portion of thin ore bed.	Y	hematite diaspore lithio-te psi-m.	Mn-m. pyrolusite	braunite
BIS	241	Very coarse recrystallized ore, massive texture with angular fragments of bixbyite-rich ore cemented by very coarse crystalline diaspore laths up to 8 cm long in dense scaffold-type intergrowth.	Y	bixbyite	diaspore	amesite hematite lithio-te psi-m. Mn-m.
BIS	242	Cauliflower aggregates of botryoidal psilomelane, from soft shaly matrix between fragmented ore.	Y	psi-m.		
BIS	243	Central portion of thin ore bed. Fine crystalline ore with discontinuous nonparallel wavy lamination is replaced by irregular, subhorizontal aggregates of massive medium crystalline ore.	N	partrid-te	lithio-te ramsd-te Mn-m. pyrolusite	braunite hematite diaspore psi-m.
BIS	244	Dense, fine crystalline ore with continuous nonparallel wavy lamination. Massive recrystallisation within shaly beds. Base of orebody.	Y	Mn-m. lithio-te	braunite partrid-te diaspore	
BIS	245	Dense fine crystalline ore with mm to cm thick continuous laminae of interbedded shaly, finely laminated dense, massive ore. Lamination appears wavy nonparallel.	Y	lithio-te hematite		braunite partrid-te pyrolusite psi-m.

UNIVERSITY OF JOHANNESBURG

Mine	S. No.	Appearance	**Analysis**	Mineral constituents		
			(Y/N)	Major	Minor	Trace
BIS	246	Discontinuous beds of massive, fine crystalline lithiophorite, dissected by subvertical cracks, are interbedded with beds of fine gritstone with a matrix of lithiophorite and hematite containing small clasts of hematite and little bixbyite and psilomelane. Top of orebody.	**Y**	lithio-te	partrid-te braunite hematite Mn-m.	diaspore
BIS	247	Coarse crystalline, vuggy bixbyite-rich ore of massive texture. Vugs are filled by amesite and ephesite. Centre of orebody.	**N**	bixbyite diaspore	Mn-m. pyrolusite lithio-te	
BIS	248	Massive medium to coarse crystalline bixbyite-rich ore, partly with box work-vugs filled by loose amesite.	**Y**	bixbyite psi-m. Mn-m.	lithio-te diaspore	hematite
BIS	249	Top of orebody. Very fine crystalline, dense ore with irregular, sharp contact to overlying red shale. Discontinuous wavy lamination inclined to the shale contact is visible. The bedding is dissected by numerous fine fractures filled by Mn-oxides.	**N**	braunite ephesite hematite Mn-m.		
BIS	250	Dense, fine crystalline ore of massive texture, with small patches of recrystallised medium grained ore.	**Y**	braunite Mn-m.	pyrolusite	diaspore
BIS	295	Hematitic shale with abundant, irregular shaped hematite pisoliths of up to 3 cm diameter.	**N**	ephesite illite	hematite	

UNIVERSITY OF JOHANNESBURG

Table II.2 Eastern Belt, PMF (including mines on Aucampsrust, Beeshoek, Doornfontein, Manganore, Kapstewel and Sishen).

Mine	S. No.	Appearance	Analysis (Y/N)	Mineral constituents Major	Minor	Trace
Aucampsrust						
AUC	198-3	Fluvial pebble of dense, massive braunitic ore ('Potato ore').	N	braunite Mn-m.	partrid-te	pyrolusite psi-m. lithio-te
AUC	199-1	Dense, shaly ore, laminated to massive texture, very fine crystalline, highly weathered.	N	hematite Mn-m. illite		braunite lithio-te
AUC	199-2	Lens of mature, fine-grained quartzite. Little interstitial hematite and supergene goethite.	N	quartz		hematite goethite
AUC	199-3	Lens of massive recrystallised manganese ore, enclosed in shaly ore (199-1). Ore is of heterogenous texture, small vugs are lined by pyrolusite crystals.	N	haus-te Mn-m. pyrolusite		partrid-te illite hematite
AUC	200	Base of orebody. Massive ore with shale patches and streaks. Numerous thin pyrolusite veinlets crosscut the ore.	Y	hematite	lithio-te braunite pyrolusite Mn-m.	psi-m. illite
AUC	201	Matrix supported conglomerate with well rounded, 2 cm large clasts of hematitized BIF, unaltered BIF and red shale. The matrix consists of massive, fine crystalline braunite. Base of orebody.	Y	hematite braunite Mn-m.		illite
AUC	202	Highly weathered shaly ore from top of orebody.	Y	braunite illite Mn-m.	quartz hematite	lithio-m.
AUC	203	Massive textured, fine crystalline ore with poor bedding. Few rounded pebbles of massive hematite occur enclosed in the matrix. Numerous fractures are lined by braunite and filled by manganomelane and pyrolusite.	N	hematite braunite Mn-m.	lithio-te	pyrolusite
AUC	204	Wolhaarkop breccia with well rounded quartz clasts cemented and replaced by a matrix of fine crystalline braunite.	Y	braunite quartz	Mn-m.	chlorite pyrolusite goethite
AUC	205	Massive, medium to coarse crystalline ore with chaotic, streaky texture. Small streaky patches of red shale and numerous small, barite filled vugs.	Y	braunite barite	hematite quartz	goethite pyrolusite Mn-m lithio-te psi-m.

UNIVERSITY OF JOHANNESBURG

Mine	S. No.	Appearance	Analysis (Y/N)	Mineral constituents Major	Minor	Trace
AUC	206	Illitic sandstone replaced by fine crystalline braunite n turn strongly weathered to manganomelane. Irregular sandstone clasts remain in a matrix of densely intergrown braunite, enclosing corroded quartz grains. Up to 2.5 m thick massive orebody on dolomite.	N	quartz Mn-m.	braunite	hematite psi-m.
Beeshoek						
BEE	207.1	Dense, fine crystalline braunite ore from base of sheet-like orebody within Wolhaarkop breccia.	N	braunite quartz	Mn-m.	hematite
BEE	207.2	Contact between dense silica-rich ore and Wolhaarkop breccia.	N	quartz Mn-m.	braunite	hematite
BEE	208	Massive ore with dense texture and rare small vugs lined by 0.2 mm large braunite crystals and filled by earthy Mn-Fe-oxides.	N	braunite Mn-m.	Psi-m.	
BEE	209	Massive, streaky textured ore. Vugs lined by euhedral braunite.	N	Mn-m. braunite	pyrolusite	psi-m.
BEE	210	Upper contact of orebody to overlying Doornfontein Conglomerate. Brecciated, sheared texture with small hematite, hematite-illite and illite fragments in a dense hematite-illite matrix. Botryoidal hematite aggregates and vug linings of specularite.	N	illite hematite	pyrolusite	braunite psi-m.
BEE	211	Massive, braunite-rich ore with breccia-like 'fragments' of coarse crystalline barite and streaks of red shale. Barite 'fragments' are 0.1 mm to 1.5 cm large, mono to oligocrystalline. Outlines are angular to subrounded, they are intensively intergrown with the surrounding braunite. Top portion of Wolhaarkop breccia.	Y	barite psi-m.	braunite	
BEE	212	Massive braunite-rich ore bed just below 211. Small patches of recrystallized oxides in fine crystalline matrix.	Y	braunite Mn-m.	hematite	partrid-te
BEE	213	Massive, fine to medium crystalline braunite-rich ore with rare small quartz crystals. Sample from 30 cm wide, 2 m long vein-like, discordant ore shoot in red shale above Wolhaarkop breccia. Immediate hanging wall of 211.	Y	braunite hematite		Mn-m. lithio-te psi-m.

UNIVERSITY OF JOHANNESBURG

Mine	S. No.	Appearance	Analysis (Y/N)	Mineral constituents Major	Minor	Trace
BEE	214	Lensoidal orebodies within red shale above the Wolhaarkop breccia. Ore with shaly interbeds and streaks between layers and aggregates of massive to medium crystalline braunite-partridgeite-hematite ore. These contain rare clasts of hematite. Strong supergene weathering.	Y	Mn-m.	braunite hematite	partrid-te illite pyrolusite psi-m.
Doornfontein						
DO	162	Dense, massive manganomelane-rich ore with corroded remnants of braunite.	N	Mn-m.	braunite	partrid-te quartz hematite
DO	163	Fe-rich Wolhaarkop breccia with up to cm-large, chert fragments. The matrix consists of fine crystalline hematite. Top of Wolhaarkop breccia.	N	quartz hematite		braunite Mn-m.
DO	165	Wolhaarkop breccia with flat lenses of typical breccia with recrystallised chert clasts in ferruginous matrix, interbedded with shaly, evenly laminated Mn-rich beds.	N	quartz hematite	illite	braunite Mn-m.
DO	166.1	Fine and evenly laminated shaly manganomelane-rich ore with thin sandy interbeds. Quartz grains appear in short seams and isolated, they are 0.1 - 0.5 mm large, poorly rounded and corroded. Replacement by Mn-oxides is apparent. The ore consists of fine crystalline oxides and rare visible illite flakes.	Y	quartz hematite Mn-m. illite	braunite psi-m.	pyrolusite
DO	167.1	Massively textured, recrystallized ore (grain sizes up to 1 mm). Manganomelane along crosscutting fractures.	Y	braunite partrid-te Mn-m.	illite psi-m. hematite	lithio-te pyrolusite
DO	167.2	Shaly ore type with streaky distribution of illitic shale material in a dense, braunite-rich matrix. Strongly weathered appearance.	Y	hematite psi-m. illite	braunite quartz Mn-m.	
DO	168	Medium to coarse grained (grin sizes 0.1 - 1 mm), massive braunite-partridgeite-rich ore with rare vugs lined by euhedral braunite crystals.	Y	braunite partrid-te psi-m.	Mn-m.	illite pyrolusite
DO	169	Massive, medium grained (grains up to 0.3 mm size), vuggy braunite-rich ore. Vugs lined by euhedral braunite crystals. Euhedral apatite crystals are intergrown with the matrix braunite.	N	braunite psi-m. Mn-m.	apatite pyrolusite	partrid-te lithio-te

UNIVERSITY OF JOHANNESBURG

Mine	S. No.	Appearance	**Analysis**	Mineral constituents		
			(Y/N)	Major	Minor	Trace
DO	170	Dense, fine crystalline shaly ore from immediate contact to underlying dolomite. Strong weathering indicated by dominance of manganomelane. Fine non parallel wavy lamination with small lenses of recrystallised braunite.	**N**	psi-m. Mn-m.	braunite	goethite
DO	171	Fine crystalline, vuggy ore with chaotic texture. Small patches of medium-grained, recrystallised braunite. Strongly weathered.	**Y**	Mn-m. psi-m.	quartz braunite partrid-te	
Manganore						
MAN	235	Well mineralized Wolhaarkop breccia. Up to 3 cm large, subrounded chert clasts are replaced by fine crystalline braunite along the clast boundaries as well as along fractures criss-crossing through the clasts.	**N**	quartz Mn-m.	braunite hematite	
MAN	236	Fine to medium grained braunite-rich ore with massive, vuggy texture from small (20 m long, 50 cm thick) stratiform ore lens in Wolhaarkop breccia.	**N**	quartz braunite Mn-m.		hematite
MAN	237	Massive, very dense and fine crystalline braunite-rich ore from small ore lens in Wolhaarkop breccia.	**Y**	Mn-m. braunite		hematite pyrolusite Psi-m.
MAN	238	Fine crystalline braunite-rich ore with small patches of recrystallised material. Massive texture. Rare vugs are coated with secondary chalcedony. Irregular shaped orebody in Wolhaarkop breccia.	**Y**			
MAN	239	Well mineralised chert breccia. Up to 1 cm large chert clasts are partly replaced by braunite. Contact of irregular shaped orebody (238) to enclosing Wolhaarkop breccia.	**Y**	quartz braunite Mn-m.		Psi-m.
Kapstewel						
KAP	225	Fine crystalline braunite-rich ore with massive texture. From sheet-like orebody directly overlying a layer of red shale.	**Y**	braunite psi-m.	pyrolusite	hematite lithio-te
KAP	226	Ferruginous shale lens interbedded with Wolhaarkop breccia.	**Y**	hematite quartz illite		braunite psi-m.

UNIVERSITY OF JOHANNESBURG

Mine	S. No.	Appearance	Analysis	Mineral constituents		
			(Y/N)	Major	Minor	Trace
KAP	227	Massively textured, fine crystalline braunite-rich ore from a lensoidal orebody enclosed by red shale. Along contact between shale and ore veinlets and streaks of Mn-oxides protrude into and replace shale material.	N	psi-m. braunite quartz	illite hematite	pyrolusite goethite
KAP	228/1	Medium grained, massive and vuggy braunite-rich ore from within the Wolhaarkop breccia. Primary recrystallised chert clasts as well as secondary fracture-filling quartz are visible. Vugs are lined by euhedral braunite (up to 1 mm), covered by supergene oxides. Contact to botryoidal hematite-filled fracture lined by a selvage of up to 3 mm long pyrolusite needles.	Y	braunite quartz	psi-m.	hematite lithio-te pyrolusite
KAP	228/2	Botryoidal hematite, massively filling up to 15 cm wide fracture crosscutting the Wolhaarkop breccia.	N	specularit e		
KAP	229	Typical Wolhaarkop breccia with recrystallised chert fragments in dense braunite matrix.	Y	quartz braunite	psi-m. Mn-m. pyrolusite	hematite
KAP	230	Massive braunite-rich ore from an ore bed underlying a thin bed of red illitic shale. The ore is fine crystalline with patches of recrystallised medium grained braunite and rare vugs.	Y	braunite Mn-m. psi-m.		quartz pyrolusite hematite
KAP	230b	Red illitic shale from shale lens directly overlying 230.	Y			
KAP	231	Same occurrence as 230. Massive, fine crystalline braunite-rich ore typical for this occurrence.	Y	braunite quartz psi-m.		partrid-te lithio-te pyrolusite
KAP	232	Massive, medium grained braunite-rich ore from sheet-like orebody completely enclosed in Wolhaarkop breccia. Ore is crosscut by many subvertical, up to 5 mm wide fractures massively filled by pyrolusite prisms.	N	braunite pyrolusite	Mn-m.	partrid-te lithio-te psi-m.
KAP	233	Same occurrence as 230. Massive, medium grained braunite-rich ore replaces (?) fine crystalline, dense precursor material which is preserved in small irregular patches.	N	Mn-m. braunite		quartz psi-m.
KAP	234	Wolhaarkop breccia with increasing degree of mineralisation towards overlying lens of red shale.	N	quartz braunite Mn-m.		

UNIVERSITY OF JOHANNESBURG

Mine	S. No.	Appearance	**Analysis**	Mineral constituents		
			(Y/N)	Major	Minor	Trace
Sishen						
SIS	81	Oxide-rich bed in Wolhaarkop breccia. Strongly weathered braunite precursor transformed into manganomelane.	**N**	Mn-m. Psi-m.		pyrolusite
SIS	304	Top of Wolhaarkop breccia. Chert seems to form rather a continuous bed than well defined clasts. Only small amount of manganomelane in between the quartz grains.	**N**	quartz	Mn-m.	

UNIVERSITY OF JOHANNESBURG

II.2 Groups of samples from the Kalahari manganese field

Mine	Sample group/ section	Sample number(s)
HZ	Profile across N-S striking, vertically dipping 3 m wide ferruginized fault zone that displaces the lower orebody. N-face of small subdivision of N-pit. Total length: 13 m.	HZ-130..HZ-140
HZ	Profile from the ferruginized eastern main graben fault to the centre of the orebody. Lower orebody sampled along S-face of North pit. About 1.5 m above pit floor. Sampling direction E-W. Total length: 233 m.	HZ-153b..HZ-162, joined to the E by HZ-141..HZ-149
HZ	Samples from ferruginization halo along the western main graben fault (HZ-150) and the immediately adjoining high-grade ore (HZ-151). Lower orebody; western access road to N-pit. Total length: 5 m. Sampling direction W-E.	HZ-150..HZ-151
MMT	Profile across chalcedony veinlet with symmetric, 25 cm wide hematitization halo. Total length: 1.8 m. Top Cut, W-face in open pit, sampling direction N-S.	MMT-82..MMT-88
MMT	Botryoidal manganomelane in calcrete formed in supergene altered, brecciated ore close to the suboutcrop of the lower orebody against calcrete of the Kalahari Formation. Top Cut, W-face in open pit.	MMT-89..MMT-90
MMT	Profile across 6 m wide fault zone. Fault zone strikes WSW-ENE, has about 2-5 m vertical displacement and dips approximately vertical. Total length: 56.5 m. Bottom Cut, W-face of open pit, sampling direction N-S in H-zone of orebody.	MMT-91..MMT-110
MMT	Profile across 6 m wide fault zone. Fault zone strikes WSW-ENE, has about 2-5 m vertical displacement and dips vertically. Total length: 30.5 m. Middle Cut, W-face of open pit, sampling direction N-S in M-zone of orebody.	MMT-111..MMT-125
MMT	Profile across pyrite-carbonate-chalcedony (tridymite) veinlet enclosed by a asymmetric 10 to 50 cm wide, zoned hematitization halo. Total length: 1.6 m. E-face of crusher pillar in open pit. Bottom cut, sampling direction N-S in H-zone of orebody. Sample MMT-129 was taken from adjoining W-face of open pit, about 10 m West of pillar, from within the same veinlet.	MMT-126..MMT-129
NC2	Profile studied and described by Gutzmer and Beukes (1995, Appendix 7). Traverse between zones of ferruginization along major N-S striking faults across marginal altered high- grade Wessels-type ore and into least low-grade ore. Block 23S; sampling direction W-E, height: 1.5 m above floor. Total length: 160 m.	NC-4..NC-14
NC2	Profile studied and described by Gutzmer and Beukes (1995, Appendix 7). Traverse across E-W striking normal fault surrounded by a 2.5 m wide zone of ferruginization and successive zones of high-grade ore. Block 23S; sampling direction N-S, height: approximately 1.5 m above floor. Total length 7 m.	NC-16..NC-21

UNIVERSITY OF JOHANNESBURG

Mine	Sample group/ section	Sample number(s)
NC2	Profile studied and described by Gutzmer and Beukes (1995, Appendix 7). Traverse between zones of highest-grade hausmannite ore across an approximately 3 m wide, E-W striking zone of silification and ferruginization that grades laterally into high-grade ore. Profile is centred by a subvertical vein filled with calcite and calc-silicates. Block 48S. Total length 11 m. Sampling direction N-S, height: 1.5 m above floor.	NC-26..NC-33
WES	Profile across a 4.6 m wide, ENE-WSW striking microsyenite ('bostonite') dyke. Samples WES-322 to WES-325 are from within the dyke, remaining samples from the adjacent lower orebody. Block 5.5. Sampling direction S-N, height: approximately 1.5 m above floor. Total length: 37.8 m.	WES-310..WES-325, joined to the N by WES-351..WES-357
WES	Profile from high-grade ore across an approximately 3.5 m wide ENE-WSW striking microsyenite ('bostonite') dyke. Normal faulting is observed along the dyke, with an approximate downthrow of 12.5 m towards the S. Profile extends from high-grade ore (samples WES-333 to WES-338-1) into the dyke (WES-338-4 to WES345, also WES-327) and back into the transition zone between lower altered hematite lutite and lower altered orebody (WES-346 to WES-349). Sampling direction: S-N; Total length: 31 m. Samples WES-327, WES-333 to WES-338-4 are from stope J8N, Westblock (sampling height: 1.5 m above floor) samples WES-339 to WES-349 have been taken from drillcore UG125 (drilled subhorizontal at +20° in NNW direction, extending from stope J8N).	WES-333..WES-349, also WES-327
WES	Section into and across a 38 m wide, NNE-SSW striking microsyenite ('bostonite') dyke. Samples WES-370 to WES-373 are from within the dyke, the remaining samples from the adjacent lower orebody. Block 5.5. Sampling direction approximately WNW-ESE, height: Approximately 1.5m above floor. Total length: 50m.	WES-358..WES-375
WES	Samples of silicate pods occurring isolated within the lower high-grade orebody, especially along the footwall contact to the underlying altered hematite-lutite. The occurrence of the silicate pods shows no relation to faulting or veining. Samples from within Area 3.6, Eastblock.	WES-377..WES-378
WES	Profile N100 studied and described by Beukes et al. (1995, Appendix 8). Traverse from low-grade Mamatwan-type ore through high-grade Wessels-type ore towards the contact of the ferruginized area around a major N-S striking normal fault. Total length 200 m; sampling height: approx. 1.1 m below grade-line; sampling direction E-W.	

Mine	Sample group/ section	Sample number(s)
WES	Profile N200 studied and described by Beukes et al. (1995, Appendix 8). Section from low-grade Mamatwan-type ore through high-grade Wessels-type ore towards the contact of the ferruginized area around a major N-S striking normal fault. Total length: 40 m; Sampling height: approximately 1.1 m below grade-line. Sampling direction E-W.	WES-N201..WES-N210
WES	Profile N500 studied and described by Beukes et al. (1995, Appendix 8). Section extends from a zone of high-grade ore through an approximately 5 m wide, E-W striking ferruginized graben-type fault structure back into high-grade ore. No fault displacement or ferruginization is observed between the orebodies on either side of the faulted area. Total length: 67 m; Sampling height: approximately 1.1 m below grade-line (where visible). Sampling direction S-N.	WES-N501..N512

UNIVERSITY OF JOHANNESBURG

Appendix III

Whole rock geochemical data

This Appendix contains all chemical data obtained for whole rock samples. Section III.1 lists major and trace element contents as well as densities of manganese ore samples from the KMF and PMF. The analytical method used for each sample is specified. Section III.2 contains whole rock analyses of bostonite samples from the KMF and samples from the Campbellrand dolomite. Section III.3 lists trace element concentrations of 40 selected ore samples obtained by MINTEK by ICP-MS.

Major element concentrations are expressed in weight percent (wt %), trace element concentrations in µg/g (ppm). Densities are calculated in g/cm^3. Mn/Fe ratios have been calculated from the element rather than the oxide concentrations. Analytical totals (Sum) have only been calculated by adding up major element concentrations. This leads to low apparent totals for some samples from the PMF, as Ba concentrations are extremely high.

UNIVERSITY OF JOHANNESBURG

Abbreviations used in this Appendix:

RHO: Density

tech.: Analytical technique

XRF, ICP-MS, L.O.I.: see Appendix I.

W/X: XRF data combined with titrimetric Fe(total) determination.

LLD: Lower than limit of detection

n.d.: not determined

III.1 Major and trace element compositions (XRF), manganese ores.

Table III.1.1 Major element contents of Mn-ores, KMF.

Sample No.	SiO_2	TiO_2	Al_2O_3	Fe_2O_3	Mn_3O_4	MgO	CaO	Na_2O	K_2O	P_2O_5	SO_3	H_2O^-	CO_2	LOI	**SUM**	Mn/Fe	RHO	tech.
Mamatwan																		
MMT-82	2.01	0.05	0.3	6.61	27.1	2.31	29.3	0.34	0.16	0.018	0.014	0.45	28.2	30.2	**98.4**	4.30	2.75	XRF
MMT-83	0.83	0.04	0.22	17.6	4.04	3.05	38.3	0.03	LLD	0.012	0.02	<0.05	35.7	36.2	**100.4**	0.24	2.82	XRF
MMT-84	4.09	0.05	0.36	24.2	8.71	9.14	21.4	0.04	0.04	0.012	0.003	0.21	31.8	32.5	**100.6**	0.38	2.96	XRF
MMT-85	1.43	0.05	0.31	17.8	3.06	1.18	40.7	0.05	0.01	0.014	0.016	0.11	34.5	35.3	**99.9**	0.18	2.75	XRF
MMT-86-Mn	3.46	0.05	0.38	7.42	30.4	2.37	26.6	0.37	0.37	0.029	0.04	0.62	24.5	28.1	**99.5**	4.29	2.83	XRF
MMT-86-He	1.78	0.05	0.34	17.9	2.88	2.25	39.3	0.14	0.02	0.013	0.019	0.19	34.5	35.3	**100.0**	0.17	2.83	XRF
MMT-87	2.62	0.05	0.34	7.62	32.5	2.61	26	0.34	0.25	0.022	0.013	0.65	25.1	27.9	**100.2**	4.46	2.82	XRF
MMT-88	2.66	0.05	0.32	7.28	34.4	2.21	25.1	0.28	0.34	0.02	0.01	0.57	24.2	26.8	**99.4**	4.95	2.98	XRF
MMT-90	9.88	0.17	2.06	8.53	29.1	2.95	20.2	0.25	1.15	1.691	0.107	1.52	n.d.	24.9	**101.0**	3.58	n.d.	XRF
MMT-91	3.44	0.05	0.07	7	70.2	1.74	4.69	0.41	0.08	0.011	LLD	0.72	3.87	12.1	**99.8**	10.51	3.16	XRF
MMT-92	7.54	0.05	0.22	12.3	37.1	1.7	19.4	0.59	0.11	0.058	0.042	0.69	14.5	21.9	**100.9**	3.17	2.55	XRF
MMT-93	4.65	0.05	0.03	6.88	66.5	2.79	1.41	0.48	0.87	0.015	LLD	0.66	0.1	16.0	**99.7**	10.14	2.94	XRF
MMT-94	1.2	0.05	LLD	6.07	73.5	1.58	2.12	0.82	0.56	0.019	LLD	0.7	0.13	14.4	**100.3**	12.69	2.33	XRF
MMT-95	6.99	0.05	LLD	6.75	67.1	1.18	2.07	0.82	1.08	0.021	LLD	1.03	0.11	14.1	**100.2**	10.42	2.58	XRF
MMT-96	15.9	0.05	0.01	6.74	59.1	0.55	2.73	0.68	1.04	0.025	LLD	0.95	0.52	12.4	**99.3**	9.19	3.31	XRF
MMT-97	50.4	0.04	0.09	7.44	30.9	0.39	1.12	0.53	0.65	0.023	LLD	0.66	0.22	8.1	**99.6**	4.35	3.11	XRF
MMT-98	42.1	0.04	0.17	5.35	39.2	0.64	1	0.48	1.53	0.046	LLD	0.52	0.21	9.3	**99.8**	7.67	n.d.	XRF
MMT-99/2	15	0.04	0.34	64.8	10.3	0.69	4.27	0.12	0.04	0.003	LLD	0.21	2.76	4.6	**100.2**	0.17	n.d.	W/X

UNIVERSITY OF JOHANNESBURG

Sample No.	SiO_2	TiO_2	Al_2O_3	Fe_2O_3	Mn_3O_4	MgO	CaO	Na_2O	K_2O	P_2O_5	SO_3	H_2O^-	CO_2	LOI	SUM	Mn/Fe	RHO	tech.
MMT-100	61.5	0.05	0.22	17.8	5.95	0.46	6.23	LLD	0.03	0.085	LLD	0.44	3.47	7.4	**99.7**	0.35	n.d.	XRF
MMT-101	12	0.04	0.06	80.5	0.1	0.12	LLD	LLD	LLD	LLD	0.164	0.07	1.57	3.4	**96.4**	0.00	n.d.	XRF
MMT-102	60	0.04	0.33	13.6	3.5	0.41	12.7	LLD	0.08	0.085	0.01	0.31	6.17	9.3	**100.1**	0.27	n.d.	XRF
MMT-103	63.7	0.05	1.03	10.2	7.16	0.67	8.82	0.07	0.22	0.071	0.029	1.41	2	8.0	**100.0**	0.74	n.d.	XRF
MMT-104	14.2	0.05	0.11	6.77	50	1.4	12.7	0.79	1.14	0.008	LLD	0.85	1.71	13.5	**100.7**	7.75	2.96	XRF
MMT-105	5.3	0.05	0.17	5.54	50.2	1.47	15.2	0.79	1.49	0.014	0.014	0.82	8.6	20.3	**100.6**	9.50	2.52	XRF
MMT-106	1.6	0.05	0.21	5.63	36.4	1.1	27.4	0.45	0.2	0.013	0.03	0.58	19.8	25.2	**98.2**	6.77	2.83	XRF
MMT-107	2.86	0.05	0.36	6.18	52.6	1.36	16.7	0.64	0.11	0.009	0.006	0.89	9.8	19.3	**100.2**	8.92	2.83	XRF
MMT-108	3.1	0.05	0.18	4.96	51.4	3.4	17.7	0.33	0.05	0.016	0.003	0.45	14.5	19.1	**100.2**	10.86	3.03	XRF
MMT-109	0.67	0.05	0.09	3.78	57.6	1.04	17.2	0.92	0.09	LLD	0.068	0.45	10.6	19.7	**101.1**	15.96	3.25	XRF
MMT-110	3.55	0.05	0.16	5.1	45.7	5.04	19.3	0.04	LLD	0.008	0.004	0.08	20.1	20.1	**99.0**	9.39	3.32	XRF
MMT-126	3.6	0.05	0.36	5.04	42.4	6.23	20.2	0.17	LLD	0.001	0.055	0.09	21.8	21.8	**99.9**	8.81	3.53	XRF
MMT-127	3.02	0.04	0.14	34.5	12.7	4.48	22.1	LLD	LLD	0.014	0.03	0.08	23.7	23.3	**100.4**	0.39	3.32	XRF
MMT-128	2.92	0.05	0.13	5.2	44	4.96	20.4	0.06	LLD	LLD	0.015	0.07	21.2	21.3	**99.0**	8.86	3.48	XRF
M2-44	4.97	0.09	<0.4	7.96	29.8	4.11	24.4	LLD	0.1	0.19	n.d.	0.11	24.4	26.9	**98.8**	3.81	3.20	XRF
M2-45	6.2	0.06	<0.4	9.77	47.2	3.2	14.6	LLD	0.1	0.24	n.d.	0.09	15.3	20.7	**123.6**	5.50	3.68	XRF
M2-47b	4.61	0.08	<0.4	4.91	49.4	2.14	17.9	LLD	0.14	0.21	n.d.	0.07	17.7	20.4	**125.5**	9.42	3.62	XRF
M2-49b	6.79	0.04	<0.4	5.96	60.9	1.56	11.3	LLD	0.12	0.23	n.d.	0.05	11.2	11.7	**117.0**	10.58	3.96	XRF
M2-49c	3.99	0.06	<0.4	9.61	30.3	2.59	24.6	LLD	0.09	0.22	n.d.	0.05	23.7	24.1	**121.3**	6.22	3.43	XRF
Nchwaning II																		
NC-4	9.79	0.09	0.1	11.5	77.9	0.1	4.44	0.02	0.01	LLD	0.036	0.15	0.847	1.9	**105.9**	7.10	4.16	XRF
NC-5	3.8	0.06	0.05	13.9	76.5	0.13	3.57	0.04	0.01	0.02	n.d.	0.08	n.d.	0.5	**98.6**	5.77	3.87	XRF

UNIVERSITY OF JOHANNESBURG

Sample No.	SiO_2	TiO_2	Al_2O_3	Fe_2O_3	Mn_3O_4	MgO	CaO	Na_2O	K_2O	P_2O_5	SO_3	H_2O	CO_2	LOI	SUM	Mn/Fe	RHO	tech.
NC-6	0.78	0.03	<0.4	12.0	70.4	0.26	9.84	LLD	0.01	0.03	2.2	0.22	0.8	2.4	**97.6**	6.15	4.22	XRF
NC-7	0.84	0.03	LLD	9.1	67.9	0.38	20.2	LLD	LLD	0.05	n.d.	0.08	n.d.	0.6	**99.0**	7.85	4.17	XRF
NC-8	0.89	0.04	<0.4	5.9	79.9	0.56	6.45	LLD	LLD	0.03	0.024	0.21	0.11	4.8	**98.5**	14.19	4.01	XRF
NC-9	4.71	0.02	<0.4	12.7	71.5	0.02	7.2	0.02	0.01	0.04	n.d.	0.2	n.d.	1.3	**97.9**	5.90	3.76	XRF
NC-10	7.74	0.03	<0.4	7.2	63.7	0.35	12.4	0.03	0.04	0.06	0.051	0.12	6.5	7.4	**99.0**	9.27	4.07	XRF
NC-11	5.7	0.04	<0.4	11.0	49.8	0.73	17.8	0.05	0.02	0.07	n.d.	0.12	13.4	14.4	**99.6**	4.74	3.62	XRF
NC-12	0.83	0.08	0.03	19.8	68.6	0.52	2.42	0.03	0.01	0.04	2.72	0.45	LLD	3.0	**98.1**	3.59	4.20	XRF
NC-13	0.52	0.03	0.14	28.3	64.3	0.56	2.18	LLD	LLD	0.02	n.d.	0.35	n.d.	4.6	**100.7**	2.35	3.98	XRF
NC-14	0.69	0.07	0.23	23.0	73.5	0.25	0.49	LLD	0.12	0.07	0.085	0.1	0.56	-1.9	**98.6**	3.31	3.87	XRF
NC-18	1.91	0.05	0.62	93.1	0.6	1.92	1.45	LLD	0.04	0.36	n.d.	0.05	0.16	1.5	**101.2**	0.01	4.47	XRF
NC-26	0.12	0.01	<0.4	4.7	96.5	0.26	0.29	LLD	LLD	LLD	0.121	<0.05	0.1	-1.3	**100.7**	20.93	3.71	XRF
NC-27	2.85	0.02	<0.4	13.3	80.5	0.09	2.74	LLD	0.01	0.03	0.03	<0.05	<0.1	-0.5	**99.1**	6.02	3.95	XRF
NC-28	12.1	0.03	<0.4	7.4	72.7	1.62	4.19	0.05	0.03	0.04	0.052	0.07	<0.1	0.7	**98.9**	9.79	3.61	XRF
NC-29	60.6	0.02	0.77	25.1	2.7	0.56	3.41	3.68	0.96	0.19	0.045	0.17	0.17	0.4	**98.4**	0.09	2.78	XRF
NC-30	52.9	0.02	0.45	32.3	3.8	0.03	3.74	4.11	0.24	0.06	n.d.	0.07	<0.1	3.0	**98.0**	0.12	2.79	XRF
NC-31	8.96	0.02	0.77	9.0	71.9	0.16	6.51	0.03	0.03	0.06	n.d.	<0.05	0.16	0.4	**97.8**	8.25	4.07	XRF
NC-32	<0.2	0.01	0.4	7.31	91.2	0.15	0.28	0.01	0.02	0.09	n.d.	<0.05	<0.1	-0.0	**99.5**	8.99	3.89	XRF
NC-33	<0.1	0.001	0.42	0.52	96.9	0.04	0.17	LLD	0.02	0.02	n.d.	LLD	<0.1	-0.1	**98.0**	128.50	3.97	XRF
Wessels																		
WES-276	35.9	0.04	2.12	29.2	4.35	2.83	13	2.27	0.02	0.108	LLD	0.16	n.d.	1.1	**90.9**	0.16	n.d.	XRF
WES-277	15.5	0.05	0.16	51.3	22	0.72	4.95	0.04	LLD	0.147	0.539	0.46	n.d.	2.4	**97.8**	0.45	n.d.	XRF
WES-278	5.6	0.05	0.42	30.4	54.8	1.4	4.76	0.03	LLD	0.035	0.146	0.07	n.d.	2.3	**99.9**	1.89	n.d.	XRF

UNIVERSITY OF JOHANNESBURG

Sample No.	SiO_2	TiO_2	Al_2O_3	Fe_2O_3	Mn_3O_4	MgO	CaO	Na_2O	K_2O	P_2O_5	SO_3	H_2O^-	CO_2	LOI	SUM	Mn/Fe	RHO	tech.
WES-310	6.89	0.04	0.28	7.31	77	0.9	3.65	0.02	LLD	0.028	0.206	<0.05	n.d.	1.7	**98.0**	11.04	4.34	XRF
WES-311-a	9.24	0.05	0.75	15.52	69.1	2.17	2.58	LLD	LLD	0.053	LLD	<0.05	n.d.	1.8	**101.2**	4.67	4.06	XRF
WES311-b	4.93	0.04	0.27	7.61	83	0.42	3.91	0.03	LLD	0.048	0.023	<0.05	n.d.	0.3	**100.6**	11.43	4.14	XRF
WES-312	8.79	0.05	0.12	7.86	78.3	0.46	2.94	LLD	LLD	0.028	0.007	<0.05	<0.1	1.5	**100.1**	10.44	4.25	XRF
WES-313	5.35	0.04	0.32	10.4	75.3	0.96	5.12	LLD	LLD	0.019	LLD	<0.05	n.d.	2.6	**100.1**	7.59	4.27	XRF
WES-314	6.21	0.04	0.34	18.1	67.3	0.7	4.78	LLD	LLD	0.062	LLD	<0.05	n.d.	1.1	**98.7**	3.90	4.23	XRF
WES-315	8.28	0.05	0.58	19.9	56.2	1.42	7.65	LLD	LLD	0.055	0.009	<0.05	n.d.	5.4	**99.5**	2.96	3.92	XRF
WES-316	5.42	0.04	0.29	8.73	80	0.66	3.37	0.02	LLD	0.025	0.035	<0.05	0	1.0	**99.6**	9.60	4.36	XRF
WES-317	9.96	0.05	0.08	6.32	78.3	0.27	3.63	LLD	LLD	0.033	LLD	<0.05	n.d.	1.4	**100.0**	12.98	4.18	XRF
WES-318	6.33	0.05	0.28	12	74.8	0.56	4.75	0.02	LLD	0.035	0.019	0.36	<0.1	0.7	**99.5**	6.53	4.28	XRF
WES-319	6.18	0.05	0.28	16.4	62.5	0.6	7.77	LLD	LLD	0.122	0.004	0.06	3.03	4.5	**98.4**	3.99	4.40	XRF
WES-320	8.61	0.05	0.17	8.42	75.9	0.26	3.84	LLD	LLD	0.019	LLD	<0.05	n.d.	0.5	**97.8**	9.45	4.28	XRF
WES-321	8.58	0.05	0.27	6.61	77.2	0.36	4.1	0.01	LLD	0.025	LLD	0.13	n.d.	0.5	**97.7**	12.24	4.35	XRF
WES-351	11.4	0.05	0.3	13	66.2	0.49	4.68	LLD	LLD	0.077	0.039	0.06	n.d.	2.3	**98.5**	5.34	n.d.	XRF
WES-352	11.7	0.05	0.58	15.9	62.6	1.01	4.87	LLD	LLD	0.075	LLD	<0.05	n.d.	2.6	**99.4**	4.13	n.d.	XRF
WES-353	7.9	0.04	0.25	9.23	76.3	0.36	3.8	LLD	LLD	0.025	LLD	<0.05	n.d.	1.3	**99.2**	8.66	n.d.	XRF
WES-354	11.3	0.05	0.49	20.2	59.1	0.72	5.56	LLD	LLD	0.059	0.019	0.06	n.d.	1.9	**99.3**	3.07	n.d.	XRF
WES-355	5.06	0.05	0.08	32.3	56.7	0.25	3.97	LLD	LLD	0.122	LLD	0.08	n.d.	0.8	**99.3**	1.84	n.d.	XRF
WES-356	3.51	0.05	0.1	15.2	76.4	0.26	2.97	LLD	LLD	0.031	LLD	0.07	n.d.	0.6	**99.2**	5.27	n.d.	XRF
WES-357	4.11	0.05	0.58	8.93	79.8	0.34	3.5	0.03	LLD	0.036	1.3	<0.05	n.d.	0.6	**99.2**	9.37	n.d.	XRF
WES-327-2	37.3	3.13	23.5	11.4	0.45	1.42	1.57	0.51	5.41	0.019	LLD	0.26	n.d.	6.3	**91.0**	0.04	n.d.	XRF
WES-333	0.07	0.05	0.54	21.1	56.9	0.82	9.85	LLD	LLD	0.071	0.144	<0.05	n.d.	10.9	**100.4**	2.83	n.d.	XRF

UNIVERSITY OF JOHANNESBURG

Sample No.	SiO_2	TiO_2	Al_2O_3	Fe_2O_3	Mn_3O_4	MgO	CaO	Na_2O	K_2O	P_2O_5	SO_3	H_2O^-	CO_2	LOI	SUM	Mn/Fe	RHO	tech.
WES-334	0.53	0.05	0.4	8.11	66.1	0.95	14.6	0.02	LLD	0.087	0.041	<0.05	n.d.	9.9	**100.8**	8.54	n.d.	XRF
WES-335	1.31	0.05	0.55	8.27	68.2	2.4	9.76	0.11	0.01	0.126	0.097	0.09	n.d.	8.7	**99.6**	8.64	n.d.	XRF
WES-336	0.35	0.06	0.3	9.27	75.7	0.93	4.88	0.08	0.01	0.098	1.66	0.26	n.d.	5.6	**99.0**	8.56	n.d.	XRF
WES-337	2.63	0.09	0.78	8.33	79.7	0.96	2.84	LLD	0.02	0.09	LLD	0.09	n.d.	4.4	**99.8**	10.03	n.d.	XRF
WES-338-I	2.26	0.07	0.46	11.8	70.3	0.61	6.99	LLD	LLD	0.552	0.093	<0.05	n.d.	5.6	**98.7**	6.24	n.d.	XRF
WES-338-II	6.31	0.16	2.87	20.6	54.4	3.78	5.29	0.29	0.07	1.52	0.021	0.05	n.d.	4.8	**100.2**	2.77	n.d.	XRF
WES-358	5.23	0.05	0.84	7.35	69.3	1.17	7.87	0.12	LLD	0.022	1.436	<0.05	n.d.	5.2	**98.6**	9.88	n.d.	XRF
WES-359	3.86	0.06	0.24	8.1	68.4	0.43	9.58	0.08	LLD	0.012	1.938	<0.05	n.d.	5.9	**98.6**	8.85	n.d.	XRF
WES-360-C	5.59	0.05	0.54	10.3	69	0.97	6.67	0.22	LLD	0.137	1.17	<0.05	n.d.	4.4	**99.1**	7.02	n.d.	XRF
WES-361	7.71	0.05	0.83	11.4	66.2	1.75	6.4	0.09	LLD	0.103	0.294	<0.05	n.d.	3.3	**98.1**	6.09	n.d.	XRF
WES-364	12	0.05	1.35	4.2	70.9	2.8	4.67	LLD	LLD	0.052	0.027	0.26	n.d.	3.3	**99.4**	17.69	n.d.	XRF
WES-365	4.87	0.05	0.54	8.06	59.3	1.07	15.4	0.02	LLD	0.098	0.234	<0.05	n.d.	8.6	**98.2**	7.71	n.d.	XRF
WES-368	9.9	0.04	0.85	4.91	63.9	1.57	8.34	LLD	LLD	0.129	0.03	0.07	n.d.	2.3	**92.0**	13.64	n.d.	XRF
WES-374-Mn	7.34	0.13	2.47	39.8	23.7	5.76	11.5	0.05	LLD	0.216	0.162	0.12	n.d.	9.7	**100.8**	0.62	n.d.	XRF
WES-375	2.48	0.07	0.31	6.83	72.9	1.27	3.14	3.09	LLD	0.041	3.56	<0.05	n.d.	1.4	**95.1**	11.19	n.d.	XRF
WES-378-I	27.2	0.04	2.6	9.31	14.8	21.4	14.1	0.01	LLD	LLD	0.138	0.16	n.d.	8.7	**98.3**	1.67	n.d.	XRF
WES-378-II	8.81	0.04	1.38	6.46	60.6	11.3	7.34	0.01	LLD	0.031	0.053	0.16	n.d.	8.8	**104.8**	9.83	n.d.	XRF
WES-378-III	6.08	0.05	1.42	7.21	67.3	8.12	6.07	0.09	LLD	0.147	LLD	0.28	n.d.	4.9	**101.3**	9.78	n.d.	XRF
WES-379-1	32.9	0.06	4.39	16.8	9.19	6.44	21.7	LLD	0.02	0.032	0.056	0.16	n.d.	8.5	**100.1**	0.57	n.d.	XRF
WES-379-2-I	5.65	0.04	0.38	10.5	76	0.61	3.9	LLD	LLD	0.093	0.024	0.1	n.d.	3.4	**100.6**	7.59	n.d.	XRF
WES-379-2-II	4.33	0.04	0.25	9.53	78.3	0.58	3.58	LLD	LLD	0.047	0.253	0.21	n.d.	2.3	**99.2**	8.61	n.d.	XRF

UNIVERSITY OF JOHANNESBURG

Sample No.	SiO_2	TiO_2	Al_2O_3	Fe_2O_3	Mn_3O_4	MgO	CaO	Na_2O	K_2O	P_2O_5	SO_3	H_2O^-	CO_2	LOI	SUM	Mn/Fe	RHO	tech.
Hotazel																		
HZ-141	0.68	0.05	0.3	8.94	88.8	1.03	0.39	LLD	LLD	0.112	LLD	0.06	n.d.	0.2	**100.5**	10.41	3.82	XRF
HZ-142	4.79	0.05	0.1	7.71	85.1	0.48	0.95	0.07	LLD	0.022	LLD	0.11	n.d.	0.6	**99.8**	11.57	4.19	XRF
HZ-143	3	0.04	0.51	4.97	88	1.55	1.99	0.1	LLD	0.072	0.036	<0.05	n.d.	0.6	**100.8**	18.56	4.07	XRF
HZ-144	3.62	0.04	0.03	6.95	87	0.32	1.53	LLD	LLD	0.011	LLD	<0.05	n.d.	0.4	**99.9**	13.12	4.26	XRF
HZ-145	4.63	0.05	0.11	7.6	84.3	0.37	1.68	0.06	0.01	0.029	LLD	<0.05	n.d.	0.7	**99.6**	11.62	4.31	XRF
HZ-146	4.16	0.05	0.07	7.2	85.4	0.42	0.91	LLD	LLD	0.039	LLD	0.19	n.d.	0.4	**98.6**	12.43	4.20	XRF
HZ-147	4.91	0.04	0.08	6.13	82.4	1.55	3.5	0.09	LLD	0.025	LLD	0.25	n.d.	0.7	**99.4**	14.09	4.14	XRF
HZ-148	7.02	0.05	0.18	5.72	84.3	0.7	1.04	LLD	LLD	0.025	LLD	0.11	n.d.	0.7	**99.7**	15.45	3.96	XRF
HZ-149	4.62	0.05	0.14	8.8	83.2	0.52	1.49	0.04	LLD	0.024	LLD	0.08	n.d.	0.7	**99.5**	9.91	4.36	XRF
HZ-150	0.44	0.04	0.01	4.24	85.8	0.18	0.36	1.28	0.83	0.002	LLD	0.56	n.d.	7.3	**100.5**	21.21	4.24	XRF
HZ-151	2.39	0.05	0.11	94.2	0.52	0.12	0.47	0.05	0.02	0.057	0.072	0.36	n.d.	1.2	**99.3**	0.01	4.07	W/X
HZ-153B	5.35	0.05	0.36	90.3	0.9	0.08	0.1	0.03	0.02	0.014	0.035	0.15	n.d.	3.6	**100.8**	0.01	3.77	W/X
HZ-153	0.88	0.05	0.18	12.1	74.7	0.72	0.57	1.07	1.86	0.032	LLD	0.77	n.d.	9.1	**101.2**	6.47	3.98	XRF
HZ-154	0.97	0.05	0.26	6.34	91.5	0.21	0.13	0.05	LLD	0.039	LLD	0.11	n.d.	0.5	**100.1**	15.12	4.43	XRF
HZ-155	1.44	0.05	0.05	7.1	87.5	0.13	0.03	0.8	0.04	0.07	LLD	0.28	n.d.	4.3	**101.5**	12.92	4.15	XRF
HZ-156	1.56	0.04	0.09	10.5	82.1	0.14	LLD	1.72	LLD	0.052	LLD	0.11	n.d.	3.8	**100.0**	8.19	4.07	XRF
HZ-157B	11	0.06	0.22	71.1	1.08	6.28	5.19	0.04	0.02	LLD	0.038	0.15	n.d.	5.5	**100.6**	0.02	3.85	W/X
HZ-157	1.91	0.05	0.85	8.56	85.3	0.5	0.37	LLD	LLD	0.168	LLD	0.12	n.d.	1.8	**99.5**	10.44	4.05	XRF
HZ-158	3.77	0.05	0.1	94.2	0.45	0.03	0.08	0.03	0.02	0.022	0.044	0.08	n.d.	0.6	**99.4**	0.01	4.37	W/X
HZ-159	2.35	0.05	0.26	94.6	0.5	0.23	0.11	0.03	0.02	0.034	0.033	0.11	n.d.	0.5	**98.7**	0.01	4.44	W/X
HZ-160	2.99	0.05	0.05	6.35	85.7	0.27	0.49	0.98	0.01	LLD	LLD	0.17	n.d.	1.9	**98.8**	14.14	4.15	XRF

UNIVERSITY OF JOHANNESBURG

Sample No.	SiO_2	TiO_2	Al_2O_3	Fe_2O_3	Mn_3O_4	MgO	CaO	Na_2O	K_2O	P_2O_5	SO_3	H_2O^-	CO_2	LOI	SUM	Mn/Fe	RHO	tech.
HZ-161	2.64	0.05	0.16	6.3	88.8	0.31	0.86	0.39	0.03	0.032	LLD	0.08	n.d.	1.5	**101.1**	14.77	4.08	XRF
HZ-162	5.07	0.05	0.09	8.08	80.2	0.39	6	0.04	LLD	0.039	LLD	<0.05	n.d.	0.9	**100.9**	10.40	4.22	XRF
Hz-304-Mn	4.42	0.05	0.24	8.14	40.3	5.28	21.5	0.01	0.01	0.026	0.045	<0.05	n.d.	19.8	**99.8**	5.19	3.41	XRF
Hz-304-Fe	3.47	0.05	0.26	12.2	32.7	6.05	23.6	0.1	0.01	0.041	0.05	0.07	n.d.	21.6	**100.1**	2.81	3.40	XRF
Wessels (samples from Burger, 1994)																		
WES-N101	5.39	0.05	0.92	55.4	12.6	3.1	9.13	n.d.	n.d.	n.d.	n.d.	0.13	6.17	6.1	**92.7**	0.23	3.89	ICP
WES-N102	6.42	0.04	0.87	16.4	64.4	0.33	8.01	n.d.	n.d.	n.d.	n.d.	0.1	2.1	3.1	**99.6**	4.03	3.80	ICP
WES-N106	1.75	0.03	<0.4	7.39	74.3	1.06	6.56	n.d.	n.d.	n.d.	n.d.	0.1	2.28	3.5	**94.6**	10.35	3.87	ICP
WES-N116	11.4	0.03	2.93	7.03	63	6.06	5.86	n.d.	n.d.	n.d.	n.d.	0.13	0.1	-0.5	**95.8**	9.19	3.76	ICP

UNIVERSITY OF JOHANNESBURG

Table III.1.2 Trace element concentrations Mn-ore, KMF.

Sample No.	V	Cr	Co	Ni	Cu	Zn	Rb	Sr	Zr	Mo	Sn	Ba	Pb	Th	tech.
Mamatwan															
MMT-82	14	11	30	9	LLD	4	7	897	23	LLD	3	222	LLD	2	XRF
MMT-83	16	13	LLD	4	LLD	LLD	4	198	LLD	LLD	1	78	LLD	1	XRF
MMT-84	21	19	10	14	LLD	LLD	2	113	LLD	LLD	LLD	83	LLD	LLD	XRF
MMT-85	11	23	3	1	LLD	LLD	1	268	1	LLD	LLD	142	1	LLD	XRF
MMT-86-Mn	22	14	24	9	LLD	19	3	670	15	LLD	1	145	LLD	LLD	XRF
MMT-86-He	13	LLD	3	LLD	LLD	LLD	3	175	LLD	LLD	LLD	137	2	LLD	XRF
MMT-87	14	9	47	8	LLD	LLD	6	737	17	LLD	5	170	LLD	3	XRF
MMT-88	12	20	42	LLD	LLD	LLD	5	722	16	LLD	2	201	LLD	2	XRF
MMT-90	160	32	274	117	91	46	18	3315	157	9	LLD	1893	3	4	XRF
MMT-91	20	17	51	LLD	LLD	57	5	125	LLD	LLD	2	896	5	LLD	XRF
MMT-92	22	LLD	41	LLD	LLD	96	LLD	260	LLD	LLD	1	2379	9	LLD	XRF
MMT-93	22	14	49	1	LLD	129	4	111	LLD	LLD	4	85	LLD	LLD	XRF
MMT-94	12	26	34	LLD	LLD	332	3	144	LLD	LLD	2	1472	8	LLD	XRF
MMT-95	11	3	38	6	LLD	273	5	125	LLD	LLD	3	367	LLD	LLD	XRF
MMT-96	11	35	46	19	LLD	655	6	186	LLD	LLD	LLD	80	8	LLD	XRF
MMT-97	14	43	41	18	LLD	964	LLD	180	LLD	LLD	LLD	41	19	1	XRF
MMT-98	12	16	57	8	1	557	LLD	341	9	LLD	3	18	2	LLD	XRF
MMT-99/2	46	59	24	15	LLD	227	5	66	LLD	LLD	LLD	44	LLD	LLD	XRF
MMT-100	23	73	68	21	4013	4	1	75	LLD	LLD	1	3937	16	2	XRF
MMT-101	60	89	LLD	11	40000	7	LLD	23	LLD	3	LLD	97	LLD	LLD	XRF

UNIVERSITY OF JOHANNESBURG

Sample No.	V	Cr	Co	Ni	Cu	Zn	Rb	Sr	Zr	Mo	Sn	Ba	Pb	Th	tech.
MMT-102	27	116	16	9	788	3	4	106	LLD	LLD	LLD	401	LLD	2	XRF
MMT-103	32	55	52	20	65	26	4	256	5	2	LLD	1105	6	4	XRF
MMT-104	19	16	60	11	LLD	75	6	259	6	LLD	LLD	518	9	1	XRF
MMT-105	17	LLD	62	LLD	LLD	65	9	480	4	LLD	1	527	LLD	1	XRF
MMT-106	7	11	27	LLD	23	66	4	263	LLD	LLD	2	566	LLD	1	XRF
MMT-107	23	22	35	LLD	LLD	73	LLD	238	LLD	LLD	5	175	LLD	LLD	XRF
MMT-108	18	20	47	2	LLD	23	2	191	LLD	LLD	LLD	907	LLD	3	XRF
MMT-109	12	4	20	2	LLD	LLD	3	283	LLD	LLD	1	2563	LLD	2	XRF
MMT-110	12	18	33	5	LLD	24	2	121	LLD	1	4	242	LLD	LLD	XRF
MMT-126	20	13	35	23	LLD	71	2	92	LLD	LLD	1	210	LLD	LLD	XRF
MMT-127	20	30	29	LLD	LLD	LLD	2	98	LLD	LLD	1	122	7	LLD	XRF
MMT-128	11	8	38	8	LLD	15	1	89	LLD	LLD	7	113	LLD	4	XRF
Wessels															
WES-276	36	236	35	28	3	40	1	45	LLD	4	2	44	55	2	XRF
WES-277	22	90	33	11	LLD	126	1	74	LLD	LLD	2	3427	LLD	LLD	XRF
WES-278	19	28	45	1	116	105	3	55	LLD	LLD	2	229	31	LLD	XRF
WES-310	14	80	13	2	11	14	2	69	LLD	LLD	2	2657	74	LLD	XRF
WES-311-a	11	45	53	10	LLD	20	3	30	LLD	LLD	2	52	31	LLD	XRF
WES311-b	14	30	20	LLD	9	4	LLD	25	LLD	LLD	2	74	98	LLD	XRF
WES-312	9	74	45	21	21	22	1	31	LLD	LLD	2	303	39	LLD	XRF
WES-313	7	38	39	LLD	LLD	5	LLD	377	LLD	LLD	2	94	181		XRF
WES-314	11	49	27	13	11	13	3	26	LLD	LLD	2	74	130	LLD	XRF
WES-315	11	49	29	39	LLD	7	2	187	LLD	LLD	2	98	62	LLD	XRF

UNIVERSITY OF JOHANNESBURG

Sample No.	V	Cr	Co	Ni	Cu	Zn	Rb	Sr	Zr	Mo	Sn	Ba	Pb	Th	tech.
WES-316	10	46	31	12	LLD	1	8	25	LLD	1	2	65	253	2	XRF
WES-317	14	104	49	13	LLD	5	4	24	LLD	LLD	2	45	62	LLD	XRF
WES-318	10	32	38	7	21	111	LLD	30	LLD	LLD	2	315	195	1	XRF
WES-319	9	44	39	34	LLD	31	2	157	LLD	LLD	2	114	109	LLD	XRF
WES-320	10	111	22	LLD	LLD	14	LLD	32	LLD	LLD	2	84	97	LLD	XRF
WES-321	14	58	44	3	LLD	119	LLD	32	LLD	LLD	2	65	213	LLD	XRF
WES-322	46	167	33	94	4	111	<5	7854	64	<1		104	904	7	XRF
WES-351	14	111	22	LLD	LLD	LLD	LLD	47	LLD	LLD	2	370	19	LLD	XRF
WES-352	19	120	33	19	LLD	22	1	25	LLD	1	2	46	20	LLD	XRF
WES-353	18	87	22	LLD	LLD	LLD	1	40	LLD	LLD	2	87	27	LLD	XRF
WES-354	18	82	15	9	LLD	LLD	LLD	27	LLD	LLD	2	98	41	1	XRF
WES-355	14	61	5	16	LLD	LLD	2	30	LLD	LLD	2	53	27	LLD	XRF
WES-356	14	54	28	13	LLD	LLD	3	32	LLD	LLD	2	175	26	LLD	XRF
WES-357	20	34	LLD	25	LLD	42	LLD	165	LLD	LLD	1	15892	79	LLD	XRF
WES-327-2	206	76	59	197	8	50	105	530	LLD	LLD	2	5351	23	4	XRF
WES-333	46	52	62	LLD	89	55	LLD	396	3	LLD	2	99	260	3	XRF
WES-334	12	29	42	4	76	27	LLD	1135	17	LLD	2	376	16	2	XRF
WES-335	37	52	82	LLD	144	94	3	518	2	LLD	1	1190	26	4	XRF
WES-336	74	53	33	19	98	27	3	2468	55	LLD	2	12588	26	LLD	XRF
WES-337	35	91	43	LLD	266	36	2	148	LLD	LLD	1	149	11	LLD	XRF
WES-338-I	93	94	54	4	77	LLD	LLD	809	24	LLD	2	314	LLD	LLD	XRF
WES-338-II	105	93	291	175	81	608	6	285	30	LLD	2	261	69	LLD	XRF
WES-338-III	130	54	469	231	210	220	52	393	130	LLD	LLD	4785	914	LLD	XRF

UNIVERSITY OF JOHANNESBURG

Sample No.	V	Cr	Co	Ni	Cu	Zn	Rb	Sr	Zr	Mo	Sn	Ba	Pb	Th	
WES-358	21	38	45	11	LLD	35	3	1761	40	2	2	14425	71	LLD	XRF
WES-359	17	42	56	8	LLD	6	LLD	1737	33	LLD	1	18634	19	LLD	XRF
WES-360-C	15	95	23	22	LLD	8	4	596	4	LLD	1	11225	9	LLD	XRF
WES-361	17	93	53	LLD	LLD	35	2	163	LLD	LLD	1	2910	11	1	XRF
WES-364	40	59	71	6	154	40	LLD	42	LLD	LLD	2	584	40	LLD	XRF
WES-365	16	36	51	13	41	41	3	1510	23	LLD	2	2718	44	LLD	XRF
WES-368	21	26	77	LLD	LLD	71	3	72	LLD	LLD	2	128	104	LLD	XRF
WES-374-Mn	109	42	53	72	LLD	96	2	316	13	2	2	2093	240	LLD	XRF
WES-375	32	20	174	10	LLD	7707	2	487	3	LLD	1	43563	240	3	XRF
WES-378-I	12	17	53	52	13	23	LLD	48	LLD	LLD	2	62	145	4	XRF
WES-378-II	14	45	46	22	10	74	2	27	LLD	1	2	146	144	3	XRF
WES-378-III	17	35	75	18	LLD	236	1	29	LLD	LLD	2	95	45	LLD	XRF
WES-379-1	36	39	14	12	202	67	LLD	803	15	LLD	2	73	208	1	XRF
WES-379-2-I	19	51	49	9	LLD	3	4	159	LLD	LLD	2	96	52	LLD	XRF
WES-379-2-II	11	98	35	14	11	33	3	94	LLD	LLD	2	2984	128	2	XRF
Hotazel															
HZ-141	20	44	LLD	1	LLD	24	2	24	LLD	LLD	10	18	15	LLD	XRF
HZ-142	8	43	38	LLD	LLD	260	3	25	LLD	LLD	4	24	51	LLD	XRF
HZ-143	12	41	31	18	LLD	152	2	30	LLD	LLD	LLD	51	41	LLD	XRF
HZ-144	20	86	40	LLD	LLD	30	4	29	LLD	LLD	5	26	30	LLD	XRF
HZ-145	17	101	14	7	LLD	111	LLD	36	LLD	LLD	6	78	32	LLD	XRF
HZ-146	24	55	59	27	LLD	36	3	29	LLD	LLD	LLD	58	4	LLD	XRF
HZ-147	17	39	36	LLD	LLD	273	2	26	LLD	LLD	LLD	232	98	1	XRF

UNIVERSITY OF JOHANNESBURG

Sample No.	V	Cr	Co	Ni	Cu	Zn	Rb	Sr	Zr	Mo	Sn	Ba	Pb	Th	tech.
HZ-148	15	60	35	LLD	LLD	11	LLD	25	LLD	LLD	LLD	26	LLD	LLD	XRF
HZ-149	18	90	47	9	LLD	158	1	25	LLD	LLD	LLD	41	61	LLD	XRF
HZ-150	17	63	21	LLD	LLD	2297	3	501	21	LLD	2	22	84	1	XRF
HZ-151	36	57	16	LLD	LLD	LLD	LLD	7	LLD	LLD	3	83	14	LLD	XRF
HZ-153B	81	24	LLD	LLD	LLD	LLD	5	16	LLD	LLD	3	107	7	LLD	XRF
HZ-153	862	49	49	6	LLD	2178	4	1372	102	5	2	52	181	4	XRF
HZ-154	18	43	8	12	LLD	266	LLD	21	LLD	LLD	6	52	141	3	XRF
HZ-155	27	38	3	11	LLD	2112	1	44	LLD	LLD	2	41	90	4	XRF
HZ-156	32	37	14	13	LLD	4336	2	22	LLD	LLD	LLD	30	90	LLD	XRF
HZ-157B	13	34	9	9	LLD	27	1	33	LLD	LLD	LLD	170	27	LLD	XRF
HZ-157	18	26	LLD	LLD	LLD	131	LLD	23	LLD	LLD	2	28	45	LLD	XRF
HZ-158	49	78	16	LLD	LLD	4	6	7	LLD	LLD	3	94	1	LLD	XRF
HZ-159	41	49	LLD	LLD	LLD	LLD	2	9	LLD	LLD	4	93	LLD	LLD	XRF
HZ-160	12	49	34	LLD	LLD	2586	4	32	LLD	LLD	5	80	104	LLD	XRF
HZ-161	14	46	38	LLD	LLD	1199	2	30	LLD	LLD	LLD	35	83	LLD	XRF
HZ-162	14	56	47	7	LLD	208	LLD	37	LLD	LLD	LLD	326	61	LLD	XRF
Hz-304-Mn	18	10	30	14	LLD	97	LLD	173	LLD	LLD	1	71	14	LLD	XRF
Hz-304-Fe	20	7	31	2	LLD	228	3	190	LLD	LLD	2	102	28	LLD	XRF

UNIVERSITY OF JOHANNESBURG

Table III.1.3 Major element concentrations Mn-ore, PMF.

Sample No.	SiO_2	TiO_2	Al_2O_3	Fe_2O_3	Mn_3O_4	MgO	CaO	Na_2O	K_2O	P_2O_5	SO_3	H_2O^-	LOI	SUM	Mn/Fe	RHO	tech.
Aucampsrust																	
AUC-200	3.5	0.1	2.15	26.6	56.8	0.17	0.31	0.28	0.39	0.084	LLD	0.33	7.7	**98.3**	2.2	4.10	XRF
AUC-201	4.16	0.09	2.46	23.7	61	0.34	0.74	LLD	0.38	0.078	LLD	0.26	5.7	**99.0**	2.7	4.27	XRF
AUC-202	7.14	0.54	10.84	37.9	27.8	0.2	0.31	0.05	0.4	0.042	LLD	0.41	7.2	**92.8**	0.8	3.67	XRF
AUC-204	21.2	0.05	0.98	0.99	62.2	0.61	0.54	0.37	1.53	0.024	LLD	0.77	9.3	**98.5**	64.7	3.41	XRF
AUC-205	21.4	0.08	1.26	3.21	62.6	0.17	1.44	1.14	0.01	0.014	2.661	0.15	3.1	**97.2**	20.1	3.94	XRF
Beeshoek																	
BEE-211	1.97	0.19	0.32	5.23	44.2	0.07	0.06	0.27	0.29	0.006	13.3	0.21	5.5	**71.6**	8.7	4.06	XRF
BEE-212	4.56	0.07	0.28	5.13	80.4	0.14	0.73	0.12	0.25	0.074	1.096	0.14	4.2	**97.2**	16.1	4.33	XRF
BEE-213	4.11	0.13	1.53	10.6	72.9	0.25	0.74	0.06	0.85	0.209	LLD	0.22	5.5	**97.0**	7.1	4.42	XRF
BEE-214	8.22	0.11	2.68	8.75	69.5	0.09	0.95	0.02	0.74	0.316	0.174	0.21	5.2	**96.9**	8.2	3.95	XRF
Manganore																	
MAN-237	4.95	0.08	1.27	17.8	62.7	0.14	0.21	0.16	2.17	0.127	LLD	0.29	9.7	**99.5**	3.6	4.13	XRF
MAN-238	8.76	0.04	0.09	1.24	78.3	0.15	0.17	0.23	0.51	0.042	LLD	0.23	10.4	**100.1**	65.0	3.57	XRF
MAN-239	43.9	0.04	0.28	2.88	44.6	0.21	0.18	0.43	0.4	0.04	0.003	0.23	5.9	**99.2**	16.0	2.99	XRF
Kapstewel																	
KAP-225	5.5	0.14	1.73	5.27	78.6	0.28	0.9	0.35	0.65	0.102	LLD	0.3	6.1	**99.9**	15.4	4.34	XRF
KAP-226	18.8	0.2	11.36	11.7	40.6	0.59	0.01	0.15	4.15	0.003	LLD	0.19	8.3	**96.0**	3.6	3.42	XRF
KAP-228/1	14.6	0.05	1.08	1.4	75.5	0.24	0.93	0.08	0.5	0.064	0.025	0.16	3.7	**98.3**	55.6	3.55	XRF
KAP-229	57	0.05	0.35	0.99	35.8	0.23	0.35	0.1	0.17	LLD	0.564	0.09	2.4	**98.1**	37.2	3.24	XRF
KAP-230	8.79	0.05	1.69	1.93	72.4	0.23	0.2	0.37	2.26	0.012	0.136	0.23	10.5	**98.8**	38.6	3.91	XRF

UNIVERSITY OF JOHANNESBURG

Sample No.	SiO_2	TiO_2	Al_2O_3	Fe_2O_3	Mn_3O_4	MgO	CaO	Na_2O	K_2O	P_2O_5	SO_3	H_2O^-	LOI	SUM	Mn/Fe	RHO	tech.
KAP-230B	63.2	0.81	21.2	2.2	0.27	1.14	0.05	0.1	7.8	0.009	0.01	0.35	3.6	**100.8**	0.1	2.00	XRF
KAP-231	10.7	0.16	4.37	4.39	63.7	0.59	0.24	0.18	2.4	0.031	LLD	0.43	9.5	**96.8**	15.0	4 12	XRF
Doornfontein																	
DO-166/1	33	0.14	3.49	22.7	29.5	0.4	0.06	LLD	1.51	LLD	LLD	0.32	6.2	**97.3**	1.3	3.59	XRF
DO-167/1	4.84	0.11	2.92	4.93	79.1	0.24	1	LLD	0.62	0.03	LLD	0.15	4.5	**98.4**	16.5	4.28	XRF
DO-167/2	8.14	1.21	5.16	37	33.6	0.21	0.07	0.01	2.25	0.079	LLD	0.14	6.8	**94.7**	0.9	3.94	XRF
DO-168	1.7	0.07	0.47	1.85	82	0.1	0.13	0.08	0.22	0.019	1.25	0.18	8.7	**96.7**	45.6	4.35	XRF
DO-171	3.71	0.07	2.35	2.16	75.5	0.6	0.55	0.31	1.87	0.068	LLD	0.39	10.1	**97.7**	36.0	2.87	XRF
Paling																	
PAL-215	1.01	0.11	3.21	33.6	48.9	0.64	0.82	0.21	1.41	LLD	LLD	0.82	11.7	**102.4**	1.5	2.80	XRF
PAL-216	2.77	0.3	11.68	31.4	44.9	0.85	0.53	0.11	0.31	0.04	LLD	0.28	7.4	**100.5**	1.5	3.91	XRF
PAL-217	5.51	0.15	16.13	13	55.7	1.38	0.54	0.05	0.12	0.078	LLD	0.32	7.8	**100.7**	4.4	3.74	XRF
PAL-218	4.47	0.68	9.63	48.4	30.3	0.74	0.4	0.34	0.11	0.069	LLD	0.33	4.6	**100.1**	0.6	3.93	W/F
PAL-219	1.65	0.07	1.98	7.66	83.7	0.46	0.53	0.06	0.07	0.002	LLD	0.16	3.8	**100.1**	11.3	4.36	XRF
PAL-220	2.11	0.16	3.02	25.1	58.3	0.26	0.55	0.1	0.49	0.103	LLD	0.2	6.0	**96.4**	2.4	3.96	XRF
PAL-221	2.96	0.24	10.5	12	63	0.41	0.8	0.08	0.82	0.062	LLD	0.37	9.1	**100.3**	5.4	3.89	XRF
PAL-222	3.79	0.24	6.34	50.6	30.9	0.27	0.4	0.09	0.32	0.066	LLD	0.23	7.7	**101.2**	0.6	3.79	W/X
Glosam																	
GLO-184	7.12	0.75	17.3	45.1	20.8	0.43	0.07	1.42	0.41	0.052	LLD	<0.05	6.3	**99.7**	0.5	3.77	XRF
GLO-185	2.5	0.22	14.1	15.2	58.6	0.28	0.61	0.17	0.37	0.052	LLD	0.06	6.5	**98.6**	4.0	4.48	XRF
GLO-186	1.52	0.54	9.87	16.4	57.8	0.94	0.2	0.01	0.83	0.02	LLD	0.14	10.7	**99.0**	3.6	3.67	XRF
GLO-187	6.35	0.42	12.7	23.1	46.7	0.35	0.17	2.35	0.76	0.022	LLD	0.21	7.2	**100.4**	2.1	3.86	XRF

UNIVERSITY OF JOHANNESBURG

Sample No.	SiO_2	TiO_2	Al_2O_3	Fe_2O_3	Mn_3O_4	MgO	CaO	Na_2O	K_2O	P_2O_5	SO_3	H_2O^-	LOI	SUM	Mn/Fe	RHO	tech.
GLO-189	0.44	0.1	0.36	98.4	0.08	LLD	0.02	LLD	0.051	LLD	0.051	<0.05	0.5	**100.1**	0.0	4.69	W/X
GLO-190	4.53	0.05	0.63	92.9	0.16	0.02	0.08	0.012	0.048	0.003	0.046	<0.05	0.4	**98.8**	0.0	4.05	W/X
GLO-192/2	6.22	0.24	6.8	8.09	54.4	0.57	0.1	0.12	1.23	0.217	LLD	0.54	11.8	**90.3**	6.9	3.81	XRF
GLO-194	1.59	0.06	1.85	94.8	0.04	0.01	0.02	0.011	0.13	0.148	0.1	<0.05	0.6	**99.4**	0.0	4.80	W/X
GLO-196	5.55	0.19	9.12	58.2	20.1	0.45	0.04	1.04	0.01	0.013	0.05	0.06	3.2	**98.0**	0.4	3.74	XRF
GLO-197/1	4.01	0.31	6.09	13.7	63.9	1.87	0.68	0.11	0.78	0.036	LLD	0.35	8.4	**100.2**	4.8	3.89	XRF
GLO-291	20.7	0.37	7.21	12.5	34.3	1.16	1.07	0.05	1.49	LLD	0.075	0.8	12.5	**92.2**	2.8	1.65	XRF
Lohatla																	
LOH-176	18	0.55	35.9	11.2	20.8	1.69	0.05	6.21	0.9	0.02	LLD	0.06	5.0	**100.5**	1.9	3.87	XRF
LOH-177	8.14	0.47	10.2	24.2	47.7	0.37	0.12	0.52	1.62	0.147	LLD	0.11	6.1	**99.7**	2.0	4.21	XRF
LOH-178	2.55	0.08	5.75	12.6	70.4	0.16	0.14	0.66	0.6	0.09	LLD	0.09	5.7	**98.8**	5.8	3.91	XRF
LOH-179	2.63	0.14	4.34	3.65	77.1	0.27	0.8	0.13	1.08	0.094	LLD	0.13	7.5	**97.9**	21.8	3.32	XRF
LOH-180	0.71	0.11	4.42	30.1	57.3	0.22	0.13	LLD	0.77	0.04	LLD	0.08	6.3	**100.1**	2.0	4.35	XRF
LOH-182	7.24	0.19	4.59	6.93	47.7	2.28	5.77	LLD	1.31	LLD	0.048	2.88	21.7	**100.6**	7.5	0.38	XRF
LOH-294	6.48	0.21	3.44	21.4	36.5	0.98	1.24	0.18	0.87	0.264	0.039	4.77	20.8	**97.2**	1.8	1.16	XRF
Bishop																	
BIS-240	3.85	0.49	14.5	29.5	38.2	0.58	0.14	0.65	0.72	0.047	LLD	0.1	9.8	**98.4**	1.3	3.81	XRF
BIS-241	2.14	0.38	29.6	9.38	49.9	1.19	LLD	LLD	0.06	0.001	LLD	<0.05	7.4	**100.0**	5.5	4.04	XRF
BIS-242	2.19	0.13	1.6	0.57	68.8	0.23	0.2	0.19	0.2	0.465	LLD	0.47	12.0	**87.0**	124.3	3.66	XRF
BIS-244	0.33	0.09	18	12.5	52.6	1.29	LLD	0.08	0.17	LLD	LLD	<0.05	14.9	**100.0**	4.3	4.23	XRF
BIS-245	0.35	0.32	3.32	19.9	57.9	0.24	0.15	0.11	2.55	0.006	LLD	0.08	8.7	**93.6**	3.0	4.21	XRF
BIS-246	3.62	0.23	18.5	11.4	56.6	0.87	0.04	1.2	0.44	LLD	LLD	0.07	6.6	**99.5**	5.1	3.51	XRF
BIS-248	3.07	0.23	5.81	17.4	66.7	0.25	0.22	0.01	0.11	0.364	LLD	0.08	5.3	**99.5**	4.0	4.10	XRF

UNIVERSITY OF JOHANNESBURG

Sample No.	SiO_2	TiO_2	Al_2O_3	Fe_2O_3	Mn_3O_4	MgO	CaO	Na_2O	K_2O	P_2O_5	SO_3	H_2O^-	LOI	**SUM**	Mn/Fe	RHO	tech.
BIS-250	4	0.15	4.44	18	67.3	0.15	0.47	0.04	0.65	0.015	LLD	0.08	5.1	**100.4**	3.9	4.35	XRF

UNIVERSITY OF JOHANNESBURG

Table III.1.4 Trace element concentrations, manganese ore, PMF.

Sample No.	V	Cr	Co	Ni	Cu	Zn	Rb	Sr	Zr	Mo	Sn	Ba	Pb	Th	tech.
Aucampsrust															
AUC-200	51	98	182	49	253	16	4	125	16	1	LLD	16300	73	LLD	XRF
AUC-201	118	117	212	94	341	55	3	158	28	LLD	LLD	24569	205	LLD	XRF
AUC-202	120	243	412	512	386	74	11	74	50	5	LLD	71515	1254	20	XRF
AUC-204	64	66	45	214	288	50	21	347	9	LLD	LLD	18199	27	LLD	XRF
AUC-205	92	93	62	70	387	61	4	43	LLD	LLD	LLD	32487	98	1	XRF
Beeshoek															
BEE-211	60	6	99	LLD	590	LLD	LLD	682	18	LLD	LLD	281170	LLD	LLD	XRF
BEE-212	70	144	107	65	223	4	1	129	LLD	LLD	LLD	28052	11	LLD	XRF
BEE-213	67	243	159	214	225	89	5	133	20	1	LLD	18271	122	LLD	XRF
BEE-214	92	131	156	191	221	74	2	173	3	LLD	LLD	26968	127	1	XRF
Manganore															
MAN-237	112	111	202	304	120	40	12	302	19	1	LLD	18833	6	LLD	XRF
MAN-238	30	237	88	149	30	29	5	56	LLD	LLD	3	1159	15	LLD	XRF
MAN-239	25	246	120	112	79	18	4	77	LLD	1	LLD	4731	27	2	XRF
Kapstewel															
KAP-225	39	144	119	238	87	29	14	103	11	LLD	1	2781	16	LLD	XRF
KAP-226	55	25	54	143	LLD	50	70	307	32	LLD	LLD	29440	2496	41	XRF
KAP-228/1	97	167	83	219	303	28	2	86	LLD	LLD	LLD	11688	148	0	XRF
KAP-229	21	251	42	50	147	17	1	57	LLD	LLD	LLD	9285	30	3	XRF
KAP-230	127	100	113	284	294	35	12	159	3	LLD	LLD	14985	58	3	XRF

UNIVERSITY OF JOHANNESBURG

Sample No.	V	Cr	Co	Ni	Cu	Zn	Rb	Sr	Zr	Mo	Sn	Ba	Pb	Th	tech.
KAP-230B	26	79	19	404	11	21	152	11	124	4	3	250	14	22	XRF
KAP-231	93	92	131	662	202	109	28	247	23	LLD	LLD	31661	446	13	XRF
Doornfontein															
DO-166/1	91	64	18	47	15	32	28	257	31	LLD	LLD	34279	2864	47	XRF
DO-167/1	96	156	51	77	201	56	8	97	5	LLD	LLD	16228	265	3	XRF
DO-167/2	32	72	49	41	LLD	40	33	263	112	LLD	LLD	37696	1438	21	XRF
DO-168	68	134	49	86	328	LLD	2	127	LLD	LLD	LLD	39424	LLD	LLD	XRF
DO-171	318	53	39	109	257	70	16	459	21	LLD	LLD	27928	44	LLD	XRF
Paling															
PAL-215	187	94	43	215	281	117	12	483	64	LLD	LLD	833	178	LLD	XRF
PAL-216	94	206	84	259	28	177	3	114	48	LLD	LLD	8586	352	9	XRF
PAL-217	164	116	141	214	167	180	LLD	72	29	2	LLD	10630	102	LLD	XRF
PAL-218	79	168	190	578	111	111	LLD	90	316	LLD	3	3669	559	18	XRF
PAL-219	102	142	22	LLD	80	28	2	76	LLD	LLD	8	1571	322	3	XRF
PAL-220	79	93	36	36	69	43	6	216	23	LLD	LLD	30530	326	8	XRF
PAL-221	58	118	199	199	55	103	6	419	156	LLD	6	731	28	1	XRF
PAL-222	65	129	49	49	LLD	54	8	237	79	LLD	5	2255	32	LLD	XRF
Glosam															
GLO-184	71	132	181	240	120	22	2	123	158	LLD	LLD	10761	353	15	XRF
GLO-185	111	156	69	125	85	47	3	55	71	LLD	LLD	6859	31	2	XRF
GLO-186	66	174	158	253	LLD	70	12	103	33	LLD	LLD	25121	1249	24	XRF
GLO-187	314	117	69	239	14	36	2	204	76	LLD	3	6858	538	11	XRF

UNIVERSITY OF JOHANNESBURG

Sample No.	V	Cr	Co	Ni	Cu	Zn	Rb	Sr	Zr	Mo	Sn	Ba	Pb	Th	tech.
GLO-189	68	19	LLD	LLD	LLD	LLD	3	7	LLD	LLD	22	145	14	LLD	XRF
GLO-190	76	51	25	50	LLD	1	6	7	LLD	LLD	12	336	7	LLD	XRF
GLO-192/2	134	71	78	29	LLD	89	19	131	19	LLD	LLD	100592	LLD	LLD	XRF
GLO-194	345	430	10	15	20	LLD	6	882	69	1	6	121	5	LLD	XRF
GLO-196	53	82	128	200	100	196	2	53	12	LLD	LLD	4492	200	10	XRF
GLO-197/1	56	132	14	49	13	33	13	340	108	LLD	LLD	5822	5	LLD	XRF
GLO-291	75	42	26	72	45	5	27	237	45	LLD	LLD	79200	LLD	LLD	XRF
Lohatla															
LOH-176	18	89	93	261	40	35	9	122	98	LLD	LLD	1925	26	6	XRF
LOH-177	216	283	107	353	168	27	18	134	346	1	LLD	5944	46	6	XRF
LOH-178	248	164	285	566	1451	703	3	112	109	9	LLD	13978	4	3	XRF
LOH-179	413	116	37	213	73	29	17	469	38	LLD	LLD	19448	LLD	1	XRF
LOH-180	141	179	52	84	105	14	6	210	38	LLD	LLD	1414	52	LLD	XRF
LOH-182	48	80	27	16	LLD	32	31	324	24	LLD	3	781	16	2	XRF
LOH-294	305	26	29	286	LLD	75	15	104	2	1	LLD	81664	LLD	1	XRF
Bishop															
BIS-240	49	110	243	423	25	55	9	97	152	1	LLD	19669	467	8	XRF
BIS-241	22	212	149	345	45	42	3	33	47	LLD	LLD	1674	22	1	XRF
BIS-242	155	22	510	198	7	317	3	119	LLD	LLD	LLD	141041	LLD	LLD	XRF
BIS-244	42	121	136	769	LLD	143	6	84	6	LLD	LLD	2593	275	5	XRF
BIS-245	83	57	42	64	LLD	64	36	421	56	LLD	LLD	48559	4212	72	XRF
BIS-246	64	189	226	375	159	16	5	93	23	LLD	LLD	4203	9	LLD	XRF
BIS-248	12	178	157	344	23	4	7	67	7	LLD	LLD	9070	88	1	XRF

UNIVERSITY OF JOHANNESBURG

Sample No.	V	Cr	Co	Ni	Cu	Zn	Rb	Sr	Zr	Mo	Sn	Ba	Pb	Th	tech.
BIS-250	63	157	59	41	106	5	LLD	41	16	3	3	3388	33	LLD	XRF

UNIVERSITY OF JOHANNESBURG

III.2 Major and trace data of various rocks associated with manganese ore in the KMF and the PMF.

Table III.2.1 Major element composition of Campbellrand dolomite (analyses by MINTEK).

Sample No.	SiO_2	TiO_2	Al_2O_3	Fe_2O_3	Mn_3O_4	M_gO	CaO	$N_{a2}O$	K_2O	P_2O_5	SO_3	H_2O-	LOI	SUM	Mn/Fe	RHO
LOH-309-1	0.33	<0.04	0.4	0.5	2.85	19.3	30.4	0.022	0.045	0.015	<0.01	0.2	45.4	**99.4**	5.9	2.79
LOH-309-2	0.7	<0.04	0.54	4.32	3.69	16.1	29.8	0.023	0.12	0.019	<0.01	<0.1	43.7	**99.0**	0.9	2.83
BOETSAP	<0.2	<0.04	0.27	0.52	2.53	19.3	30.6	0.023	0.018	0.02	<0.01	0.3	45.9	**99.5**	5.1	2.79

Table III.2.2 Trace element composition of, Campbellrand dolomite (analyses by MINTEK).

Sample No.	V	Cr	Co	Ni	Cu	Zn	Rb	Sr	Zr	Mo	Sn	Ba	Pb	Th
LOH-309-1	<8	<8	<5	LLD	14	5	<5	11	4	<3	n.d.	<8	<5	<5
LOH-309-2	<5	<5	<1	LLD	<1	<5	<1	26	<5	<1	n.d.	6	<1	<1
BOETSAP	58	<5	<1	LLD	2	6	<1	16	<5	<1	n.d.	32	<1	<1

UNIVERSITY OF JOHANNESBURG

Table III.2.3 Major element composition of bostonite dykes, KMF (analyses by MINTEK).

Sample No.	SiO_2	TiO_2	Al_2O_3	Fe_2O_3	Mn_3O_4	MgO	CaO	Na_2O	K_2O	P_2O_5	SO_3	H_2O^-	LOI	SUM	Mn/Fe	RHO
WES-322	38.8	0.78	13.1	9.22	3.5	5.4	23.8	0.49	0.027	<0.05	<0.01	<0.1	2.1	97.2	0.39	3.26
WES-323	52.6	1	15	10.2	0.43	4.82	6.01	3.1	4.18	0.11	<0.01	0.2	1.6	99.3	0.04	2.78
WES-324	52.4	1.01	15.1	10.4	0.37	4.86	5.24	5.27	1.25	0.12	<0.01	0.3	1.9	98.2	0.04	2.76
WES-325	54.7	0.99	15	10.5	0.16	4.98	5.28	2.3	2.12	0.11	<0.01	0.2	2.0	98.3	0.02	2.77
WES-338-IV	25.4	2.63	15.4	22	3.5	12.7	2.88	3.4	4.08	0.097	0.075	0.1	5.4	97.7	0.16	n.d.
WES-340	37.6	3.11	23.1	9.07	0.44	2.49	1.78	0.55	4.99	0.555	LLD	0.34	6.9	91.0	0.05	2.93
WES-370	32.6	1.46	12.7	10.5	0.79	1.85	35.5	0.038	0.089	<0.05	<0.01	0.4	4.0	99.9	0.08	2.90
WES-371	51.2	1.5	14.7	10.5	0.43	3.54	5.1	4.83	1.75	0.14	<0.01	0.3	4.1	98.1	0.04	2.78
WES-372	51.8	1.3	14.3	12.7	0.17	6.33	3.61	2.83	2.16	0.11	<0.01	0.2	2.9	98.4	0.01	2.71
WES-373	32.8	1.89	19.9	9.63	0.57	3.67	24.6	0.04	0.13	<0.05	<0.01	<0.05	3.4	96.6	0.06	3.19
WES-374-Dyke	31.9	1.31	11.6	17.5	0.77	2.75	29.5	0.034	0.26	<0.05	<0.01	<0.05	2.9	98.5	0.05	3.20
HZ-288	52.6	0.53	12.6	11	0.17	9.02	5.75	1.34	2.63	0.06	<0.01	0.7	2.7	99.1	0.02	2.96

Table III.2.4 Trace element composition of bostonite dykes, KMF (analyses by Mintek).

Sample No.	V	Cr	Co	Ni	Cu	Zn	Rb	Sr	Zr	Mo	Sn	Ba	Pb	Th
WES-322	46	167	33	94	4	111	<5	7854	64	<1	LLD	104	904	7
WES-323	260	126	32	89	8	1064	107	426	119	3	LLD	3473	403	7
WES-324	152	132	32	55	4	22	30	224	52	<1	LLD	1820	28	8
WES-325	174	133	33	63	5	<5	72	228	71	2	LLD	710	13	8
WES-338-IV	110	49	249	79	150	145	109	1908	118	LLD	LLD	9578	1790	LLD
WES-340	137	52	106	100	13	86	111	471	233	1	2	3379	19	8
WES-370	35	131	1	10	2	<5	<5	402	80	<1	LLD	301	181	3
WES-371	151	70	31	51	5	82	82	95	89	<1	LLD	559	10	3
WES-372	289	85	46	89	2	48	58	176	20	<1	LLD	501	5	3
WES-373	61	165	17	67	73	64	<5	1788	123	1	LLD	15000	200	4
WES-374-Dyke	16	75	21	87	4	79	12	1908	80	<1	LLD	501	278	LLD
HZ-288	207	909	37	140	2	36	75	151	3	<1	LLD	1015	8	LLD

UNIVERSITY OF JOHANNESBURG

III.3 Trace element and REE composition (ICP-MS) of manganese ore, KMF.

Table III.3.1 Trace element concentrations in Mn-ores, KMF.

Sample No.	B	Ti	Co	Ni	Cu	Zn	Rb	Sr	Y	Zr	Mo	Sn	Ba	Pb	U	Th
Hz-145	910	80	24	8.2	<2	105	<2	43	11	<2	<2	<2	38	74	<1	<1
Hz-147	150	150	22	5.6	<2	320	<2	161	6.2	<2	<2	<2	140	150	<1	<1
Hz-156	90	97	7.1	1.3	<2	4700	<2	3.7	6.5	<2	<2	<2	2.7	140	1.2	<1
Hz-157	40	50	2.5	3.5	<2	140	<2	3	2.6	7.2	<2	<2	<2	80	<1	1 2
Hz-159	60	70	1.6	13	<2	9.3	<2	12	8.5	8.2	<2	<2	30	6.3	<1	<1
MMT-96	20	13	50	50	<2	1600	4.5	930	13	14	<2	<2	60	23	2.1	1.4
MMT-97	LLD	87	38	23	<2	2100	2.6	790	7.3	3	<2	<2	36	15	<1	1
MMT-105	7.1	320	30	25	<2	160	5.6	920	22	5.8	<2	<2	490	<1	2.1	1.2
MMT-110	1200	350	25	17	<2	60	<2	180	7.6	<2	<2	<2	140	<1	<1	<1
MMT-126	1200	340	20	24	<2	10	<2	130	6.8	6	<2	<2	20	<1	<1	<1
MMT-127	50	460	15	24	<2	6.1	<2	110	2.4	24.1	<2	1.7	47	15	<1	<1
MMT-128	770	390	25	6.5	<2	<1	<2	90	5.1	<2	<2	3.6	23	20	<1	<1
NC-8	230	190	270	17	56	790	<2	5800	3.7	20	2.4	7.1	1900	240	<1	<1
NC-10	467	157	21	130	16	60	<2	205	130	<2	<2	<2	5	46	<1	<1
NC-11	375	235	15	79	5	45	<2	301	<5	<2	<2	<2	22	55	<1	<1
NC-13	380	140	60	21	23	100	<2	290	14	20	<2	<1	1200	30	<1	<1
NC-18	40	300	20	12	3.8	19	<2	13	20	30	<2	<1	20	7.1	2.2	<1
NC-26	110	60	20	12	36	5.8	<2	40	6.9	2.4	<2	2.2	980	16	<1	<1
NC-27	315	115	83	8.7	2.5	7.3	<2	3.4	4.1	5.8	<2	3.5	13500	3	<1	<1

UNIVERSITY OF JOHANNESBURG

Sample No.	B	Ti	Co	Ni	Cu	Zn	Rb	Sr	Y	Zr	Mo	Sn	Ba	Pb	U	Th
NC-28	1800	160	25	17	74	11	<2	10	6.4	11	<2	<1	16000	<1	<1	2.2
NC-29	110	110	5.5	17	<2	<1	<2	100	2.3	8.5	<2	4.4	56	10	<1	1.3
NC-30	100	140	9.1	30	2.4	4.1	<2	190	3.8	9	<2	3.6	100	20	<1	1.8
NC-31	1850	140	23	25	<2	13	<1	16	3.6	45	3.1	3.2	180	36	1.1	<1
NC-32	270	60	20	3.3	<2	210	<1	12	3	11	<2	1.6	210	100	<1	<1
NC-33	85	6.5	20	3.8	<2	50	<1	3.3	2.2	<2	<2	1.5	14	220	<1	<1
WES-312	990	110	33	10	<2	35	<1	19	9.7	<2	<2	1.4	180	73	<1	<1
WES-316	390	120	20	5.5	<2	20	<1	10	5.8	3.1	<2	1.7	16	370	<1	<1
WES-318	<2	170	15	10	<2	160	<1	14	6.2	<2	<2	2.2	150	280	<1	<1
WES-319	495	220	25	13	<2	43	<1	160	8.4	<2	<2	1.6	35	135	<1	1.4
WES-320	870	120	18	7	<2	25	<1	16	6.1	<2	<2	1.4	38	120	<1	<1
WES-321	450	140	22	13	<2	160	<1	16	6.4	<2	6.7	1.3	11	290	<1	<1
WES-N101	460	270	12	30	<2	340	<1	150	6.8	<2	2	2.5	86	55	<1	1.2
WES-N102	935	210	20	31	<2	29	<1	18	8.8	4.8	2.5	1.4	1.8	29	<1	<1
WES-N107	2800	200	31	23	<2	10	<1	26	12	<2	<2	1.3	33	23	<1	<1
WES-N116	170	180	14	<2	<2	29	<1	6.4	12	<2	<2	5	4.3	60	<1	<1
M2-44	360	560	23	13	<2	<2	1.1	210	6.5	2.1	<2	1.9	53	<1	<1	<1
M2-45	530	350	30	264	<2	18	1.4	94	5.2	12	<2	1.7	77	13	<1	<1
M2-47B	610	460	24	25	<2	110	1.3	110	5.1	20	<2	2.6	250	170	<1	<1
M2-49B	865	265	27	15	<2	14	1.2	83	4.2	<2	<2	<2	185	<2	<1	<1
M2-49C	540	630	23	44	<2	160	1.7	170	10	90	<2	1.9	45	190	<1	2

UNIVERSITY OF JOHANNESBURG

Table III.3.2 REE concentrations (ICP-MS) in Mn-ores, KMF.

Sample No.	La	Ce	Pr	Nd	Sm	Eu	Gd	Tb	Dy	Ho	Er	Tm	Yb	Lu
Hz-145	9.8	4.2	2.2	7.3	1.4	<1	1.8	<1	1.3	<1	<1	<1	<1	<1
Hz-147	8.5	1.8	1.3	5.6	<1	<1	1.1	<1	1.3	<1	<1	<1	<1	<1
Hz-156	3	5.2	<1	4.2	1	<1	1.3	<1	1.2	<1	<1	<1	1.1	<1
Hz-157	2.5	4.8	<1	3.1	<1	<1	<1	<1	<1	<1	<1	<1	<1	<1
Hz-159	8.2	23	2.2	13	2.4	<1	3.3	<1	2.5	<1	1.1	<1	<1	<1
MMT-96	11	16	2.3	11	2.2	<1	2	<1	1.8	<1	1.3	<1	1.6	<1
MMT-97	2.2	4	<1	3.9	<1	<1	<1	<1	<1	<1	<1	<1	<1	<1
MMT-105	9.6	5.9	2.1	9.8	2.5	<1	3	<1	2.8	<1	2.2	<1	1.8	<1
MMT-110	8.1	4.4	1.2	5	<1	<1	1.5	<1	1.3	<1	<1	<1	1.1	<1
MMT-126	7	3.3	<1	4.7	<1	<1	1.1	<1	1.1	<1	<1	<1	<1	<1
MMT-127	14	5.5	1.4	5.5	<1	<1	<1	<1	<1	<1	<1	<1	<1	<1
MMT-128	70	20	<1	2.8	<1	<1	<1	<1	<1	<1	<1	<1	<1	<1
NC-8	560	4.6	<1	2.7	<1	1.2	<1	<1	<1	<1	<1	<1	<1	<1
NC-10	4	4	<1	2	1	<1	1	<1	1	<1	<1	<1	<1	<1
NC-11	4	7	<1	1	2	<1	<1	<1	2	<1	<1	<1	<1	<1
NC-13	1500	8.1	18	9.2	1	1.1	1.6	<1	2.3	<1	1.6	<1	1.4	<1
NC-18	290	30	2.4	20	5.2	1.3	4.3	<1	3.9	<1	1.8	<1	1.8	<1
NC-26	3	3.3	1.2	5.9	1.3	1.2	<1	<1	1.2	<1	<1	<1	<1	<1
NC-27	19	5.4	2.8	16.5	1.7	<1	1.3	<1	1.2	<1	<1	<1	<1	<1
NC-28	8	6	1.4	6.1	1.4	<1	<1	<1	1.2	<1	<1	<1	<1	<1
NC-29	3.5	5	1.3	6	1.1	<1	<1	<1	1	<1	<1	<1	<1	<1

UNIVERSITY OF JOHANNESBURG

Sample No.	La	Ce	Pr	Nd	Sm	Eu	Gd	Tb	Dy	Ho	Er	Tm	Yb	Lu
NC-30	5.7	5	1.4	7.6	1.3	<1	1.3	<1	1.1	<1	<1	<1	<1	<1
NC-31	3.3	5.3	1.2	5.4	<1	<1	<1	<1	1	<1	<1	<1	<1	<1
NC-32	2.5	3.4	<1	2.5	<1	<1	<1	<1	<1	<1	<1	<1	<1	<1
NC-33	1.1	<1	<1	<1	<1	<1	<1	<1	<1	<1	<1	<1	<1	<1
WES-312	1.1	4.2	2.7	10	1.2	<1	2.9	<1	1.3	<1	<1	<1	<1	<1
WES-316	29	2.5	<1	4.4	<1	<1	<1	<1	1	<1	1.1	<1	<1	<1
WES-318	1.4	2.5	<1	2.3	<1	<1	1.1	<1	<1	<1	<1	<1	<1	<1
WES-319	5.9	3.9	1	4.5	<1	<1	1.6	<1	1.7	<1	1.2	<1	<1	<1
WES-320	2.8	2.9	<1	4.2	<1	<1	1.2	<1	1.1	<1	1	<1	<1	<1
WES-321	4	3.2	<1	3.9	1.1	<1	<1	<1	1.1	<1	<1	<1	<1	<1
WES-N101	6.2	27	1.4	9	1.9	<1	2.3	<1	1.7	<1	1.1	<1	<1	<1
WES-N102	8.6	18	2.3	15	2.9	1.3	3.9	<1	1.6	<1	<1	<1	1.3	<1
WES-N107	1.8	4.7	1.1	5.9	<1	<1	1.4	<1	1.7	<1	1.3	<1	1.2	<1
WES-N116	12	2.3	1.6	11	1.2	<1	2	<1	1.3	<1	<1	<1	<1	<1
M2-44	13	4.3	1.2	5.5	<1	<1	<1	<1	<1	<1	<1	<1	<1	<1
M2-45	3.2	3.1	1	4.1	<1	<1	<1	<1	<1	<1	<1	<1	<1	<1
M2-47B	3.9	4	<1	4.6	<1	<1	1.2	<1	<1	<1	<1	<1	1.2	<1
M2-49B	2.6	2.6	<1	3.4	<1	<1	<1	<1	<1	<1	<1	<1	<1	<1
M2-49C	6.8	6.9	1.4	6.8	1.2	<1	1.4	<1	1.5	<1	1.2	<1	1.1	<1

UNIVERSITY OF JOHANNESBURG

Appendix IV

Phase chemistry data

Mineral compositions obtained by EMPA analyses are listed in this Appendix. Section IV.1 contains compositions of the lower oxides of manganese, section IV.2 contains data of the Mn^{4+}-oxides, in section IV.3 compositions of silicates directly associated with the hydrothermal alteration of manganese ores (and Olifantshoek Shales) are recorded, section VI.4 lists carbonate compositions in the KMF, section IV.5 contains compositional data for sulphates and other mineral groups associated with the manganese ores. Section IV.6 is devoted to mineral phases related to intrusive bostonite dykes and their alteration products.

UNIVERSITY OF JOHANNESBURG

Abbreviations used in this chapter:

N number of spot analyses used to calculate mean composition.

S. No. sample number.

LLD concentration below the detection limit.

VI.1 Lower oxides of manganese

Table VI.1.1 Composition of hausmannite from the KMF and the PMF.

Mine	S. No.	N	SiO_2	TiO_2	Al_2O_3	Fe_2O_3	Mn_2O_3	MnO	MgO	CaO	BaO	Na_2O	K_2O	TOTAL	Remark
KMF															
MMT	107	3	0.10	0.03	0.20	1.47	64.6	33.5	LLD	LLD	0.03	0.10	LLD	100.1	hydrothermal
HZ	141	5	0.18	0.08	0.13	1.66	64.2	33.6	0.05	LLD	0.05	0.15	LLD	100.1	hydrothermal
HZ	148	3	0.30	LLD	0.03	0.48	65.3	33.7	0.03	0.10	0.07	0.10	LLD	100.1	hydrothermal
HZ	153	1	0.1	0.1	LLD	1.09	67.2	29.9	0.72	0.4	LLD	0.4	0.2	100.1	hydrothermal
HZ	154	5	0.49	LLD	0.05	4.85	60.3	34.2	0.07	0.05	0.10	0.08	0.05	100.3	hydrothermal
HZ	156	3	0.20	0.07	0.10	2.58	64.1	32.3	0.17	LLD	LLD	0.66	LLD	100.2	hydrothermal
HZ	157	3	0.17	0.03	0.13	0.56	65.5	33.4	LLD	0.07	0.03	0.20	LLD	100.0	hydrothermal
HZ	160	5	0.14	0.04	0.10	1.50	65.2	32.4	0.14	0.02	0.06	0.51	0.02	100.1	hydrothermal
HZ	161	3	0.20	LLD	0.10	1.66	64.8	32.9	0.13	0.07	0.03	0.23	0.03	100.1	hydrothermal
HZ	304	3	0.30	0.08	0.17	LLD	65.8	33.0	0.10	0.07	0.03	0.48	LLD	100.0	hydrothermal
NC2	4.1	5	0.2	0.1	0.1	2.75	59.4	36.2	0.25	1.21	LLD	LLD	LLD	100.2	hydrothermal
NC2	4.2	5	0.5	LLD	LLD	3.41	62.5	33.6	0.23	LLD	LLD	LLD	LLD	100.2	hydrothermal
NC2	5	2	LLD	LLD	0.05	3.33	63.5	32.3	0.52	LLD	0.53	LLD	LLD	100.1	hydrothermal
NC2	8	1	LLD	LLD	LLD	6.61	60.3	33.1	0.16	LLD	LLD	LLD	LLD	100.2	hydrothermal
NC2	10	1	LLD	LLD	LLD	2.49	62.5	31.5	2.67	1.04	0.1	LLD	LLD	100.3	diagenetic
NC2	15	3	0.39	LLD	0.08	2.39	64.3	31.1	1.56	0.21	0.10	LLD	LLD	100.1	hydrothermal
NC2	22	1	LLD	0.1	0.11	7.68	60.6	29	2.75	LLD	LLD	LLD	LLD	100.2	hydrothermal
NC2	23	3	0.10	LLD	LLD	2.25	65.1	30.5	1.04	1.04	0.03	LLD	LLD	100.0	hydrothermal
NC2	27	1	LLD	LLD	0.1	3.6	64.2	30.6	1.36	LLD	0.1	LLD	LLD	100.0	hydrothermal
NC2	31	1	0.75	LLD	LLD	0.36	64.6	33.9	0.27	LLD	LLD	LLD	LLD	99.9	hydrothermal, vug
NC2	33	2	LLD	LLD	0.62	0.60	65.2	33.1	0.36	0.10	0.10	LLD	LLD	100.1	hydrothermal, vug
NC2	286	2	0.17	0.03	0.75	LLD	65.3	33.5	0.03	0.10	LLD	0.10	LLD	100.0	hydrothermal
WES	HMN-7	6	0.17	0.03	0.22	5.74	61.2	32.3	0.47	0.02	0.08	0.10	0.02	100.3	hydrothermal, magnetic
WES	HMN-9	2	0.15	0.05	0.05	5.09	62.2	32.1	0.57	LLD	0.05	0.10	LLD	100.3	hydrothermal, magnetic

UNIVERSITY OF JOHANNESBURG

Mine	S. No.	Mineral	N	SiO_2	TiO_2	Al_2O_3	Fe_2O_3	Mn_2O_3	MnO	MgO	CaO	BaO	Na_2O	K_2O	TOTAL	Remark
WES	365	braunite II	3	5.27	0.07	0.03	11.9	77.6		0.03	5.01	0.07	0.10	0.03	100.2	hydrothermal
NC2	6	braunite (new)	1	2.49	LLD	0.2	19.1	74.6		0.26	2.57	0.33	LLD	LLD	99.6	hydrothermal
NC2	8	braunite (new)	1	2.5	LLD	0.2	15	77.3		0.2	3.39	0.2	LLD	LLD	98.8	hydrothermal
NC2	20	braunite (new)	1	1.72	LLD	0.1	12.4	78.8		0.22	3.96	0.1	LLD	LLD	97.3	hydrothermal
WES	HMN-7	braunite (new)	5	1.06	0.07	0.08	14.3	83.7		0.08	0.89	0.02	0.07	LLD	100.2	hydrothermal
WES	HMN-9	braunite (new)	2	1.62	0.05	0.47	18.0	78.2		0.05	1.56	0.05	0.05	LLD	100.0	hydrothermal
MMT	107	partridgeite	8	0.14	0.01	0.16	1.52	97.8		0.05	0.06	0.03	0.09	LLD	99.8	diagenetic
MMT	109	partridgeite	8	0.19	0.03	0.31	1.53	97.8		0.08	0.16	0.04	0.10	0.01	100.2	diagenetic
NC2	286	partridgeite	1	0.2	LLD	0.2	0.27	98.1		0.3	0.4	LLD	0.1	LLD	99.6	diagenetic
NC2	12	bixbyite	1	1.64	LLD	0.1	20.7	75.3		0.2	1.63	LLD	LLD	LLD	99.6	hydrothermal
NC2	13	bixbyite	2	0.05	LLD	0.4	21.5	75.7		0.36	0.12	0.10	LLD	0.05	98.2	hydrothermal
WES	330	bixbyite	2	0.40	0.05	LLD	10.1	89.2		0.25	0.05	0.05	0.15	0.05	100.2	hydrothermal
WES	HMN-7	bixbyite	5	0.22	0.11	0.24	6.58	92.6		0.30	0.09	0.05	0.08	LLD	100.2	hydrothermal
WES	HMN-9	bixbyite	7	0.15	0.05	0.32	17.8	81.6		0.17	0.03	0.04	0.16	0.03	100.3	hydrothermal
PMF																
AUC	198.2	braunite	4	10.3	0.05	0.35	0.34	78.6	8.58	0.08	1.52	0.24	0.03	0.05	100.1	Br-Ptr-ore
AUC	198.3	braunite	5	10.4	0.06	0.24	0.04	79.4	8.00	0.12	1.60	0.16	0.18	0.04	100.2	Br-Ptr-ore
AUC	201.1	braunite	8	10.3	0.1	1.5	5.1	72.8	8.9	0.1	1.3	0.2	0.1	0.1	100.4	Br-ore
AUC	201.2	braunite	5	9.9	0.0	1.5	3.3	78.0	4.2	0.2	2.5	0.3	0.1	0.3	100.3	Br-ore
AUC	204.1	braunite	5	10.6	0.06	0.4	0.31	77.8	9.06	0.06	1.61	0.04	0.06	0.04	100.0	Br-ore
AUC	204.2	braunite	5	10.4	LLD	0.46	0.4	78.2	8.97	0.1	1.39	0.10	0.08	0.00	100.1	Br-ore
AUC	204.3	braunite	5	10.4	0.04	0.55	0.24	78.0	9.15	0.04	1.50	0.00	0.08	0.00	100.1	Br-ore
AUC	205	braunite	5	11.1	0.04	0.91	1.17	75.7	9.47	0.06	1.66	0.02	0.04	0.02	100.2	Br-ore
BEE	208	braunite	20	10.8	LLD	1.1	0.1	76.7	10.0	0.1	1.2	0.2	0.1	LLD	100.3	Br-ore
BEE	213	braunite	5	10.5	0.1	0.5	5.0	72.4	11.1	LLD	0.7	0.1	0.1	LLD	100.4	Br-ore
BEE	214	braunite	10	10.3	0.04	1.27	2.51	75.4	9.07	0.07	1.24	0.12	0.17	0.06	100.2	Br-Ptr-ore
DO	161	braunite	5	11.2	0.00	3.73	2.06	72.9	7.58	0.14	1.79	0.29	0.1	0.51	100.2	Br-Ptr-ore
DO	169	braunite	3	10.8	0.0	0.8	1.8	75.7	9.8	0.1	1.2	0.1	0.1	LLD	100.4	Br-ore
DO	171	braunite	5	11.5	0.06	0.63	0.22	77.8	7.22	0.20	2.36	0.04	0.14	0.06	100.3	Br-ore
GLO	185.1	braunite	8	10.6	0.01	1.27	0.06	78.4	7.98	0.06	1.85	0.06	0.09	0.03	100.4	Br-BrII-Ptr-ore

UNIVERSITY OF JOHANNESBURG

Mine	S. No.	Mineral	N	SiO_2	TiO_2	Al_2O_3	Fe_2O_3	Mn_2O_3	MnO	MgO	CaO	BaO	Na_2O	K_2O	TOTAL	Remark
GLO	185.2	braunite	10	10.7	0.03	1.67	1.67	78.3	4.56	0.11	3.08	0.07	0.1	0.04	100.3	Br-BrII-Ptr-ore
GLO	185.3	braunite	5	10.4	0.06	1.30	2.21	78.7	4.41	0.12	2.95	0.13	0.12	0.04	100.5	Br-BrII-Ptr-ore
GLO	187	braunite	3	9.78	0.98	1.06	4.19	71.4	10.8	0.2	0.54	0.27	0.17	0.59	100.0	Br-Ptr-ore
GLO	Ll-01	braunite	3	8.90	0.2	0.6	2.43	80.0	4.69	0.2	1.72	0.74	0.1	0.45	100.0	lithiophorite
KAP	228.1	braunite	5	10.8	0.06	1.05	3.37	73.5	10.1	0.1	1.20	0.04	0.08	0.04	100.3	Br-ore
KAP	228.2	braunite	5	11.1	0.02	1.14	4.11	72.7	9.27	0.08	1.62	0.08	0.12	0.02	100.3	Br-ore
KAP	229	braunite	5	10.9	0.1	1.06	0.7	75.8	9.77	0.02	1.47	0.14	0.12	0.02	100.1	Br-ore
KAP	230	braunite	7	10.6	LLD	1.41	0.16	76.9	9.38	0.13	1.3	0.13	0.06	0.06	100.1	Br-ore
LOH	176	braunite	5	9.1	1.05	1.28	2.87	73.0	12.4	0.08	0.3	0.04	0.08	0.04	100.2	Br-Ptr-ore
LOH	178	braunite	5	9.11	0.1	1.74	5.93	72.7	9.47	0.06	0.3	0.12	0.34	0.32	100.2	Br-Ptr-ore
LOH	179	braunite	10	10.0	0.09	0.58	0.42	76.7	11.8	0.15	0.15	0.05	0.15	0.03	100.1	Br-Ptr-ore
MAN	238	braunite	6	10.7	0.02	0.51	4.58	72.7	10.5	0.08	0.96	0.05	0.15	LLD	100.2	Br-ore
PAL	216.1	braunite	5	9.81	0.41	1.14	5.42	70.6	12.6	0.06	0.09	0.08	0.08	0.04	100.3	Br-Ptr-ore
PAL	216.2	braunite	5	9.18	0.47	1.08	4.20	73.8	10.7	0.13	0.5	LLD	0.10	LLD	100.2	Br-Ptr-ore
PAL	219	braunite	3	9.52	0.08	1.64	4.32	76.1	6.14	0.14	1.89	0.16	0.12	0.08	100.2	Br-Ptr-ore
GLO	185.1	braunite II	10	4.19	0.04	3.99	LLD	92.2		0.1	1.21	0.06	0.13	0.02	102.0	Br-BrII-Ptr-ore
GLO	185.3	braunite II	10	4.07	0.05	3.03	3.54	89.8		0.08	1.16	0.07	0.1	0.01	101.9	Br-BrII-Ptr-ore
GLO	185.4	braunite II	10	3.36	0.08	2.71	2.61	90.7		0.03	1.18	0.04	0.08	0.02	100.8	Br-BrII-Ptr-ore
AUC	198	partridgeite	1	0.3	LLD	0.54	LLD	99.0		LLD	0.1	0.5	0.1	LLD	100.5	Br-Ptr-ore
BEE	214.1	partridgeite	5	0.95	LLD	0.54	0.40	98.0		0.06	0.12	0.04	0.08	0.02	100.2	Br-Ptr-ore
BEE	214.2	partridgeite	5	0.5	0.04	0.99	0.04	98.5		0.04	0.1	0.1	0.06	0.02	100.4	Br-Ptr-ore
DO	161	partridgeite	3	0.57	0.05	0.45	0.24	98.7		0.08	0.13	0.05	0.15	LLD	100.4	Br-Ptr-ore
GLO	185.2	partridgeite	10	0.22	0.04	1.42	LLD	98.4		0.1	0.02	0.04	0.08	0.02	100.4	Br-BrII-Ptr-ore
GLO	185.3	partridgeite	5	0.28	0.02	0.61	0.67	98.6		0.08	0.06	0.04	0.04	0.08	100.5	Br-BrII-Ptr-ore
GLO	187	partridgeite	3	0.23	0.03	1.81	0.20	98.1		0.03	LLD	LLD	0.03	LLD	100.5	Br-Ptr-ore
GLO	193	partridgeite	3	0.69	0.13	1.12	0.54	97.5		0.03	0.2	0.03	0.03	LLD	100.3	Br-Ptr-ore
LOH	179	partridgeite	10	0.78	0.09	1.55	1.15	95.3		0.03	0.91	0.1	0.12	0.02	100.0	Br-Ptr-ore
LOH	79.1	partridgeite	5	0.32	0.12	2.25	4.59	92.7		0.18	0.1	LLD	0.12	0.02	100.4	Ptr-He-ore
LOH	79.2	partridgeite	5	0.20	0.14	2.21	1.59	95.7		0.12	0.1	LLD	0.06	LLD	100.2	Ptr-He-ore
LOH	178.1	partridgeite	5	0.46	0.06	2.38	3.25	93.5		0.12	0.04	0.1	0.16	0.04	100.1	Br-Ptr-ore

UNIVERSITY OF JOHANNESBURG

Mine	S. No.	Mineral	N	SiO_2	TiO_2	Al_2O_3	Fe_2O_3	Mn_2O_3	MnO	MgO	CaO	BaO	Na_2O	K_2O	TOTAL	Remark
LOH	178.2	partridgeite	3	0.20	LLD	2.80	2.15	95.3		0.13	LLD	0.03	0.07	LLD	100.7	Br-Ptr-ore
PAL	219.3	partridgeite	5	1.30	0.04	1.62	1.08	95.4		0.12	0.39	0.08	0.12	LLD	100.2	Br-Ptr-ore
PAL	219.4	partridgeite	2	0.65	0.05	1.25	1.90	96.7		0.2	0.1	0.1	LLD	LLD	100.9	Br-Ptr-ore
BIS	241	bixbyite	10	0.14	0.45	2.89	13.9	82.6		0.09	0.02	0.03	0.08	0.01	100.2	Bx-ore
BIS	243	bixbyite	3	0.13	0.37	1.88	20.5	76.4		0.07	0.07	0.07	0.07	LLD	99.5	Bx-ore
BIS	247	bixbyite	3	0.07	0.07	2.30	20.0	76.9		0.10	0.03	0.1	0.23	LLD	99.9	Bx-ore
BIS	289.3	bixbyite	10	0.20	0.06	2.18	14.5	83.0		0.04	0.02	0.1	0.12	0.02	100.3	Bx-ore
GLO	Mn10-63	bixbyite	5	1.39	0.41	1.41	16.6	79.0		LLD	0.65	0.09	0.06	LLD	99.7	Bx-ore
PAL	219	bixbyite	5	1.48	0.16	1.97	12.4	84.0		0.14	0.43	0.02	0.1	0.02	100.7	Bx-ore
PAL	224	bixbyite	5	0.32	0.68	1.77	19.5	78.0		0.12	0.06	0.04	0.08	0.02	100.6	Bx-ore
PAL	228.1	bixbyite	9	0.48	0.55	1.58	18.6	78.6		0.07	0.1	0.06	0.11	0.01	100.1	Bx-ore
PAL	228.2	bixbyite	4	0.45	0.58	1.80	18.8	78.4		0.03	0.03	0.03	0.18	0.03	100.3	Bx-ore

UNIVERSITY OF JOHANNESBURG

Table IV.1.3 Composition of jakobsite, manganite and marokite from the KMF.

Mine	S. No.	Mineral	N.	SiO_2	TiO_2	Al_2O_3	Fe_2O_3	Mn_2O_3	MnO	MgO	CaO	BaO	Na_2O	K_2O	TOTAL	Remark
HZ	133	jakobsite	3	0.27	0.03	LLD	67.0		31.5	0.91	0.07	0.07	0.23	0.07	100.1	hydrothermal, gel-type
HZ	152	jakobsite	3	0.17	LLD	LLD	71.7		28.4	0.55	0.40	0.07	0.33	LLD	101.6	hydrothermal, breccia
HZ	154.1	jakobsite	3	0.23	0.10	0.07	55.4		44.8	0.20	0.10	0.03	0.13	0.03	101.1	hydrothermal
HZ	154.2	jakobsite	3	0.41	0.10	0.45	55.5		42.9	0.99	LLD	0.05	0.20	LLD	100.6	hydrothermal
HZ	156	jakobsite	3	0.89	0.10	LLD	56.6		41.3	0.20	0.03	0.03	0.30	LLD	99.5	hydrothermal, vein
MMT	92	jakobsite	5	0.46	0.10	LLD	57.9		41.2	0.24	0.08	0.06	0.20	0.04	100.2	hydrothermal, vein
MMT	99.1	jakobsite	5	0.95	0.02	0.06	65.2		32.7	0.47	0.44	0.06	0.30	LLD	100.2	hydrothermal, vein
MMT	99.2	jakobsite	3	1.44	0.07	0.13	65.2		32.4	0.84	LLD	LLD	0.23	LLD	100.3	hydrothermal, vein
NC2	23	jakobsite	5	0.28	LLD	LLD	58.4		38.7	0.60	0.36	LLD	LLD	LLD	98.3	hydrothermal
WES	351	jakobsite	3	LLD	0.07	0.60	62.3		35.7	0.63	LLD	LLD	0.41	LLD	99.7	dyke contact
WES	LVB37	jakobsite	5	1.11	0.06	LLD	54.42		42.9	0.57	0.12	0.04	0.20	0.02	99.4	hydrothermal, vug
HZ	156	manganite	2	0.25	0.05	0.05	0.46	85.7		LLD	LLD	0.05	0.10	LLD	86.7	hydrothermal
NC2	6	manganite	1	LLD	LLD	LLD	0.10	88.8		0.10	0.20	LLD	LLD	LLD	89.2	hydrothermal
NC2	8	manganite	2	LLD	LLD	LLD	0.26	89.1		0.10	0.05	LLD	LLD	LLD	89.5	hydrothermal
NC2	10	manganite	2	0.35	0.05	LLD	0.32	88.9		0.05	0.28	LLD	LLD	LLD	89.9	hydrothermal
NC2	12	manganite	3	0.03	LLD	LLD	0.57	87.8		0.16	0.90	LLD	LLD	LLD	89.5	hydrothermal
NC2	13	manganite	1	0.10	LLD	LLD	2.88	83.1		0.63	0.31	LLD	LLD	LLD	87.0	hydrothermal
NC2	286	manganite	3	0.27	LLD	0.20	LLD	87.3		0.10	0.10	0.03	0.16	LLD	88.1	hydrothermal, vein
NC2	6	marokite	3	LLD	LLD	0.03	0.41	74.1		LLD	25.6	0.03	LLD	LLD	100.1	hydrothermal
WES	N510	marokite	10	0.24	LLD	LLD	3.52	72.1		LLD	24.5	LLD	LLD	LLD	100.4	hydrothermal

UNIVERSITY OF JOHANNESBURG

N	ne	S. No.	N	SiO_2	TiO_2	Al_2O_3	Fe_2O_3	Mn_2O_3	MnO	MgO	CaO	BaO	Na_2O	K_2O	TOTAL	Remark
V	ES	HWS-8.1	10	0.11	0.04	LLD	6.27	62.0	30.9	0.95	0.01	0.03	0.07	0.01	100.3	hydrothermal, magnetic
V	ES	320	3	0.30	LLD	0.03	0.29	65.2	34.2	LLD	LLD	0.03	0.03	LLD	100.0	hydrothermal, vein
V	ES	362	5	0.18	0.03	0.03	11.2	56.3	31.7	0.59	0.10	0.08	0.12	LLD	100.3	hydrothermal, magnetic
V	ES	366	20	0.20	0.03	LLD	8.47	58.5	32.5	0.27	0.24	0.05	0.08	0.01	100.4	hydrothermal, magnetic
P	MF															
P	L	219	9	0.25	0.07	1.51	1.07	63.3	33.4	0.25	0.07	0.07	0.06	0.03	100.1	Ptr-Br-ore

T ble VI.1.2 Composition of braunite-bixbyite group minerals from the KMF and the PMF.

N	ne	S. No.	Mineral	N	SiO_2	TiO_2	Al_2O_3	Fe_2O_3	Mn_2O_3	MnO	MgO	CaO	BaO	Na_2O	K_2O	TOTAL	Remark
K	MF																
H		146	braunite	5	9.81	0.02	0.18	4.81	74.3	10.1	0.08	0.70	0.02	0.12	0.04	100.2	diagenetic
H		148	braunite	3	9.80	0.03	0.13	4.60	74.2	10.6	0.13	0.57	0.03	0.07	LLD	100.1	diagenetic
N	MT	93	braunite	5	10.2	0.02	0.12	4.62	72.9	11.6	0.17	0.20	0.06	0.19	LLD	100.1	diagenetic
N	MT	125	braunite	4	10.3	0.03	0.03	6.48	72.9	8.77	0.33	1.13	0.03	0.10	0.05	100.1	diagenetic
N	MT	127.3	braunite	5	9.71	0.02	0.61	4.00	76.5	7.72	0.45	1.08	0.06	0.06	LLD	100.2	diagenetic
N	'2	10	braunite	2	9.76	0.02	0.46	4.00	77.0	6.94	0.30	1.61	0.02	0.06	LLD	100.1	diagenetic
N	'2	15	braunite	2	9.18	0.05	0.15	5.60	81.7	2.60	0.63	3.93	0.20	LLD	LLD	100.1	hydrothermal
N	'2	286	braunite	3	9.84	0.05	0.15	6.00	79.1	4.81	0.68	3.27	0.20	0.10	LLD	100.2	diagenetic
V	ES	N505	braunite	3	11.1	0.03	LLD	1.99	76.5	8.27	0.07	2.05	0.10	0.07	0.03	100.2	skarn
V	ES	364	braunite-Ca	10	12.0	0.08	0.02	4.7	70.5	7.40	0.14	5.21	0.20	0.11	0.02	100.3	hydrothermal
N	'2	5	braunite II	2	4.44	0.05	LLD	10.6	79.8		0.30	4.13	0.75	LLD	LLD	100.1	hydrothermal
N	'2	8	braunite II	2	5.09	LLD	0.15	12.4	77.7		0.15	4.77	LLD	LLD	LLD	100.2	hydrothermal
N	'2	9	braunite II	1	5.14	LLD	0.1	14.2	76.5		0.1	5.24	0.1	LLD	LLD	101.4	hydrothermal
N	'2	27	braunite II	1	4.9	LLD	0.1	15.2	73.9		LLD	4.52	0.21	LLD	LLD	98.8	hydrothermal
V	ES	330	braunite II	1	6.8	LLD	0.2	10.3	77.6		0.2	6.08	LLD	LLD	LLD	101.2	hydrothermal
V	ES	359	braunite II	3	5.36	LLD	0.03	10.4	79.3		0.13	5.02	0.07	0.13	0.03	100.5	hydrothermal, vug

JOHANNESBURG UNIVERSITY OF

IV.2 Higher manganese oxides

Table IV.3.1 Composition of Mn^{4+}-oxides (KMF and PMF).

Mine	S. No.	Mineral	N	SiO_2	TiO_2	Al_2O_3	Fe_2O_3	MnO_2	MgO	CaO	BaO	Na_2O	K_2O	TOTAL	Remark
KMF															
HZ	130	manganomelane	5	0.77	LLD	0.28	2.27	85.4	1.16	1.45	0.06	0.99	2.95	95.4	supergene
HZ	133	manganomelane	3	0.40	LLD	LLD	1.58	85.8	0.40	1.04	0.07	0.64	3.72	93.6	supergene
HZ	152	manganomelane	5	0.49	LLD	0.39	3.46	84.4	0.52	1.19	0.06	1.36	0.95	92.8	supergene
HZ	153	manganomelane	5	0.59	0.10	0.38	2.01	85.9	1.12	1.38	LLD	0.97	1.94	94.4	supergene
MMT	90.1	manganomelane	5	0.26	0.08	0.08	1.10	84.7	0.73	0.96	0.18	0.48	5.10	93.6	supergene
MMT	90.2	manganomelane	3	0.23	0.03	0.13	0.37	82.5	1.16	1.37	0.43	0.56	3.19	89.9	supergene
MMT	98	manganomelane	10	0.51	0.05	0.19	1.78	87.2	0.84	1.60	0.05	0.85	0.36	93.4	hydrothermal breccia clasts
MMT	104	manganomelane	5	0.45	0.02	0.10	1.55	88.9	0.52	1.11	LLD	0.45	0.34	93.4	supergene
MMT	108	manganomelane	5	0.32	0.02	0.14	0.63	84.1	1.27	2.04	2.22	1.09	0.32	92.2	supergene
MMT	118	manganomelane	5	1.18	LLD	0.21	1.09	87.9	0.76	1.45	0.13	0.76	0.70	94.2	dendrite, supergene
MMT	119.1	manganomelane	7	0.55	0.06	0.09	4.50	84.0	1.50	1.38	0.04	0.93	0.82	93.8	dendrite, supergene
MMT	119.2	manganomelane	5	0.66	LLD	0.15	4.56	85.7	0.84	1.31	0.10	0.73	0.45	94.5	supergene
HZ	152	ramsdellite	5	0.96	LLD	0.02	0.78	92.6	0.12	0.30	0.06	0.22	0.22	95.3	ore
WES	350.1	romanechite	5	0.14	LLD	0.06	1.51	73.7	0.06	0.42	20.2	0.40	LLD	96.6	supergene
WES	350.2	romanechite	3	0.13	LLD	0.07	1.50	69.3	0.10	0.30	24.2	0.47	0.03	96.1	supergene
HZ	140	todorokite	6	1.57	0.05	0.73	1.11	84.7	3.40	1.05	0.03	2.25	0.55	95.4	supergene
MMT	87	todorokite	5	0.46	LLD	0.16	1.13	80.2	2.33	2.95	0.04	1.17	0.84	89.2	supergene
MMT	92	todorokite	6	0.63	LLD	0.07	1.28	83.1	1.17	1.92	1.83	0.79	0.30	91.1	vein
MMT	105	todorokite	5	0.30	0.02	0.42	1.12	81.3	2.89	2.25	0.06	1.34	0.34	90.0	supergene
NC2	23	todorokite	1	0.10	LLD	0.10	2.06	77.5	9.20	0.46	LLD	0.10	LLD	89.6	supergene
NC2	286	todorokite	1	0.20	0.10	0.10	0.18	82.9	2.30	2.28	LLD	1.65	0.10	89.8	supergene
SMA	todo1.1	todorokite	10	0.19	0.05	LLD	1.26	80.4	3.15	0.91	0.33	1.67	0.57	88.6	vein

Mine	S. No.	Mineral	N	SiO_2	TiO_2	Al_2O_3	Fe_2O_3	MnO_2	MgO	CaO	BaO	Na_2O	K_2O	TOTAL	Remark
SMA	todo1.2	todorokite	8	0.24	0.01	LLD	1.32	78.7	2.42	1.69	0.90	1.02	0.94	87.2	matrix
HZ	154	(?) unknown	5	4.36	LLD	2.64	0.62	87.4	0.32	0.10	0.06	0.08	0.02	95.6	supergene
PMF															
BIS	247	cryptomelane	3	0.83	LLD	3.74	6.16	76.8	0.30	0.23	0.76	0.27	5.34	94.5	supergene
DO	171	cryptomelane	6	0.52	0.12	1.33	LLD	87.8	0.27	0.17	0.43	0.45	5.42	96.5	supergene
LOH	79	cryptomelane	5	0.88	0.02	3.50	0.93	82.8	0.72	0.06	1.99	0.18	4.92	96.0	supergene
PAL	216	goethite	3	0.10	0.40	0.10	87.1	2.5	0.03	0.03	0.10	0.17	0.03	90.5	veinlet, supergene
GLO	Ll-01	lithiophorite	5	LLD	0.41	26.8	0.63	58.4	1.61	0.02	0.10	0.10	0.02	88.2	vug (Li_2O 3.31 %)
LOH	79	lithiophorite	3	0.07	0.20	25.9	2.16	56.1	2.48	0.20	0.07	LLD	0.10	87.3	layer
AUC	198	manganomelane	5	0.40	0.06	1.21	0.89	86.5	0.12	0.20	3.67	1.12	3.06	97.2	supergene
BIS	243	manganomelane	5	0.72	0.13	3.15	10.8	69.3	0.68	0.39	4.15	0.48	1.97	91.7	supergene
GLO	185	manganomelane	3	1.12	0.07	2.01	LLD	89.1	0.03	0.84	0.07	1.58	0.23	95.0	supergene
GLO	187	manganomelane	3	1.25	1.24	1.81	21.0	63.1	0.40	0.10	4.62	0.37	2.52	96.4	supergene
MAN	238	manganomelane	5	0.80	0.04	0.98	2.90	85.5	0.12	0.14	0.91	1.61	1.55	94.6	supergene
AUC	198	nsutite	2	0.35	0.10	0.67	0.83	92.8	0.10	0.50	0.35	0.20	0.30	96.2	supergene
KAP	229	nsutite	5	0.78	0.06	0.85	LLD	95.9	0.02	0.02	0.08	0.12	LLD	97.9	supergene
AUC	199.2	pyrolusite	5	0.63	0.02	0.87	LLD	96.0	0.06	0.08	0.10	0.26	0.12	98.1	supergene
BIS	243	pyrolusite	3	0.55	0.07	0.27	0.29	95.2	LLD	0.07	0.44	0.13	0.33	97.3	supergene
DO	169	pyrolusite	3	2.28	0.07	0.30	LLD	94.6	0.03	0.20	0.50	0.13	0.10	98.2	supergene
PAL	216	pyrolusite	3	0.88	0.03	0.50	LLD	93.9	0.03	0.41	0.10	0.13	0.10	96.1	veinlet, supergene
AUC	198	romanechite	2	0.25	0.05	1.32	1.17	82.2	0.15	0.20	9.78	1.01	1.63	97.8	supergene
AUC	199	romanechite	3	0.70	LLD	1.29	1.44	79.6	0.40	0.95	6.85	0.59	1.44	93.2	supergene
BEE	211	romanechite	5	0.34	LLD	0.42	0.65	78.8	0.22	0.10	13.3	0.39	0.86	95.1	supergene
BIS	244	romanechite	5	0.36	LLD	0.38	0.06	77.2	0.20	0.24	14.3	0.36	0.25	93.3	supergene
DO	161	romanechite	3	0.33	0.38	1.85	7.88	75.9	0.13	0.10	8.30	0.23	3.55	98.7	supergene
DO	169	romanechite	3	0.47	0.03	0.23	LLD	82.0	0.07	0.27	13.2	0.23	0.17	96.7	supergene
GLO	185	romanechite	5	0.51	0.38	1.99	1.65	79.8	0.12	0.18	9.01	0.59	1.38	95.6	supergene
GLO	192	romanechite	5	0.46	0.12	0.28	LLD	76.5	0.32	0.34	13.9	0.44	0.24	92.6	supergene
KAP	229	romanechite	3	0.20	LLD	0.20	0.07	80.5	0.07	LLD	15.4	0.30	0.03	96.7	supergene
LOH	178	romanechite	3	0.86	0.20	3.63	4.93	70.2	0.17	0.23	9.83	0.17	1.77	92.0	supergene

JOHANNESBURG UNIVERSITY

Mine	S. No.	Mineral	N	SiO_2	TiO_2	Al_2O_3	Fe_2O_3	MnO_2	MgO	CaO	BaO	Na_2O	K_2O	TOTAL	Remark
LOH	179	romanechite	3	0.45	0.03	1.06	0.35	78.7	0.03	0.23	15.7	0.37	LLD	96.9	supergene
PAL	216	romanechite	5	0.45	LLD	0.57	LLD	80.8	0.24	1.09	8.65	0.36	0.68	92.8	supergene

IV.3 Silicates associated with the manganese ores

Table IV.3.1 Garnet associated with Wessels-type ore, KMF.

Mine	S. No.	Mineral	N	SiO_2	TiO_2	Al_2O_3	Fe_2O_3	MnO	MgO	CaO	Na_2O	K_2O	TOTAL	Remark
HZ	148	andradite	3	34.4	0.15	1.38	26.4	4.44	0.38	33.0	0.07	0.03	100.3	mottled ore
HZ	154	andradite	5	35.3	0.08	0.55	29.2	1.94	0.20	33.1	0.10	LLD	100.4	mottled ore
NC2	1	andradite	3	35.3	0.23	1.61	28.0	4.44	0.17	30.6	LLD	LLD	100.4	mottled ore
NC2	4	andradite	4	35.4	0.23	1.59	28.1	4.52	0.14	30.9	LLD	LLD	100.9	ore
NC2	15	andradite	2	34.2	0.10	2.60	27.0	1.41	1.20	33.9	LLD	LLD	100.3	ore
NC2	18	andradite	2	32.8	0.05	1.09	28.7	1.28	0.43	33.6	LLD	LLD	97.9	ore
NC2	31	andradite	3	32.2	0.07	1.91	25.1	4.31	0.43	32.4	LLD	LLD	96.4	ore
WES	276.1	andradite	3	34.9	0.10	4.05	25.0	3.67	0.08	31.9	0.24	0.03	100.0	skarn
WES	276.5	andradite	4	34.4	0.03	4.38	25.4	4.63	0.03	31.0	0.10	0.10	99.9	skarn
WES	276.6	andradite	3	36.1	LLD	8.05	19.4	3.39	0.10	32.9	0.09	LLD	100.0	skarn
WES	279	andradite	2	34.4	LLD	0.76	29.3	8.15	0.17	27.7	LLD	LLD	100.4	skarn
WES	320	andradite	3	35.7	LLD	2.69	24.1	3.96	LLD	34.0	LLD	LLD	100.4	vein

UNIVERSITY OF JOHANNESBURG

Mine	S. No.	Mineral	N	SiO_2	TiO_2	Al_2O_3	Fe_2O_3	MnO	MgO	CaO	Na_2O	K_2O	TOTAL	Remark
WES	362	andradite	3	34.9	LLD	0.57	29.3	1.70	0.10	33.1	LLD	LLD	99.7	ore
WES	366	andradite	5	35.6	LLD	1.02	28.8	1.40	0.08	33.8	LLD	LLD	100.7	ore
WES	367.1	andradite	3	29.7	LLD	2.40	24.7	2.74	0.42	35.0	LLD	LLD	95.0	vein
WES	373	andradite	4	36.0	1.71	11.2	14.1	0.81	0.84	34.9	0.15	LLD	99.7	vein
WES	N505	andradite	3	34.9	LLD	0.07	29.4	1.62	0.17	33.6	0.17	0.03	99.9	skarn
WES	SHALE.1	andradite	8	34.3	0.01	0.18	31.1	0.19	0.06	33.7	LLD	LLD	99.5	shale

Table IV.3.2 Pyroxene associated with Wessels-type ore, KMF.

Mine	S. No.	Mineral	N	SiO_2	TiO_2	Al_2O_3	Cr_2O_3	Fe_2O_3	MnO	MgO	CaO	Na_2O	K_2O	TOTAL	Remark
NC2	30	aegirine	4	51.1	0.10	0.36	LLD	28.9	1.90	1.76	3.56	12.5	LLD	100.1	skarn
WES	276.b	aegirine	4	51.1	LLD	0.54	LLD	25.2	3.00	2.94	6.19	11.0	LLD	100.0	vug
WES	276.2	aegirine	3	53.6	LLD	0.19	LLD	11.1	6.68	9.83	5.00	13.3	0.04	99.7	skarn
WES	276.4	aegirine	3	52.4	0.03	0.39	LLD	25.6	2.12	2.89	5.17	11.6	LLD	100.2	skarn
WES	378	aegirine	6	51.9	0.03	LLD	0.02	32.8	1.45	0.05	0.10	13.4	0.03	99.8	skarn
WES	N505.1a	aegirine	3	51.4	LLD	LLD	LLD	28.5	0.28	2.96	4.00	12.2	0.03	99.5	skarn
WES	N505.1b	aegirine	5	51.4	0.02	0.02	0.06	27.0	5.52	1.12	1.47	13.5	0.06	100.2	skarn
WES	N505.2	aegirine	3	51.0	0.07	LLD	0.03	33.2	0.54	0.36	0.45	14.2	LLD	99.9	skarn
WES	SHALE.1	aegirine	5	52.2	0.18	0.90	0.02	31.9	0.37	0.18	1.38	12.8	LLD	100.0	skarn
WES	LVB3.5	johannsenite	10	48.1	0.03	LLD	LLD	0.05	28.9	0.17	23.1	0.03	0.01	100.3	skarn

Table IV.3.3 Amphiboles associated with Wessels-type ore, KMF.

Mine	S. No.	Mineral	N	SiO_2	TiO_2	Al_2O_3	FeO	MnO	MgO	CaO	Na_2O	K_2O	TOTAL	Remark
NC2	30	Mn-richterite	10	51.0	LLD	LLD	LLD	21.8	0.10	15.2	8.94	LLD	97.0	skarn
WES	378.1a	K-richterite	5	58.4	LLD	LLD	1.24	1.22	22.3	6.14	4.78	3.04	97.1	skarn
WES	378.1b	arfedsonite	5	57.9	LLD	LLD	5.98	5.34	16.2	1.44	7.10	3.04	97.0	skarn

Table IV.3.4 Manganese-rich silicates from Wessels-type ore, KMF.

Mine	S. No.	Mineral	N	SiO_2	TiO_2	Al_2O_3	FeO	MnO	MgO	CaO	Na_2O	TOTAL	Remark
NC2	29	orientite	15	29.8	LLD	0.70	LLD	20.2	1.99	27.2	LLD	79.9	vein
NC2	30	pectolite	5	51.1	LLD	LLD	0.10	2.38	LLD	31.2	9.30	94.1	skarn
WES	378.1	pectolite	5	53.9	LLD	LLD	0.06	11.2	0.12	24.8	8.19	98.2	skarn
WES	276	rhodonite	3	47.8	0.03	LLD	0.10	41.7	0.92	9.08	0.17	99.8	vein
WES	279	rhodonite	5	47.7	LLD	LLD	LLD	42.6	0.78	8.89	LLD	100.0	skarn
WES	378.2	ruizite	5	25.9	LLD	1.33	2.56	25.5	0.12	35.7	0.06	91.2	skarn
HZ	289	tephroite	5	30.4	LLD	LLD	0.02	68.3	1.24	0.18	0.06	100.2	vein
WES	351.1	tephroite	3	29.8	LLD	LLD	1.16	67.2	0.80	0.77	0.20	100.1	vug
WES	351.2	tephroite	3	30.4	0.03	LLD	1.64	64.4	1.07	2.24	0.17	99.9	vug
WES	351.3	tephroite	3	30.2	LLD	0.03	0.59	66.9	0.65	1.20	0.13	99.7	vug
WES	LVB3.7	tephroite	6	28.8	0.02	LLD	LLD	70.0	0.48	0.32	0.10	99.7	vug
WES	320	vesuvianite	3	36.3	0.03	15.7	0.29	5.19	1.60	36.1	LLD	89.7	vein

Table IV.3.5 Ca-Hydroxysilicates from Wessels-type ore, KMF.

Mine	S. No.	Mineral	N	SiO_2	Al_2O_3	FeO	MnO	MgO	CaO	SrO	Na_2O	TOTAL	Remark
NC2	29b	datolite	3	36.6	LLD	LLD	0.10	1.32	32.1	LLD	LLD	70.1	vein
WES	320	datolite	1	33.8	0.20	LLD	LLD	LLD	34.3	LLD	LLD	68.3	vein
WES	BCM95.3	datolite	5	35.6	0.06	LLD	0.02	0.02	33.3	LLD	LLD	69.0	vug
WES	LVB3.12	datolite	5	35.7	0.08	0.04	0.04	LLD	33.8	LLD	LLD	69.6	vug
WES	276.b	thomsonite	6	35.0	31.8	LLD	LLD	LLD	7.16	10.3	3.61	87.8	vug
WES	LVB3.4	tobermorite	10	51.2	0.14	0.06	0.13	LLD	34.0	LLD	LLD	85.4	vug
WES	LVB3.6	tobermorite	21	49.3	0.14	0.09	0.70	LLD	35.0	LLD	LLD	85.2	vug
NC2	29b	xonotlite	2	48.4	LLD	LLD	0.33	0.05	45.8	LLD	LLD	94.5	vein
WES	LVB3.4	xonotlite	6	50.1	0.15	LLD	0.26	LLD	47.0	LLD	LLD	97.4	vug

Table IV.3.6 Silicates associated with manganese ore, PMF.

Mine	S. No.	Mineral	N	SiO_2	TiO_2	Al_2O_3	FeO	MnO	MgO	CaO	BaO	Na_2O	K_2O	TOTAL	Remark
AUC	202	Ba-margarite	5	32.7	0.10	39.6	0.45	0.89	0.22	0.02	20.5	0.37	3.37	98.2	Br-ore
BIS	241	amesite	5	22.2	0.08	35.7	0.16	0.42	26.6	LLD	LLD	LLD	LLD	85.1	Bx-ore
GLO	197	amesite	5	23.7	LLD	35.3	0.40	1.07	28.5	LLD	LLD	0.04	LLD	89.0	Bx-ore
GLO	187	ephesite	3	32.3	LLD	52.1	1.68	1.60	0.34	0.03	n.d.	7.75	0.13	95.9	Bx-ore
LOH	82	ephesite	5	34.3	0.02	52.7	0.26	0.10	0.00	0.10	n.d.	5.10	0.08	92.6	Bx-ore
LOH	176	ephesite	3	32.1	0.13	52.6	1.24	1.33	0.24	0.07	n.d.	7.35	0.10	95.2	vein
LOH	181	ephesite	5	33.5	0.08	52.2	0.34	0.08	0.00	0.10	n.d.	4.94	0.14	91.4	vein

IV.4 Composition of carbonates associated with manganese ores

Table IV.4.1 Carbonates, KMF

Mine	S. No.	Mineral	N	SiO_2	Al_2O_3	FeO	Mn_2O_3	MnO	MgO	CaO	SrO	BaO	Na_2O	TOTAL	Remark
HZ	289	calcite	5	LLD	LLD	LLD		2.13	LLD	54.3	LLD	LLD	LLD	57.8	hydrothermal vein
HZ	304	calcite	2	LLD	LLD	LLD		2.31	LLD	51.1	LLD	LLD	LLD	56.1	hydrothermal vein
MMT	84	calcite	5	LLD	LLD	LLD		2.05	0.49	51.9	LLD	0.06	LLD	57.3	vein
MMT	90	calcite	3	0.15	LLD	LLD		0.18	0.39	52.6	LLD	LLD	LLD	54.5	calcrete
MMT	92	calcite	3	0.17	0.07	LLD		6.46	0.27	46.0	LLD	0.07	0.10	54.2	vein
MMT	98	calcite	4	0.15	LLD	LLD		LLD	1.65	55.1	LLD	0.10	0.10	58.1	fault breccia
MMT	99	calcite	4	0.16	LLD	0.15		0.05	0.58	51.5	LLD	0.14	0.08	53.7	fault breccia
MMT	105	calcite	3	0.14	LLD	0.06		0.20	0.53	53.6	LLD	LLD	0.07	55.7	MMT-type ore
MMT	108.1	calcite	5	0.15	LLD	LLD		4.94	0.34	49.0	LLD	0.09	0.08	55.7	MMT-type ore
MMT	108.2	calcite	5	0.16	LLD	0.08		2.56	0.28	49.8	LLD	0.10	0.08	55.1	MMT-type ore
MMT	118	calcite	5	0.15	LLD	0.08		0.05	0.72	53.8	LLD	0.08	0.07	57.0	vein
MMT	125	calcite	8	0.17	LLD	0.12		2.38	0.43	50.3	LLD	LLD	0.13	54.6	MMT-type ore
MMT	127.2	calcite	5	0.14	LLD	0.50		7.93	0.55	46.9	LLD	0.09	LLD	57.2	MMT-type ore
MMT	127.3	calcite	5	0.16	LLD	LLD		11.56	0.06	45.8	0.22	0.07	LLD	60.0	vein
NC2	1	calcite	1	LLD	LLD	0.25		4.15	0.37	50.5	LLD	0.10	LLD	61.4	vein
NC2	4	calcite	2	LLD	LLD	0.05		2.87	LLD	60.7	LLD	LLD	LLD	68.6	WES-type ore
NC2	6	calcite	1	LLD	LLD	LLD		0.12	LLD	57.4	LLD	LLD	LLD	58.5	WES-type ore, vug
NC2	9	calcite	1	LLD	LLD	LLD		0.10	LLD	59.7	LLD	LLD	LLD	60.8	WES-type ore
NC2	10	calcite	5	LLD	LLD	0.34		2.77	0.31	54.0	LLD	LLD	LLD	59.4	MMT-type ore
NC2	13	calcite	2	LLD	LLD	5.61		0.20	0.05	53.2	LLD	0.08	LLD	61.1	WES-type ore, vein
NC2	15	calcite	5	LLD	LLD	1.28		3.21	0.33	54.1	LLD	LLD	LLD	61.4	ferruginized ore
NC2	18	calcite	1	LLD	LLD	0.17		0.40	0.34	57.4	LLD	LLD	LLD	61.3	fault, vein
NC2	20	calcite	2	LLD	LLD	LLD		0.31	LLD	57.8	LLD	LLD	LLD	59.1	WES-type ore
NC2	23	calcite	1	LLD	LLD	1.88		2.86	0.34	53.8	LLD	0.24	LLD	60.2	MMT-type ore
NC2	29b	calcite	1	LLD	LLD	LLD		0.59	LLD	58.4	LLD	LLD	LLD	60.0	skarn, vein

Mine	S. No.	Mineral	N	SiO_2	Al_2O_3	FeO	Mn_2O_3	MnO	MgO	CaO	SrO	BaO	Na_2O	TOTAL	Remark
NC2	30	calcite	1	LLD	LLD	0.1		0.47	LLD	56.6	LLD	LLD	LLD	60.2	skarn
NC2	286	calcite	1	0.11	LLD	0.23		1.32	LLD	54.6	LLD	LLD	0.10	57.4	WES-type ore
WES	359	calcite	1	0.1	LLD	LLD		0.13	LLD	52.5	LLD	LLD	LLD	54.7	WES-type ore, pore
WES	365	calcite	3	0.1	LLD	0.12		0.2	LLD	52.3	LLD	LLD	LLD	54.1	WES-type ore, pore
WES	366	calcite	1	0.1	0.1	LLD		0.3	0.1	58.8	LLD	LLD	LLD	61.6	WES-type ore, pore
WES	367	calcite	1	0.1	0.05	LLD		LLD	LLD	51.2	LLD	LLD	LLD	52.3	WES-type ore, vein
WES	LVB6.06	calcite	1	0.18	0.1	LLD		0.38	LLD	55.1	LLD	LLD	0.17	56.9	WES-type ore, vug
WES	Shale.1	calcite	5	0.21	LLD	0.1		5.44	0.1	52.8	LLD	LLD	LLD	60.8	altered quartzite
MMT	98	dolomite	2	0.15	LLD	LLD		LLD	20.2	33.7	LLD	LLD	0.15	56.2	fault-breccia
NC2	9	gaudefroyite	5	0.1	0.2	LLD	39.1		LLD	37.1	n.d.	n.d.	n.d.	76.5	WES-type ore
NC2	12	gaudefroyite	5	0.1	0.3	LLD	38.6		LLD	36.3	n.d.	n.d.	n.d.	75.3	WES-type ore
NC2	26	gaudefroyite	5	LLD	0.1	LLD	37.2		LLD	36.6	n.d.	n.d.	n.d.	73.9	WES-type ore
NC2	32	gaudefroyite	5	0.1	0.2	LLD	36.9		LLD	36.8	n.d.	n.d.	n.d.	74.0	WES-type ore
HZ	304.3	kutnahorite	2	0.16	LLD	0.33		3.90	23.2	28.7	LLD	LLD	0.05	59.4	MMT-type ore
HZ	304.4	kutnahorite	3	0.15	LLD	0.15		4.71	19.9	29.9	LLD	LLD	0.07	58.9	MMT-type ore
HZ	304.5	kutnahorite	3	0.11	LLD	0.16		4.80	22.3	28.9	LLD	LLD	0.10	61.3	MMT-type ore
HZ	304.6	kutnahorite	1	0.17	LLD	0.29		5.44	21.0	29.0	LLD	LLD	0.10	62.0	MMT-type ore
HZ	305	kutnahorite	1	0.26	LLD	0.23		4.27	23.2	29.7	LLD	LLD	0.10	63.8	MMT-type ore
MMT	83.1	kutnahorite	3	0.58	LLD	1.25		10.0	1.00	39.6	0.20	0.03	0.07	53.8	MMT-type ore
MMT	83.2	kutnahorite	5	0.11	0.02	0.05		11.2	0.23	42.7	LLD	0.03	0.08	56.5	MMT-type ore
MMT	83.3	kutnahorite	4	0.27	0.03	1.12		6.84	1.63	43.5	0.07	0.08	0.05	56.6	MMT-type ore
MMT	84	kutnahorite	11	0.27	0.01	3.37		8.41	8.79	34.8	0.03	0.02	0.13	56.9	MMT-type ore
MMT	87	kutnahorite	6	0.30	0.01	0.29		12.7	1.42	42.7	0.13	0.05	0.13	58.8	MMT-type ore
MMT	109	kutnahorite	5	0.14	LLD	0.1		5.29	0.62	48.7	0.02	0.06	0.04	57.0	MMT-type ore
MMT	127.1.1	kutnahorite	10	0.26	0.05	0.76		7.73	4.00	43.2	0.09	0.03	0.08	57.9	MMT-type ore
MMT	127.1.2	kutnahorite	5	0.17	LLD	0.17		15.7	14.2	27.7	0.06	0.04	0.12	60.2	MMT-type ore
MMT	127.1.3	kutnahorite	5	0.63	LLD	0.4		17.7	12.1	25.3	0.04	0.02	0.18	59.5	MMT-type ore
MMT	127.3	kutnahorite	5	0.41	LLD	0.26		17.3	13.4	25.9	0.08	0.04	0.12	58.7	MMT-type ore
MMT	129.3	kutnahorite	5	0.14	LLD	2.09		11.3	4.64	37.4	0.02	LLD	0.06	58.6	MMT-type ore
MMT	129.4	kutnahorite	5	0.32	LLD	1.78		13.9	12.1	26.2	0.08	LLD	0.12	58.5	MMT-type ore

IV.5 Composition of hydroxides, sulphates, phosphates and vanadates associated with manganese ore, PMF

Table IV.5.1 Diaspore, PMF

Mine	S. No.	Mineral	N	SiO_2	TiO_2	Al_2O_3	Fe_2O_3	Mn_2O_3	MgO	CaO	BaO	Na_2O	K_2O	H_2O	TOTAL	remark
BIS	241	diaspore	10	LLD	0.13	84.2	0.54	0.60	0.08	0.03	LLD	0.03	LLD	14.6	100.2*	Bx-ore
GLO	289	diaspore	10	LLD	0.02	84.6	0.31	0.21	0.03	0.02	LLD	0.04	LLD	14.9	100.1*	Bx-ore
PAL	228	diaspore	9	LLD	0.04	84.7	0.34	0.21	0.08	LLD	LLD	0.03	LLD	14.5.	99.9	Bx-ore

* H_2O content determined by Penfieldt method (Nyfeler, 1994, pers. comm.).

Table IV.5.2 Barite associated with Wessels-type ore of the KMF and with ore of the PMF

Mine	S. No.	Mineral	N	CaO	SrO	BaO	SO_3	TOTAL	Remark
KMF									
NC2	5	Sr-barite	3	0.03	12.2	51.4	35.1	99.9	WES-type ore, pore
NC2	9	Sr-barite	2	0.19	32.9	27.4	39.0	100.1	WES-type ore, pore
NC2	12	Sr-barite	1	0.15	22.7	39.3	36.6	100.0	WES-type ore, veinlet
WES	272	barite	5	LLD	1.88	64.1	34.0	99.9	WES-type ore, vein
WES	SHALE6.b	barite	5	LLD	1.21	65.0	33.1	99.9	altered shale
PMF									
GLO	290	barite	5	LLD	1.20	64.6	34.4	99.0	massive barite lens
JAP	302	barite	5	LLD	2.27	64.5	34.7	99.2	massive barite lens
KAP	297	barite	5	LLD	1.16	64.6	34.4	98.8	Ba+illite+diaspore vein
LAH	166	barite	5	LLD	0.28	65.0	34.2	99.2	in Br-ore
LOH	293	barite	5	LLD	1.45	64.7	34.4	99.1	massive Ba+hematite lens
BEE	211	barite	5	LLD	0.77	64.7	34.1	98.8	in Br-ore

Table IV.5.3 Apatite, PMF

Mine	S. No.	Mineral	N	SiO_2	TiO_2	Al_2O_3	FeO	MnO	MgO	CaO	SrO	BaO	Na_2O	K_2O	P_2O_5	F	TOTAL	Remark
DO	169	apatite	8	0.18	0.06	LLD	0.04	0.61	0.08	57.3	LLD	LLD	0.03	LLD	40.6	present	98.8	Br-ore

Table IV.5.4 Gamagarite, PMF

Mine	S. No.	Mineral	N	SiO_2	TiO_2	Al_2O_3	Fe_2O_3	Mn_2O_3	MgO	CaO	BaO	V_2O_5	TOTAL	Remark
GLO	Mn10-63	gamagarite	5	0.17	LLD	0.19	7.13	5.93	0.11	0.04	52.5	32.1	98.1	Bx-ore

UNIVERSITY OF JOHANNESBURG

IV.6 Minerals associated with bostonite dykes, KMF

Primary igneous as well as alteration phases occurring within bostonite dykes in the KMF have been analysed and are complied in VI.6.1 (primary igneous minerals) and IV.6.2 (alteration phases).

IV.6.1 Igneous phases

Table IV.6.1.1 Feldspar.

Mine	S. No.	Mineral	N	SiO_2	Al_2O_3	FeO	MnO	MgO	CaO	Na_2O	K_2O	TOTAL	Remark
WES	276.3	albite	3	67.8	20.4	0.18	0.26	LLD	LLD	11.5	LLD	100.1	dyke
WES	324.1	albite	5	67.6	20.8	0.26	0.09	LLD	0.43	10.5	0.29	100.0	dyke
WES	324.2	albite	5	67.7	20.7	0.26	0.00	LLD	0.18	11.1	0.12	100.1	dyke
WES	371	albite	10	68.2	20.4	0.11	0.04	LLD	0.10	11.0	0.06	99.8	dyke
HZ	288	labradorite	5	51.4	29.7	1.23	0.05	LLD	13.6	3.87	0.43	100.3	dyke

Table IV.6.1.2 Pyroxene and amphibole.

Mine	S. No.	Mineral	N	SiO_2	TiO_2	Al_2O_3	Cr_2O_3	FeO	MnO	MgO	CaO	Na_2O	K_2O	TOTAL	Remark
HZ	288	diopsidic augite	10	51.9	0.34	3.29	0.29	9.39	0.29	17.2	17.2	LLD	LLD	99.9	dyke
WES	372	diopsidic augite	5	52.4	0.38	1.93	0.06	9.78	0.33	16.7	18.1	0.25	0.02	100.0	dyke
WES	372	diopsidic salite	5	53.5	0.78	0.45	0.09	6.07	1.19	15.1	22.3	0.64	LLD	100.2	dyke
WES	372	Fe-edenite	5	46.8	1.28	5.16	LLD	24.9	0.36	8.26	9.94	1.86	0.70	99.2	dyke

UNIVERSITY OF JOHANNESBURG

Table IV.6.2.1 Unknown oxide, $CaTi_6O_{13}$

Mine	S. No.	Mineral	N	SiO_2	TiO_2	Al_2O_3	FeO	MnO	MgO	CaO	Na_2O	K_2O	TOTAL	Remark
WES	327.1	$CaTi_6O_{13}$	3	0.43	85.9	0.40	1.75	0.24	0.07	11.5	0.54	0.07	100.9	veinlet, dyke margin

Table IV.6.2.2 Tephroite (chilled and altered margins of dykes).

Mine	S. No.	Mineral	N	SiO_2	TiO_2	Al_2O_3	FeO	MnO	MgO	CaO	Na_2O	TOTAL	Remark
WES	351.1	tephroite	3	29.8	LLD	LLD	1.16	67.2	0.80	0.77	0.20	100.1	chilled margin, ore
WES	351.2	tephroite	3	30.4	0.03	LLD	1.64	64.4	1.07	2.24	0.17	99.9	chilledmargin, contact
WES	351.3	tephroite	3	30.2	LLD	0.03	0.59	66.9	0.65	1.20	0.13	99.7	chilled margin, dyke

JOHANNESBURG UNIVERSITY OF

Table IV.6.2.3 Garnets from chilled and altered margins of dykes

Mine	S. No.	Mineral	N	SiO_2	TiO_2	Al_2O_3	Fe_2O_3	FeO	MnO	MgO	CaO	Na_2O	K_2O	TOTAL	Remark
WES	322	andradite	5	34.9	1.34	5.63	23.5		0.51	0.25	33.3	0.22	LLD	99.7	chilled margin
WES	351.1	andradite	3	34.1	LLD	1.03	27.8		10.50	0.32	27.0	0.17	LLD	101.0	ore
WES	351.2	andradite	3	35.9	LLD	1.04	28.4		3.97	0.27	31.1	0.07	LLD	100.8	ore
WES	351.3	andradite	3	35.2	0.03	2.89	26.7		4.53	0.10	30.6	0.13	LLD	100.2	chilled contact
WES	378.1	andradite	6	31.7	LLD	1.03	21.2		8.58	0.41	34.6	0.07	LLD	97.5	chilled margin
WES	378.2a	andradite	5	34.0	LLD	0.54	22.5		7.59	0.27	34.0	LLD	LLD	98.9	chilled margin
WES	378.2b	andradite	5	29.8	0.08	0.44	22.6		7.00	0.35	34.0	0.10	LLD	94.3	chilled margin
WES	322	grossulare	3	38.4	0.38	21,6		1.33	6.42	0.07	31.9	0.00	LLD	100.1	chilled margin
WES	327.1a	grossulare	3	37.8	0.20	20.1		4.36	0.48	0.61	33.8	1.03	0.47	98.9	chilled margin
WES	327.1b	grossulare	3	34.8	1.01	20.0		2.47	2.08	2.83	32.3	0.23	0.13	95.9	chilled margin
WES	373	grossulare	3	38.3	0.03	25.7		9.80	0.42	0.07	23.6	0.07	0.03	98.0	chilled margin

Table IV.6.2.4 Pyoxene (chilled and altered margins)

Mine	S. No.	Mineral	N	SiO_2	TiO_2	Al_2O_3	Cr_2O_3	FeO	MnO	MgO	CaO	Na_2O	K_2O	TOTAL	Remark
WES	324	Mn-diopside	3	55.4	0.03	LLD	0.03	0.07	1.90	17.4	25.3	LLD	LLD	100.0	dyke
WES	320.2	Mn-diopside	3	53.7	LLD	LLD	0.13	0.09	3.21	17.0	25.9	LLD	LLD	100.0	dyke
WES	322	Mn-diopside	3	50.6	LLD	2.13	0.05	1.77	10.80	10.7	22.9	0.52	0.13	99.7	dyke
WES	351	Mn-diopside	3	52.8	LLD	LLD	0.13	0.84	8.82	12.4	24.9	LLD	LLD	99.9	dyke

UNIVERSITY JOHANNESBURG

Appendix V

Stable Isotope Data

Stable and radiogenic isotope data that were collected during this study are listed. $\delta^{13}C$ and $\delta^{18}O$ isotope compositions of sedimentary and hydrothermal carbonates from the KMF are listed in table V.1. Table V.II contains a compilation of $\delta^{34}S$ and $^{87}Sr/^{86}Sr$ isotope compositions of barite and celestite associated with Mn-ores in the PMF and KMF.

Table V.1 $\delta^{13}C$ and $\delta^{18}O$ isotope ratios of carbonate samples. Data were collected by Hsueh-Wen Yeh (Taipe). Samples marked (*) were analysed by S. Talma (CSIR, Pretoria) and those marked (#) by H. Strauß (Bochum, Germany). Samples are mineral separates, whole rock samples are specifically mentioned.

Sample No.	Carbonate	$\delta^{13}C_{(PDB)}$	$\delta^{18}O_{(PDB)}$	Sample Description
Wessels-type ores				
WES-276	calcite	-21.1	-13.7	Stringers in skarn assemblage.
WES-279	calcite	-15.1	-14.4	Vug infill in rhodonite skarn.
WES-273#	calcite	-7.7	-12.5	Sparite, in banded barite-pyrite vein.
WES-326	calcite	-15.5	-13.2	Vug infill in altered BIF fault breccia.
WES-329*	calcite	-10.8	-8.4	Brittle, central infill in calcite-pyrite vein.
WES-330	calcite	-10.7	-8.7	Sparite, vein infill.
WES-332	calcite	-11.3	-12.9	Sparite, vein infill associated with massive andradite-clinochlore assemblage.
WES-362*	calcite	-7.9	-12.5	Calcite vug infill, associated with andradite, clinochlore, in Hs-Br II ore. Whole rock sample. Close to calcite-pyrochroite vein.
WES-363-1	calcite	-8.1	-19.5	Banded calcite-pyrochroite vein. Oldest calcite generation along selvage, with pyrite.
WES-363-2	calcite	-10.7	-15.2	Banded calcite vein, second generation.
WES-363-3	calcite	-7.8	-12.9	Banded calcite vein, third generation.
WES-363-4	calcite	-8.8	-9.9	Banded vein, central infill (fourth generation) of calcite-gypsum and pyrochroite assemblage.

UNIVERSITY OF JOHANNESBURG

Sample No.	Carbonate	$\delta^{13}C_{(PDB)}$	$\delta^{18}O_{(PDB)}$	Sample Description
WES-364*	calcite	-11.6	-10.8	Vug infill in Hs-Br II ore, associated with andradite, clinochlore. Whole rock sample taken close to calcite-pyrochroite vein.
WES-365*	calcite	-10.4	-15.1	Vug infill in Hs-Br II ore. Whole rock sample taken close to calcite-pyrochroite vein
WES-367*	calcite	-4.6	-8.4	Sparite vein, with barite, andradite, specularite.
WES-370	calcite	-2.9	-15.8	Sparite vein, associated with acmite and andradite. Vein crosscuts margin of altered bostonite dyke.
WES-Shale-1*	calcite	-9.4	-10.4	Stringers in hydrothermally altered Mapedi quartzite, associated with acmite and andradite. On fault plane.
PDB1-00	calcite	-10.3	-13.6	Vug assemblage with jacobsite, andradite. Wessels. Source: De Bruin
LVB5-34	calcite	-10.4	-15.1	Infill of hausmannite lined vug. Wessels. Source: Von Bezing.
LVB6-06-Rim	calcite	-12.0	-15.8	Large calcite scalenohedron, associated with pyrite. Vein crosscuts altered BIF. Wessels. Source: Von Bezing.
LVB5-33	Mn-calcite	-8.1	-10.5	Mn-calcite-sparite overgrowing pyrite cluster. Wessels. Source: Von Bezing.
WES-N504-2	calcite	-7.9	-8.5	Central portion of strata bound veinlet, associated with barite, Br-II-rich ore. Wessels. Source: Burger.
WES-N504-3	calcite	-22.3	-13.6	Upper selvage of strata bound veinlet, Br-II-rich ore. Wessels. Source: Burger.
WES-N504-4	calcite	-17.1	-12.0	Upper portion of strata bound veinlet, Br-II-rich ore. Wessels. Source: Burger
WES-N504-5	calcite	-11.1	-9.7	Lower portion of strata bound veinlet, Br-II-rich ore. Wessels. Source: Burger
WES-N504-6	calcite	-14.8	-13.9	Vug infill in vuggy, coarse crystalline Hs-rich ore. Wessels. Source: Burger.
WES-N205	calcite	-11.5	-4.2	Vug infill in vuggy, coarse-crystalline Hs-rich ore. Wessels. Source: Burger.
WES-N208	calcite	-13.1	-1.5	Vug infill un Br II-Hs-rich ore, associated with feitknechtite. Wessels. Source: Burger.
WES-N228	calcite	-7.5	-11.6	Sparitic calcite in ferruginized fault plane. Wessels. Source: Burger.

UNIVERSITY OF JOHANNESBURG

Sample No.	Carbonate	$\delta^{13}C_{(PDB)}$	$\delta^{18}O_{(PDB)}$	Sample Description
LVB3-03	calcite	-8.7	-30.9	Sparitic rhombs coating vugs that are lined by hausmannite. Hs-rich ore. Nchwaning II.
LVB6-06#	calcite	-63.3	-17.6	Vug lining of large scalenohedra, with galena, celestite, on caryopilite. Nchwaning II. Source: Von Bezing.
NC-10*	calcite	-6.2	-15.2	Mamatwan-type ore, weakly altered. Whole rock sample.
NC-11*	calcite	-6.0	-16.0	Mamatwan-type, weakly altered. Whole rock sample.
NC-15a*	calcite	-8.2	-15.5	Massive lens of sparitic calcite and hematite. Close to ferruginized fault. Whole rock sample.
NC-18a*	calcite	-9.1	-15.1	Sparitic, with hematite, andradite. On fault plane. Whole rock sample.
NC-22*	calcite	-8.4	-14.6	Sparitic vug infill, in massive hausmannite ore, associated with clinochlore. Whole rock sample.
NC-26*	calcite	-10.7	-13.9	Sparitic vug infill, in coarse-crystalline, vuggy Hs-rich ore. Whole rock sample.
NC-29b*	calcite	-16.3	-19.3	Sparitic vein infill. Associated with ruizite, xonotlite, clinochlore. Fault plane centring a silicified and ferruginized halo.
LVB1-34	calcite	-10.5	-15.3	Skarn assemblage, calcspar with pink grossulare. Nchwaning II. Source: Von Bezing.
LVB6-28	calcite	-17.3	-18.4	Sparite vug infill, coating hausmannite, specularite in vuggy, coarse Hs-rich ore. Nchwaning II. Source: Von Bezing.
LVB5-36	calcite	-24.1	-18.1	Sparitic vein/ vug linings, on altered BIF-breccia in fault plane. Associated with pyrite. Nchwaning II. Source: Von Bezing
LVB6-29	calcite	-12.9	-14	Sparitic overgrowth of hausmannite. Vug infill in vuggy, coarse crystalline Hs-rich ore. Nchwaning II. Source: Von Bezing.
LVB1-34	calcite	-10.5	-15.3	Sparitic, intergrown with pink grossulare. Skarn assemblage. Nchwaning II. Source: Von Bezing.
Hz-304	calcite	-9.9	-14.8	Sparite associated with hausmannite-partridgeite, in vein crosscutting weakly altered ore, upper orebody, Northern pit. Diffuse ferruginization halo.

Sample No.	Carbonate	$\delta^{13}C_{(PDB)}$	$\delta^{18}O_{(PDB)}$	Sample Description
Hz-289	calcite	-8.1 1	-15.1	Sparite in association with tephroite and Mn-pectolite in vein that crosscuts massive Hs-rich ore. Lower orebody, Southern pit.
Hz-157	calcite	-9.3	-5.2	Vug infill, associated with clinochlore, andradite. Massive Hs-rich ore. Whole rock sample.
LVB5-37	Mn-calcite	-10.3	-20.5	Lensoidal crystals with pyrite on altered BIF breccia in fault plane. Gloria Mine
LVB5-30-1-Rh	rhodochrosite	-19.7	-17.8	Small crystals, complex habitus, vein assemblage with shigaite, hematite, jacobsite, caryopilite, leucophoenicite. Nchwaning II. Source: Von Bezing.
LVB5-30-2-Rh	rhodochrosite	-36.9	-18.7	Small, rose-red rhombs. Nchwaning II. Source: Von Bezing.
LVB5-30-3-Rh	rhodochrosite	-38.6	-15.6	Dense mass. Nchwaning II. Source: Von Bezing
LVB5-31-1-Rh	rhodochrosite	-12.1	-4.7	Coarse crystalline, deep red scalenohedra, with manganite. Hotazel. Source: Von Bezing.
LVB5-31-2-Rh	rhodochrosite	-7.6	-4.4	Vug infill of globular rhodochrosite. Hotazel. Source: Von Bezing.
LVB5-31-3-Rh	rhodochrosite	-4.4	-4.8	Rose-red rhombs, associated with manganite, vein or vug infill. Hotazel. Source: Von Bezing.
LVB5-31-4-Rh	rhodochrosite	-3.8	-3.8	Aggregates of interfering discs, vug filling. Hotazel. Source: Von Bezing.
LVB5-32-Rh	rhodochrosite	-6.9	-3.9	Large globular aggregates. Nchwaning I. Source: Von Bezing.
MMT-82	calcite	-8.1	-12.8	MMT-type ore. Whole rock sample.
	kutnahorite	-8.3	-12.3	
MMT-83	calcite	-5.2	-14.2	MMT-type ore, weakly ferruginized. Whole rock sample.
	kutnahorite	-5.0	-13.2	
MMT-84	calcite	-4.4	-8.6	MMT-type ore, strongly ferruginized, close to veinlet. Visible recrystallization. Whole rock sample.
	kutnahorite	-3.6	-7.6	

UNIVERSITY OF JOHANNESBURG

Sample No.	Carbonate	$\delta^{13}C_{(PDB)}$	$\delta^{18}O_{(PDB)}$	Sample Description
MMT-84-vein	calcite	-4.5	-11.1	Calcite-chalcedony veinlet, centring ferruginized halo. Whole rock sample.
MMT-85	calcite	-4.8	-13.2	Weakly ferruginized MMT-type ore. Whole rock sample.
	kutnahorite	-4.5	-9.9	
MMT-86-He	calcite	-5.5	-14.4	Weakly ferruginized MMT-type ore, diffuse contact to unaltered ore. Whole rock sample.
	kutnahorite	-5.7	-13.6	
MMT-86-Mn	calcite	-7.9	-12.1	Unaltered MMT-type ore. Diffuse contact to weakly ferruginized ore. Whole rock sample.
MMT-87	calcite	-8.0	-12.5	MMT-type ore. Whole rock sample.
	kutnahorite	-8.7	-11.8	
MMT-88	calcite	-7.8	-13.1	MMT-type ore. Whole rock sample.
	kutnahorite	-8.2	-11.8	
MMT-91	kutnahorite	-10.8	-12.1	MMT-type ore. Whole rock sample.
MMT-92	kutnahorite	-10	-11.2	MMT-type ore. Whole rock sample.
MMT-96	calcite	-8.4	-6.0	Completely altered MMT-type ore. Whole rock sample.
MMT-97	calcite	-8.2	-5.7	Sparitic vein crosscutting altered ore.
MMT-98	calcite	-9.0	-5.7	Vuggy, sparitic cement of brecciated and rounded fragments of altered MMT-type ore. Close to contact fault-zone . Associated with chalcedony.
MMT-102	calcite	-7.6	-5.2	Cement of hydrofractured and ferruginized MMT-type ore. Calcite scalenohedra. Contact fault zone to ore.
MMT-103	calcite	-8.1	-5.7	Sparitic and vuggy cement of brecciated, ferruginized and altered ore fragments. Nontronite associated.
MMT-104	calcite	-7.6	-4.8	Altered MMT-type ore. Whole rock sample.
MMT-105	calcite	-7.4	-6.6	Altered MMT-type ore. Whole rock sample.
MMT-106	calcite	-7.4	-8.2	Weakly altered MMT-type ore with partridgeite and hausmannite. Whole rock sample.
MMT-107	calcite	-8.6	-11.3	Weakly altered MMT-type ore with partridgeite and hausmannite. Whole rock sample.

UNIVERSITY OF JOHANNESBURG

Sample No.	Carbonate	$\delta^{13}C_{(PDB)}$	$\delta^{18}O_{(PDB)}$	Sample Description
MMT-108	calcite	-9.6	-11.7	MMT-type ore. with hausmannite, partridgeite. Whole rock sample.
	kutnahorite	-10.7	-13.6	
MMT-109	calcite	-11.0	-13.9	MMT-type ore. Whole rock sample.
MMT-110	calcite	-11.1	-14.1	MMT-type ore. Whole rock sample.
	kutnahorite	-11.0	-13.6	MMT-type ore. Whole rock sample.
MMT-126	calcite	-11.2	-13.7	MMT-type ore. Whole rock sample.
	kutnahorite	-11.4	-13.4	
MMT-127	calcite	-10.3	-13.8	Weakly ferruginized MMT-type ore. Whole rock sample.
	kutnahorite	-10.8	-13.6	
MMT-128	calcite	-11.3	-13.9	MMT-type ore. Whole rock sample.
	kutnahorite	-11.4	-13.5	
MMT-129-I	Mn-dolomite	-10.1	-12.1	Massive matrix of pyritized and carbonatized MMT-type ore fragment in fault plane.
MMT-129-II	Mn-dolomite	-12.4	-13.0	Rounded crystals. associated with pyrite, covered by tridymite. Cement between altered MMT-type ore fragments.
MMT-307-I	calcite	-5.7	-4.2	Older generation of calcite cement (white, sparitic) between altered Mn-ore fragments in fault zone.
MMT-307-II	calcite	-8.2	-6.0	Younger generation of calcite cement (yellowish, sparitic). Overgrowing MMT- 307-I.
MMT-90-1*	calcite	-6.0	-3.1	Calcrete with manganomelane. Top of lower orebody.
MMT-90-2*	calcite	-4.3	-0.8	Calcrete, small rhombs in vug in botryoidal manganomelane. Top of lower orebody.
SM-TODO-Cc	calcite	-9.2	-5.2	Lens-like crystals in strata bound veins, in association with todorokite. Smartt mine.
Drill core M2 (Mamatwan, lower, unaltered orebody) (Data from Beukes, unpublished)				
MMT-M2/47B/1	Mn-calcite	-11.5	-5.8	Diagenetic carbonate ovoids.
MMT-M2/47B/2	Mn-calcite	-11.7	-6.7	Flat diagenetic carbonate lenses.
MMT-M2/47B/3	kutnahorite	-12.5	-6.8	Whole rock sample.
MMT-M2/49B/1	Mn-calcite	-11.3	-9.1	Diagenetic carbonate ovoids.

Table V.2 $\delta^{34}S$ and $^{87}Sr/^{86}Sr$ isotope ratios of sulphates from the KMF and the PMF. Data collected by H. Strauß (Bochum, Germany).

Sample No.	Sulphate	$\delta^{34}S_{(CDT)}$	$^{87}Sr/^{86}Sr$	Sample description
KMF				
BR-Ba	barite	+17.9	0.710755	Barite-hematite vein, Black Rock
LVB3-Ba	barite	+24.8	0.726785	Nchwaning II, vein barite
WES-272-Ba	barite	+29.1	0.758615	Wessels, white barite. Vein-assemblage with calcite and pyrite
LVB6-06-Ce	celestite	+23.5	0.727162	Nchwaning II, vug assemblage with calcite, galena, on caryopilite
PMF				
BEE-211-Ba	barite	+24.2	0.712440	Barite patches in siliceous manganese ore (braunite). Beeshoek.
GLO-290-Ba	barite	+27.0	0.730696	Barite lens at contact between dolomite and ferruginous Mn-ore, surrounded by Ba-rich wad. Glosam Mine.
KAP-297-Ba	barite	+29.2	0.716190	Thin barite-illite-diaspore vein on fault plane. Kapstewel Fe-mine.
KAP-TVM-Ba	barite	+23.4	0.724283	Barite intergrown with braunite, siliceous manganese ore. Kapstewel. Source: Transvaal Museum
KLI-TVM-Ba	barite	+23.5	0.714462	Barite-hematite lens in siliceous manganese ore. Klipfontein. Source: Transvaal Museum.
JAP-302-Ba	barite	+48.7	0.720423	Barite from Japiesrust. Barite lens on Blackridge thrust (?).
LOH-293-Ba	barite	+22.7	0.708447	Barite lens with botryoidal hematite, surrounded by Ba-rich wad in ferruginous Mn-ore. Lohatla.

Appendix VI

Fluid Inclusion Data

Data sheets are presented for the various samples on which microthermometric fluid inclusion studies were conducted. Each data sheet contains short descriptions of the sample itself, and of the different populations of fluid inclusions that were recognized. Furthermore histograms and some statistical data (mean, minima and maxima), obtained from the measurement of the final melting temperature (T_{mf}) and the homogenization temperature (T_h), are displayed. The data sheet contains further information regarding some characteristics of the inclusion behaviour during melting.

The following abbreviations are used in the Data sheets:

N	number of measurements
T_f	freezing temperature
T_h	homogenization temperature
T_{m1}	Eutectic temperature, first melting process.
T_{m2}	Cotectic temperature, second melting process.
T_{m3}	Cotectic temperature, third melting process.
T_{mf}	Final melting temperature.
L	Monophase liquid inclusions.
LV	Liquid-vapour inclusions.
F	Degree of filling of fluid inclusion by liquid phase.

UNIVERSITY OF JOHANNESBURG

The term 'crazy paving' is used as defined by Shepherd et al. (1985) to describe the granular polycrystalline appearance of the fluid inclusion content during the melting process.

All temperatures are listed in °C.

Data sheet VI.1 BCM-95-1 (Nchwaning II) **datolite**

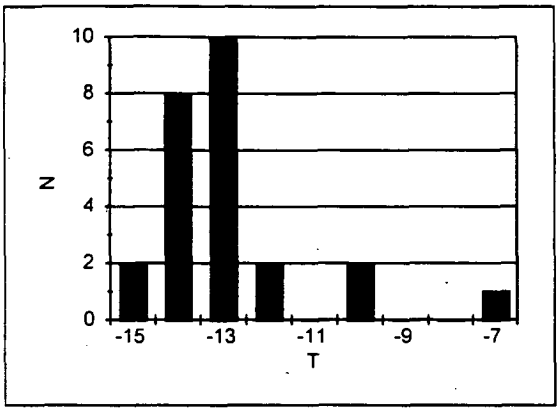

Figure VI.1 T_{mf} histogram, sample BCM-95-1. N=25, T in °C.

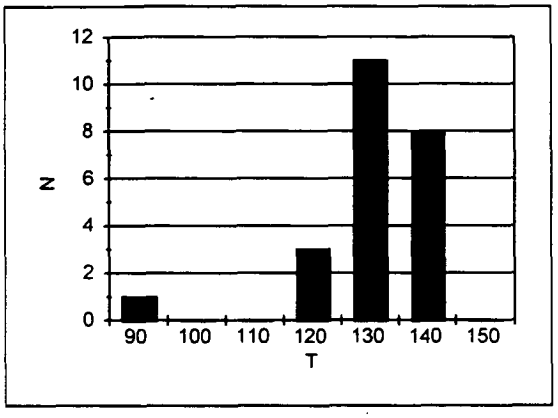

Figure VI.2 T_h histogram, sample BCM-95-1. N=23, T in °C.

T_{mf} statistics:

Mean:	-12.4 °C
Maximum:	-6.4 °C
Minimum:	-14.4 °C

T_h statistics:

Mean:	135.1 °C
Maximum:	95 °C
Minimum:	149 °C

UNIVERSITY OF JOHANNESBURG

Sample description: Centimeter-large, rose-red subhedral datolite crystals. Vug or vein mineralisation. Source: B. Cairncross.

Description of fluid inclusion generations:

Primary: Small clusters of 5 - 15 µm large, ellipsoidal inclusions. F= 99-100 %. Aqueous L and LV inclusions.

Pseudosecondary: Short intracrystalline trails of 1-30 µm large elongated inclusions of irregular shape. F=99-100 %. Aqueous L and LV inclusions.

Measured

Primary and pseudosecondary inclusions show identical behaviour.

T_f: Inclusions freeze at -50 to -60 °C to form clear, in some cases visibly polycrystalline solid.

T_{m1}: First melting at -29.3 to -35.1 °C indicated by darkening and intensive 'crazy paving' of the inclusion content. *$MgCl_2 \cdot 12\ H_2O$ melting.*

T_{m2}: 'Crazy paving' and colouration disappear at - 20 to -22 °C. *Hydrohalite melting.*

T_{mf}: The last of few large clear crystals with low relief melts between -94 to 149 °C. *Ice melting.*

Data sheet VI.2 HZ-289 **calcite**

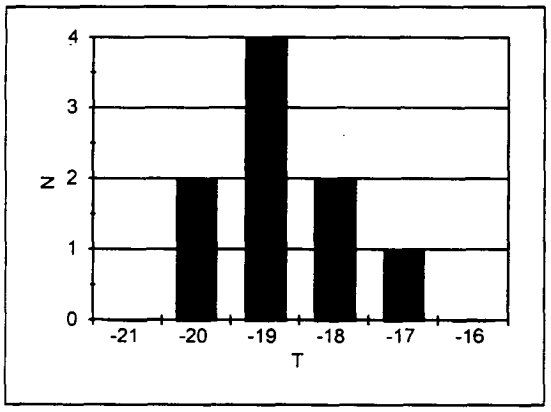

Figure VI.3 T_{mf} histogram, sample HZ-289. N=10, T in °C.

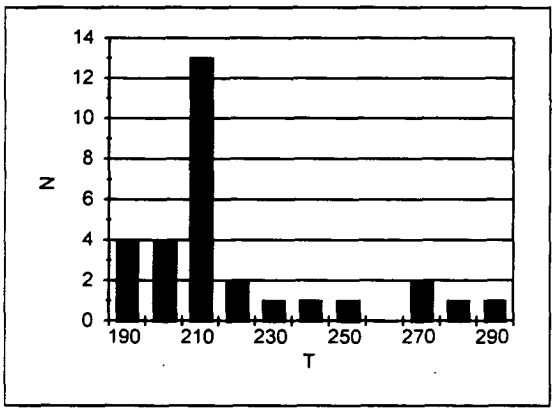

Figure VI.4 T_h histogram, sample HZ-289. N=35, T in °C.

T_{mf} statistics:

Mean:	-18.5 °C
Maximum:	-16.6 °C
Minimum:	-21.6 °C

T_h statistics:

Mean:	218 °C
Maximum:	311 °C
Minimum:	183 °C

UNIVERSITY OF JOHANNESBURG

Sample description: Vein infill of sparitic white calcite, massively intergrown with bluish tephroite and dense rose-coloured Mn-pectolite.

Description of fluid inclusion generations:

Primary: Large number of erratically distributed, ellipsoidal to polygonal shaped inclusions. Size: 5-15 µm, F = 98 - 100 %, aqueous L and LV inclusions.

Secondary: Indistinct trails of small polygonal inclusions that crosscut grain boundaries. Size 1 - 3 µm, F=98-100%, aqueous L and LV inclusions.

Measured

Primary inclusions only.

T_f: Freezing not exactly observable, clear solid, vapour bubble does not shrink.

T_{m1}: First melting at -31.1 to -39.5 °C indicated by darkening and 'crazy paving' of inclusion content. *$MgCl_2 \cdot 12 H_2O$ melting.*

T_{m2}: Dark colour and polycrystallinity disappear at approximately -23 to -25 °C. *Hydrohalite melting.*

T_{mf}: Final melting of remaining large clear crystals with low relief in the region -17.1 to -21.8 °C. *Ice melting.*

Data sheet VI.3 WES-359 **calcite**

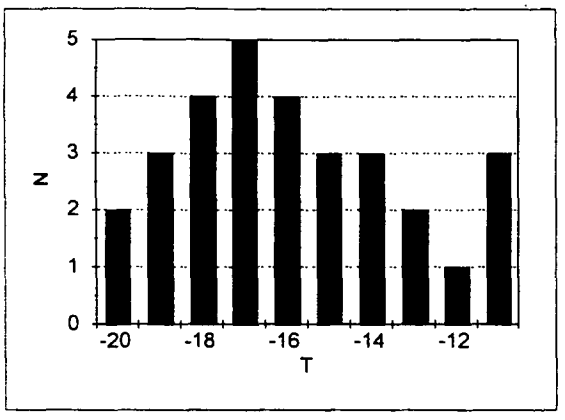

Figure VI.5 T_{mf} histogram, sample WES-359. N=30, T in °C.

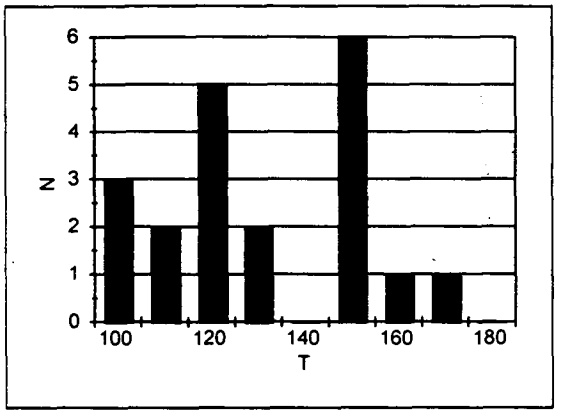

Figure VI.6 T_h histogram, sample WES-359. N=20, T in °C.

T_{mf} statistics:

Mean:	-15.5 °C
Maximum:	-10.6 °C
Minimum:	-20.0 °C

T_h statistics:

Mean:	136 °C
Maximum:	175 °C
Minimum:	102 °C

UNIVERSITY OF JOHANNESBURG

Sample description: Pore fills of calcspar, associated with andradite and clinochlore, in Hs-BrII- He-rich ore. Lamellar intergrowth of calcite and braunite II.

Description of fluid inclusion generations:

Primary: Abundant rhomb-shaped and irregular inclusions that occur disperse and in small clusters. Clinochlore flakes seem to form parts of inclusion walls. Size: 3-50 µm, F = 95-100 %, aqueous L and LV inclusions.

Pseudosecondary: Intracrystalline inclusion trails, not parallel to cleavage. Shape rhombohedral, size 1-6 µm, F=98-100%, aqueous L and LV inclusions.

Secondary: Trails of minute inclusions that crosscut grain boundaries. Aqueous L inclusions.

Measured

Primary and pseudosecondary inclusions show identical behaviour.

T_f: Freezing at -45 to 70 °C to form a clear solid.

T_{m1}: First melting at -33.8 to -39 °C indicated by considerable darkening and strong 'crazy paving' of inclusion content. *$MgCl_2 \cdot 12\ H_2O$ melting.*

T_{m2}: Dark colour and granularity disappear at approximately -29 to -26 °C. *Hydrohalite melting.*

T_{mf}: Final melting of remaining large clear crystals with low relief around -11 to -20 °C. *Ice melting.*

Data sheet VI.4 WES-365 **calcite**

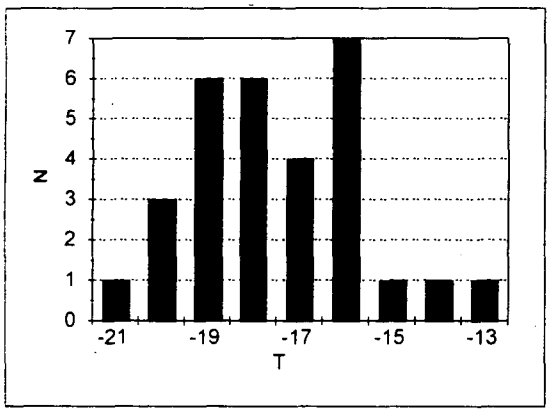

Figure VI.7 T_{mf} histogram, sample WES-365. N=30, T in °C.

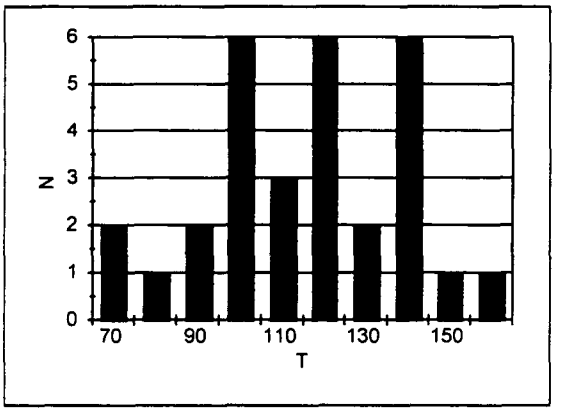

Figure VI.8 T_h histogram, sample WES-365. N=30, T in °C.

T_{mf} statistics:

Mean:	-15.5 °C
Maximum:	-10.6 °C
Minimum:	-20.0 °C

T_h statistics:

Mean:	136 °C
Maximum:	175 °C
Minimum:	102 °C

UNIVERSITY OF JOHANNESBURG

Sample description: Pore fills of calcspar, associated with andradite and clinochlore, in hausmannite-rich ore.

Description of fluid inclusion generations:

Pseudosecondary: Straight, parallel arranged intracrystalline trails of ellipsoidal to rhombohedral shaped inclusions. Size 5-30 µm, F=95-100%, aqueous L and LV inclusions. Signs of leaking and decrepitation common.

Secondary: Trails of minute inclusions that crosscut grain boundaries. Size 1-3 µm, F=99-100%. Aqueous L and LV inclusions.

Measured

Pseudosecondary inclusions only.

T_f: Freezing at -50 to 75 °C is difficult to observe. A clear solid forms.

T_{m1}: First melting rarely observed, at about -55 °C indicated by slight darkening. Antarcticite melting.

T_{m2}: 'Crazy paving' appears and content darkens considerably at -33 to -40.2 °C. *$MgCl_2 \cdot 12\ H_2O$ melting.*

T_{m3}: Dark colour and granularity disappear at approximately -24.8 to -21.1 °C. *Hydrohalite melting.*

T_{mf}: Final melting of remaining large clear crystals with low relief in the region -12 to -20 °C. *Ice melting.*

Data sheet VI.5 Sample WES-367-1 **calcite**

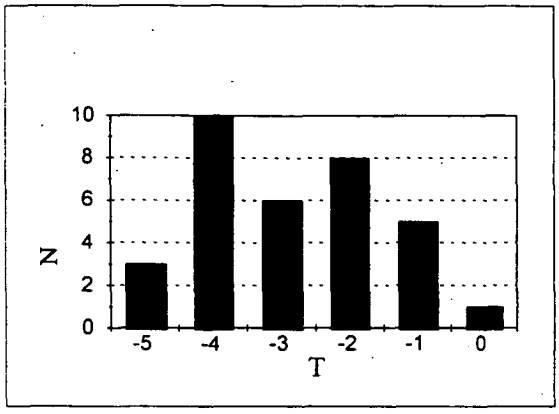

Figure VI.9: T_{mf} histogram, sample WES-367-1.
N = 30; T in °C.

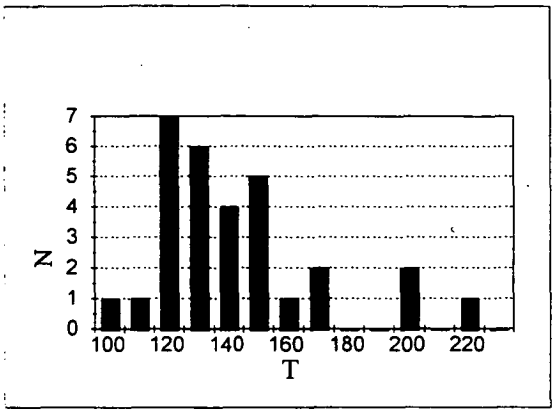

Figure VI.10: T_h histogram, sample WES-367-1.
N = 30; T in °C.

T_{mf} statistics:

Mean:	-2.42 °C
Maximum:	0 °C
Minimum:	-4.8 °C

T_h statistics:

Mean:	146 °C
Maximum:	104 °C
Minimum:	222 °C

UNIVERSITY OF JOHANNESBURG

Sample description: White calcspar, intergrown with barite and clinochlore. Massive filling of the centre of a banded vein. Succession of vein mineralization is: specularite + andradite - calcite + barite + clinochlore.

Description of fluid inclusion generations:

Primary: Isometric with indicated rhombohedral outline. Dispersed occurrence in specific. Size: < 50 µm, F = 99 - 100 %, aqueous L and LV inclusions. Indications for leaking are common.

Secondary: Short trails of small inclusions that crosscut grain boundaries. Ellipsoidal shape, elongated. Size 2-5 µm, F=99 - 100%, aqueous L inclusions.

Measured

Primary and secondary inclusions show identical behaviour.

T_f: Inclusion content freezes at about - 40 °C to form a brownish, polycrystalline mass.

T_{m1}: First melting at -33.8 to -36.5 °C results in decolouring and coarsening of the crystallinity. *$MgCl_2 \cdot 12\ H_2O$ melting.*

T_{m2}: Continuous melting process, difficult to observe. Polycrystallinity disappears with last melting of high relief phase at approximately -21 °C. *Hydrohalite melting.*

T_{mf}: Large clear crystals with low relief melt in the region -4 to 0 °C. *Ice melting.*

Data sheet VI.6 WES-370 **calcite**

Table VI.1 Fluid inclusion data for sample WES-370.

N	T_f	T_{m1}	T_{m2}	T_{mf}	T_h
1	-72.1	-51.2		-19.5	113.9
2	-70.6	-52.0		-21.3	239.3
3	-75.2	-51.0		-18.5	188.5
4		-51.3		-17.2	195.2
5		-50.9		-17.5	172.6
6					206.0

T_{mf} statistics:

Mean: -18.8 °C

Maximum: -17.2 °C

Minimum: -21.3 °C

T_h statistics:

Mean: 186 °C

Maximum: 239 °C

Minimum: 113 °C

UNIVERSITY OF JOHANNESBURG

Sample description: Calcspar associated with acmite and andradite, fills vein that cuts through the altered margin of a bostonite dyke.

Description of fluid inclusion generations:

Primary: Rare cluster of inclusions of slightly irregular rhombohedral shape. Size: 3 - 15 μm, F = 98 - 100 %, aqueous L and LV inclusions.

Secondary: Short, bended trails projecting from grain boundaries inwards. Very small inclusions of less than 1 μm size, F= 100%, aqueous L inclusions.

Measured

Primary inclusions only.

T_f: Inclusion content freezes at about -70 to -75 °C to form a clear solid.

T_{m1}: First melting at -51 to -52 °C. A slight brownish tint and 'crazy paving' appear. *Antarcticite melting.*

T_{m2}: Not clearly observable, continuous decolouring and disappearance of granular appearance between -35 and -21 °C. *Hydrohalite* and *$MgCl_2 \cdot 12\ H_2O$ melting (?).*

T_{mf}: Final melting of large, clear crystals with low relief at -17.2 to-21.3 °C. *Ice melting.*

Data sheet VI.7 LVB-6-06 **calcite**

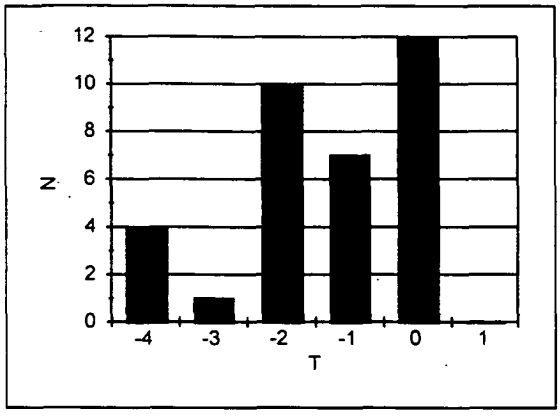

Figure IV.11 T_{mf} histogram, sample LVB6-06. N=34, T in °C.

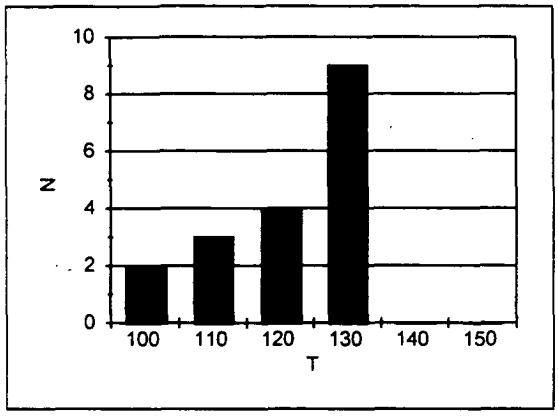

Figure VI.12 T_h histogram, sample LVB6-06. N=19, T in °C.

T_{mf} statistics:

Mean:	-0.9 °C
Maximum:	+0.6 °C
Minimum:	-3.9 °C

T_h statistics:

Mean:	124 °C
Maximum:	137 °C
Minimum:	98 °C

UNIVERSITY OF JOHANNESBURG

Sample description: Scalenohedral, light amber coloured calcite crystals, associated with celestite and galena in vug assemblage. Matrix is dense caryopilite. Nchwaning II mine.

Description of fluid inclusion generations:

Secondary: Straight and bended trails of elongated, ellipsoidal inclusions that pinch out within crystal, but are doubtlessly located in healed fractures as they show no crystallographic control. Size ranges from 5 - 500 µm, F = 90 - 100 %, aqueous L and LV inclusions.

Measured

Secondary inclusions only.

T_f: Inclusion content freezes at -30 to -40 °C to form a clear solid. Freezing is difficult to observe.

T_{ml}: No initial melting is observed.

T_{mf}: Final melting of large, clear crystals with low relief melt at -3.9 to 0 °C. *Ice melting.*

Data sheet VI.8 NC-29b **calcite**

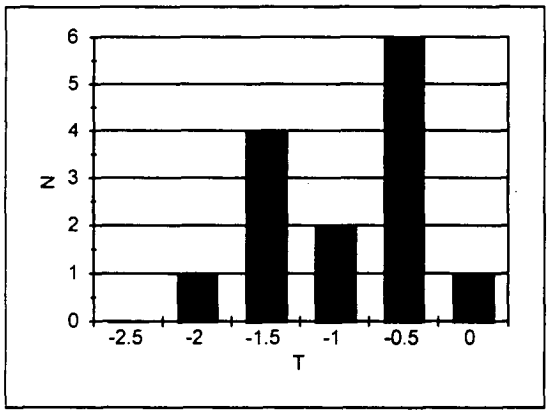

Figure VI.13 T_{mf} histogram, sample NC-29b. N=14, T in °C.

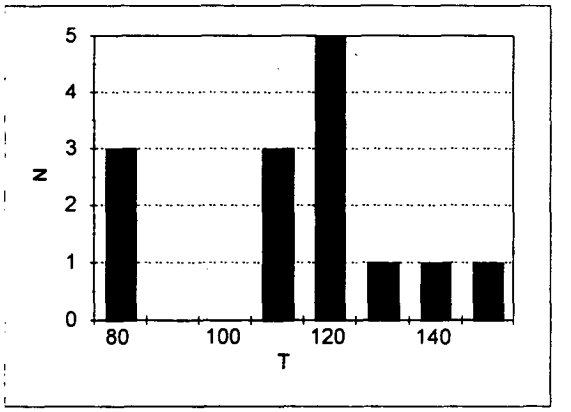

Figure VI.14 T_h histogram, sample NC-29b. N=14, T in °C.

T_{mf} statistics:

Mean:	-0.8 °C
Maximum:	-0 °C
Minimum:	-2 °C

T_h statistics:

Mean:	119 °C
Maximum:	154 °C
Minimum:	81 °C

UNIVERSITY OF JOHANNESBURG

Sample description: Calcspar associated with datolite, ruizite and xonotlite, fills vein surrounded by silicification and ferruginization halo.

Description of fluid inclusion generations:

Primary: Disperse distributed with ellipsoidal to irregular outline. Closely associated with xonotlite needles protruding into calcite. Size: 3 - 5 µm, rarely up to 30 µm, F = 95-100 %, aqueous L and LV inclusions. Indications of leaking and stretching common.

Pseudosecondary: Straight intracrystalline trails of ellipsoidal inclusions in parallel arrangement. Control by cleavage suspected. Size 1-10 µm, F=99-100, aqueous L and LV inclusions.

Secondary: Trails crosscutting grain boundaries. Sigmoidal shape of 1 µm large inclusions, aqueous L inclusions.

Measured

Primary and pseudosecondary inclusions show identical behaviour.

T_f: Inclusion content freezes at -50 to -60 °C to form a clear solid.

T_{m1}: First melting observed only once at -52 °C as 'crazy paving' appeared. *Antarcticite melting.*

T_{m2}: Not observed.

T_{mf}: Final melting of large, clear crystals with low relief at -2 to 0 °C. *Ice melting.*

Data sheet IV.9 WES-332 **calcite**

Table VI.2 Fluid inclusion data for sample WES-332.

N	T_f	T_{m1}	T_{m2}	T_{mf}	T_h
1	-26.5			-1.1	139.8
2				-0.3	
3	-26.6			0.3	80.6
4				0.8	
5				-0.4	

T_{mf} statistics:

Mean: -0.8 °C
Maximum: -0 °C
Minimum: -2 °C

T_h statistics:

Mean: 119 °C
Maximum: 154 °C
Minimum: 81 °C

Sample description: Massive calcspar associated with andradite and clinochlore, fills subhorizontal fracture along the base of the orebody

UNIVERSITY OF JOHANNESBURG

Description of fluid inclusion generations:

Primary: Few scattered primary inclusions. Polygonal rhombohedral or ellipsoidal shape. Size: 5 - 50 μm, F = 95-100 %, aqueous L and LV inclusions.

Secondary: Bended trails along healed fractures protrude from grain boundaries inwards. Extremely elongated inclusions of up to 30 μm length, aqueous L inclusions. Signs of leaking and necking.

Measured

Primary inclusions only.

T_f: Inclusion content freezes at -50 to -60 °C to form a clear solid.

T_{m1}: Not observed.

T_{m2}: Not observed.

T_{mf}: Final melting of large, clear crystals with low relief at -1.1 to 0.8 °C. *Ice melting.*

Data sheet VI.10 LAH-166 **barite**

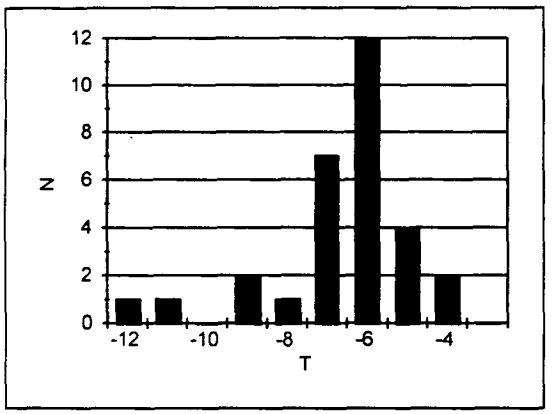

Figure VI.15 T_{mf} histogram, sample LAH-166. N=30, T in °C.

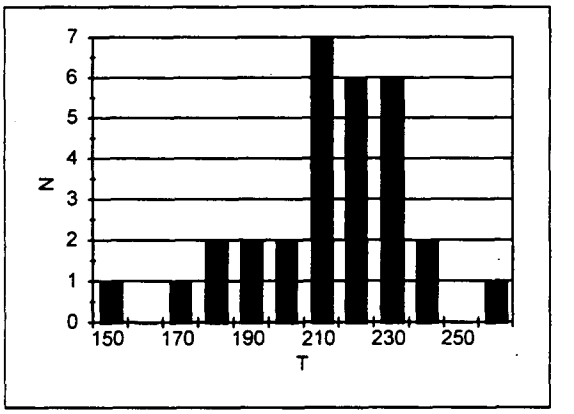

Figure VI.16 T_h histogram, sample LAH-166. N=30, T in °C.

T_{mf} statistics:

Mean:	-6.0 °C
Maximum:	-11.3 °C
Minimum:	-3.6 °C

T_h statistics:

Mean:	218 °C
Maximum:	263 °C
Minimum:	150 °C

UNIVERSITY OF JOHANNESBURG

Sample description: Klipfontein Mine (sample from Transvaal Museum). Coarse crystalline barite intergrown with massive braunite of Woolhaarkop breccia. Many solid inclusions of hematite and psilomelane.

Description of fluid inclusion generations:

Primary: Disperse distributed inclusions of irregular rounded outline. Size: 1-30 µm, F = 98-100 %, aqueous L and LV inclusions.

Secondary: Yield cracks, healed fractures with trails of inclusions. Size 1-5 µm, aqueous L inclusions.

Measured

Primary inclusions only.

T_f: Inclusion content freezes at -70 to -80 °C to form a clear solid. Difficult to observe.

T_{m1}: First melting observed in some inclusions at -47.2 to -52.4 °C as 'crazy paving' appears and inclusion content assumes a brownish colour. *Antarcticite melting.*

T_{m2}: 'Crazy paving' and brownish tint faint as high relief phase melts at -25.2 to -31.2 °C. *Hydrohalite melting.*

T_{mf}: Final melting of large, slightly brownish crystals with low relief at - 3.6 to -11.9 °C. *Ice melting.*

Data sheet VI.11 BEE-211 **barite**

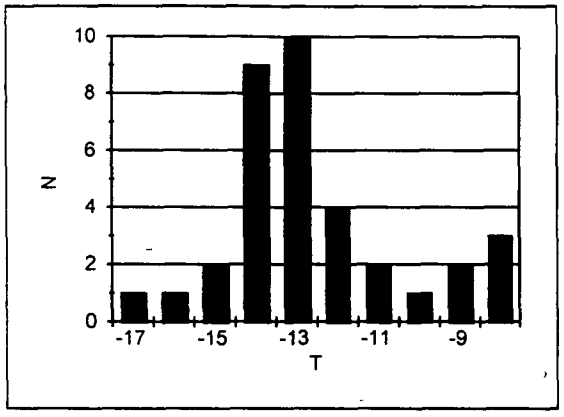

Figure VI.17 T_{mf} histogram, sample BEE-211. N=36, T in °C.

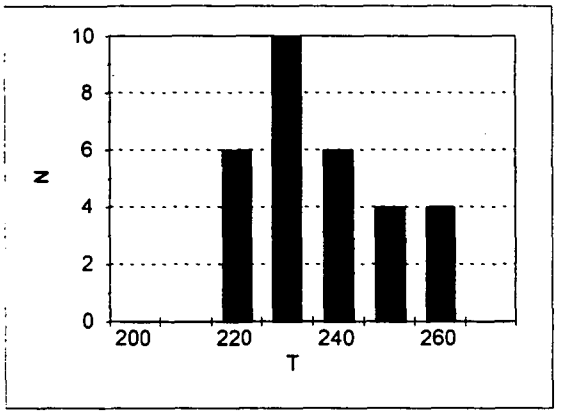

Figure VI.18 T_h histogram, sample BEE-211. N=30, T in °C.

T_{mf} statistics:

Mean:	-11.8 °C
Maximum:	-6.3 °C
Minimum:	-16.9 °C

T_h statistics:

Mean:	242 °C
Maximum:	268 °C
Minimum:	220 °C

UNIVERSITY OF JOHANNESBURG

Sample description: Coarse crystalline barite forms clast-like patches in a lens-like body within the Woolhaarkop breccia. Barite contains hematite and braunite inclusions. Supergene psilomelane.

Description of fluid inclusion generations:

Primary: Abundant, disperse distributed inclusions of irregular rounded shape. Size: 5 -70 µm, F = 90-100 %, aqueous L and LV inclusions. Indications of leaking common in those inclusions with low F.

Pseudosecondary: Straight plains within single grains that carry numerous inclusions. No crystallographic control visible. Inclusions are polygonal (negative crystal shape) or ellipsoidal. Size 2-15 µm, F=95-100%, aqueous L and LV inclusions.

Secondary: Yield cracks, bended trails projecting from grain boundaries inside. Inclusions of irregular, elongated shape. Length up to 5 µm, aqueous L inclusions.

Measured

Primary and pseudosecondary inclusions show identical behaviour.

T_f: Inclusion content freezes at -75.3 to -80.5 °C to form a clear solid. Difficult to observe.

T_{m1}: First melting observed in many inclusions at -56.4 to -47.7 °C as 'crazy paving' appeared and inclusion content assumes a brownish colour. *Antarcticite melting.*

T_{m2}: 'Crazy paving' and brownish tint disappear as high relief phase melts at -23.8 to -27 °C. *Hydrohalite melting.*

T_{mf}: Final melting of large, slightly brownish crystals with low relief at -16.9 to -6.3 °C. *Ice melting.*

Data sheet VI.12 GLO-290 **barite**

Table VI.3 Inclusion data for sample GLO-290.

N	T_f	T_{m1}	T_{m2}	T_{mf}	T_h
1				-14.6	116.8
2					107.4
3				-8.7	114.8
4				-8.8	
5					203.5
6					211.3
7					248.0
8					248.0

T_{mf} statistics:

Mean: -10.7 °C
Maximum: -6.3 °C
Minimum: -16.9 °C

T_h statistics:

Mean: 179 °C
Maximum: 107 °C
Minimum: 248 °C

UNIVERSITY OF JOHANNESBURG

Sample description: Massive barite lens, located on the contact between dolomite and ferruginous manganese ore. Surrounded by Ba-rich wad.

Description of fluid inclusion generations:

Primary: Rounded inclusions occur disperse, but also in parallel arranged trails within barite grains. Size: 1-10 µm, F = 98-100 %, aqueous L and rarely LV inclusions.

Secondary: Yield cracks, bended trails projecting from grain boundaries inside. Inclusions of irregular, elongated shape. Size less than 5 µm, aqueous L inclusions.

Measured

Primary inclusions only.

T_f: Not observed.

T_{m1}: Not observed.

T_{m2}: Not observed.

T_{mf}: Final melting very difficult to observe. First sudden movement of vapour bubble was assumed to be an indication for completed melting.

Data sheet VI.13 LOH-293 **barite**

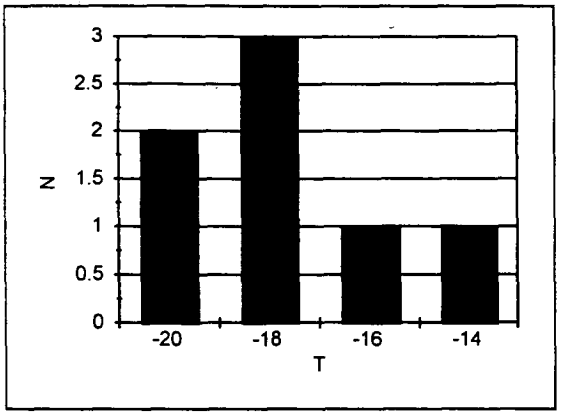

Figure VI.19 T_{mf} histogram, sample LOH-293. N=7, T in °C.

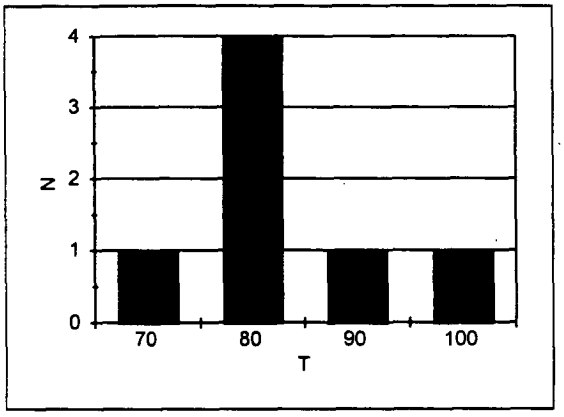

Figure VI.20 T_h histogram, sample LOH-293. N=9, T in °C.

T_{mf} statistics:

Mean:	-16.5 °C
Maximum:	-13.5 °C
Minimum:	-28.9 °C

T_h statistics:

Mean:	84 °C
Maximum:	102 °C
Minimum:	69 °C

UNIVERSITY JOHANNESBURG

Sample description: Massive barite lens with small aggregates of botryoidal hematite, surrounded by Ba-rich wad in proximity to contact of dolomite and ferruginous manganese ore.

Description of fluid inclusion generations:

Primary: Abundant, disperse distribution of inclusions having ellipsoidal to irregular rounded shape. Size: less than 5 μm, F = 98-100 %, aqueous L and rarely LV inclusions.

Pseudosecondary: Short, diffuse trails of ellipsoidal inclusions within single grains. Size smaller than 2 μm, aqueous L inclusions.

Measured

Primary inclusions only.

T_f: Not observed.

T_{m1}: Not observed.

T_{m2}: Strong melting occurs at -22.4 to -29.2 °C. Very difficult to observe. *Hydrohalite melting.*

T_{mf}: Bubble in some inclusions moves suddenly at -18.9 to -13.5 °C. Very difficult to observe. *Ice melting.*

Data sheet VI.14 KAP-297

barite

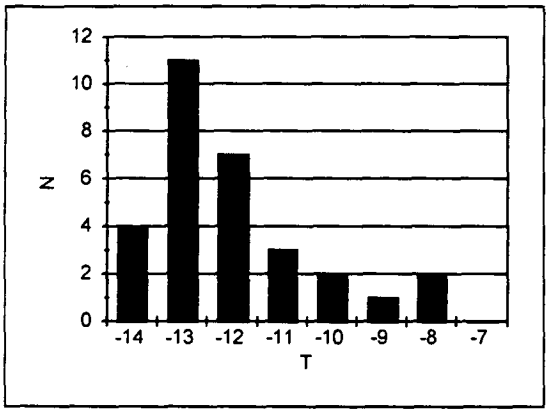

Figure VI.21 T_{mf} histogram, sample KAP-297. N=30, T in °C.

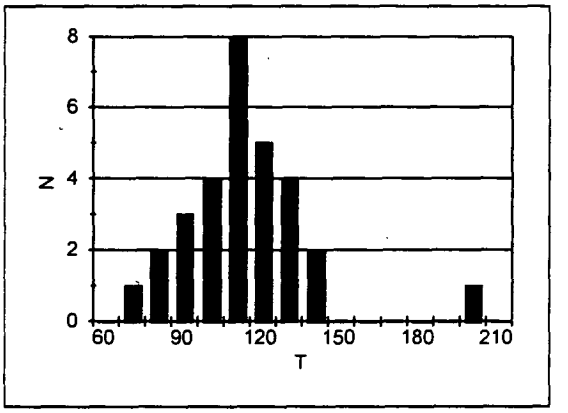

Figure VI.22 T_h histogram, sample KAP-297. N=30, T in °C.

T_{mf} statistics:

Mean:	-11.6 °C
Maximum:	-7.5 °C
Minimum:	-13.9 °C

T_h statistics:

Mean:	117 °C
Maximum:	207 °C
Minimum:	74 °C

UNIVERSITY OF JOHANNESBURG

Sample description: Thin vein along fault plane filled by green diaspore, illite and coarse barite. Fault dislocates two blocks of hematitized conglomeratic iron ore.

Description of fluid inclusion generations:

Primary: Abundant, disperse distribution of inclusions having irregular rounded or ellipsoidal shape. Size: 1 -10 μm, F = 95-100 %, aqueous L and rarely LV inclusions. Indications of leaking in those inclusions with low F.

Pseudosecondary: Short, bended trails of minute inclusions of ellipsoidal shape within single grains. Size less than 2 μm, aqueous L inclusions.

Measured

Primary inclusions only.

Tf: Freezing of inclusion content difficult to observe, at about -60 to -70 °C to form a clear solid.

Tm1: First melting observed in many inclusions at -55.3 to -53.4 °C as 'crazy paving' appears and inclusion content assumes a brownish colour. *Antarcticite melting.*

Tm2: 'Crazy paving' and brownish tint disappear as high relief phase melts at -22 to -20.5 °C. Only few observations. *Hydrohalite melting.*

Tmf: Final melting of large, slightly brownish crystals with low relief at -13.9 to -7.8 °C. *Ice melting.*

Data sheet VI.15 JAP-302 **barite**

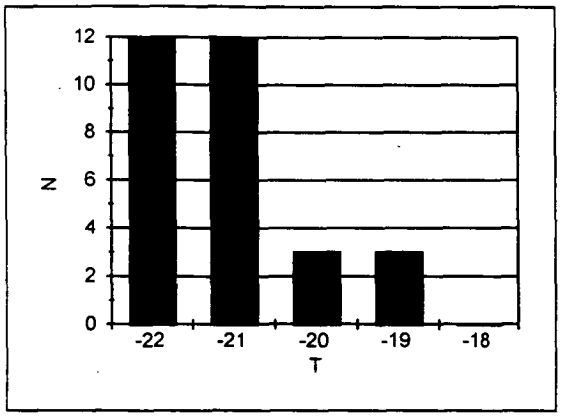

Figure VI.23 T_{mf} histogram, sample JAP-302. N=30, T in °C.

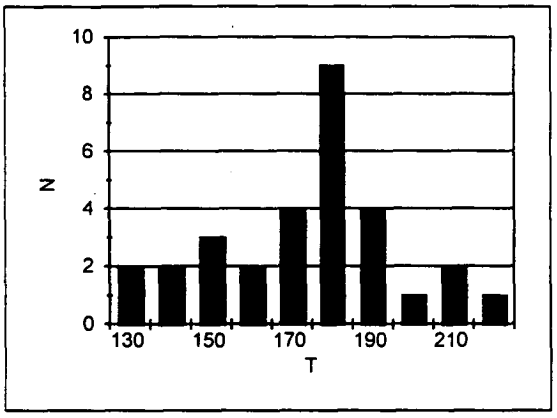

Figure VI.24 T_h histogram, sample JAP-302. N=30, T in °C.

T_{mf} statistics:

Mean:	-20.7 °C
Maximum:	-18.1 °C
Minimum:	-21.9 °C

T_h statistics:

Mean:	179 °C
Maximum:	228 °C
Minimum:	131 °C

UNIVERSITY OF JOHANNESBURG

Sample description: Sample of massive barite from lens-like barite deposit on Japiesrust. Barite lens located on Blackridge thrust plane.

Description of fluid inclusion generations:

Primary: Inclusions are all orientated in short, straight trails that are commonly parallel orientated. Very dense population of inclusions with ellipsoidal shape. Size: 1-5 µm, F = 98-100 %, aqueous L and rarely LV inclusions.

Pseudosecondary: Distinction from primary inclusions is impossible.

Measured

Primary (and pseudosecondary ?) inclusions only.

T_f: Freezing of inclusion content at -71.2 to -75.6 °C to form a clear solid.

T_{m1}: First melting observed in many inclusions at -48.9 to -49.9 °C as 'crazy paving' texture appears. *Antarcticite melting.*

T_{m2}: 'Crazy paving' disappears slowly as high relief phase melts. No definite temperature determination. *Hydrohalite melting.*

T_{mf}: Final melting of large crystals with low relief at -18.1 to -21.9 °C. *Ice melting.*

Appendix VII

Fault controlled metasomatic alteration of Early Proterozoic sedimentary manganese ores in the Kalahari manganese field, South Africa

(published in: Economic Geology, 90, 823-844, 1995)

J. Gutzmer and N. J. Beukes

Abstract

Low-grade Mamatwan-type sedimentary manganese ore has been upgraded to high-grade Wessels-type ore in the Kalahari manganese field. The alteration appears to be of hydrothermal (metasomatic) origin closely related to zones of ferruginization (hematitization) developed along major north-south and minor east-west trending normal faults and fractures. The faults and fractures appear to have acted as channelways for the hydrothermal fluid causing metasomatic alteration of the manganese ore.

The manganese ores display a very consistent zonation from zones of ferruginization along faults to unaltered sedimentary manganese ore in the cores of fault blocks. This zonation is as follows: Least altered Mamatwan-type sedimentary ore, finely laminated, and composed of finely intergrown braunite and Ca-Mn carbonates with minor hematite and abundant carbonate ovoids. Parallel to normal faults and zones of ferruginization the ore has been sequentially altered to braunite (II) - braunite (new), bixbyite - hausmannite and hausmannite-rich ore. Immediately adjacent to zones of ferruginization a second stage of braunite-rich ore has been developed. The high-grade ore appears porous and massive and original sedimentary bedding is obliterated.

The formation of high-grade ore appears to be related to a process of silica and carbonate leaching from sedimentary protore by hydrothermal fluids. In proximity to the feeder channels for the hydrothermal fluids the manganese ore was replaced by hematite. Some of the manganese was reprecipitated to form very high-grade (>50 wt % Mn) manganese ore immediately adjacent to zones of ferruginization. During waning stages of hydrothermal fluid flow, silica and some calcium carbonate leached from sedimentary manganese ore apparently reprecipitated close to and within the fluid channelways. This led to the formation of a secondary stage of braunitic manganese ore

UNIVERSITY OF JOHANNESBURG

developed as a transition between zones of ferruginization and high-grade hausmannite-rich ore. At the same time zones of ferruginization became calcified and some rare silicate minerals were formed.

Introduction

The Kalahari manganese field, situated some 60 km northwest of Kuruman in the Northern Cape Province, South Africa (Fig. 1), is the largest known land-based manganese deposit with an estimated resource of 13 billion metric tons of ore with grades varying from 20-48 wt % Mn (Taljaardt, 1982).

However, of this resresource only approximately 2.75 percent, i.e. 360 million tons is of high grade, > 40 wt % Mn content (Taljaardt, 1982). The high-grade ore is derived from hydrothermal alteration of a low-grade sedimentary precursor ore (Kleyenstüber, 1984; Miyano and Beukes, 1987) interbedded with iron-formation of the Early Proterozoic Hotazel Formation of the Transvaal Supergroup. Zones of iron-enrichment (ferruginization) intersect the high-grade ore.

UNIVERSITY OF JOHANNESBURG

Controls on the processes of hydrothermal upgrading of low-grade sedimentary ore and ferruginzation of high-grade ore are poorly understood. In addition the effect of ferruginization on the mineral composition of the high-grade ore is unknown. The aim of this study was to establish a model for the origin of ferruginization through detailed study of mineral paragenesis, and to investigate possible links between ferruginization and alteration of primary sedimentary manganese ore to high-grade ore. A petrographic-geochemical study was undertaken across several zones of ferruginization, and along a traverse in which low-grade sedimentary manganese ore grades laterally into high-grade manganese ore (Gutzmer and Beukes, 1993; Gutzmer, 1993).

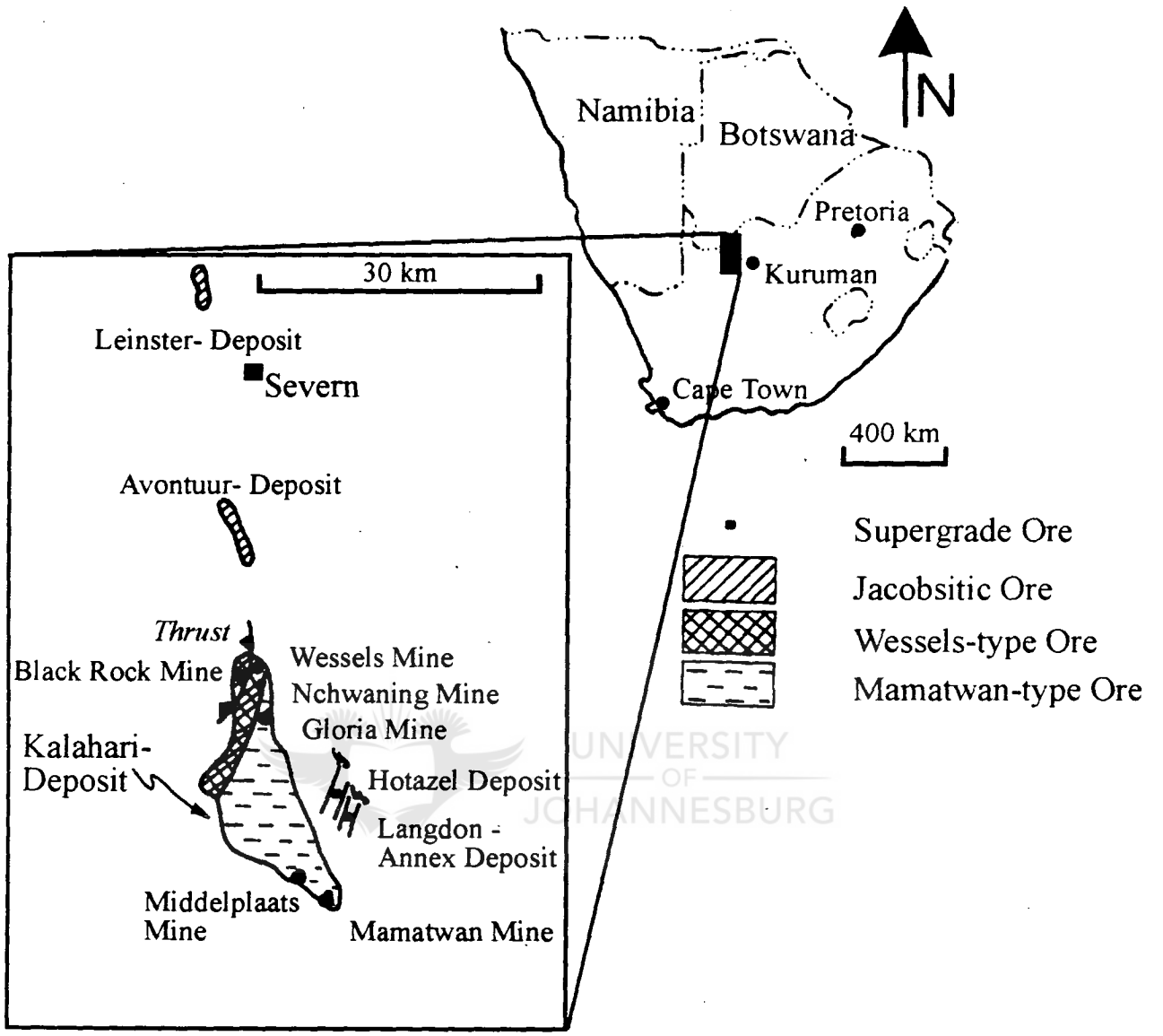

Figure 1: Regional map of the Kalahari manganese field showing the location of five erosionally preserved deposits and the distribution of thrusting, major normal faulting, and ore types and location of mines (modified after Nel et al., 1986).

Regional Geology

The Kalahari manganese field comprises five known deposits of which the braunitic Kalahari deposit is by far the largest and of greatest economic importance measuring some 35 km x 15 km in dimension (Fig. 1). Small high-grade deposits at Hotazel and Langdon-Annex (Fig. 1) have been

mined out. Manganese beds in the Leinster and Avontuur deposits are jacobsitic in composition (Fig. 1), of low-grade and contain no economically viable reserves.

The Kalahari manganese deposits represent structurally preserved erosional relicts of the manganese-bearing Hotazel Formation below younger cover of late Palaeoproterozoic Olifantshoek red beds, late Carboniferous-early Permian Dwyka diamictite of the Karoo Supergroup and Tertiary Kalahari beds. Virtually all the deposits are covered by these younger sequences and natural outcrops

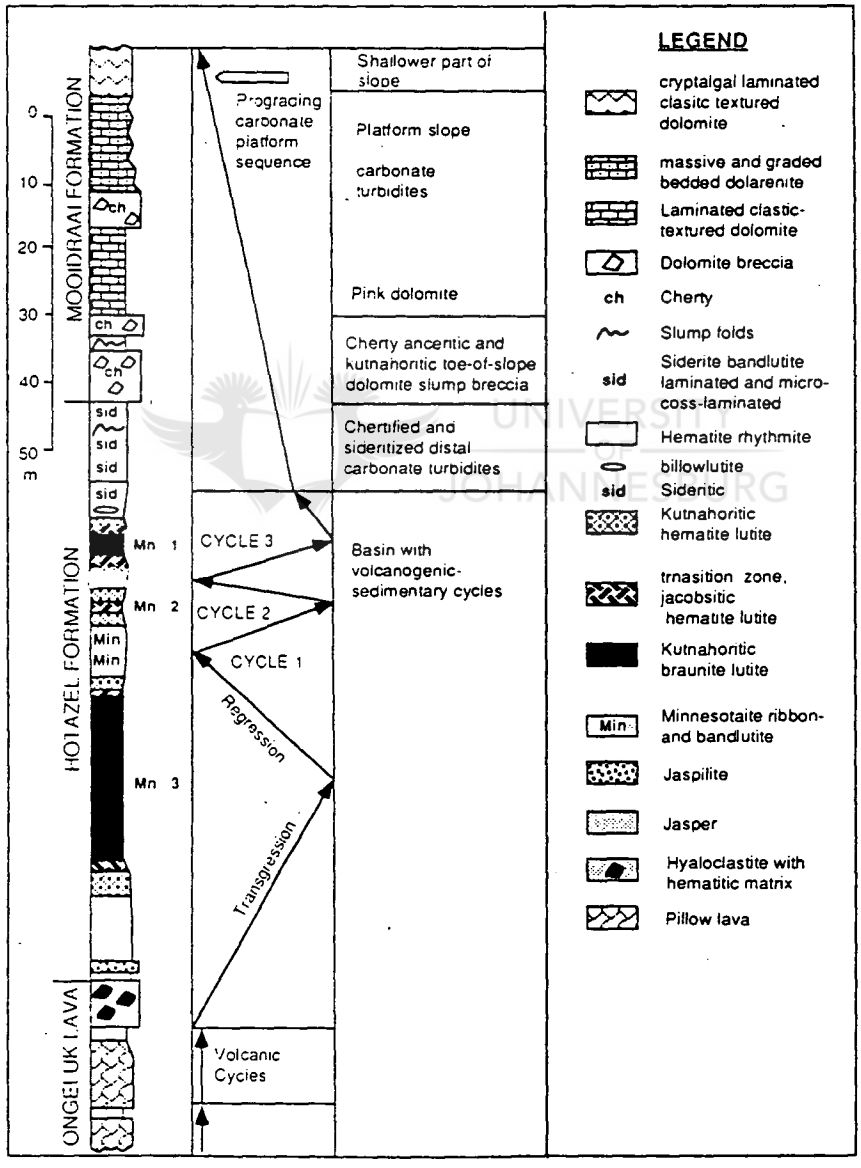

Figure 2: Type profile of the Hotazel and Moodraai Formations showing the stratigraphic setting of the three manganse ore units interbedded with iron-formation. Note the cyclical repetition of lithofacies in the Hotazel Formaation and the jaspilites interbedded with hyaloclastite and pillow lava of the Ongeluk Formation (modified after Nel et al., 1986). Abbreviations: ch = chlorite, min - minnesotaite, sid - siderite.

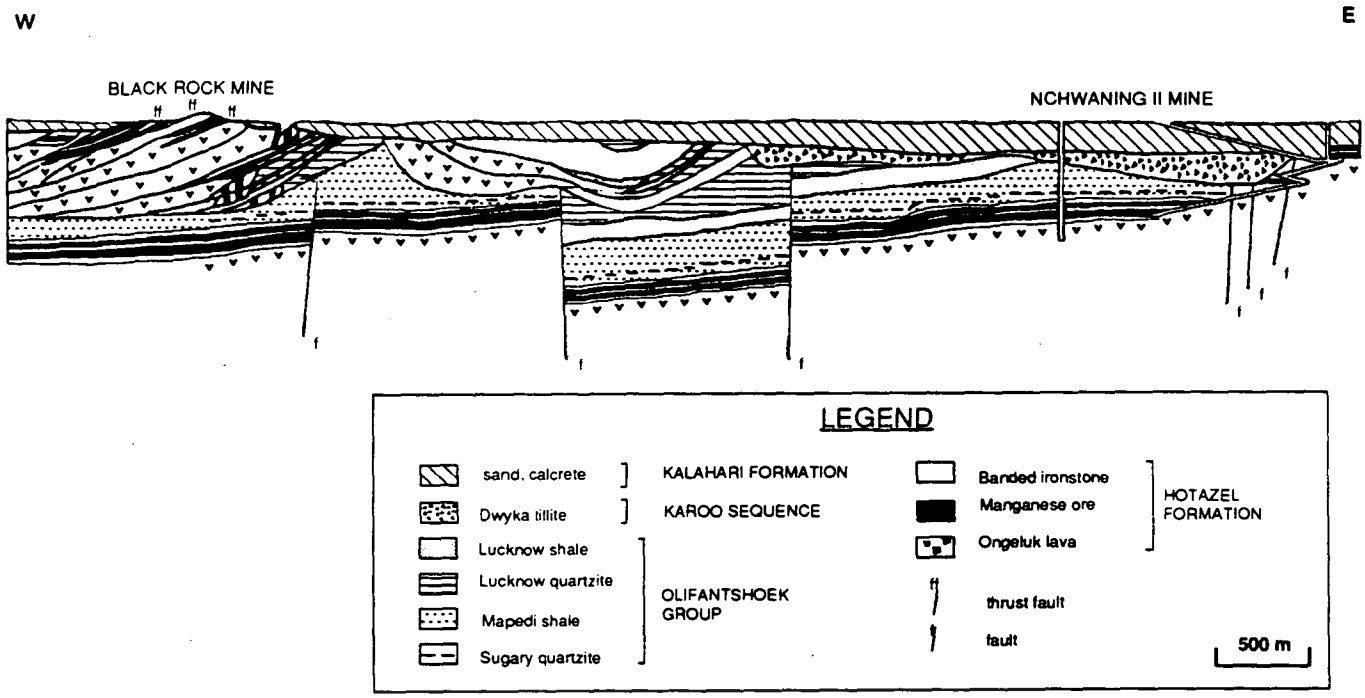

Figure 3: Cross section through the Black Rock and Nchwaning mines showing stratigraphic setting and location of the two mines (modified after AMMOSAL, 1992).

are restricted to Black Rock, a small hill near Hotazel, at what is now Black Rock Mine (Fig. 1).

The manganese-bearing Hotazel Formation is conformably underlain by pillow lava, hyaloclastite and jaspilite of the Ongeluk Formation and overlain by Mooidraai dolomite (Fig. 2). Three manganese beds are present in the Hotazel Formation, each forming the center of three symmetrical iron-formation – hematite lutite – braunite lutite sedimentary cycles (Fig. 2). Virtually all manganese ore reserves and production come from the lower manganese bed which reaches a maximum known thickness of about 45 m at Mamatwan Mine and ranges between 4 - 8 m in the Wessels and Nchwaning mining areas (Fig. 1). The upper manganese bed has been mined locally where it reaches a thickness of up to 4 m. The central manganese bed is of no economic significance, being on average less than 1 m thick (De Villiers, 1970).

In the Kalahari deposit strata dip gently to the west at about 8°. However, near the western margin of the deposit, Ongeluk lava and Hotazel Formation have been duplicated by thrusting from the west (Fig. 3) (Boardman, 1941; Beukes and Smit, 1987). The sequence has also been affected by a series of north-trending normal faults. These faults post-date deposition of the overlying late

Palaeoproterozoic Olifantshoek red beds, but pre-date the thrust event (Fig. 3). Thrusting is related to formation of the Kheiss orogen some 1700 - 1800 m.y. ago (Stowe, 1986; Beukes and Smit, 1987).

Distribution of Major Ore Types and Zones of Ferruginization

Two major types of ore are present in the Kalahari deposit, namely low-grade sedimentary Mamatwan-type ore and high-grade hydrothermally altered Wessels-type ore (Kleyenstüber, 1984). Mamatwan-type ore is a diagenetic to very low grade metamorphic carbonate-bearing braunitic manganolutite with a manganese content of 30 - 39 wt %. Some units in this ore bed average up to 38.4 wt % Mn (Table 1). The ore is typically microcrystalline, laminated and composed of finely intergrown braunite, hematite, kutnahorite and manganocalcite with small concretionary ovoids of manganese-bearing calcite.

Table 1: Comparison of average chemical compositions of Wessels-type ore from the Nchwaning mine and Mamatwan-type ore from the Gloria mine (in wt %, AMMOSAL, 1992)

	Wessels-type ore	Mamatwan-type ore
Mn	51.0	38.4
Fe	10.5	5.0
SiO_2	3.8	5.9
CaO	0.4	3.3
MgO	n.d.	0.3

In contrast, high-grade Wessels-type ore is carbonate-poor and coarse crystalline. It is derived from alteration of Mamatwan-type ore. Major ore minerals are braunite II, braunite (new) (term coined by Kleyenstuber (1984) for a member of the braunite group defined by textural and compositional characteristics, however not a mineral species recognized by the IMA commission on new minerals), bixbyite and hausmannite. The manganese content may be as high as 51 wt % on average (Table 1). Preservation of original sedimentary structures range from good to absent in Wessels-type ore.

Transitions from Wessels-type ore to low grade Mamatwan-type ore may be sharp or gradational. Main ore and gangue minerals of the Kalahari manganese fields are listed in Table 2.

Table 2: Mineral encountered in this study. Names and chemical composition. Abbreviations from Fig. 9a-h

Mineral (abbreviation)	Chemical formula
Hematite (he)	$Fe_2^{3+}O_3$
Specularite (sp)	$Fe_2^{3+}O_3$ (coarse recrystallized hematite)
Braunite (br)	Mn^{2+} (Mn, Fe)$_6^{3+}SiO_{12}$
Braunite II (br 2)	$Ca_{0.5}$(Mn, Fe)$_7^{3+}Si_{0.5}O_{12}$
Braunite (new) (br n) [1]	$Ca_{0.34}$(Mn, Fe)$_6^{3+}Si_{0.34}O_{10}$
Bixbyite (bx)	(Mn, Fe)$_2^{3+}O_3$
Hausmannite (hs)	$Mn^{2+}Mn_2^{3+}O_4$
Manganite (mn)	$Mn^{3+}OOH$
Marokite (ma)	$CaMn_2^{3+}O_4$
Calcite (cc)	$CaCO_3$
Kutnohorite	$CaMn^{2+}(CO_3)_2$
Manganocalcite	(Ca, Mn^{2+})CO_3
Barite	$BaSO_4$
Sr barite	(Ba, Sr)SO_4
Gaudefroyite	$Ca_4Mn_{3-4}^{3+}[(CO_3)(O, OH)_3(BO_3)_3]$
Quartz	SiO_2
Andradite	$Ca_3Fe_2^{3+}[SiO_4]_3$
Datolite	$CaBSi_4(OH)$
Pectolite	$NaCa_2Si_3O_8(OH)$
Xonotlite	$Ca_6Si_6O_{17}(OH)_2$
Aegirine-augite	(Na, Ca) (Fe^{3+}, Fe^{2+}, Mn, Mg)Si_2O_6
Mn richterite	Na_2Ca(Mg, Mn, Fe)$_5[(OH)_2/Si_8O_{22}]$
Clinochlor	(Mg, Fe^{2+})$_{10}Al_2[(OH)_{16}/Si_6Al_2O_{20}]$

Abbreviations from Figure 9a–h

[1] Braunite (new) is not a mineral recognized by the IMA; however, it has been observed and described by Kleyenstüber (1984) and was given a separate name by him due to its characteristic skeletal texture and consistent composition

Wessels-type ore appears to be restricted to the northwestern part of the Kalahari deposit in the area of thrust duplication and normal faulting of strata (Fig. 1). Kleyenstüber (1985) suggested that formation of the high-grade ore was related to the process of thrust deformation. However, this is also an area of relatively intense deformation by north-trending normal faults and a possible link between these faults and formation of high-grade ore and/or ferruginization needs to be investigated. Such an investigation is of economic importance, because it is known that the formation of high-grade ores in the Hotazel and Langdon-Annex deposits are related to the system of north-trending normal faults bounding these deposits (De Villiers, 1970; Miyano and Beukes, 1987).

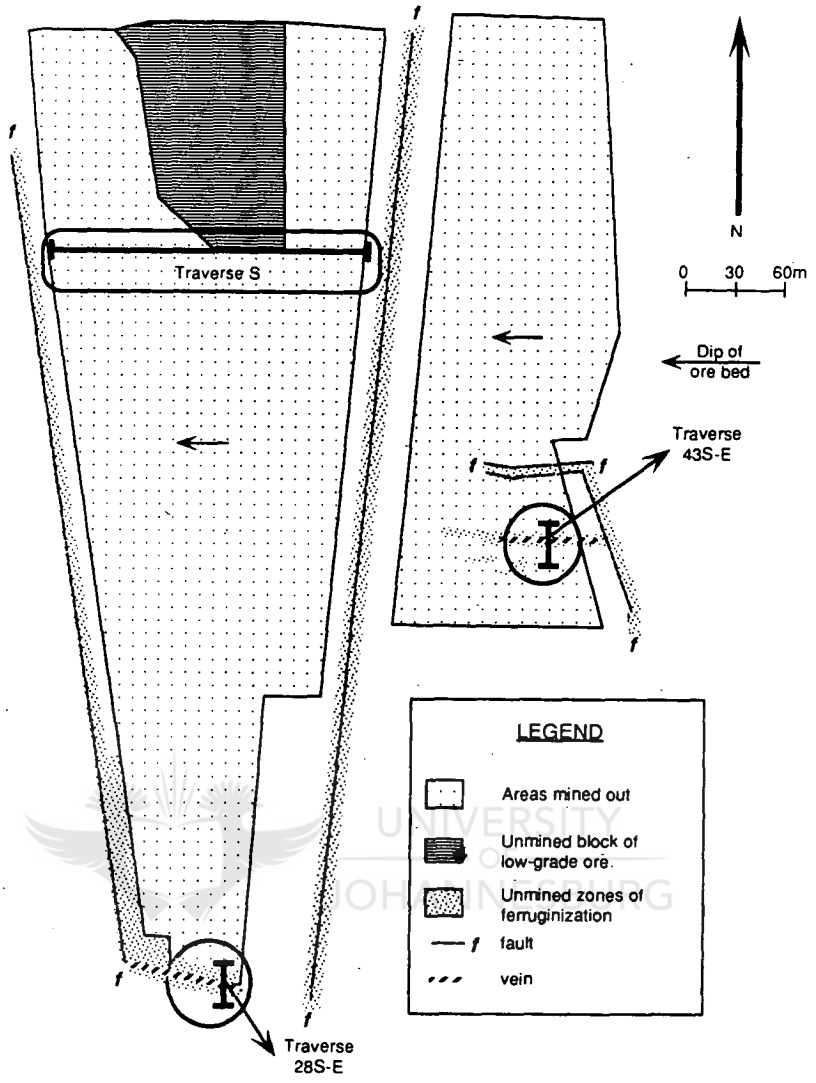

Figure 4: Simplified stope plan of sampling area at the Nchwaning mine showing sampled traverses in relation to blocks of low-grade ore placed centrally within blocks of high-grade ore restricted by zones of ferruginization along normal faults and veins.

Underground room and pillar mining of high-grade ores of the lower manganese bed takes place at Nchwaning Mine up to a depth of 400 m below surface. The simplified stope plan of an area mined at Nchwaning (Fig. 4) illustrates a relationship between normal faulting, zones of ferruginization and the distribution of high-grade Wessels-type ore versus low-grade Mamatwan-type ore. Mining practice is to exploit only the highest-grade ores with manganese contents close to 50 weight percent and a Mn/Fe ratio above 4.8. Mined-out ore blocks indicating high-grade ore, are elongated in a north-south direction parallel to the system of normal faults. Ore immediately alongside north-south

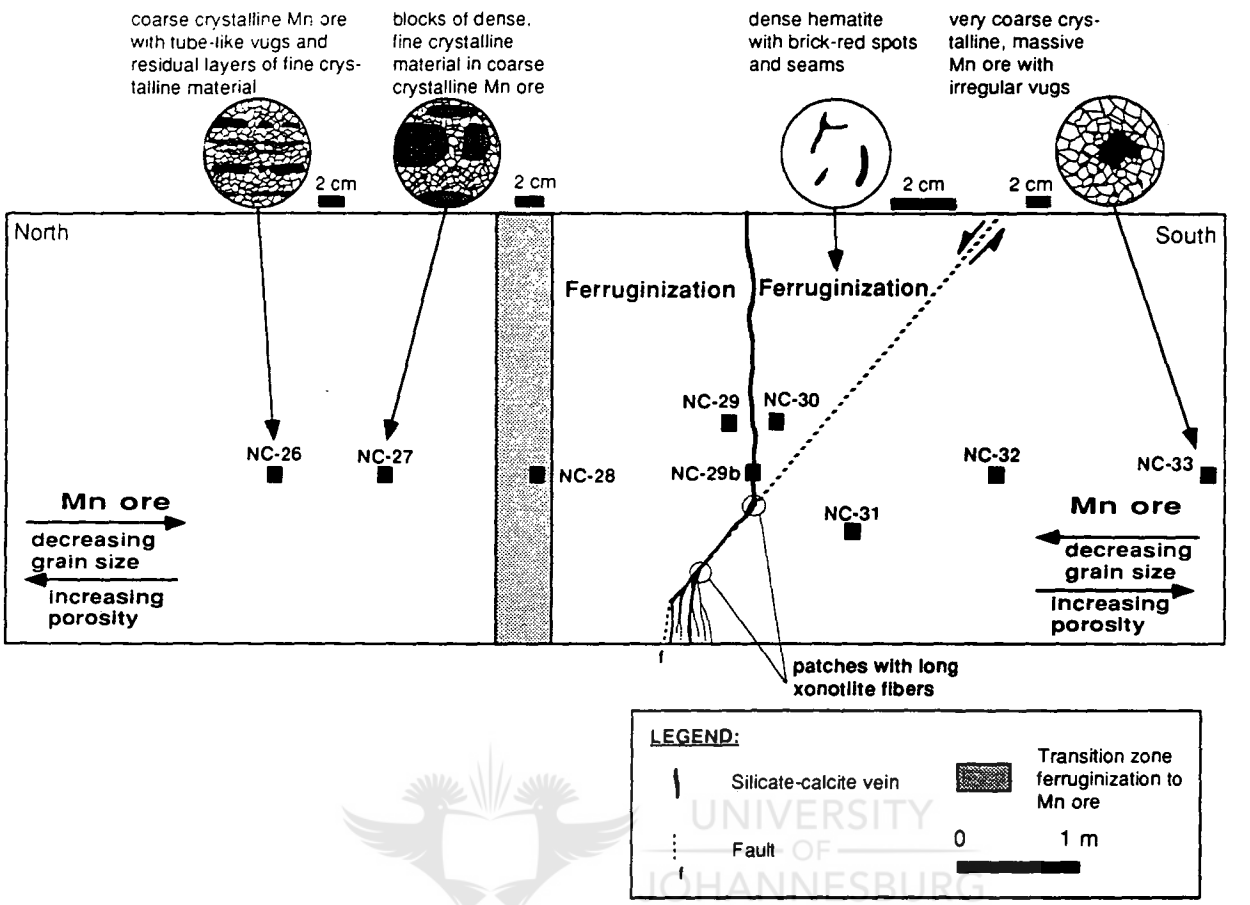

Figure 5: Traverse 43S-E, stope map and sample positions.

trending faults is not mined due to high iron contents i.e. ferruginization. In contrast, relicts of low-grade Mamatwan-type ore are preserved in the core of some fault blocks. Highest-grade ore appears to be developed intermediate between zones of ferruginzation along normal faults, and relicts of Mamatwan-type ore in the central part of fault blocks (Fig. 4, traverse S).

A second, less well pronounced, direction of ferruginization is associated with a system of east-west trending minor faults and veins (Fig. 4, traverse 28S-E, traverse 43S-E). North-south trending zones of ferruginization may be in the order of a few tenths of meters wide and more than a kilometer long. In contrast the east-west trending zones of ferruginization are only in the order of a few meters wide and have been traced along strike lengths of up to 200 m.

Sampling

Samples were taken at Nchwaning Mine in north-south traverses across two typical east-west trending zones of ferruginization i.e. traverse 43S-E (Fig. 5) and traverse 28S-E (Fig. 6). Another set of samples came from an east-west traverse covering different ore types between two zones of ferruginization associated with north-south trending normal faults (traverse S, Fig. 7). Because vertical variations are present in the mineralogical composition of precursor Mamatwan-type ore (Nel et al., 1986), samples were taken at approximately constant level in the manganese ore bed i.e., 1.5 - 1.7 m above the floor of stopes.

In traverse 43S-E (Fig. 5) and traverse 28S-E (Fig. 6) the zones of ferruginization are composed of

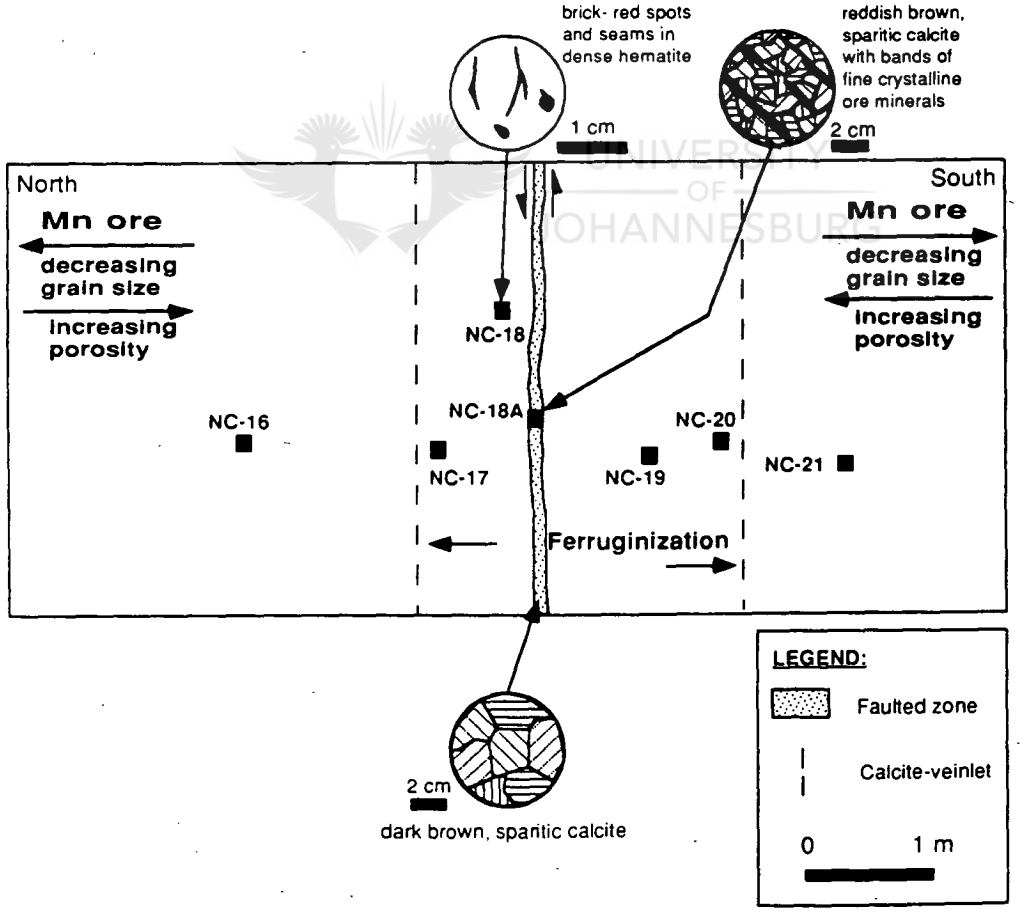

Figure 6: Traverse 28S-E, stope map and sample positions.

microcrystalline dense steel-grey hematite with minor brick-red spots and seams of calcite intergrown with the hematite. In traverse 43 S-E dense silicate-hematite rock is present in the ferruginized areas (Fig. 8a). The ferruginized zone in traverse 43S-E is centered by a 1-3 cm wide vein filled by a complex Ca-Mn-silicate-carbonate mineral assemblage, with patches of long xonotlite fibers. The vein is displaced by a small reverse fault (Fig. 5). The silicate-hematite mineral assemblage grades laterally into dense, very fine grained and massive manganese ore with semi-metallic greyish-brown colour, a brownish tint and irregular strings of hematite. In turn this ore grades laterally, away from the zone of ferruginzation, into coarse crystalline, massive manganese ore of metallic lead-grey colour. Grain size and porosity increase away from the zone of ferruginization (Fig. 5).

A coarse-grained, irregularly banded hematite-rich calcspar body, associated with a fault, is developed in the central part of the ferruginized zone of traverse 28S-E (Fig. 6). The massive hematite associated with this fault grades laterally into very coarse-grained metallic lead-grey manganese ore with high porosity. Further outwards the grain size of the manganese ore decreases, the porosity diminishes and the massive texture grades into ore with 'residual' sedimentary lamination.

UNIVERSITY OF JOHANNESBURG

In traverse S, ferruginized ore flanking normal faults, could not be sampled due to lack of underground exposure (Fig. 7). However in this traverse high-grade manganese ore types are symmetrically distributed relative to a central core of low-grade ore (Samples NC-1a-10 and NC-1a-11, Fig. 7). The low-grade ore is composed of laminated micro-crystalline

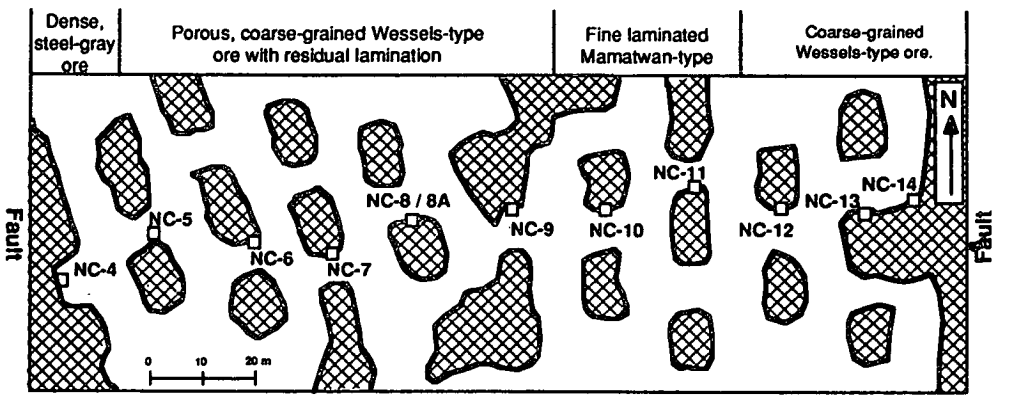

Figure 7: Traverse S, stope map and sample positions. Hatched areas are sidewalls and pillars, blank areas are mined out.

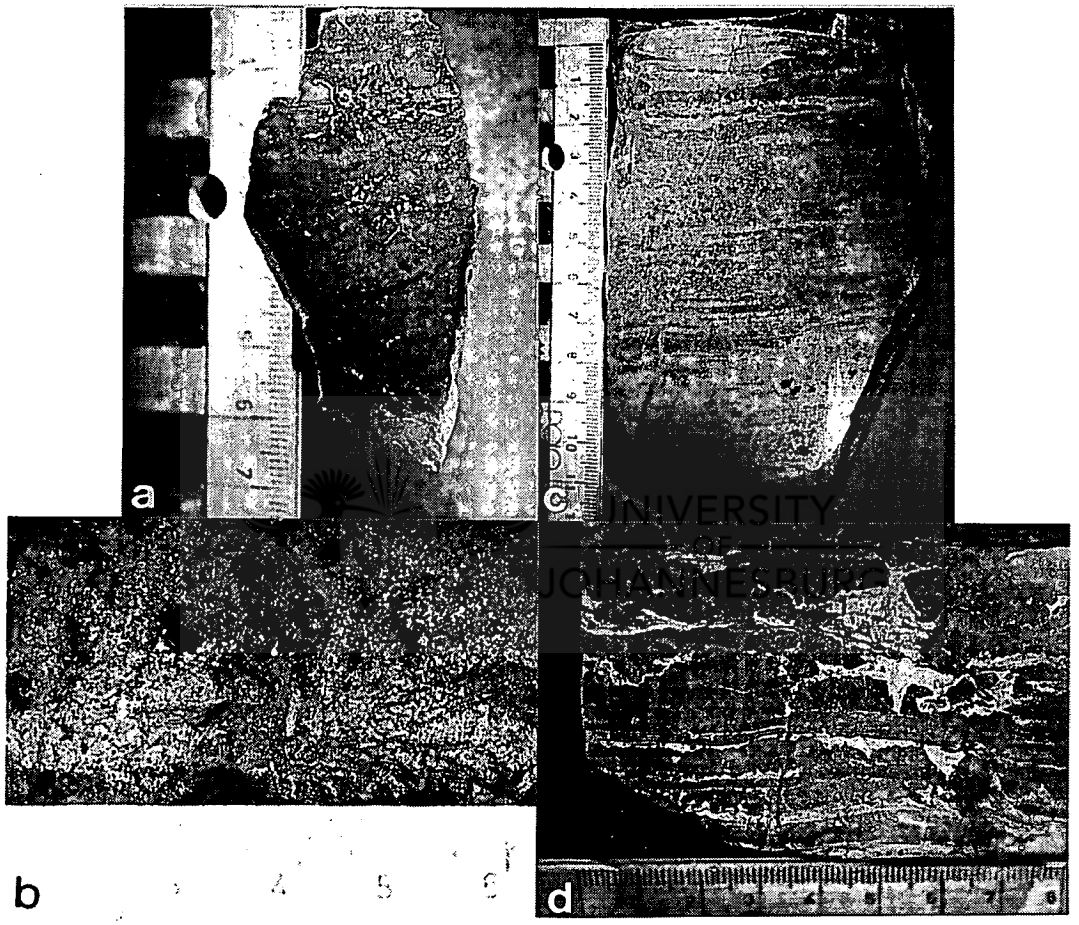

UNIVERSITY OF JOHANNESBURG

Figure 8: a. Ferruginized and strongly silicified wallrock of calc-silicate vein. White streaks and pods consist of pectolite and quartz, red matrix of densely intergrown ailicates and hematite (NC-1b-29b). b. Very coarse crystalline hausmannite ore (NC-1b-33). c. Example of residual layering. Discontinuous, fine crystalline braunite II-braunite (new) laminae in coarse crystalline hausmannite-marokite-specularite matrix (NC-1a-6). d. Irregular aggregates of dense hematite (light gray) replacing coarse crystalline hausmannite along bedding planes (NC-1a-14).

braunite-carbonate ore with abundant millimeter-sized carbonate ovoids. This ore grades to the east and west into porous and vuggy coarse grained ore which is either massive or displays

residual sedimentary lamination (Fig. 8c). Pores and vugs are filled or partly filled by calcspar or Sr-barite. At the western end of the traverse, in proximity to the ferruginized ore zone, the manganese bed is composed of very dense fine grained and massive ore with a semi-metallic greyish-brown colour (sample NC-1a-4, Fig. 7). The eastern end of the traverse S is characterized by very coarse crystalline porous ore with metallic lead-grey colour and irregular aggregates of massive hematite (sample NC-1a-14, Fig's. 7 and 8d). Samples 4 and 14 therefore resemble ore types found immediately adjacent to the ferruginized zones in traverses 43S-E and 28S-E respectively.

Mineralogical Variations

Mineralogical variations along the three traverses, as determined by X-ray Diffraction (XRD) and microscopic analysis of samples, are summarized in Table 3. In both traverses 43S-E and 28S-E there appears to be a consistent symmetrical lateral variation in mineralogical composition of manganese ores relative to central zones of ferruginization. Samples from the zone of ferruginization are essentially composed of hematite with associated sparitic calcite in traverse 28S-E. However, in traverse 43 S-E an assemblage of quartz, Mn-richterite, pectolite and aegirine-augite is associated with the hematite. The zone of ferruginization in traverse 43 S-E is bordered by massive dense manganese ore composed of braunite with subordinate hausmannite, hematite, andradite and clinochlore. These braunite-rich zones, on either side of the zone of ferruginization are bordered by zones composed of hausmannite - braunite II ore and are in turn flanked by ore composed essentially of hausmannite (Table 3). In traverse 28S-E the ferruginized zone grades laterally into manganese ore composed of hausmannite with traces of braunite (new), grading into virtually pure hausmannite ore. One of the hausmannite-rich samples contains abundant bixbyite (Table 3).

Traverse S provides insight into mineralogical variations from unaltered sedimentary protore into zones of high-grade ore adjacent to ferruginized faults. On the western side of the traverse, sample NC-1a-4, in proximity to a zone of ferruginization, is composed of massive braunite-rich ore similar to that bordering the zone of ferruginization in traverse 43S-E (Table 3). This sample thus provides

Table 3: Mineralogical composition of samples along traverses.

	Traverse S												Traverse 28S-E							Traverse 43S-E							
	W	Samples NC-1a										E	N	Samples NC-1b					S	N	Samples NC-1b						S
Mineral	4	5	6	7	8	8a	9	10	11	12	13	14	16	17	18a	18	19	20	21	26	27	28	29	29b	30	31	32	33
Braunite	XXX					XX		XXX	XXX							X						XXX				XXX		
Braunite II		XXX	XX	XX	XX	XX	XXX	X	X												XXX						X	
Braunite (new)		XXX	XXX		XX		XX														X							
Bixbyite				X	X					XX	XX		XX															
Hausmannite	X	XX	X	X	XX	X		X	X	XX	XXX	XXX	XXX	XXX		X		XXX	XXX		XXX	XXX				X	X	
Marokite			XXX	XXX	XX	X																						
Manganite			XX	X	XX	X		X		XX	XX																	
Hematite	XX	X	X	X	X			XX	XX	X	X		X	X	XXX	XXX	XXX	X	X		X	X	XXX	XXX	XXX	XX	X	
Specularite	X	X	X	X						X	X	X	X	X				X	X	X	X						X	X
Microsparite								XXX	XXX																			
Calcspar	X		X				X	X		X					XX	XXX	X						XX					
Quartz																							XX		XX			
Brucite																												
Gaudefroyite		X			X		X			X				X														
Gypsum																												
Sr barite											X			X					X									
Andradite															X	X	X					X				X		
Pectolite																							XX		XX			
Acmite																							XX		XX			
Mn richterite																							XX		XX			
Clinochlore												X		X		X		X	X			X				X		
Orthoclase																							X		X			
Ore type	G	F	C	C	C	C	B	A	A	D	D	E	D	E	H	H	H	E	E	E	F	G	HS		HS	G	F	E

Composition: XXX = dominant (>30%), XX = important (10–30%), X = subordinate (1–10%), I = trace (<1%) Ore type: A = braunite-calcmicrospar, B = braunite II-braunite (new), C = braunite II-marokite-hausmannite-manganite, D = bixbyite-hausmannite, E = hausmannite, F = hausmannite-braunite II, G = braunite, H = hematite-sparitic calcite, HS = hematite-quartz-silicate

UNIVERSITY OF JOHANNESBURG

a link between the zone of ferruginization in traverse 43S-E and the mineralogical variation towards Mamatwan-type ore. Similar to the situation in traverse 43S-E, the western-most braunite-rich sample in traverse S is flanked, to the east, by ore composed of hausmannite, braunite II and braunite (new). To the east of this (samples NC-1a-6, 7 and 8), marokite and manganite are prominent in association with hausmannite, braunite II and braunite (new). Immediately adjacent to the area of Mamatwan-type ore, samples are composed of braunite II and braunite (new) with minor braunite (Table 3).

Towards the east of the central core of Mamatwan-type ore in traverse S, sample NC-1a-14, most proximal to the zone of ferruginization, is essentially composed of hausmannite, partly replaced by hematite. This sample is similar in composition to the hausmannite-rich samples bordering the zone of ferruginization in traverse 28S-E. A link is thus provided between the zone of ferruginization on the eastern side of traverse S and Mamatwan-type ore in the central core. This central core of Mamatwan-type ore is separated from the hausmannite-rich ore of sample NC-1a-14 by ore composed of hausmannite with abundant bixbyite and manganite (Table 3). The central area of Mamatwan-type ore is composed of microcrystalline braunite and microsparitic calcite with subordinate hematite, braunite II, hausmannite and sparitic calcite (Table 3).

Laterally, from zones of ferruginization to areas of Mamatwan-type ore, nine main types of ore are thus developed. These could be defined as i) braunite-calcmicrospar, ii) braunite II-braunite (new), iii) braunite II-marokite-hausmannite-manganite, iv) hausmannite-bixbyite, v) hausmannite, vi) hausmannite-braunite II, vii) braunite, viii) hematite-calcspar, ix) hematite-silicate ores (Table 3).

Petrographical Variations

Western Side of Traverse S

On the western side of traverse S lateral variation from Mamatwan-type braunite-calcmicrospar ore through braunite II-braunite (new) and braunite II-marokite-manganite-hausmannite ore into braunite ore is present.The braunite-calcmicrospar ore (samples NC-1a-10 and 11, Table 3) is typically very fine crystalline, dense and laminated. Laminae are in the order of 1 mm thick and defined by variations in the ratio of ore minerals to calcmicrospar. This ratio fluctuates between approximately

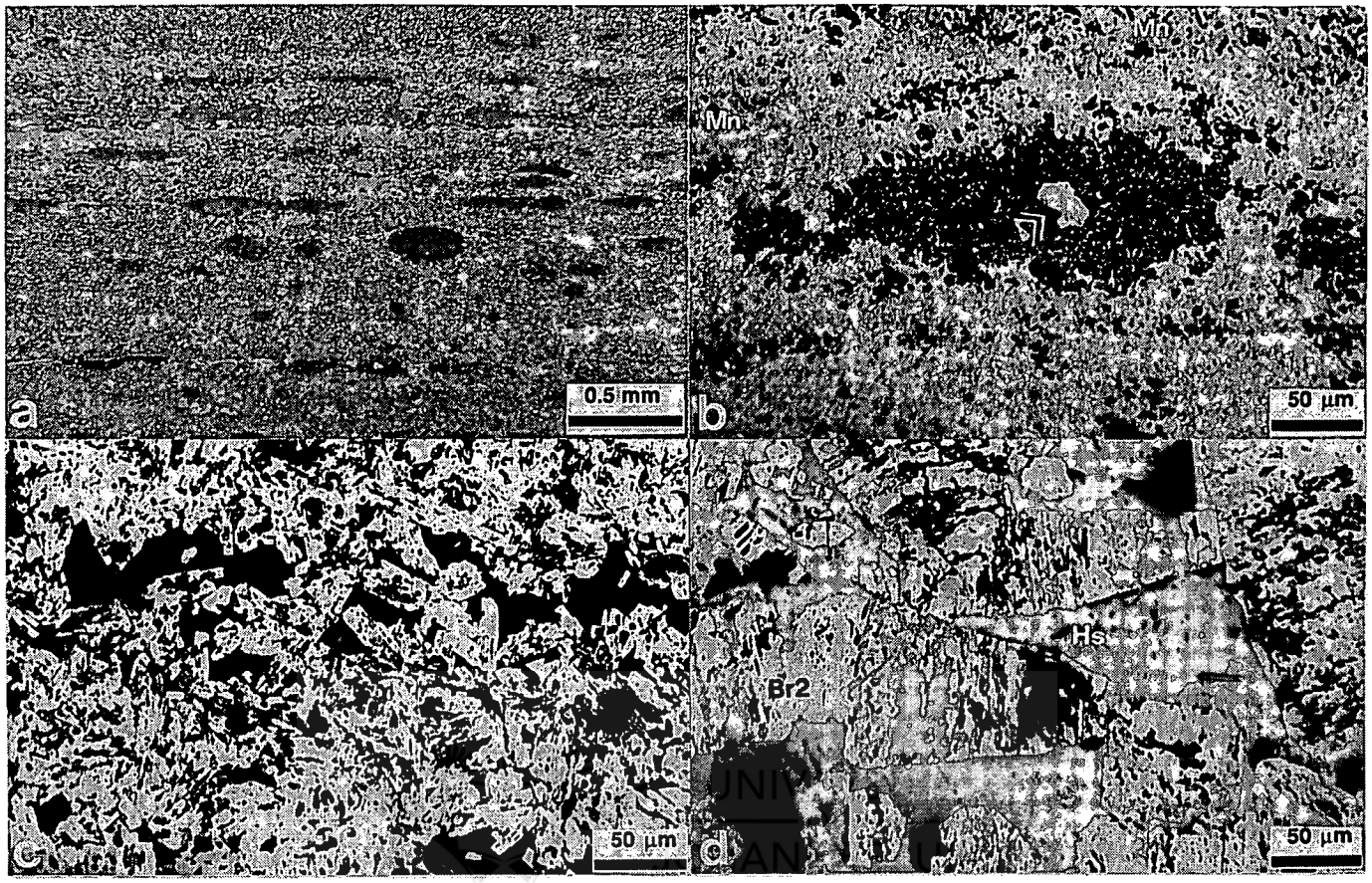

Figure 9: Reflected light photomicrographs. a.Least altered ore. Fine crystalline braunite-hematite (both light-gray) and calcite (dark gray) matrix, finely laminated and with numerous lensoidal calcite seams and ovoids. b. Subhedral, coarse crystalline hausmannite (arrow) in ovoid replacing caalcite. Surrounding matrix consists of very fine crystalline anhedral braunite (gray), hematite (white), calcite (black) and aggregates of secondary manganite (Mn, dark gray) (oil immersion). c. Skeletal prisms of braunite (new) form a very porous intergrowth in highly altered ore (oil immersion). d. Remnants of euhedral braunite II (Br 2) bipyramids replaced by anhedral hausmannie (Hs) (oil immersion).

4:1 in ore-rich laminae to 2:3 in calcmicrospar-rich laminae. Numerous calcite ovoids, from 0.2 to 1 mm in diameter, are present especially in ore-rich bands (Fig. 9a). The braunite-calcmicrospar is composed of finely intergrown anhedral braunite, calcite and minor hematite (5-10 vol %). Braunite and calcmicrospar grains are typically in the order of 5 µm in diameter and hematite grains between 1 and 3 mm in diameter. Braunite II, in aggregates about 100 - 200 µm in size, replaces the braunite-calcmicrospar-hematite assemblage locally. The braunite-calcmicrospar ore preserved along traverse S closely resembles typical sedimentary Mamatwan-type ore in sedimentary structures,

texture and mineral assemblage. However, there are some important differences like the absence of kutnahorite which has been replaced by calcite intergrown with braunite, the presence of secondary porosity especially along calcmicrospar-rich laminae, and also higher manganese concentrations at the expense of the carbonate content (see below). However, this type of least altered ore has still been named Mamatwan-type ore throughout this study.

The braunite-calcmicrospar Mamatwan-type ore of traverse S grades laterally towards the west into braunite II-braunite (new) ore (sample NC-1a-9 and 8a, Table 3). This ore is more porous than the braunite-calcmicrospar ore and composed of finely intergrown braunite II and braunite (new). Sedimentary lamination is preserved but now defined by differences in porosity and concentrations of braunite II and braunite (new). Braunite II-rich laminae, apparently developed after original braunite-rich laminae, are more coarse grained than the adjacent braunite (new)-rich laminae. Grain sizes of braunite II are in the order of 50 - 150 mm, while those of braunite (new) are in the order of 20 - 50 mm. The braunite II-rich laminae are dense with little porosity. In contrast, laminae rich in braunite (new), apparently representing original calcmicrospar-rich laminae, are composed of a porous intergrowth of skeletal prismatic braunite (new) crystals (Fig. 9c), and minor braunite II. It is interesting to note that all calcmicrospar and hematite have been replaced by braunite II and braunite (new).

UNIVERSITY OF JOHANNESBURG

The braunite II-braunite (new) ore grades laterally into brauniteII-marokite-manganite- hausmannite ore (samples NC-1a-5 to 8, Table 3). This ore displays rather poor preservation of sedimentary lamination in a massive recrystallized matrix. Residual sedimentary lamination is poorly defined by horizontal seams of braunite II and braunite (new), enclosed and replaced by a very coarse grained assemblage of marokite, manganite and hausmannite (Fig. 9d). Replacement is most intense in sample NC-1a-5 and declines rapidly towards NC-1a-7 and NC-1a-8a (Table 3). The replacement mineral assemblage crosscuts sedimentary bedding, eliminating it and resulting in recrystallized massive and dense marokite ore with grain sizes between 50 and 150 μm.

In sample NC-1a-7, corroded and porous secondary bixbyite crystals, up to 0.5 mm in diameter, are replaced by anhedral marokite grains (Fig. 9e). Subordinate manganite and hausmannite with minor specularite may fill interstices between marokite grains. In all these samples marokite, manganite, hausmannite and rarely bixbyite contain small hematite inclusions. It is important to note that in

some samples euhedral crystals of marokite and braunite II grow into secondary vugs. These vugs may further be filled by specularite (definition of use of terms hematite specularite in Table 2). This is an indication of a second stage of formation of braunite II, marokite and hematite. The late phases of braunite II, marokite and hematite become more abundant towards the fault zone on the west side of traverse S.

The braunite ore developed at the western end of traverse S (sample NC-1a-4) is composed of a massive dense mosaic-textured intergrowth of subhedral 10 to 30 µm sized braunite crystals in association with specularite (the latter comprising up to 20 vol %) and minor hausmannite. Small

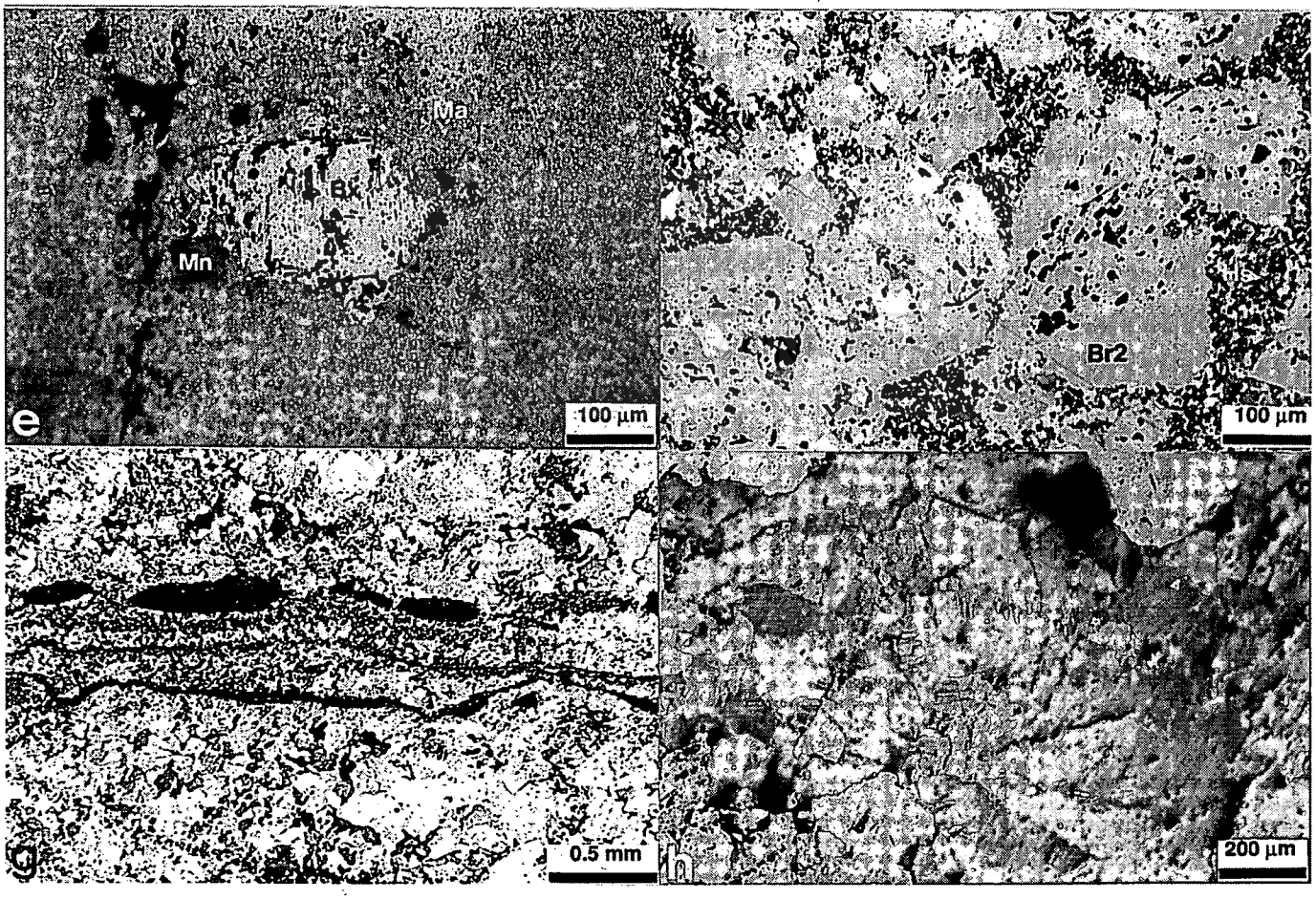

Figure 9 (cont.) e. Large bixbyite crystal (Bx) massively replaced by surrounding marokite (Ma) and manganite (Mn). f. Pseudocubic braunite II crystals (Br II) along grain boundaries and irregular replaced by fine crystalline hausmannite (Hs, strong anisotropy) and minor hematite (white) (oil immersion, crossed nicols). g. Coarse crystalline, massive intergrowth of hausmannite with horizontally elongated vugs indicating residual layering. h. Coarse crystalline, massive intergrowth of hausmannite with serrated grain boundaries and fine lamellar twinning.

amounts of andradite and sparitic calcite may fill interstitial pores between braunite and specularite grains. The ore is massive except for some faint banding caused by enrichment of hematite or andradite along certain bands. In some cases, cube- and brick-shaped pseudomorphs are preserved in the matrix of braunite. The pseudomorphic outlines may well represent remains of large bixbyite crystals observed in adjacent braunite II-marokite-manganite-hausmannite ore. They are up to 200 μm large and defined by a highly porous intergrowth of subhedral to euhedral braunite crystals.

Ovoids in the Mamatwan-type braunite-calcmicrospar ore (Fig. 9a) are filled by sparitic calcite, poikilotopically enclosing small braunite crystals. Relatively large subhedral hausmannite crystals, up to 100 μm in diameter, may be developed within these ovoids (Fig. 9b). Such hausmannite has also been observed in unaltered diagenetic Mamatwan-type ore from Mamatwan Mine (Nel et al., 1986). In contrast original manganese bearing calcite ovoids have been replaced by massive braunite II in the braunite II - braunite (new) ore. Ovoids in braunite II - marokite - manganite - hausmannite ore are rimmed by massive braunite II and filled by coarse crystalline hausmannite, manganite and marokite with cores of sparitic calcite poikilotopically including braunite II. No ovoids are preserved in the massive braunite ore at the western end of traverse S.

Scarce minerals such as gaudefroyite, and gangue components such as Sr-barite and sparitic calcite fill veinlets, vugs and secondary pores. In one case, sample NC-1a-6, small brucite fibers occur in association with calcite. In the braunite ore of sample NC-1a-4, at the western end of traverse S, andradite and calcite fill pore spaces.

Eastern Side of Traverse S

The braunite-calcmicrospar ore of traverse S is flanked to the east by vuggy coarse crystalline bixbyite-hausmannite ore (Table 3). This ore, represented by samples NC-1a-12 and 13, is mainly composed of pseudocubic euhedral to subhedral bixbyite grains. Hausmannite, gaudefroyite and specularite fill interstitial space and secondary vugs between bixbyite crystals. In sample NC-1a-12 anhedral manganite, in aggregates of up to 0.5 mm in diameter, encloses euhedral hausmannite grains, up to 50 μm large. Manganite also replaces bixbyite and in such cases contains small rounded inclusions of hematite. Some of the bixbyite crystals display atoll structures i.e., replacement of crystal cores by very fine crystalline porous intergrowth of manganite, hausmannite and minor

hematite. Other bixbyite crystals are microfractured and display a corroded grain shape. The coarse crystalline bixbyite-rich matrix of sample NC-1a-13 is also invaded by 10 - 50 μm wide subhorizontal seams of fine crystalline anhedral hematite (grain size up to 10 μm) in association with minor sparitic calcite and gypsum.

The bixbyite-hausmannite ore grades further to the east into hausmannite ore. This ore is composed of a massive intergrowth of coarse crystalline anhedral hausmannite grains, up to 0.5 mm in length, and minor interstital specularite. Small interstitial pores and vugs are preferentially concentrated along horizontal bands, leading to a residual layered appearance. The hausmannite ore is locally invaded and replaced by patches of very fine crystalline hematite.

Traverse 28S-E

Traverse 28S-E displays the transition from coarse crystalline hausmannite ore, with faint residual sedimentary lamination (samples NC-1b-16 and 21), through massive hausmannite ore (samples NC-1b-17 and 20), into a central zone of ferruginzation i.e., hematite-calcspar ore of samples NC-1b-18 and 19 (Table 3). At the northern end of the traverse the residual laminated hausmannite-rich ore contains bixbyite and can be classified as bixbyite-hausmannite ore. The transition from bixbyite-hausmannite ore into massive hausmannite ore is almost identical to that on the eastern end of traverse S described above.

In the bixbyite-hausmannite ore (NC-1b-16) anhedral hausmannite, in a porous intergrowth of 10 to 200 mm large crystals, replaces euhedral to subhedral bixbyite crystals, up to 200 μm in diameter. Residual bixbyite appears in single grains or small aggregates isolated in the hausmannite. Microfractures in the bixbyite crystals are filled by hausmannite and the margins of bixbyite grains appear corroded. The residual lamination results from laminae composed of a fine crystalline porous intergrowth of anhedral hausmannite, specularite and clinochlore (grain size below 50 μm) alternating with laminae composed of densely intergrown hausmannite with grain size varying between 0.1 and 2 mm. The large hausmannite crystals carry small rounded inclusions of hematite. Contacts between laminae are gradual. Sample NC-1b-21, at the southern end of traverse 28S-E, is similar in texture to NC-1b-16 but it contains no bixbyite.

The massive hausmannite ore immediately adjacent to the zone of ferruginization (samples NC-1b-17 and 20, Table 3) is composed of very coarse crystalline and densely intergrown hausmannite crystals with grain size up to 2 mm (Fig. 9h) containing rounded inclusions of hematite.

Horizontally elongated vugs are common in the hausmannite ore (Fig. 9g). They indicate residual sedimentary lamination. The vugs are lined by small euhedral hausmannite crystals and filled by calcite, specularite and clinochlore. Microfractures and small veinlets, filled with mineral assemblages similar to those forming vug fills, crosscut the hausmannite-rich ores.

The fault in traverse 28S-E is filled by a hematite-calcspar assemblage, composed of sparitic calcite poikilotopically enclosing hematite associated with minor braunite, hausmannite, andradite and clinochlore. The sparitic calcite forms up to 1 mm large anhedral grains. The hematite forms needle-shaped subhedral grains, 1-5 μm long and sometimes forms globular shaped aggregates (sample NC-1b-18a).

Crosscutting stringers and patches of sparitic calcite are present in the massive hematite of the ferruginization zone around the fault (NC-1b-18, NC-1b-19). It is associated with 10-60 μm large andradite crystals and fine fibrous clinochlore.

UNIVERSITY JOHANNESBURG

Traverse 43S-E

The distribution of ore types in traverse 43S-E is symmetrical around the central zone of ferruginization (Table 3). Very coarse to coarse grained and porous hausmannite ore, either massive or with vague residual sedimentary lamination, grades laterally into coarse grained porous hausmannite-braunite II ore with residual sedimentary lamination, in turn grading into massive dense braunite ore and a central zone of massive fine-crystalline hematite-quartz-silicate rock. The center of the traverse, sample NC-1b-29b, is formed by a vein filled by calcspar and various silicate minerals.

The hausmannite ore consists of massively intergrown anhedral hausmannite grains, each about 0.1 to 1.5 mm large. The hausmannite is free of hematite inclusions but minor specularite occurs as interstitial pore fill.

The hausmannite-braunite II ore of sample NC-1b-27 and NC-1b-32 is composed of a massive equigranular intergrowth of subhedral braunite II grains, 200 - 500 μm long, that are partly replaced by hausmannite. All stages of replacement of braunite II grains by hausmannite are present. The initial stage is represented by braunite II grains corroded and surrounded by a rim of porously intergrown, rather small, anhedral hausmannite grains (Fig. 9f). The result is massive hausmannite with small hematite inclusions (Fig. 9h). Rare specularite occurs as interstitial pore fill.

A mosaic-textured intergrowth of 20 to 50 μm large braunite polygons is characteristic for the ore adjacent to the zone of ferruginization (samples NC-1b-28 and 31, Table 3). Up to 500 μm large cube- to brick-like pseudomorphic outlines, perhaps after hausmannite or bixbyite, are filled by a porous intergrowth of braunite, andradite and minor specularite. The dense braunite matrix may locally be replaced by subhedral hematite needles (up to 5 μm long) associated with andradite and clinochlore.

Vugs in the manganese ores of traverse 43S-E may be lined or filled by hausmannite. In some cases these hausmannite crystals are corroded and overgrown by specularite. Other vugs are filled by gaudefroyite and clinochlore. In the braunite ore, next to the zone of ferruginization, vugs may be rimmed by euhedral braunite and filled by andradite, specularite and hausmannite.

The ferruginized zone in traverse 43S-E is composed of very irregular and inconsistent bands and areas of steel-grey fine grained massive hematite, surrounded by a wine-red fine crystalline hematite-quartz-silicate matrix with irregular white to cream coloured spots and veins of silicate minerals. The massive hematite bands are made up by a very dense intergrowth of platy specularite grains, 1 - 50 μm in diameter, enclosing zoned idiomorphic secondary quartz grains, defined as quartz I, that are up to 300 μm large. Anhedral dark honey-brown aegirine-augite, defined as aegirine-augite I, is typically developed as reaction rims along the contact between quartz I crystals and specularite.

The wine-red hematite-quartz-silicate matrix consists of quartz II as anhedral grains up to 100 μm, potassium feldspar, aegirine-augite, a Na-Ca-Mn amphibole and pectolite. Aegirine-augite associated with quartz II is light yellow in colour and defined as aegirine-augite II.

The silicate-carbonate vein, in the center of the ferruginized zone, is composed of sparitic calcite and Ca-silicates (xonotlite and datolite).

Table 4: Selected electron microprobe analyses of various manganese oxides (data in wt %).

	Braunite NC10-2/1	Braunite NC15b-1	Braunite II NCS-1/4	Braunite II NC27-1/1	Braunite (new) NC6-4/3	Bixbyite NC13-2/1	Hausmannite NC27-2/1	Manganite NCS-1/2	Marokite NC6-4/1
SiO_2	9.81	8.41	5.13	4.90	2.49		0.01	0.01	
TiO_2		0.01			0.02	0.04	0.04		
Al_2O	0.07	0.02	0.22	0.07	0.24	0.41	0.05	0.04	0.04
Fe_2O^1	4.08	2.68	13.5	15.2	19.1	20.9	3.60	0.41	0.04
Mn_2O_3	76.8	80.5	75.6	73.9	74.6	75.07	64.2[3]	89.7	73.6
MnO	5.50	6.21				0.36	30.6		
MgO	0.26	0.12	0.20	0.03	0.26	0.36	1.37		
CaO	3.47	1.95	4.87	4.52	2.57	0.07	0.03	0.07	26.6
BaO			0.04	0.21	0.33	0.07	0.05	0.07	0.08
H_2O^2						0.05		9.70	
Total	100.1	99.9	99.6	98.8	99.6	98.1	100.0	100.0	100.4

[1] Total Fe calculated as Fe_2O_3
[2] H_2O by difference
[3] Data have been recalculated to balance MnO and Mn_2O_3 according to Kleyenstüber (1984)

Mineral Chemistry

Representative electron-microprobe analyses of manganese oxides and some silicates are listed in Tables 4 and 5 respectively. Generally speaking mineral compositions remain rather constant independent of the manganese ore type. A strong inverse correlation exists between silica and iron in the braunite - bixbyite group. SiO_2-content decreases from close to 10 wt % in braunite (theoretical maximum) to bixbyite containing no silica. In contrast the Fe_2O_3 content increases from about 4 wt % in braunite to 20 wt % in bixbyite. Calcium is only a minor impurity in bixbyite but comprises about 5 wt % in braunite II and 3 wt % in braunite (new). The ternary SiO_2-Fe_2O_3-CaO diagram (Fig. 10) indicates a virtually complete range of compositions between the end members braunite and bixbyite, also showing the composition of the Ca end member of the braunite-bixbyite group, neltnerite. This confirms the results of De Villiers and Buseck (1989), who proposed a polysomatic layered model for the different minerals in the braunite-bixbyite group.

UNIVERSITY JOHANNESBURG

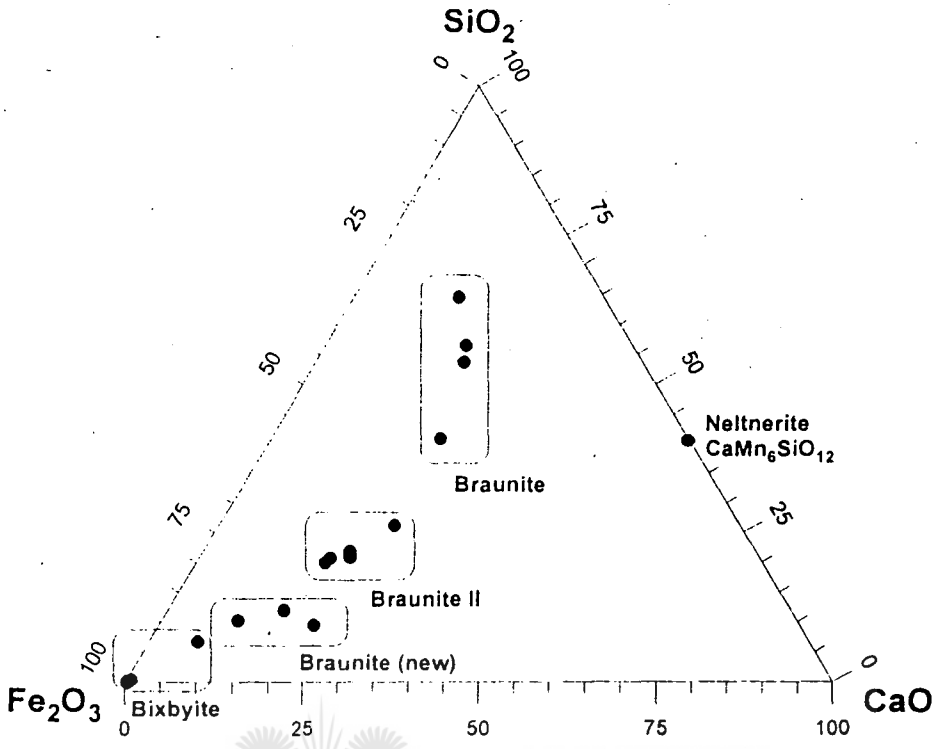

Figure 10: Ternary plot SiO_2-Fe_2O_3-CaO of electron microprobe analyses of minerals belonging to the braunite-bixbyite group. Note the positions of the Ca-rich endmember neltnerite $CaMn_6^{3+}SiO_{12}$ and braunite $Mn^{2+}Mn_6^{3+}SiO_{12}$.

Hausmannite has chemical compositions close to that of the ideal formula (Table 4). Main impurities are MgO (0.1 - 4.31 wt %) and Fe_2O_3 (0.4 - 8.3 wt %), bound into the lattice in place of Mn^{2+} and Mn^{3+} (Roy, 1981), respectively (Table 4). The compositions of manganite, and marokite are close to that of their ideal stoichiometric composition (Table 4).

All garnet grains analysed proved to be andradite with Al_2O_3 contents below 3 wt % and MnO concentrations at 4 - 5 wt % (Table 5). The mean formula for the garnet is $(Ca_{5.5\text{-}6}Mn^{2+}_{0.2\text{-}0.6},Mg_{0.01\text{-}0.2})(Fe_{3.3\text{-}3.7},Al_{0.2\text{-}0.5})[Si_6O_{24}]$. Garnet of similar composition has been reported by various authors (De Villiers, 1970; Kleyenstüber, 1984; Dixon, 1989).

Chlorite intergrown with andradite and sparitic calcite has the composition of clinochlore (Table 5). with an approximate formula of $(Mg_{4.8}Al_1Fe_{0.1}Mn_{0.1})[(OH)_8/(Si_{2.75}Al_{1.25})O_{10}]$. This corresponds to almost pure clinochlore. Clinochlore with similar composition has also ben described by Kleyenstüber (1984, 1985) from Wessels-type ore.

Table 5: Selected electron microprobe analyses of gangue minerals (data in wt %).

	Andradite NC1-7/6	Clinochlore N15b-3/9	Xonotlite[1]	Datolite[2]	Aegirine-augite I[3] NC30-4/1	Aegirine-augite II[4] NC30-8/3	Mn richterite[5]	Pectolite[6]
SiO_2	34.3	31.5	48.3	36.2	48.2	49.4	51.0	51.0
TiO_2	0.10				0.09	0.11		
Al_2O_3	2.39	17.9	0.01	0.02	0.24	0.39	0.01	0.02
Fe_2O_3	27.4	0.49			33.1[7]	30.4[7]		
Mn_2O_3								
FeO		1.42	0.02	0.02			0.05	0.07
MnO	1.34	1.72	0.33	0.12	1.24[8]	2.31[8]	21.8	2.38
NiO						0.11		
MgO	0.57	34.7	0.05	1.20	0.99	3.06	0.10	
CaO	34.0	0.08	45.8	32.3	2.36	4.99	15.9	31.2
Na_2O		0.05	0.02		12.9	11.4	8.94	9.30
K_2O				0.01	0.02	0.01	0.01	
H_2O^+	n.d.	12.7	n.d.	n.d.	n.d.	n.d.	1.90	n.d.
Total	100.1	100.6	94.5	69.9	99.1	102.2	99.7	94.0

[1] Mean of two analyses
[2] Mean of eight analyses
[3] Mean of 15 analyses
[4] Mean of five analyses
[5] Mean of ten analyses
[6] Mean of five analyses
[7] Total Fe as Fe(III)
[8] Total Mn as Mn(II)
[9] For amphibole and chlorite by stoichiometric calculation

UNIVERSITY OF JOHANNESBURG

The compositions of some of the silicate minerals present in the silicate-vein and the ferruginized zone of traverse 43S-E are also given in Table 5. Xonotlite and datolite appear slightly depleted in SiO_2 and CaO but enriched in MgO and MnO relative to their theoretical composition.

Honey-brown aegirine-augite I is enriched in total iron and depleted in Al_2O_3, MnO, MgO, CaO and Fe^{2+} relative to the light yellow aegirine-augite II.

The amphibole in this assemblage contains up to 21.8 wt. % MnO (Table 5). It has been defined as Mn-rich richterite. Pectolite (Table 5) associated with quartz II is slightly enriched in MnO and depleted in SiO_2 and CaO relative to the theoretical composition.

Table 6: Whole rock geochemical composition.

A. Samples from profiles 28S-E (NC-Hb-16 - NC-Hb-21) and 43S-E (NC-Hb-26-NC-Hb-33).

Sample no.	NC-Hb-16	NC-Hb-17	NC-Hb-18	NC-Hb-19	NC-Hb-20	NC-Hb-21	NC-Hb-26	NC-Hb-27	NC-Hb-28	NC-Hb-29	NC-Hb-30	NC-Hb-31	NC-Hb-32	NC-Hb-33
Ore type[1]	D	E	H	H	E	E	E	F	G	HS	HS	G	F	E
Main elements (wt %)														
SiO_2	0.72	0.80	1.62	1.73	0.21	0.27	0.12	1.95	11.0	62.9	55.8	10.9	0.40	0.12
TiO_2	0.09	0.05	0.08	0.08	0.08	0.07	0.05	0.06	0.08	0.03	0.03	0.06	0.03	0.07
Al_2O_3	0.13	0.56	0.63	0.28	0.25	0.04	0.00	0.04	0.58	1.63	0.71	0.79	0.08	0.32
Fe	6.3	8.2	67.4	64.2	9.07	7.75	4.43	8.51	9.63	21.1	24.3	9.55	3.82	0.93
Mn	63.4	60.5	0.8	0.54	60.8	63.2	66.0	60.8	49.5	1.20	3.28	52.4	68.0	70.6
MgO	0.53	1.53	1.92	2.13	1.13	0.74	0.26	0.09	0.94	0.30	0.03	0.16	0.15	0.04
CaO	0.91	1.88	1.45	4.03	1.75	0.19	0.19	2.04	4.69	3.48	3.36	4.65	0.37	0.04
Na_2O	0.00	0.04	0.00	0.00	0.00	0.00	0.00	0.00	0.05	3.68	4.11	0.03	0.01	0.00
K_2O	0.01	0.02	0.04	0.01	0.00	0.00	0.00	0.01	0.03	0.96	0.24	0.03	0.02	0.02
P_2O_5	0.03	0.05	0.36	0.03	0.14	0.13	0.00	0.03	0.04	0.19	0.06	0.06	0.09	0.02
SO_4^{2-}	n.d.	n.d.	n.d	0.055	n.d.	n.d.	0.121	0.030	0.052	0.045	n.d.	n.d.	n.d.	n.d.
CO_2	n.d.	n.d.	n.d.	1.51	n.d.	n.d.	<0.2	<0.2	<0.2	<0.2	n.d.	n.d.	n.d.	n.d.
H_2O	0.06	0.07	0.05	0.05	0.06	0.04	0.02	0.03	0.07	0.17	0.07	0.03	0.01	0.00
LOI[1]	0.56	1.59	1.45	3.18	1.01	−1.84	−1.26	−0.47	0.68	0.40	0.30	0.43	−0.02	−0.11
Trace elements (ppm)														
Zn	1,310	3,590	92	58	576	324	21	64	23	33	31	33	162	88
Cu	266	256	263	253	274	271	288	260	231	81	95	258	288	286
Ni	96	89	129	99	77	69	72	57	83	309	147	99	78	29
Ga	<4	<4	<4	<4	<4	7	<4	<4	<4	<4	<4	<4	<4	<4
Mo	32	20	47	35	29	24	13	19	26	66	41	37	19	6
Nb	24	26	26	26	23	30	29	22	24	9	14	22	24	30
Zr	<3	<3	<3	<3	<3	<3	<3	<3	<3	7	3	<3	<3	<3
Y	<3	11	4	<3	4	7	<3	<3	<3	5	3	3	<3	<3
Sr	7	11	20	32	12	3	23	<3	9	253	211	5	32	4
Rb	<2	<2	<2	<2	<2	5	5	<2	<2	16	10	<2	<2	6
U	<5	<5	<5	<5	6	<5	<5	8	<5	<5	9	5	<5	<5
Th	<5	<5	<5	5	<5	<5	<5	9	<5	<5	<5	<5	<5	7
Pb	38	102	13	38	59	59	31	29	14	24	20	53	141	221
Co	6	9	29	73	<7	<7	<6	5	<6	68	21	12	<6	<7
Cr	59	87	425	287	55	18	14	48	143	602	512	162	54	55
V	<8	<8	<8	<8	<8	<7	<7	<6	<9	65	47	<7	<8	<8
Ba	<8	<8	<8	<8	<7	<8	1,373	<9	21	64	152	<8	1,829	136
Sc	<6	<6	<6	<6	<6	<6	<6	<6	<6	<6	<7	<7	<7	<7
As	36	<8	377	220	29	22	<8	20	107	70	79	101	<8	24
Cl	170	540	82	71	326	131	<20	58	77	<20	24	41	35	32
F[1]	<100	300			1,080	1,420	<100	<100	1,290	740	740	940	1,590	
Te	<6	<6	13	9	<6	8	10	9	<6	<6	<6	<6	<6	6
Se	<5	<5	<5	<5	<5	<5	<5	<5	<5	<5	<5	<5	<5	<5

UNIVERSITY OF JOHANNESBURG

Table 6, continued.

B. Samples from traverse S

Sample no.	NC-1a-4	NC-1a-5	NC-1a-6	NC-1a-7	NC-1a-8	NC-1a-9	NC-1a-10	NC-1a-11	NC-1a-12	NC-1a-13	NC-1a-14
Ore Type[1]	C	F	C	C	C	B	A	A	D	D	E
Main elements (wt %)											
SiO_2	9.79	3.80	0.78	0.84	0.85	4.71	7.74	5.70	0.83	0.52	0.69
TiO_2	0.09	0.06	0.05	0.02	0.08	0.06	0.06	0.04	0.08	0.07	0.07
Al_2O_3	0.10	0.05	0.03	0.00	0.00	0.24	0.03	0.18	0.03	0.14	0.23
Fe	8.08	9.72	8.43	6.34	4.46	8.90	9.03	12.7	19.8	17.2	23.0
Mn	56.1	55.1	50.7	48.9	59.2	51.5	48.9	35.2	47.6	53.3	48.5
MgO	0.10	0.13	0.26	0.38	0.29	0.02	0.35	0.73	0.51	1.18	0.25
CaO	4.44	3.57	9.84	20.2	8.01	7.20	12.4	25.0	2.42	1.70	0.49
Na_2O	0.02	0.04	0.00	0.00	0.00	0.02	0.03	0.05	0.03	0.00	0.00
K_2O	0.01	0.01	0.01	0.00	0.00	0.01	0.04	0.02	0.01	0.00	0.12
P_2O_5	0.00	0.02	0.03	0.05	0.03	0.04	0.06	0.7	0.04	0.02	0.07
SO_4^{2-}	0.036	n.d.	2.20	n.d.	0.024	n.d.	0.051	n.d.	2.72	n.d.	0.085
CO_3^{2-}	0.847	n.d	0.842	n.d.	0.098	n.d.	4.50	n.d.	<0.2	n.d.	<0.2
H_2O	0.15	0.08	0.22	0.08	0.21	0.20	0.12	0.12	0.45	0.35	0.10
L.O.I.[3]	1.91	0.53	2.43	0.57	4.84	1.25	7.35	14.4	3.02	4.57	1.88
Trace elements (ppm)											
Zn	45	11	401	273	556	20	39	66	182	165	102
Cu	247	261	277	247	268	275	217	174	276	250	278
Ni	119	57	61	163	494	41	133	40	104	71	186
Ga	<4	<4	<4	<4	<4	4	<4	·	<4	<4	<4
Mo	33	9	13	42	254	7	51	12	32	15	72
Nb	26	32	22	20	25	23	23	19	26	26	32
Zr	<3	<3	<3	<3	<3	<3	<3	<3	<3	<3	<3
Y	<3	31	<3	5	<3	<3	5	9	16	9	6
Sr	75	415	4,860	1,930	2,640	8,970	208	314	3,990	397	21
Rb	5	<5	<5	<3	<5	<5	7	<2	<2	<2	<2
U	<5	8	<5	<5	<5	<5	<5	<5	<5	<5	<5
Th	<5	<5	<5	<5	8	<5	<5	<5	<5	<5	<5
Pb	121	60	130	71	320	24	52	74	39	38	120
Co	6	<5	9	55	58	9	9	31	24	15	8
Cr	120	13	34	297	1,188	<9	242	<8	104	58	332
V	<8	<8	<8	<8	<7	<8	<6	<8	<8	<8	<8
Ba	<14	3,043	20,128	2,782	1,421	7,186	<18	<8	7,840	2,849	<8
Sc	<5	<8	<7	<7	<6	<6	<7	<6	<6	<6	<6
As	34	<8	<8	<8	<8	<8	<8	<8	<8	<8	<8
Cl	868	780	70	46	60	1,140	44	30	118	400	1,440
F	1,800	2,190	2,040	1,330	300	2,900	<100	2,010	2,560	<100	3,300
Te	<6	<6	<6	<6	<6	<6	<6	9	17	<6	<6
Se	<5	<5	<5	<5	<5	<5	<5	<5	<5	<5	<5

[1] Different ore types as defined in Table 3
[2] SO_4 and CO_2 analyses only for selected samples
[3] Negative loss on ignition due to partial oxidation of Mn^{2+} (hausmannite) to Mn^{3+}
[4] At very high Fe concentrations no reliable detection of F (XRF)

UNIVERSITY OF JOHANNESBURG

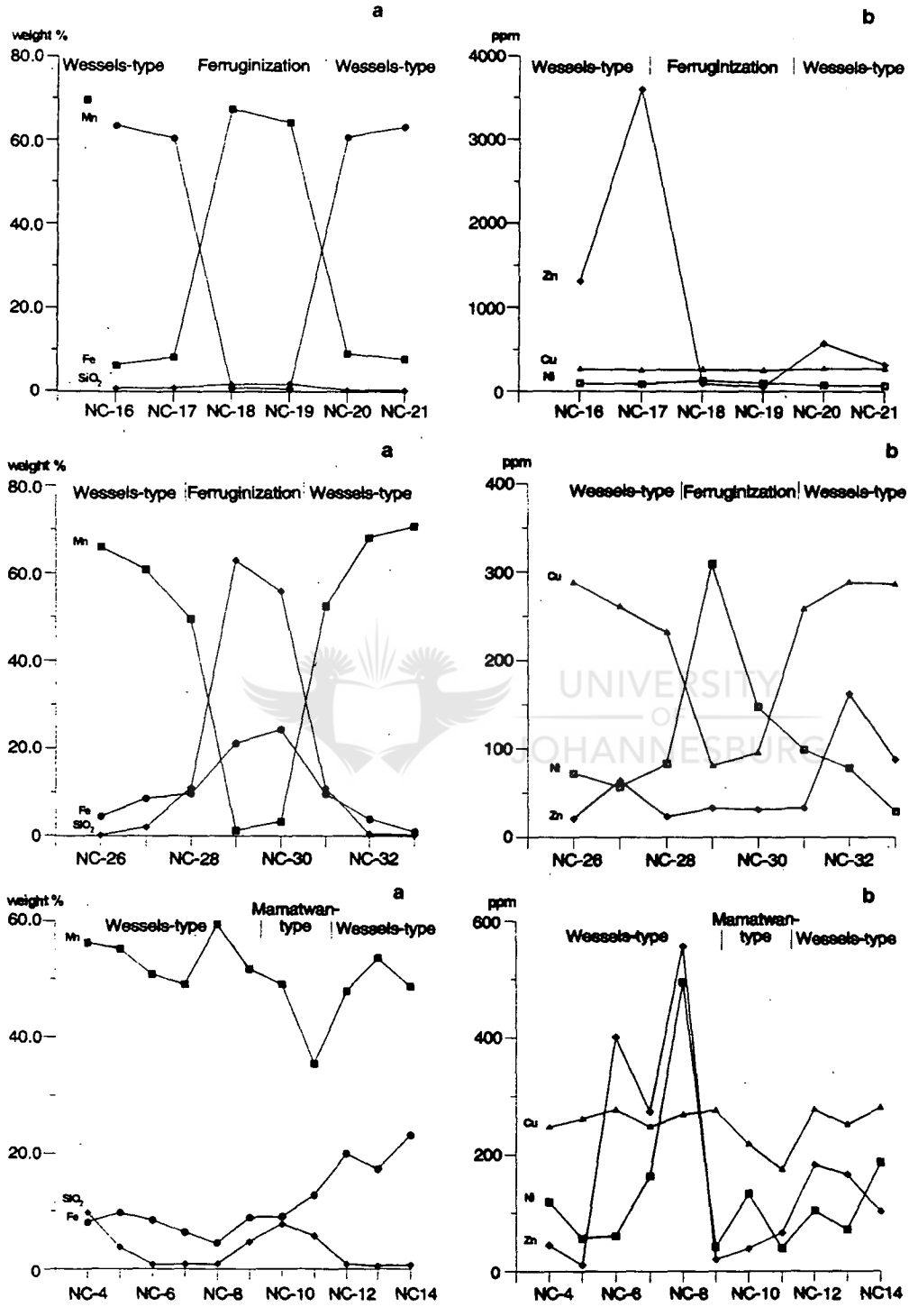

Figure 11: Variation of major element (a) and trace element (b) concentrations in traverse 28S-E.
Figure 12: Variation of major element (a) and trace element (b) concentrations in traverse 43S-E.
Figure 13: Variation of major element (a) and trace element (b) concentrations in traverse S.

Whole Rock Geochemistry

Results of whole rock chemical analyses are presented in tables 6A and 6B. In traverses 43S-E and 28S-E (Table 6A, Fig's. 11 and 12), concentrations of major elements vary symmetrically relative to central zones of ferruginization which are enriched in iron and depleted in manganese. Manganese contents sharply decrease to values of less than 5 wt % in zones of ferruginization and reach maximum values of 65 - 70 wt % in hausmannite-rich ores towards the sides of the traverses. In contrast iron concentrations may be as high as 60 % in ferruginized zones, whereas in manganese ores its concentrations vary from less than 1 wt % to about 10 wt %.

Minor components SiO_2, Al_2O_3, MgO, CaO and P_2O_5 (Fig.11a) are positively correlated with Fe in traverse 28S-E. Similarly the trace elements Co, Ni, Cr, Mo, As, Te and Sr are positively correlated with Fe (Fig.11b). These trace elements could be incorporated into the hematite-lattice except for Sr which has been found as celestite (Von Bezing et al., 1991) or may replace Ba in barite as well as Ca in calcite.

Traverse 43S-E is characterized by the strong positive correlation of Fe and SiO_2. The SiO_2 concentration increases in an almost perfect symmetrical pattern relative to the central calc-silicate vein in the ferruginized zone (Fig. 12a). It increases from 0.12 wt % in hausmannite-rich ores distant from the vein to 62.9 wt % in the ferruginized and silicified wallrock of the calc-silicate vein. Almost all minor components and trace elements correlate positively with Fe in traverse 43S-E. Noteworthy is the strong enrichment of the alkali elements in the ferruginization zone. However, Pb, Zn and Cu are depleted in the ferruginized and silicified samples (Fig.12b).

Ba, Cl, F and SO_3 display highly variable concentrations along traverses 28S-E and 43S-E (Table 6A). Appearance of minerals containing these elements such as barite, gypsum and other rare phases (Von Bezing et al., 1991), is confined to microfractures, veinlets and secondary pores which are irregularly distributed in the rock samples.

In traverse S, lowest concentrations of Mn (35.2 wt %) are found within the Mamatwan-type ore (Samples NC-1a-10 and 11, Table 6B and Fig. 13). Mn concentration of 48.9 wt % and carbonate content of only 4.5 wt % CO_2 in sample NC-1a-10 deviates considerably from typical Mamatwan-type ore (35-39 wt % Mn, 15-17 wt % CO_2, Nel et al., 1986). However, the existing

close mineralogical and textural resemblance of this sample to Mamatwan-type ore defines it as only slightly altered.

The manganese contents increase from Mamatwan-type ore to a mean of more than 50 wt % in Wessels-type ores. Iron concentration reaches a low of 4.46 wt % in the sample with highest Mn content of 59.2 wt % (sample NC-1a-8, Table 6B and Fig. 13). The hausmannite-rich ore of sample NC-1b-14 displays the highest iron concentration of 23 wt % due to replacement of hausmannite by secondary hematite. Iron concentration in Mamatwan-type ore is typically well below 10 wt % (Table 1).

SiO_2 and CO_2 tend to be depleted in Wessels-type ore relative to Mamatwan-type ore precursor (Table 6B). Concentrations of SiO_2 are between 5.70 and 7.74 wt % in the Mamatwan-type samples and decrease to a low of 0.52 wt % in Wessels-type bixbyite-hausmannite ore (sample NC-1b-13). An exception is the braunite-rich sample with 9.79 weight percent SiO_2 adjacent to the western boundary fault.

Mamatwan-type samples are furthermore enriched in CO_2 relative to Wessels-type ore. The concentration of CO_2 in Mamatwan-type ore is 4.5 wt %. In Wessels-type ores concentrations are typically below 1 wt % (Table 6B and Fig. 6).

CaO and MgO are generally positively correlated with CO_2. However, marokite ($CaMnO_4$)-rich Wessels-type ore may contain 10 - 20 wt % CaO and less than 1 wt % CO_2 (NC-1a-6 and NC-1a-7, Table 6B). In contrast, marokite-poor Wessels-type ores contain less than 5 wt % CaO. Calcite-rich Mamatwan-type samples contain more than 10 wt % CaO (NC-1a-10 and NC-1a-11, Table 6B). Ba, Sr and SO_3 are positively correlated and enriched in Wessels-type ore relative to Mamatwan-type ore (Table 6B). High concentrations of Ba (up to 8 wt %), SO_3 (up to 2.2 wt %) and Sr (up to 0.5 wt %) are associated with samples containing Sr-barite (Tables 3 and 6B).

Concentrations of some minor and trace elements appear to be either very low but consistent (TiO_2, Nb) or to show random scattering (MgO, P_2O_5, Zn, Pb, Ni, Co, Cr, F, Cl). Contents of most other elements are just too low for any interpretation.

Discussion

General Paragenetic Model

The alteration of low-grade to high-grade manganese ore, associated with faulting and ferruginization, along the various traverses sampled, bear so many similarities that a general paragenetic model may be constructed. In constructing the model (Fig. 14) hausmannite ore in traverse 28S-E has been correlated with that at the eastern end of traverse S (Table 3). Similarly, massive braunite ore in traverse 43S-E has been correlated with braunite ore at the western end of traverse S (Table 3).

The model comprises precursor sedimentary braunite-hematite-kutnahorite-manganocalcite Mamatwan-type ore (Nel et al., 1986) that originally extended over the entire ore bed now found to be altered. In this area, most distal to zones of ferruginization and normal faulting, the first signs of alteration of Mamatwan-type ore is found to be the alteration of braunite to braunite II and kutnahorite to hausmannite and calcite (Fig. 14). This alteration probably took place through reactions such as

UNIVERSITY OF JOHANNESBURG

I.

$$6\ Mn^{2+}Mn^{3+}{}_6SiO_{12} + 3\ Fe_2O_3 + 3\ CaCO_3 + O_2(aq) \rightarrow$$

braunite hematite calcite →

$$6\ Ca_{0.5}(Mn,Fe)^{3+}{}_7Si_{0.5}O_{12} + 2\ Mn_3O_4 + 3\ SiO_{2(aq)} + 3\ CO_{2(aq)}$$

braunite II hausmannite

II.

$$3\ CaMn^{2+}(CO_3)_2 + 1/2\ O_2(aq) \rightarrow Mn^{2+}Mn^{3+}{}_2O_4 + 3\ CaCO_3 + 3\ CO_{2(aq)}$$

kutnahorite → hausmannite calcite

It is important to note that these initial alteration reactions involve dissolution of silica (i.e. SiO_2) and CO_2 from the original low grade sedimentary ore, replacement of hematite and oxidation of Mn^{2+} from the carbonate to Mn^{3+} in hausmannite. The ore also acquires secondary porosity due to leaching of carbonate and SiO_2 from the system.

Slightly more proximal to zones of faulting or ferruginization, alteration of the ore is taken a step further by more leaching of silica from the system and the development of braunite (new) in the ore and resulting higher porosity (Fig. 14). Braunite (new) may have formed from braunite with hematite and calcite or entirely from braunite II:

IIIa.

$$6\ Mn^{2+}Mn^{3+}{}_6SiO_{12} + 3\ Fe_2O_3 + 2\ CaCO_3 + 3/2\ O_{2(aq)} \rightarrow$$

braunite hematite calcite →

$$6\ Ca_{0.34}(Mn,Fe)^{3+}{}_6Si_{0.34}O_{10} + 3Mn^{3+}{}_2O_3 + 4SiO_{2(aq)} + 2\ CO_{2(aq)}$$

braunite (new) bixbyite

IIIb.

$$300\ Ca_{0.5}(Mn,Fe)^{3+}{}_7Si_{0.5}O_{12} \rightarrow$$

braunite II →

$$348\ Ca_{0.33}(Mn,Fe)^{3+}{}_6Si_{0.33}O_{10} + 6\ Mn^{3+}{}_2O_3 + 35\ CaO + 35\ SiO_2(aq)$$

braunite (new) bixbyite

In some cases it appears as if braunite (new) developed from laminae which originally consisted mainly of manganocalcite and kutnahorite with small amounts of braunite. This resulted in the very porous laminae composed of skeletal braunite (new) crystals (Fig. 9c) and the reaction involved may have been as follows:

IV.

$$4\ Mn_7SiO_{12} + 2\ CaMn[CO_3]_2 + 3\ Fe_2O_3 + 3/2\ O_{2(aq)} \rightarrow$$

braunite + kutnahorite + hematite →

$$6\ Ca(Mn,Fe)_{21}SiO_{34} + 2\ SiO_{2(aq)} + 4\ CO_{2(aq)}$$

braunite (new)

The final step of leaching of silica and carbonate from the system involves the formation of bixbyite and marokite-bearing ores (Fig. 14) probably through reactions such as:

V.

$$2\ Mn^{2+}Mn^{3+}{}_6SiO_{12} + Fe_2O_3 + 1/2\ O_2\ (aq) \rightarrow 8\ (Mn,Fe)^{3+}{}_2O_3 + 2\ SiO_{2(aq)}$$

braunite hematite → bixbyite

VI.

$$Mn^{3+}{}_2O_3 + CaCO_3 \rightarrow CaMn^{3+}{}_2O_4 + CO_{2(aq)}$$

bixbyite calcite → marokite

Reactions involving dissolution of silica and carbonate are by then virtually complete and reactions involving the reduction of Mn^{3+} to Mn^{2+} in order to form hausmannite become prominent.

In the zone of ferruginization (Fig. 14) manganese ore is replaced by hematite. One possibility is that ferrous iron carried in solution acted as reductant for Mn^{3+} leading to reactions such as

VII.

$$Mn^{3+}{}_2O_3 + Fe^{2+}{}_{(aq)} \rightarrow Fe^{3+}{}_2O_3 + Mn^{2+}(aq)$$

The Mn^{2+} thus liberated may in turn be precipitated to form the very high-grade hausmannite-rich ores preferentially developed immediately adjacent to zones of ferruginization (Fig. 14). One possibility is that an Mn^{3+} phase e.g. bixbyite was replaced by hausmannite through a reaction such as

VIII.

$$Mn^{3+}{}_2O_3 + Mn^{2+}{}_{(aq)} + O^{2-}{}_{(aq)} \rightarrow Mn^{2+}Mn_2{}^{3+}O_4$$

bixbyite hausmannite

However, this whole assemblage of alteration zones related to fault or vein systems, is overprinted in proximity to zones of ferruginization by a secondary phase of silica enrichment and carbonatization. It is represented by the formation of massive braunite-rich ores in the transition zone

between hematite and hausmannite ores and the precipitation of coarse-grained sparitic calcite in the zone of ferruginization. The braunite may have formed from reactions such as

IX.

$$7\ Mn^{2+}Mn^{3+}{}_2O_4 + 3\ SiO_{2(aq)} + O_{2(aq)} \rightarrow 3\ Mn^{2+}Mn^{3+}6SiO_{12}$$

hausmannite braunite

Closely associated with the formation of secondary braunite-rich ores is the formation of second phase braunite II and braunite (new) partly filling vugs and pores in proximity to zones of ferruginization. Quartz and Ca-silicates such as andradite, as well as calcite, are closely associated with the hematite in zones of ferruginization, indicating high concentration of silica, carbonate and Ca^{2+}. Further away from the fault zones, gangue minerals are mainly restricted to vug and vein fills of gaudefroyite, clinochlore, Sr-barite, gypsum and very little calcite. Characteristic is the association of clinochlore and gaudefroyite with hausmannite-rich ores. Sr-barite, gypsum and calcite vein fillings seem not to be restricted to certain mineral assemblages.

UNIVERSITY OF JOHANNESBURG

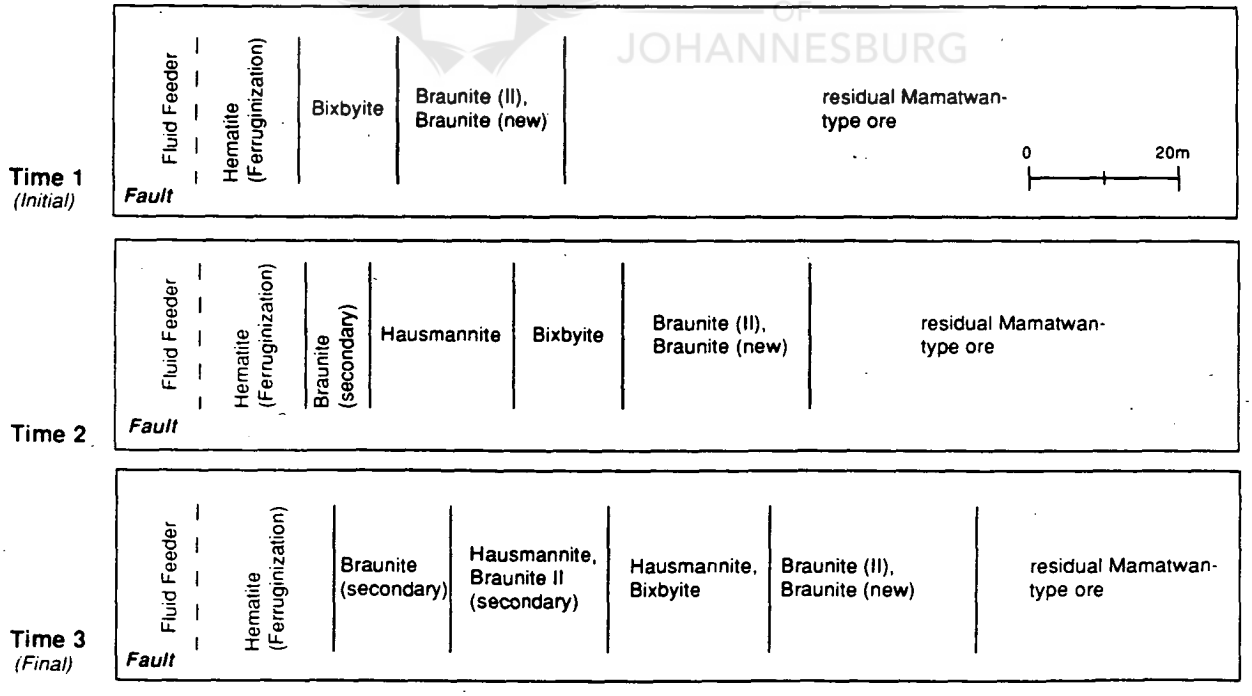

Figure 15: Paragenetic model for the temporal and spatial development of zones of different manganese ore types relative to the ferruginized fluid feeder along a fault. Paragenetic zones develop symmetrially to fluid feeder, only right half of developing system is displayed. Scale only approximate.

Conceptual Hydrothermal Model

The alteration of low-grade Mamatwan-type ore to high-grade Wessels-type ore in the Kalahari manganese field is perhaps best explained by a fault controlled hydrothermal-metasomatic system. Normal faults and fractures apparently served as conduits for hydrothermal fluids from where they penetrated laterally into the manganese ore beds (Fig's 14 to 16). The presence of fluids involved in the alteration process is clearly illustrated by the development of secondary porosity in the manganese ores, the precipitation of hydrothermal minerals in veins and pores, the replacement of manganese ores by hematite along fault zones, and introduction of elements such as Na and K into the system in proximity to feeder channels.

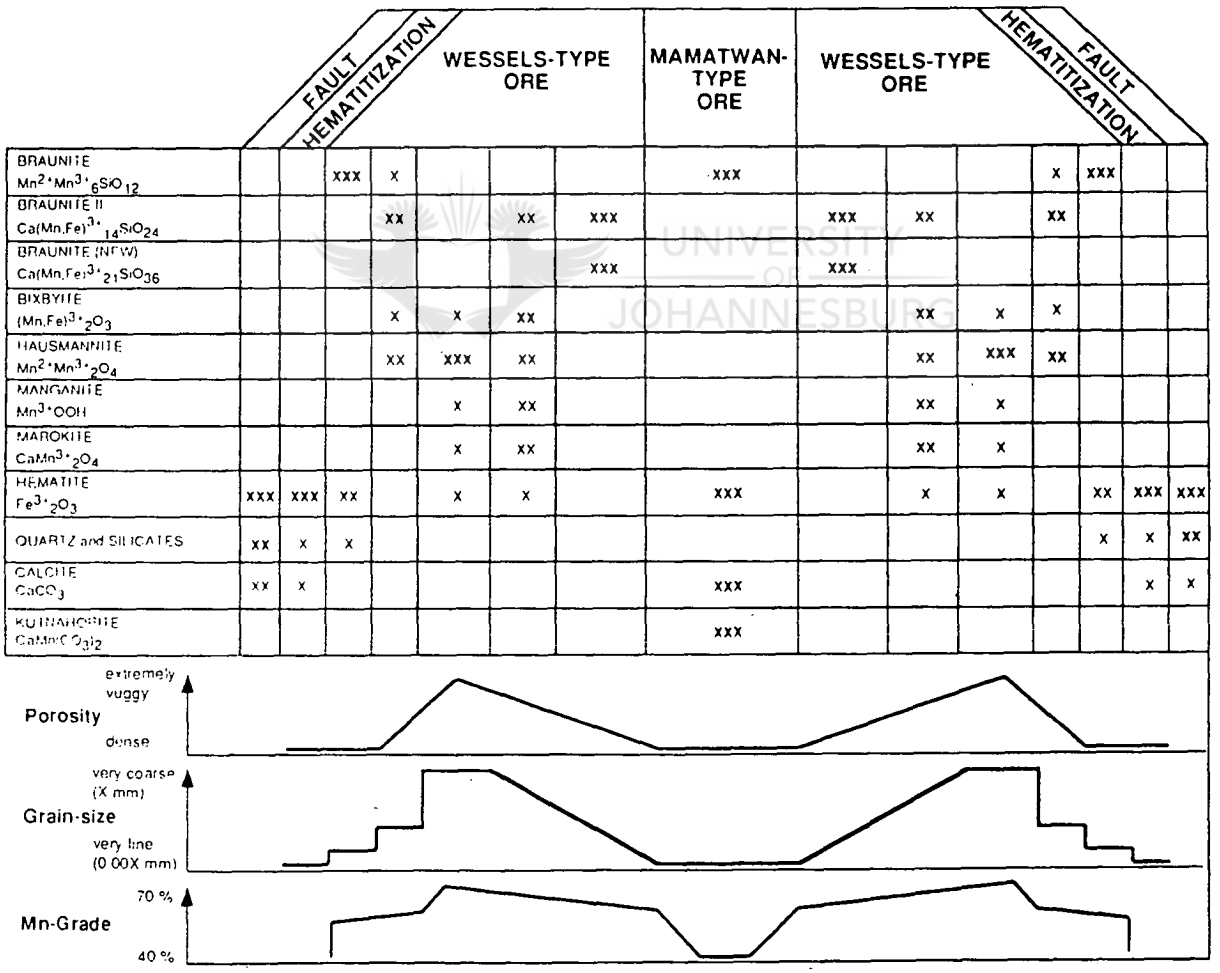

Figure 14: Idealized profile between two normal faults at the Nchwaning mine showing qualitative lateral distribution of ore mineral assemblage, porosity, grain size, and Mn-grade. XXX- dominant (> 30 Vol %); XX - important (10-30 Vol %), X - subordinate (1-10 Vol %).

From the main feeder channels a front of hydrothermal fluids apparently percolated and reacted its way laterally into the primary sedimentary manganese ore bed dissolving carbonates, leaching silica, creating secondary porosity and causing precipitation of hydrothermal manganese ore minerals. This front clearly developed lateral physico-chemical gradients as indicated by the different zones of manganese ore types (Fig. 14).

With time the zone of alteration adjacent to feeder channels also widened as indicated by overprinting of one ore type by another (Fig. 15). A good example is the replacement of braunite II and braunite (new) ore by bixbyite ore with the latter in turn being replaced by hausmannite ore.

This model may be based on theories of hydrothermal metasomatic zoning presented by Khorshinskij (1965, 1970). By applying thermodynamic principles various features of complex natural metasomatic systems e.g. skarn formation in carbonate rocks or zoned wallrock alteration around hydrothermal veins in silicate rocks may be explained. By sequential reaction fronts developing within a pervasive fluid system in a rock unit that taps a structurally controlled fluid source, features formed during alteration of sedimentary manganese ores described above, may be accomplished.

UNIVERSITY OF JOHANNESBURG

Replacement of manganese ore by hematite along major feeder channels suggests that the primary hydrothermal fluid must have been reducing in order to have carried ferrous iron in solution. The fluid must also have been undersaturated with regards of CO_2 to allow dissolution of carbonates and alkaline to facilitate leaching of silica from braunite and from the primary sedimentary manganese ore. However, an alkaline pH may also have been developed solely due to leaching of carbonates. As the fluid penetrated into the manganese ore beds the presence of Mn^{3+}-bearing oxides allowed precipitation of hematite and dissolution of Mn^{2+} that was reprecipitated as hausmannite in the very high-grade hausmannite rich ore zones. Towards the margin of the hydrothermal front this alkaline fluid caused transformation of braunite into braunite II, braunite (new) or bixbyite through leaching of silica and oxidation of manganese-bearing carbonates to Mn-oxides, for example hausmannite,

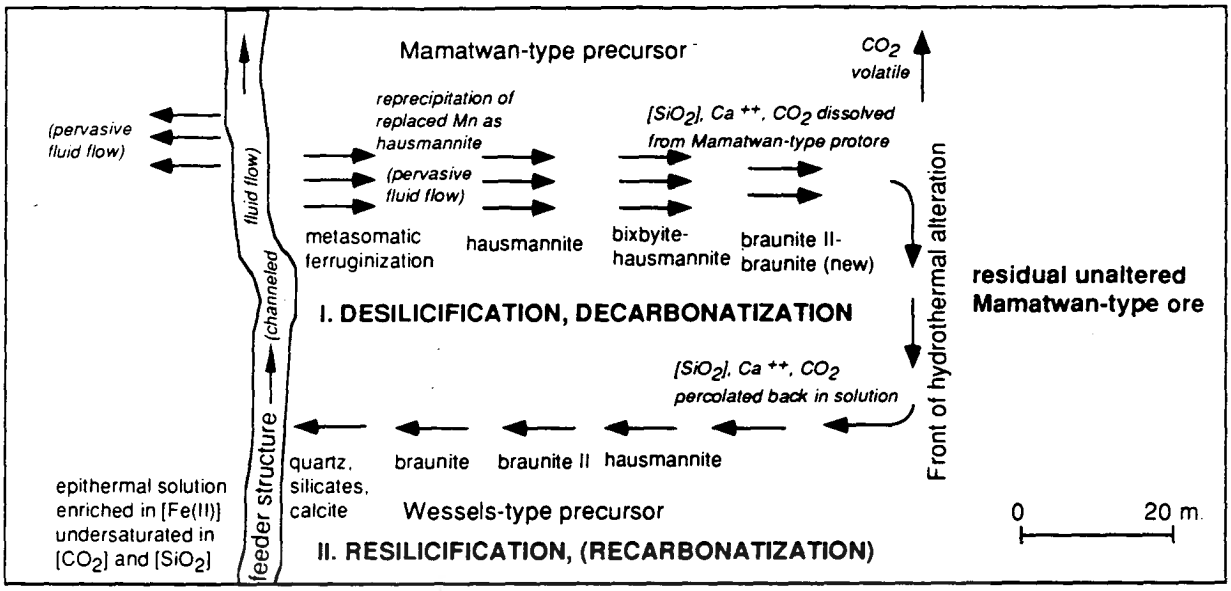

Figure 16: Conceptual model of a closed hydrothermal system responsible for alteration and ferruginization of ores in the Kalahari manganese field. Fluid flow symmetrical to that of the central fluid feeder, only right half of fluid flow scheme is displayed. Scale only approximate.

and calcite with liberation of CO_2 (Fig. 16).It seems quite possible that some type of convection developed because of temperature gradients, with dissolved components such as SiO_2, Ca^{2+} and CO_2 being percolated back to the main feeder channel (Fig. 16). It is envisaged that during waning stages of fluid flow and cooling down of the system some silica was reprecipitated in proximity to main fluid channelways to form secondary braunite-rich ore zones, as well as quartz and silicates in ferruginized zones. Channelways apparently finally became plugged by reprecipitation of secondary quartz, calcite and various silicates (Fig. 16). A good example of final plugging of a fluid channelway may be the xonotlite-datolite vein of traverse 43S-E.

Initially only very narrow zones next to feeder channels may have been altered by the hydrothermal fluids. However, with time the zones probably widened (Fig. 15). The wide zones of alteration relative to feeder channels (up to 100 m wide on either side) suggest very long term periods of effective fluid flow to heat up country rock and cause widespread metasomatic alteration of primary sedimentary manganese ores.

Widespread alteration would also only have been possible through continuous input of 'fresh' (new) hydrothermal fluid into the system. This would imply high fluid-rock ratios.

The temperature gradient in the hydrothermal system has yet not been very well defined. Miyano and Beukes (1987) suggest a temperature range in the order of 300 - 400 °C. Dixon (1989) proposed a hydrothermal system with temperatures reaching up to 450 °C for the formation of sugilite in the high-grade ore deposits, while Gutzmer (1993) envisaged a temperature range between 250 and 400 °C, an estimation based on stability fields of various ore and gangue minerals.

The origin of the fluids and the age of the alteration process are at present uncertain. The normal faults predate thrusting (Fig. 3), but Kleyenstüber (1984, 1985) also noticed hydrothermal alteration along planes of thrust faults. It is thus likely that some of the hydrothermal fluids were derived from tectonic loading during the thrust event that took place some 1800 - 2000 m.y. ago (Beukes and Smit, 1987). However, it is possible that fluids were derived from intrusion of the nearby Kameel mafic igneous body (Holland and Beukes, 1990), but this remains pure speculation. Dixon (1989) estimated the age of the hydrothermal event at approximately 1300 m.y. based on dating galena (Pb) from vug mineralisation, as well as dense sugilite (Rb-Sr, Pb). However, the significance of galena and sugilite to the main alteration event still remains uncertain. These various unknown parameters are targets of ongoing research in the area.

UNIVERSITY OF JOHANNESBURG

Conclusions

Low-grade Mamatwan-type ore of sedimentary origin upgraded by hydrothermal fluids to high-grade Wessels-type ore in the northwestern part of the Kalahari manganese field. North striking normal faults and eastward trending veins and minor faults served as feeder channels for the hydrothermal fluids. Manganese ores became ferruginized in the immediate vicinity of the feeder channels by complete metasomatic replacement of manganese oxides by hematite.

Two stages of hydrothermal alteration are characterized by a specific lateral variation in mineralogical composition of the manganese ores from zones of ferruginization towards zones of less altered ores. Stage I desilicified and decarbonatized the ore. The ideal lateral sequence of ore types, from zones of ferruginization towards zones of unaltered Mamatwan-type ore, appears to be

hematite + calcite - hausmannite - bixbyite+hausmannite - braunite II + braunite(new) + marokite + hausmannite + manganite - braunite II + braunite (new) - braunite + hematite + carbonate (Mamatwan-type ore).

The second stage of alteration resilicifies ores previously altered by stage I in proximity to feeder channels. The lateral sequence of ore-types appears to be hematite+quartz+silicate+calcite - braunite+andradite - braunite II+hausmannite - hausmannite. The stages of hydrothermal alteration have been assigned to the prograding and retreating periods of a complex hydrothermal system with channeled vertical fluid flow along feeder structures but pervasive lateral flow within the manganese ore beds.

Acknowledgements

This project was supported by the Associated Manganese Mines of South Africa (AMMOSAL). The authors are indebted to Willem Grobbelaar, Technical Manager of AMMOSAL, and Awie Pretorius, geologist at Nchwaning mine, for their assistance with accomodation, sampling and transport during the project. We would also like to thank Arno Kleyenstüber, MINTEK, for his kind support and a critical review of the manuscript as well as E. Gierth and A. K. Schuster (TU Clausthal) for their assistance in taking the photographs.

References

AMMOSAL (1992). Brochure describing the manganese and iron ore interests of the Associated Manganese Mines of South Africa Ltd. AMMOSAL, Mancorp Mine, 6 pp.

Beukes, N.J., and Smit, C. A., (1987). New evidence for thrust faulting in Griqualand West, South Africa: Implications for stratigraphy and the age of red beds. Trans. Geol. Soc. S. Afr., 90, 378-394.

Boardman, L.G. (1941). The Black Rock manganese deposit in the Southeastern Kalahari. Trans. Geol. Soc. S. Afr., 44, 51-60.

De Villiers, J.P.R., and Buseck, P.R. (1989). Stacking variations and non-stoichiometry in the bixbyite-braunite polysomatic mineral group. Amer. Mineral., 74, 1325-1336.

De Villiers, P.R. (1970). The geology and mineralogy of the Kalahari manganese-field north of Sishen, Cape Province. Mem. geol. Surv. S. Afr., 59, Pretoria, 84 pp.

Dixon, R. D. (1989). Sugilite and associated metamorphic silicate minerals from Wessels mine, Kalahari manganese field. Bull. geol. Surv.. S. Afr., 93, Pretoria, 47 pp.

Gutzmer, J. (1993). Hydrothermale Alteration von Manganerzen der Nchwaning-Mine, Kalahari-Manganerzfeld, Südafrika. Unpubl. Diplom thesis, Technische Universität Clausthal, 161 pp.

Gutzmer, J., and Beukes, N.J. (1993). Hydrothermal alteration and ferruginization of sedimentary manganese ore at the Nchwaning mine, Kalahari manganese field, Early Proterozoic Transvaal Supergroup, South Africa. Unpubl. report, Johannesburg, 152 pp.

Holland, D., and Beukes, N.J. (1990). A palaeoweathering profile from Griqualand West, South Africa: Evidence for dramatic rise in atmospheric oxygen between 2.2 and 1.9 BYBP. Am.J.Sci., 290A, 1-34.

Khorshinskij, D.S. (1965). Abriss der metasomatischen Prozesse. Akademie Verlag, Berlin, 195 pp.

Khorshinskij, D.S. (1970). Theory of metasomatic zoning. Clarendon Press, New York, 162 pp.

Kleyenstüber , A. S. E. (1984). The mineralogy of the manganese bearing Hotazel Formation of the Proterozoic Transvaal Sequence in Griqualand West, South Africa. Trans. geol. Soc. S. Afr., 87, 257-272.

Kleyenstüber , A. S. E. (1985). A regional mineralogical study of the manganese bearing Voëlwater Subgroup in the northern Cape Province. Unpubl. Ph.D thesis, RAU, Johannesburg, 328 pp.

Miyano, T., and Beukes, N.J. (1987). Physicochemical environments for the formation of quartz-free manganese oxide ores from the Early Proterozoic Hotazel Formation. Kalahari manganese field, South Africa. Econ.Geol., 82, 706-718.

Nel, C.J., Beukes, N.J., and De Villiers, J.P.R. (1986). The Mamatwan manganese mine of the Kalahari manganese field. In: Mineral deposits of Southern Africa (Annhaeusser, C.R., and Maske, S., eds.), Geol. Soc. S. Afr., Johannesburg, 963-978.

Roy, S. (1981). Manganese deposits. Academic Press, London, 458 pp.

Stowe, C. W. (1986). Synthesis and interpretation of structures along the north-eastern boundary of the Namaqua tectonic province, South Africa. Trans.geol. Soc. S. Afr., 89, 185-198.

Taljaardt, J.J. (1982). Major manganese ore fields, Republic of South Africa. Unpubl. report, SAMANCOR, Johannesburg, 7 pp.

Von Bezing, K.L., Dixon, R.D., Pohl, D., and Cavallo, C. (1991). The Kalahari manganese field: An update. Miner. Record, 24, 7/8, 10-27.

UNIVERSITY JOHANNESBURG

Appendix VIII

Fault controlled hydrothermal alteration of Palaeoproterozoic manganese ore in Wessels Mine, Kalahari manganese field.

(published in: South African Journal of Geology, 98, 430-451, 1995)

N.J. Beukes, A.M. Burger*, and J. Gutzmer

Abstract

The Kalahari manganese field, situated some 60 km northwest of Kuruman in the Northern Cape Province, is the largest known land-based manganese deposit. Low-grade sedimentary Mamatwan-type ore (containing up to 38 wt % Mn) dominates and constitutes about 97 % of the ore reserves. It is composed of finely intergrown braunite and Mn-rich carbonates. High-grade Wessels-type ore (containing on average 42 to 48 wt % Mn) constitutes about 3 % of the known reserves, and occurs in the northwestern part of the main Kalahari deposit. Here the sequence is displaced by a system of north-south striking normal faults. Fault zones are ferruginized and alongside faults sedimentary Mamatwan-type ore has been upgraded by hydrothermal alteration to Wessels-type ore. Pockets of Mamatwan-type ore are present in cores of fault blocks. Wessels-type ore consists mainly of hausmannite, bixbyite, braunite II and manganite and subordinate gangue minerals such as calcite, clinochlore and andradite. Hydrothermal alteration of Mamatwan-type ore to Wessels-type ore involved leaching of SiO_2 and oxidation of manganese-bearing carbonates to manganes oxides. In weakly altered Mamatwan-type ore, Mn-calcite ovoids are replaced by hausmannite and calcite, and braunite is altered to braunite II. The next stage of alteration involves the transformation of braunite II into bixbyite and hausmannite. Gangue minerals such as barite, andradite, sparitic calcite and clinochlore formed during alteration. The highest-grade Wessels-type ore consists predominantly of hausmannite. In proximity to fault zones hematitization of manganese ores took place. The transition zone between hematite-rich fault zones and high-grade hausmannite-rich Wessels-type ore is characterized by the development of a secondary phase of massive braunite-rich ore. The hematite-rich ores fault zones may contain abundant calcite and some andradite. Normal faults apparently acted as conduits for hydrothermal fluids. Hydrothermal alteration appears to

have taken place in a type of convection cell with SiO_2 and CO_2, leached from Mamatwan-type ore, reprecipitated in proximity to the normal faults as secondary braunite and calcite.

Introduction

The Kalahari manganese field, situated some 60 km to the northwest of Kuruman in the Northern Cape Province of South Africa (Fig. 1A), is the largest known land-based manganese deposit in the world containing about 13,500 Mt of indicated manganese ore reserves at 20-60 mass% Mn (Taljaardt, 1982). The primary manganese ores are of sedimentary origin and interbedded with iron-formation of the Hotazel Formation of the Palaeoproterozoic Postmasburg Group of the Transvaal Supergroup. The manganese field consists of five known, structurally preserved, erosional relics of the manganese-bearing Hotazel Formation (Nel et al., 1986), of which the Kalahari deposit is by far the largest (Fig. 1B).

Two main ore types are present, namely low-grade primary sedimentary Mamatwan-type ore, with Mn contents of 20-38 wt %, and secondary high-grade Wessels-type ore containing 45-60 wt % Mn (Kleyenstüber, 1984). High-grade Wessels-type ore isrepresents an alteration product of low-grade sedimentary Mamatwan-type ore (Kleyenstüber, 1984) and is economically economically the most sought after ore in the Kalahari deposit. However, it constitutes only about three percent of the known reserves (Taljaardt, 1982). Part of this high-grade reserve is not minable because of the presence of "zones of ferruginization". It is therefore important to establish the origin of the high-grade ores and controls on their distribution, including that of ferruginized zones, for purposes of mine planning and exploration for new high-grade ore reserves. These factors have not been studied in any detail in Wessels mine (Fig. 1C), the type locality for Wessels-type ore (Kleyenstüber, 1984). A study by Gutzmer and Beukes (1995) at Nchwaning mine, immediately adjacent to Wessels mine (Fig. 1C), indicated that Wessels-type ore was formed by hydrothermal alteration of primary Mamatwan-type.

Alteration took place along a system of north-south and east-west striking normal faults with zones of ferruginization are preferentially developed immediately adjacent. Low-grade Mamatwan-type ore may be preserved in cores of fault blocks. The study presented in this paper was designed to

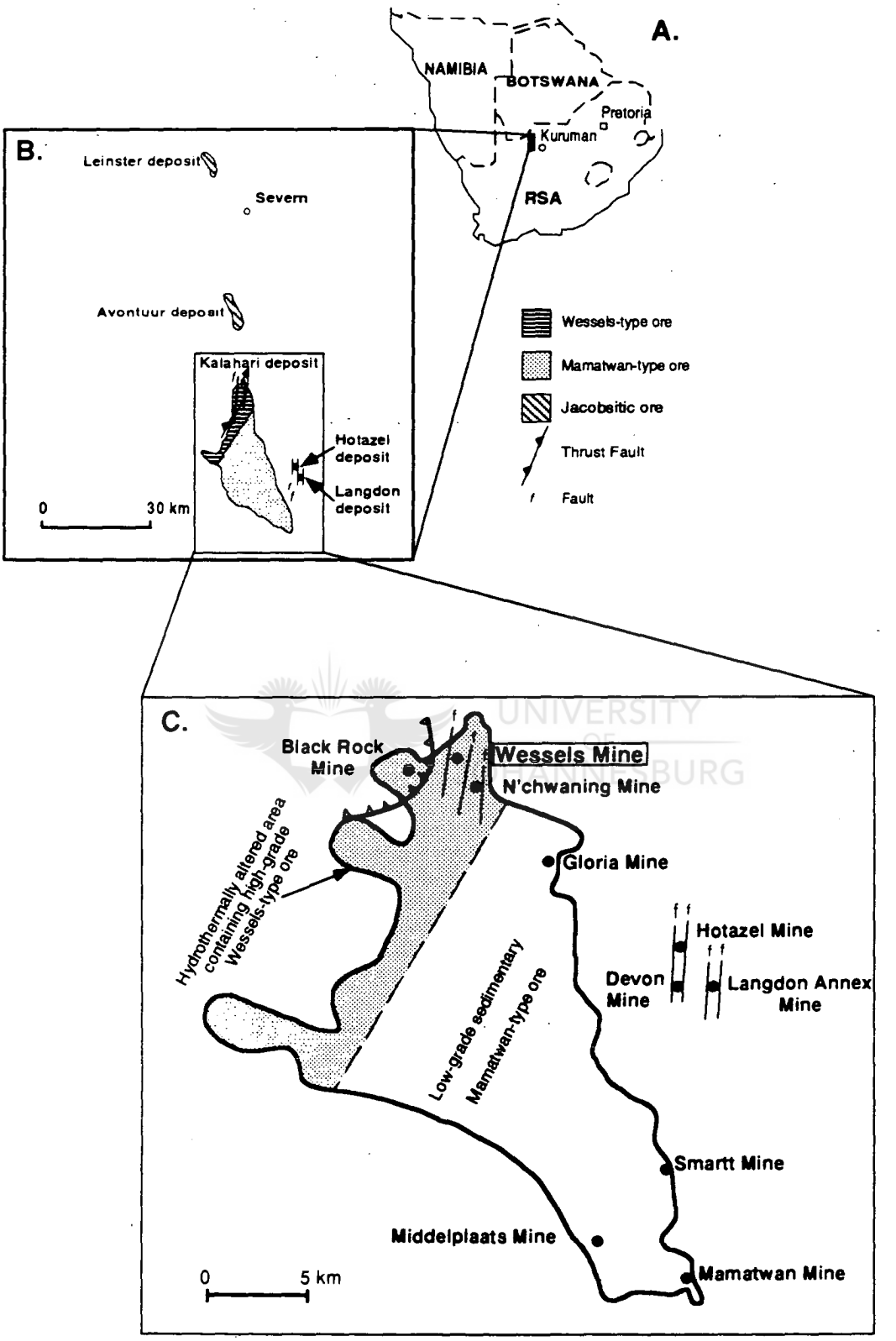

Figure 1: Locality map of the Kalahari manganese field (A) showing the location of five erosionally preserved deposits (B) and the distribution of thrusting, major normal faulting, ore types, and location of mines (C).

establish whether similar geological parameters could be identified as responsible for the distribution of high-grade manganese ores and zones of ferruginization in Wessels mine.

Wessels mine, like Nchwaning mine, is an underground operation ideally suited for such a study. The room and pillar mining technique applied in both of these two mines provides excellent opportunities for sampling transitions between high-grade Wessels-type ore and low-grade Mamatwan-type ore in mined-out areas. Another advantage is that the structure of the area is well known because of mining operations. Drives also crosscut faults and zones of ferruginization, so that their relationship to different types of manganese ores can also be studied.

Regional geological setting

At Wessels mine the manganese-bearing Hotazel Formation occurs at a depth of between 350 and 400 m below surface. The manganese beds are covered by very late Palaeoproterozoic red shale and quartzites of the Mapedi Formation of the Olifantshoek Group (Beukes and Smit, 1987), late Carboniferous to early Permian glaciogenic diamictite of the Dwyka Group of the Karoo Supergroup and Tertiary to Quarternary clay, calcrete, gravel and sand of the Kalahari Formation (Fig. 2).

The Hotazel Formation dips gently at between 2 and 15 degrees to the west. It is conformably underlain by pillow lavas and hyaloclastites of the Ongeluk Formation and unconformably overlain by red shale of the Mapedi Formation of the Olifantshoek Group (Fig. 2). A thin chert and hematite small-pebble conglomerate is developed along the unconformity at the base of the Mapedi Formation (Wiggering and Beukes, 1990).

The Hotazel Formation contains three manganese beds, each forming the centre of three symmetrical sedimentary cycles, composed of iron-formation ↔ hematite-lutite ↔ manganese-lutite (Beukes, 1983). The lowermost manganese ore bed is the best developed and thickest.

It is on average between 4 and 8 m thick at Wessels mine, but known to reach a thickness of up to 45 m at Mamatwan mine some 35 km to the south of Wessels mine (Fig. 1C). All the ore mined at Wessels is from this lower manganese bed. The middle bed is only poorly developed, seldom exceeding more than one meter in thickness, and may be absent in some areas of the Kalahari deposit (De Villiers, 1970). The upper bed is of the order of 2 to 4 m thick and consists mainly of low-grade

manganese ore which has been mined on a local scale. Bostonite dykes, trending north-east south-west, intrude the Hotazel Formation. These dykes do not intrude the overlying Mapedi Formation of the Olifantshoek Group (W.J. Grobbelaar, personal communication, 1995).

North-south striking normal faults displace the manganese ore beds in the Wessels-mine with a mean throw of between 5 and 10 m (Fig. 2). Some faults have virtually no displacement, whereas others are known to have displacements of up to 60 m. Downthrows are almost invariably to the west. Minor east-west striking faults are also present. The system of normal faults apparently also preserve the Hotazel and Langdon deposits in graben structures below the Kalahari Formation to the east of Wessels mine (Fig. 1C).

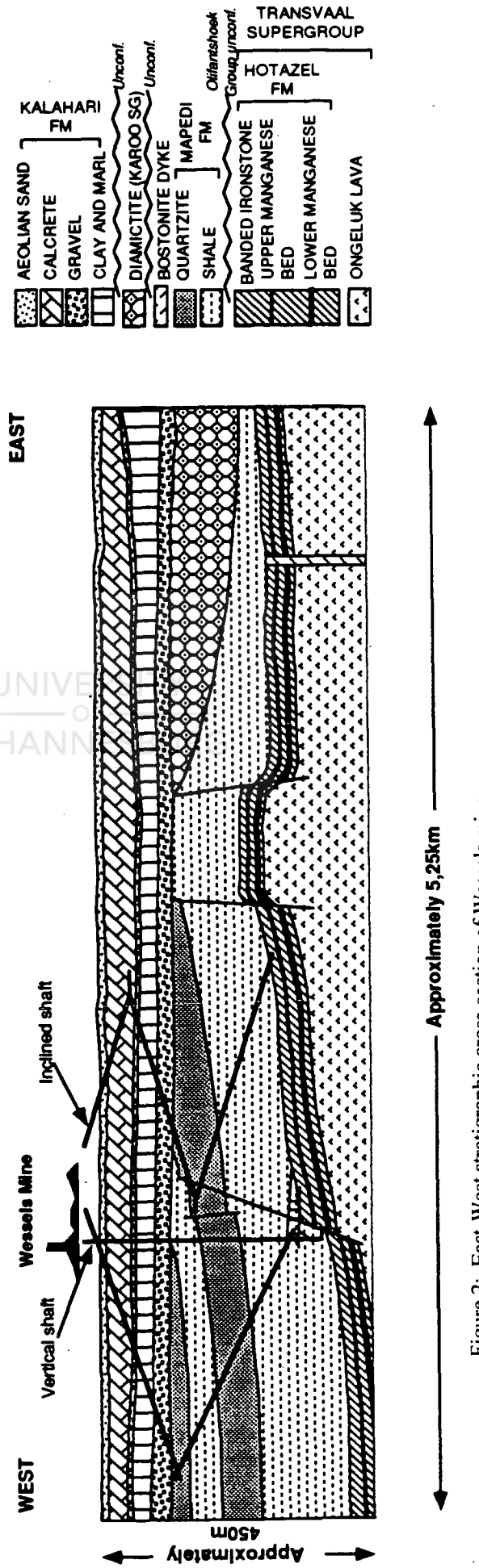

Figure 2: East-West stratigraphic cross-section of Wessels mine.

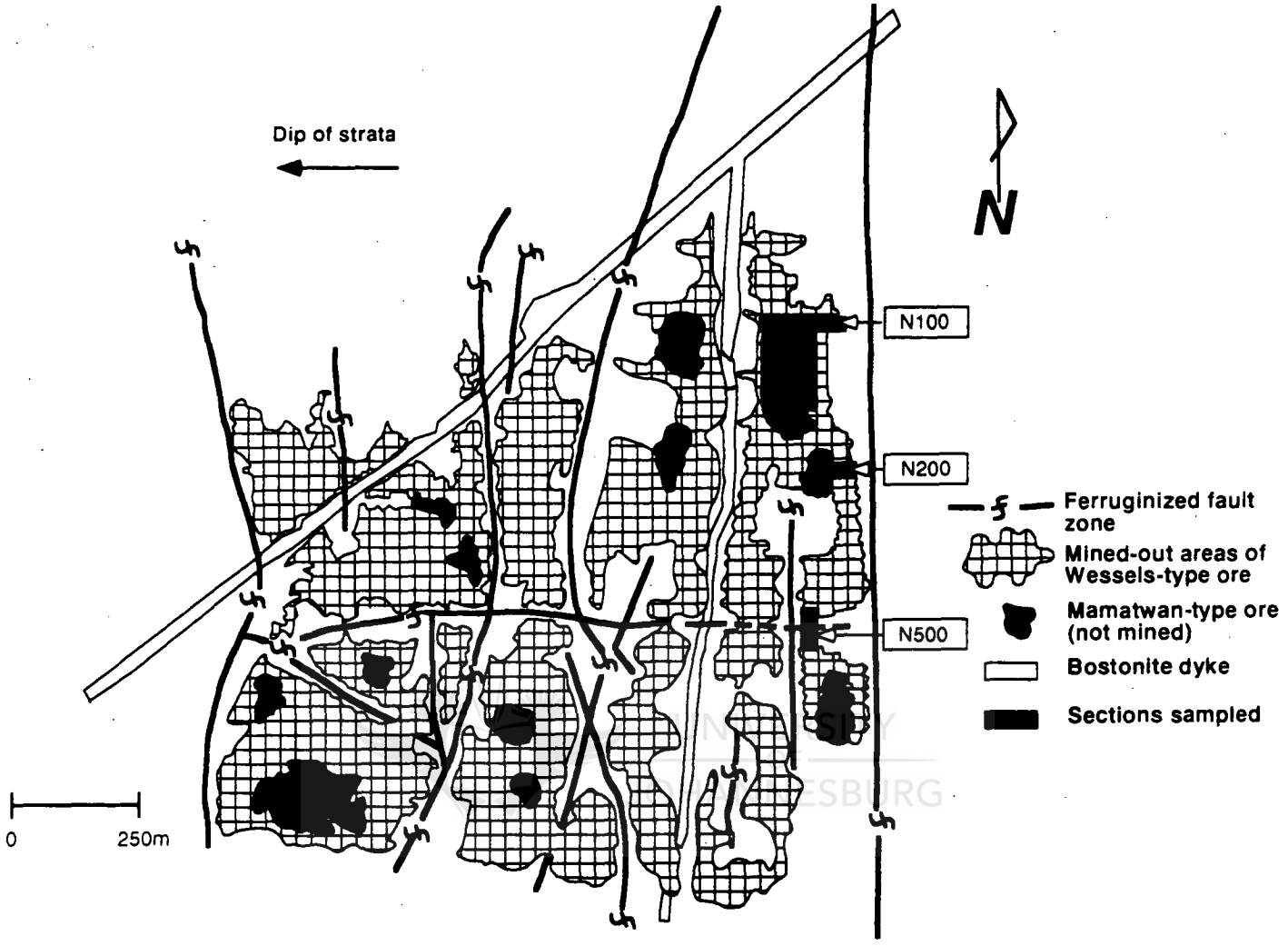

Figure 3: Simplified stope plan of the sampling area in Wessels mine. Traverses sampled are indicated.

Towards the west of Wessels mine there is evidence of large scale overthrusting. The thrust duplicated the sequence and also formed the Black Rock outcrop (Fig. 1C). The normal faults apparently post-date the deposition of the red beds of the overlying Olifantshoek Group (Fig. 2), but predate the thrust event (Fig. 1C). Thrusting is related to the formation of the Kheiss orogen (1700 - 1800 m.y.) (Stowe, 1986; Beukes and Smit, 1987). Development of high-grade Wessels-type ore is apparently relatd to this area of normal faulting and thrust deformation in the northwestern part of the Kalahari deposit (Kleyenstüber, 1984) (Fig. 1C).

The age of the Hotazel Formation is not very well constrained. Ongeluk lavas conformably underlying the Hotazel Formation, have a Pb-Pb apparent age of 2239±90 m.y. (Armstrong, 1987). In contrast the Hartley lava of the overlying Olifantshoek Group, above the Lucknow quartzites, define a Rb-Sr isochron that indicates and age of 2026±180 m.y. with a Pb-Pb age of 1830±400 m.y. (Armstrong, 1987). This implies that the Hotazel Formation was deposited between 2100-2200 m.y. ago.

Detailed geological setting

A map of Wessels mine on which normal faults, ferruginized zones and bostonite dykes are shown, relative to mined-out areas, indicate that manganes ore is not mined adjacent to major normal faults (Fig. 3). There appear to be two main reasons for this, namely loss of ground due to normal faulting and ferruginization of manganese ores along the faults. North-south trending faults are dominant and most of th ferruginization is present alongside them. Ferruginization is also associated with some of the east-west trending normal faults (Fig. 3). It is important to note that unmined areas of low-grade Mamatwan-type ore occur in the center of fault blocks (Fig. 3). High-grade Wessels-type ore is developed between areas of unmined Mamatwan-type ore and the ferruginized zones along faults.

Wessels-type manganese ore is usually coarse-grained and massive or vuggy, with a metallic luster. This contrasts with the dull, very fine-grained appearance of primary sedimentary Mamatwan-type ore preserved in central parts of fault blocks. Mamatwan-type ore has got a spotted appearance due to the presence of tiny ovoidal carbonate concretions. Ferruginized zones along fault planes are very fine-grained wit a bluish metallic lustre and irregular subhorizontal to vertical banding. The iron-formation overlying and underlying the manganese ore beds are also known to be altered in areas where high-grade Wessels-type ore is developed. Magnetite and ankerite are replaced by hematite in altered iron-rormation with some acmite developed as a secondary mineral in chert mesobands (Kleyenstüber, 1985). Leaching and recrystallisation of chert bands in altered iron-formation resulted in development of considerable amounts of porosity of secondary origin.

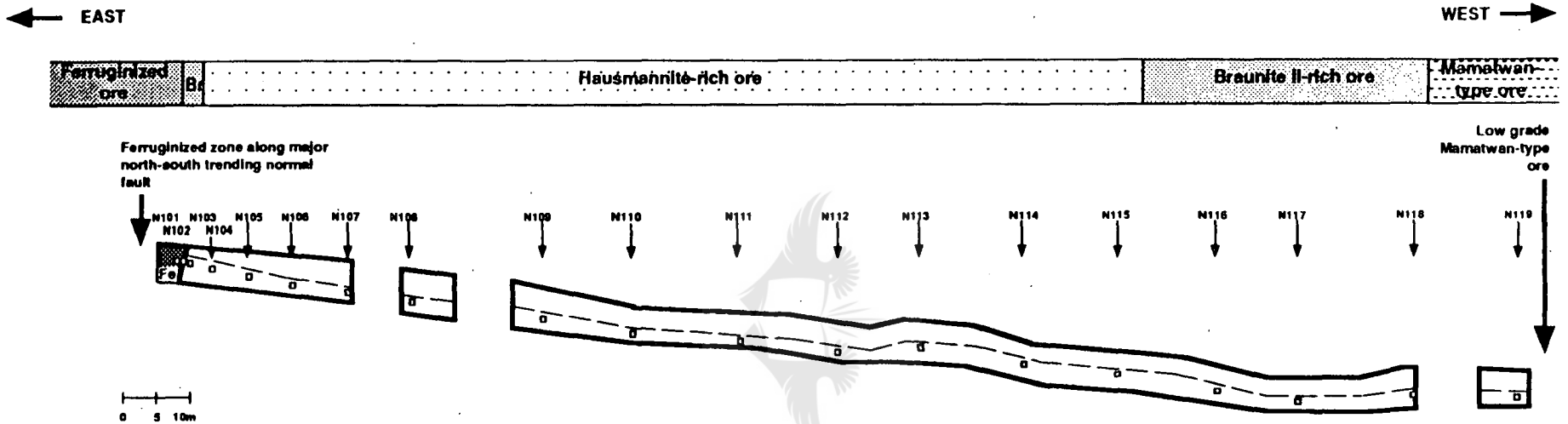

	N101	N102	N103	N104	N105	N106	N107	N108	N109	N110	N111	N112	N113	N114	N115	N116	N117	N118	N119
HAUSMANNITE		X	XXX	XXX	XXX	XXX	XXX	XX	XXX	XXX	XXX	XXX	XXX	XXX	XXX	XX	X	X	X
BIXBYITE			X			XXX	XXX	XX	X		X								
BRAUNITE II	X	XXX	X	X	X	XX	XX	X	XX		X	XX	XXX	XX	XX	XXX	XX	X	XX
BRAUNITE	X	XX	X							X							XXX	XXX	XXX
MANGANITE								XXX	X	X									
HEMATITE	XXX	X	X	X				X	X					X		X			
CALCITE	XX	XXX				XX		X	X	X					X	X			X
BARITE					X	X		X		X			X		X	X		X	
BRUCITE					X							X	X						
ANDRADITE								X					X				X		
CLINOCHLORE			X	X				X	X	X	X	X	X	X	X	X	X		
NATROLITE														X	X				
CRYPTOMELANE										X	X								
GAUDEFROYITE			X		X	X	X		X		X				X				

Figure 4: Mineralogical composition of ores along traverse N100 as determined by XRD analyses. (xxx - dominant mineral phase, > 30 vol %; xx - important mineral phase, 10-30 vol ;, x- subordinate or minor mineral phase, < 10 vol %)

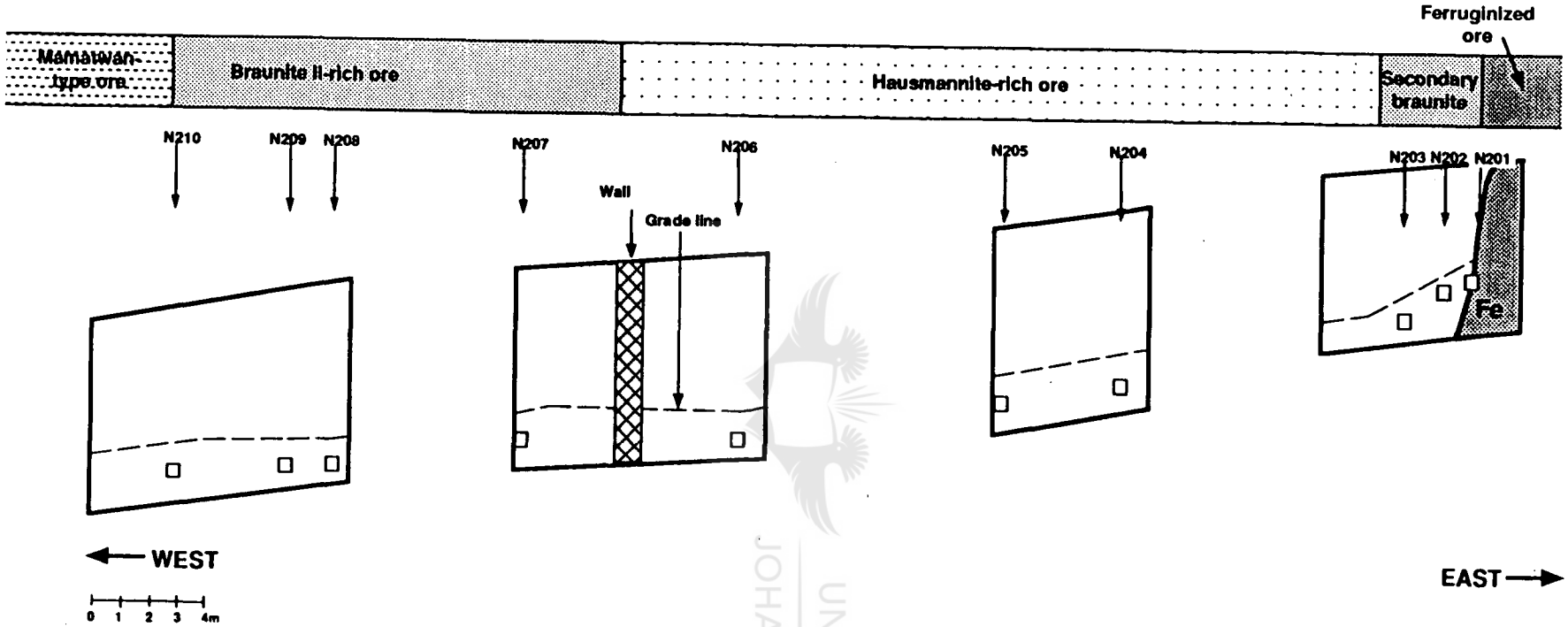

	N210	N209	N208	N207	N206	N205	N204	N203	N202	N201
HAUSMANNITE	xx	xx	xx	xxx	xxx	xxx	xxx	xxx	xx	
JACOBSITE									x	
BRAUNITE II		xxx	xxx	xx	xx	x		x	xxx	
BRAUNITE	xxx	xx	xx						xx	xxx
BIXBYITE			x		x	xx	x	x	x	x
MANGANITE										
HEMATITE			x	x	x	x	x		xx	xx
CALCITE	x	x				x	x	x	xx	xxx
BARITE	x		x				x	x	x	
BRUCITE				x	x		x			
ANDRADITE								x		xx
CLINOCHLORE	x	x	x		x	x	x	x	x	
NATROLITE			x							
CRYPTOMELANE	x									
FEITKNECHTITE			x		x					

Figure 5: Mineralogical composition of ores along traverse N200 as determined by XRD analyses. (xxx - dominant mineral phase, > 30 vol %; xx - important mineral phase, 10-30 vol %; x - subordinate mineral phase, < 10 vol %).

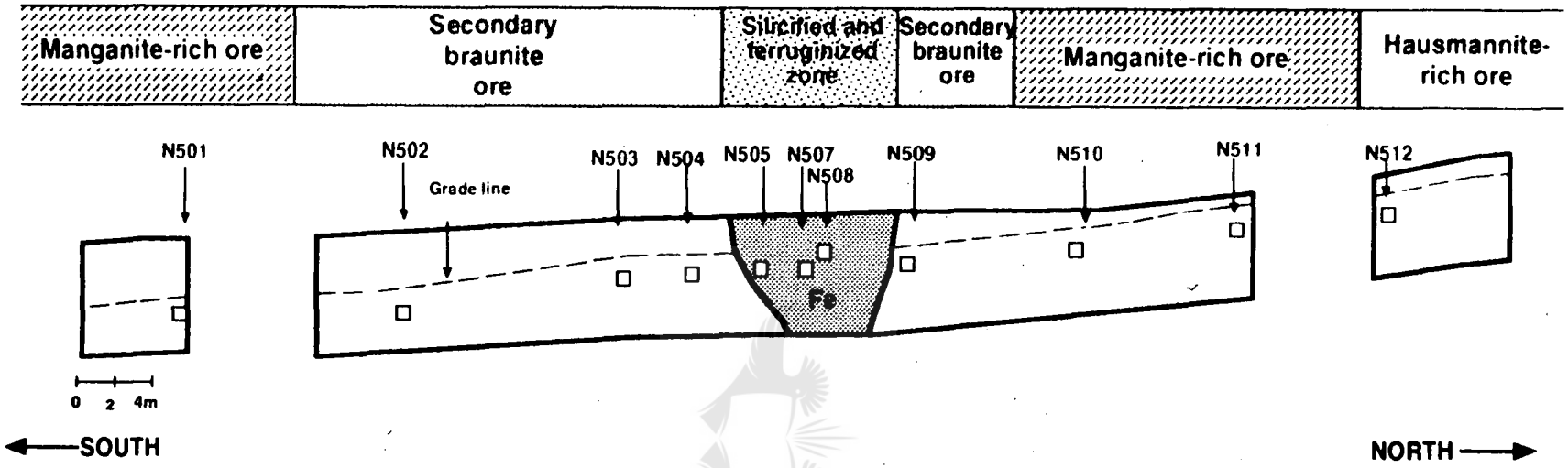

	N501	N502	N503	N504	N505	N507	N508	N509	N510	N511	N512
HAUSMANNITE				x					X	XX	XX
BRAUNITE II	X	XXX	XXX	XXX	XX			XXX	x	X	X
BIXBYITE	XXX							XXX			
MANGANITE	XXX	XX	XX	X				x	XXX	XXX	XXX
HEMATITE					XX	X	XXX				
CALCITE		X	X	X		X		X	XX	X	x
BARITE											
BRUCITE	X	X	X	X				X			
CLINOCHLORE			X				X				
CRYPTOMELANE			X	X				X			
FEITKNECHTITE			X					X			
AEGIRINE					XXX	XXX	XXX				
GAUDEFROYITE		X									
INESITE			X								
QUARTZ						XXX	XX				

Figure 6: Mineralogical composition of ores along traverse N500 as determined by XRD analyses (xxx - dominant mineral phase, > 30 vol %, xx - important mineral phase, 10-30 vol %; x - subrdinate or minor mineral phase, < 10 vol %).

For this study only the lower manganese bed was sampled. Samples were taken along two sections (N100 and N200) displaying lateral transitions from low-grade Mamatwan-type ore through zones of high-grade Wessels-type ore into zones of ferruginization along north-south trending normal faults. A third section (N500) was sampled through a zone of ferruginization and silicification associated with an east-west trending normal fault (Fig. 3).

Selected hand samples were collected for petrographic and geochemical analysis. In order to eliminate possible effects of vertical zonation in ore beds, samples were taken 100-120 cm below the "grade line" in the ore bed. The "grade line" is a thin red hematite lamina approximately 4 mm thick, that occurs consistently in the middle of the lower manganese ore bed at Wessels mine.

Section N100 is some 200 m long and extends from low-grade Mamatwan-type ore in the west, through high-grade Wessels-type ore, into a ferruginized zone along a major north-south trending normal fault in the east (Figs. 3 and 4). Samples were taken along a north facing stope wall. Samples N101 and N102, on the eastern end of the section, were taken in close proximity to each other, with sample N101 in the ferruginized ore and sample N102 on the border between ferruginized ore and high-grade Wessels-type ore. The other samples were evenly spaced, about 10 m apart. Sample N119 is of Mamatwan-type ore, and the other samples, N102 - N118, of Wessels-type manganese ore.

Section N200 is some 40 m long (Figs 3 and 5). This section represents a transition from a low-grade Mamatwan-type ore, in the central part of a fault block in the west, through high-grade Wessels-type ore, into a ferruginized zone along a major north-south trending normal fault in the east. In both sections N100 and N200 the grade line is slightly undulating due to the presence of wide open folds with amplitudes of a metre or two and wavelengths of 30 to 40 m.

Section N500 extends across a zone of ferruginization bordered by Wessels-type ore (Figs 3 and 6). In hand sample clasts of banded quartz-rich rock cemented by secondary quartz are present in the ferruginized fault zone. The "grade line" is not displaced by the fault zone (Fig. 7), which may suggest either the presence of a small graben structure or a strike-slip fault component.

Definition of ore types and lateral zonation along sections

A study of the various sections resulted in the distinction of six principle ore-types, namely hematite-rich ore, massive fine-grained secondary braunite-rich ore, massive coarse-grained hausmannite-rich ore, vuggy coarse-grained hausmannite-rich ore, braunite II-rich ore and Mamatwan-type ore.

Zones of ferruginization are characterized by very fine-grained, massive to irregularly banded hematite. Botryoidal hematite are often filling the central fracture or vein of ferruginized fault zones (Fig. 7A). Massive, fine-grained braunite-rich ore is typically developed along the contact between the ferruginized zones and high-grade ore. This ore-type will be referred to as secondary braunite-rich ore. The highest-grade ore, referred to as massive hausmannite-rich ore, is medium- to coarse-grained with a massive appearance (Fig. 7B). Fracture and cleavage planes of hausmannite grains display a typical metallic lustre. Tiny specks of light coloured gangue minerals are present. This is in contrast to another type of high-grade ore, referred to as vuggy hausmannite-rich ore, which is coarse-grained and very porous with abundant light coloured gangue minerals filling vugs and pores (Fig. 7C).

UNIVERSITY OF JOHANNESBURG

The very high-grade massive hausmannite-rich ore appears to be developed in transition zones between vuggy hausmannite-rich ore and massive secondary braunite-rich ore. A fourth common

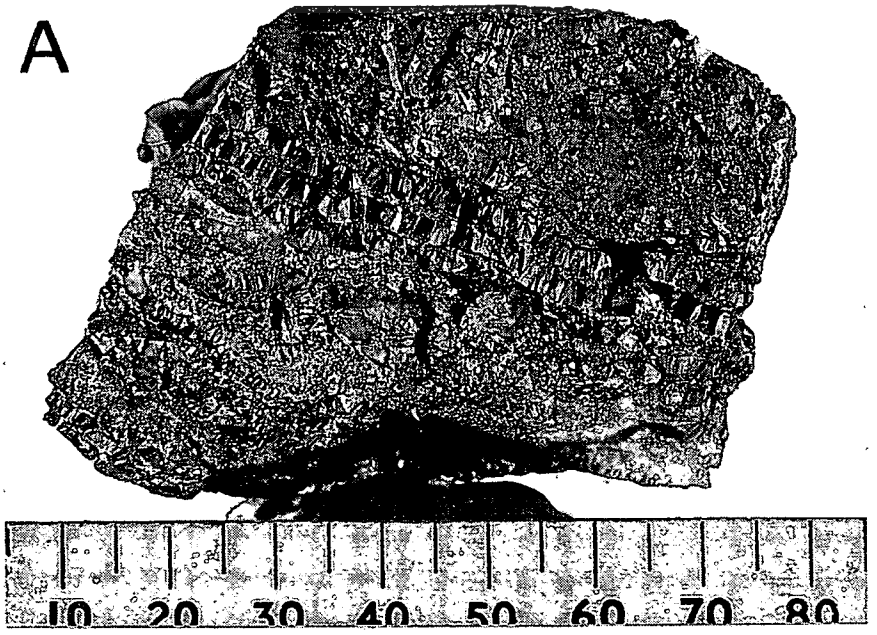

Figure 7: (A) Botryoidal hematite typically developed along central parts of ferruginized fault zones.

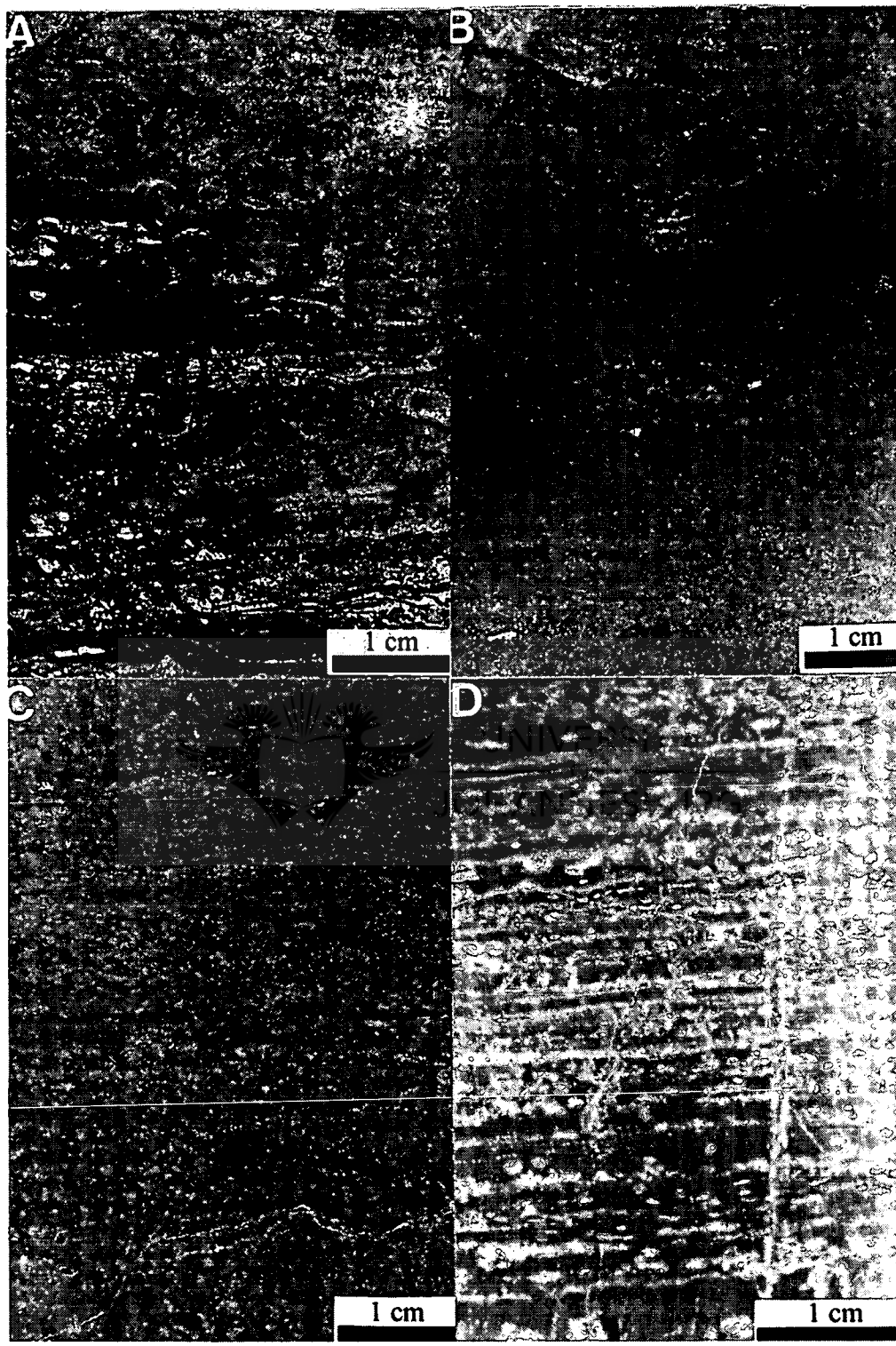

Figure 7 (cont.): (B) massive hausmannite-rich ore, with poorly preserved sedimentary texture. (C) Vuggy, coarse crystalline hausmannite-rich ore, crosscut by an irregular aggregate of massive coarse crystalline hausmannite. (D) Braunite II-rich ore with well preserved sedimentary lamination. (E) Finely laminated carbonate-rich Mamatwan-type ore with numerous kutnahorite ovoids.

type of high-grade ore is medium- to fine-grained with visible remnant sedimentary lamination and abundant calcite-filled vugs. Braunite II is always present and it is therefore referred to as braunite II-rich ore. This ore-type (Fig. 7D) is typically developed in the transition zone between vuggy hausmannite-rich ore and residual low-grade Mamatwan-type ore. Mamatwan-type ore is very fine grained and laminated with abundant small carbonate ovoids (Fig. 7E).

Slight variations in lateral zonation are present along the three sections studied in detail. Along section N100 the low-grade Mamatwan-type ore, composed of carbonate ovoids set in a laminated very fine-grained braunite-rich matrix, is followed eastward, towards the zone of ferruginization, by medium-grained braunite II-rich ore with remnant lamination (Fig. 4). Partial obliteration of original sedimentary lamination took place during the alteration process. Small vugs and secondary pores are present, apparently developed by dissolution of carbonate ovoids and grains that were present in Mamatwan-type ore precursor. Nearer to the ferruginized zone some higher-grade braunite II-rich ore is developed displaying poorly preserved lamination and containign abundant small secondary vugs partly filled with white calcite.

In close proximity to the ferruginized zone, coarse grained vuggy hausmannite-rich ore is developed with abundant calcite-filled vugs (Fig. 4). Original lamination is virtually obliterated. In between this vuggy ore and the massive secondary braunite-rich ore, developed immediately adjacent to the ferruginized fault zone, massive coarse-grained hausmannite-rich ore, almost devoid of secondary vugs or pores, is present. The massive, fine-grained secondary braunite-rich ore is restricted to a very narrow zone, some 2 m wide, next to the ferruginized fault zone. The secondary braunite-rich ore appears to replace coarse-grained hausmannite-rich ore (Fig. 4) and displays little sign of original bedding. In the ferruginized fault zone, irregularly banded dense bluish-grey hematite-rich ore is developed.

Sampling of section N200 started in the transition zone between Wessels- and Mamatwan-type ores (Fig. 5). In this transition zone, Mamatwan-type ore is preserved in which original kutnahorite ovoids have been replaced by hausmannite. Towards the ferruginized fault zone, all ovoids are replaced by hausmannite and lamination is partly obliterated by replacement of the original braunite-lutite by braunite II-rich ore. The latter is followed by coarse-grained calcitic and vuggy hausmannite-rich ore in which no original sedimentary lamination is preserved. More proximal to the ferruginized zone, high-grade massive coarse-grained hausmannite-rich ore with a few secondary pores and minor

gangue minerals are present. Secondary braunite-rich ore is developed immediately adjacent to the ferruginized zone (Fig. 5). This ore is very fine-grained and displays irregular undulating banding composed of alternating hematite- and braunite-rich bands.

The different ore-types along section N500 (Fig. 6) are symmetrically distributed on both sides of a ferruginized fault zone. Coarse-grained hausmannite-rich ore is developed furthest away from the fault zone. The ore is transitional into a medium-grained massive black manganite-rich ore with veinlets of barite and calcite as in sample N503 (Fig. 6). Ore immediately adjacent to the fault zone is composed of fine-grained massive braunite. In the fault zone a fine-grained yellow-brown bended silicified fault rock is developed containing fragments of silicified iron-formation. Red hematite stains the margins of the siliceous fault rock. The central par of the fault rock is composed of quartz and acmite. On the eastern side of the adit, in sample N506 along the fault zone (Fig. 6), a pocket of sugilite is developed surrounded by quartz.

UNIVERSITY OF JOHANNESBURG

Lateral mineralogical variations

All samples collected along the three sections were analysed by X-ray powder diffraction to identify major and minor mineral phases. Analyses were undertaken with a Siemens D-500 diffractometer, using Cu K_α radiation, a step size of 0.04° 2θ and a counting time of 0.5 sec/step between 4 ° and 80° 2θ. Minerals encountered and their ideal chemical formulae are summarized in Table 1.

The results define a systematic mineralogical zonation along the various sections. Along section N100 Mamatwan-type ore (sample N119), at the western end of the section, is composed of braunite with minor amounts of braunite II and traces of hausmannite and calcite (Fig. 4). The trace amounts of hausmannite and calcite are most probably present in remnant kutnahorite ovoids as the transformation of kutnahorite into calcite and hausmannite in such ovoids has been observed in Mamatwan-type ore by Kleyenstüber (1985). Samples N118 and N117 contain similar mineral assemblages to that of N119, but calcite is absent (Fig. 4). Trace amounts of barite, andradite, clinochlore and gaudefroyite are present in the two samples. In the transition zone to Wessels-type ore braunite disappears (sample N116) and abundant braunite II and hausmannite are present (Fig. 4). High-grade ore, with hausmannite as the dominant phase, associated with minor braunite II,

occurs from sample N115 to sample N112. Bixbyite appears in sample N111 and becomes prominent more proximal to the fault zone in samples N106 and N107.

Immediately adjacent to the ferruginized fault zone braunite predominates again and it is especially abundant in sample N102 with trace amounts of hausmannite (Fig. 4). Hematite is the dominant mineral in the ferruginized zone, together with calcite (Fig. 4). Gangue minerals such as barite, brucite, andradite and clinochlore occur sporadically in trace amounts in Wessels-type ore. However, gaudefroyite appears more persistently close to the ferruginized fault zone. These gangue minerals are absent in the fault zone. Cryptomelane is present in trace amounts in samples N110 and N111 (Fig. 4).

Table 1: Minerals encound in the manganese ores during petrographic and powder diffraction studies.

Mineral	Ideal composition	Group
Hausmannite	Mn_3O_4	Oxides + Hydroxides
Bixbyite	Mn_2O_3	
Braunite II	$Ca_{0.5}(Mn,Fe)_7Si_{0.5}O_{12}$	
Braunite	Mn_7SiO_{12}	
Manganite	α-MnOOH	
Feitknechtite	ß-MnOOH	
Marokite	$CaMn_2O_4$	
Jacobsite	$MnFe_2O_4$	
Cryptomelane	KMn_8O_{16}	
Hematite	Fe_2O_3	
Quartz	SiO_2	
Brucite	$Mg(OH)_2$	
Calcite	$CaCO_3$	Carbonates
Gaudefroyite	$Ca_4Mn_3[(O,OH)_3\(BO_3)_3\CO_3]$	
Barite	$BaSO_4$	Sulphates
Andradite	$Ca_3Fe_2[SiO_4]_3$	Silicates
Aegirine/Acmite	$NaFe[Si_2O_6]$	
Inesite	$Ca_2Mn_7[(OH)_2\Si_{10}O_{28}]\cdot 5H_2O$	
Sugilite	$(K,Na)(Na,Fe)_2(Li_2,Fe)[Si_{12}O_{30}]$	
Clinochlore	$Mg_5[(OH)_8\AlSi_3O_{10}]$	
Natrolite	$Na_2[AlSi_3O_{10}]\cdot 2H_2O$	

UNIVERSITY OF JOHANNESBURG

Braunite is the dominant phase, associated with minor hausmannite and trace amounts of calcite and clinochlore (Fig. 5) on the western side of section N200, in proximity to Mamatwan-type ore (sample N210). Away from the Mamatwan-type ore, braunite II becomes the dominant mineral phase (samples N208 and N209), with minor hausmannite and braunite, and trace amounts of barite and clinochlore. Braunite disappears within the higher-grade hausmannite-rich ores (samples N203 to N207) and the amount of braunite II decreases considerably (samples N206 and N207). Trace amounts of calcite, clinochlore, brucite, barite, natrolite and andradite are present (Fig. 5). Very close to the ferruginized fault zone (sample N202) braunite II is the main mineral, associated with minor amounts of hausmannite, braunite, hematite, jacobsite and calcite (Fig. 5). Immediately adjacent to the ferruginized fault zone, in sample N201, hausmannite and braunite II are absent and braunite and calcite represent major phases together with minor hematite and andradite.

Section N500 displays symmetrical variation of manganese mineral assemblages on both sides of the ferruginized fault zone (Fig. 6). Most distal to the fault zone, manganite is the major mineral in high-grade ore with subordinate hausmannite and braunite II. To the south of the fault zone bixbyite occurs together with the manganite. Towards the ferruginized zone, braunite II becomes predominant, associated with minor amounts of manganite. Trace amounts of brucite and calcite are present as gangue minerals. In the fault zone itself only minor braunite is present, associated with large amounts of acmite, hematite and calcite (Fig. 6). Quartz is a major constituent of the mineral assemblage in the centre of the ferruginized zone. Some cryptomelane, feitknechtite, gaudefroyite and inesite are present immediately adjacent to the ferruginized zone in braunite II-rich ore (Fig. 6). The occurrence of small amounts of clinochlore is restricted to ores immediately adjacent to the fault zone (Fig. 6).

Lateral petrographic zonation and paragenetic relationships

Polished thin sections were used to study the petrographic characteristics of the various ore types in reflected and transmitted light. Sedimentary Mamatwan-type ore consists of an intergrowth of very fine-grained braunite and kutnahorite (grain size ranging from 1 to 20 μm). Tiny specks of hematite (generally less than 5 μm in diameter) are present as inclusions in braunite and kutnahorite. Fine sedimentary bedding is defined by thin laminae with varying concentrations of kutnahorite and

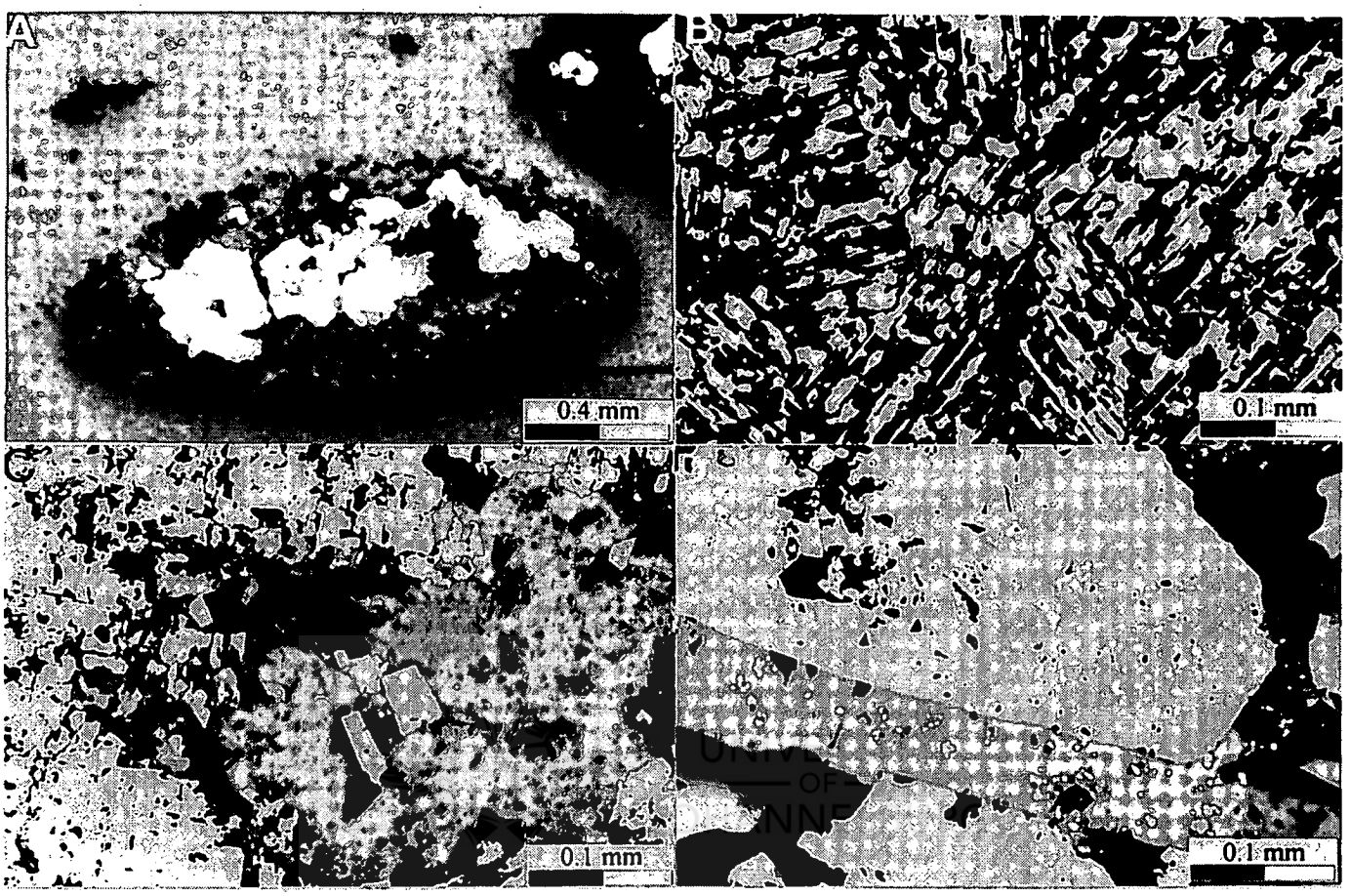

Figure 8: Reflected light photomicrographs: (A) Carbonate ovoid filled by sparitic calcite and euhedral hausmannite crystals, set in a braunite-hematite-calcite matrix. (B) Very porous, skeletal intergrowth of braunite II and braunite (new) (both light gray). (C) Large, anhedral manganite grain (gray), enclosing euhedral hausmannite crystals (light gray), asssociated with gaudefroyite (very dark gray), surrounded by braunite II (white). (D) Stubby prismatic and long prismatic marokite crysals with tiny hematite (white) and gaudefroyite inclusions (black).

braunite and abundant carbonate ovoids that consist of kutnahorite and manganoan calcite. These ovoids are in many cases replaced by hausmannite and calcite (Fig. 8A). This replacement process represents the first sign of alteration of the primary sedimentary manganese ores.

Fine-grained braunite and kutnahorite are replaced by braunite II in braunite II-rich ore; preferentially developed transitional between residual Mamatwan-type ore and high-grade hausmannite-rich ores. The braunite II crystals are generally subhedral or euhedral with a bipyramidal shape and they are considerably larger in size (up to 250 μm in diameter) than the primary braunite in the matrix of Mamatwan-type ore. Tiny hematite specks are common as inclusions in the braunite II.

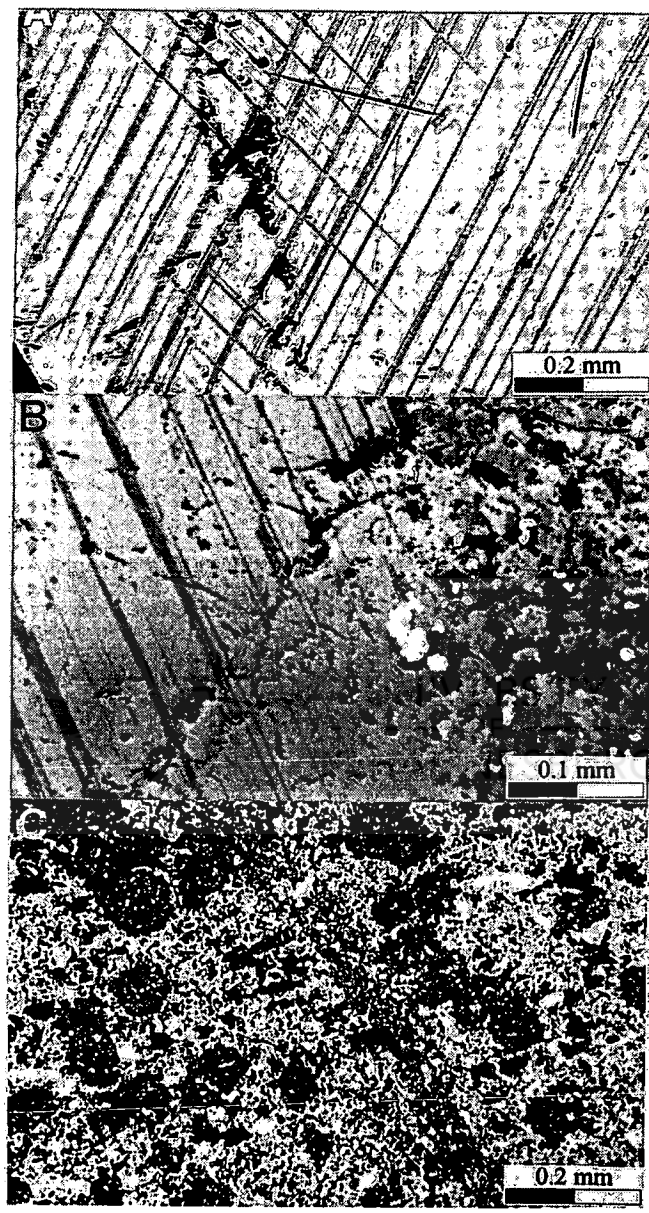

Figure 9: Reflected light photomicrographs. (A) Coarse crystalline hausmannite with typical polysynthetic twinning. (B) Fine crystalline magnetic hausmannite associated with andradite (dark gray) and hematite (white), replaced by coarse crystalline non-magnetic anhedral hausmannite displaying polysynthetic twinning (left half). (C) Mottled texture, with large round andradite 'mottles' dispersed in a fine crystalline matrix of magnetic hausmannite (gray) and hematite (white).

Braunite II forms at the expense of kutnahorite-rich laminae first, with the result that kutnahorite is always absent in braunite II-rich ores, whereas some primary braunite may still be preserved. Many of the original carbonate ovoids are replaced by secondary sparitic calcite and euhedral hausmannite crystals, which are generally concentrated in the centre of ovoids. (Fig. 8A). Veinlets filled with gaudefroyite and hausmannite may crosscut braunite II-rich ore. Gaudefroyite and andradite also occur as infilling of pores and small vugs in the ore. These pores and vugs apparently develop from preferential dissolution of kutnahorite matrix or primary carbonate ovoids.

A variety of braunite with very low silica contents (< 5 wt %) (Fig. 8B), referred to as 'braunite (new)' by Kleyenstüber (1985) was identified in a few samples. Identification is based on the characteristic prismatic habit and skeletal texture of the crystals that replace braunite II and the hematite inclusions normally present in braunite II. Braunite (new) thus appears to form at the expense of braunite II and hematite inclusions in the braunite II.

The transition zone between braunite II and hausmannite-rich ores is marked by the replacement of braunite II by hausmannite. Vugs in hausmannite-rich ores are lined by euhedral hausmannite crystals and filled by sparitic calcite, associated in many cases with barite, clinochlore and gaudefroyite. Braunite II and skeletal braunite (new) are absent or only present in trace amounts in highest-grade hausmannite-rich ores. Large euhedral bixbyite grains (isometric cubes of up to 2 mm), manganite (Fig. 8C)and marokite (Fig. 8D) are locally abundant in the highest-grade ore. Manganite forms very large anhedral grains (up to 5 mm in diameter) and encloses small euhedral hausmannite grains (Fig. 8C). Marokite forms euhedral prismatic to stubby short-prismatic crystals up to 0.5 mm in length (Fig. 8D).

Hausmannite-rich ore is characterized by its massive, very coarse-grained to medium-grained texture with considerable secondary porosity (Fig. 9A). These secondary vugs may be filled by calcite, gaudefroyite, andradite, barite and clinochlore. The increase in pore and vug space is closely related to the process of leaching of carbonate and silica from Mamatwan-type ore precursor.

Coarse-grained hausmannite appears to replace an earlier, very fine-grained assemblage of hausmannite, hematite and andradite (Fig. 9B), an observation already made by Kleyenstüber (1985).

In some samples of fine-grained hausmannite-rich ore the replacement of carbonate ovoids by andradite results in a characteristic mottled appearance of the ore (Fig. 9C).

Subhedral andradite grains, finely intergrown with hausmannite and hematite, may have formed by the reaction:

braunite + hematite + kutnahorite → andradite + hausmannite (±hematite)

(Mamatwan-type ore) (Wessels-type ore)

In the transition zone between hausmannite-rich ore and massive secondary braunite-rich ore, immediately adjacent to the ferruginized fault zones, hausmannite is being replaced by braunite II along twin lamellae in the hausmannite. This braunite II contains anhedral inclusions of remnant hausmannite and appears to be closely associated with braunite. Vugs filled with gaudefroyite and veinlets filled with specularite and calcite are present. The massive secondary braunite-rich ore, developed along the margins of zones of ferruginization, is composed of a mosaic-texture intergrowth of braunite crystals. The braunite crystals are associated with and replaced by specularite. In rare cases outlines of primary carbonate ovoids, completely replaced by sparitic calcite, may be preserved in the secondary braunite-rich ore.

Hematite-rich ores of the ferruginized zones are composed of very fine crystalline dusty hematite, needle-like specularite and calcite. Specularite is also associated with rare euhedral andradite crystals. Specularite infiltrates massive secondary braunite-rich ore, replacing braunite crystals from the outside inwards. Veinlets filled with hausmannite, calcite and specularite are common in the massive secondary braunite-rich ore. Veinlets filled by calcite and specularite are also present in the ferruginized zones. The silicified and ferruginized zone in section N500 (Fig. 7) is composed of a very fine and dense intergrowth of anhedral acmite, clinochlore, sugilite and quartz. The original lamination of the sedimentary precursor is in places well preserved due to variations in the concentrations of hematite and silicate minerals. The central part of the ferruginized fault zone is brecciated with clasts set in a quartz-hematite matrix. Breccia fragments are silicified and composed of ferruginized manganese ore and altered acmite-rich iron-formation.

It has to be emphasized that the alteration of Mamatwan-type ore to Wessels-type ore is by no means gradational. Rather, it appears to be related to metasomatism caused by fluids that infiltrated primary sedimentary ore beds along bedding planes and a system of fractures or faults (Fig. 10).

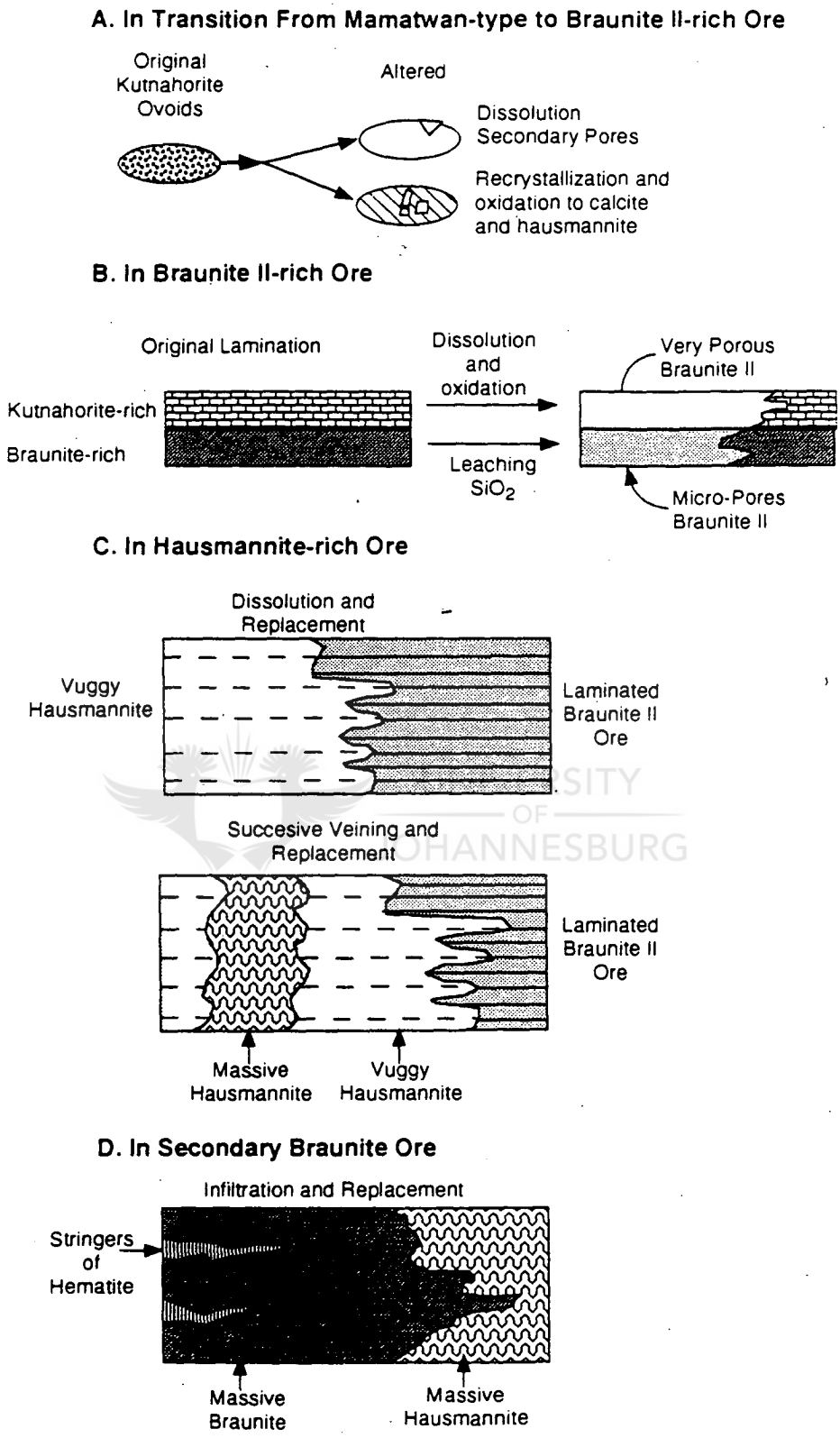

Figure 10: Diagram illustrating characteristic textural changes with increasing degree of alteration during the transformation of low-grade Mamatwan-type ore to high-grade Wessels-type ore.

In some cases contacts between Mamatwan-type ore and high-grade Wessels-type ore may thus be very sharply defined on a micro- to macroscopic scale. Metasomatic alteration is also indicated by transformation of primary kutnahorite ovoids into ovoids composed of calcite with a core of hausmannite, suggesting penecontemporaneous dissolution, oxidation and reprecipitation of the components of the ovoid (Fig. 10A). Slightly more proximal to zones of ferruginization in transition zones to braunite II-rich ores, infiltration of fluids apparently led to the transformation of original braunite-kutnahorite laminae in the Mamatwan-type ore to porous braunite II-rich laminae (Fig. 10B). Original carbonate-rich laminae in Mamatwan-type ore become especially porous when altered to braunite II (Fig. 10B). In transition zones to hausmannite-rich ores, the braunite II-rich ores may in turn be replaced by fronts or veins of cross-cutting massive coarse-grained hausmannite-rich ore (Fig. 10C). High-grade hausmannite-rich ore is in turn replaced by cross-cutting secondary braunite-rich ore with stringers of secondary hematite (Fig.10D). During final stages of alteration, fluid movement took place along a system of veinlets which were sealed by hausmannite or gangue minerals such as calcite, gaudefroyite or andradite.

UNIVERSITY OF JOHANNESBURG

Chemical composition of selected minerals

A Cameca CAMEBAX electron microprobe coupled to a Link eXL II driven energy dispersive spectrometer was used to analyse the different minerals. An absorbed current of 15 nA on MgO and an acceleration voltage of 15 kV were used for analyses.

Chemical compositions of hausmannite range from iron-poor, with 1-2 wt % Fe_2O_3, to iron-rich, containing 5-11.3 wt % Fe_2O_3 (Table 2). In hausmannite-rich ores, composed of fine-grained hausmannite overgrown by coarse crystalline hausmannite, the fine grained crystals are enriched in iron compared to the coarse-crystalline hausmannite crystals (Fig. 11A). It is interesting to note that the iron-rich hausmannite is strongly magnetic at room temperature and can easily be separated from the iron-poor hausmannite with a simple hand magnet. The presence of magnetic hausmannite is extremely unusual, as it is supposed to be paramagnetic above the Curie temperature of 42.5 °K (Boucher et al., 1970). The nature of the magnetic hausmannite is described in detail by Gutzmer et al. (1995) and the magnetic properties ascribed to exchange of Mn^{3+} by Fe^{3+} on the octahedrally coordinated sites of the distorted spinel-type structure of hausmannite. In lateral sense, both fine-

grained magnetic and coarse-grained non-magnetic hausmannite display an increase in Fe_2O_3-contents from Mamatwan-type ore towards ferruginized fault zones (Fig. 11B).

Table 2: Chemical composition of hausmannite.

Sample	N202M	N203	N203M	N204	N204M	N205	N205M	N207	N207M	N209	N210	N119
No. of analyses	7	9	5	9	15	4	5	3	4	12	2	14
SiO_2	0.2								0.2			0.7
Al_2O_3												
MnO*	32.5	32.6	33.1	32.5	32.5	32.6	31.8	31.1	32.3	31.1	32.1	31.27
Fe_2O_3	5.27	1.95	3.77	2.76	4.81	1.12	11.3	2.47	6.24	4.93	2.97	1.82
Mn_2O_3	61.7	65.0	62.9	64.4	62.6	65.8	57.1	65.8	61.2	63.1	64.7	64.0
MgO	0.5								0.3	0.9		
CaO												
Total	100.1	99.6	99.8	99.7	99.9	99.5	100.2	99.4	100.2	100.0	99.8	98.2

* MnO – Mn_2O_3 charge balance has been calculated

All data are calculated means from several electron microprobe spot analyses

Braunite contains on average between 9 and 11 wt % SiO_2 and 0.6-3.7 wt % CaO (Table 3). The iron content of braunite varies between 2.73 and 10.8 wt % Fe_2O_3. The Fe_2O_3 contents increase rather systematically from that in low-grade Mamatwan-type ore (analysis N119, Table 3) to that

Table 3: Composition of different manganese oxides.

Mineral	Braunite	Braunite	Braunite	Braunite	Braunite II	Braunite II	Braunite (new)	Bixbyite	Marokite
Sample No.	N119	N201	N206	N210	N106	N208	N107	N512	N510
No. of analyses	14	1	6	11	5	19	7	4	3
SiO_2	10.7	9.41	11.7	10.7	4.88	5.15	3.01	0.8	0.2
Al_2O_3	LLD	LLD	LLD	LLD	LLD	LLD	0.35	LLD	LLD
Fe_2O_3	3.23	8.89	5.89	4.54	13.0	14.6	13.4	20.6	3.52
Mn_2O_3	84.1	81.2	78.2	82.7	76.8	75.1	80.9	78.9	72.1
MgO	0.5	LLD	0.6	LLD	LLD	0.8	LLD	LLD	LLD
CaO	1.78	0.76	3.73	2.31	4.89	4.59	3.01	0.6	24.5
Total	100.3	100.3	99.9	100.3	99.6	100.2	100.7	100.9	100.3

Most data are calculated means from several electron microprobe spot analyses. LLD – lower than limit of detection

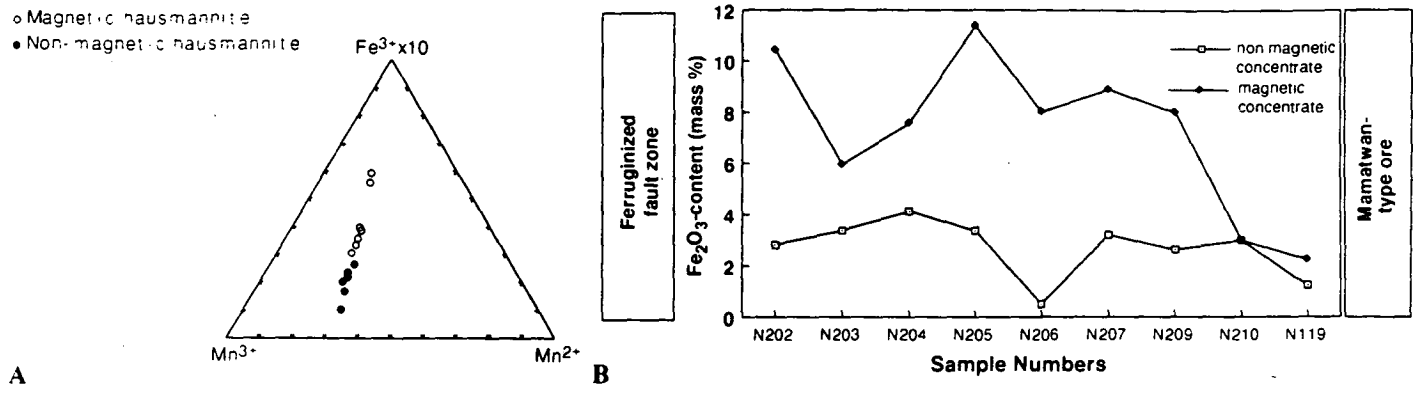

Figure 11: (A) Compositions of magnetic and non-magnetic hausmannite plotted in a Fe^{3+}-Mn^{3+}-Mn^{2+} triangular diagram (each spot represents the average composition calculated from several EDS electron microprobe analyses on one sample/ hausmannite separate (modified from Gutzmer et al., 1995). (B) Average Fe_2O_3 content of magnetic and non-magnetic hausmannite separates in traverse N200 (and sample N119 as example of Mamatwan-type ore) as anlysed by EDS electron microprobe.

in samples bordering ferruginized zones (analysis N201, Table 3) (Fig. 12A). These values of Fe_2O_3 are very similar to that reported by Kleyenstüber (1985) and Gutzmer (1993) from braunite at Hotazel and Nchwaning mines respectively.

UNIVERSITY OF JOHANNESBURG

Braunite II consistently displays higher Fe_2O_3 concentrations than the associated braunite (Table 3). Values range from 3.4 wt % in weakly altered Mamatwan-type ore to 12.7 and 14.6 wt % in Wessels-type ore (Table 3). Highest Fe_2O_3 concentrations are present in close proximity to ferruginized fault zones (Fig. 12B).

The SiO_2 content of braunite II ranges between 4.9 and 5.4 wt %. Braunite (new) as defined by Kleyenstüber (1985), was found only as parts of fine skeletal crystals, that consist predominantly of braunite II (Table 3). SiO_2 and CaO concentrations are at about 3 wt % and the Fe_2O_3 contents are between 13 and 15 wt % (Table 3). Bixbyite, replacing braunite II in hausmannite-rich ore, contains 20.7 - 25.2 wt % Fe_2O_3 (Table 3). No hematite inclusions are present in the bixbyite grains, but they are abundant in the surrounding hausmannite and braunite II. This would suggest incorporation of iron, derived from hematite, into bixbyite during the replacement of braunite II. Analyses of marokite indicated the composition to be very close to the ideal composition of pure $CaMn_2O_4$ with 72.1 wt

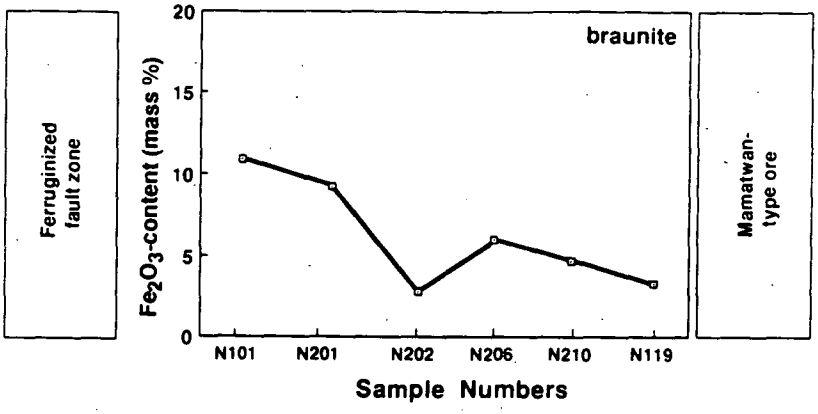

Figure 12A: Average Fe_2O_3 content of braunite in samples of different degrees of alteration as analysed by electron microprobe.

% Mn_2O_3 and 24.5 wt % CaO. However, the marokite in Wessels-type ore contains about 3 wt % Fe_2O_3 (Table 3); the trivalent iron most probably replacing a small amount of Mn^{3+} in the marokite structure.

UNIVERSITY OF JOHANNESBURG

Two texturally distinct types of andradite were recognized, namely andradite replacing carbonate ovoids in braunite II rich ore, and andradite occurring as subhedral to euhedral pore fillings associated with braunite II and hausmannite (Table 4). The andradite in ovoids contains on average about 34.7 wt % CaO in contrast to those intergrown with hausmannite and braunite II which contain

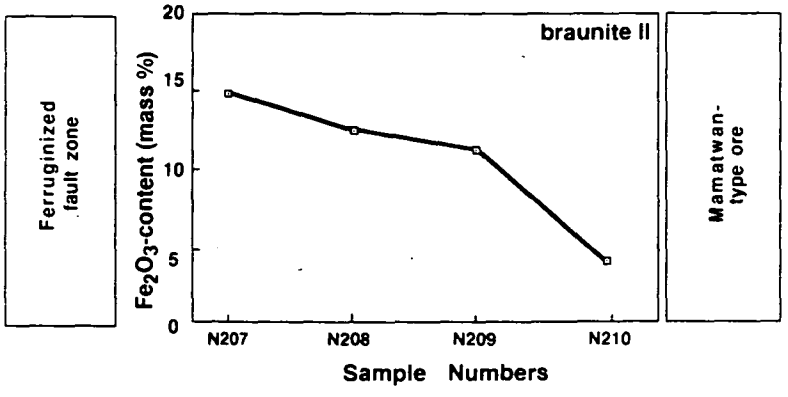

Figure 12B: Average Fe_2O_3 content of braunite II in the central part of traverse N200 as analysed by electron microprobe.

Table 4: Composition of gangue minerals.

Mineral	Andradite	Andradite	Andradite	Calcite*	Mn-Calcite*
Sample No.	N113	N203	N210	N202	N206
SiO_2	34.9	34.0	33.3	LLD	LLD
Al_2O_3	4.2		0.4	LLD	LLD
FeO				0.6	0.4
MnO				1.0	11.2
Fe_2O_3	24.2	31.4	22.0		
Mn_2O_3	2.09	5.1	11.5		
MgO	LLD	LLD	LLD	LLD	LLD
CaO	34.7	29.2	33.2	60.0	51.3
CO_2**				38.4	37.1
Total	100.1	99.7	100.4	100.0	100.0

All data are calculated means from several electron microprobe spot analyses. LLD – lower than limit of detection

* Semiquantitative analyses, calculated CO_2 content is too low

** By difference

29 - 33.2 wt % CaO. In turn the andradite replacing ovoids contain less iron (24 wt %) than those associated with hausmannite and braunite II (up to 34.1 wt %).

Two compositionally distinct types of sparitic calcite are present, both occurring as secondary vug infills. They include namely manganoan calcite, containing 9-14.6 wt % MnO and 0.5 wt % FeO, and manganese-poor calcite which contains between 0.9 - 1.3 wt % MnO and 0.2 - 0.4 wt % FeO (Table 4).

Whole rock geochemistry

A set of samples from section N 200 was analysed to determine lateral variations in chemical composition of the manganese ore from a zone of ferruginization through high-grade Wessels-type ore into low-grade Mamatwan-type ore. Two samples were selected from section N100 to represent material from a ferruginized fault zone proper (sample N101) and from Mamatwan-type ore (sample N119).

Table 5: Bulk rock chemical analyses for selected samples (ICP analyses, MINTEK).

	N101	N201	N202	N203	N204	N205	N206	N207	N208	N209	N210	N119
SiO_2	7.4	8.1	4.4	3.8	0.7	3.5	10.0	3.8	4.7	3.1	11.7	7.3
Al_2O_3	LLD	LLD	LLD	LLD	LLD	LLD	0.9	LLD	LLD	LLD	LLD	LLD
Fe	39.3	5.8	7.6	5.1	3.5	7.4	3.8	6.3	4.8	5.5	4.8	5.1
Mn	12.2	49.2	62.3	66.8	60.2	47.8	49.1	55.6	55.7	54.4	53.9	44.0
MgO	4.0	LLD	1.2	LLD	LLD	LLD	2.6	8.0	LLD	1.3	LLD	1.5
CaO	15.5	6.5	14.6	3.0	2.2	3.4	7.5	4.1	6.9	6.6	5.0	8.8
Na (ppm)	N.D.	94	302	286	170	171	120	600	60	209	199	100
K (ppm)	N.D.	13	39	14	15	10	13	10	3	14	9	17
P_2O_5 (ppm)	N.D.	365	616	528	519	674	397	802	312	816	490	485
CO_2	N.D.	4.5	10.1	0.5	1.5	0.5	3.3	0.5	1.6	2.0	0.5	7.5
H_2O^-	N.D.	0.2	LLD	LLD	LLD	0.1	0.1	LLD	0.1	LLD	LLD	0.1
Mn/Fe	0.3	8.5	8.2	13.1	17.2	6.5	12.9	8.8	11.6	9.9	11.2	8.6
ore type	F	B	B	H	H	H	BII	BII	BII	BII	BII	M

Codes used to describe various ore-types are: M- Mamatwan-type ore, BII- braunite II-rich ore, H-hausmannite-rich ore, B-secondary braunite-rich ore, F- ferruginized ore, N.D. – not determined, LLD – lower than limit of detection

The chemical compositions of the ores display some very interesting lateral variations. Most important perhaps is the fact that highest MnO-contents of 77.7 - 86.2 wt % are present in the massive hausmannite-rich ores, immediately adjacent to secondary braunite-rich ores bordering ferruginized fault zones (Table 5, Fig. 13A). On both sides of the very high-grade ores the MnO content decreases to values between 63.5 and 61.7 wt % (Fig. 13A). Braunite II-rich ores next to

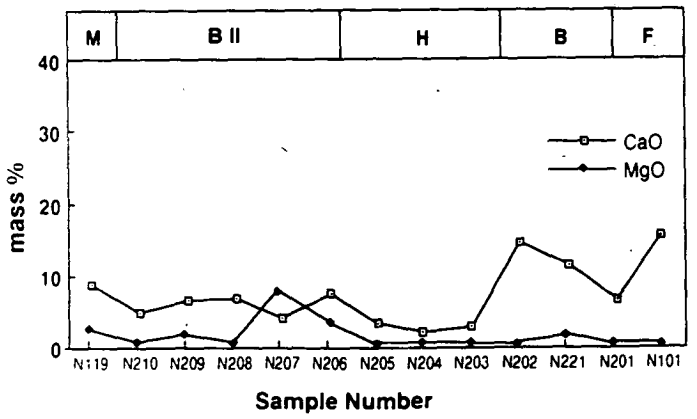

Figure 13C: Variation of CaO and MgO concentrations in traverse N200 in relation to the distribution of ore-types. Sample N101 is added as an example of ferruginized manganese ore, sample N119 as an example for Mamatwan-type ore.

Mamatwan-type ore display very consistent MnO-contents of between 64 and 72 wt % (Table 5, Fig. 13A). The MnO-contents decrease to 56.8 wt % in Mamatwan-type ore of sample N119. This value is higher than in totally unaltered Mamatwan-type ore, which seldom, if ever, contains more than 49 wt % MnO. This implies that Mamatwan-type ore from sample N119 has already undergone some enrichment in manganese. The Fe_2O_3 content of the ores remains rather constant at between 5 and 10.9 wt % (Table 5, Fig. 13A). However, it increases drastically to 56.1 wt % Fe_2O_3 in the ferruginized zone, accompanied by a decrease in MnO concentration to 15.7 wt % (Table 5, Fig. 13A). SiO_2 contents are at lowest (0.7 - 3.5 wt %) in hausmannite-rich ores and slightly higher (3.1 - 4.7 wt %) in braunite II-rich ores (Table 5, Fig. 13B). High concentrations of SiO_2 in braunite II-rich ores (10 - 11.7 wt %) may be related to the presence of abundant andradite. Secondary braunite ore next to the fault zone contains some 8.1 wt % SiO_2 and Mamatwan-type ore about 7.3 wt % SiO_2 (Table 5, Fig. 13B).

CaO and MgO concentrations do not display very obvious lateral variations. However, there appears to be a definite increase of both components towards the ferruginized fault zone and Mamatwan-type ore. MgO values are often below the detection limit of 0.1 wt % in Wessels-type ore, whereas Mamatwan-type ore may contain up to 1.5 wt % MgO and ferruginized fault zones up to 4 wt % MgO. One braunite II-rich sample (N207) contains 8 wt % MgO which may be explained by the presence of brucite in the sample.

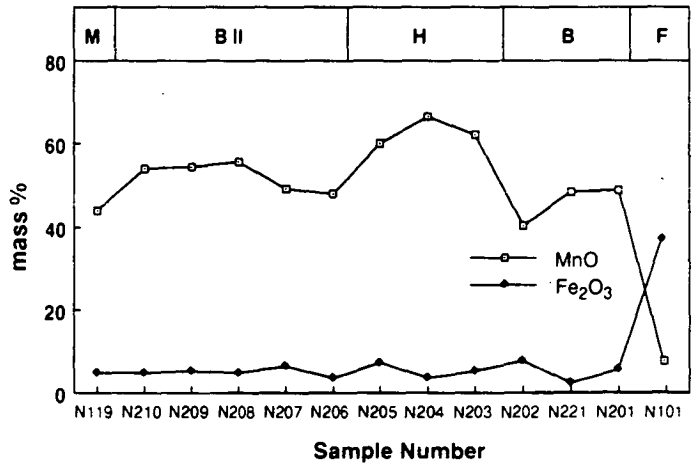

Figure 13A: Variation of MnO and Fe_2O_3 concentrations in traverse N200 in relation to the distribution of ore types. Sample N101 is added as an example of ferruginized mangense ore, sample N119 as an example for Mamatwan-type ore.

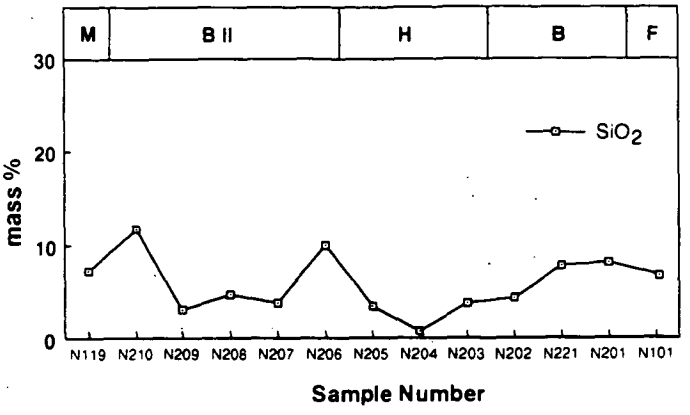

Figure 13B: Variation of SiO_2 concentrations in traverse N200 in relation to the distribution of ore-types. Sample N101 is added as an example of ferruginized manganese ore, sample N119 as an example for Mamatwan-type ore.

The high MgO content is not related to the presence of carbonate minerals, as the CO_2 content for this sample is very low (0.5 wt %). CaO contents are generally below 7.5 wt % in Wessels-type ore, increasing to 8.8 wt % in Mamatwan-type ore and to 15.5 wt % in the zone of ferruginization (Table 5). CaO concentrations tend to correlate positively with CO_2 contents, indicating that most of the CaO is present in the form of calcite. Ores are generally very low in P_2O_5 (365-802 ppm). The same is valid for concentrations of K (9-39 ppm) and Na (94-600 ppm) (Table 5).

Integrated model of lateral zonation in ores

An integrated model describing the lateral zonation of ore types in Wessels mine can be constructed from the data presented above. According to this model (Fig. 14) primary sedimentary Mamatwan-type ore becomes increasingly altered towards zones of ferruginization along a system of normal faults. Alteration apparently took place through infiltration of strata by fluids along bedding planes, fractures, joints and faults. Fluid movement caused dissolution and recrystallization of parent sedimentary manganese ore and precipitation of new manganese and gangue minerals (Fig. 14).

Primary Mamatwan-type ore, preserved in the centre of fault blocks, is finely crystalline and well laminated with abundant small kutnahorite ovoids. The first alteration reaction observed is the transformation of kutnahorite into hausmannite and calcite. This reaction is most prominently

displayed in carbonate ovoids. However, this transformation process has also been observed in areas far removed from high-grade Wessels-type manganese ores, such as at Mamatwan mine (Kleyenstüber, 1985; Nel et al., 1986). It is therefore not known if this specific transformation process is due to diagenesis, very low-grade metamorphism or related to hydrothermal fluid infiltration. Thin calcite and/or hausmannite-filled veinlets may crosscut Mamatwan-type ore. In the transition zone between Wessels and Mamatwan-type ores, the ore becomes medium-grained and sedimentary lamination less well defined, grading into thicker residual layering (Fig. 14). The mineral assemblage changes from braunite-hematite-kutnahorite into braunite II and hausmannite, with small amounts of calcite. With increasing intensity of alteration, closer to zones of ferruginization, calcite is replaced by manganese oxides such as braunite II and hausmannite. The ores are massive and hausmannite occurs as the dominant manganese ore mineral.

In closer proximity to the ferruginized fault zones, vuggy and coarse-grained massive hausmannite-rich ores predominate (Fig. 14). Vugs apparently formed by dissolution and leaching of certain components, especially carbonate. In some cases these vugs are filled by gaudefroyite or light-coloured gangue minerals such as clinochlore, calcite and barite. Towards fault zones the vuggy hausmannite ore becomes dense and massive with very little gangue minerals present. This massive hausmannite-rich ore represents the highest-grade of Wessels-type ore (Fig. 14).

Immediately adjacent to ferruginized fault zones this massive hausmannite-rich ore is in turn replaced by fine-grained massive braunite-rich ore (Fig. 14). Ferruginized zones are typically composed of densely banded hematitized, and in places silicified ores. Brecciation is common within fault zones and clasts of silicified and hematitized manganese ores have been found together with fragments of altered iron-formation cemented by quartz, other silicates and/or calcite.

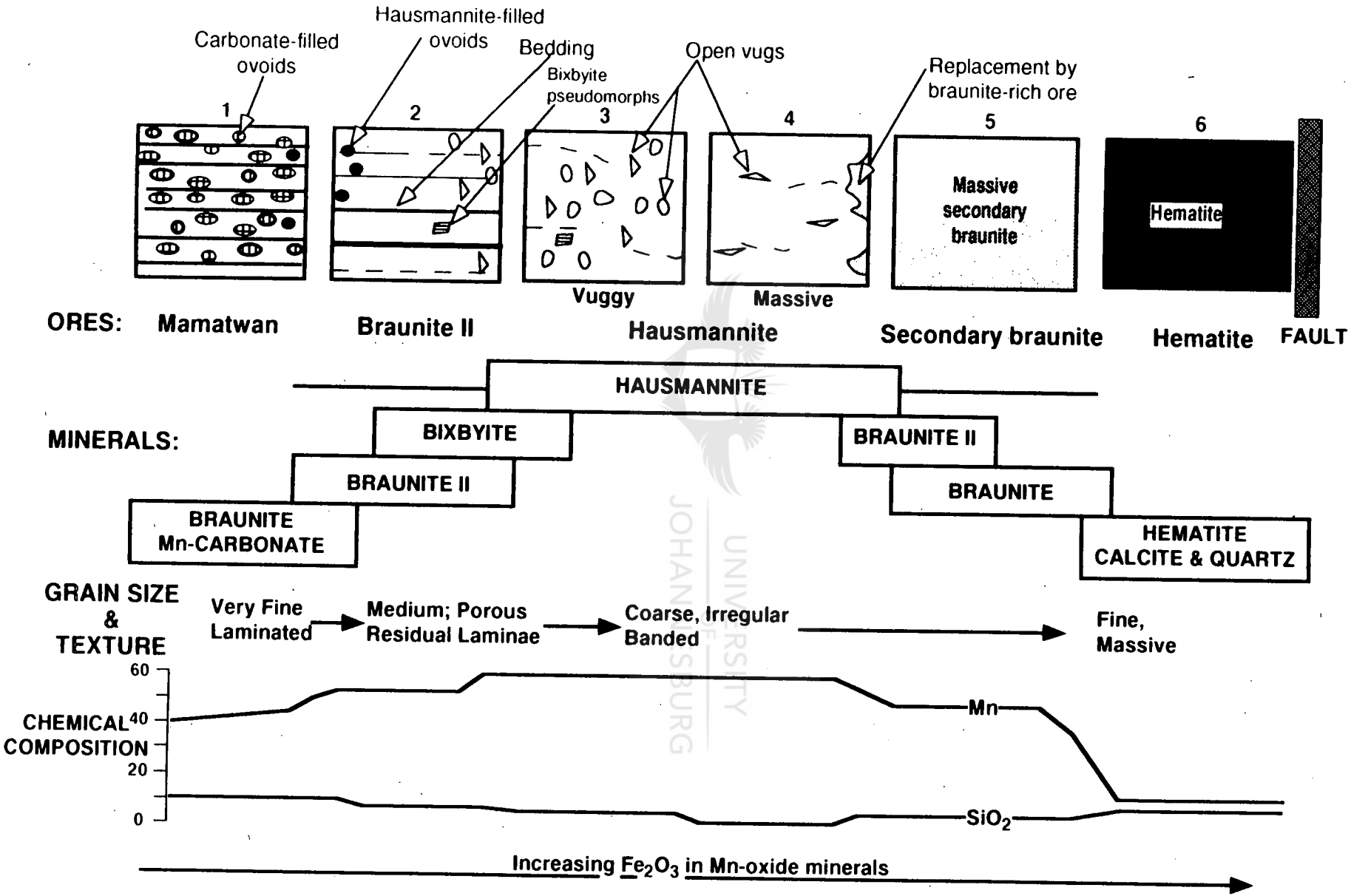

Figure 14: Composite diagram illustrating the systematic zonation of the different manganese ore-types from sedimentary Mamatwan-type ore to ferruginized fault zones in an idealized profile. Characteristic ore textures, dominant mineral assemblages, and the chemical zonation displayed by Mn and SiO_2 are related to the various ore types.

The systematic zonation of ore-types indicates a gradual loss of silica during alteration of low-grade primary sedimentary Mamatwan-type ore to the high-grade Wessels-type ore. This observation is based on the fact that braunite with a content of about 10 wt % SiO_2, present in the primary Mamatwan-type, is replaced by braunite II (with about 5 wt % SiO_2). The braunite II is in turn replaced by hausmannite and bixbyite which contain no silica. The silica content in hausmannite-rich ores is present in trace amounts of andradite and clinochlore. In proximity to the ferruginized fault zone, silica is re-introduced into the system with the formation of secondary generations of braunite II and braunite, replacing hausmannite in Wessels-type ores (Fig. 14). The iron content of the different manganese oxide mineral phases such as braunite, braunite II, and hausmannite, increases in the direction of the ferruginized fault zones (Fig. 14).

Conceptual genetic model

The most important observation of this study is that alteration of Mamatwan-type ore to Wessels-type ore is closely related to north-south trending normal faults. Highest grade Wessels-type ore occurs immediately adjacent to the ferruginized fault zones. Alteration of Mamatwan-type ore to Wessels-type ore is accompanied by an increase in the porosity of ores, recrystallization of the primary fine-grained Mamatwan-type ore to a coarser grain-size, dissolution of carbonates, and leaching of silica from braunites. This type of alteration is best explained by a hydrothermal-metasomatic alteration. The proposed model is that hydrothermal fluids moved from fault conduits into the adjacent diagenetic Mamatwan-type ores and altered these to finally produce high-grade Wessels-type ore (Fig. 15). A very similar model was derived by Gutzmer and Beukes (1993; 1995) for the alteration of the ores at the neighbouring Nchwaning Mine.

In the transition zone between primary Mamatwan-type ore and Wessels-type ore, most distal from major fluid conduits along faults (Fig. 15), the first sign of alteration is represented by the transformation of kutnahorite into calcite and hausmannite, probably through a reaction such as:

$$3CaMn(CO_3)_2 + 1/2\ O_2 \rightarrow Mn_3O_4 + 3\ CaCO_3 + 3CO_2.$$

Moving laterally into zones of higher degrees of alteration, desilicification and further decarbonatization of the ores took place and braunite was transformed first into braunite II, and then into bixbyite (Fig. 15). The following reactions may have been taken place:

braunite + hematite + calcite + O_2 → braunite II + CO_2 + SiO_2

and

braunite II + hematite → bixbyite + CaO + SiO_2.

The next step appears to have been the formation of hausmannite-rich ore formed by the reduction of some trivalent manganese to the divalent state. This transformation must have been accompanied by a loss of silica in the replacement of braunite II and braunite (new) by hausmannite. However, in cases where hausmannite appears pseudomorph after bixbyite, the transformation process must have involved reduction of some of the trivalent manganese present in the bixbyite.

Very high-grade Wessels-type ore, which consists almost entirely of hausmannite, developed close to the faults which acted as conduits for hydrothermal fluids. These ores may have been enriched by manganese, that was leached from the zones of ferruginization along faults (Fig. 15). Mobilization of manganese may have been made possible by reduction of Mn^{3+} to Mn^{2+} by ferrous iron.

The ferric iron would have precipitated as hematite to form the ferruginized zone along faults, with manganese transported further into the manganese bed to form hausmannite-rich ores. Recrystallization or replacement of the fine-grained Fe-bearing hausmannite by coarse-grained Fe-poor hausmannite possibly took place due to introduction of the Mn^{2+}-rich fluids.

The secondary braunite-rich zone, developed between the ferruginized zone and the very high-grade hausmannite-rich ore, may have formed due to the reprecipitation of silica leached from braunites in the low-grade ores situated further away from fluid conduits (Fig. 15). Cooling of the hydrothermal fluid and resulting oversaturation of silica may have led to reprecipitation of the SiO_2 (Fournier, 1986) either as quartz or in braunite.

This mechanism could also explain the presence of quartz and silicates in some of the ferruginized zones. Dissolved silica was apparently also precipitated in the form of andradite in secondary pores

or as a replacement product of carbonate ovoids. The latter transformation may have taken place through the reaction:

$3CaCO_3 + Fe_2O_3 + 3SiO_2 \rightarrow Ca_3Fe_2Si_3O_{12} + 3\ CO_2$ (Kleyenstüber, 1985).

calcite hematite andradite

Calcium liberated from the carbonates was precipitated in the form of secondary calcite, braunite II, marokite, andradite and gaudefroyite. Carbon dioxide released during the alteration process, reacted with calcium and manganese to form secondary calcite and manganoan calcite (Fig. 15).

In addition to ferrous iron, certain amounts of sodium and potassium must have been introduced by the hydrothermal fluids into the system, and others were redistributed, to form gangue minerals such as barite, clinochlore and andradite. Gutzmer and Beukes (1995) describe potassium feldspar, acmite, richterite, xonotlite and datolite as further gangue minerals associated with Wessels-type ore at Nchwaning Mine. Kleyenstüber (1984, 1985) identified diaspore and hydrogrossulare in veinlets associated with Wessels-type ore.

UNIVERSITY OF JOHANNESBURG

It is important to note that the alteration process is described as a series of metasomatic fronts that invaded Mamatwan-type ore from a fluid conduit along a normal fault (Fig. 15). Successive fronts thus overprint each other laterally as the zone of alteration next to the fault zone widened away from the fault conduit (Khorshinskij, 1970). During waning stages of hydrothermal activity the metasomatic front receded and at that time resilicification and carbonatization took place in the vicinity of the fault zones with the formation of secondary braunite ore next to the ferruginized zone and precipitation of quartz and calcite in the fault zone (Fig. 15).

It is suggested that the hydrothermal fluid evolved through time as it infiltrated the ore bed. "Primary" fluids that moved along fault conduits must have been acidic and reducing in order to transport considerable amounts of ferrous iron in solution. The fluids must also have carried certain amounts of alkalies, aluminium and barium and were undersaturated with respect to SiO_2 and CO_2. As the fluids infiltrated surrounding Mamatwan-type ore, the dissolved ferrous iron reacted with the trivalent manganese in braunite, leading to precipitation of hematite and dissolution of divalent

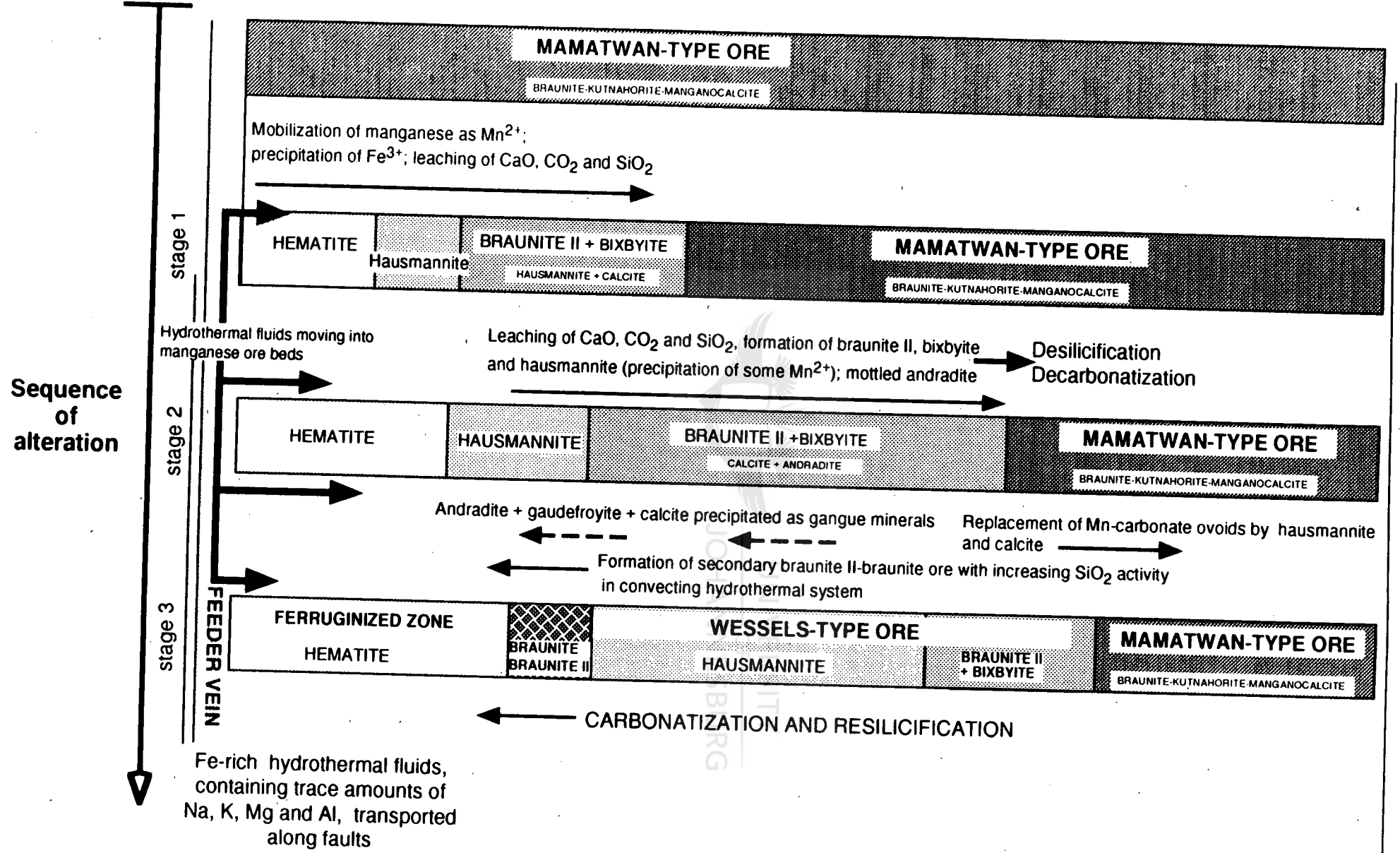

Figure 15: Simplified model for the temporal and spatial development of the hydrothermal alteration of sedimentary Mamatwan-type ores in association with fault zones acting as feeder channels for hydrothermal fluids. From stage 1 to stage 3 successive metasomatic fronts develop, progressing from the fault into the manganese ore. Each metasomatic front is characterized by a specific alteration reaction, resulting in a change of mineral paragenesis. Stages 1 and 2 illustrate the progressing phase of alteration leading to decarbonatization, desilification, and hematitization; stage 3 illustrates the regressing phase, caracterized by resilification and carbonatization close to the fault zone.

manganese. Reaction with carbonates in the sedimentary manganese ore (Gutzmer, 1993) most probably led to an increase in the alkalinity of the fluid enhancing the dissolution of SiO_2. The fluid temperature on the other hand would have decreased with increasing distance from major conduits. During final stages of hydrothermal activity, coincident with decreasing temperature, fluids would have become oversaturated in silica. At this stage precipitation of secondary braunite and quartz in proximity to the fault zones is envisaged (Fig. 15).

The timing of hydrothermal alteration is uncertain. Kleyenstüber (1985) describes a hydrothermal mineral assemblage from planes of thrust faults in the Kalahari manganese field. It is thus assumed that hydrothermal alteration developed during or after the thrust event. However, no evidence is available directly linking the hydrothermal mineral assemblage along planes of thrust faults with that associated with normal faults. Dixon (1989) dated the hydrothermal alteration event in the Kalahari manganese field at 1350-1250 m.y. by Rb-Sr dating of sugilite and Pb-Pb dating of galena. Bostonite dykes, partly altered by the hydrothermal event, give a Rb-Sr age of 1350 m.y. (Dixon, 1989).

The geological history of the Kalahari manganese field can thus be summarized as follows: Deposition of primary sedimentary ore took place some 2240 to 2100 m.y. ago. Then follows a period of folding, uplift and erosion prior to deposition of the Mapedi red beds and Hartley lava some 1900 m.y. ago. Bostonite dykes must have intruded after folding but prior to erosion of the Hotazel Formation, in pre-Mapedi times. The Mapedi red beds display rapid thickness variations (Beukes, 1983, Beukes and Smit, 1987), which may suggest that deposition took place in a rift setting. The system of normal faults, along which ferruginization of manganese ores took place, may thus have developed during deposition of the Mapedi Formation. Thrust faulting took place during the Kheiss orogeny some 1750 m.y. ago (Beukes and Smit, 1987). However, hydrothermal alteration of ores and dykes may only have taken some 1250-1350 m.y. ago.

UNIVERSITY OF JOHANNESBURG

Conclusions

In the northwestern part of the Kalahari manganese deposit, at Wessels Mine, north-south trending normal faults, with subordinate east-west trending normal faults, acted as feeder channels for hydrothermal fluids which reconstituted and thereby upgraded low-grade, primary sedimentary diagenetic Mamatwan-type ore to high-grade Wessels-type ore. The manganese ores in immediate

vicinity of the faults are hematitized, and no primary sedimentary structures and textures are preserved. A systematic zonation of mineralogically and texturally distinct manganese ore are developed in association with ferruginized fault zones. Zones of ferruginized ore are bounded by zones of massive secondary braunite ore in turn followed by zones of porous coarse-grained high-grade hausmannite-rich ore, slightly porous braunite II-rich ore, and dense microcrystalline laminated primary sedimentary Mamatwan-type ore.

Metasomatic alteration was apparently caused by a hydrothermal fluid containing abundant ferrous iron in solution, and containing lesser amounts of Na and K. These fluids mobilized SiO_2, CO_2 and CaO as they migrated through the ore beds. Mn^{2+}, liberated by reduction of Mn^{3+} by Fe^{2+} with precipitation of hematite in the fault zones, repercipitated adjacent to fault zones to form very high-grade hausmannite-rich Wessels-type ore. In the transition zone to primary Mamatwan-type ore kutnahorite was altered to hausmannite and calcite and silica leached from braunite to form braunite II, braunite (new), bixbyite and hausmannite. Secondary minerals which precipitated from the hydrothermal fluids include gaudefroyite, clinochlore, barite and andradite.

The origin of the hydrothermal fluids is unknown and the exact timing of the main metasomatic event is not certain. Data presented by Dixon (1989) indicate that hydrothermal alteration may have taken place some 1350 - 1250 m.y. ago.

UNIVERSITY OF JOHANNESBURG

Acknowledgements

We would like to thank the management of SAMANCOR for permission to undertake the investigation at Wessels Mine. Special thanks to Carol Lathy for assistance during underground mapping at the mine. Arno Kleyenstüber of MINTEK is thanked for his valuable advise during XRD and petrographic analyses as well as his critical review of the manuscript. The manuscript was further improved by reviews by Johan de Villiers and Rudi Boer. The authors are grateful to Bruce Cairncross who improved the English of an earlier version of the manuscript.

References

Armstrong, R.A. (1987). Geochronological studies on Archean and Proterozoic formations of the foreland of the Namaqualand front and possible correlates on the Kaapvaal craton. Ph.D. thesis (unpubl.), Univ. of the Witwatersrand, Johannesburg, 274 pp.

Beukes, N.J. (1983). Palaeoenvironmental setting of iron formations in the depositional basin of the Transvaal Supergroup, South Africa. In: Trendall, A.F. & Morris, R.C. (eds.). Iron formations, facts and problems. Elsevier, Amsterdam, 131-209.

Beukes, N.J., and Smit, C. A., (1987). New evidence for thrust faulting in Griqualand West, South Africa: Implications for stratigraphy and the age of red beds. Trans. Geol. Soc. S. Afr., 90, 378-394.

Boucher, B., Buhl, R. & Perrin, M. (1970). Proprietes et structure magnetique de Mn_3O_4. J. of phys. chem. Sol., 32, 2429-2437.

De Villiers, P.R. (1970). The geology and mineralogy of the Kalahari manganese-field north of Sishen, Cape Province. Mem. geol. Surv. S. Afr., 59, Pretoria, 84 pp.

Dixon, R. D. (1989). Sugilite and associated metamorphic silicate minerals from Wessels mine, Kalahari manganese field. Bull. geol. Surv. S. Afr., 93, Pretoria, 47 pp.

Fournier (1986). The behaviour of silica in hydrothermal solutions. In: Berger, B.R. & Bethke, P.M. (eds.): Geology and Geochemistry of epithermal systems. Reviews in Econ. Geol., 2, 45-59.

Gutzmer, J. (1993). Hydrothermale Alteration von Manganerzen der Nchwaning-Mine, Kalahari-Manganerzfeld, Südafrika. Unpubl. Diplom thesis, Technische Universität Clausthal, 161 pp.

Gutzmer, J., and Beukes, N.J. (1995). Hydrothermal alteration and ferruginization of sedimentary manganese ore at the Nchwaning mine, Kalahari manganese field, Early Proterozoic Transvaal Supergroup, South Africa. Econ. Geol., 90, 823-844.

Gutzmer, J., Kleyenstüber, A.S.E., Beukes, N.J. & Burger, A.M. (1995). Magnetic hausmannite from hydrothermally altered manganese ore in the Palaeoproterozoic Kalahari manganese deposit, Transvaal Supergroup, South Africa. Min. Mag., 59, 703-716.

Khorshinskij, D.S. (1970). Theory of metasomatic zoning. Clarendon Press, New York, 162 pp.

Kleyenstüber , A. S. E. (1984). The mineralogy of the manganese bearing Hotazel Formation of the Proterozoic Transvaal Sequence in Griqualand West, South Africa. Trans. geol. Soc. S. Afr., 87, 257-272.

Kleyenstüber , A. S. E. (1985). A regional mineralogical study of the manganese bearing Voëlwater Subgroup in the northern Cape Province. Unpubl. Ph.D thesis, RAU, Johannesburg, 328 pp.

Stowe, C. W. (1986). Synthesis and interpretation of structures along the north-eastern boundary of the Namaqua tectonic province, South Africa. Trans.geol. Soc. S. Afr., 89, 185-198.

Taljaardt, J.J. (1982). Major manganese ore fields, Republic of South Africa. Unpubl. report, SAMANCOR, Johannesburg, 7 pp.

Wiggering, H., and Beukes, N.J. (1990). Petrography and geochemistry of a 2100 - 2200 m.y. old hematitic paleoalteration profile on Ongeluk basalt of the Transvaal Supergroup, Griqualand West, South Africa. Precambr. Res., 46 , 241-258.

Appendix IX

Magnetic hausmannite from hydrothermally altered manganese ore in the Palaeoproterozoic Kalahari manganese deposit, Transvaal Supergroup, South Africa

(published in: Mineralogical Magazine, 59, 703-716, 1995)

J. Gutzmer, N.J. Beukes, A.S.E Kleyenstüber and A.M. Burger

Abstract

Hausmannite (Mn_3O_4), a manganese oxide with tetragonally distorted spinel structure, is considered to be ferrimagnetic with a very low Curie temperature of 42.5 K. However, strongly magnetic hausmannite has been discovered in some of the hydrothermally altered high-grade manganese ores of the giant Kalahari manganese deposit in South Africa. EDS-electron microprobe analyses indicate magnetic hausmannite to contain on average between 3 and 11.3 wt. % Fe_2O_3. In contrast non-magnetic hausmannite contains on average about 1-3 wt. % Fe_2O_3. X-ray powder diffraction analyses reveal small changes in cell dimensions of the magnetic hausmannite related to the high iron content. Mössbauer spectroscopy suggests that all iron is in the trivalent state. Optical microscopy and scanning electron microscopy (electron back-scatter imaging) proved the magnetic hausmannite to be homogeneous in composition, containing only a few minute inclusions of hematite. Magnetic blocking temperatures of the iron-rich hausmannite, approximating the Curie temperature, is in the order of 750 K. It is suggested that the ferrimagnetic state of hausmannite is stabilized and enhanced by replacement of Mn^{3+} by Fe^{3+}.

UNIVERSITY OF JOHANNESBURG

Introduction

Hausmannite, the manganese oxide ($Mn^{2+}Mn^{3+}{}_2O_4$) has a tetragonally distorted spinel-type structure. According to Mason (1943) and Frenzel (1980) naturally occurring hausmannite contains up to 6.9 wt. % Fe_2O_3. Hausmannite is paramagnetic at room temperature (Frenzel, 1980) and ferrimagnetic below a Curie temperature of between 40 and 45 K (Boucher et al.,

1970, Olés, 1976). The magnetic characteristics have been described by Frenzel (1980) to vary only slightly due to increasing content of iron.

However, during a study of high-grade manganese ores in the Kalahari manganese field highly magnetic, iron-rich hausmannite was discovered. The magnetic hausmannite is, similar to magnetite and hausmannite, strongly attracted by a hand magnet. This paper documents the geological setting and composition of this unusual hausmannite. Information is also provided on the magnetic properties of the hausmannite.

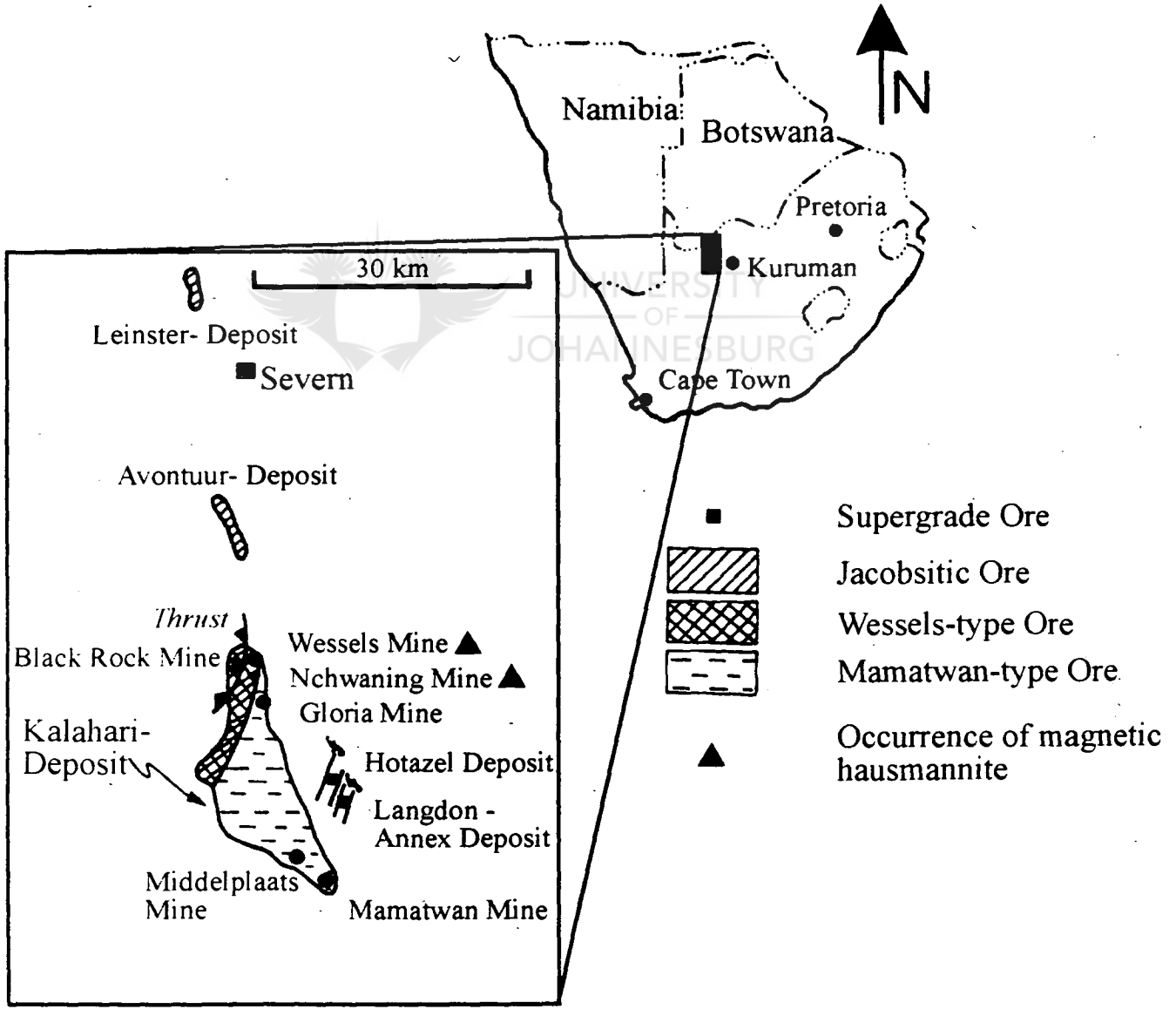

Figure 1: Locality map showing the occurrence of magnetic hausmannite relative to the distribution of ore-types, and structural erosionally preserved deposits of the Kalahari manganese field, South Africa (modified after Nel et al., 1986).

Geological setting

The Palaeoproterozoic sedimentary Kalahari manganese field is situated in the Northwestern Cape Province of South Africa in the Kalahari desert (Fig. 1). The manganese ore beds are interbedded with iron-formation of the Hotazel Formation and preserved in five erosional relict basins. The largest of these erosional relicts covers an area of about 35 km by 15 km (Fig. 1) and contains the Kalahari manganese deposit with known reserves of about 13500 Mt of manganese ores at grade varying between 20 and 60 wt. % Mn.

Three manganese ore beds are present, each forming the center of symmetrical iron-formation - hematite-lutite - braunite-lutite sedimentary cycles (Beukes, 1983; Nel et al., 1986). Virtually all manganese ore reserves and production come from the lower manganese bed, which reaches a maximum known thickness of about 45 m in the southwestern part of the manganese field at Mamatwan mine (Fig. 1). Further to the north, at Wessels and Nchwaning mines (Fig. 1), this bed is on average between 4 and 8 m thick.

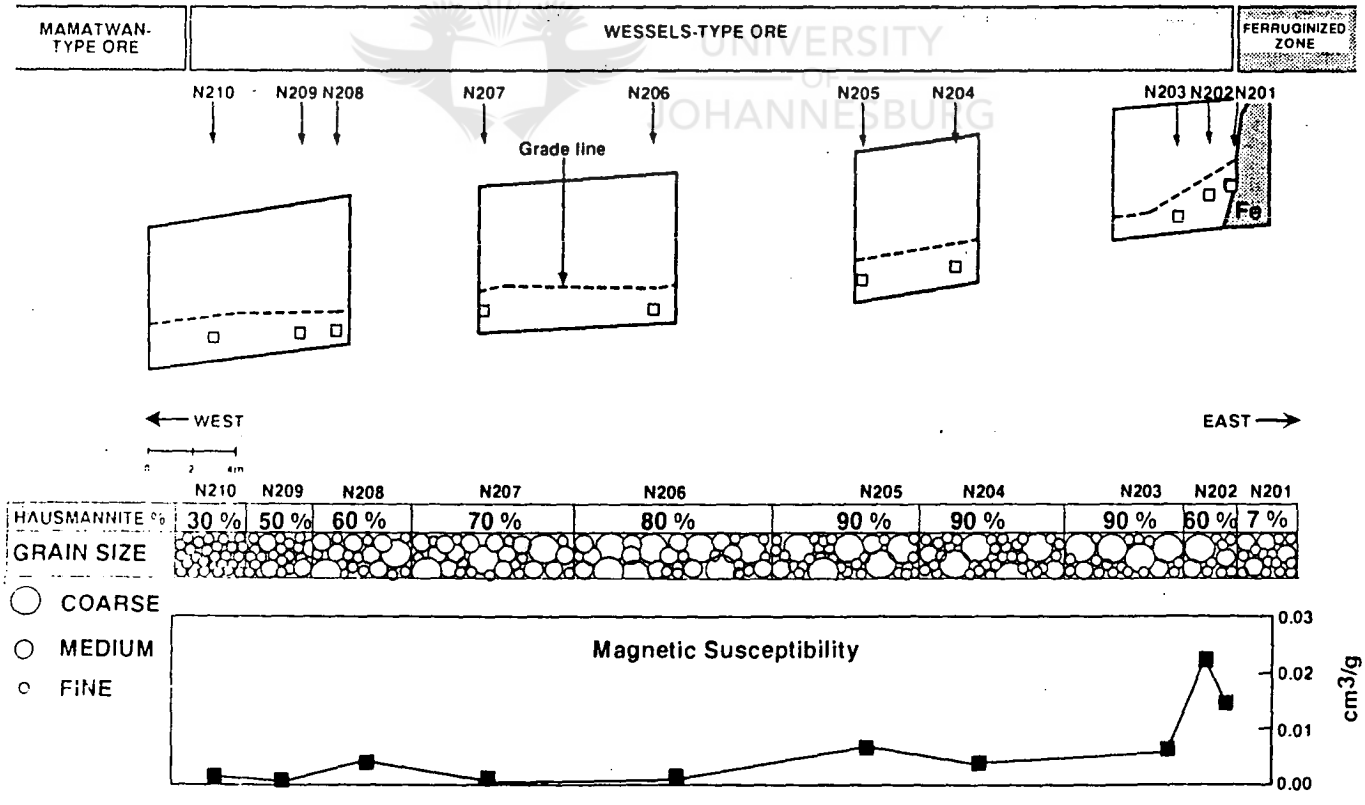

Figure 2: Sampled traverse at Wessels mine, from unaltered Mamatwan-type ore through Wessels-type ore into a zone of ferruginization surrounding a fault. The hausmannite content, as estimated by optical microscopy, varies from 50 % to more than 90 % in the samples of Wessels-type ore. Fine-grained magnetic hausmannite and coarse-grained non-magnetic hausmannite are intimately intergrown in variable proportions. A thin hematitic layer, the grade line, was used as reference height of sampling position. Magnetic susceptibility data for whole-rock samples indicate a large increase towards the zone of ferruginization.

Two major types of ore are present, namely diagenetic to very low-grade metamorphic sedimentary Mamatwan-type ore and hydrothermally altered Wessels-type ore (Kleyenstüber, 1984). Mamatwan-type ore is of relatively low-grade containing 30-39 wt. % Mn. The ore is microcrystalline, laminated and composed of finely intergrown braunite, hematite, kutnahorite and manganocalcite with abundant small concretionary ovoids of maganese-bearing calcite. Hausmannite is common as a diagenetic oxidation product replacing carbonate ovoids and laminae. This diagenetic/ low temperature hausmannite contains up to 4.5 wt. % Fe_2O_3 (Nel et al., 1986).

The high-grade Wessels-type ore, containing 46-60 wt. % Mn, was derived from hydrothermal alteration of Mamatwan-type ore in association with a system of normal N-S trending faults present in the Wessels-Nchwaning area (Gutzmer, 1993, Gutzmer and Beukes, 1993). Only about three percent of the estimated ore reserves are of the Wessels-type and it is concentrated in the intensively faulted northwestern part of the Kalahari deposit (Fig. 1). The normal faults apparently act as conduits for the hydrothermal fluids leading to hematitization of manganese ores along fault planes and the development of Wessels-type ore adjacent to them (Gutzmer and Beukes, 1993). The high-grade Wessels-type ore is coarse-grained and vuggy composed mainly of hausmannite, bixbyite, braunite II and braunite with minor manganite, marokite and hematite. Gangue minerals include gaudefroyite, andradite, calcite and clinochlore (Kleyenstüber, 1984).

The magnetic hausmannite is associated with a specific part of the Wessels-type ore assemblage. During systematic studies of the metasomatic alteration process from sedimentary Mamatwan-type precursor ore to hydrothermally altered Wessels-type ore, whole rock magnetic susceptibility data were gathered along sample profiles. Unusually high susceptibilities were gained from some hausmannite-rich samples immediately adjacent to ferruginized fault zones (Fig. 2). Tests indicated that in these ores, with high magnetic susceptiblity, a phase of hausmannite could be separated by using a simple hand magnet. In fact one of the authors (A.S.E.K.) found similar strong magnetic hausmannite in a sample from Nchwaning II mine (Fig. 1) in 1986 but at that time the specific geological setting of the material was not realized.

Petrography and sample preparation

Detailed petrographic studies indicated that very coarse crystalline vuggy hausmannite ores, with hausmannite grain sizes in the order of 0.5-3 mm, do not contain magnetic hausmannite. The magnetic hausmannite is rather developed in massive fine-grained hausmannite-rich ore. This

ore-type contains two generations of hausmannite, namely a fine crystalline generation with grain sizes of 100-500 μm, overgrown by younger, very coarse crystalline hausmannite. The fine crystalline hausmannite is highly magnetic and attracted by a hand magnet. The coarse crystalline phase does not display this feature.

Minor amounts of bixbyite and braunite II are present in the massive fine-grained magnetic hausmannite-rich ores. Gangue minerals in both magnetic and non-magnetic hausmannite ores include minor hematite, barite, calcite, clinochlore and gaudefroyite.

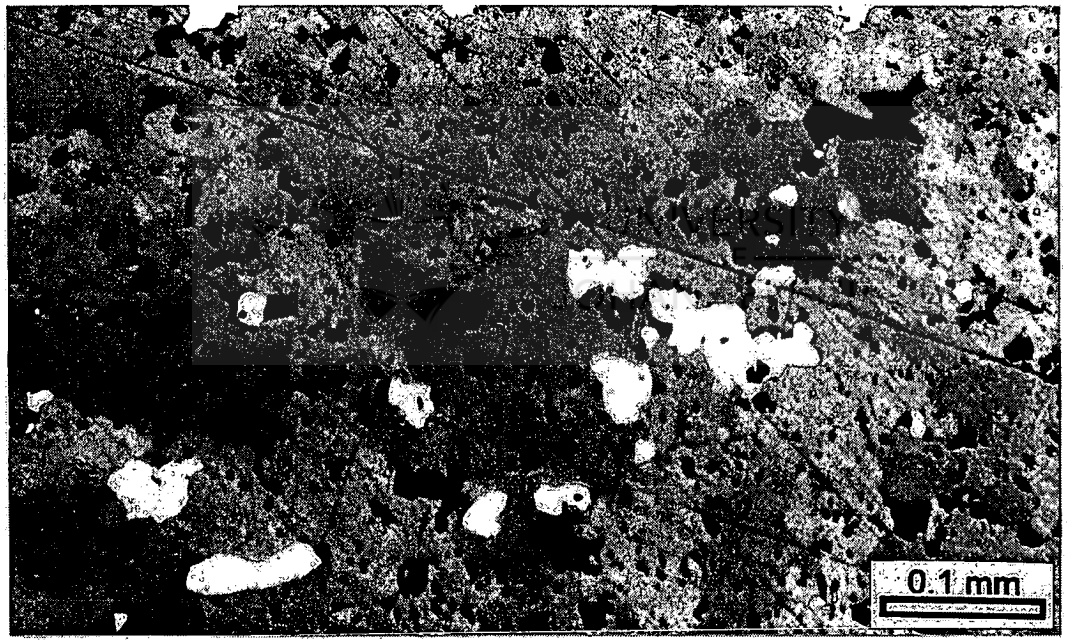

Figure 3: Reflected light photomicrograph (200x, oil immersion) showing typically fine crystalline, anhedral magnetic ausmannite grains (various shades of gray) intergrown with subhedral to euhedral hematite platelets.

The intimate intergrowth of the two hausmannite phases in massive ores prohibits complete separation. Samples for chemical, crystallographic and magnetic studies were prepared by stepwise concentration of sieved grain fractions using an isodynamic Frantz magnetic separator. The least magnetic hausmannite fraction was labelled 'non-magnetic', whereas the 'magnetic'

fraction was further concentrated by hand-picking magnetic hausmannite grains with a pair of magnetized steel tweezers. However, absolutely pure separates could not be obtained, results of different separates should therefore be regarded as mean values. In addition the properties ofsome

Table 1: Mean composition (electron microprobe) and calculated unit cell constants of pure, iron-free hausmannite and hausmannite containing low, intermediate and high concentrations of iron.

sample	syn. Mn_3O_4 [a]	syn. Mn_3O_4 (this study)[b]	LVB404 low Fe	N204 intermediate Fe		N205 high Fe	
separate				magnetic	non magnetic	magnetic	non magnetic
Fe_2O_3			1.20	4.30	2.23	11.3	1.12
Mn_2O_3	69.0	69.0	65.2	62.7	64.5	57.1	65.8
MnO	31.0	31.0	33.1	32.7	32.6	31.8	32.6
MgO			0.36	0.21	LLD	LLD	LLD
Total	100.0	100.0	99.9	99.9	99.4	99.2	99.5
number of analyses		1[c]	5	15	9	5	5
R=(Mn/Mn+Fe)	1	1	0.99	0.96		0.89	
unit cell constants	a_0= 5.7621 c_0= 9.4696 c_0/a_0= 1.643	a_0=5.764(8) c_0=9.470(3) c_0/a_0=1.643	a_0= 5.764(7) c_0= 9.45(8) c_0/a_0= 1.641	a_0= 5.771(3) c_0= 9.41(7) c_0/a_0= 1.632		a_0= 5.772(6) c_0= 9.41(6) c_0/a_0= 1.631	

a) Values of synthetic Mn_3O_4 from National Bureau of Standards (1972).
b) Synthetic hausmannite prepared by heating of $MnCO_3$.
c) Synthetic hausmannite has been wet chemically analyzed for Mn and Fe.

UNIVERSITY OF JOHANNESBURG

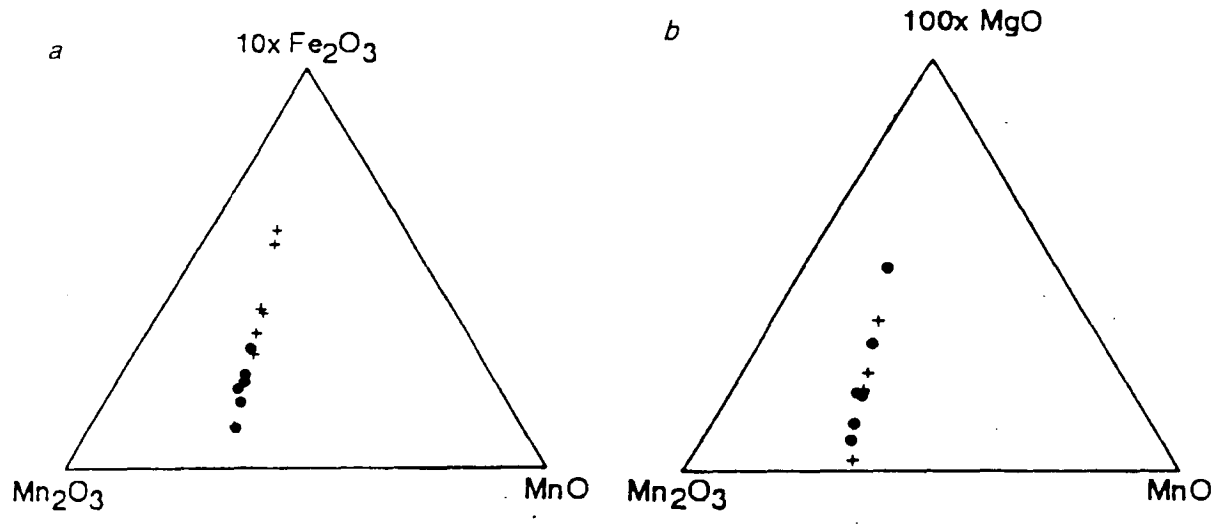

Figure 4: Mean of EDS-electron-microprobe analyses of magnetic (crosses) and non-magnetic (circles) hausmannite separates from sample traverse N200 plotted in triangular diagrams (a) Mn_2O_3-MnO-10xFe_2O_3 and (b) Mn_2O_3-MnO-100xMgO. Magnetic separates are clearly discriminated from non-magnetic separates by their higher iron content, whereas contents of magnesia are irregularly distributed.

UNIVERSITY OF JOHANNESBURG

"non-magnetic" hausmannite, filling vugs in the high-grade ore, have been studied for comparison with the magnetic hausmannite concentrates.

Backscattered electron imaging on mounted grain separates indicated the hausmannite phase to be very pure and of homogenous chemical composition. The only impurities detected were tiny subspherical hematite inclusions of up to 10 microns in diameter (Fig. 3). Careful consideration was given to the possibility that the hausmannites may include minute grains of jacobsite but no such material could be detected. For the same reason X-ray powder diffraction analyses were undertaken. Fine powder for X-ray diffractometry was prepared by milling grain concentrates for 2 minutes in a swingmill and then for 10 minutes in a McCrone micronizing mill using Propan-2-ol as milling medium. X-ray powder mounts were formed by side loading to determine peak intensities and by back loading and pressing to obtain accurate peak positions. For each technique three pellets were prepared and measured independently. Results were averaged.

Mineral chemistry

Grains of magnetic and non-magnetic separates were analyzed with EDS electron microprobe to determine systematic chemical variations. Analyses of Si, Ti, Al, Fe, Mn, Mg, Ca, Na and K indicated that only concentrations of Mn, Fe and Mg are above the detection limit. The mean results from five samples (magnetic and non-magnetic separates of two ore samples and as reference a non-magnetic hausmannite crystal from a vug in Wessels mine) are listed in Table 1 and compared to synthetic Mn_3O_4. The charge balance between Mn_3O and MnO was calculated following Kleyenstüber (1984). The results indicate that the magnetic hausmannite is iron-rich with Fe_2O_3 contents in order of 3-12 wt. %. In contrast non-magnetic fractions contain between 1 and 5 wt. % Fe_2O_3 (Fig. 4a). Mössbauer spectroscopy on a grain separate of magnetic hausmannite indicated that all iron is present in the trivalent state. Magnesium concentrations are

Table 2: List of peak positions and relative intensities for magnetic (magnetic separates of samples N204, N205) non-magnetic natural (LVB404) and synthetic (MINTEK sample) hausmannite samples. Listed peak positions were corrected and were used to calculate unit cell constants listed in Table 1. Position data were aquired using pressed, back-loaded powder mounts, intensity data were obtained from side-loaded powder mounts. Each listed data set represents average values of measurements on three independently prepared mounts of each sample.

(*hkl*)	Synthetic Mn_3O_4		LVB404		N204		N205	
	d (C)	*I* (rel.)	*d* (C)	*I* (rel.)	*d* (C)	*I* (rel.)	*d* (C)	*I* (rel.)
1 0 1	4.918	35	4.907	40	4.909	54	4.913	65
1 1 2	3.089	48	3.084	84	3.079	70	3.081	65
2 0 0	2.882	24	2.880	32	2.882	22	2.884	16
1 0 3	2.768	63	2.764	93	2.756	100	2.756	73
2 1 1	2.488	100	2.487	100	2.487	98	2.489	100
2 0 2	2.462	20	2.460	7	2.458	9	2.460	14
0 0 4	2.367	21	2.362	84	2.354	62	2.353	67
2 2 0	2.0385	25	2.0377	40	2.0404	26	2.0398	27
2 0 4	1.8296	4	1.8269	6	1.8237	5	1.8232	5
1 0 5	1.7993	15	1.7974	22	1.7902	18	1.7905	14
3 1 2	1.7010	8	1.7008	7	1.7009	8	1.7025	7
3 0 3	1.6417	7	1.6353	5	1.6340	7	1.6376	8
3 2 1	1.5766	22	1.5762	26	1.5777	20	1.5783	18
2 2 4	1.5449	34	1.5438	59	1.5418	52	1.5433	44
4 0 0	1.4411	18	1.4412	32	1.4426	11	1.4428	11
3 0 5	1.3489	3	1.3481	3.6	1.3579	23	1.3453	3
4 1 3	1.2784	6	1.2781	6	1.2787	5	1.2790	5
4 2 2	1.2438	4	1.2461	2	1.2452	1	1.2461	1
4 0 4	1.2310	4	1.2306	3	1.2304	5	1.2307	5
0 0 8	1.1836	2	1.1864	6	1.1920	4	1.1908	4
4 1 5	1.1248	4	1.1244	4	1.1242	4	1.1236	4
4 3 3	1.0826	4	1.0827	5	1.0834	3	1.0836	4

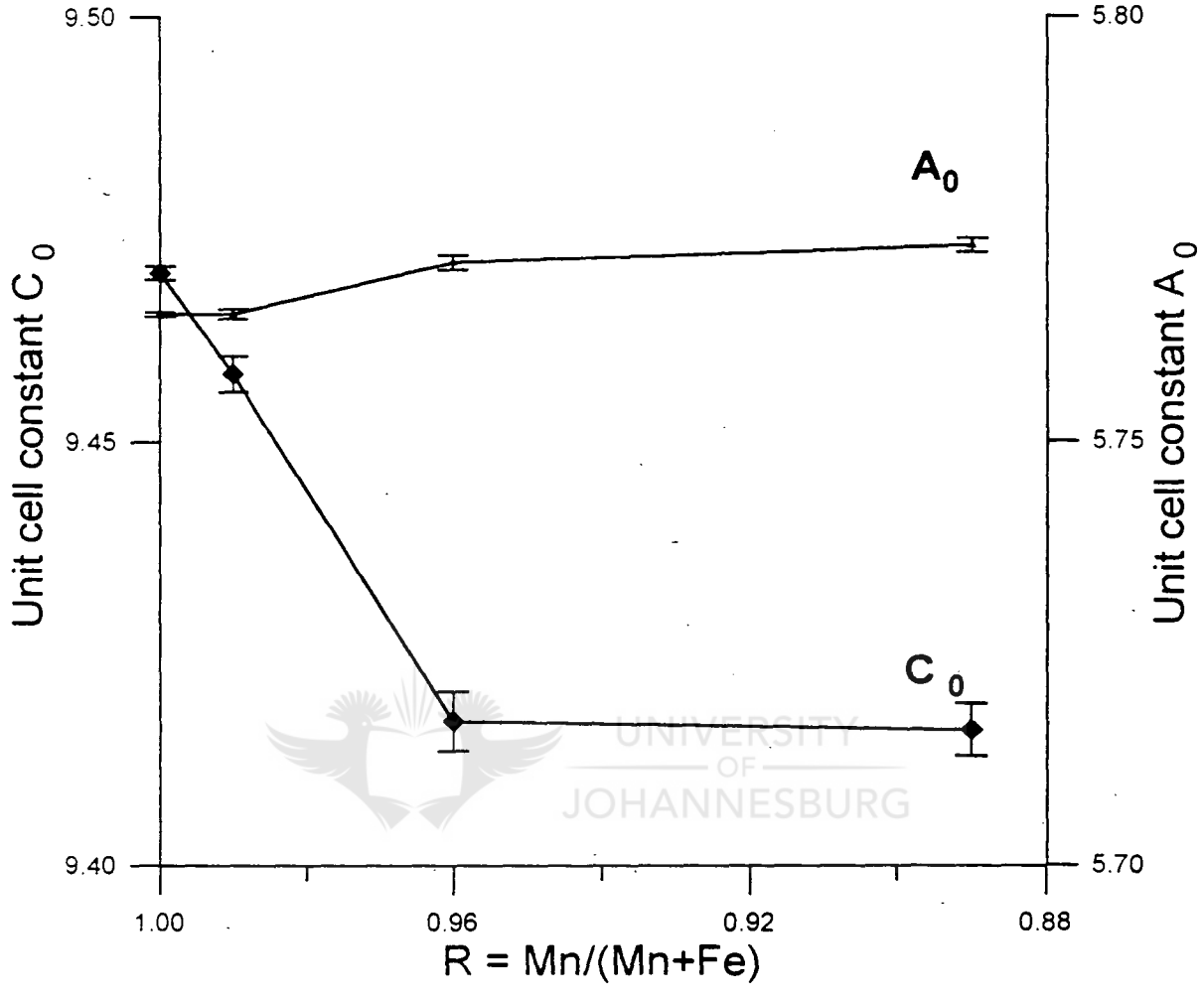

Figure 5: Variation of unit cell parameters a_0 and c_0 of hausmannite with decreasing parameter R=(Mn/(Fe+Mn) e.g. increasing iron content.

very low (less than 1 wt. % MgO). The distribution of magnesium between magnetic and non-magnetic concentrates appears erratic (Fig. 4b).

Crystallography

X-ray powder diffraction analyses were undertaken on mineral separates with different iron contents in order to obtain information on possible changes of unit cell dimensions as a result of exchange of Mn by Fe. A Philips PW 1710 based vertical goniometer equipped with an iron tube was used. The scan speed was 0.004° sec^{-1} and data were collected from 20° to 140°2θ. During

this exercise the diffractometer was calibrated with an external standard (NBS 640b, silicon) to an accuracy of ≤ 0.01° 2θ deviation in the range of data acquisition. The same material was added as an internal standard to the pressed mounts to perform a zero point refinement prior to unit cell constant calculation. Cell constants of the different hausmannite samples were calculated from 20 peak positions of the powder pattern with the PC-version of the Appleman-Evans program (Benoit, 1987). Patterns are recorded in Table 2, Table 1 includes the calculated unit cell constants for the different samples.

A small increase of the cell parameter a_o and a much larger decrease of c (resulting in a distortion parameter c_o/a_o closer to 1) are observed in the magnetic hausmannite samples (N204, N205) relative to the non-magnetic samples (synthetic Mn_3O_4 and LVB4-04) (Fig. 4). However, there is only a marginal difference between the unit cell parameters of the two magnetic samples, indicating thus, that the change of the cell parameters does take place in discrete steps and not gradually with increasing iron content.

UNIVERSITY OF JOHANNESBURG

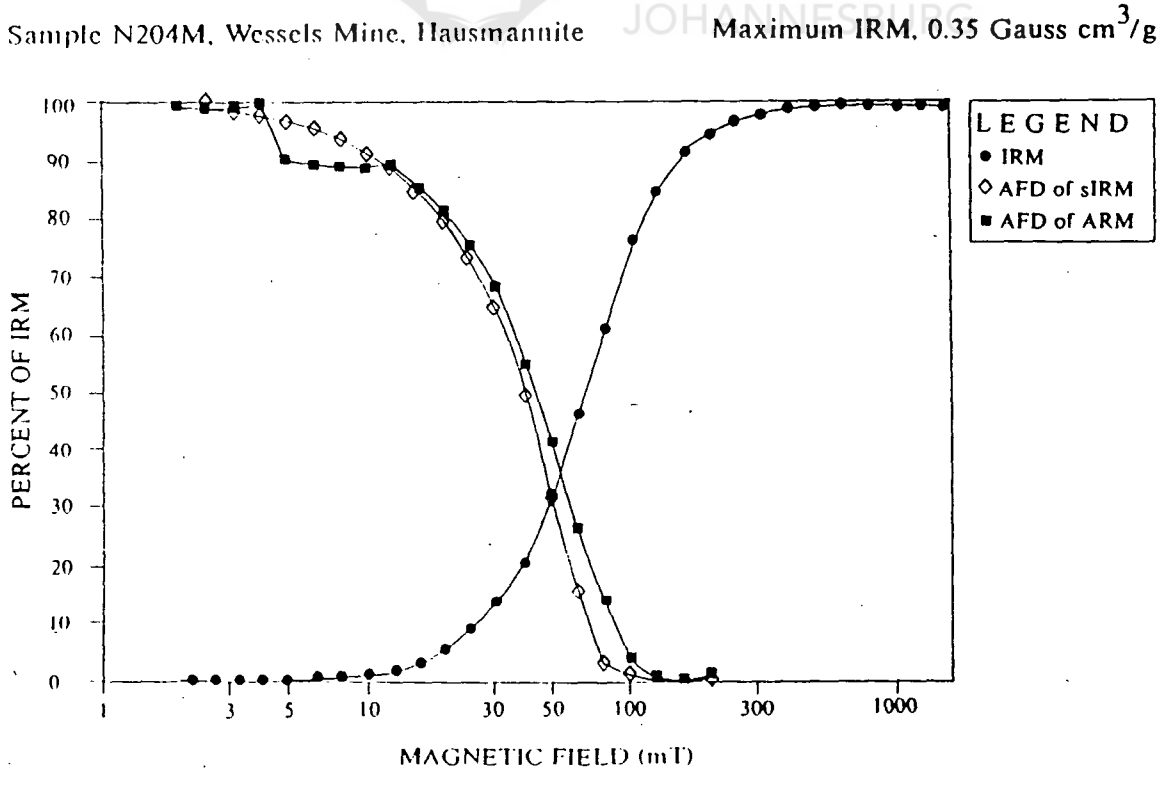

Figure 6: Coercitivity spectrum of hausmannite sample N205 (block sample). Triangles are for IRM acquisition, solid squares for AF demagnetization, open squares for AF demagnetization of ARM.

Magnetic mineralogy

Magnetic mineralogy of grain separates and block samples was determined by one of the authors (N.J.B.) in the laboratories of J. Kirshvink at the California Institute of Technology. Coercivity spectra were acquired (Fig. 6) and samples were demagnetized thermally through step heating under atmospheric conditions (Fig. 6).

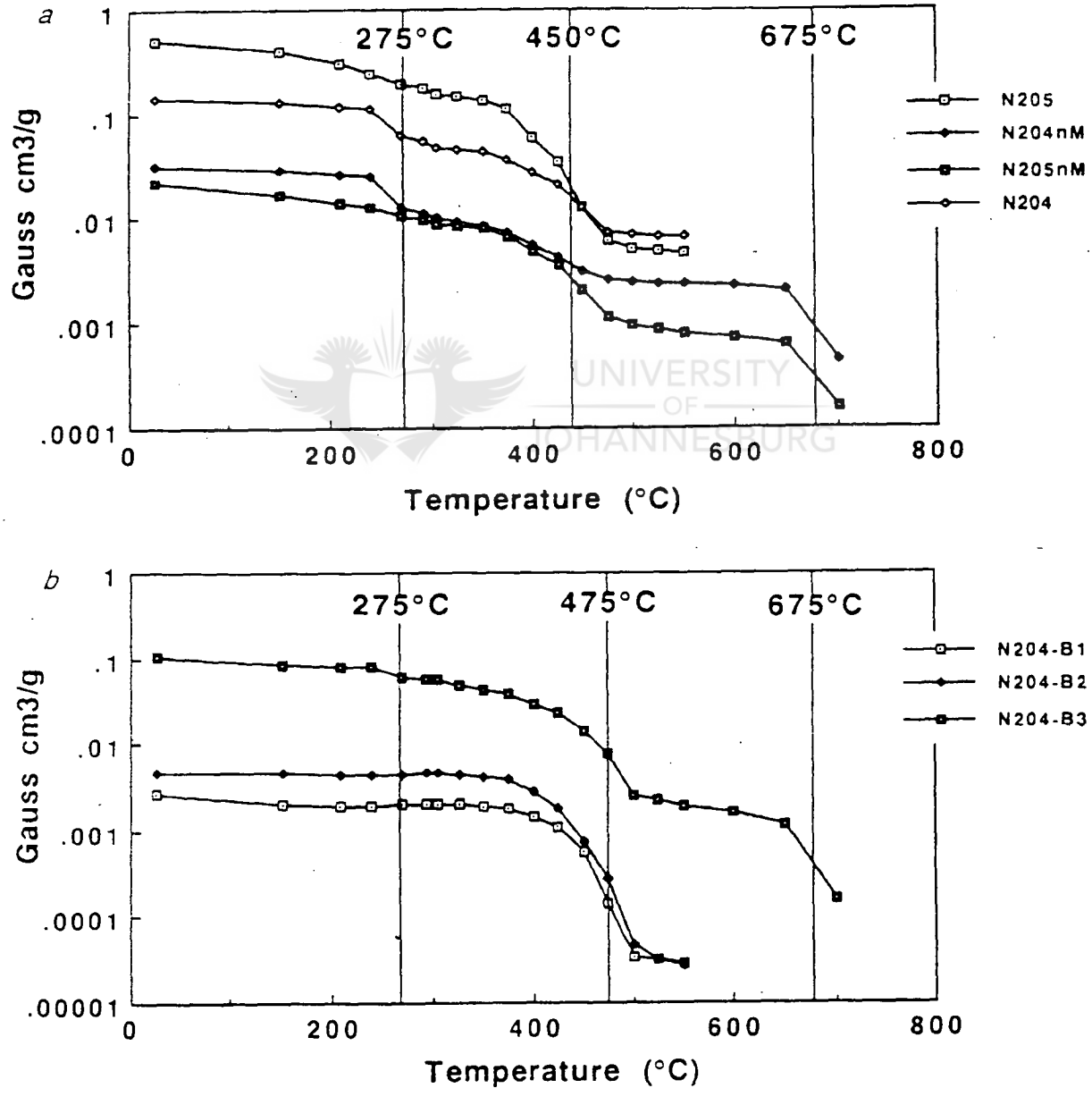

Figure 7: Thermal demagnetization data of powdered magnetic (M) and non-magnetic (nM) separates (a), and blocks (b) of samples N204 and N205. Marked are losses of magnetization at 275, 450-475 and 675°C. These correspond to soft demagnetization of multidomain hausmannite grains, the demagnetization of magnetic hausmannite, and the demagnetization of small amounts of hematite respectively.

Studies of magnetic and non-magnetic concentrates showed that separation between different generations of hausmannite was not completely accomplished. So called 'non-magnetic' concentrates have similar characteristics as the 'magnetic' concentrates although on a much lower absolute magnetic level (Fig. 7).

The coercitivity spectrum of the magnetic hausmannite is very similar to that of magnetite as reported by Yamazaki et al. (1991) (Fig. 6). Natural remanent magnetization (NRM) of small block samples are in the order of 0.002 - 0.1 Gauss cm^3 g^{-1}. Isothermal remanent magnetization curves (IRM) are characterized by a steep initial increase and saturation at applied magnetic field strength of 0.25 to 0.5 T. Moments of IRM acquisition reached maxima of between 0.15 and 0.67 Gauss cm^3 g^{-1}. Positive isothermal Laurie-Fuller tests suggest that the remanent magnetization is dominantly carried by single domain hausmannite crystals. Perturbations at low field strength are probably grain size related.

Blocking temperatures, which appear in the thermal demagnetization curve (Fig. 7) as points of major loss of magnetization, approximate the Curie temperature of the demagnetized phase (Butler, 1992). They consistently fall in in the range of 720 - 775 K (450-500 °C). Small kinks in the demagnetization curve occur also at about 530-550 K (260-280 °C) and 920-970 K (650-700 °C). The kink at 920-970 K is the result of demagnetization of hematite inclusions in hausmannite grains. Magnetism due to hematite normally accounts for less than one percent of the initial NRM (natural remanent magnetism) of block samples or magnetic separates. The cause for the drop of magnetization 530-550 K remains uncertain, but may be related to soft magnetism in multidomain hausmannite grains.

Discussion

Good introductions into the magnetic properties of Fe-Mn spinels, so called ferrites, are provided by Smit and Wijn (1959) and Goodenough (1966) and a detailed description of the properties of the physical ang chemical properties of hausmannite is given by Frenzel (1980).

Data of well studied members of the Mn-Fe spinels are listed in Table 3. Hausmannite has a tetragonally distorted structure and may be compared to more iron-rich members of the group of ferrites (Table 3). Half of the octahedrally coordinated interstices in the f.c.c oxygen lattice are occupied by trivalent manganese and one eighth of the tetrahedrally coordinated sites are

Table 3: Intrinsic properties of hausmannite-magnetite series ferrites. Data from Goodenough (1966), Olés et al. (1976); data for iwakiite from Matsubara et al. (1979), for hausmannite from NBS (1972) (lattice constants) and Boucher et al. (1970) spin configuration, for magnetic hausmannite sample N205, this study.

	hausmannite	magnetic hausmannite	synthetic ferrite	synthetic ferrite	iwakiite	jacobsite	magnetite
composition	$Mn^{2+}Mn^{3+}_2O_4$	$Mn^{2+}(Mn,Fe)^{3+}_2O_4$	$Mn^{2+}Mn^{3+}FeO_4$	Mn_3FeO_4	$MnFe_2O_4$	$MnFe_2O_4$	$Fe^{3+}(Fe^{2+},Fe^{3+})_2O_4$
site occupation	normal	normal (?)	normal or partly inverted	normal or partly inverted	?	normal or partly inverted	inverted
crystallographic system	tetragonal	tetragonal	tetragonal	cubic	tetragonal	cubic	cubic
unit cell constants (Å)	a=5.7621 c=9.4696 c/a=1.638	a=5.772 c=9.416 c/a=1.631	a=8.34 c=8.88 c/a=1.06	a=8.49	a=8.52 c=8.54 c/a=1.002	a=8.52	a=8.40
magnetism				electron spin only			
type of magnetic order	similar to Yafet-Kittel order	Yafet-Kittel or Neel order (?)	Neel order	Neel order	?	Neel order	Neel order
A-B spin orientations	8 discrete directions of spin orientation	?	antiparallel in (001)	antiparallel	?	antiparallel	antiparallel
Curie temperature (K)	42.5	750	413	?	?	563	858

UNIVERSITY OF JOHANNESBURG

occupied by divalent manganese cations. The tetragonal lattice distortion is an expression of a cooperative Jahn-Teller effect around the octahedrally coordinated Mn^{3+} sites, stretching the spinel-lattice along (001). The degree of inversion is commonly small (Wickham, 1969). The oxygen parameter *u*, a measure for non-stoichiometry, may be an function in understanding the physical properties of hausmannite (Wickham, 1969; Tanaka, 1974), but it is not well studied.

Table 4: Intrinsic properties of the divalent and trivalent cations of iron and manganese.

cation	Mn^{2+}	Mn^{3+}	Fe^{2+}	Fe^{3+}
ionic radius (pm)	83	66	78	65
orbital electron configuration	$3d^5$	$3d^4$	$3d^6$	$3d^5$
bonding electron configuration	$t_{2g}^4 e_g^2$	$t_{2g}^3 e_g^1$	$t_{2g}^6 e_g^0$	$t_{2g}^4 e_g^2$
theoretical magnetic moment (μ_B)	5	4	4	5
Curie constant per gram ion	4.38	3.00	3.00	4.38

The lattice distortion diminishes with increasing amounts of iron in the compositional series between Mn_3O_4 and Fe_3O_4 and it disappears at compositions $MnFeO_4$ and $MnFe_2O_4$ where cubic, as well slightly distorted modifications are known (Table 3) (Goodenough, 1966; Matsubara et al.,1979).

Ferrimagnetism in Mn-Fe spinels is caused exclusively by the orientation of bonding electron spin moments of the cations. The so called orbital magnetic moment is effectively quenched in these compounds (Goodenough, 1966). Only the spins of unpaired electrons can contribute to the magnetic moment of a molecule. Manganese and iron are both transitional metals with respectively 7 and 8 outer electrons in 3d and 4s orbitals. Their divalent and trivalent cations therefore have electron configurations with 4 ($3d^4$, $3d^6$) or 5 ($3d^5$) unpaired electrons resulting in large theoretical magnetic moments and high Curie constants (Table 4). Mn^{2+} and Fe^{3+} have identical electron configurations and therefore identical magnetic properties. The latter is also true for Mn^{3+} and Fe^{2+} which have equivalent electron configurations with respectively four and six electrons in the outer d-orbital.

The magnetic structure of hausmannite below the Curie point is fairly complex (Kasper, 1959; Boucher et al., 1970; Bonnet et al, 1974). According to Boucher et al. (1970) the electron spins of the B-site cations form an umbrella of two-fold symmetry around [010] with six distinctive

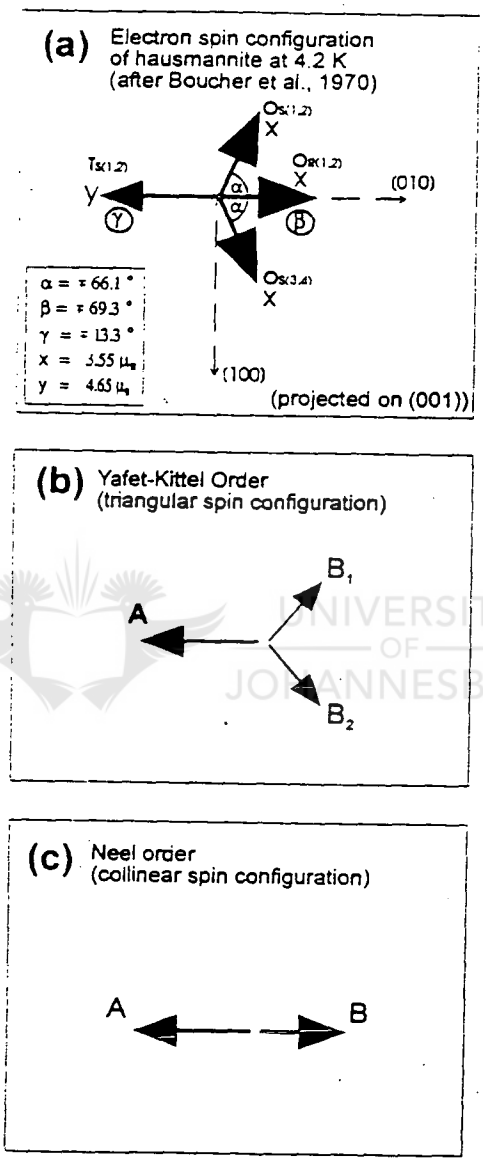

Figure 8: (a) The electron spin configuration of hausmannite at 4.2 K after Boucher et al. (1970), projected on (001) Eight discrete directions of electron spin orientation (equivalent to eight magnetic sublattices) are notable, six of these (O_1-O_6) of cations in octahedral positions, two (T_1, T_2) of cations in tetrahedral coordination. (b) Yaffet-Kittel model of triangular spin ordering in a two-sublattice mode, resembling the projection of the hausmannite configuration. (c) Simple antiparalel Neel order with collinear electron spins in a two-sublattice mode. This model is valid for Mn_3O_4-Fe_3O_4 series ferrites with the exeption of hausmannite.

spin orientations. In contrast the electron spins of the A-site cations are orientated into two distinctive directions antiparallel to [010]. The magnetic structure of hausmannite has therefore to be described in an orthorhombic cell doubled along [010] relative to the crystallographic cell. The two crystallographic sublattices A (tetrahedrally coordinated) and B (octahedrally coordinated) have to be subdivided into 2 distinctive A-site sublattices (T1 - T2) and 6 distinctive B sublattices (O1-O6), each characterized by a distinctive direction of spin orientation (Boucher et al., 1970). However, projected onto (001) (Fig. 8a) this structure resembles that of a plane triangular Yafet-Kittel spin configuration (Fig. 8b). This is in contrast to the simple antiparallel Neel configuration (Fig. 8c) of the two crystallographic sublattices characteristic for all other ferrites (Table 3).

The bonding electrons of the cations of different sublattices interact via next-neighbor cation-anion-cation superexchange (Goodenough, 1966, Smit and Wijn, 1959). This coupling is stronger, the smaller the distance between cations and oxygen and the closer the angle between the two cation-oxygen bond is to 180 ° (Smit and Wijn, 1959).

UNIVERSITY of JOHANNESBURG

The ordering of the electron spins by magnetic coupling is disturbed by thermal excitation. Transformation from the state of ordered spins, to the paramagnetic state of disordered spins, occurs at the so called Curie point, a material specific temperature. The Curie temperature is therefore a measure of the strength of magnetic coupling. This coupling appears to be very weak in the case of the complex magnetic structure of iron-free hausmannite, resulting in a very low Curie temperature of 40-45 K. However, the coupling apparently becomes stronger in compounds where manganese is replaced by iron, as suggested by increasing Curie temperatures of ferrite compounds with simple Neel ordering, with diminishing manganese content. It is for example 858 K in magnetite (Table 3).

The same principle may apply to the iron-rich magnetic hausmannite with unknown magnetic order scheme. With an iron content of a few weight percent, stability of the ferrimagnetic state e.g. strong coupling of electron spins, may be accomplished and the Curie temperature increased from 40-45 K to 750 K, i.e. not far off from the Curie temperature of magnetite.

The Mn^{3+}-Fe^{3+} exchange apparently enforces the spin coupling and stabilizes the ferrimagnetic state (Fig. 8a). This stabilization could result from simplification of the magnetic ordering from Yafet-Kittel to Neel order or simply from stronger spin coupling between individual cation sites due to increase of the mean magnetic moment.

The magnetic hausmannite is distinctively different from ordinary hausmannite not only in its magnetic properties but also in its remarkably high iron content and its unit cell parameters. The iron content can be expressed in the parameter R = Mn/ (Mn+Fe). R reaches a maximum value of 0.89 in the magnetic hausmannite (12 wt % Fe_2O_3). This is considerably higher than R=0.93 (or 6.9 wt % Fe_2O_3) envisaged by Mason (1943); Van Hook and Keith (1958), Halba et al. (1973), and Osawa et al. (1992) as the room temperature stability limit for the solubility of iron in the hausmannite lattice in the system Mn_3O_4 - $MnFe_2O_4$. The composition reported for the magnetic hausmannite falls, according to all these studies, into the two phase region, the single phase 'magnetic hausmannite' should therefore be unstable.

However, the observed change of the unit cell parameters for magnetic hausmannite relative to non-magnetic hausmannite, may indicate a distinct change within the crystal structure due to the high iron content.

Unfortunately no other quantitative conclusion cannot be drawn as neutron diffraction data to determine the exact spin configuration and the distribution of iron and manganese between the different lattice sites, are not available at this stage. Work is in progress to obtain such information, however, it remains a major problem to obtain pure phases suitable for analysis.

UNIVERSITY OF JOHANNESBURG

Conclusions

Unusually magnetic hausmannite, that clings to a hand magnet, is present in hydrothermally altered sedimentary manganese ores of the Kalahari manganese deposit in South Africa. The magnetic hausmannite is very fine-grained and intergrown with coarse-grained, non-magnetic hausmannite in the manganese ores. The only impurities present in the magnetic hausmannite are small inclusions of hematite. The magnetic hausmannite is enriched in iron relative to non-magnetic hausmannite and occurs immediately adjacent to ferruginized fault zones in the manganese field.

The magnetic hausmannites have thermal blocking temperatures, approximating the Curie temperature, of about 750 K. This is in contrast to pure iron-free hausmannite with Curie temperatures of 40-45 K. The high blocking temperature appears to be related to the increased iron contents in the hausmannite. Exchange of manganese by iron in hausmannite may stabilize ferrimagnetic ordering in the crystal structure and increase the temperature at which transformation from the ferrimagnetic state to the paramagnetic state (the Curie temperature)

takes place. A similar effect is seen in other spinels with Neel ordering, where Curie temperature increases from 563 K in jacobsite to 858 K in magnetite.

Knowledge of the characteristics and the distribution of the magnetic hausmannite may in future be of value in geophysical exploration for high-grade ores in the Kalahari manganese field. In scientific sense recognition of the magnetic hausmannite phase indicates that there may be need for careful examination of the magnetic properties of hausmannite from other manganese deposits. In this connection it is interesting to note that Fan et al. (1993) describe an jacobsite-type phase with compositional and magnetic properties fairly similar to the magnetic hausmannite described here.

Acknowledgements

Special thanks to Joe Kirshvink (CALTECH) for supporting studies by one of us (N.J.B.) at his laboratory. Thanks also to Ina Penberthy (MINTEK) for performing the image processing on the SEM and to Faan Waanders (Potchefstroom University) for doing Mössbauer spectroscopy on the hausmannite. We are indebted to Hendrik Alberts (RAU) for constructive discussions about the magnetic properties of spinels.

References

Benoit, P.H. (1987). Adaption to microcomputer of the Appleman-Evans program for indexing and least-square refinement of powder-diffraction data for unit-cell dimension. Amer. Mineral., 72, 1018-1019.

Beukes, N.J. (1983). Palaeoenvironmental setting of iron formations in the depositional basin of the Transvaal Supergroup, South Africa. In: Iron formations, facts and problems (Trendall, A.F. and Morris, R.C., eds.). Elsevier, Amsterdam: 131-209.

Bonnet, A., Delapalme, A. and Tcheou, F. (1974). In: Proceedings of the International Conference on Magnetism, 5, 605.

Boucher, B., Buhl, R. and Perrin, M. (1970). Proprietes et structure magnetique de Mn_3O_4. J. Phys. Chem. Sol., 32,.2429-2437.

Butler, R.F. (1992). Palaeomagnetism. Blackwell, Cambridge, 319pp.

Fan, D., Hariya, Y., Li, J., Miura, H., and Ye, J. (1993). Study on strongly metamorphosed ferro-manganese oxide minerals in Wafangzi deposit, P.R. China. Ressource Geol., 17, 50-56.

Frenzel, G. (1980). The manganese ore minerals. In: The geology and geochemistry of manganese (Varentsov, I.M. and Grasselly, G., eds.). Schweizerbarth, Stuttgart, 1, 25-157.

Goodenough, J.B.(1966). Magnetism and the chemical bond. Interscience Publishers, New York, 393 pp.

Gutzmer, J. (1993). Hydrothermale Alteration von Manganerzen der Nchwaning Mine, Kalahari Manganerzfeld, Südafrika. M.Sc. thesis (unpubl.), TU Clausthal, Clausthal-Zellerfeld, 161 pp.

Gutzmer, J. and Beukes, N.J. (1993). Fault controlled hematitization and upgrading of manganese ores in the Kalahari manganese field, South Africa. In: Extended Abstracts16'th Colloquium of African Geology, (Maphalala, R. and Mabuza, M., eds.). Geological Survey and Mines Mbabane, Swaziland, 139-141.

Halba, P., Khilla, M.A. and Kripicka, S. (1973). On the miscibility gap of spinels $MnxFe_{3-x}O_{4+y}$. J. Phys. Chem. Sol., 34, 387-395.

Kasper, J.S. (1959). Magnetic structure of hausmannite, Mn_3O_4. Bull. Amer. Phys. Soc., Series 2, 4, 178.

Kleyenstüber, A.S.E. (1984). A regional mineralogical study of the manganese bearing Voelwater Subgroup in the Northern Cape Province. PhD thesis (unpubl.), RAU, Johannesburg, 328 pp.

Mason, B. (1943). Mineralogical aspects of the system $FeO-Fe_2O_3-MnO-Mn_2O_3$. Geol. Foren. Forhandl., Norway, 65, 95 - 180.

Matsubara, S., Kato, A. and Nagashima, K. (1979). Iwakiite, $Mn^{2+}(Fe^{3+}, Mn^{3+})_2O_4$, a new tetragonal spinelloid mineral from the Gozaisho mine, Fukushima Prefecture. Japan. Mineral. Jour. Japan, 9, 383.

National Bureau of Standards (1972). National Bureau of Standards Monograph, 25, 38.

Nel, C.J., Beukes, N.J. and De Villiers, J.P.R. (1986). The Mamatwan mine of the Kalahari manganese field. In: Mineral deposits of Southern Africa (Anhaeusser, C.R. and Maske, S., eds.), 1, 963-978.

Osawa, S., Kikuchi, T. and Hariya, Y. (1992). Phase equilibria in the system $MnFe_2O_4$ - Mn_3O_4. Mineral. Jour. Japan, 16, 28-39.

Olés, A., Kajzar, F., Kucab, M. and Sikora, W. (1976). Magnetic structures determined by neutron diffraction. Warzow, 727 pp.

Smit, J. and Wijn, H.P.J. (1959). Ferrites. Philips Technical Library, Almeloh, 369 pp.

Tanaka, T. (1974). Lattice constant and nonstoichiometry in Mn-Fe ferrites. Japan. Jour.Appl. Phys., 13, 1235-1237.

Van Hook, H.J. and Keith, M.L. (1958). The system Mn_3O_4 - Fe_3O_4. Amer. Mineral., 43, 69 -83.

Wickham, D.G. (1969). The chemical composition of spinels in the system Fe_3O_4-Mn_3O_4. Jour. inorg. nucl. Chem., 31, 313-320.

Yamazaki, T., Katsura, I. and Marumo, K. (1991). Origin of stable remanent magnetization of siliceous sediments in the central equatorial Pacific. Earth Planet. Sci. Lett., 105, 81-93.

UNIVERSITY OF JOHANNESBURG